Developing chemical tools to understand the lipid interactome and identify targets of lipid signalling

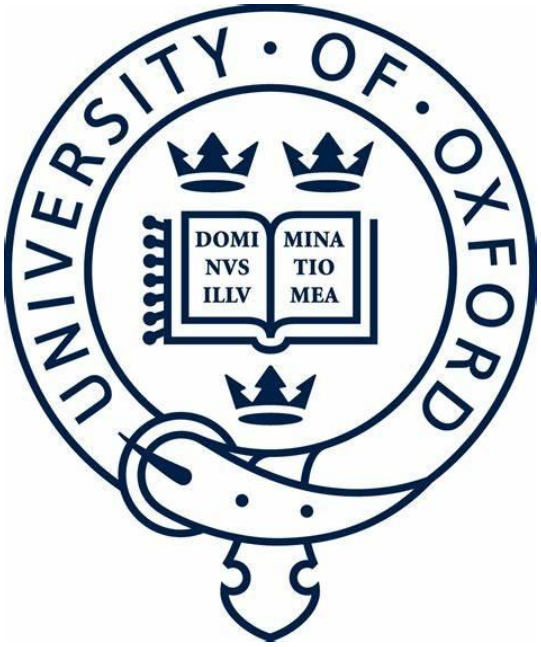

Ríona Devereux

St. Hugh's College

Chemistry in Cells Doctoral Training Programme

Department of Chemistry and Department of Physiology, Anatomy and Genetics

University of Oxford

This dissertation is submitted for the degree of Doctor of Philosophy

October 2024

Dedicated to my parents.

Declaration of authorship

The work presented in this thesis is my own, except where otherwise stated. No part of this thesis has been submitted for any other degree at this or any other university.

_____

Ríona Devereux

October 2024

Acknowledgements

I would like to begin by expressing my sincere gratitude to my funding body, the Wellcome Trust, whose support made this research possible. I am also deeply thankful to the Chemistry in Cells programme for providing the invaluable support and the opportunity to pursue my D.Phil. at Oxford. I would also like to say a huge thank you to the services and facilities teams in both departments, without whom I would not have been able to carry out my research.

I would like to especially thank Angie for sharing her extensive chemistry knowledge and for fostering such a positive and collaborative research culture within her group. To Lisa, thank you for helping me, as a chemist, to begin to understand and truly appreciate the world of metabolism. I'm also grateful for your excellent TV recommendations and our daily pop culture updates, which always brighten up my day. Finally, a heartfelt thank you to Josie for her support and invaluable expertise throughout my D.Phil.

A huge thanks goes to both my research groups in Oxford, without whom I wouldn't have made it through. To the AJR group over the years—too many to mention—thank you for all the much-needed coffee breaks (and many, many pints), for your constant support, and for putting up with me as I ran around the lab like a headless chicken. A special thank you to Carole, Pol, and Max for all their help over the years, and to Hannah, Adam, and Caroline for being such incredible friends. Congratulations and thank you to Dr. Pinqi Wang—it's hard to believe we've already finished! To the CMRG group, thank you all for welcoming a loud and crazy chemist into your world; I felt at home from day one. A special shoutout to Marcos, my 'Cell Yoda,' for teaching me the ways of cell culture—I'll definitely miss our days in the culture room. A big thank you to Eline for all her hard work in helping me with the validation steps and wishing her all the best with her PhD. Thanks to Ryan and Aaron for always answering my many bioinformatics questions and to Claudia, Kaitie, and Steph for their help, support, friendship, and our cocktail trips. Lastly, thank you to Tom for always being there when I needed him and for being as addicted to coffee as I am. A massive thank you to Jack for all his computational wisdom and for always being such a big fan of my project! Sarah and Iolanda, thank you both so much for all your help with the proteomics, I have learned so much.

I want to thank all my friends in Oxford, from work, college, and spontaneous encounters, for making this journey memorable. Special thanks to Claire and Nick for the countless coffee dates and pub nights and for always asking about the cells – you guys were my family away from home! To Matt, Alex, Sam, and Dom, thank you for always being up for a drink, a laugh and a boogie, and for adding so much fun to the Oxford experience. Thank you to Katie, for being a fantastic housemate and always being up for watching reality TV with a glass of wine at the end of a long day. A heartfelt thank you to my friends from home, Meghan and Róisín, whom I met at school and who have always been there for me, no matter what.

Big thank you to all the team at Horsebox, my go-to coffee spot, for keeping me both caffeinated and sane (almost) every day.

I am deeply grateful to my family for their unwavering support. To my dad, who was my first inspiration as a chemist - his incredible career and constant encouragement have been invaluable, and I can't thank him enough. To my mum, who patiently sat with me for hours helping with schoolwork, especially maths and science, and who now is always just a phone call away (thank you also for keeping me well-fed during the past few months!). Finally, to my sister Maeve and my brother Conor, thank you for always keeping me humble and for being ready to grab a pint and chat whenever I needed it.

I would like to express my deepest gratitude to my boyfriend, Andrew, for his unwavering support and love throughout my journey to Oxford to pursue my D.Phil. Thank you for standing by me at every step, being my constant voice of reason, and for your endless encouragement through all the challenges. I couldn’t have done it without you.

I would like to sincerely thank Ms. Carroll, my chemistry schoolteacher, for inspiring me to pursue a career in chemistry. Your passion for the subject and commitment to ensuring I never forgot the ‘basics’ have been invaluable to my journey. I would also like to extend my heartfelt thanks to my first supervisor, Prof. Isabel Rozas at Trinity College Dublin, for pushing me to be the best I could be and for all her invaluable support in helping me get to where I am today.

Abstract

Lipids are essential molecules that play critical roles in cellular function, serving as key components of cell membranes, sources of energy, and signalling molecules that regulate various metabolic and biological processes. In the Western diet, the intake of lipids, particularly saturated fatty acids, has increased significantly, often contributing to metabolic disorders such as obesity, diabetes, and cardiovascular diseases. Despite their well-established roles in metabolism, we still have an incomplete understanding of how these fatty acids interact with cellular proteins and signalling pathways. The consequences of these interactions, especially in excess, remain unclear, underscoring the need for deeper exploration into how fatty acids impact cellular function and contribute to health and disease outcomes. Chemical probe techniques offer a powerful approach to address this knowledge gap, enabling the investigation of how fatty acids interact with specific biomolecules and pathways.

This work began with the design and synthesis of several fatty acid chemical probes, based on both photoaffinity and photocatalytic labelling techniques. Two palmitic acid probes were synthesised: a photoaffinity probe, produced in five steps, and a photocatalytic probe, synthesised in eleven steps. Building on the palmitic acid photoaffinity probe, two additional palmitic acid metabolite probes were developed: palmitoyl-CoA and palmitoyl-carnitine photoaffinity probes, both one step from the palmitic acid photoaffinity probe. These probes were all shown to be activated under suitable conditions (UV or blue light) using mass spectrometry. Two oleic acid probes were designed, and their synthesis was initiated: a photoaffinity oleic acid probe, which reached the penultimate step, and a photocatalytic oleic acid probe, two steps from completion. However, challenges in synthesising the *Z*-alkene hindered the finalisation of both probes.

This thesis then utilised the photoaffinity palmitic acid probe *in vitro* to investigate its interactions, in two biological contexts: cancer and the heart. The probe interacted with expected pathways, such as metabolism, protein localisation, trafficking, and signalling pathways (including PPARs and mTOR), confirming its role in fundamental cellular processes. Additionally, novel pathways were uncovered by the probe, including chromatin organisation, RNA metabolism, and cytoskeletal

regulation, which are not typically associated with fatty acid metabolism. These findings suggest that palmitic acid may influence post-transcriptional gene regulation, chromatin structure, and cellular architecture, indicating a more complex role in cellular function. Additionally, the probe's interaction with signalling pathways such as TGFβ, VEGF, Rho, and Rac highlight its involvement in processes related to cell growth, differentiation, migration, and angiogenesis. Furthermore, its effect on sex hormone signalling suggests potential regulatory roles in hormonal pathways, which could have implications for diseases such as cancer and cardiovascular conditions.

Lastly, this thesis explored the use of a novel photocatalytic palmitic acid probe in *MDA-MB-231* cells. The findings from this probe heavily overlapped with those from the photoaffinity probe, with the exception of an increased number of nuclear pathways crucial for maintaining the structural and functional integrity of the nucleus, which were enriched by the photocatalytic probe. These findings may be genuine palmitic acid targets, or they may be non-specific binding due to the bulky photocatalyst of the probe and contributing towards the increased cell toxicity compared with the photoaffinity probe. One important thing to consider when designing chemical probes is to ensure the native structure is minimally perturbed. *In silico* alignment demonstrated that the photoaffinity palmitic acid and palmitoyl-carnitine probe were structurally similar to their parent fatty acids, but that the photoaffinity palmitoyl-CoA and photocatalytic palmitic acid probe deviated somewhat, potentially due to the diazirine or bulky photocatalyst, respectively.

In conclusion, this work reveals that palmitic acid has broad and complex effects on key cellular processes, influencing metabolism, cytoskeletal dynamics, and signalling pathways in both cancer cells and cardiomyocytes. These palmitic acid probes were shown to shift metabolism, modulate hormone signalling, and regulate cytoskeletal organization, affecting cell proliferation, migration, and contractility. Unexpectedly, they also interacted with proteins involved in RNA metabolism, nuclear organisation, and chromatin regulation, suggesting that fatty acids play a more extensive role in gene regulation and cellular architecture than previously understood. These findings provide new insights into how lipid signalling integrates with essential cellular functions and highlight potential pathways that could be targeted in diseases like cancer and heart disease.

Table of Contents

Declaration ..... **i**

Acknowledgements ..... **ii**

Abstract ..... **iv**

Table of contents ..... **vi**

Abbreviations and Symbols ..... **xi**

1. General Introduction **1**

1.1 *Lipids* 2

1.2 *Lipid Functions in Cellular Biology* 4

1.3 *Lipids in Disease* 10

1.4 *Types of Fatty Acid Interactions* 15

1.5 *Methods for Profiling Lipid-Protein Interactions In Vitro* 17

1.6 *Thesis Aims* 24

2. Materials & Methods **25**

2.1 *In Vitro Labelling with Photoaffinity Fatty Acid Probes* 26

2.2 *Metabolite Measurements in Cell Media* 29

2.3 *Mitochondrial Network Staining* 30

2.4 *Proteomic Analysis of Fatty Acid Probes* 30

2.5 Western Blotting 32

2.6 Transcriptomic Analysis 33

2.7 Gene Expression Analysis Using Quantitative PCR (qPCR) 35

2.8 Statistical Analysis 36

3. Design and Synthesis of Fatty Acid Probes for Target ID Experiments **37**

3.1 *Abstract* 38

3.2 *Introduction* 39

3.3 *Chapter Aims* 41

3.5 *Results* 42

3.5.1 *Synthesis of Palmitic Acid Photoaffinity Probe **1*** 42

3.5.2 *Synthesis of Palmitoyl-CoA Photoaffinity Probe **2*** 48

3.5.3 *Synthesis of Palmitoyl Carnitine Photoaffinity Probe **3*** 49

3.5.4 *Synthesis of Palmitic Acid Photocatalytic Probe **4*** 50

3.5.5 *Attempted Synthesis of Oleic Acid Photoaffinity Probe **5*** 56

3.5.6 *Attempted Synthesis of Oleic Acid Photocatalytic Probe **6*** 58

3.6 *Discussion & Conclusion* 60

4. Development and Optimisation of the Photoaffinity Palmitate Probe 1 Workflow in *MDA-MB-231* cells **62**

4.1 *Abstract* 63

4.2 *Introduction* 64

4.3 *Chapter Aims* 65

4.4 *Methods* 66

3.4.1 *Lipid Droplet Staining* 66

3.4.2 *Mitochondrial Isolation and Respiration* 66

4.5 *Results* 68

4.5.1 *Probe **1** was an Effective Reagent in the CuAAC Reaction* 68

4.5.2 *Concentration-Dependent Covalent Incorporation of Probe **1** In Vitro* 69

4.5.3 *Non-covalent Incorporation of Probe **1** In Vitro Following UV Irradiation* 71

4.5.4 *Probe **1** Interactions Mimicking Endogenous Palmitate Interactions* 72

4.5.5 *Cellular Uptake of Probe 1 was Confirmed by Confocal Microscopy* 73

4.5.6 *Probe **1** was not Cytotoxic at 30 μM Labelling Concentration* 74

4.5.7 *Probe **1** was not Causing Mitochondrial Fragmentation* 76

4.5.8 *Probe **1** Increases Lipid Droplet Number in Cells* 77

4.5.9 *Mitochondria do not Fully Oxidise Probe **1*** 78

4.5.10 *Nuclear Integrity Following UV Irradiation* 82

4.5.11 *Neutravidin-Biotin Pulldown Optimisation* 84

4.6 *Discussion* 86

5. Identification of Palmitic Acid Targets in *MDA-MB-231* cells Using Photoaffinity Palmitate Probe 1 ..... **88**

5.1 *Abstract* 89

5.2 *Introduction* 90

5.3 *Chapter Aims* 91

5.4 *Methods* 92

5.4.1 *Colocalisation of Probe **1** with Mitochondrially-Encoded Cytochrome C Oxidase II (MT-CO2)* 92

5.4.2 *F-Actin Staining* 92

5.4.3 *Measuring Probe **1** Colocalisation with Lipid Droplets* 92
5.4.4 *Assessing Cell Metabolism Using Radiolabelled Compounds* 93
(a) *Measuring Glycolysis* 93
(b) *Measuring Fatty Acid Oxidation* 94
5.5 *Results* 95
5.5.1 *Proteomic Analysis in MDA-MB-231 Cells* 95
5.5.1.1 *Proteomic Analysis in MDA-MB-231 Cells Treated with 30 µM Probe **1** (no UV)* 96
5.5.1.2 *Proteomic Analysis in MDA-MB-231 Cells Treated with 30 µM Probe **1** (with UV)* 99
5.5.2 *Validation of Probe **1** Protein Targets in MDA-MB-231 Cells* 102
5.5.3 *Transcriptomic Analysis of Probe **1**-Treated MDA-MB-231 Cells* 106
5.5.4 *Validation of Transcriptomic Targets of Probe **1** in MDA-MB-231 Cells* 116
5.5.5 *Comparison of Proteomic and Transcriptomic Analyses of Probe **1** in MDA-MB-231 Cells* 121
5.6 *Discussion* 123

6. Target Identification in hiPSC Cardiomyocytes Using Photoaffinity Probe 1 ..... **127**
6.1 *Abstract* 128
6.2 *Introduction* 129
6.3 *Chapter Aims* 130
6.4 *Methods* 131
6.4.1 *Cell Culture of Human-Induced Pluripotent Stem Cell-Derived Cardiomyocytes (hiPSC-CMs)* 131
6.5 *Results* 132
6.5.1 *Labelling of hiPSC-CMs with Probe **1*** 132
6.5.2 *Cell Viability of hiPSC-CMs Following Probe **1** Treatment* 134
6.5.3 *Proteomic analysis of hiPSC-CMs treated with probe **1*** 135
6.5.3.1 *Proteins Interactors of 30 µM Probe **1** (with UV)* 138
6.5.3.2 *Proteins Interactors of 100 µM Probe **1** (no UV)* 142
6.5.3.3 *Proteins Interactors of 100 µM Probe **1** (with UV)* 145
6.5.4 *Validation of Identified Targets from Proteomic Analysis* 150
6.5.4.1 *Validation of Protein Interactors of Probe **1*** 150
6.5.4.2 *Effects of Probe **1** on Mitochondrial Networks in hiPSC-CMs* 153

6.5.6.3 *Effects of Probe **1** on OXPHOS Protein Levels* 154

6.5.5 *Transcriptomics Captures Changes in Gene Expression Induced by Probe 1 or Palmitate Treatment* 155

6.5.6 *Transcriptomic Analysis of Probe **1** Treatment* 156

6.5.6.1 *Analysis of Upregulated Genes Following Probe **1** Treatment* 157

6.5.6.2 *Analysis of Downregulated Genes Following Probe **1** Treatment* 161

6.5.6.3 *Gene Set Enrichment Analysis Following Probe **1** Treatment* 166

6.5.7 *Transcriptomic Analysis of Palmitic Acid Treatment* 168

6.5.7.1 *Analysis of Upregulated Genes Following Palmitic Acid Treatment* 169

6.5.7.2 *Analysis of Downregulated Genes Following Palmitic Acid Treatment* 172

6.5.7.3 *Gene Set Enrichment Analysis Following Palmitic Acid Treatment* 176

6.5.8 *Comparison of the Pathway Changes Following Probe **1** or Palmitic Acid Treatment* 178

6.5.8.1 *Analysis of Upregulated Pathways* 178

6.5.8.2 *Analysis of Downregulated Pathways* 179

6.5.9 *Validation of Transcriptomic Changes in hiPSC-CMs* 181

6.6 *Discussion* 183

7. Optimisation and Development of Further Palmitate and Palmitate Metabolite Probes **188**

7.1 *Abstract* 189

7.2 *Introduction* 190

7.3 *Chapter Aims* 193

7.4 *Methods* 194

7.4.1 *Chemical Synthesis* 194

7.4.2 *Metabolic Incorporation of Probe **4** into MDA-MB-231 Cells* 194

7.4.3 *Live Cell Imaging of Blue Light-Sensitive Probe **4** Using Fluorescence Microscopy* 194

7.4.4 *Ab Initio Computational Methods for Structural Behaviour Analysis of Probes **1** and **3** and Parent Molecules* 194

7.4.5 *Energy Minimisation of Small Molecules Using Molecular Operation Environment (MOE) and Structural Alignment via PyMOL for Comparative Analysis of Probes **1-4** and Parent Molecules* 195

7.5 *Results* 197

7.5.1 *Cell Viability of MDA-MB-231 Cells with Photocatalytic Probe **4*** 197

7.5.2 *Protein Labelling of MDA-MB-231 Cells with Probe **4*** 198

7.5.3 *Proteomic Analysis of MDA-MB-231 Cells Treated with Probe **4*** 199

7.5.4 *Comparison of the Proteins and Pathways Enriched by Probe **4** with Probe **1*** 208

7.5.5 *Computational Methods to Analyse Probe Structures* 213

7.6 *Discussion* 218

8. General Discussion **221**

8.1 *General Discussion* 221

8.2 *Research Limitations* 224

8.3 *Future Work* 225

8.4 *Conclusion* 227

9. Chemistry Experimental **229**

Bibliography **264**

Appendix **283**

Abbreviations and symbols

°C	degree Celsius
µm	Micrometre
µM	Micromolar
Å	Angstrom, 10^{-10} metres
acac	Acetylacetone
ACSL	Acyl-CoA synthetase
ADP	Adenine diphosphate
aq.	Aqueous
ATP	Adenine triphosphate
BSA	Bovine Serum Albumin
CD36	Fatty acid translocase
CDI	Carbonyldiimidazole
CoA	Coenzyme A
CPTI	Carnitine palmitoyl-transferase I
CPTII	Carnitine palmitoyl-transferase II
CuAAC	Copper(I)-catalysed azide-alkyne cycloaddition
DAG	Diacylglycerol
DAPI	4′,6-Diamidino-2-phenylindole dihydrochloride
dH_2O	Deionised water
DIPEA	*N*,*N*-Diisopropylethylamine
DMF	Dimethylformamide
DMPU	*N,N*′-Dimethylpropyleneurea
DMSO	Dimethylsulfoxide
DPBS	Dulbecco's phosphate buffered saline
dppf	1,1'-Bis(diphenylphosphino)ferrocene

DTT	Dithiothreitol
EDC	1-Ethyl-3-(3-dimethylaminopropyl)carbodiimide
EDTA	Ethylenediaminetetraacetic acid
EGTA	Ethylene glycol-bis(2-aminoethylether)-*N,N,N′,N′*-tetraacetic acid
eq.	Equivalents
ETC	Electron transport chain
FA	Fatty acid
FAD	Oxidised flavin adenine dinucleotide
$FADH_2$	Reduced flavin adenine dinucleotide
FAO	Fatty acid oxidation
FFA	Free fatty acid
g	Gram
h	Hour(s)
HATU	Hexafluorophosphate azabenzotriazole tetramethyl uronium
HDL	High-density lipoprotein
HEPES	4-(2-Hydroxyethyl)piperazine-1-ethanesulfonic acid
HEPES	4-(2-hydroxyethyl)-1-piperazineethanesulfonic acid
HOSA	Hydroxylamine-*O*-sulfonic acid
HRMS	High resolution mass spectrometry
IFM	Interfibrillar mitochondria
LCFA	Long chain fatty acid
LCMS	Liquid chromatography–mass spectrometry
LC-MS/MS	Liquid chromatography–tandem mass spectrometry
LDH	Lactate dehydrogenase
LDS	Lithium dodecyl sulphate
LiHMDS	Lithium bis(trimethylsilyl)amide
LRMS	Low resolution mass spectrometry

M	Molar
m/z	Mass-to-charge ratio
MCFA	Medium chain fatty acid
min	Minute(s)
mM	Millimolar
MUFA	Monounsaturated fatty acid
NADH	Nicotinamide adenine dinucleotide
NADPH	Reduced nicotinamide adenine dinucleotide phosphate
nm	Nanometre
nM	Nanomolar
NMR	Nuclear magnetic resonance
OXPHOS	Oxidative phosphorylation
PAL	Photoaffinity labelling
PCC	Pyridinium chlorochromate
PFA	Paraformaldehyde
PUFA	Polyunsaturated fatty acid
ROS	Reactive oxygen species
rpm	Revolutions per minute
RT	Room temperature
SCFA	Short chain fatty acid
SDS	Sodium dodecyl sulphate
SFA	Saturated fatty acid
SSM	Subsarcolemmal mitochondria
TAG	Triacylglyceride
TAMRA	5-Carboxytetramethylrhodamine
TBAF	Tetra-*n*-butylammonium fluoride
TBTA	Tris[(1-benzyl-1*H*-1,2,3-triazol-4-yl)methyl]amine

TCA	Tricarboxylic acid cycle
TCEP	Tris(2-carboxyethyl)phosphine
TFA	Trifluoroacetic acid
THF	Tetrahydrofuran
TNBC	Triple negative breast cancer
UV	Ultraviolet

Chapter 1

Introduction

1.1 Lipids

Lipids play essential roles in both cellular physiology and pathology. They are the structural components of cell membranes, without which cells and life itself would not exist. In addition, lipids serve as energy stores, sources of signalling molecules and platforms for protein recruitment and are also involved in the generation of bioactive metabolites.[1]

1.1.1 Lipid Classification

Lipids are a structurally diverse group of molecules and can be either hydrophobic or amphiphilic. Most lipids consist of long hydrocarbon chains or rings, making them nonpolar and insoluble in water, yet soluble in organic solvents. Lipids can be classified into different subtypes, and these include fatty acids (FAs), glycerides, phospho-glycerides, steroids, sphingolipids and waxes, each serving unique roles in biological systems (Figure 1.1).[2]

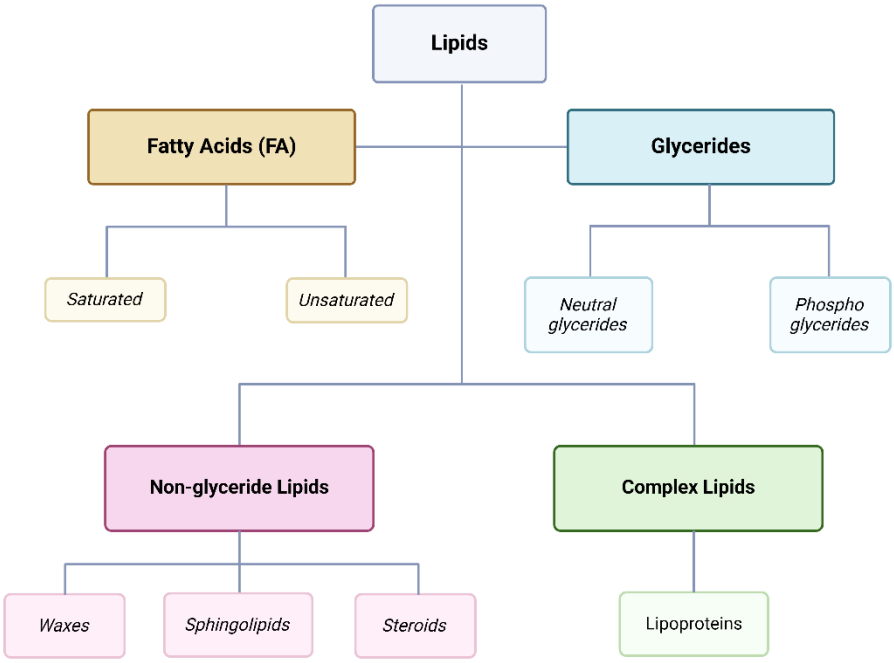

1.1.2 Fatty acids (FAs)

FAs are, structurally, the simplest form of lipids, with long hydrocarbon chains and a polar carboxyl head-group (-COOH) at one end. Based on the length of the hydrocarbon chain, FAs can be divided into 3 classes: short-chain FAs (SCFA), with aliphatic tails of less than 6 carbons; medium-chain FAs (MCFA), which have aliphatic tails of 6-12 carbons; and long-chain FAs (LCFA), having

aliphatic tails with greater than 12 carbons.[3,4] FAs can also be classified based on their degree of saturation, as a saturated FA (SFA), containing no double bonds, or unsaturated FAs, containing one (monounsaturated FA – MUFA) or more (polyunsaturated FA – PUFA) double bonds. FAs are important components of lipids, such as triglycerides (TAGs), phospholipids, cholesteryl esters, and plant sterols, which mainly contribute to energy storage and metabolism, cell membrane stability and the modulation of various cell processes.[5,6]

Some of the most abundant FAs in the Western diet are palmitic and oleic acid, both of which can be metabolised to generate large amounts of ATP. Palmitic acid (C16:0) is a saturated FA and therefore, contains no double bonds between the carbon atoms in its 16-carbon chain (Figure 1.2). Palmitic acid is usually found in animal fats and some plant oils and can be synthesised by the human body during de novo lipogenesis. It plays a role in energy storage, but is also an essential component of several lipids, including phospholipids and triglycerides, which make up cell membranes.[7,8] Palmitic acid has been implicated in lipotoxicity - where excessive levels of saturated FAs can cause damage to cells, particularly in the liver, pancreas and heart.[9–11] Oleic acid (C18:1) is a monounsaturated fatty acid with 18 carbon atoms and a single double bond between the 9th and 10th carbons (Figure 1.2). Oleic acid is primarily found in plant-based oils and is more prominent in the Mediterranean diet, which has been associated with numerous health benefits due to its higher intake of unsaturated fats.[12,13] Oleic acid is involved in various biological processes that regulate metabolism, cellular signalling, and inflammation.[14]

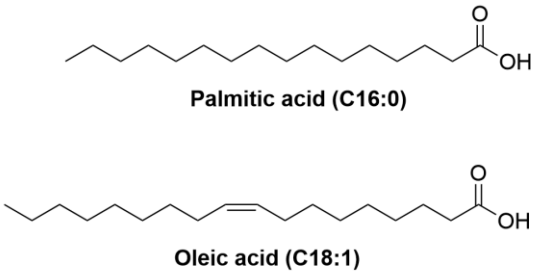

Figure 1.2: Chemical structures of palmitic and oleic acid

1.2 Lipid Functions in Cellular Biology

1.2.1 Membranes

Lipids provide the structural integrity of the cell membrane, and phospholipids are their primary structural components.[15–17] These lipid bilayers form spontaneously due to the hydrophobic effect, where nonpolar lipid tails aggregate to minimise contact with water, thus reducing the system's free energy, and polar head groups face outward, towards the aqueous environment.[18] This structure creates a semi-permeable barrier that controls the movement of substances into and out of the cell. Cholesterol, another lipid, is embedded within this phospholipid bilayer. It helps regulate membrane fluidity, preventing the membrane from changing during temperature fluctuations.[19–21] It also plays a role in changing the thickness, water penetration, compressibility and curvature of lipid bilayers. Cholesterol is also involved in the formation of lipid rafts, specialised membrane microdomains that help in the organisation and function of signalling molecules.[21] Lipids, especially phospholipids (e.g. phosphatidylserine), are essential for fusion events that occur in the membrane.[22,23] When vesicles transport proteins and other molecules within the cell, lipids play a role in the fusion of these vesicles with target membranes. This allows for the appropriate distribution and secretion of cellular materials.

1.2.2 Energy generation

Lipids play a significant role in metabolic regulation, e.g. FAs can be used as substrates for energy production when glucose levels decrease, causing a shift from carbohydrate to fat metabolism in the body.[24,25] FA metabolism is a critical biochemical process by which FAs are broken down to generate energy, particularly during periods of fasting, exercise, or low carbohydrate availability. This process mainly involves β-oxidation, the tricarboxylic acid (TCA) cycle, and oxidative phosphorylation (OXPHOS), which work together to convert FAs into adenosine triphosphate (ATP), the energy currency of the cell.

1.2.2.1 FA uptake across the cell membrane and into the mitochondria

The most commonly used FA for β-oxidation by cells is palmitic acid. Once palmitic acid reaches target tissues, it enters cells via FA transporters (e.g. CD36) before being "activated" in the cytosol by acyl-CoA synthetase (ACSL), which attaches coenzyme A (CoA) to palmitic acid to form palmitoyl-CoA. Long-chain fatty acyl-CoA molecules cannot freely cross the mitochondrial inner membrane. Therefore, they must be transported by the carnitine shuttle system (Figure 1.3).[26] Carnitine palmitoyltransferase I (CPT I) on the outer mitochondrial membrane converts palmitoyl-CoA into palmitoyl-carnitine by transferring the acyl group to carnitine.[27] Palmitoyl-carnitine is then transported across the mitochondrial inner membrane by a translocase protein. Carnitine palmitoyltransferase II (CPT II), located on the inner mitochondrial membrane, reconverts palmitoyl-carnitine back into palmitoyl-CoA and releases free carnitine, which returns to the cytosol.[26,28] This makes palmitoyl-CoA and palmitoyl-carnitine (Figure 1.4) critical intermediates in FA metabolism, particularly in the processes of energy production within cells.

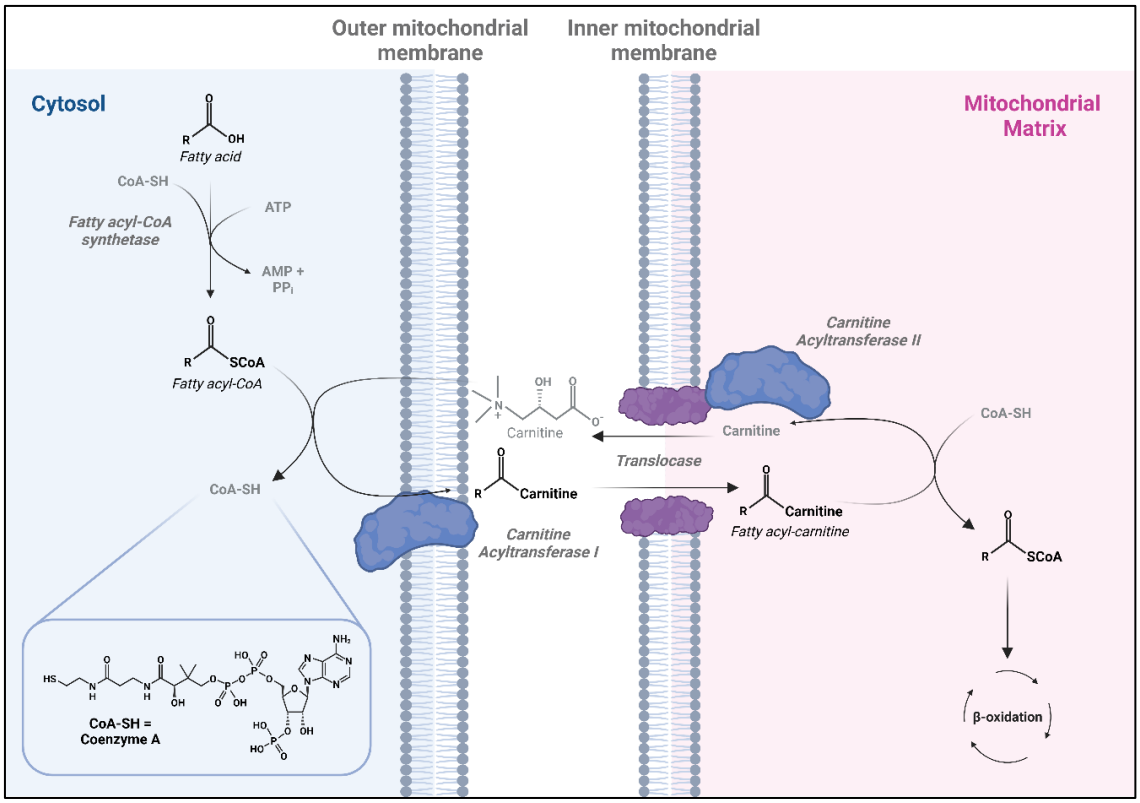

Figure 1.3: Carnitine shuttle system transports FAs into the mitochondria. Import of FAs into the inner mitochondrial membrane occurs following the conversion of the fatty acyl-CoA into a fatty acyl-carnitine by carnitine acyltransferase I (CPT1), located in the outer mitochondrial membrane. The carnitine translocase acts as an anti-porter, exchanging fatty acyl-carnitines for carnitines, thus transporting the fatty acyl-carnitine into the mitochondria. The fatty acyl-carnitine is then converted back to the fatty acyl-CoA by carnitine acyltransferase II (CPT2). The fatty acyl-CoA can then go on for oxidation.[26,28]

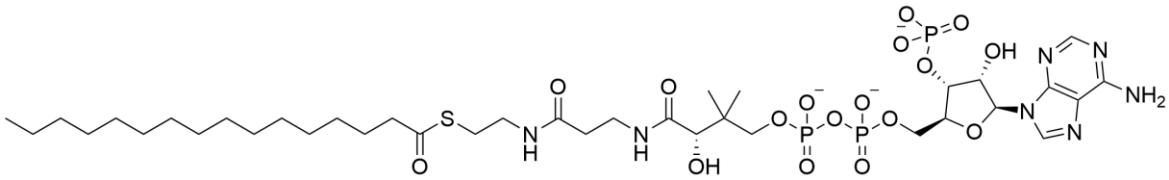

Palmitoyl-CoA

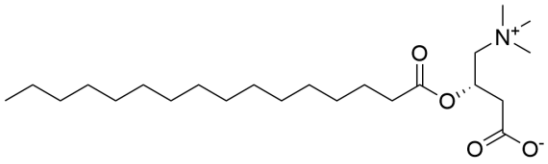

Palmitoyl-carnitine

Figure 1.4: Chemical structures of the palmitic acid metabolites: palmitoyl-CoA and palmitoyl-carnitine.

1.2.2.2 β-oxidation of FAs

Mitochondrial β-oxidation involves a repetitive four-step cycle, which progressively shortens the FA chain by two carbon atoms in each round, ultimately producing acetyl-CoA and ATP (Figure 1.5c). After β-oxidation, the generated acetyl-CoA molecules enter the TCA cycle, which occurs in the mitochondrial matrix (Figure 1.5d).[29,30] The primary function of the TCA cycle is to further oxidise acetyl-CoA to CO_2 through a number of enzymatic steps while capturing high-energy electrons in the form of NADH and $FADH_2$, which feed in the electron transport chain (ETC) to generate ATP. OXPHOS is the final stage of FA metabolism, where the NADH and $FADH_2$ produced from both β-oxidation and the TCA cycle are used to generate ATP (Figure 1.5e).[31–33] This process occurs in the inner mitochondrial membrane and involves the ETC and ATP synthase. NADH and $FADH_2$ donate high-energy electrons to the ETC, where the energy from electron transfer is used to pump protons (H^+) across the mitochondrial inner membrane, creating an electrochemical gradient (proton gradient). The accumulated protons in the intermembrane space flow back into the mitochondrial matrix through ATP synthase (Complex V). This flow of protons, called chemiosmosis, drives the production of ATP from ADP and inorganic phosphate (P_i).

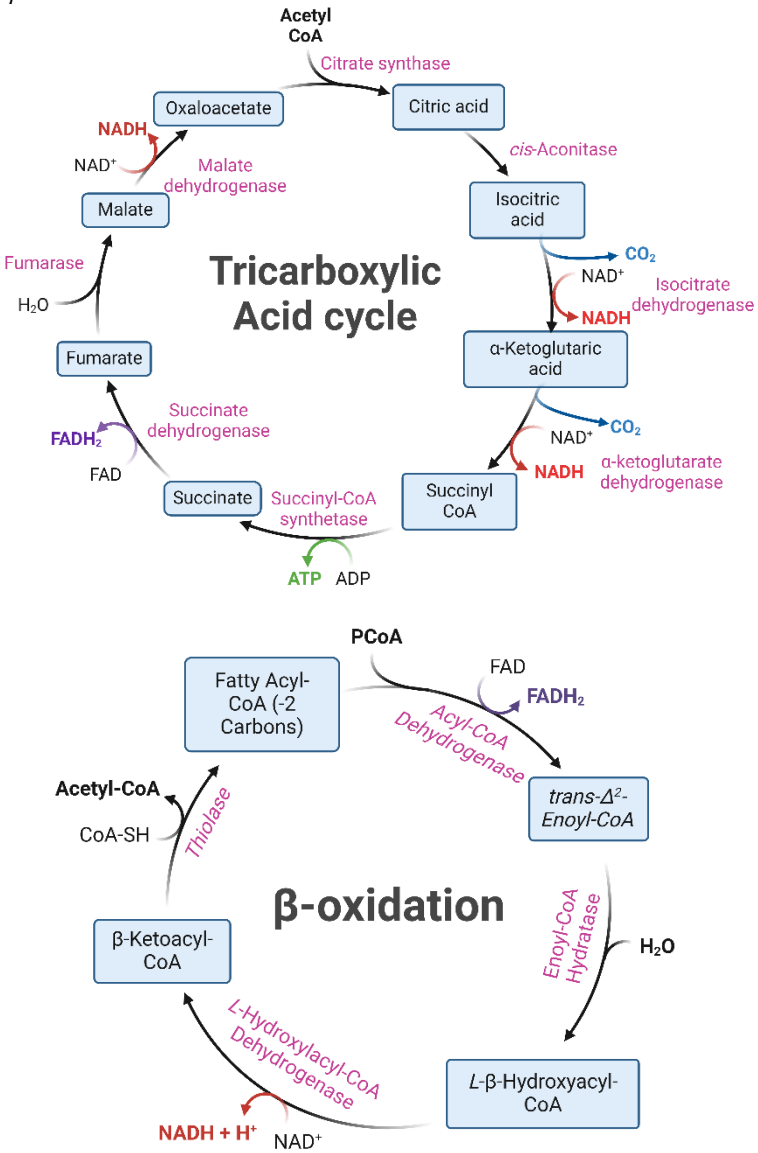

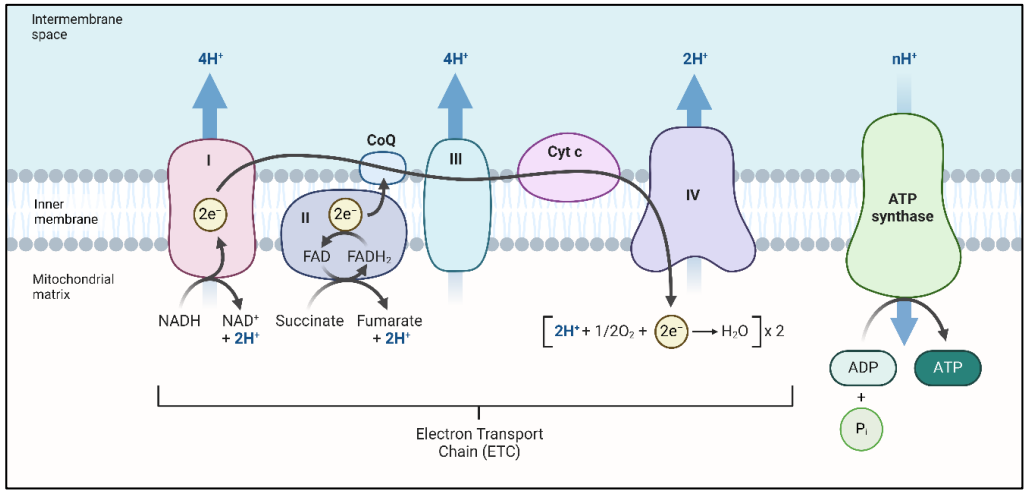

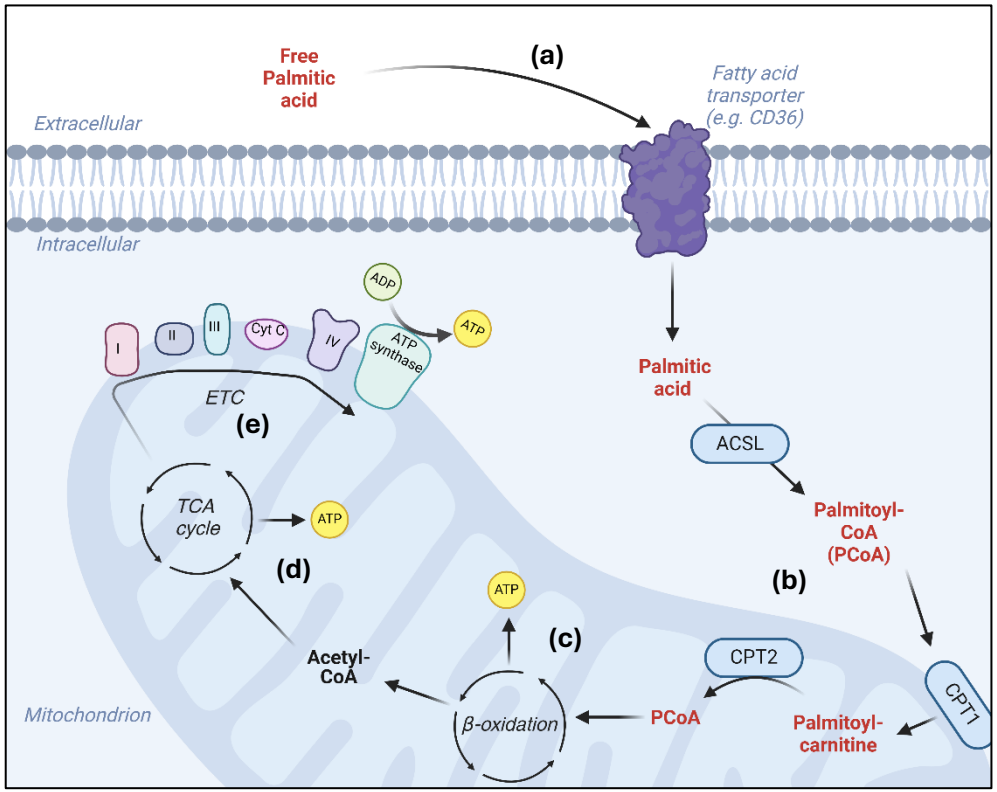

Figure 1.5: Legend on next page.

Figure 1.5 (contd.): Overview of fatty acid metabolism. (a) Palmitic acid is transported into the cells through fatty acid transporters (e.g. CD36); (b) Palmitic acid is activated and transported into the mitochondria through the carnitine shuttle system; (c) The first step of β-oxidation is the oxidation of the fatty acyl-CoA by acyl-CoA dehydrogenase, forming a double bond between the alpha and beta carbon atoms, which results in the production of trans-enoyl-CoA (Figure 1.6).[27,34,35] This reaction generates $FADH_2$, which enters the electron transport chain (ETC). The enzyme enoyl-CoA hydratase adds water across the double bond, converting trans-enoyl-CoA into 3-hydroxyacyl-CoA. 3-hydroxyacyl-CoA is oxidized by 3-hydroxyacyl-CoA dehydrogenase, producing 3-ketoacyl-CoA and generating NADH, which also enters the ETC. Finally, thiolase cleaves 3-ketoacyl-CoA by adding another molecule of CoA, producing acetyl-CoA (which enters the citric acid cycle) and a fatty acyl-CoA that is two carbons shorter. This shortened fatty acyl-CoA re-enters the β-oxidation cycle, and the process repeats until the entire FA chain is converted into acetyl-CoA units.(d) The TCA cycle, also known as the citric acid cycle or Krebs cycle, occurs in the mitochondrial matrix. Acetyl-CoA enters the cycle and combines with oxaloacetate to form citric acid. Through a series of reactions, citric acid is converted back to oxaloacetate, releasing energy-rich molecules including NADH, $FADH_2$, ATP, and CO_2. Key steps include the production of NADH at the isocitrate to α-ketoglutarate and α-ketoglutarate to succinyl-CoA steps, the production of $FADH_2$ from succinate to fumarate, and ATP generation from succinyl-CoA to succinate. These high-energy electron carriers, NADH and $FADH_2$.[29,30] Oxidative phosphorylation (OXPHOS) occurring in the inner mitochondrial membrane, throguh the electron transport chain (ETC) and ATP synthesis. Electrons ($2e^-$) from NADH and $FADH_2$ are transferred through a series of protein complexes (I-IV) and mobile carriers (CoQ and Cyt c), driving the pumping of protons (H^+) across the inner membrane into the intermembrane space. This creates a proton gradient that powers ATP synthesis via ATP synthase, which allows protons to flow back into the mitochondrial matrix, producing ATP from ADP and inorganic phosphate (P_i). Oxygen (O_2) is the final electron acceptor at Complex IV, combining with protons to form water (H_2O).[31–33]

1.2.3 Energy storage of lipids

Lipids can form dense and efficient energy stores in the form of lipid droplets which are organelles that regulate the storage and hydrolysis of neutral lipids and are found largely in the adipose tissue. TAGs are the major lipid form for storage of FAs within cells and in the plasma.[36] They consist of a polar glycerol head, covalently bonded to three FA tails (Figure 1.6). TAGs are stored in cells in lipid droplets, and they provide a long-term energy reserve that the body can break down into FAs during periods of fasting or extended physical activity and these FAs can go on to be used for ATP production through β-oxidation (Figure 1.7).

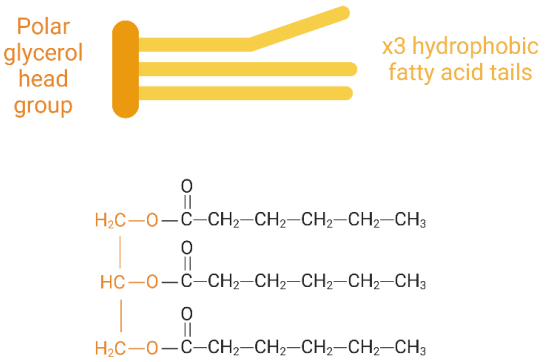

Figure 1.6: Structure of a Triglyceride (TAG): The molecular structure of a TAG consists of a polar glycerol head group bonded to three hydrophobic FA tails through ester linkages.

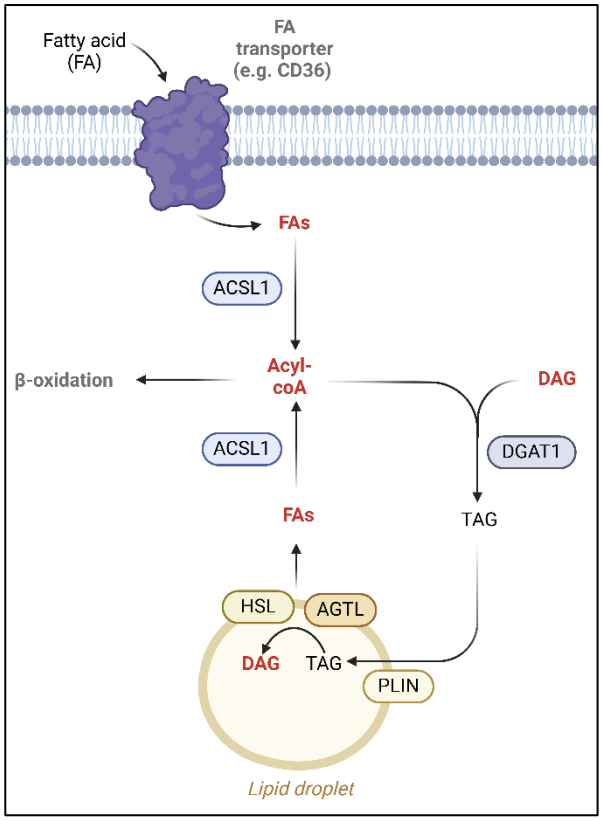

Figure 1.7: Lipid storage in lipid droplets. Fatty acids (FAs) are transported into the cell by a FA transporter (e.g. CD36) and converted into the FA acyl-CoA by acyl-CoA synthetase (ACSL). The acyl-CoA can then react with a diacylglycerol (DAG) catalysed by diacylglycerol *O*-acyltransferase 1 (DGAT1) to form a triacylglycerol (TAG). TAGs can then be transported into lipid droplets by perilipin (PLIN) where they are stored. When energy is needed, stored TAGs can be broken down. This begins with the activation of adipose triglyceride lipase (AGTL) and hormone-sensitive lipase (HSL), which hydrolyse TAG into DAG and release free fatty acids (FAs).

1.2.4 Signalling and hormones

Lipids are also involved in cell signalling, both as direct signalling molecules and as precursors to other signalling compounds. FAs are ligands for nuclear transcription factors and can thereby regulate gene transcription. FAs act as ligands for peroxisome proliferator-activated receptors (PPARs), particularly PPARα, which is highly expressed in cardiac tissue.[37,38] Activation of PPARα by FAs upregulates the expression of genes involved in FA uptake (e.g., CD36) and β-oxidation (e.g., CPT1).[39] Additionally, PPARα signalling modulates mitochondrial biogenesis and reactive oxygen species (ROS) management, both of which are crucial for maintaining mitochondrial integrity and preventing oxidative stress, which can impair heart function.[40]

Eicosanoids, derived from PUFAs (such as arachidonic acid), are potent signalling molecules that regulate inflammation, immunity, blood clotting, and other key physiological processes.[41,42] Phosphoinositides are involved in intracellular signalling pathways, such as those that regulate cell growth, survival, and differentiation.[43,44] Steroid hormones, such as estrogen, testosterone, and cortisol, are derived from cholesterol and play crucial roles in regulating metabolism, immune responses, reproduction, and responses to stress.[45,46]

Taken together, lipids are critical structural components of cell membranes and play major roles in energy storage, cellular signalling, nutrient transport, and metabolic regulation.

1.3 Lipids in disease

1.3.1 Cancer

Cancer cells reprogram metabolic pathways to meet their increased energetic, biosynthetic, and redox balance requirements. A hallmark of cancer metabolism is the Warburg effect, which describes the preference of cancer cells to rely on aerobic glycolysis rather than OXPHOS, even in the presence of ample oxygen.[47] This effect allows cancer cells to prioritise the production of metabolic intermediates needed for cell growth and division over maximal ATP yield. However, more than 100 years of research have provided insights into the integral role of FAs in tumorigenesis. Some of these

roles include the increased reliance of cancer cells on de novo lipogenesis and exogenous FA uptake, storage and oxidation to not only sustain their rapid proliferative rate, but also provide an essential energy source during conditions of metabolic stress.[48–50] These alterations in lipid metabolism are now recognized as hallmarks of cancer and the adaptations provide cancer cells with energy, membrane building blocks, signalling molecules, and protection from oxidative stress.[51]

1.3.1.1 FA Synthesis, Uptake and Storage in Cancer

Cancer cells exhibit increased de novo FA synthesis, even in the presence of abundant circulating lipids.[52] Fatty acid synthetase (FASN) is a central enzyme in the biosynthesis of FA and is frequently upregulated in many types of cancer, including breast cancer.[53] Sterol regulatory element-binding proteins (SREBPs) are transcription factors that regulate the expression of enzymes involved in lipid biosynthesis, including FASN and acetyl-CoA carboxylase (ACC).[54,55] SREBPs are activated in response to oncogenic signals, hypoxia, and nutrient availability in cancer cells, promoting lipogenesis.[55] Cancer cells can also take up exogenous FAs from the tumour microenvironment, which helps support their metabolic needs. CD36 has been shown to be overexpressed in various cancers, including breast, ovarian, and oral cancers.[56,57] The overexpression of CD36 has been associated with increased metastasis and poorer prognosis.[52] Cancer cells often accumulate lipid droplets, and these lipid stores can be mobilised during periods of metabolic stress or nutrient deprivation, providing a reservoir of energy and membrane precursors.[58]

1.3.1.2 FA Oxidation (FAO) in Cancer

FAO is upregulated in some cancer types, particularly those that grow in nutrient-limited or hypoxic environments.[48–50] Increased CPT1 expression and activity have been observed in several cancers, including prostate, breast, and pancreatic cancers.[50] FAO provides a steady supply of ATP for energy, particularly under nutrient-stressed conditions, allowing cancer cells to survive and proliferate even when glucose availability is low.[48] By producing NADPH through FAO, cancer cells can replenish their antioxidant defences, which are critical for survival in the face of high levels of ROS generated by rapid proliferation and metabolic activity.[59,60]

1.3.1.3 Oncogenic Signalling and FA Metabolism

Cancer cells often hijack key oncogenic signalling pathways to enhance FA metabolism. These pathways not only drive cell growth and proliferation but also regulate lipid metabolism at multiple levels: The PI3K/AKT/mTOR pathway signalling axis promotes cell growth, survival, and metabolism in cancer cells.[61,62] AKT can directly activate ATP citrate lyase (ACLY), which converts citrate into acetyl-CoA, the building block for FA synthesis.[63] The PI3K/AKT pathway also upregulates SREBP, promoting lipogenesis and FA synthesis.[64] c-Myc is a transcription factor that regulates cell growth, proliferation, and metabolism, often implicated in cancer due to its role in promoting oncogenic processes when overexpressed or dysregulated. c-Myc enhances the transcription of genes that drive de novo FA synthesis, such as FASN and ACC, providing cancer cells with the metabolic resources needed for rapid proliferation.[65,66]

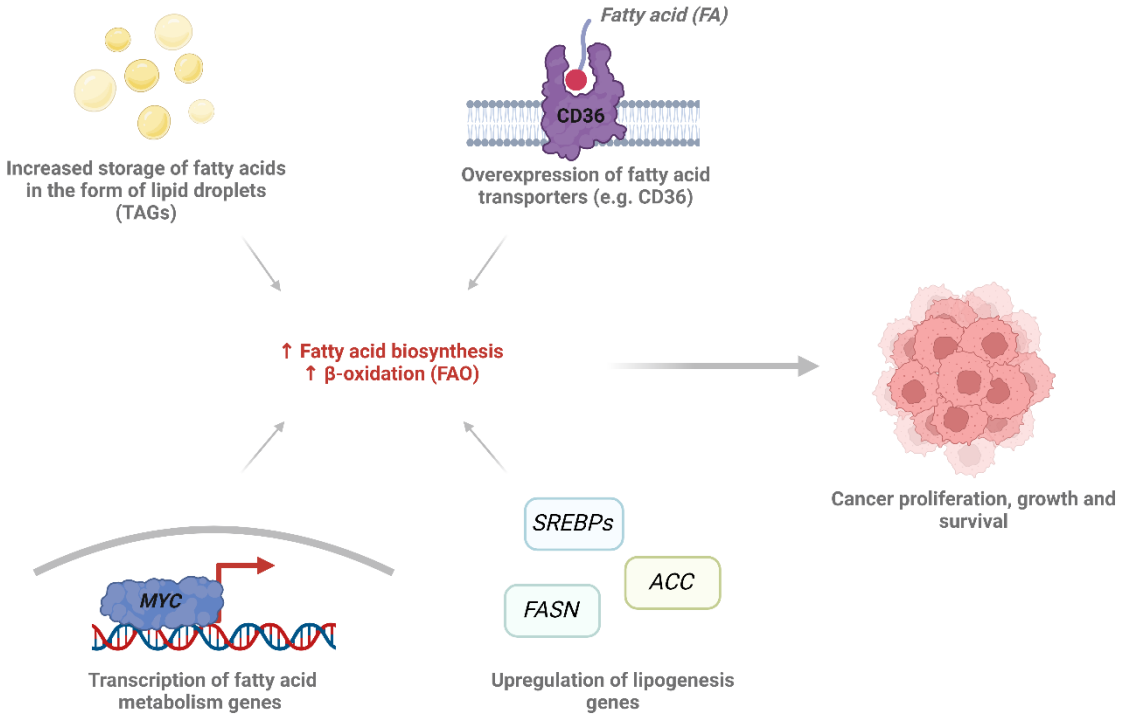

Figure 1.8: Overview of the roles of FAs in cancer. Cancer cells rely upon FAs for proliferation, growth and survival - utilising them to produce energy and membrane maintenance. Increased expression of FA transporters allows exogenous FA uptake. Increased FA storage in the form of lipid droplets. Transcription of FA metabolism genes allow for increased β-oxidation. Upregulation of lipogenesis genes. As a result, both FA biosynthesis and β-oxidation (FAO) are increased.

1.3.2 Heart Disease

1.3.2.1 FAs in the healthy heart

The human heart is an energetic omnivore, depending on the use and generation of large quantities of ATP to maintain basal metabolism and contractility.[67] In cardiomyocytes, ATP is consumed during several processes, such as ion pumping across the membrane, which helps to maintain calcium homeostasis, and in the contraction and relaxation of heart muscle cells. The heart's metabolic flexibility allows it to switch between different energetic substrates depending on availability.[67,68] Under normal conditions, the heart prioritises FAs, using β-oxidation to produce approximately 60-80% of its energy. The remainder of the energy is derived from the oxidation of other energetic substrates, such as glucose and lactate, as well as small amounts of ketone bodies and amino acids.[69,70] It is, therefore, not surprising that FAs play a crucial role in heart health, influencing everything from energy metabolism and contractility to inflammation.

1.3.2.2 FAs in Heart Disease

The relatively tight coupling between lipid uptake and oxidation prevents the accumulation of excess lipids in the cardiomyocyte. Diabetic cardiomyopathy is a heart disease that occurs specifically in people with diabetes, involving structural and functional changes in the heart, ultimately leading to heart failure.[71–73] The condition is largely driven by metabolic disturbances associated with diabetes, including increased FA uptake and metabolism, oxidative stress, inflammation and impaired cardiac function. [74,75] In certain conditions (e.g. during insulin resistance or T2D), an increased reliance on FAs as an energy substrate in the heart can occur, with increased FA uptake, the rate of which surpasses the rate of FAO, leading to the accumulations of lipid intermediates (e.g. DAGs or ceramides) in the cardiomyocytes.[76] To compensate for this, mitochondria increase FAO, however, excessive FAO can overwhelm the mitochondrial capacity and lead to mitochondrial dysfunction and ROS production

During ischaemia and in heart failure (HF), the heart's ability to oxidise FAs is impaired, due to insufficient oxygen concentrations for mitochondrial respiration, leading to an increased reliance on glucose.[77,78] The accumulation of unmetabolised FAs in the heart damages cardiac cells, contributing to the progression of heart failure. An excess of circulating FAs or accumulation of toxic FA

intermediates in the heart can alter ion channel function and electrical conduction, leading to an increased risk of arrhythmias.[79]

1.3.2.3 Cardiac Lipotoxicity

Despite its preference for FA, the heart is vulnerable to the pathological effects of lipid overload. In conditions where FA uptake by the heart exceeds its oxidative capacity, toxic FA intermediates accumulate in cardiac cells and can cause mitochondrial dysfunction, apoptosis (cell death), and inflammation (Figure 1.9).[80] This condition is referred to as lipotoxicity and is prevalent in metabolic disorders, such as obesity and type 2 diabetes (T2D).

LCFAs such as palmitic acid play a major role in lipotoxicity due to their ability to alter cellular structures, causing oxidative stress, endoplasmic reticulum (ER) stress, defective insulin signalling, mitochondrial dysfunction, inflammation, and myofibrillar dysfunction, resulting in apoptosis.[81,82] In previous studies using isolated mitochondria[83,84] or cultured cells[85,86], palmitic acid and its intermediates, palmitoyl-carnitine and palmitoyl-CoA have been shown to affect mitochondrial membrane potential ($\Delta\Psi_m$), the mitochondrial permeability transition pore (mPTP), activity of the ETC, and the generation of ROS. A sustained mitochondrial FA oversupply and incomplete FAO, therefore, results in mitochondrial accumulation of FA-CoAs and acylcarnitines. In contrast to FA-CoAs, acylcarnitines can cross membranes and end up back in the cytoplasm or in the blood.

Lipotoxicity can also promote cardiac remodelling, resulting in hypertrophy and fibrosis.[87] This is caused by the accumulation of lipids, but also the activation of inflammatory pathways in the heart, leading to increased extracellular matrix (ECM) production. A more comprehensive understanding of the proteins and molecular pathways implicated in this condition would significantly advance the development of targeted therapeutic strategies.

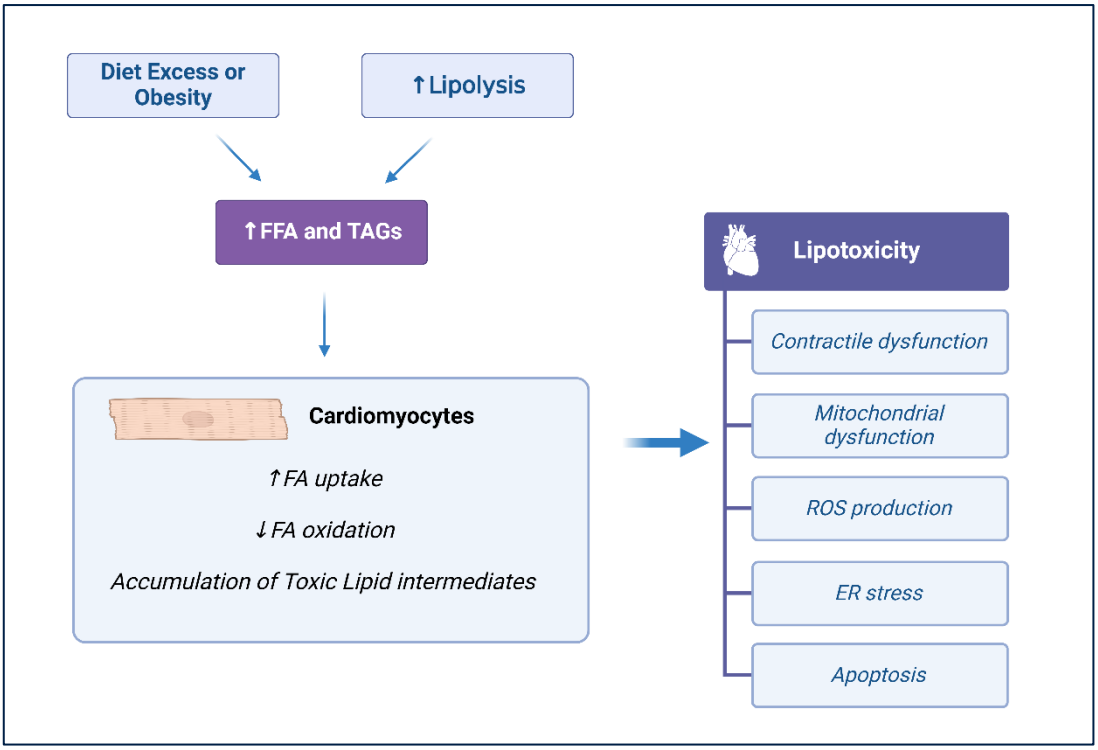

Figure 1.9: Pathophysiological mechanism leading to cardiac lipotoxicity (adapted figure).[74]

1.4 Types of FA Interactions

FAs interact with a multitude of biomolecules through both covalent and non-covalent interactions. Investigating these interactions would further help us understand how FAs function in different biological and disease contexts.

1.4.1 Covalent Interactions

Covalent interactions involving FAs result from the formation of stable bonds with other biomolecules. FAs can covalently attach to proteins through acylation, where the FA attaches to a protein via amide, ester or thioester bonds. This post-translational modification (PTM) can affect the structure, localisation, and function of proteins. Palmitoylation is a common type of acylation, where the 16-carbon SFA palmitic acid attaches to specific residues on proteins via a covalent bond.[88] This addition can be to cysteine residues through thioester linkages, to the *N*-terminal group of a protein through amide linkages and, less frequently, to serine and threonine residues through ester linkages. These are referred to as *S*-palmitoylation, *N*-palmitoylation and *O*-palmitoylation, respectively (Figure 1.10).[89] This modification occurs via a palmitoyltransferase, using the palmitic acid

intermediate, palmitoyl-CoA as the substrate and is typically reversible and regulates the anchoring of proteins to membranes, which can influence signal transduction and intracellular trafficking.[90,91] FAs also form covalent ester bonds with glycerol to produce TAGs and phospholipids.[92,93] In phospholipids, ester bonds help form the cell membrane structural components, where FAs contribute to both membrane fluidity and stability.[16,17]

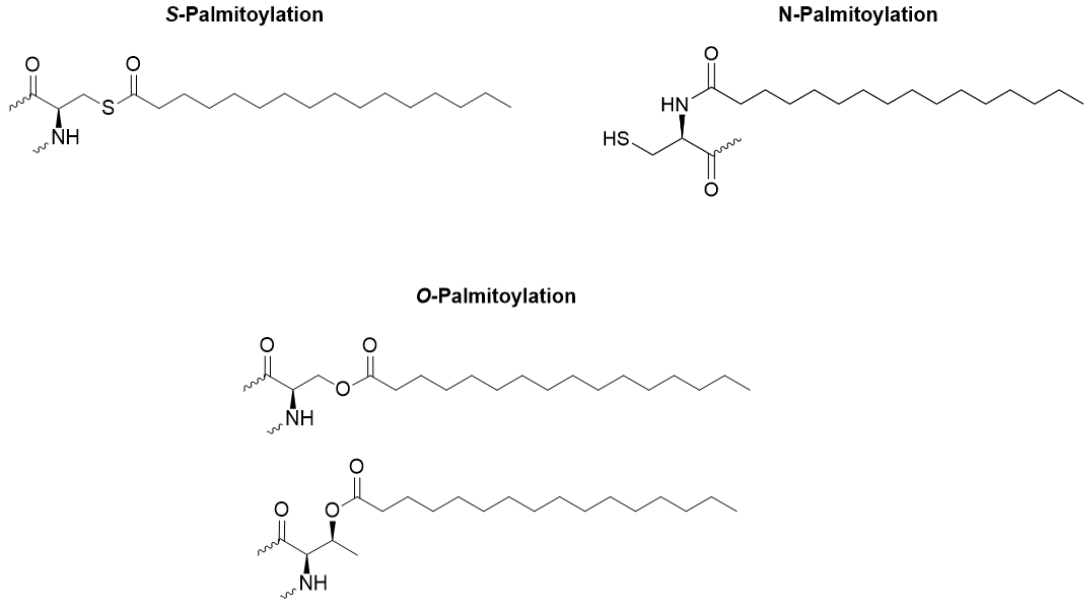

Figure 1.10: Types of cellular protein palmitoylation: *S*-palmitoylation is the attachment of a palmitoyl group to a cysteine residue to form a thioester bond. *N*-palmitoylation attaches to the *N*-terminal amino acid to form an amide bond. *O*-palmitoylation attaches to a serine or threonine amino acid, forming an ester bond.[89]

1.4.2 Non-Covalent (Hydrophobic) Interactions

Non-covalent interactions can occur through hydrophobic interactions or hydrogen bonding. FAs present in the lipid bilayer can interact with integral membrane proteins through hydrophobic interactions, where the hydrophobic tail of the FA interacts with hydrophobic amino-acid residues within the protein (Figure 1.11).[18,94] The carboxy polar head group of FAs can also participate in electrostatic interactions with positively charged residues or hydrogen bonding with polar residues.[95] Hydrophobic interactions between FAs also contribute to the formation of lipid rafts, which are

microdomains within the membrane rich in cholesterol and sphingolipids that serve as platforms for protein signalling and trafficking.[96,97] Even for proteins not associated with membranes, there can be binding pockets or surface regions where hydrophobic interactions with FAs are possible. This interaction helps transport FAs in the bloodstream, where FAs are bound to carrier proteins, e.g. albumin, in hydrophobic pockets where the interaction is driven by the hydrophobic effect.[98] Hydrophobic binding also allows FAs to interact transiently with enzymes such as lipases during fat metabolism.[99] The non-covalent, hydrophobic interactions aid in the formation and stability of cell membranes, lipid transport, and dynamic interactions with proteins.

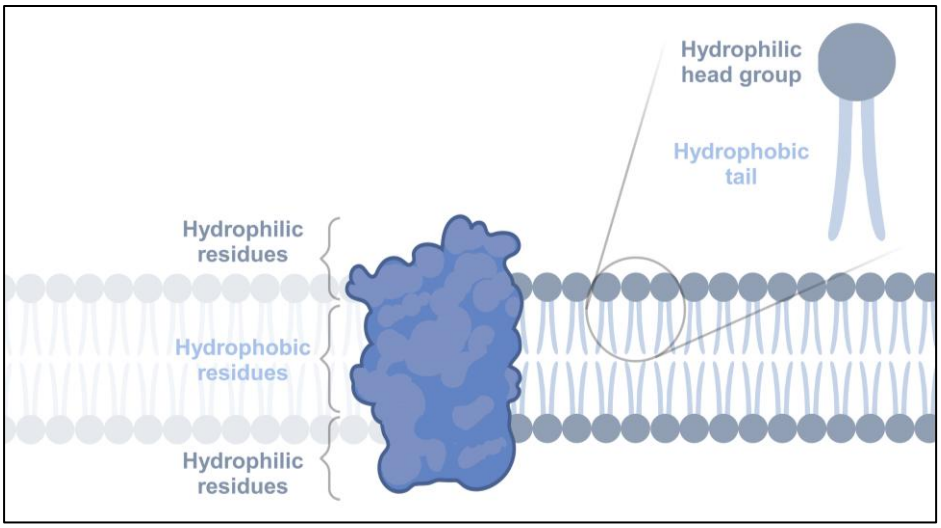

Figure 1.11: Non-covalent hydrophobic interactions of FAs and proteins: FAs non-covalently associate with proteins through interaction of the hydrophilic head group with hydrophilic amino acid residues of the protein, whereas the hydrophobic tail groups interact with hydrophobic amino acids.

1.5 Methods for Profiling Lipid-Protein Interactions *In Vitro*

Understanding lipid-protein interactions is crucial for studying cell membranes, signal transduction, and metabolic processes.[100,101] *In vitro* studies allow for controlled experimental environments where these interactions can be investigated. Several methods have been developed to analyse and quantify lipid-protein interactions, each with distinct advantages, depending on the specific lipid or protein being studied and the nature of the interaction. Below are key methods used for studying lipid-protein interactions *in vitro* (Table 1.1). It is clear that fluorescent lipid probes and radiation have inherent limitations, including steric hindrance of the fluorophores and safety concerns with radioactive

reagents. Cutting-edge techniques, including Click chemistry, photoaffinity labelling (PAL), and photocatalytic labelling, are of current interest as they each provide a different route to study the protein-lipid interactome with minimal disruption to endogenous interactions or increased labelling. Therefore, photoaffinity labelling (PAL) and photocatalytic labelling were chosen for this study and will be discussed further below.

Table 1.1: Techniques for investigating lipid-protein interactions

Technique	Advantages	Limitations
Fluorescent lipid probes[102–105]	Allows for real-time visualisation and tracking of lipid interactions.	Fluorophores can be sterically bulky and may affect endogenous interactions.
Radioisotope-labelled lipids[101,106,107]	Highly sensitive. Precise quantification and real-time tracking.	Safety concerns, decay of reagents, cost of reagents and disposal, and lack of spatial resolution.
Click Chemistry[100,108–111]	Reporter molecule (fluorophore or biotin) attached after interactions occur. Minimal disruption of endogenous interactions.	No real time tracking, reporter labelling occurs after cell lysis. Stoichiometric labelling only.
Photoaffinity labelling (PAL)[111–117]	Captures both covalent and non-covalent interactions via photocrosslinking.	No real time tracking, reporter labelling occurs after cell lysis. Stoichiometric labelling only.
Photocatalytic labelling[117–120]	Catalytic mechanism allows for increased labelling events. Reduces background noise.	Large photocatalyst may disrupt endogenous interactions.

1.5.1 Click-Chemistry for Lipid-Protein Interactions

Lipid analogues containing a terminal alkyne or azide can be used to label proteins of interest (Figure 1.13).[100] This labelling occurs using Click chemistry, a highly selective and efficient chemical reaction that enables the bioorthogonal coupling of functional groups. One example is the copper(I)-catalysed azide-alkyne cycloaddition (CuAAC) reaction, which reacts terminal alkynes with azides to form 1,2,3-triazoles.[108,109] Lipid analogues containing an azide or alkyne functional group can be incorporated into cellular membranes or used in model systems. After interaction with proteins, these lipids can be covalently "clicked" to a fluorescent dye or a biotin label, allowing detection of lipid-protein complexes. As alkynes or azides are not naturally present in biological samples, and the reactants are biorthogonal, this method is useful for detecting crosslinked proteins. Bifunctional

lipids, which incorporate both photoactivatable and clickable groups, are used in these studies to facilitate the detection of interactions (Figure 1.12).[110,111] Cells can, therefore, be fed with these lipid analogues (e.g., azido-palmitic acid or alkyne FAs), and after lipid-protein interactions, Click chemistry can be used to label and track these protein interactors. This technique can only label proteins that are covalently bound to the lipid analogue, e.g. palmitoylated proteins. Martin *et al.* performed a global profiling of palmitoylated proteins in BW5147-derived mouse T-cell hybridoma cells and captured proteins previously shown to be palmitoylated.[121]

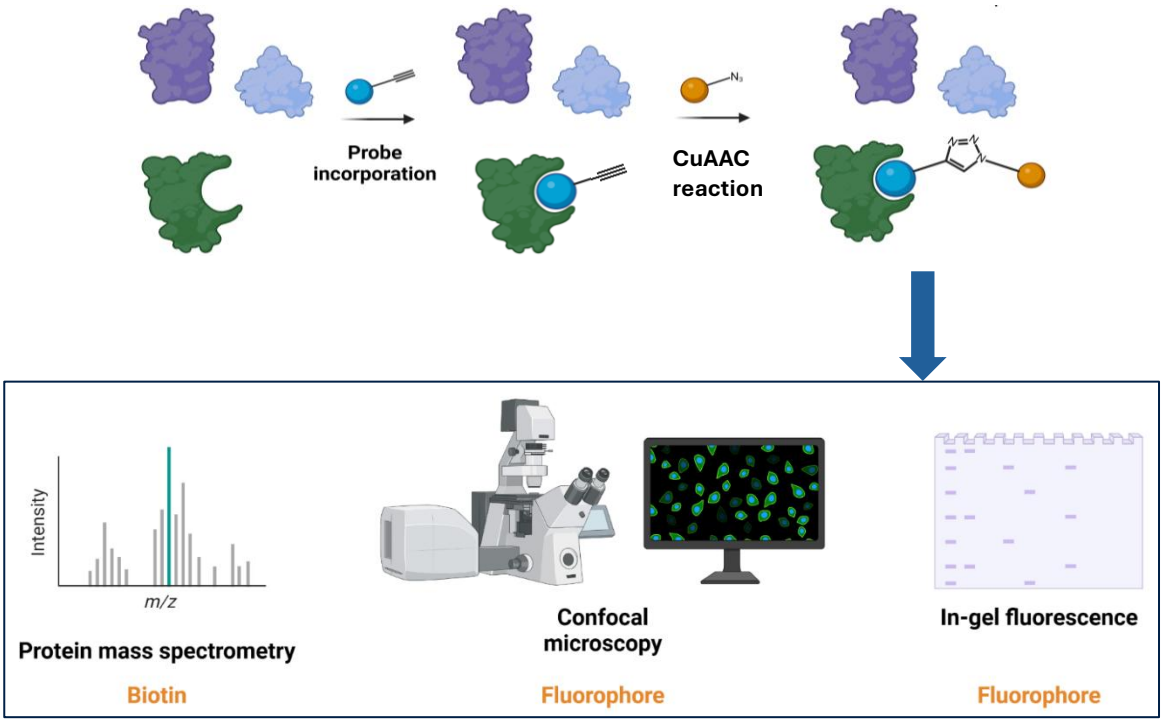

Figure 1.12: General scheme for *in vivo* profiling of cellular lipid-protein interactions using Click chemistry. Alkyne-containing probes become metabolically incorporated and Click chemistry can be used to label the alkyne group in the probe structure with biotin-N_3 or TAMRA-N_3 (denoted by orange sphere), allowing the respective enrichment and target identification (LC-MS/MS) or visualisation of the crosslinked proteins by in-gel fluorescence or fluorescence microscopy.

1.5.2 Photoaffinity Labelling (PAL) for Lipid-Protein Interactions

Photoaffinity labelling involves the use of lipid analogues modified with both a photoreactive group and a terminal alkyne handle (Figure 1.13).[111–113] Upon activation by light, these lipids form covalent bonds with interacting proteins. This technique enables the identification and characterisation of lipid-binding proteins. It involves using a small molecule or protein that, upon exposure to an

external stimulus such as UV light, generates a reactive intermediate. This intermediate, due to its short-lived nature, can cross-link with proteins only within its immediate vicinity, providing a snapshot of lipid-protein interactions. The target protein can then be tagged, using Click chemistry, with a reporter (biotin or fluorophore) to facilitate downstream immunoblotting or proteomic analyses. After UV activation, proteins covalently bound to the lipid probe are isolated using biotin pulldown. Once isolated, the crosslinked proteins can be identified using mass spectrometry, western blotting, or immunodetection methods, allowing researchers to determine the specific proteins interacting with the lipid probe.[111] Photoactivatable lipids were first introduced in the 1970s, and since then, a range of such lipids has been developed for studying lipid-protein interactions. These photoactivatable probes include phospholipids, sphingolipids, and sterols, varying in their photoactivatable group positions and chemical structures.[114] Commonly used photoactivatable groups are aryl azides, benzophenones, and diazirines, all of which are known for their chemical stability, and high reactivity upon photoactivation. For this study, diazirines were chosen due to their small size, which minimises steric interference with the biomolecules under investigation. Diazirines are activated efficiently by UV light at 350 nm, producing a highly reactive carbene. This longer wavelength minimises non-specific photocrosslinking and reduces potential photodamage to cells.[122]

The advantage of this PAL over other techniques is that the FA structure is minimally altered; therefore, the interactions between the FA and proteins are not majorly perturbed.[116] Both soluble and membrane-embedded proteins can be captured, allowing for analysis of proteome-wide lipid interactions.[111] The photo-crosslinking group allows for the investigation of both covalent and non-covalent interactions that can be affinity-purified and then either visualised or analysed via proteomic techniques. Some limitations of the technique include non-specific crosslinking, potential UV damage, perturbation of lipid interactions (due to photoreactive group) and there is limited temporal resolution.[117] For example, Fedoryshchaki *et al*. used a photoaffinity myristic acid (C14:0) probe to investigate lipid-mediated protein-protein interactions in HeLa cells.[123]

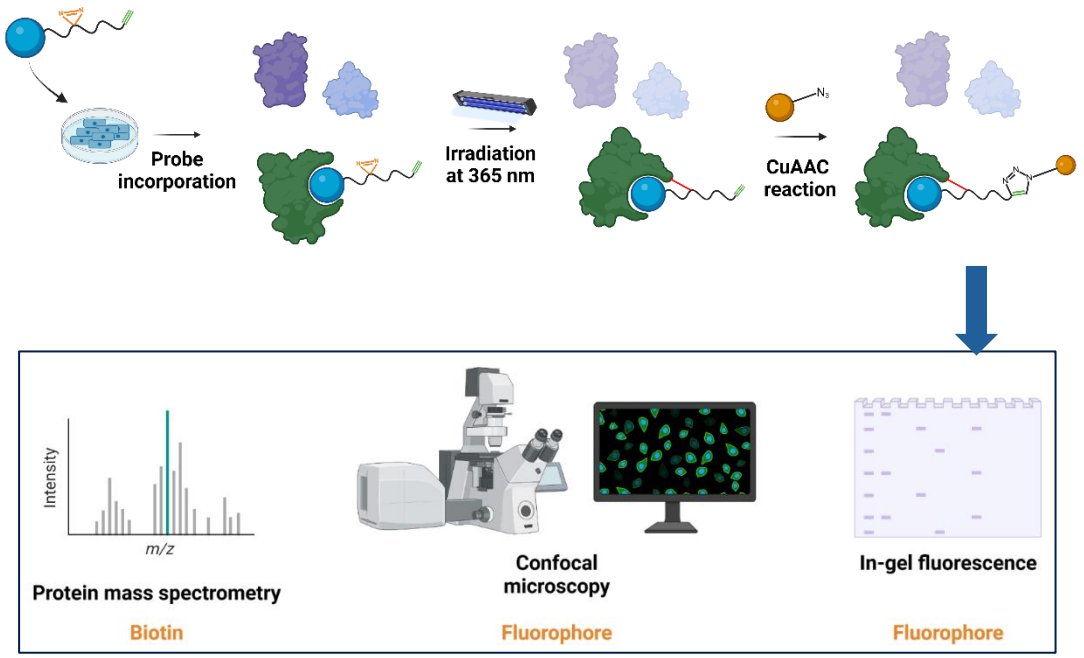

Figure 1.13: General scheme for *in vivo* profiling of cellular lipid-protein interactions using photoaffinity labelling (PAL): (a) Diazirine-containing probes can crosslink to their protein-binding partners by UV irradiation, covalently capturing lipid-protein interactions. Click chemistry can be used to label the alkyne group in the probe structure with biotin-N_3 or TAMRA-N_3 (denoted by orange sphere), allowing the respective enrichment and target identification or visualisation of the crosslinked proteins by in-gel fluorescence or fluorescence microscopy.

1.5.3 Photocatalytic Protein Labelling (µMap)

One crucial aspect of proximity labelling is the labelling radius of the reactive intermediate, which influences the resolution and precision of the labelling process.[118] A less reactive probe tends to diffuse further, capturing proteins over a larger distance and potentially resulting in numerous false-positive 'hits'. In contrast, a more reactive probe has a smaller diffusion range, helping to ensure that only the local microenvironment of the small molecule is probed. A significant challenge with using diazirine as the reactive species is its rapid quenching by water (~99% of the reactive species), leading to the formation of hydrated products.[117] This rapid quenching is important for limiting the diffusion of the reactive intermediate, but it can also result in low labelling efficiency, making it difficult to analyse low-abundance proteins. Recently, Geri *et al.* addressed this limitation with their novel µMap technology, which employs an iridium photocatalyst (Figure 1.14).[118] This catalyst absorbs blue light and becomes excited into a triplet-excited state, this then allows for the conversion of the photon into chemical energy, which is transferred to a nearby diazirine labelling molecule

through a Dexter energy transfer. This causes the formation of a triplet-excited diazirine molecule and the photocatalyst returns to its ground state. The triplet-excited diazirine then undergoes a rearrangement, with the release of nitrogen to form a highly reactive carbene intermediate. This intermediate can then go on to crosslink nearby proteins or be quenched by the aqueous environment (Figure 1.14).[120,124] One of the major advantages of this method over PAL is that it is possible for multiple labelling events to occur from a single photocatalyst if an excess diazirine labelling reagent is used. This allows continuous excitation of diazirines wandering into the radius where Dexter energy transfer can happen means improved labelling efficiency. This catalytic labelling overcomes the limitations of PAL, where only stoichiometric labelling is possible and can also allow for the enhanced capture of low abundance proteins. Photocatalytic labelling maintains a slightly larger labelling radius (4-5 nm) compared with carbenes (3 nm). However, this enables labelling of the microenvironment to occur. The initial energy transfer is confined to a distance of approximately 1 nm, resulting in a labelling radius of 4-5 nm (carbene diffusion ~3 nm), improving both resolution and precision in proximity labelling.[117] Lastly, the diazirine labelling molecule is not activated by blue light, therefore, no hydrolysis quenching of the labelling molecule occurs in areas where the photocatalyst is not bound. However, due to the increased labelling of proteins data analysis can become increasingly difficult.[120]

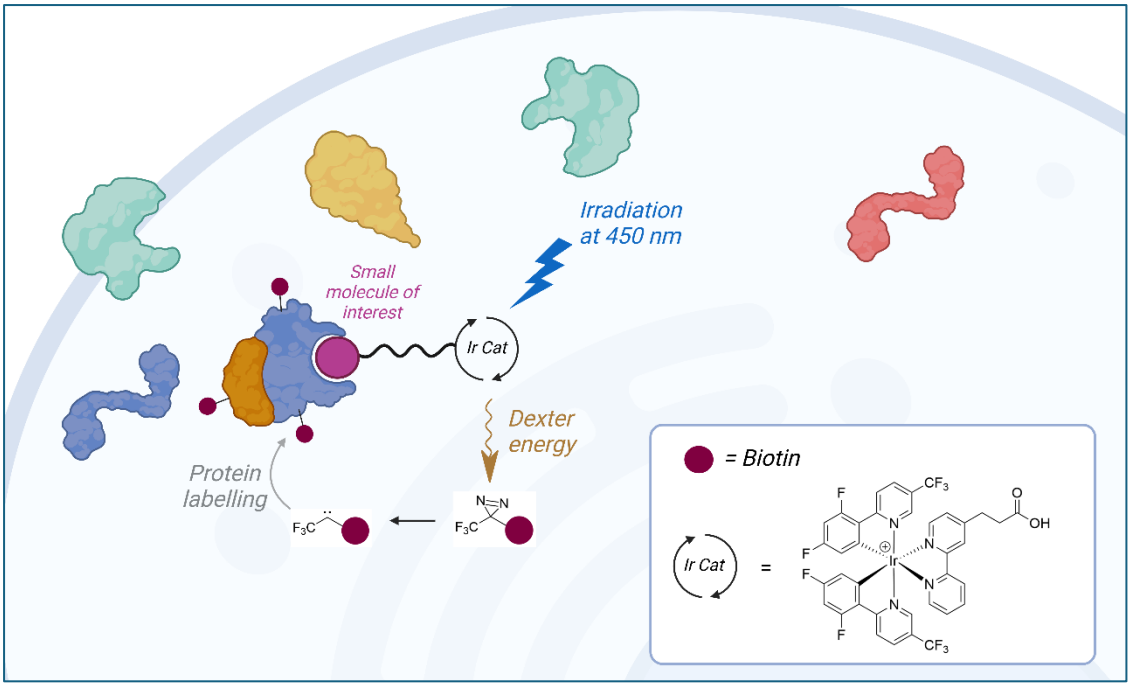

Figure 1.14: General mechanism of protein labelling by iridium-based photocatalytic chemical probes.[120,124]

1.6 Thesis Aims

The work described in this thesis intends to synthesise and utilise both photoaffinity and photocatalytic probes of different FAs and some FA metabolites to understand with which proteins specific FAs or metabolites interact in both breast cancer and heart *in vitro* models. It will further investigate the biological outcomes of these interactions, specifically changes in gene expression, protein expression and phenotype. The main aim of this chemical biology investigation is to highlight proteins or pathways of interest in each cell line for potential therapeutic target identification. This will be achieved through five chapters, focusing on:

1. Chemical design, synthesis and characterisation of various FA photoaffinity or photocatalytic probes (palmitic acid (SFA) and oleic acid (MUFA)).
2. Optimisation of the labelling workflow for a palmitic acid photoaffinity probe in triple-negative breast cancer (*MDA-MB-231*) cells.
3. Target identification through proteomic and transcriptomic analysis using a palmitic acid photoaffinity probe in breast cancer (*MDA-MB-231*) cells.
4. Target identification through proteomic and transcriptomic analysis using a palmitic acid photoaffinity probe in human-derived iPSC cardiomyocytes.
5. Optimisation and development of a photocatalytic palmitic acid probe in *MDA-MB-231* cells and computational modelling of the palmitic acid and metabolite photoaffinity probes.

Chapter 2

Materials and Methods

2.1 *In vitro* labelling with photoaffinity FA probes

2.1.1 Metabolic labelling of cells with photoaffinity FA probes

MDA-MB-231 cells were maintained in DMEM low glucose (Sigma) supplemented with 10% Fetal Bovine Serum (Sigma) (5% CO_2 and 37°C). hiPSC-cardiomyocytes were maintained in maturation media (DMEM medium supplemented with 10% horse serum, 5 µg/mL vitamin B12, 0.5 mM ascorbic acid, 0.82 µM biotin, 50 nM insulin, 400 µM oleic acid:BSA (2:1), 1x MEM non-essential amino acids, and 20 U/mL penicillin-streptomycin) (5% CO_2 and 37°C). For metabolic labelling, cells were seeded in 6 well plates and grown to 80% confluency. Cells were treated with probe (final DMSO concentration <0.3%) in serum-free media and incubated for 16 h. Following incubation cells were either collected for protein or mRNA extraction (see section 2.6.1) or irradiated with UV light (see section 2.1.2). UV irradiation was performed using EvoluChem™ PhotoRedOx box light source (365 nm, 18 W, 110V, Strem Chemicals Inc.). The cells were then washed with 1 × PBS and irradiated (3 min, 5 cm distance, 365 nm) on ice. Subsequently, cells were lysed at 4 °C with 200 µL of a buffer containing 1% SDS, 1% triton X-100 and protease inhibitors in PBS. The cells were scraped to collect the lysate and stored at -80 °C, and the total protein concentration was determined by a bicinchoninic acid protein assay (Thermo Scientific Pierce).

2.1.2 Click reaction for alkyne functionalisation & protein precipitation

Based on previously published procedure.[125] Cell lysates (100 µL at a concentration of 1 µg/µL in lysis buffer) were then clicked to either TAMRA-azide or biotin-azide (1 µL of 10 mM in DMSO stock) using a Click mix of: $CuSO_4$ (2 µL of 50 mM in H_2O stock); TCEP (2 µL of 50 mM in H_2O stock); and TBTA (1 µL of 10 mM in DMSO stock), for 1 h at RT with gentle shaking (700 rpm). The reaction was quenched upon the addition of EDTA (final concentration 0.5 mM). Excess Click reagents were removed, and proteins were precipitated by adding ice-cold methanol (400 µL), ice-cold chloroform (100 µL) and cold MS-grade water (200 µL), followed by vigorous vortexing at 3,000 rpm for 10 s. The samples were then centrifuged at 5,000 g for 2 min at RT. The top aqueous layer was discarded, and ice-cold methanol (500µl) was added and centrifuged at 17,000 g for 4 min

at RT. The supernatant was discarded, and ice-cold methanol (500 µL) was added, followed by vigorous vortexing and sonication using a probe sonicator to ensure the protein was resuspended. The samples were then centrifuged at 17,000 g for 4 min at RT. The supernatant was discarded and the protein pellet was dried for <5 min at RT, leaving the tube open and upside down on tissue paper. The proteins were then solubilized with resuspension buffer (10 µL, 2% (w/v) SDS in 50 mM HEPES) and HEPES-NaOH solution (90 µL, 50 mM stock). A Stick sonicator was used to ensure full resuspension of the protein pellets.

2.1.3 In-gel fluorescence visualization of metabolic labelling

For visualisation following the attachment of TAMRA-azide using the Click reaction, NuPAGE-reducing sample buffer was added to the samples and denatured at 95 °C for 5 min on a heating block. The samples were cooled on ice and centrifuged at 5,000 g for 1 min. Samples (30 µg of protein) were loaded on hand-poured SDS-PAGE gels (12% (w/v) polyacrylamide, *Appendix A*) and run at 90 V for 10 mins followed by 120 V until the loading dye ran off the bottom. The gel was removed from the case and placed in ice-cold dH_2O. The gel was then scanned for fluorescence on a Li-Cor Odyssey® M Imaging System using the 520 channel (λ_{ex} 520/ λ_{em} 570-610 nm) and the 630 Trans channel (λ_{ex} 631-659 nm) for the molecular weight marker (Precision Plus marker, Bio-Rad, cat. no. 1610393).

2.1.4 Pulldown enrichment using neutravidin agarose beads

For enrichment following the attachment of biotin using the Click reaction, 100 µL of a Neutravidin agarose bead suspension was used per 1 mg of protein. The beads were centrifuged at 3000 g for 1 min and the slurry supernatant was discarded. The beads were then washed three times with 0.2% SDS in Dulbecco's phosphate buffered saline (DPBS), centrifuging in between washes at 3000 g for 2 min. To aliquot the beads, 0.2 % SDS in DPBS was added and the solution was vortexed for 1 min. The beads were aliquoted into new LoBind eppendorfs (100 µL per 1 mg protein). The aliquots were then centrifuged at 3,000 g for 2 min and the supernatant was discarded. For an input sample, 15 µL of each sample was retained. The remaining sample was added to the beads and incubated

with gentle shaking (1200 rpm) for 2 h at RT. The samples were centrifuged at 3,000 g for 2 min and the supernatant was removed and stored at -20 °C. The beads were washed 3 times with 0.2% SDS in DPBS with gentle shaking (700 rpm) at RT and centrifuged at 3,000 g to remove the supernatant. For proteomics, beads were stored at -80 °C, ready for sample preparation (see section 2.4.1). For western blotting, 2% SDS in DPBS (0.75 µL/µg original protein) and NuPAGE reducing sample buffer (0.25 µL/µg original protein) were added to the beads and briefly vortexed. The beads were then heated to 95 °C for 15 min to elute the proteins. The supernatant was removed immediately and placed in a LoBind Eppendorf. NuPAGE-reducing sample buffer (0.25 µL/µg original protein) was added to the input and supernatant samples and heated to 95 °C for 5 min. Western blotting was performed as described in section 2.5.

2.1.5 Click reaction for confocal microscopy

The cell line of choice was seeded on fibronectin-coated glass coverslips in 24-well plates and allowed to adhere overnight. Cells were then incubated with various concentrations of probe **1** for 16 h. Culture media was removed; the cells were washed three times with DPBS and fixed with 4% PFA for 10 min at RT (Figure 2.1). After fixation, the cells were washed three times with DPBS and were permeabilised with 0.5% Triton X-100 in DPBS for 10 min at RT and washed three times with DPBS. The coverslips were then incubated with the Click reaction mixture: TAMRA-azide (1 µL of 10 mM stock); $CuSO_4$ (2 µL of a 50 mM stock); TCEP (2 µL of a 50 mM stock); and TBTA (1 µL of a 10 mM stock)), in the dark for 1 h at RT. The cells were washed three times with DPBS, to remove excess TAMRA-azide. Coverslips were mounted on slides using Fluoromount-G™, with DAPI (Invitrogen) and allowed to set overnight at 4 °C. The cells were imaged using a Leica TCS SP5 confocal microscope (TAMRA: λ_{ex} 546/ λ_{em} 565 nm, DAPI: λ_{ex} 358/ λ_{em} 461 nm) and acquired images were processed using Fiji software.

2.2 Metabolite measurements in cell media

All metabolite measurements were performed on culture medium (200 µL) using an ABX Pentra 400 Chemistry Analyser (Horiba). The lactate dehydrogenase (LDH) assay was performed using the

LDH CP reagent (Horiba, A11A01824). LDH was estimated using the UV kinetic method (DGKC), where LDH catalyses the conversion of pyruvate and NADH to L-lactate and NAD^+. A decrease in absorbance value at 340 nm is due to NADH oxidation to NAD^+ and is directly proportional to LDH activity. The lactate assay was also performed using the lactic acid reagent (Horiba, A11A01721). The reagent containing lactate oxidase reacts with the lactate molecules in the media, triggering the release of hydrogen peroxide. The hydrogen peroxide produces a colour, with colour intensity proportional to the amount of lactate present in the sample. The glucose assay was also performed using the Glucose PAP CP reagent (Horiba, A11A01668). The reagent containing glucose oxidase converts glucose to gluconic acid, whilst oxygen is simultaneously reduced to hydrogen peroxide. The hydrogen peroxide reacts further and produces a colour, with colour intensity proportional to the amount of glucose present in the sample. All samples were run in duplicate.

2.3 Mitochondrial network staining

Cells of interest were incubated with culture media containing 100 nM of MitoTracker Red CMXRos dye for 30 min at 37 °C. The cells were then washed three times with DPBS and fixed with 4% PFA for 10 min at RT and washed three times with DPBS. Coverslips were mounted on slides using Fluoromount-G™, with DAPI (Invitrogen) and allowed to set overnight at 4 °C. The cells were scanned using a Leica TCS SP5 confocal microscope (MitoTracker: λ_{ex} 579/ λ_{em} 599 nm, DAPI: λ_{ex} 358/ λ_{em} 461 nm) and acquired images were processed using Fiji software.

2.4 Proteomic analysis of fatty acid probes

2.4.1 On-bead trypsin digest

Trypsin digestion was performed using the Smart digest system (ThermoFisher). Smart trypsin buffer (150 µL) and Smart trypsin (2 µL) were added to the Neutravidin beads (following pulldown enrichment, see section 2.1.4), and the samples were incubated at 70 °C for 2 h at 1,400 rpm. The digestion was stopped upon the addition of trifluoroacetic acid (final concentration 1% v/v). The

samples were centrifuged for 5 min at 13,000 rpm, the supernatant was removed and placed in fresh LoBind eppendorfs.

2.4.2 Peptide desalting

Desalting was performed using Sola cartridge C18 columns. The columns were first rinsed with solution B (500 µL 65% acetonitrile, 0.1% TFA and 35% HPLC-grade water), followed by equilibration with solution A (1 mL, 2% acetonitrile, 0.1% TFA and 98% HPLC-grade water). The peptide digests were then diluted with solution A (1 mL) and run through the column. The peptides were then washed with solution A (1 mL), eluted with solution B (100 µL) and collected in fresh LoBind eppendorfs. The peptides were then dried completely by vacuum centrifugation and stored at -20 °C until ready for MS analysis.

2.4.3 LC-MS/MS analysis

The running of the samples and the acquisition of the raw data was performed by Sarah Flannery and Iolanda Vendrell from the Fischer laboratory at the Target Discovery Institute, University of Oxford.

Before LC-MS/MS analysis, peptides were reconstituted in 0.1% formic acid. The LC-MS/MS analysis was conducted using the Orbitrap Ascend Tribrid mass spectrometer (Thermo Scientific) connected to a Thermo Scientific Vanquish™ Neo UHPLC system, interfaced via a nano-EASY spray source. The Vanquish™ Neo system was run in Trap and Elute mode, using solvent A (0.1% formic acid in HPLC-grade water) and solvent B (0.1% formic acid in acetonitrile), with trifluoroacetic acid (0.1% in HPLC-grade water) used as the weak wash solution.

Tryptic peptides were initially loaded onto a PepMap Neo C18 trap column (Thermo Scientific; S/N 174500) at a flow rate of 8 µL/min (total volume 24 µL) and separated on a 50°C heated EasySpray PepMap Neo column (Thermo Scientific; S/N ES75500). The peptides were eluted using a multistep gradient starting from 2% to 18% solvent B over 40 minutes, followed by 18% to 35% solvent B over 20 minutes, with a flow rate of 300 nL/min. The column was then washed for 14 minutes with 99% solvent B, followed by rapid equilibration in the Vanquish Neo system (using control mode

with a pressure limit of 1000 bar). Simultaneously, the trap underwent a zebra wash (in-built wash function for the LC system) and was quickly equilibrated.

MS data was collected in data-independent acquisition (DIA) mode. Briefly, MS1 scans were acquired in the Orbitrap at a resolution of 45,000 (at m/z 200) across a mass range of 350–1650 m/z. The normalized automatic gain control (AGC) target for MS1 was set at 125% (5e5 ions) with a maximum injection time of 91 ms and an RF lens setting of 30%. DIA MS2 scans were acquired using the tMSn scan function at 30,000 resolutions in the Orbitrap, across 40 variable-width scan windows, with a normalized AGC target of 1000%, automatic maximum injection time, and 30% collision energy.

2.4.4 Proteomic data analysis

The raw data were analysed using DIA-NN v1.8.1 in library-free mode against the UniProt human proteome database (UP000005640, downloaded on May 13th, 2023), including common contaminants. For Trypsin/P digestion, a maximum of one missed cleavage was allowed, with cysteine carbamidomethylation specified as a fixed modification. The "Match between runs" feature was enabled, and mass accuracy was inferred from the dataset. The DIA-NN neural network classifier was configured to operate in double-pass mode. Protein intensities were normalized using RT-dependent cross-run normalization within DIA-NN.

Data analysis from here on was performed *by myself.* Data was then imported into Perseus software and processed as follows.[126] Rows were filtered based on valid values and $\log_2$-transformed. Imputation was performed using the 'replace from normal distribution' option. The data was filtered for contaminants, and the matrix was exported as a .txt file. This txt. file was converted into .csv file. R was used to visualise the data, using the *'plotPCA'* functions for PCA analysis and the *'enhancedVolcano'* function for volcano plots. Pathway enrichment analysis was then performed using Metascape on the significant ($p < 0.05$) proteins only.[127] STRING database was used for protein-protein interaction mapping.[128]

2.5 Western blotting

Protein lysates were boiled at 70°C for 10 minutes were loaded onto an SDS-PAGE gel (12% (w/v) polyacrylamide gels) and separated by gel electrophoresis. Proteins in the gel were transferred onto a nitrocellulose membrane and equal protein loading was confirmed using Ponceau staining for each membrane. The membrane was blocked for 1 h with 5% milk, incubated overnight with the primary antibody, followed by 30 mins of washing with 1×TBST, 1 h incubation with the secondary antibody and a final 30 mins of washing with 1×TBST. Blot imaging and analysis was performed using a Chemidoc XRS+ imaging system (Bio-Rad) and Image Lab Software version 6.1. The list primary and secondary antibodies used can be found in Table 2.1.

Table 2.1: Antibodies used for Western blotting

Name	Product number	Concentration	Species
Anti-4EBP1	9644S (Cell signalling)	1:1000	Rabbit
Anti-ATP5MG	16307-1-AP (ProteinTech)	1:2000	Rabbit
Anti-ATP5MG	16307-1-AP (Proteintech)	1:2000	Rabbit
Anti-Biotin	ab53494 (abcam)	1:1000	Rabbit
Anti-ENO2	9536S (Cell Signaling)	1:2000	Rabbit
Anti-H3	ab10799 (abcam)	1:1000	Mouse
Anti-MT-CO2	ab79393 (abcam)	1:10000	Rabbit
Anti-mTOR	7C10 (Cell Signaling)	1:1000	Rabbit
Anti-p-4EBP1	9455S (Cell Signaling)	1:1000	Rabbit
Anti-p70S6K	2708S (Cell Signaling)	1:1000	Rabbit
Anti-p-mTOR	D9C2 (Cell Signaling)	1:1000	Rabbit
Anti-p-p70S6K	9234S (Cell Signalling)	1:1000	Rabbit
Anti-p-S6RBP	2215S (Cell Signaling)	1:1000	Rabbit
Anti-Rab11B	PA5-31348 (Invitrogen)	1:2000	Rabbit

Anti-RPL5	145685S (Cell Signaling)	1:1000	Rabbit
Anti-S6RBP	2217S (Cell Signaling)	1:1000	Rabbit
Anti-VEGFA	ab46154 (abcam)	1:2000	Rabbit
Anti-β-Actin	ab6276 (abcam)	1:2000	Mouse
Goat Anti-Mouse (HRP)	ab6789 (abcam)	1:1000	Goat
Goat Anti-Rabbit (HRP)	ab6721 (abcam)	1:1000	Goat

2.6 Transcriptomic analysis

2.6.1 RNA extraction and cDNA conversion

RNA was extracted from cells using Trizol reagent (ThermoFisher). Total RNA was isolated and purified using the Qiagen RNeasy Mini Kit (Qiagen, Venlo, Netherlands), following the manufacturer's instructions. For RNA-sequencing sample preparation the optional DNAse step was performed. RNA concentration and purity were measured using the NanoDrop™ UV spectrometer (A_{250}:A_{280}). RNA (1 μg) was converted into cDNA using a high-capacity cDNA reverse transcriptase kit (Applied Biosciences) according to the manufacturer's protocol.

2.6.2 Differential Gene Expression Analysis

RNA from cell samples were sequenced using an Illumina stranded paired 150-bp poly-A enrichment protocol by Novogene. The RNA-seq data analysis was conducted using R and Bioconductor packages, particularly DESeq2 and pathway analysis tools.[129] The raw count data was imported from a CSV file. Non-informative columns were removed through successive filtering steps to isolate the raw counts, and the Ensembl gene IDs were mapped to Entrez gene IDs using the *'org.Hs.eg.db'* annotation package. Duplicated Entrez IDs were identified and handled by keeping only the row with the highest sum of gene counts and missing Entrez IDs were removed. Genes with low counts (less than 10 in fewer than four samples) were filtered out to reduce noise. A variance-stabilizing transformation (VST) was applied to normalize the raw counts, and the Euclidean distance was calculated between samples based on their normalized gene counts.[130] Hierarchical clustering and

Principal Component Analysis (PCA) were performed to explore the relationships between the samples. For differential expression analysis, *'DESeq'* was run. Pathway enrichment analyses were conducted using 'KEGG', evaluating upregulated and downregulated gene sets separately. Metascape was used to carry out further pathway enrichment analysis.[127] STRING database was used to analyse protein-protein interactions.[128]

2.6.3 Gene Set Enrichment Analysis (GSEA) – pathway analysis

Pathway analysis was performed using gene set enrichment techniques on RNA-seq data. Three pathway databases were utilized: WikiPathways, Hallmark, and KEGG pathways.[131,132] Gene set enrichment analysis (GSEA) was conducted using ranked gene lists. The ranks were created from DESeq2 differential expression results by converting gene names to uppercase symbols and applying the *'createRanks_new'* function, which ranks genes based on DESeq2 statistical outputs. A Fast Gene Set Enrichment Analysis (*FGSEA*) was performed.[133] Pathways with an adjusted p-value (padj) below 0.05 were considered significantly enriched. Visualization of the FGSEA results was achieved through a dot plot (*'ggdotchart'* function). The normalized enrichment scores (NES) were plotted against the top enriched pathways, ordered by NES, with colours representing the negative $\log_{10}$-transformed p-values.

2.7 Gene expression analysis using quantitative PCR (qPCR)

2.7.1 Quantitative Polymerase Chain Reaction (qPCR)

cDNA was used for qPCR using SYBR Green technology (Thermo Fisher Scientific). cDNA (20 ng) and Power SYBR Green PCR Master Mix were loaded into each well of a 96-well plate (MicroAMP fast, Applied Biosciences) and a standard SYBR cycle was applied using a Step-One Plus Real-Time PCR system. Quantification of data was performed using the double delta C_t relative quantification method.[134] Relative gene expression was normalised to the average C_t value of the housekeeping gene: Hypoxanthine Phosphoribosyltransferase 1 (HPRT1), for both *MDA-MB-231* cells and hiPSC-CMs. Primers were designed using NCBI primer-Blast (Table 2.2).

Table 2.2: Primer sequences used for qPCR analysis

Gene	Sequences
ACTN4	**FPR:** CTACGCAAGCAGTTTGGAGC **RPR:**AGGCCCTCAATCTCCTCGAT
IGF1	**FPR:** CCATGTCCTCCTCGCATCTC **RPR:** ACCCTGTGGGCTTGTTGAAA
GPR89B	**FPR:** ATCCCTTTCCCATTCTCAGCCC **RPR:**GGCAGTTGACAGCACCAAATCC
HPRT	**FPR:** CCCTGGCGTCGTGATTAGTG **RPR:**TCGAGCAAGACGTTCAGTCC
MTCO2	**FPR:** GCTGTCCCCACATTAGGCTT **RPR:**CGATGGGCATGAAACTGTGG
ND4	**FPR:** GCTCCATCTGCCTACGACAA **RPR:**CTACGAGGGCTATGTGGCTG
RAC2	**FPR:** AGTGGTTCCCAGAAGTGCG **RPR:**TCCAGGTATTTCACCGAGTCAATCT
UBC	**FPR:** CCTGGTGCTCCGTCTTAGAG **RPR:**TTTCCCAGCAAAGATCAACC
ANKRD1	**FPR:** GCCCAAGATCGAATTCCGTGA **RPR:** CGCTGTGCTGACAACTTATC
SULT1E1	**FPR:** ATTCATGCAAGGACAGGTTCC **RPR:** AGCTCCTCTGATGGCTTCCT
SCN1A	**FPR:** CCTCCCCACACCAGTCTTTG **RPR:** GCTCGCCCTCTAAAGCTGAA
SUCNR1	**FPR:** GCTGGGGATCATGGCATGGAA **RPR:** TCCAAGGACTCCCACAACGA
NPPB	**FPR:** CACAGGTGTCTGGAAGTCCC **RPR:** GCTCGCCCTCTAAAGCTGAA

2.8 Statistical analysis

Prism (version 10.1.1, GraphPad) software was used for the statistical analyses. Results, presented means ± standard error of the mean (SEM), were considered significant at $p < 0.05$. Unpaired t-tests with Welch's correction were used, along with Brown-Forsythe and Welch one-way ANOVA, followed by Dunnett's T3 multiple comparisons test. Levels of significance are denoted by asterisks, as follows: **** ≤ 0.0001, *** ≤ 0.001, ** ≤ 0.01, * ≤ 0.05, ns > 0.05.

Chapter 3

Design and synthesis of fatty acid probes for target ID experiments

3.1 Abstract

Palmitic and oleic acid are two of the most abundant FAs in the Western diet, and therefore, their biological roles and impacts on cell processes should be fully understood. Photoaffinity labelling (PAL) and photocatalytic labelling are two chemical biology methods that can identify protein interactors of ligands in cells. In this chapter, PAL and photocatalytic labelling probes were developed for both palmitic and oleic acid to explore their interactions *in vitro*.

A palmitic acid PAL probe containing a photoreactive diazirine and terminal alkyne was successfully synthesised and purified in five steps. Parallel to this, a novel photocatalytic palmitic acid probe, containing an iridium-based photocatalyst linked to the tail of a palmitic acid molecule was synthesised in eleven steps. Novel PAL probes of several important palmitic acid metabolites were also successfully synthesised: a palmitoyl-CoA and a palmitoyl-carnitine PAL probe, one step each from the palmitic acid PAL probe. A PAL and novel photocatalytic oleic acid probe had been designed, and their synthesis was attempted. Difficulties with purification or formation of the *z*-alkene in the molecules resulted in only partial synthesis, with one synthetic step left for the PAL probe and two steps for the photocatalytic probe.

In conclusion, several palmitic acid and metabolite probes were successfully synthesised, purified and characterised. These probes can be used to interrogate the different interactomes of each molecule *in vitro*.

3.2 Introduction

Design of the fatty acid and fatty acid metabolite chemical probes

A detailed understanding of the function of every protein in the human proteome remains one of the most significant challenges in biology. Importantly, there is clear evidence that protein annotation has been accelerated by the discovery of chemical probes.[135–137] A chemical probe should be a potent and selective ligand for its target protein, modulating the biochemical activity of the target in cells. When designing probes of FAs, it is critical to ensure that the chemical structures are as close to endogenous FAs as possible: containing a hydrophobic tail and a polar head group. Therefore, the design of the palmitic acid, oleic acid and metabolite probes in this chapter structurally resemble their parent FAs, with the addition of a photoreactive group and terminal alkyne or a photocatalyst and linker.

Since palmitic and oleic acid are the most abundant FAs in the Western diet, mapping their protein interactions in various cells would be of great interest. Additionally, as the palmitic acid metabolites: palmitoyl-CoA and palmitoyl-carnitine, have previously been shown to be toxic intermediates, chemical probes of these compounds would further help to understand the mechanism of this toxicity.[76] The palmitic acid photoaffinity probe **1** (Figure 3.1) in this chapter was a previously published probe by Haberkant *et al.*, where it was used to map lipid-protein interactions in CHO cells and a multicellular organism, *Caenorhabditis elegans* (*C. elegans*).[138] In this chapter, this probe was synthesised to give probe **1** and then used to synthesise the palmitic acid metabolite photoaffinity probes: palmitoyl-CoA probe **2** and palmitoyl-carnitine probe **3** (Figure 3.1). The oleic acid photoaffinity probe **5** (Figure 3.2) in this chapter was based on a previously published probe by Niphakis *et al.,* where it was used to map lipid-protein interactions in HEK293T cells.[139] The photocatalytic palmitic acid and oleic acid probes (**4** and **5**, respectively) from this chapter are novel probe designs. Trowbridge *et al.* had previously designed photocatalytic probes for small molecule drug target identification.[124] However, no FA probes had been developed.

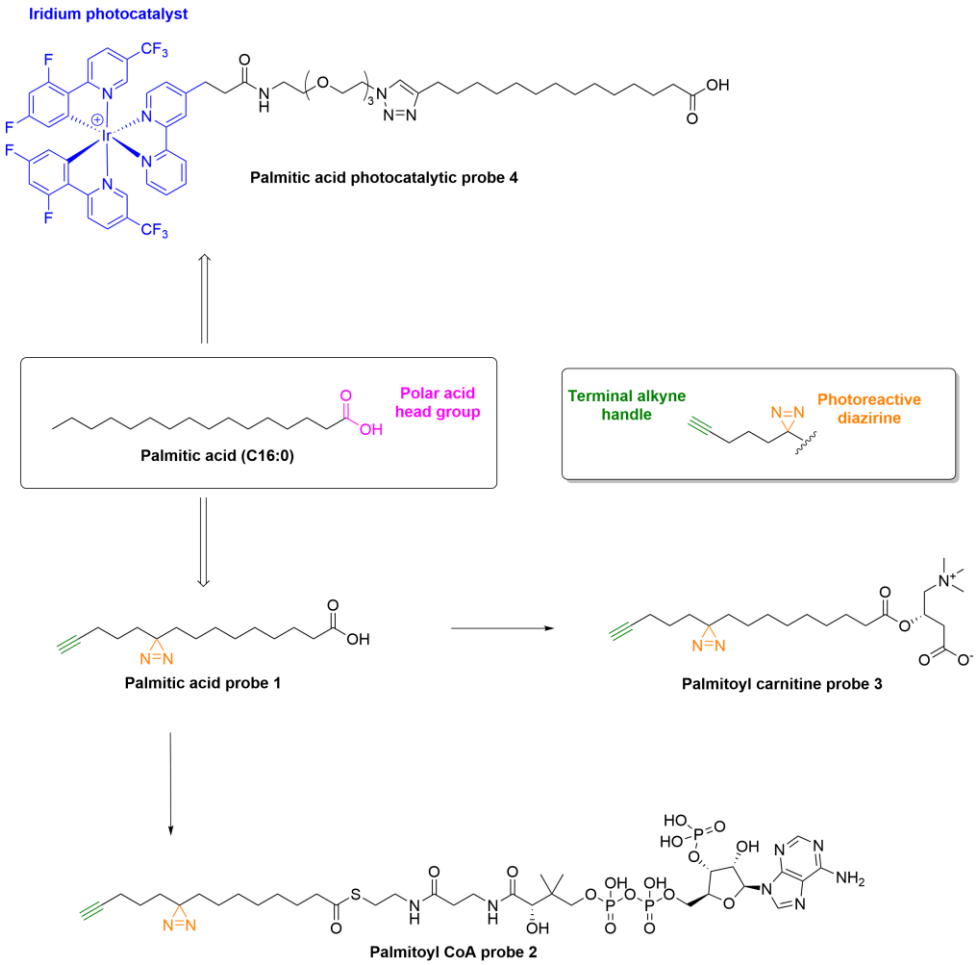

Figure 3.1 Proposed structures of palmitic acid and metabolite photoaffinity probes: 1, 2, and 3 and photocatalytic probe 4. Photoaffinity probes contain a photoreactive diazirine group (orange) and terminal alkyne (green). Photocatalytic probe contains iridium-photocatalyst (blue). All probes retain a polar acid head group.

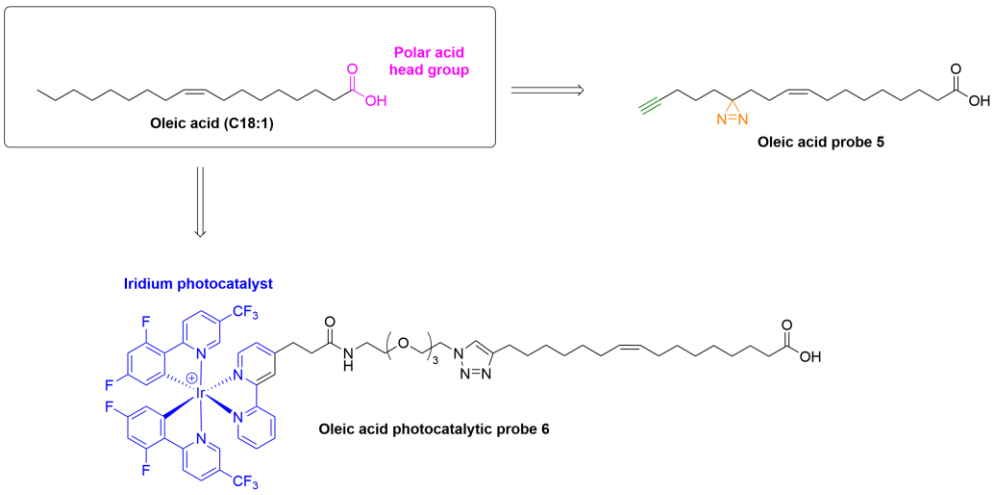

Figure 3.2: Proposed structures of oleic acid photoaffinity probe 5 and photocatalytic probe 6. Photoaffinity probe contains photoreactive diazirine group (orange) and terminal alkyne (green). Photocatalytic probe contains iridium-photocatalyst (blue). Both probes retain polar acid head group.

3.3 Chapter Aims:

Palmitic and oleic acid are two of the main FAs in the Western diet, however, an investigation into the interactomes of both FAs has not been performed in several tissues of interest, including breast cancer and the heart. This chapter, therefore, aims to synthesise both PAL and photocatalytic chemical probes of palmitic acid and oleic acid and PAL probes of some palmitic acid metabolites, with their intended use to investigate the protein interactions of both FAs in relevant cell lines. This was achieved through:

1. The design, synthesis, optimisation and purification of a palmitic acid PAL probe **1** in five synthetic steps.
2. The design, synthesis and purification of a photocatalytic palmitic acid probe **4** in eleven synthetic steps.
3. The design, synthesis and purification of two palmitic acid metabolite PAL probes: a palmitoyl-CoA and palmitoyl-carnitine PAL probes (**2** and **3**, respectively), both one step from the palmitic acid PAL probe.
4. The design and attempted synthesis of both a PAL and photocatalytic oleic acid probe (**5** and **6**, respectively).

3.4 Results:

3.4.1 Synthesis of palmitic acid photoaffinity probe 1

The synthesis of the palmitic acid probe **1** employed the route from the work of Haberkant *et al.*, which involved a synthetic route beginning with the Grignard addition of the protected alkyne **7** into an acid chloride **8**, forming ketone **9**, with subsequent silyl deprotection of the alkyne and ester hydrolysis to give acid **10** and concluded with the formation of a diazirine to form probe **1** (Scheme 3.1).[138] While this synthetic route was initially pursued, various stages of the process required optimization.

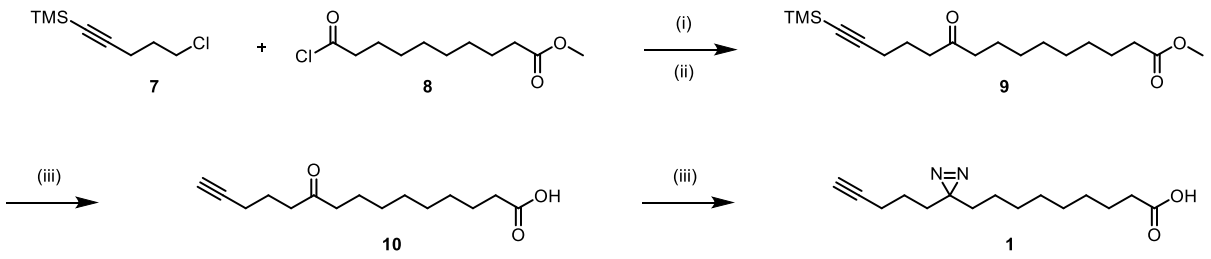

Scheme 3.1: Synthetic route to the palmitic acid probe 1 published in the literature. Reagents & conditions: (i) Mg, 1,2-dibromoethane, THF, 50°C, 12 h; (ii) THF, RT, 6 h, 66%; (iii) KOH, MeOH, 50°C, 12 h, 63%; (iv) NH_3, HOSA, I_2, MeOH, 4 °C - RT, 58%. Yields are quoted from Haberkant *et al.*[138]

The acid chloride **8** was synthesised using oxalyl chloride with catalytic DMF from the commercially available monomethyl sebacate **11** (Scheme 3.2). In exploring the selectivity of the mono-addition of the Grignard reagent, one equivalent of the commercially obtained pentylmagnesium bromide was used. This approach predominantly yielded alcohol **12**, the double addition product, with the desired ketone **13** formed as the minor product, in a 9:1 ratio, respectively. The mass balance was found to be starting material. Haberkant *et al*. synthesised ketone **9** in a reported 66% yield and did not comment on the selectivity of the reaction for addition into the acid chloride over the ester.

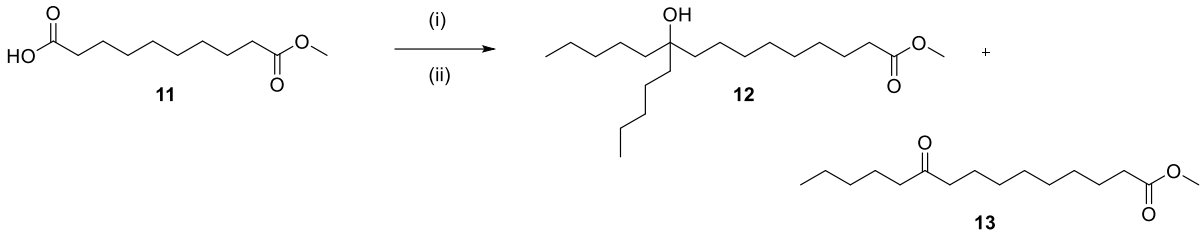

Scheme 3.2: Selectivity of the Grignard addition to give ketone 13. Reagents & conditions: (i) Oxalyl chloride, DMF (cat.), CH_2Cl_2, RT, 12 h; (ii) Pentyl magnesium bromide, THF, −78°C - RT, 12 h (9:1).

In an attempt to enhance selectivity for the monoalkylation product, catalytic amounts (3% w/w) of $Fe(acac)_3$ were introduced. Addition of $Fe(acac)_3$ increased selectivity of the reaction of acid chloride **8** and pentyl magnesium bromide for the ketone **13** to 1:1 and giving a 34% isolated yield (Scheme 3.3).[140,141]

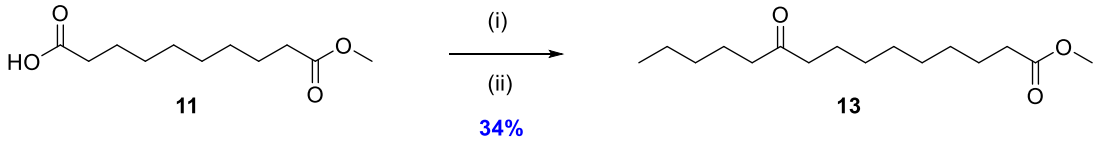

Scheme 3.3: Selectivity of the Grignard addition into the acid chloride. Reagents & conditions: (i) Oxalyl chloride, DMF (cat.), CH_2Cl_2, RT, 12 h; (ii) Pentyl magnesium bromide, $Fe(acac)_3$ (3% w/w), THF (anhyd.), −78°C - RT, 12 h, 34%.[32,33]

Due to the suboptimal selectivity of the Grignard addition into the acid chloride, an alternative method was also explored to reduce over-addition products, leading to the synthesis of the corresponding Weinreb amide **14** from **11**. The use of Weinreb amides avoids the over-addition into the carbonyl group. This is due to the stabilisation of the tetrahedral intermediate by chelation of the methoxy group to the magnesium, and therefore, at low temperature, collapsing of the tetrahedral intermediate, allowing for another addition, does not occur.[142] The synthesis of the desired Weinreb amide was achieved by subjecting monomethyl sebacate to an amide coupling with *N,O*-dimethylhydroxylamine using HATU, resulting in amide **14** in an 89% yield. Subsequent base hydrolysis of the ester **14**, using sodium hydroxide in methanol, gave the carboxylic acid **15** in 90% yield. Following this, a Grignard addition into compound **15** was examined using a commercially

available pentyl magnesium bromide solution involving the formation of the monoalkylation product, ketone **16** with a 73% yield (Scheme 3.4).

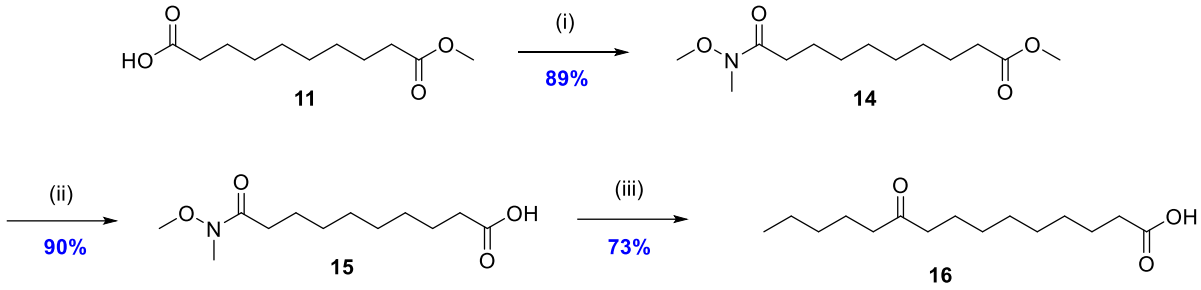

Scheme 3.4: Synthesis of ketone 16. Reagents & conditions: (i) N,O-dimethylhydroxylamine hydrochloride, HATU, NEt_3, CH_2Cl_2, RT, 20 h, 89%; (ii) NaOH, MeOH, RT, 20 h, 90%; (iii) Pentyl magnesium bromide, THF, −78°C - RT, 12 h, 73%.

After achieving adequate chemo selectivity in the Grignard addition, the addition was attempted with the required chloride **7** using the conditions developed by Haberkant *et al.* to form the Grignard reagent (Scheme 3.1). These conditions did not lead to the formation of the ketone **17** (Scheme 3.5).[138] An iodine/lithium chloride titration of the organomagnesium halide showed that the magnesium was not inserted into the C−Cl bond.[143] Therefore, more forcing conditions would be necessary to form an organomagnesium chloride. Following numerous attempts using the conditions by Haberkant *et al*. to form the desired Grignard, an alternative route was planned for the formation of the ketone **17**, where an Umpolung approach was used.

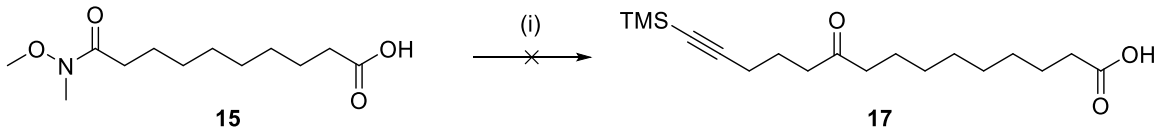

Scheme 3.5: Attempted formation of ketone 17 using a Weinreb amide approach. Reagents & conditions: (i) (5-Chloro-1-pentynyl)trimethylsilane, Mg, 1,2-dibromoethane, THF (anhyd.), −78°C - RT, 3 h.

The Umpolung approach attempted was the Corey-Seebach reaction, whereby a reversal of the reactivity of the acyl carbon atom allows for reactions with electrophiles, as the lithiated 1,3-dithiane can be used as a masked acyl anion.[144] The Umpolung approach involved the protection of 10-

hydroxydecanoic acid **18** using a TBS group to give acid **19**, which was subsequently reduced to alcohol **20**. The alcohol was then converted into a leaving group following reaction with tosyl chloride. Tosylate **21** was the electrophile for the Umpolung reaction (Scheme 3.6).

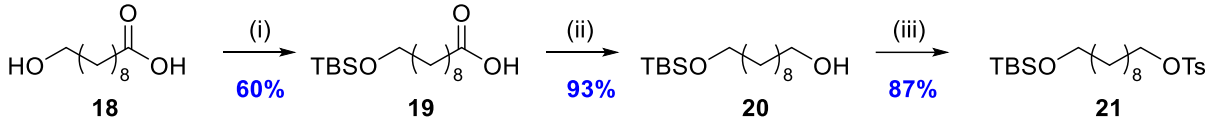

Scheme 3.6: Synthesis of tosylate 21. Reagents & conditions: (i) *Tert*-butyldimethylsilyl chloride, imidazole, DMF, 0 °C, 1h, 60%; (ii) $LiAlH_4$, THF (anhyd.), 0 °C - RT, 4h, 93%; (iii) Tosyl chloride, NEt_3, CH_2Cl_2, 0 °C, 12 h, 87%.[145–148]

The nucleophilic partner for the C-S reaction was prepared in two steps from alcohol **22**. Alcohol **22** was converted to the iodide **23** in 82% yield. 1,3-Dithiane was lithiated using *n*-BuLi and reacted with the electrophile **23**, giving the dithiane **24**. This was then subjected to another lithiation and reacted with tosylate **21** (Scheme 3.7).[144] However, the desired product **25** was not formed and an intramolecular carbo-lithiation occurred instead.[149,150] This reaction gave **26** as the product, as determined by NMR analysis (Figure 3.3).[149,150] Due to the preference for the intramolecular reaction, the tosylate **21** was used as the first electrophile to form dithiane **27** and then reacted with **23**. However, this did not result in the desired product **25** (Scheme 3.8), and only degradation of the starting material occurred. Multiple reaction attempts were performed, but compound **25** was not successfully synthesised.

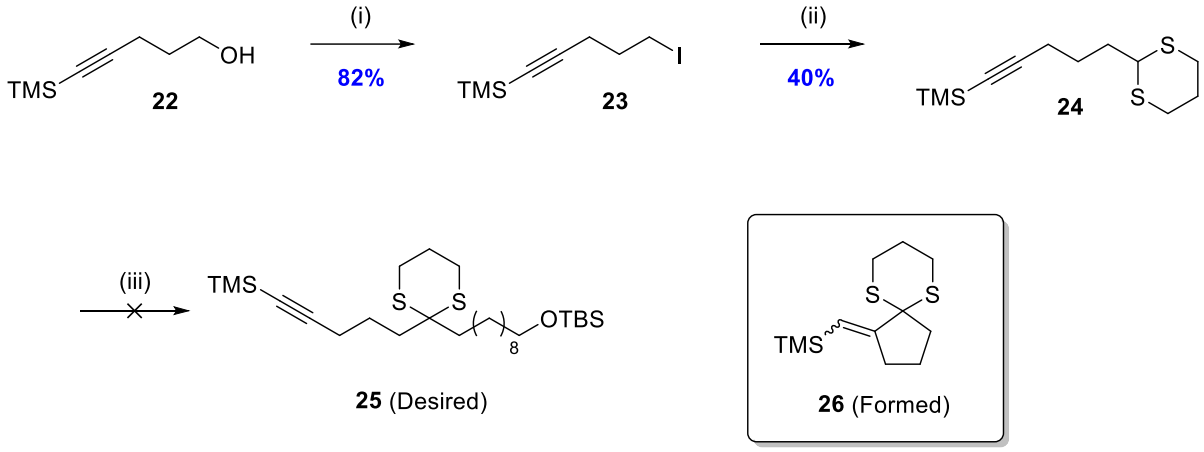

Scheme 3.7: Attempted synthesis of the protected ketone 25. Reagents & conditions: (i) I_2, PPh_3, THF (anhyd.), 0 °C - RT, 12 h, 82%; (ii) *n*-BuLi, 1,3-dithiane, THF (anhyd.), −78 °C, 4 h, 40%; (iii) *n*-BuLi, **21**, THF (anhyd.), −78 °C, 4 h.[144,151,152]

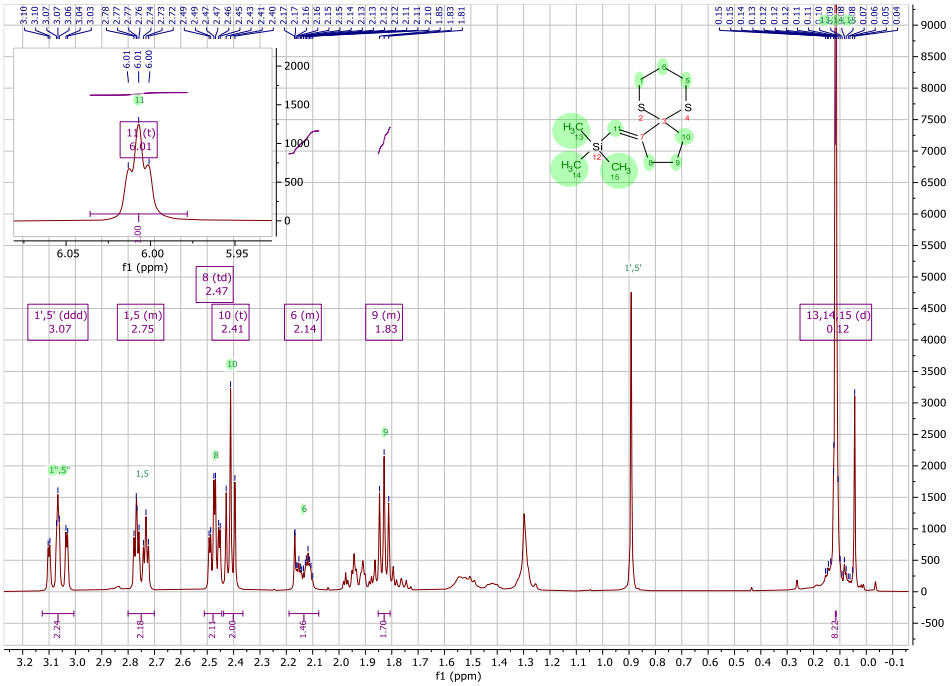

Figure 3.3: NMR assignment of the product 26 of reaction scheme 3.8.[149]

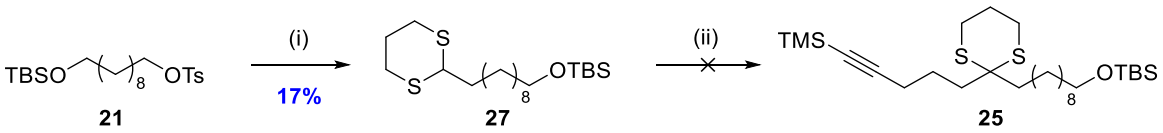

Scheme 3.8: Attempted synthesis of the protected ketone 25. Reagents & conditions: (i) *n*-BuLi, 1,3-dithiane, THF (anhyd.), −78 °C °C, 4 h, 17%; (ii) *n*-BuLi, THF (anhyd.), −78 °C °C, 4 h.[144]

Alternatively, a reaction optimisation for the Grignard formation was performed (Table 3.1) and resulted in the successful synthesis of the desired Grignard reagent. Optimised reaction conditions involved the activation of the magnesium turnings by both physical and chemical methods. Etching of the magnesium using a mortar and pestle and a combination of iodine and 1,2-dibromoethane added in catalytic amounts. Combining these methods allowed for the removal of the magnesium oxide layer from the metal turnings, allowing access for the alkyl chloride to react. The Grignard solution was then reacted with compound **15** to give ketone **17** in 79% yield (Scheme 3.9). Subsequent silyl deprotection using potassium carbonate in methanol gave compound **28**. To synthesise the photoreactive diazirine group, a solution of ketone **28** in methanol was treated with liquid ammonia, followed by hydroxylamine-*O*-sulfonic acid to obtain the diaziridine intermediate. This intermediate was then oxidised using excess iodine, giving the desired palmitic acid photoaffinity probe **1** in 20% yield.

Table 3.1: Summary of conditions used for the formation of the Grignard reagent used to synthesise ketone **17.**

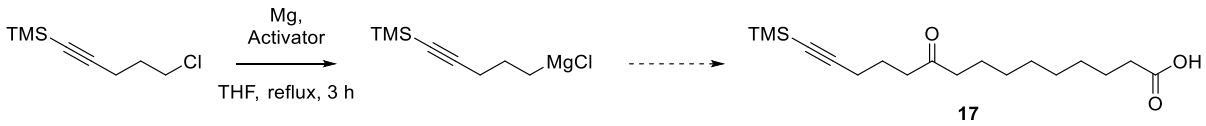

17

Entry	Activator	Mg (eq.)	Reaction outcome
1	1,2-DBE	1.2	No Grignard addition monitored by ^{1}H NMR
2	I_2	1.2	No Grignard addition monitored by ^{1}H NMR
3	I_2	2	No Grignard addition monitored by ^{1}H NMR
4	I_2 & 1,2-DBE	2	79% yield of the desired product

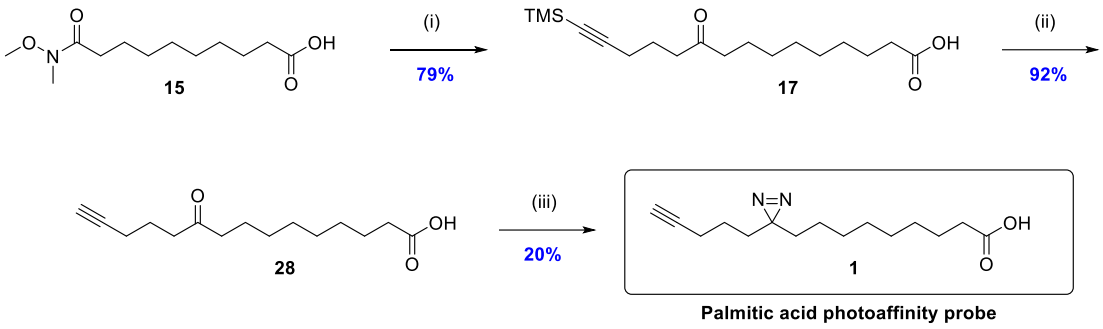

Scheme 3.9: Optimised synthesis of palmitic acid photoaffinity probe 1. Reagents & conditions: (i) (5-Chloro-1-pentynyl)trimethylsilane, Mg, 1,2-dibromoethane (cat.), I_2 (cat.), THF, −78 °C - RT, 3 h, 79%; (ii) K_2CO_3, MeOH, RT, 16 h, 92%; (iii) NH_3, HOSA, I_2, MeOH, 4°C - RT, 20%.[138]

In order to confirm that upon irradiation with a 365 nm UV lamp diazirine **1** (MW = 264 g/mol) is activated, a test reaction was performed where a sample of diazirine **1** (0.1 mg) was irradiated in methanol for 3 min. Mass spectrometry analysis confirmed the formation of the methanol and water addition product (*m/z* $[M+H]^+$ 267 and 253, respectively) following the conversion of the diazirine to the carbene and insertion of the highly reactive species into the C−H bond of the solvent and water, respectively (Figure 3.4).



Figure 3.4: Mass spectrum of the photoirradiation of probe 1 in methanol: Probe **1** (0.1 mg) was irradiated in MeOH (0.5 mL) at 365 nm for 3 min. *m/z* 263 corresponds to probe **1**, *m/z* 267 corresponds to methanol-insertion product and *m/z* 253 corresponds to water-insertion product.

3.4.2 Synthesis of palmitoyl-CoA photoaffinity probe 2

The synthesis of palmitoyl-CoA photoaffinity probe **2** was based on work by Fedoryshchak *et al.* that synthesised a myristoyl-CoA photoaffinity probe using CDI as the acid activating reagent to

form the thioester.[123] Palmitic acid photoaffinity probe **1** was first activated using CDI and was then reacted with coenzyme A in a mixture of THF and $NaHCO_3$ (aq.). Degassing of the coenzyme A solution with N_2 was necessary for the reaction, presumably to suppress oxidation of CoASH to the corresponding disulfide. These conditions allowed the formation of the palmitoyl-CoA photoaffinity probe **2** in 20% yield (Scheme 3.10).

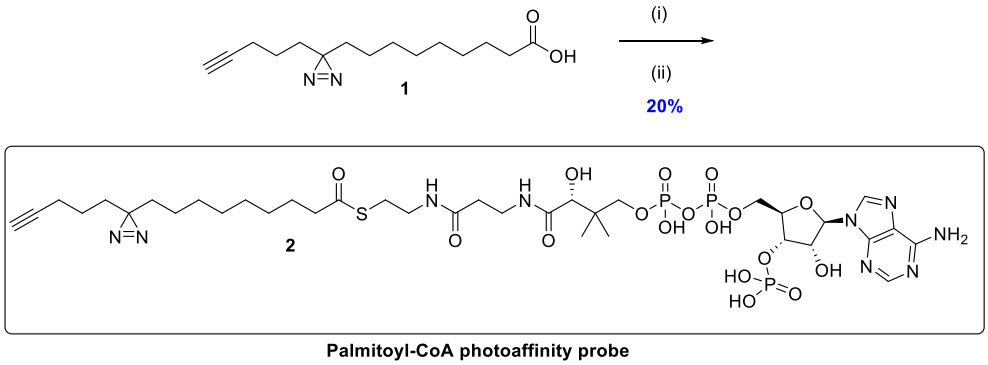

Scheme 3.10: Synthesis of palmitoyl-CoA photoaffinity probe 2. Reagents & conditions: (i) CDI, THF (anhyd.), RT, 30 min; (ii) Coenzyme A, $NaHCO_3$ (aq.) (0.5 M), THF, RT, 4 h, 20%.[123]

As with the previous probe, UV irradiation (3 min) followed by mass spectrometry confirmed the reactivity of diazirine **2** with methanol and water (*m/z* $[M+3Na]^+$ 1085 and 1071, respectively)

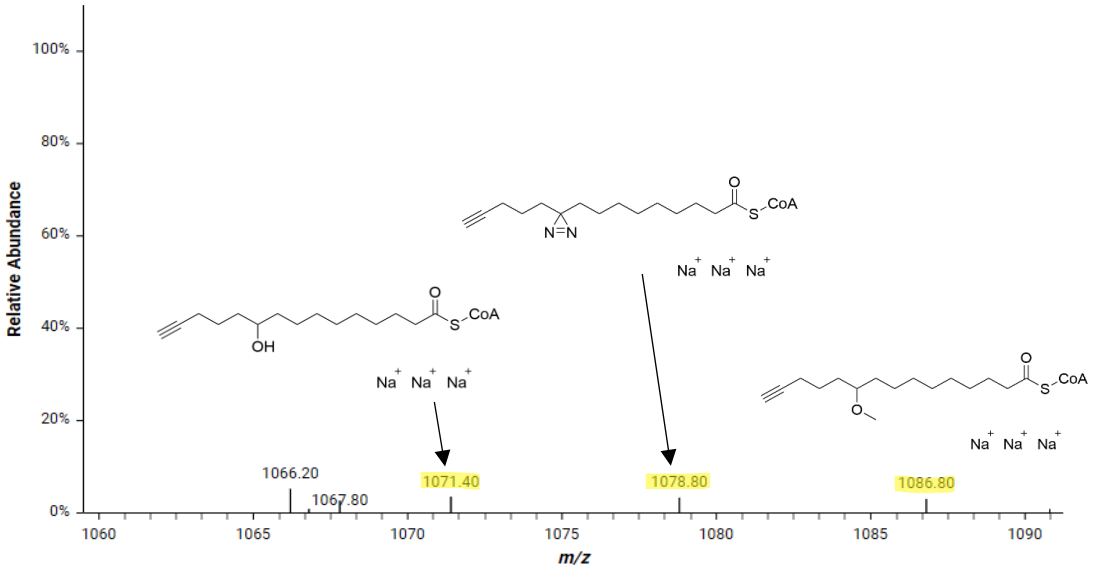

(Figure 3.5).

Figure 3.5: Mass spectrum of the photoirradiation of probe 2 in methanol: Probe **2** (0.1 mg) was irradiated in MeOH (0.5 mL) at 365 nm for 3 min. *m/z* $[M+3Na]^+$ 1078 corresponds to probe **2**, *m/z* $[M+3Na]^+$ 1086 corresponds to methanol-insertion product and *m/z* $[M+3Na]^+$ 1071 corresponds to water-insertion product.

3.4.3 Synthesis of palmitoyl-carnitine photoaffinity probe 3

Palmitic acid photoaffinity probe **1** was converted into the palmitoyl-carnitine photoaffinity probe **3** through the conversion of compound **1** into the equivalent acid chloride and immediately reacting with *L*-carnitine, giving **3** in 43% yield (Scheme 3.11).[153] No optimisation was performed for this reaction. Mass spectrometry confirmed the reactivity of diazirine **3** in methanol, giving the masses for the methanol and water insertion products (*m/z* $[M+H]^+$ 410 and 397, respectively) (Figure 3.6).

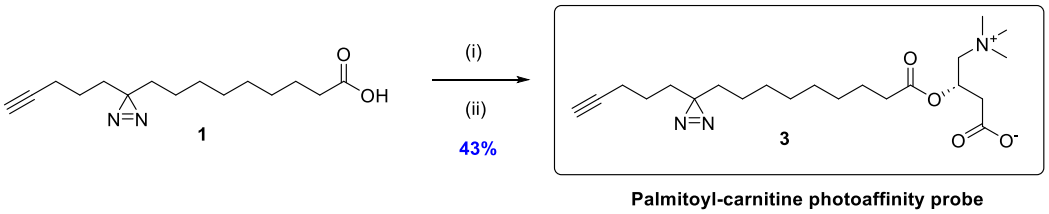

Scheme 3.11: Synthesis of palmitoyl-carnitine photoaffinity probe 3. Reagents & conditions: (i) Oxalyl chloride, DMF (cat.), CH_2Cl_2, RT, 12 h (ii) *L*-carnitine, THF, 43%.[153]

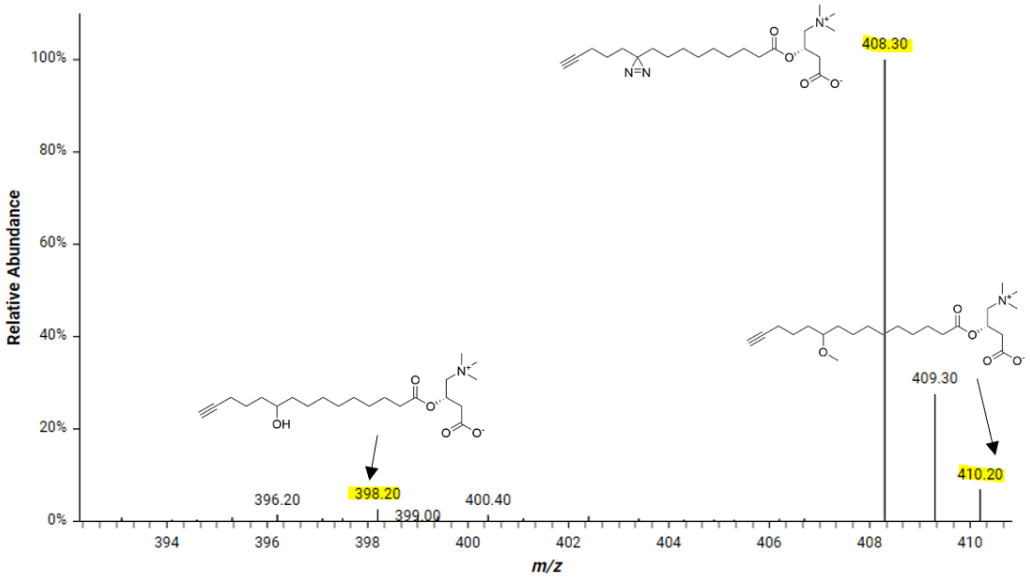

Figure 3.6: Mass spectrum of the photoirradiation of probe 3 in methanol: Probe **3** (0.1 mg) was irradiated in MeOH (0.5 mL) at 365 nm for 3 min. m/z $[M+H]^+$ 408 corresponds to probe **2**, m/z $[M+H]^+$ 410 corresponds to methanol-insertion product and m/z $[M+H]^+$ 398 corresponds to water-insertion product.

3.4.4 Synthesis of photocatalytic iridium palmitate probe 4

The synthesis of palmitic acid photocatalytic probe **4** was influenced by the methods previously developed by Geri *et al.* This synthetic route involved the synthesis of the photocatalytic iridium catalyst, the subsequent addition of a PEG linker and the attachment of the molecule of interest. The

palmitic acid unit needed to be functionalised with an alkyne to allow for attachment via a PEG-3-azide linker to the iridium photocatalyst using a CuAAC reaction (Scheme 3.12).

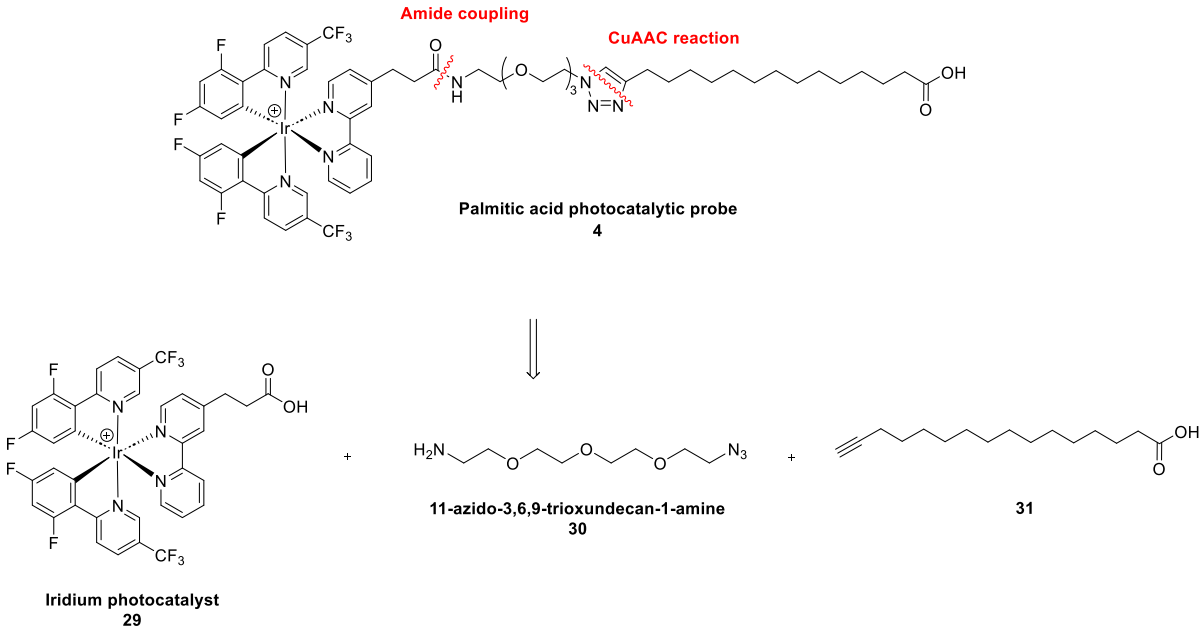

Scheme 3.12: Retrosynthetic analysis of palmitic acid photocatalytic probe 4

The initial stage of the synthetic route focused on the cell-permeable photocatalyst **29**. The synthesis of the first ligand for the catalyst, was achieved through the alkylation of bipyridine **32** with ethyl 2-bromoacetate in the presence of LDA. This reaction yielded ester **33** in 55% yield. This then underwent a base ester hydrolysis using lithium hydroxide, producing ligand **34** in 85% yield (Scheme 3.13). The second ligand for the photocatalyst, ligand **35** was synthesised through a Suzuki coupling yielding ligand **35** in a 63% (Scheme 3.14).

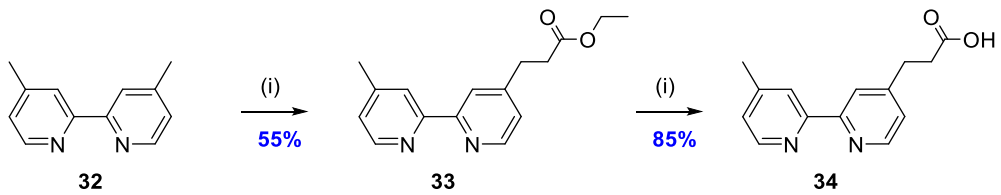

Scheme 3.13: Synthesis of ligand 34. Reagents & conditions: (i) Lithium diisopropylamide (1.0 M in THF/heptane/ethylbenzene), ethyl 2-bromoacetate, THF, −78 °C - RT, 16 h, 55%; (ii) LiOH, THF, RT, 16 h, 85%.[124]

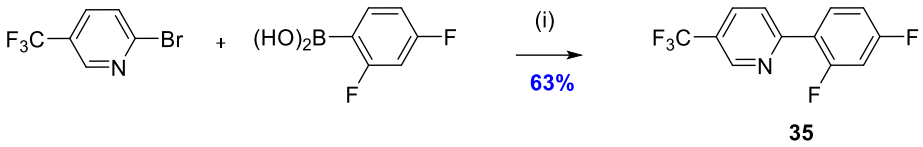

Scheme 3.14: Synthesis of ligand 35. Reagents & conditions: (i) $Pd(dppf)Cl_2$, Cs_2CO_3, 1,4-dioxane, 100 °C, 16 h, 63%.[154,155]

The synthesis of the palmitate unit of probe **4** started with the reduction of 14-tetradecanoic acid **36** using lithium aluminium hydride to produce the bis-alcohol **37** in 85% yield. This was followed by mono-bromination with hydrobromic acid, resulting in compound **38** with 52% yield. This reaction was monitored by TLC to avoid over-bromination occurring, to maximise the yield of the reaction. Compound **38** was then oxidised using Jones' reagent to yield the carboxylic acid **39** in 78% yield. A subsequent lithiation of (trimethylsilyl)acetylene and S_N2 reaction with the bromide **39** led to the formation of the silyl-protected alkyne **40** in 50% yield. The final stage involved the silyl deprotection using potassium carbonate in methanol, which produced the palmitic acid-alkyne **31** with 79% yield (Scheme 3.15).

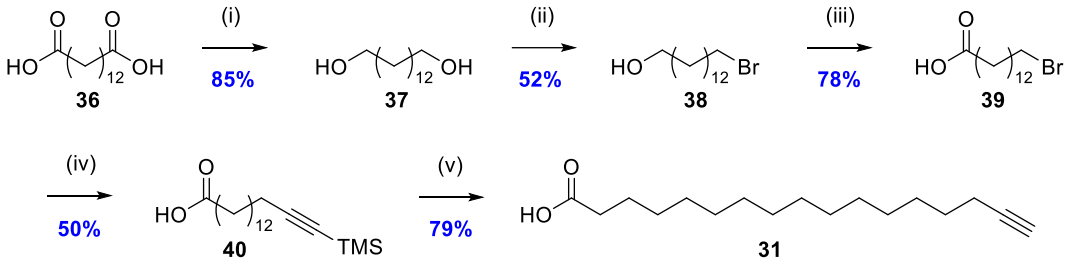

Scheme 3.15: Synthesis of palmitic acid-alkyne 31. Reagents & conditions: (i) $LiAlH_4$ (1.0 M in THF), THF, 0 ˚C - RT, 20 h, 85%; (ii) HBr (48%), C_6H_{12}, reflux, 16 h, 52%; (iii) Jones' reagent (2.0 M CrO_3 in aq. H_2SO_4), acetone, 16 h, 78%; (iv) (trimethylsilyl)acetylene, *n*-BuLi, THF, −78 °C - RT 16 h, 50%; (v) K_2CO_3, MeOH, RT, 79%.[156–159]

The iridium photocatalyst was synthesised by reacting $IrCl_3$ with 2.0 equivalents of ligand **35**, resulting in the formation of iridium dimer **41** with a yield 71%. This dimer was then transformed into the iridium monomer **42** with a yield of 58%, using silver hexafluorophosphate in acetonitrile. Following the reaction of ligand **34** with monomer **42**, the iridium photocatalyst **29** was obtained in 95% yield (Scheme 3.16). The final steps of the photocatalytic probe synthesis were to combine the three building blocks, using an amide coupling and CuAAC reaction. The amide coupling reaction

between **29** and azido **30** was performed using EDC as the coupling agent and DMAP as the base, resulting in the iridium-linker conjugate **43** with 67% yield. The final step involved a CuAAC reaction between **43** and palmitic acid-alkyne **31**, using copper(II) sulphate, DIPEA, and sodium ascorbate, achieving a yield of 65% (Scheme 3.16).

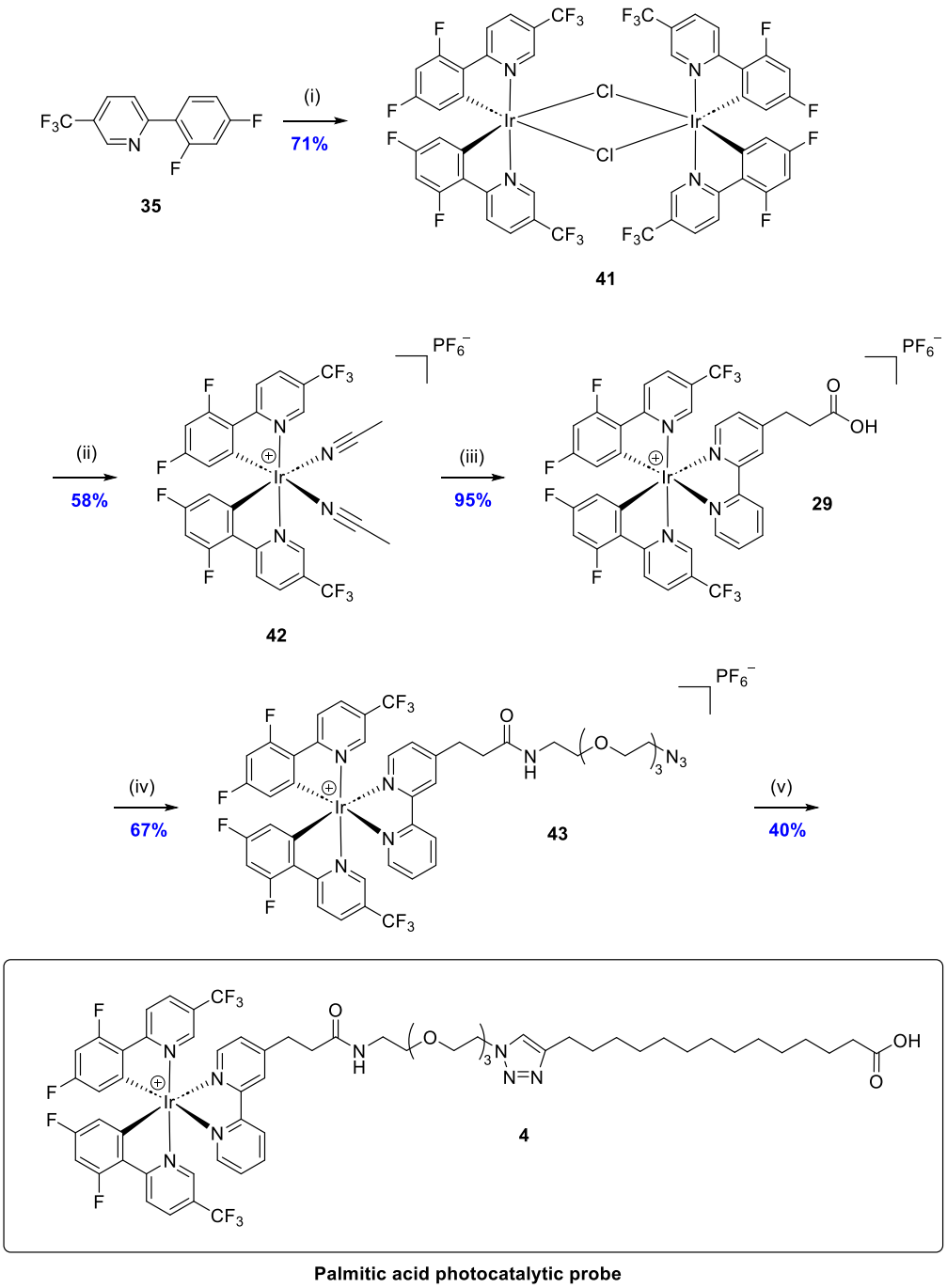

Scheme 3.16: Synthesis of the palmitic acid photocatalytic probe 4. Reagents & conditions: (i) $IrCl_3.H_2O$, 2-ethoxyethanol, H_2O, 135 °C, 12 h, 71%; (ii) $AgPF_6$, CH_2Cl_2 (anhyd.), MeCN, 55 °C, 20 h, 58%; (iii) **34**, CH_2Cl_2/EtOH, 30 °C, 16 h, 95%; (iv) **30**, NEt_3, EDC, DMAP, MeCN, RT, 12 h, 67%; (v) **31**, DIPEA, $CuSO_4$, sodium ascorbate, MeCN/H_2O, RT, 16 h, 40%.[124]

The synthesis of the diazirine-biotin labelling reagent **44** involved an amide coupling reaction between (4-(3-(trifluoromethyl)-3*H*-diazirin-3-yl)phenyl)methanamine hydrochloride and a biotin-PEG3-NHS-ester. This reaction yielded the diazirine-biotin-conjugate **44** in 60% yield (Scheme 3.17).

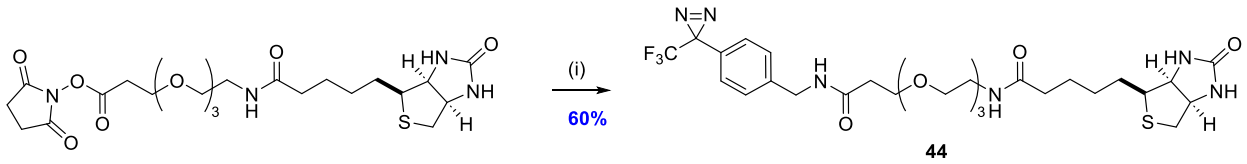

Figure 3.17: Synthesis of biotin-diazirine conjugate 44. Reagents & conditions: (i) (4-(3-(trifluoromethyl)-3*H*-diazirin-3-yl)phenyl)methanamine hydrochloride, DMF, RT, 16 h, 60%.[124]

To confirm that upon photoirradiation of the palmitic acid photocatalytic probe **4** with 440 nm, the Dexter energy transfer (Figure 3.7) to the biotin-diazirine conjugate **44** was occurring, a test reaction was performed. Probe **4** (0.1 mg, 0.072 µmol) was added to a solution of **44** (0.05 mg, 0.072 µmol) in methanol. This solution was irradiated for 3 min and subjected to mass spectrometry (Figure 3.8). The mass spectrum confirmed the presence of **44** (*m/z* $[M+K]^+$ 683), but also the presence of the methanol insertion product (*m/z* $[M+K]^+$ 687) and water insertion product (*m/z* $[M+K]^+$ 673). The same experiment was repeated without the presence of the photocatalyst present (Figure 3.9). The mass spectrum only found the mass corresponding to the labelling reagent **44** but not the methanol or water insertion products. This result confirmed that the Dexter energy transfer was only occurring when the photocatalyst was present and activation of the biotin labelling molecule was not occurring at 440 nm.

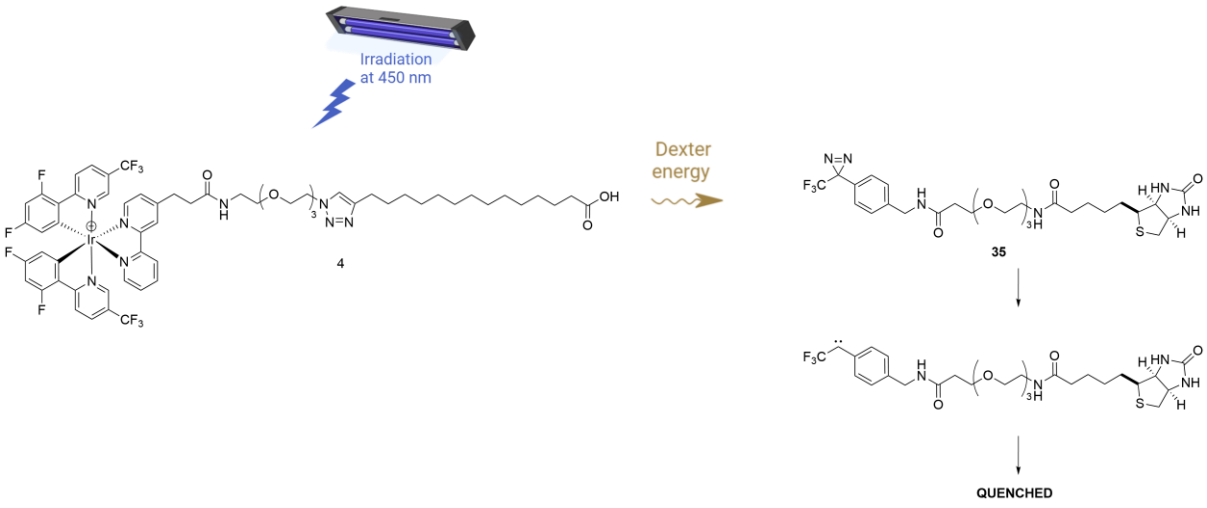

Figure 3.7: Mechanism of the Dexter energy transfer from probe 4 to biotin-diazirine conjugate 44 following irradiation with 440 nm.[124]

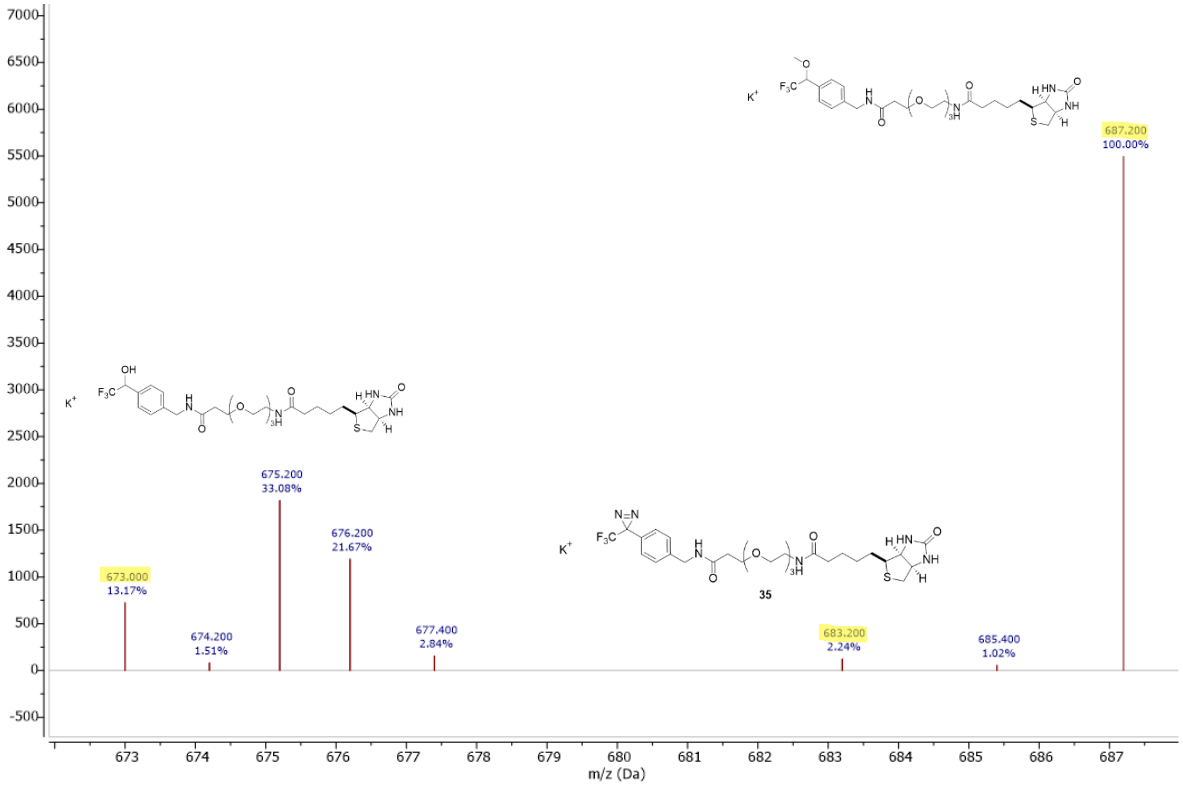

Figure 3.8: Mass spectrum of the photoirradiation of probe 4 and biotin-diazirine conjugate 44 in methanol: Probe **4** (144 µM) and biotin-diazirine conjugate **44** (144 µM) were irradiated in MeOH (0.5 mL) at 440 nm for 3 min. *m/z* 683 corresponds to **44**, *m/z* 687 corresponds to methanol-insertion product and *m/z* 673 corresponds to water-insertion product.

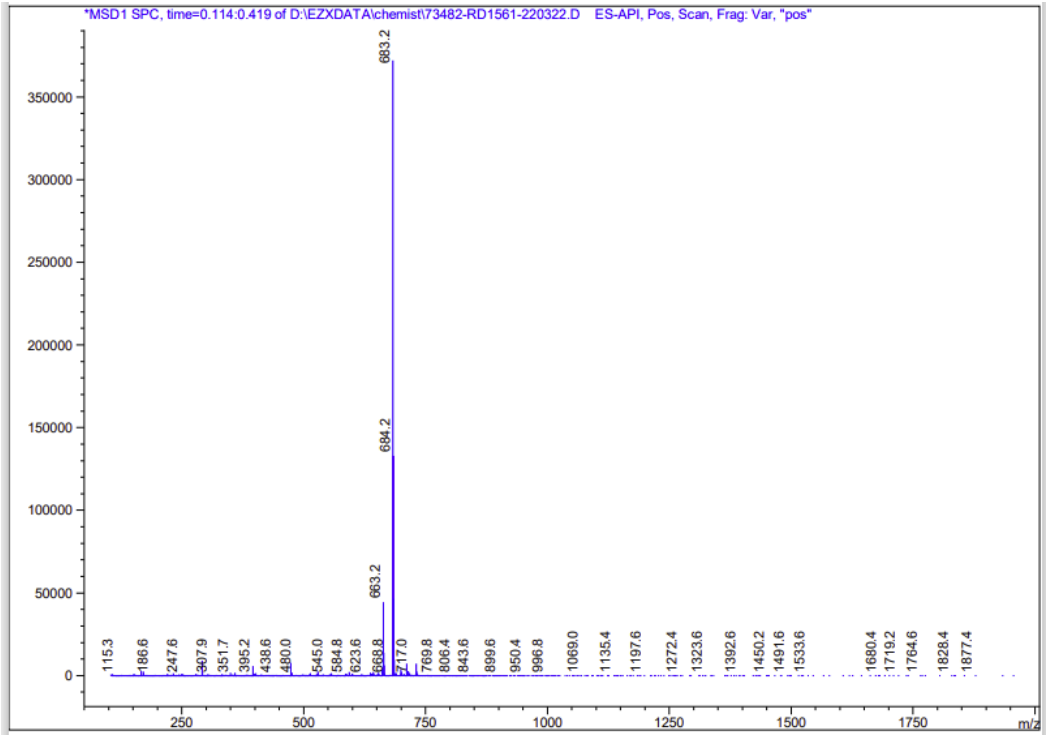

Figure 3.9: Mass spectrum of the photoirradiation of 44 in the absence of the probe 4 using 440 nm: 44 (144 µM) was irradiated in MeOH (0.5 mL) at 440 nm for 3 min. *m/z* 683 corresponds to **44.** No masses corresponding to the methanol or water insertion products (m/z $[M+K]^+$ 687 or m/z $[M+K]^+$ 673, respectively) were obtained.

3.4.5 Attempted synthesis of oleic acid photoaffinity probe 5

The synthesis of oleic acid photocatalytic probe **5** (Figure 3.10) was influenced by the methods previously developed by Niphakis *et al.*[139] Butane-1,4-diol was mono-protected using a *tert*-butyl silyl group to give **45**, which was oxidised using the Swern oxidation method to the aldehyde **46**. A Grignard addition was performed on aldehyde **46** using the Grignard conditions optimised in Table 3.1 and (5-chloro-1-pentynyl)trimethylsilane, to give alcohol **47**, which was deprotected using TBAF, giving the bis alcohol **48**. The purification of **48** proved difficult, as tetrabutylammonium salts were difficult to remove. Therefore, following reaction completion, the crude mixture was stirred with Dowex 50WX8 (200-400 mesh) following the conditions optimised by McDermott *et al.*[160] This resulted in removing TBA from the mixture and gave product **48** in 74% yield. The bis-alcohol **48** was then oxidised using Swern oxidation conditions to give compound **49**. This was the aldehyde used in the Wittig reaction to form the alkene of oleic acid (Scheme 3.18).

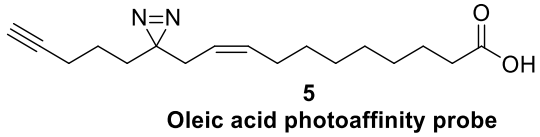

5
Oleic acid photoaffinity probe

Figure 3.10: Chemical structure of oleic acid photoaffinity probe 5

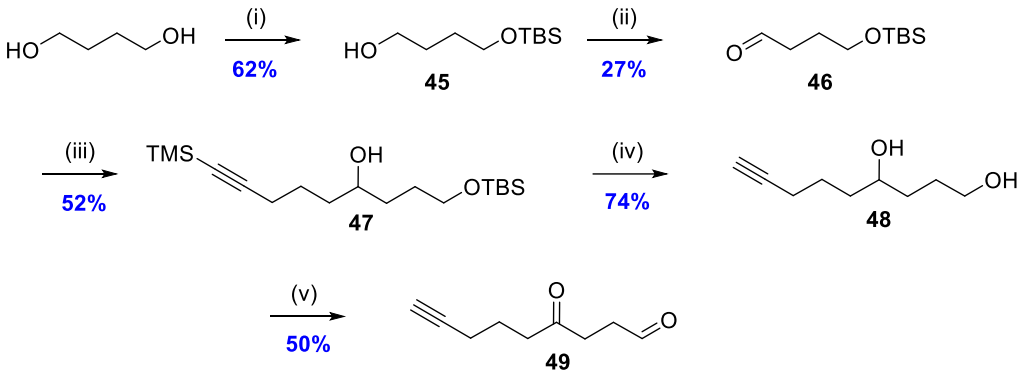

Scheme 3.18: Synthesis of aldehyde 49. Reagents & conditions: (i) *tert*-Butyldimethylsilyl chloride, imidazole, DMF (anhyd.), 0 °C, 1 h, 62%; (ii) DMSO, oxalyl chloride, CH_2Cl_2 (anhyd.), −78 °C - RT, 2 h, 27%; (iii) (5-chloro-1-pentynyl)trimethylsilane, Mg, 1,2-dibromoethane, I_2, THF (anhyd.), −78 °C - RT, 3 h, 52%; (iv) TBAF, THF (anhyd.), 0 °C - RT, 2 h, 74%; (v) DMSO, oxalyl chloride, CH_2Cl_2 (anhyd.), −78 °C - RT, 2 h, 50%.[139,160–162]

For the Wittig reaction, phosphonium salt was synthesized starting from 9-bromononan-1-ol. The alcohol was oxidised using Jones' reagent to carboxylic acid **50**. The phosphonium salt **51** was synthesised by the alkylation of triphenylphosphine with the alkyl bromide **50**, giving the quaternary phosphonium **51** in 87% yield, without chromatographic purification (Scheme 3.19).

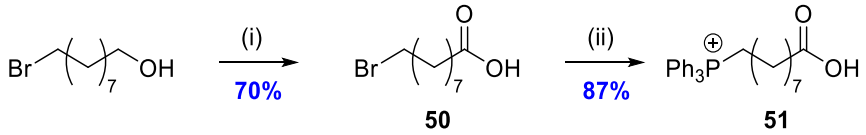

Scheme 3.19: Synthesis of phosphonium salt 51. Reagents & conditions: (i) Jones' reagent (2.0 M CrO_3 in aq. H_2SO_4), acetone, RT, 20 h, 70%; (ii) PPh_3, MeCN, reflux, 48 h, 87%.[163,164]

The phosphonium salt **51** was then deprotonated to give an ylide intermediate which was reacted with aldehyde **49** to give both the *Z* (**52**) and the *E* (**53**) geometric alkene isomers in an 85:15 ratio (Scheme 3.20). The desired isomer for the oleic acid probe was the *Z*-alkene (**52**), therefore separation of the isomers was necessary. This proved to be very difficult, as using $AgNO_3$ impregnated silica (2.5% w/w) for chromatography did not result in successful separation of the isomers. Also due to lack of material and time, the diazirine reaction using ketone **52** (Scheme 3.21) to form the oleic acid photoaffinity probe **5** was not attempted, as this reaction's yield averages between 10-45% yield.[165]

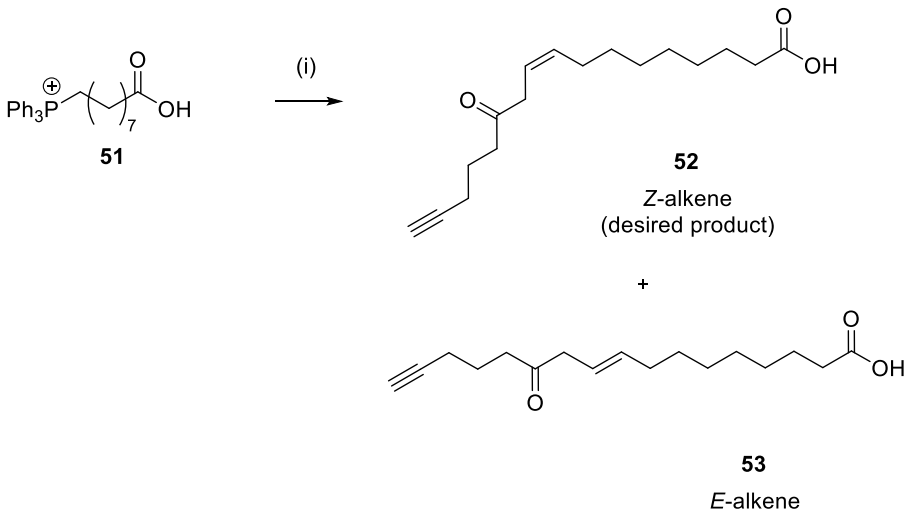

Scheme 3.20: Synthesis of alkene 52 for probe 5. Reagents & conditions: (i) **49**, LiHMDS, DMPU, THF (anhyd.), −78 °C, 1 h.[139]

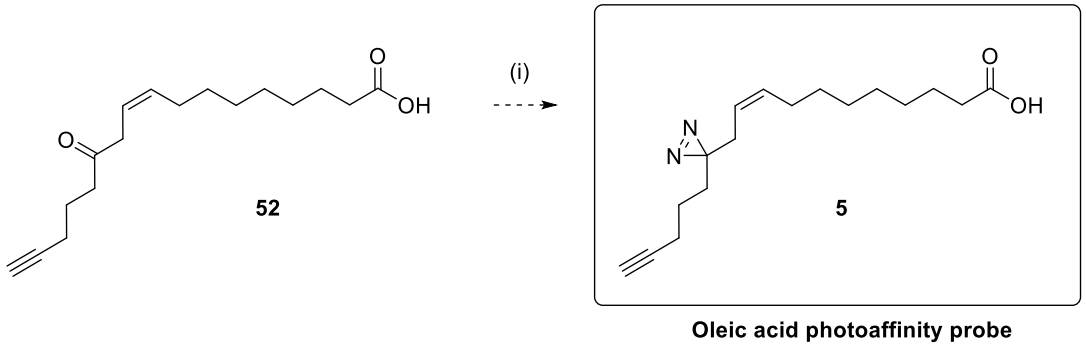

Scheme 3.21: Proposed final step for the formation of the diazirine of probe 5 from ketone 52. Reagents & conditions: (i) $NH_{3\,(g)}$, HOSA, I_2, MeOH, 4°C - RT.[139]

3.4.6 Attempted synthesis of oleic acid photocatalytic probe 6

The synthesis of a photocatalytic probe of oleic acid was also planned and attempted. The route involved a Wittig reaction to form the alkene of the oleate unit and then a CuAAC Click reaction to attach the oleate unit to the iridium photocatalyst (Scheme 3.22)

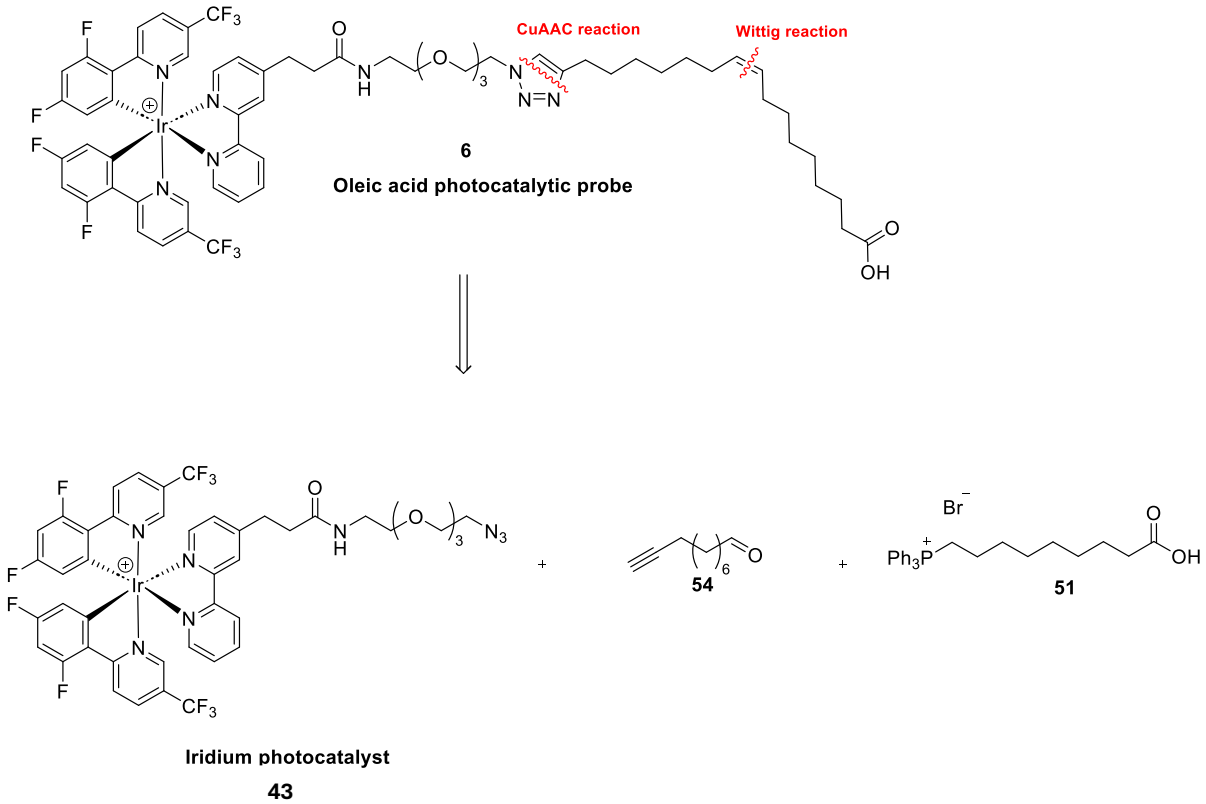

Scheme 3.22: Retrosynthetic analysis of palmitic acid photocatalytic probe 6

This route involved the oxidation of dec-9-yn-1-ol to the equivalent aldehyde **54** using the PCC oxidation method. This aldehyde was then reacted with the quaternary phosphonium salt **51** from Scheme 3.19 in a Wittig reaction, but this did not result in the formation of the alkene product **55** (Scheme 3.23). By NMR analysis, the starting materials were still present, with no product formation. However, if compound **55** had been successfully synthesised, the final step would have been a CuAAC reaction with the iridium-linker conjugate **43** from Scheme 3.16 to give the final photocatalytic oleic acid probe **6** (Scheme 3.24).

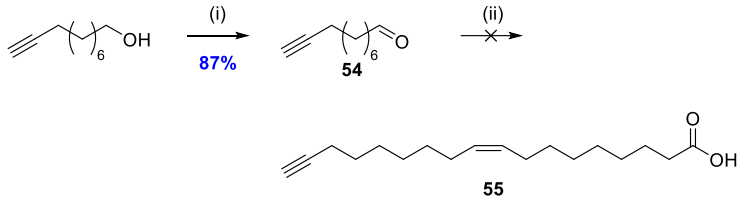

Scheme 3.23: Synthesis of alkene 55. Reagents & conditions: (i) PCC, MS4Å, CH_2Cl_2 (anhyd.), RT, 30 min, 87%; (ii) LiHMDS, DMPU, THF (anhyd.), −78 °C, 1 h.[166]

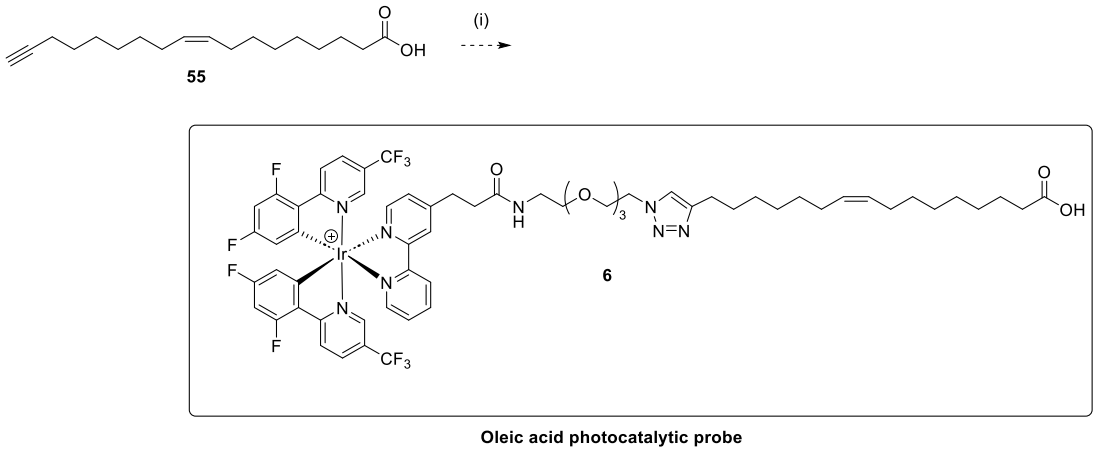

Scheme 3.24: Proposed final step for the formation of probe 6. Reagents & conditions: (i) **43**, DIPEA, $CuSO_4$, sodium ascorbate, MeCN/H_2O, RT, 16 h.[124]

3.5 Discussion & Conclusion

This chapter describes the design and synthesis of several FA and FA metabolite photoaffinity and photocatalytic probes, compounds **1**, **2**, **3**, **4**, **5** and **6** (chemical structures in Figure 3.10). Probes **1** and **4** are based on the structure of palmitic acid, a 16-carbon FA, with probes **2** and **3** based on metabolites of palmitic acid, palmitoyl-CoA and palmitoyl-carnitine, respectively. The other two probes, **5** and **6** are based on the structure of the monounsaturated 18-carbon FA, oleic acid. The photoaffinity probes (**1**, **2**, **3** and **4**) contain a diazirine photoreactive group, for tagging proteins and a terminal alkyne handle for further functionalisation (biotin or fluorophore). The photocatalytic probes are based on a recently published labelling technique, consisting of the FAs of interest linked to an iridium-centred photocatalyst.[124] This photocatalyst, once photo-irradiated at 440 nm, can initiate protein labelling via a Dexter energy transfer to a biotin-diazirine conjugate. Mass spectrometry confirmed that successfully synthesised probes **1**, **2**, **3** and **4** were activated upon photoirradiation and formed the reactive carbene species necessary for protein labelling. The oleic acid probe synthesis for both the photoaffinity and photocatalytic probes was unsuccessful at forming the alkene. Further optimisation of both the reaction conditions and the purification technique would be necessary to successfully obtain **5** and **6** as the correct geometric isomers.

In conclusion, probes **1 – 4** were taken forward, probe **1** (the palmitic acid photoaffinity probe) was used in *Chapters 4, 5 & 6* and probes **2**, **3** and **4** (the palmitoyl-CoA and palmitoyl-carnitine photoaffinity probes and photocatalytic palmitic acid probe, respectively) were used in *Chapter 7*.

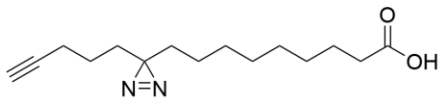

Palmitic acid photoaffinity probe **1**

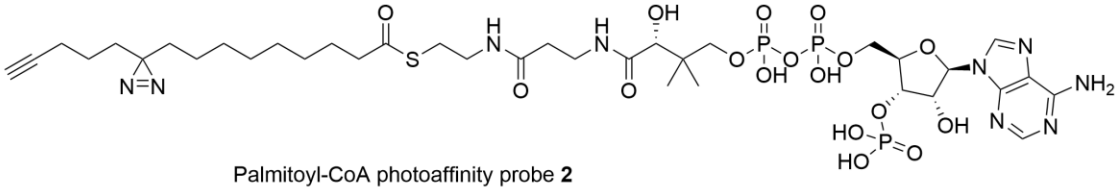

Palmitoyl-CoA photoaffinity probe **2**

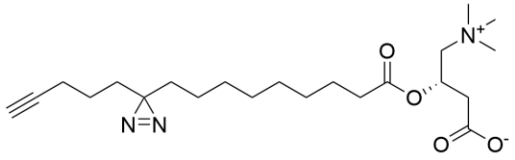

Palmitoyl-carnitine photoaffinity probe **3**

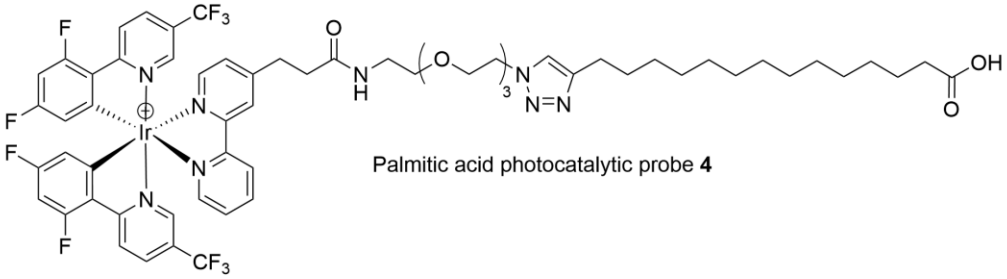

Palmitic acid photocatalytic probe **4**

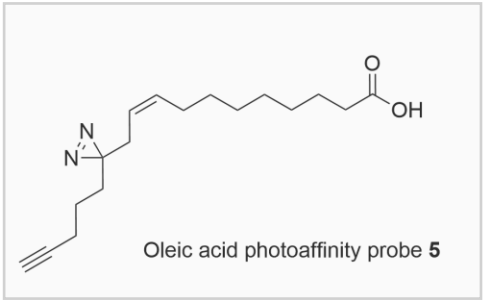

Oleic acid photoaffinity probe **5**

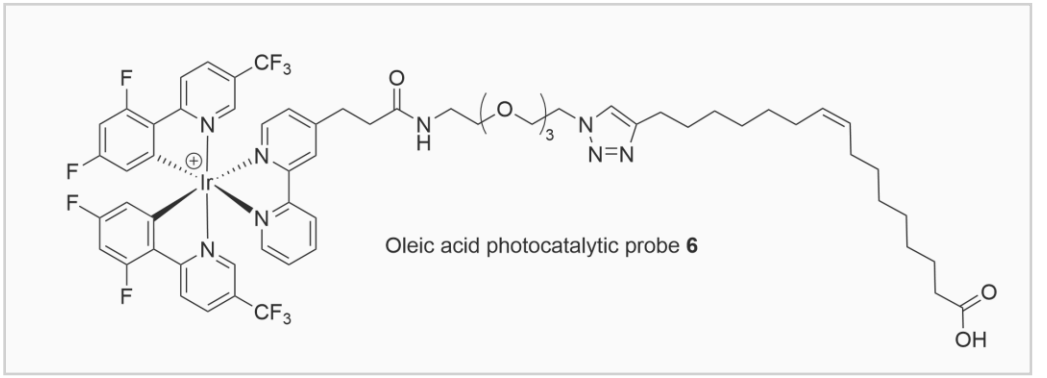

Oleic acid photocatalytic probe **6**

Figure 3.10: Chemical structures of fatty acid probes. Structures in grey could not be prepared.

Chapter 4

Development and Optimisation of a Photoaffinity Palmitate Probe **1** Workflow in *MDA-MB-231* cells

4.1 Abstract

FAs are the predominant fuel in the body, and they have many important functions. Too much FA metabolism can contribute to many diseases including cardiac complications that occur in type 2 diabetes. However, we do not currently understand with which proteins fatty acids, or their metabolites interact within cells, and how this regulates cell function. In this chapter, techniques for utilising probe **1**, a photoaffinity palmitate probe, were developed and optimised in *MDA-MB-231* cells, and the effects of probe **1** on cell function were investigated.

MD-MB-231 cells were incubated with probe **1** at various concentrations, with and without UV radiation, and the effect on protein labelling was confirmed using Click chemistry and Western blotting. Protein labelling occurred in the absence of UV irradiation, most likely due to covalent interactions and this labelling was concentration dependent. With the addition of the UV irradiation step, more proteins were labelled, most likely due to capturing the additional non-covalent interactions. Palmitate is known to interact with proteins in both a covalent (palmitoylation) and non-covalent manner. Protein labelling was decreased when cells were co-treated with palmitate, demonstrating that probe **1** was capturing palmitate interactors. Confocal microscopy was used for visualisation of probe **1** in cells, and this highlighted localisation in both the cell cytoplasm and nucleus and demonstrated that mitochondrial fragmentation was not occurring. Nuclear integrity following UV irradiation was shown to be unaffected by probe **1** treatment, confirming that the localisation of probe **1** in the nucleus was due to uptake and not nuclear damage. Incubation of probe **1** did not result in an increase in glycolysis, as measured by lactate production and glucose consumption rates in cell media. Probe **1** was shown to not be metabolised by isolated mitochondria for ADP-stimulated state 3 respiration when compared with palmitoyl-CoA and palmitate. Optimisation of a neutravidin-biotin pulldown allowed for further analysis of these protein interactors by proteomics.

Collectively, these results demonstrate that probe **1** is a suitable mimic for palmitate and that a workflow had been optimised to explore various elements of palmitate metabolism and biology in different cell lines.

4.2 Introduction

According to the World Health Organisation (WHO) breast cancer is the most frequently diagnosed cancer in women worldwide, with 2.3 million women diagnosed in 2022.[167] The *MDA-MB-231* cell line, isolated from a patient with invasive ductal carcinoma, is commonly used to model late-stage breast cancer.[168] This cell line is estrogen receptor (ER), progesterone receptor (PR), and human epidermal growth factor receptor 2 (HER2) negative and expresses mutated p53, a tumour suppressor protein [169] , therefore, these cells represent a good model of triple-negative breast cancer (TNBC). Dysregulation of FA metabolism is now recognised as playing a role in many different cancer types, including breast. As these cells are cancer cells, they preferentially utilise glycolysis (Warburg effect) for energy production but can shift their metabolism towards β-oxidation depending on substrate availability.[47] Therefore, as these cells are highly proliferative, an advantage when large numbers of cells are required for probe labelling experiments, and can metabolise FAs but had not been exposed to them prior to probe labelling studies, it was decided that this cell line would be a good model for testing the metabolic incorporation of probe **1** (Figure 4.1). [182]

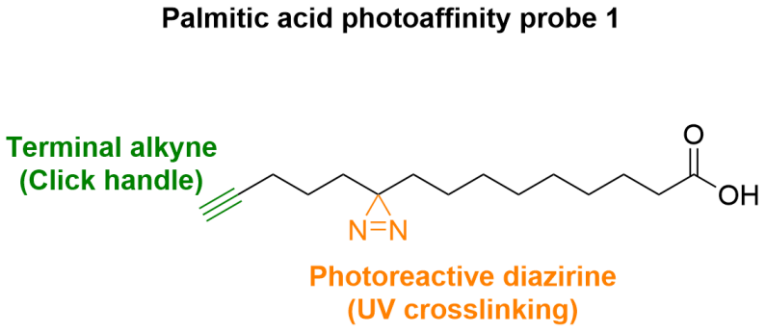

Figure 4.1: Chemical structure of palmitic acid photoaffinity probe 1

The work in this chapter was necessary as a probe labelling workflow needed to be optimised *in vitro*. Cell labelling concentration optimisation and competition experiments were performed to ensure probe **1** was mimicking endogenous palmitic acid. Lastly, the pulldown enrichment of probe **1**-labelled proteins was optimised to ensure optimal labelling and enrichment for proteomic workflows. This experiments also needed to be performed, whilst avoiding cell death, as this would have falsely led to identification of death processes as being regulated by FAs.

4.3 Chapter Aims

This chapter aims to optimise the protein labelling workflow for the photoaffinity palmitate probe **1** in *MDA-MB-231* cells, a workflow that was used in subsequent chapters. This was achieved through:

1. Optimisation of the Click reaction conditions necessary for optimal protein labelling using probe **1** and further functionalisation allowing for in-gel fluorescence or protein enrichment for proteomics.
2. Investigation of the level of proteins that are covalently and non-covalently interacting with probe **1** in the cell and to determine if these interactions were outcompeted with palmitate, the parent fatty acid.
3. The use of confocal microscopy to visualise the localisation of probe **1** in cells and to investigate the effects of probe **1** on cell and organelle structures.
4. Investigation of cell viability following incubation with probe **1** at the optimal labelling concentration of 30 μM.
5. Investigation of probe **1** as a metabolic substrate for β-oxidation in isolated respiring mitochondria and comparing respiration to that of both palmitate and palmitoyl-CoA.
6. Optimisation of the use of neutravidin agarose beads for the enrichment of proteins interacting with probe **1** and the optimisation of the experimental conditions to ensure the highest yield of enriched proteins for proteomic analysis.

4.4 Methods

4.4.1 Lipid droplet staining

Lipid droplets in cells were stained using an HCS LipidTOX™ Green neutral lipid stain (Invitrogen). The cells were washed twice with DPBS and fixed with 4% PFA for 10 min at RT. The cells were treated with HCS LipidTOX™ Green (1:200) in DPBS for 30 min at RT. The cells were washed 3 times with DPBS to remove excess stain. Cover slips were mounted on slides using Fluoromount-G™, with DAPI (Invitrogen) and allowed to set overnight at 4 °C. The cells were scanned using a Leica TCS SP5 confocal microscope (LipidTOX: λ_{ex} 495/ λ_{em} 505 nm, DAPI: λ_{ex} 358/ λ_{em} 461 nm) and acquired images were processed using Fiji software.

4.4.2 Mitochondrial isolation and respiration

Subsarcolemmal (SSM) and interfibrillar (IFM) mitochondria were isolated from rat hearts, according to the method of Palmer et al., using a modified Chappell–Perry buffer (100 mM KCl, 50 mM MOPS, 5 mM $MgSO_4 \cdot 7H_2O$, 1 mM EDTA, 1 mM ATP, 0.2 % (w/v) BSA, pH 7.4)[170]. SSM were isolated by polytron and Potter-Elvejhem homogenisation. IFM were isolated using trypsin digestion (5 mg/gww) and further homogenisation. Mitochondria were resuspended in KME (100 mM KCl, 50 mM MOPS, 0.5 mM EGTA, pH 7.4) and protein concentrations were determined by bicinchoninic acid assay (Pierce, UK). Mitochondrial respiration was measured using a Clark-type oxygen electrode (Strathkelvin, UK, MS200) at 30 °C, as previously described (Figure 4.2).[171] Mitochondria (0.15 mg of protein) were incubated in 500 µL respiratory media (100 mM KCl, 50 mM MOPS, 1 mM EGTA, 5 mM KH_2PO_4, 1 mg ml^{-1} BSA, pH 7.4). Mitochondrial respiration was measured using palmitoyl-CoA (PCoA) (0.1 mM final) with carnitine (50 µM final) and malate (50 µM final). State 3 respiration was stimulated by ADP (0.2 mM final), and respiration rates were measured. For measuring the respiration of palmitate by mitochondria, a protocol was modified for synthesis of the fatty acyl CoA.[172]A solution containing of 0.15 mg of mitochondrial protein, $MgCl_2$, (0.24 µM final), ATP (0.24 µM final), CoA (0.135 µM final), *L*-carnitine (45 µM final), and malate

(0.375 µM stock) in 500 µL of respiratory mixture (100 mM KCl, 50 mM MOPS, 1 mM EGTA, 5 mM KH_2PO_4, 1 mg mL^{-1} BSA, pH 7.4) was preincubated in the chamber. After the depletion of endogenous substrates, fatty acid substrate (0.1 mM final of palmitate or 0.103 µM final of probe **1**) was added and the oxygen consumption rates were measured. Data was analysed to determine oxygen consumption rates (nmol O_2/mg/min).

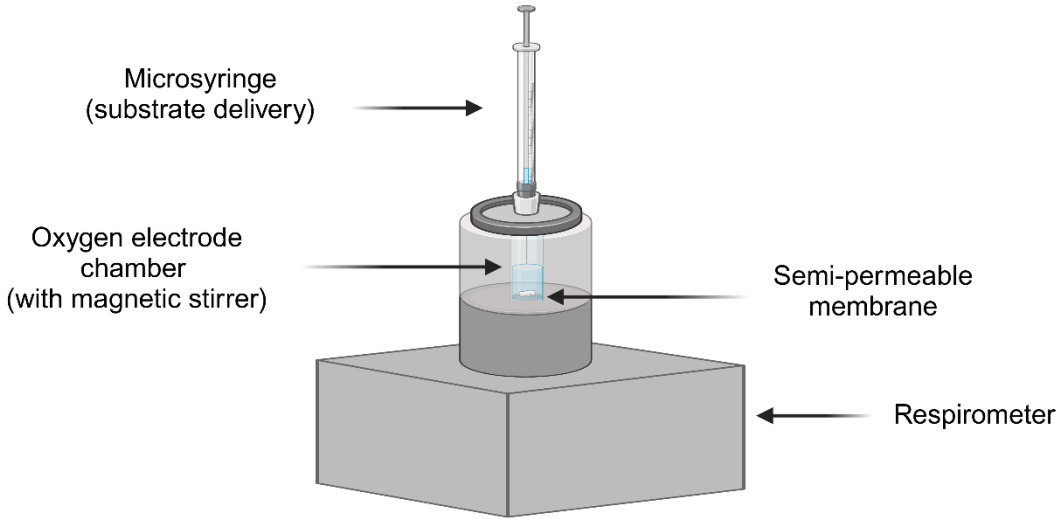

Figure 4.2: Experimental apparatus setup for mitochondrial respiration measurements.

4.5 Results

4.5.1 Probe 1 was an effective reactant in the CuAAC reaction

Downstream analysis of the probe **1**-protein interactome will require a CuAAC reaction to attach either a fluorophore (Carboxytetramethylrhodamine - TAMRA) or a biotin molecule. To test the suitability of probe **1** for CuAAC, a test reaction of probe **1** with TAMRA-azide and biotin-azide was performed in a mass spectrometry vial using $CuSO_4$, TCEP and TBTA. The reaction was completed under identical conditions utilised during biological sample labelling.

Using mass spectrometry, probe **1** (MW = 264 g/mol), TAMRA-azide (MW = 631 g/mol) and biotin-azide (MW = 615 g/mol) were analysed separately, resulting in peaks at 263, 632 and 614 m/z, respectively (Table 4.2). Probe **1** was then mixed with the appropriate azide, $CuSO_4$, TCEP and TBTA, and stirred for 1 h at RT. The expected MW for the biotin- and TAMRA-CuAAC products were 880.16 g/mol and 894.46 g/mol, respectively. Using negative ion mode, mass peaks were observed at 879 m/z and 893 m/z, respectively (Table 4.1). This confirmed that the CuAAC reaction was occurring between probe **1** and both the TAMRA-azide and biotin-azide under these reaction conditions.

Table 4.1: Mass Spectrometry mass values of analysed CuAAC reaction reagents

Compound	MW (g/mol)	Charge state	m/z
Probe **1**	264.37	$[M-H]^-$	263
TAMRA-azide (760757 - Sigma Aldrich)	631.70	$[M+H]^+$	632
Biotin-azide (B10184 – ThermoFisher)	615.79	$[M-H]^-$	614
TAMRA-CuAAC product	894.46	$[M-H]^-$	893
Biotin-CuAAC product	880.16	$[M-H]^-$	879

4.5.2 Concentration-dependent covalent incorporation of probe 1 *in vitro*

Probe **1** was then cultured with cells to determine if it could be covalently incorporated into proteins in a concentration-dependent manner. In unpublished data from the group, it was shown *MDA-MB-231* cells can metabolise and store palmitate without evidence of toxicity up to concentrations of 0.5 mM. These cells were cultured in the absence of fatty acids prior to introduction of probe **1** to the media, and we hypothesised that if probe **1** were behaving like the endogenous fatty acid it would interact with proteins known to be regulated by palmitate. Cells were cultured with varying concentrations of probe **1** for 16 h and lysed, followed by a Click reaction with the bifunctional TAMRA-biotin-azide (Figure 4.3a,b). Using in-gel fluorescence, the TAMRA fluorophore was visualised, and there was a clear concentration-dependent increase in proteins labelled with probe **1** from 1-30 μM (Figure 4.3c). This result confirmed that probe **1** was being incorporated into the cells and successfully labelling protein interactors. Optimal protein labelling occurred at 30 μM, as no additional protein labelling was evident at the increased concentrations of 50 or 100 μM. Labelled proteins result from only covalent interactions of probe **1** as the UV irradiation step was not performed for these samples.

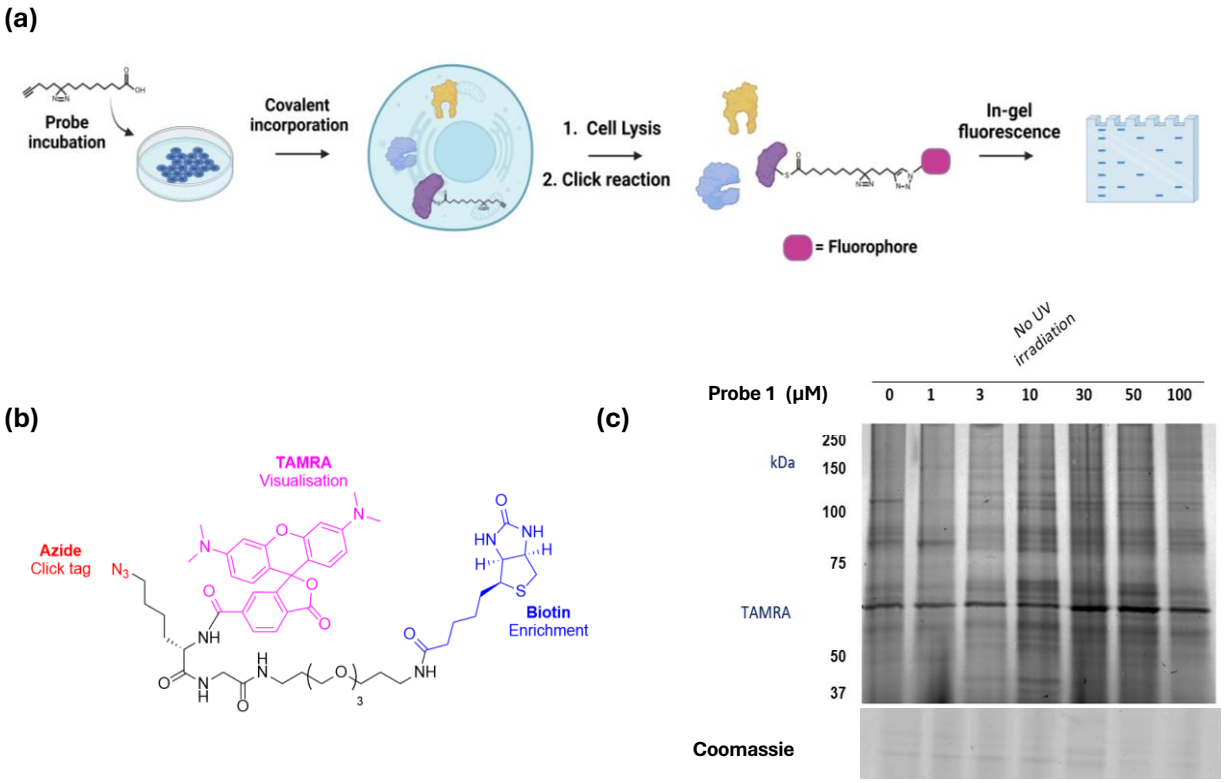

Figure 4.3: Covalent incorporation of probe 1 *in vitro*: (a) Workflow for the attachment of a fluorophore to probe **1**-labelled proteins using the CuAAC reaction. (b) Chemical structure of the TAMRA-biotin-azide used in CuAAC reaction. (c) In-gel fluorescence highlights the concentration-dependence of protein labelling by probe **1** (16 h). Total protein staining using Coomassie blue.

In-gel fluorescence demonstrated that using the TAMRA-biotin-azide resulted in protein labelling in the negative control lane (Figure 4.3c). To test whether this was non-specific binding of the bifunctional TAMRA-biotin-azide, a Click reaction was performed on samples using TAMRA-azide only (Figure 4.4a). This led to a reduction in non-specific binding and labelling (Figure 4.4b). These non-specific interactions may be due to the biotin portion of the TAMRA-biotin-azide interacting with proteins in the cells. A concentration dependence was still evident using TAMRA-azide, with optimum labelling at 30 μM of probe **1**.

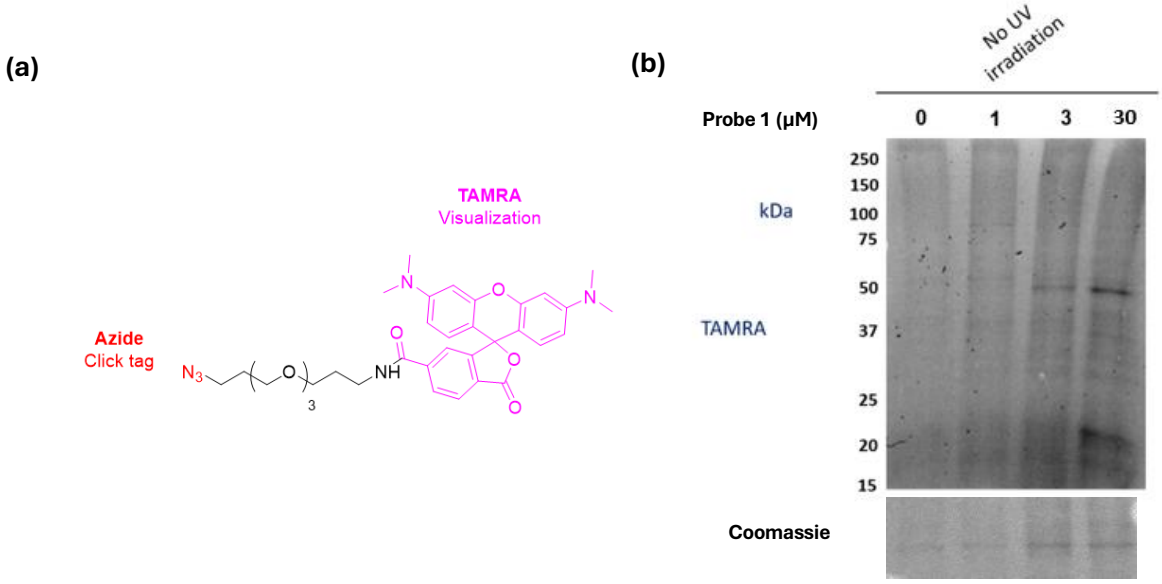

Figure 4.4: Reducing non-specific protein labelling: (a) Chemical structure of the TAMRA-azide used in the CuAAC reaction. (b) In-gel fluorescence shows reduced non-specific protein labelling in control cells (16 h) when using TAMRA-azide. Total protein staining using Coomassie blue.

4.5.3 Non-covalent incorporation of probe 1 *in vitro* following UV irradiation

Employing the photoaffinity diazirine group, non-covalent labelling with probe **1** was investigated (Figure 4.5a). The addition of the UV irradiation step in PAL allows for the capture of both covalently and non-covalently interacting proteins, as it results in the formation of a covalent bond between the proteins and probes. Cells were treated with 30 μM of probe **1** for 16 h, UV irradiated for 3 min, lysed and clicked to TAMRA-azide (Figure 4.5b). The negative control and UV only lanes contained no evidence of protein labelling, suggesting that probe **1** was needed to guide TAMRA labelling and that UV irradiation also had no effect on labelling in the absence of probe **1**. Probe **1**, in the absence of UV irradiation, resulted in lower protein labelling, which increased upon UV irradiation. Therefore, this confirmed that the addition of the UV irradiation step for probe **1** captures more protein interactors.

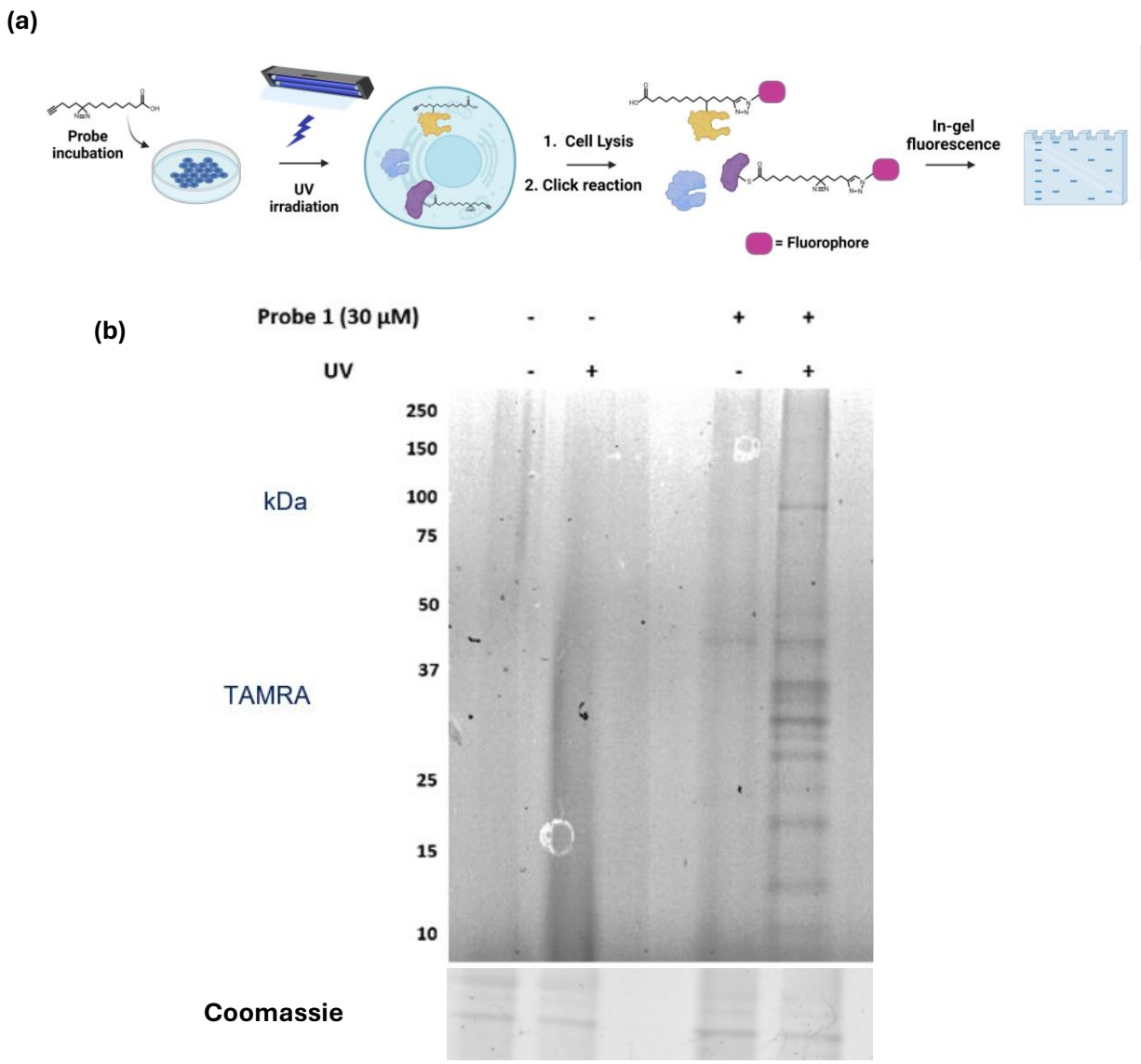

Figure 4.5: Non-covalent incorporation of probe 1 *in vitro*: (a) Workflow for the crosslinking of the probe to proteins and subsequent attachment of a fluorophore using the CuAAC reaction. (b) In-gel fluorescence shows increased protein labelling by probe **1** (30 µM, 16 h) following UV irradiation. Total protein staining using Coomassie blue.

4.5.4 Probe 1 interactions mimicking endogenous palmitate interactions

To confirm that the addition of the photoaffinity diazirine group and the terminal alkyne handle into probe **1** structure had not affected the endogenous lipid-protein interactions, a competition experiment was performed. Cells were treated with probe **1** and compared to cells co-treated with palmitate and probe **1,** for 16 hours followed by UV irradiation (Figure 4.6). Negative control (DMSO) and palmitate only lanes showed no evidence of labelling, due to the absence of probe **1**.

Only lanes containing probe **1** showed protein labelling (TAMRA fluorescence). Comparing probe **1**-only lane (lane 2) to probe **1** plus 0.1 µM palmitic acid (lane 4) did not reveal a changed in protein labelling. However, when the concentration of probe **1** to palmitic acid was a 1:1 ratio (lane 5), the protein labelling with probe **1** was decreased. This confirmed that probe **1** was mimicking palmitic acid in its interactions as labelling could be outcompeted by endogenous palmitic acid.

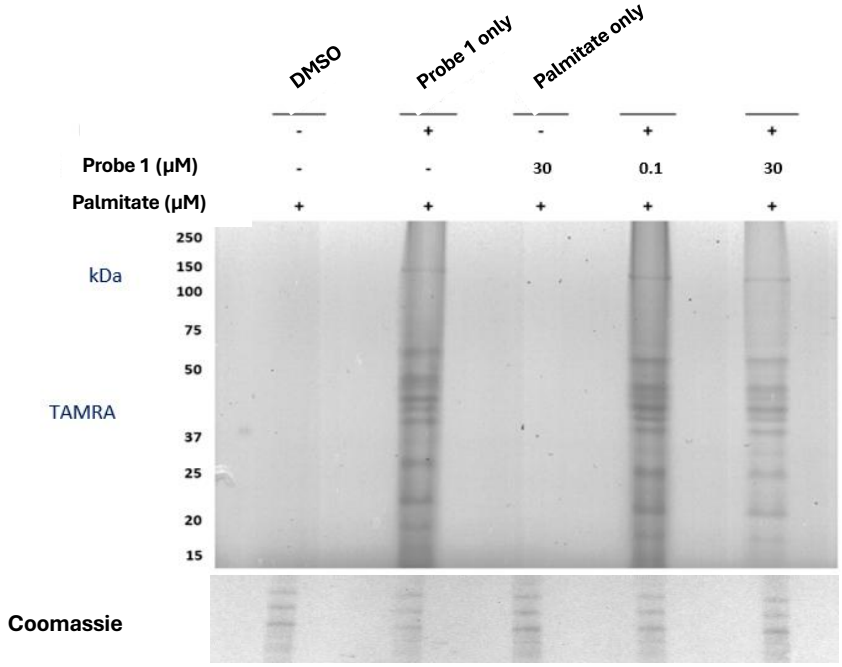

Figure 4.6: Competition experiment using palmitate: In-gel fluorescence highlights a reduction in protein labelling when probe **1**-treated (30 µM, 16 h) cells were co-treated with palmitate (30 µM, 16 h). Total protein staining using Coomassie Blue.

4.5.5 Cellular uptake of probe 1 was confirmed by confocal microscopy

Cells were cultured with probe **1** for 16 h and then fixed using PFA. Following fixation, the cells were incubated with the Click mixture, to attach the TAMRA fluorophore via the CuAAC reaction. Imaging the TAMRA fluorophore by confocal microscopy allowed for the visualisation of probe **1** localisation in specific regions inside of the cell (Figure 4.7a,b). This visualisation confirmed that probe **1** was not just localised in cell membranes but was entering into the cytosol. Additionally, probe **1** was colocalising with the DAPI nuclear stain, demonstrating that probe **1** was entering the nucleus. Compared to untreated control cells, the probe **1**-treated cells had a significant increase in TAMRA labelling (Figure 4.7c).

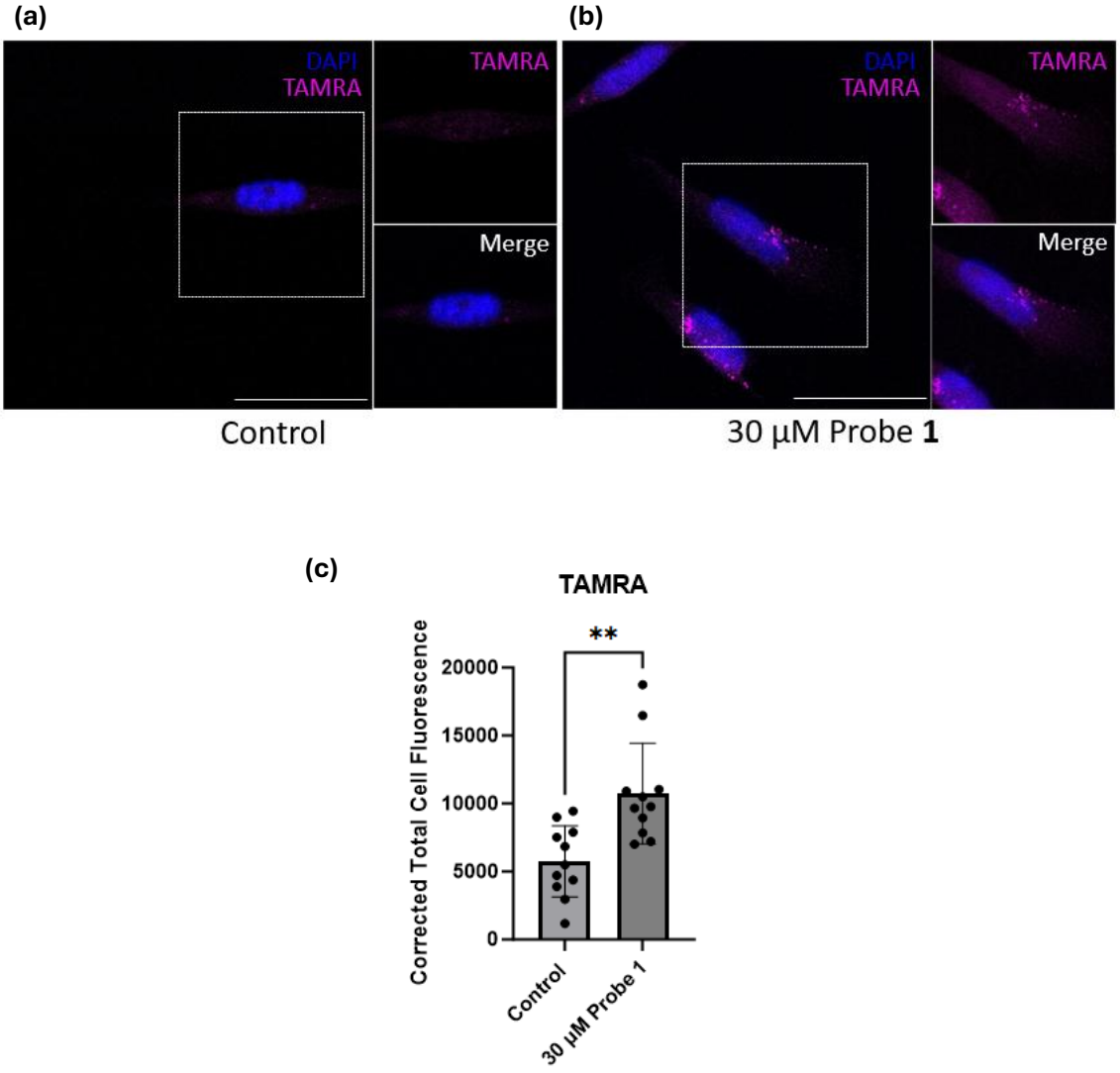

Figure 4.7: Confocal microscopy images of probe 1 using CuAAC reaction: Imaging for TAMRA (magenta) and nuclear staining with DAPI (blue), as (a) control or after treatment for 16 h with (b) 30 µM probe; scale bar is 50 µm with ×2 zoom to the right with (c) corrected total cell fluorescence quantified (n = 11).

4.5.6 Probe 1 was not cytotoxic at 30 µM labelling concentration

To investigate the potential cytotoxicity of probe **1,** *MDA-MB-231* cells were treated with 30 µM of probe **1** for 16 h. Lactate dehydrogenase (LDH) release, lactate production and glucose consumption rates were measured using a Pentra C400 clinical chemistry analyser (Figure 4.8).

LDH is a cytoplasmic enzyme that catalyses the interconversions of pyruvate to lactate and NADH to NAD^+ during glycolysis.[173] When cells become damaged, LDH is released from the cytoplasm into the extracellular environment. LDH has been shown to be stable in cell media and may be used as a measurement of cell damage and toxicity.[174] There was no significant difference in the LDH release rates compared with control cells (Figure 4.8a), demonstrating that at 30 μM probe **1** is not toxic to the cells.

As discussed above anaerobic glycolysis breaks down glucose into two molecules of pyruvate, which is reduced to lactate. Therefore, glucose and lactate can be used as indicators of the metabolic status of cells.[175] There was no significant difference in the lactate production and glucose consumption rates of probe **1**-treated cells compared with controls (Figure 4.8b,c), suggesting that the cells were not becoming more glycolytic following probe **1** treatment. If cells were becoming metabolically stressed (e.g. inhibition of OXPHOS or FAO) the lactate production rate would increase and the glucose consumption rate would increase. As this did not occur following probe **1** treatment, it suggested that probe **1** was not causing metabolic stress in the cells.

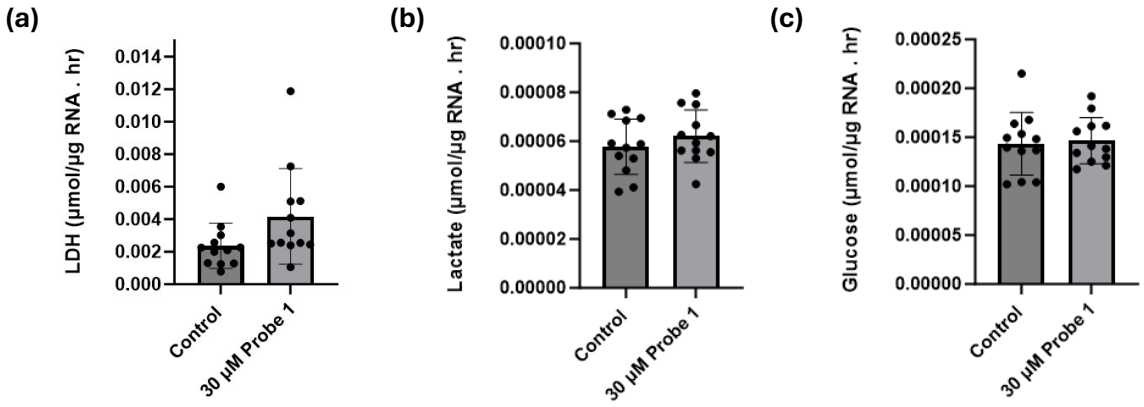

Figure 4.8: Lactate dehydrogenase (LDH), glucose and lactate levels following probe 1 treatment: (a) LDH, (b) glucose and (c) lactate levels in cell media were measured (n=12).

Using a brightfield microscope, cells did not have any visible changes in morphology following 16 h treatment with 30 μM probe **1** (Figure 4.9). This suggests probe **1** was not affecting adherence or morphology.

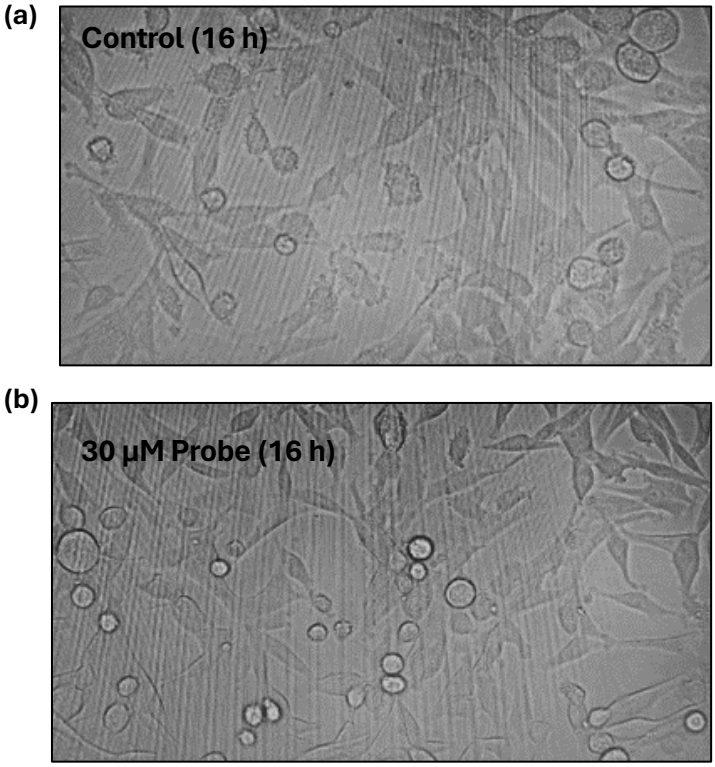

Figure 4.9: Probe 1 does not alter cell morphology of *MDA-MB-231* cells: Brightfield images of MDA-MB-231 cells, either (a) control or (b) treated with 30 µM probe **1** for 16 h. Spherical objects are bubbles in the PBS during imaging.

4.5.7 Probe 1 is not causing mitochondrial fragmentation

Palmitic acid is known to regulate mitochondrial morphology, with high concentrations causing deleterious mitochondrial fragmentation in several cell types.[176] Control, 30 µM palmitate and 30 µM probe **1**-treated cells were stained using MitoTracker™ Red CMXRos (Figure 4.10). This dye is used to stain active mitochondrial networks in live cells. The MitoAnalzyer plugin for ImageJ (version 1.54d) was used to analyse mitochondrial morphology for each of the conditions, resulting in a skeletonised network. There was no significant difference in branching of the mitochondrial

networks, though there was a trend in both 30 µM palmitate or 30 µM probe **1** treatment towards increasing network branching (Figure 4.10b).

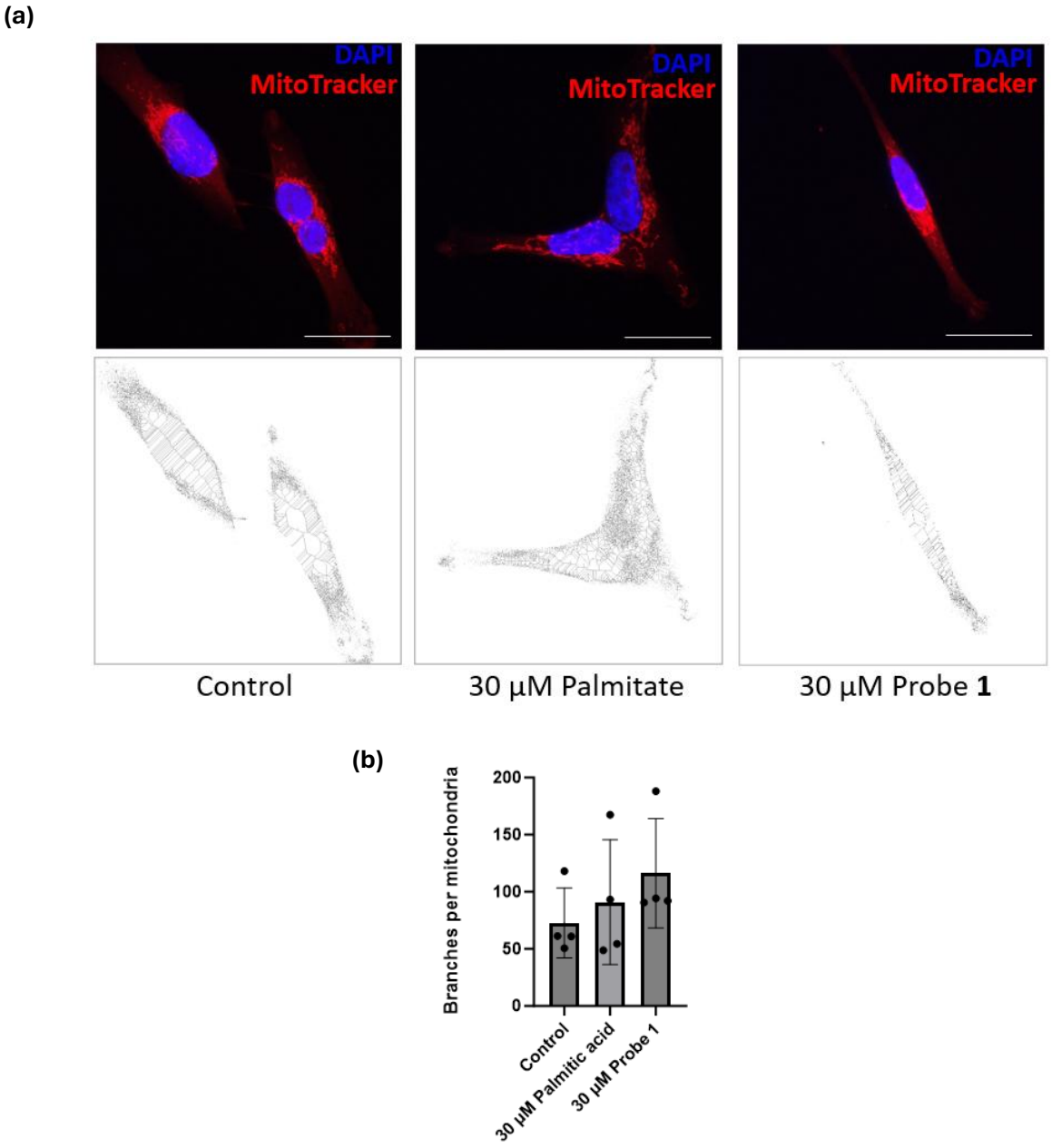

Figure 4.10: Confocal microscopy images of mitochondrial networks: (a) Top row - Staining using MitoTracker CMXRos (red) with DAPI (blue), in control cells, 30 µM palmitic acid or 30 µM probe **1** treated cells. Bottom row – skeletonised images of mitochondrial networks (ImageJ) highlight increase in network branching following probe **1** treatment. Scale bar is 50 µm. (b) quantification of mitochondrial network branching (n = 4).

4.5.8 Probe 1 increased lipid droplet number in cells

To further investigate the localisation of probe **1**, HCS LipidTOX™ staining was used to visualise lipid droplets in the cells (Figure 4.11). For this experiment, cells were either untreated or treated with 30 µM palmitate or 30 µM probe **1**. When comparing control and palmitate-treated cells there was no significant difference in lipid droplet numbers (Figure 4.11d). However, when comparing probe **1**-treated cells with both control cells and palmitate-treated cells, there was a statistically significant increase in lipid droplet numbers. These results suggested that probe **1** was transcriptionally upregulating lipid storage or is inhibiting FAO, or was being stored (lipid droplets) and could not be oxidised.

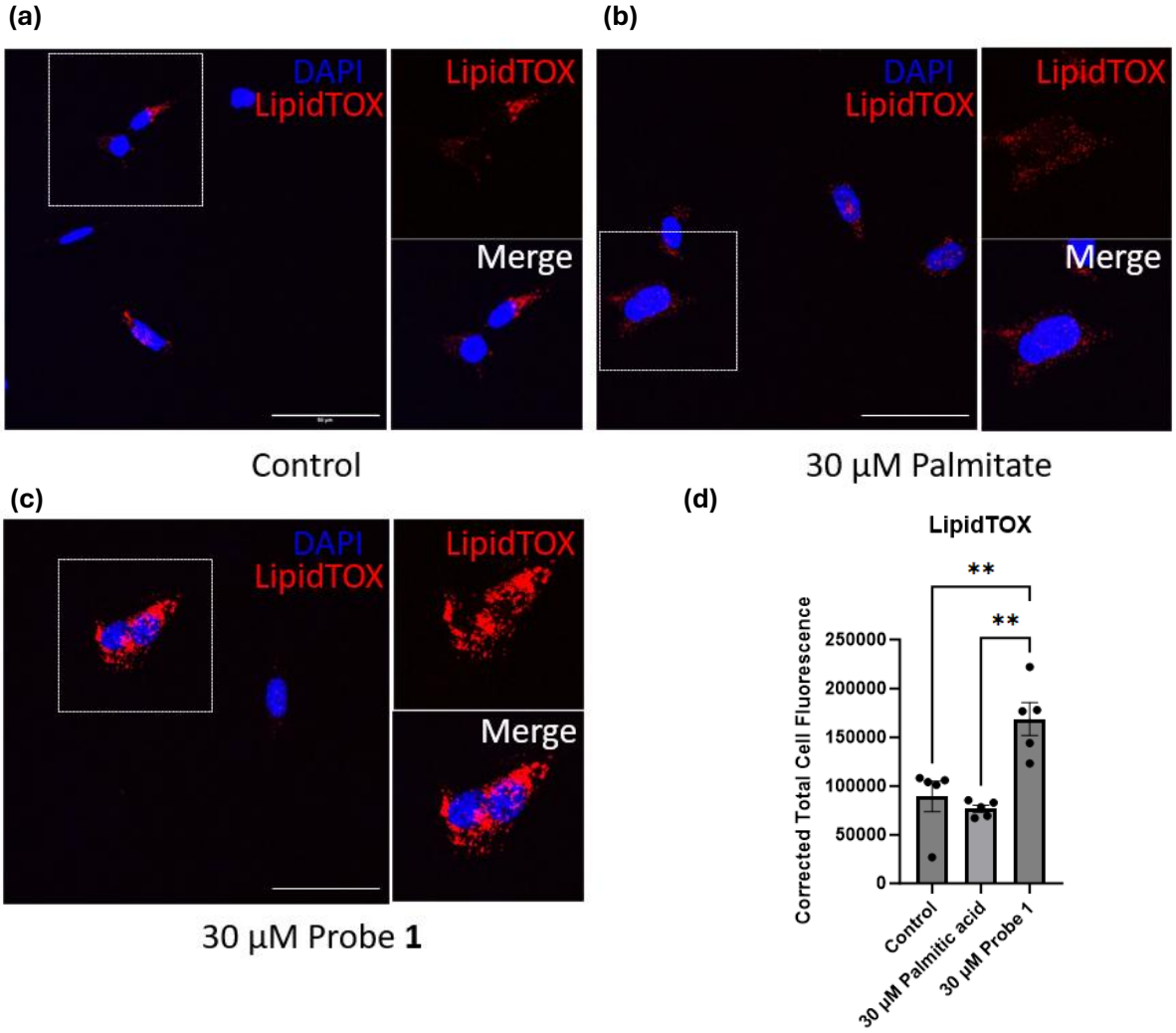

Figure 4.11: Confocal microscopy images of lipid droplets: Staining using HCS LipidTOX (red) with DAPI (blue), as (a) control or after treatment for 16 h with (b) 30 µM palmitate or (c) 30 µM probe **1**; scale bar is 50 µm with ×2 zoom to the right and (d) corrected total cell fluorescence was quantified (n = 5).

4.5.9 Mitochondria do not fully oxidise probe 1

One of the main roles of palmitic acid is in energy production by β-oxidation in the mitochondria. To test whether probe **1** was a mitochondrial substrate, a protocol for respiring FFA in isolated mitochondria was developed, based on a previously published protocol.[177] This involved the formation of the activated fatty acyl-CoA *in situ*, leading to uptake into the mitochondria via the carnitine shuttle system and, ultimately, respiration. Subsarcolemmal (SSM) and interfibrillar (IFM) mitochondria populations were isolated from a rat heart, and rates of respiration were calculated by measuring oxygen consumption using a high-resolution respirometer.

Initially, palmitoyl-CoA was used as a positive control substrate, as this is a known substrate for mitochondrial fatty acid uptake and β-oxidation.[178] Palmitoyl-CoA resulted in high rates of state 3 respiration in the isolated mitochondria, confirming that the mitochondria were intact and functioning (Table 4.2 and Figure 4.12a). Using the protocol developed for the FFAs, palmitic acid was tested as a substrate, where palmitic acid was incubated with Mg^{2+}, coenzyme A and ATP to allow acyl-CoA synthetase (ACS) to form palmitoyl-CoA *in situ* (Figure 4.12b). The rates of respiration of palmitic acid were 177 and 182 nmol O_2/min/mg mitochondrial protein, in SSM and IFM, respectively (Table 4.2 and Figure 4.12b), which were similar to palmitoyl-CoA. Given that the protocol developed for FFAs successfully respires palmitic acid, the same approach was used with probe **1** (Table 4.2 and Figure 4.13). This resulted in respiration rates of 88 and 80 nmol O_2/min/mg mitochondrial protein, in SSM and IFM, respectively. These rates were similar to the baseline respiration rates when only malate was present (90 and 82 nmol O_2/min/mg mitochondrial protein) (Table 4.2 and Figure 4.14).

Table 4.2: State 3 respiration values for various substrates: Average oxygen consumption values of various substrates (n=1 or n=3)

Substrate	SSM*	IFM*
Palmitoyl-CoA†	193	259
Palmitic acid	177	182
Probe **1**	88	80
Malate	90	82
Palmitic acid post-probe **1**	122	185

*nmol O_2/min/mg mitochondrial protein
† n=1 per population

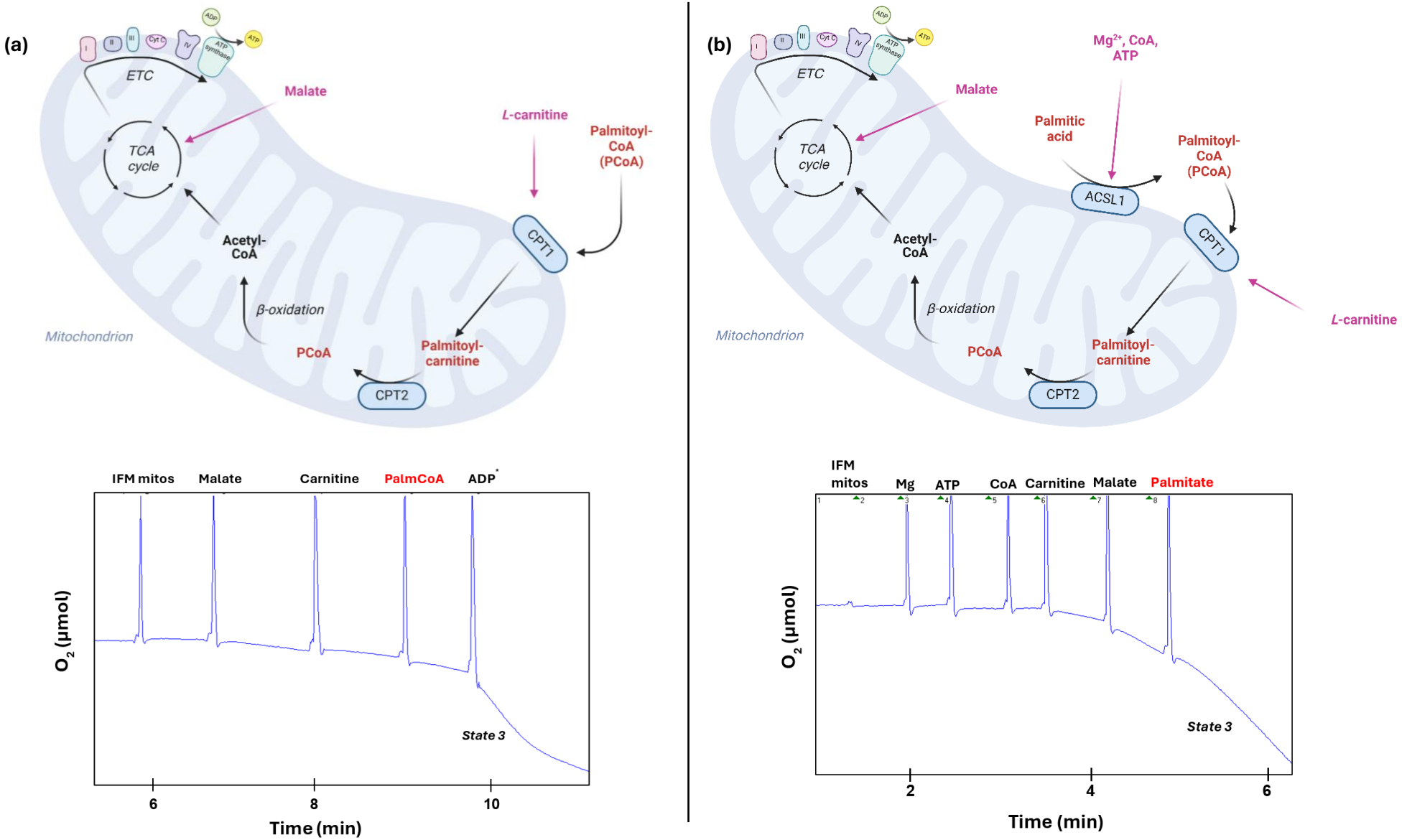

Figure 4.12: Respiration traces of palmitoyl-CoA (PCoA) and palmitic acid by interfibrillar mitochondria (IFM). (a) Respiration of PCoA using malate and *L*-carnitine as reagents resulted in state 3 respiration; (b) Respiration of palmitic acid using magnesium (Mg^{2+}), coenzyme A (CoA), ATP, malate and *L*-carnitine as reagents resulted in state 3 respiration.

These results suggest that probe **1** is not being used as a substrate for β-oxidation (Figure 4.14). This may result from the inability of the mitochondria to use probe **1** as a β-oxidation substrate. Alternatively, probe **1** may not be binding to the necessary enzymes required to convert it into the acyl-CoA or acyl-carnitine. However, probe **1** does not inhibit the mitochondria from respiring, as the addition of palmitate following probe **1** on the same run resulted in state 3 respiration (Table 4.2 and Figure 4.13).

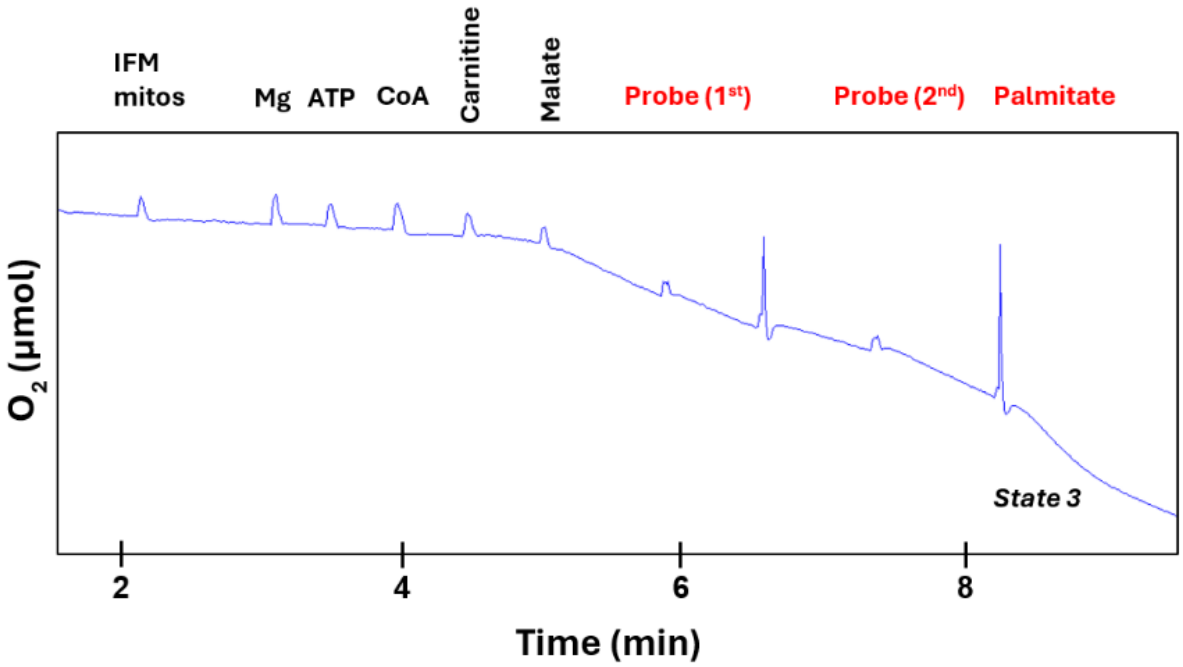

Figure 4.13: Respiration traces of probe 1, followed by palmitic acid by interfibrillar mitochondria (IFM). Respiration of probe **1** using magnesium (Mg^{2+}), coenzyme A (CoA), ATP, malate and *L*-carnitine as reagents did not result in state 3 respiration. A second addition of probe **1** also did not result in state 3 respiration. A final addition of palmitic acid did result in state 3 respiration, confirming the mitochondria were still intact and not inhibited.

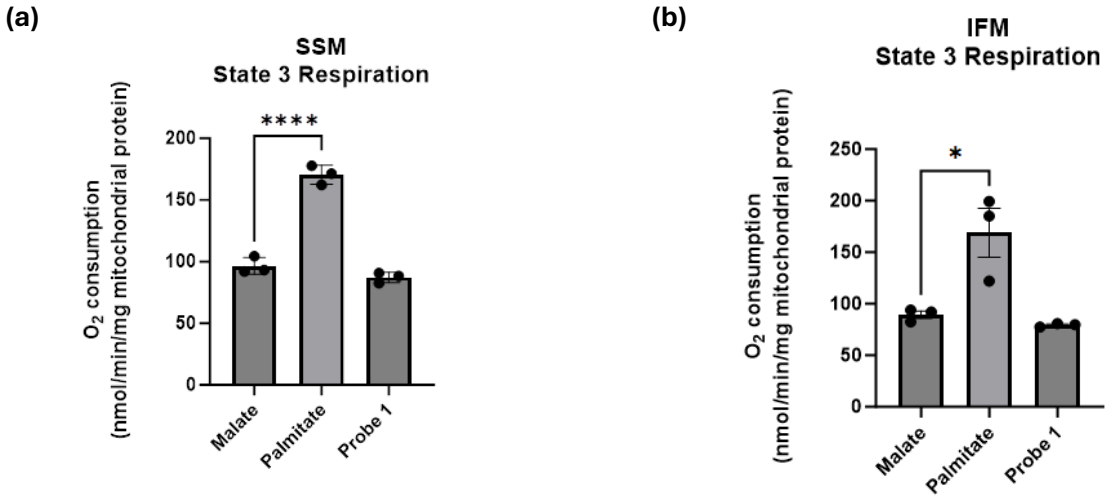

Figure 4.14: The probe 1 is not a substrate for state 3 respiration. State 3 respiration rates in isolated (a) SSM and (b) IFM mitochondria (rat heart) when respiring on malate alone or malate + palmitate + CoA (Palmitate), or malate + probe **1** + CoA (Probe **1**) (n=3).

4.5.10 Nuclear integrity following UV irradiation

To ensure that the 3 min UV irradiation at 365 nm did not have any effect on the structure of the nucleus, nuclear Lamins were stained using a Lamin A/C antibody. Nuclear Lamins are critical in maintaining nuclear envelope integrity and nuclear morphology. Control and probe **1**-treated cells were compared with and without UV irradiation following immediate fixation (Figure 4.15). There appeared to be no difference in the Lamin staining between groups. This suggests that the nuclear membrane is not damaged following probe **1** treatment or UV irradiation.

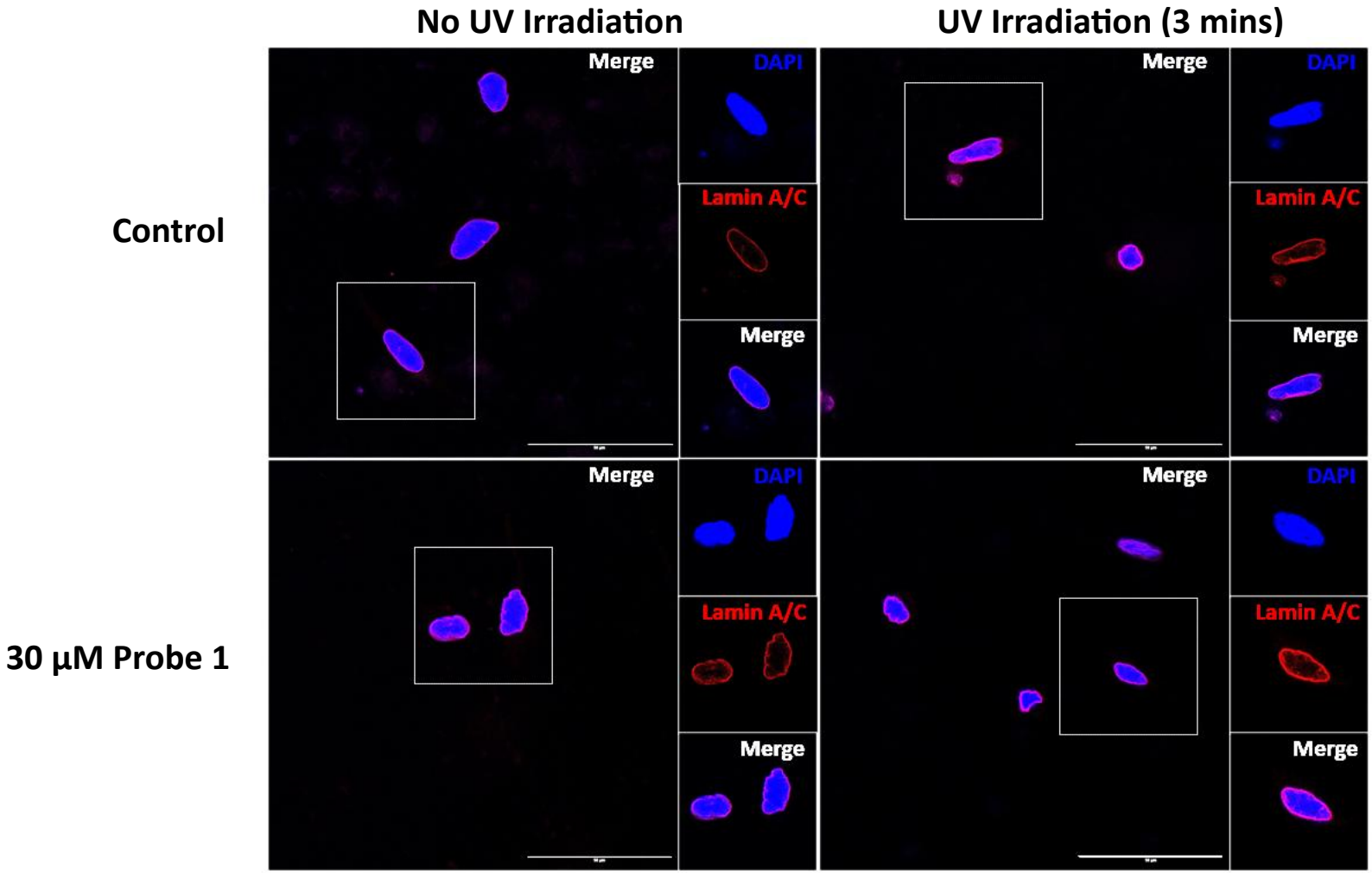

Figure 4.15: Confocal microscopy images of Lamin A/C: Images showing the distribution of Lamin A/C in *MDA-MB-231* cells, highlighting structural integrity of the nuclear membrane. Lamin structure, after 16 h, is compared between control, control + UV irradiation (3 min), 30 µM probe **1** and 30 µM probe **1** + UV irradiation (3 min). Cells were immediately fixed after irradiation.

4.5.11 Neutravidin-biotin pulldown optimisation

With protein interaction and non-toxicity confirmed, the next step in the workflow was to pulldown the lipid-protein interacting partners for proteomic analysis. Enrichment of interactor proteins was necessary to allow for further analysis. Therefore, this was performed using a neutravidin-biotin pulldown using neutravidin beads. The elution of biotin-labelled proteins from the beads had to be optimised to ensure maximum yield of enriched proteins. Firstly, elution in sodium dodecyl sulfate (SDS) and lithium dodecyl sulfate (LDS) buffers were compared (Figure 4.16a). Proteins did not elute off the beads in the SDS buffer but did using LDS buffer. Therefore, LDS loading buffer was chosen as the optimal elution buffer. Following this, a temperature comparison was performed to compare the amounts of eluted proteins 95 °C and 70 °C (Figure 4.16b). Upon comparison, there was a greater level of eluted proteins after 15 min when the beads were heated at 95°C compared with 70°C.

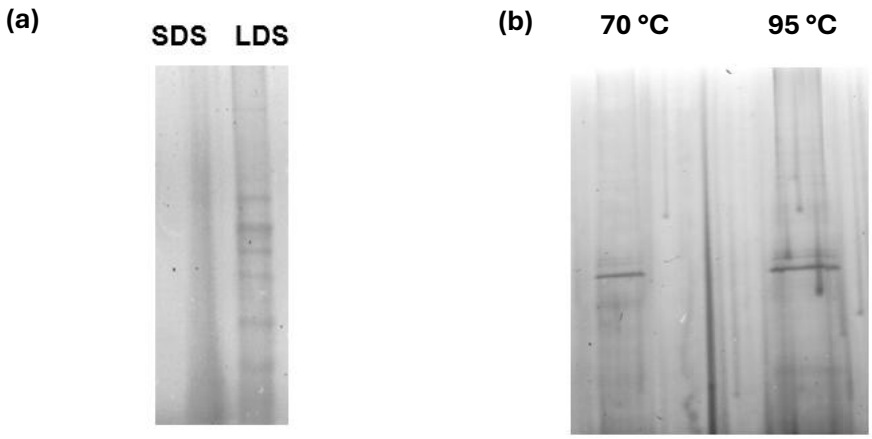

Figure 4.16: Neutravidin-biotin pulldown optimisation: (a) Levels of eluted proteins (30 µM probe **1**, 16 h, 3 min UV irradiation) when using either SDS- or LDS-based elution buffers. (b) Levels of eluted proteins (30 µM probe **1**, 16 h) when heating neutravidin beads at 70 °C or 95 °C.

With the elution conditions optimised, four sample groups were compared: control, control with UV, 30 µM probe 1, and 30 µM probe **1** with UV (Figure 4.17a). These samples underwent the optimised pull-down protocol followed by western blotting using an anti-biotin antibody. Post-pulldown lanes

demonstrated enrichment of proteins in the native control and UV only lanes, due to endogenous protein biotinylation. This is expected as a neutravidin pulldown would also enrich all endogenously biotinylated proteins in the samples. The UV-only lane has less proteins enriched compared to the control lane, suggesting UV irradiation may be decreasing endogenous biotinylation. The enrichment of proteins increased when probe **1** was present, and further increased with UV irradiation. This was also confirmed by Coomassie staining of the probe **1**-treated samples (Figure 4.17b). These results demonstrated that the neutravidin pulldown protocol was working and could be used for proteomic sample preparation, to further investigate the protein interactors of probe **1**.

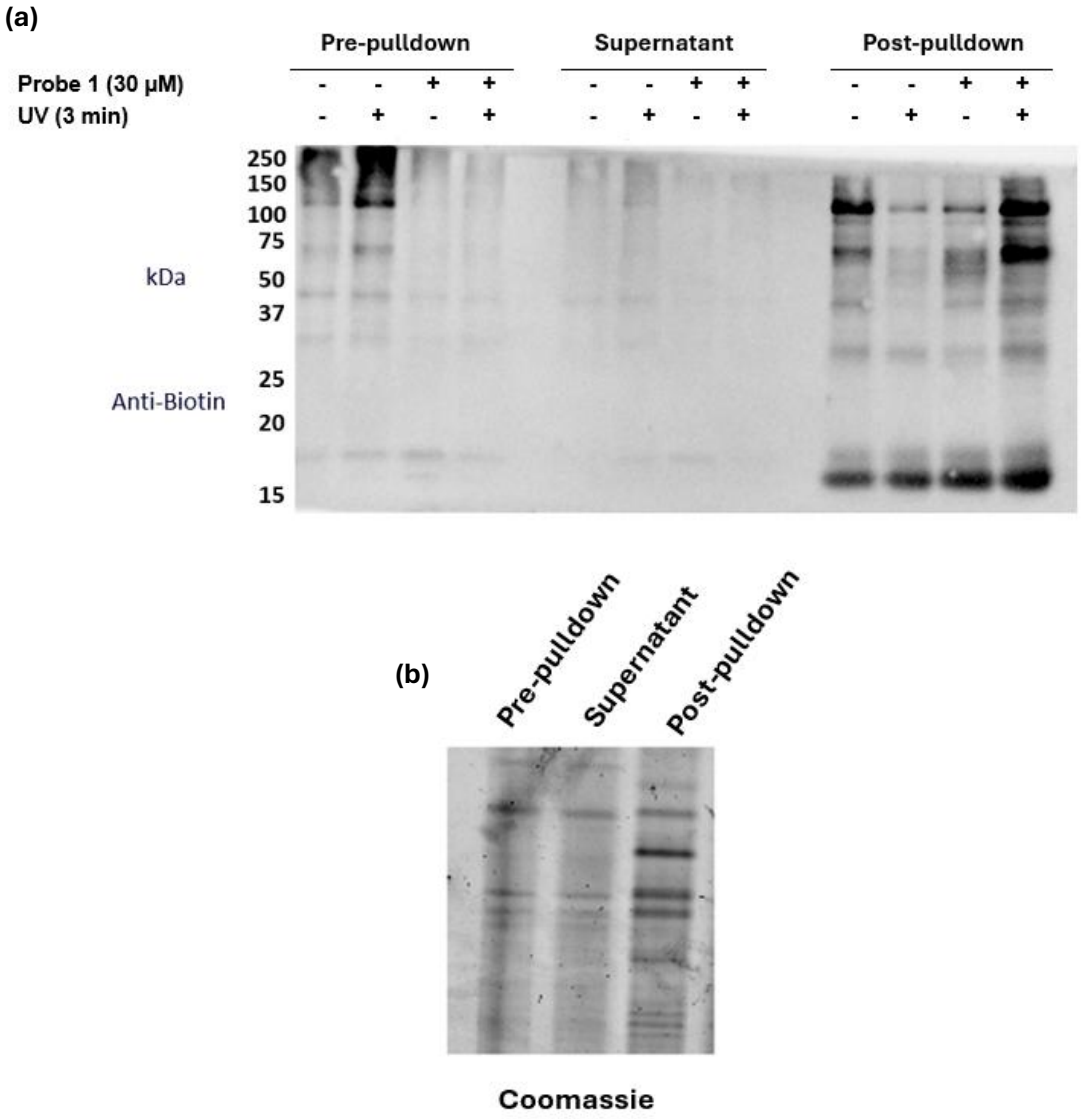

Figure 4.17: Neutravidin-biotin pulldown: The enrichment of probe **1**-labelled proteins (30 µM, 16 h, ±UV) following neutravidin-biotin pulldown highlighted by (a) Western blotting and (b) Coomassie (total protein) staining. Post-pulldown = proteins eluted off Neutravidin beads.

4.6 Discussion

In this chapter, a protocol for the use of palmitic acid photoaffinity probe **1** in *MDA-MB-231* cells was optimised. Using this protocol, it was shown that probe **1** enters into cells and becomes metabolically incorporated, resulting in protein labelling. Probe **1** was also shown to cause changes in mitochondrial structures and lipid storage, but it did not cause cell toxicity. This provided a working protocol for the use of probe **1** as a chemical tool *in vitro*.

Palmitic acid can interact with proteins covalently (e.g. palmitoylation) and non-covalently (hydrophobic).[88,94] Due to the chemical structure of probe **1**, containing the photoreactive diazirine, in theory both these types of interactions could be captured. Proteins captured by the non-UV irradiated *MDA-MB-231* samples (16 h incubation) are hypothesised to be proteins that undergo covalent attachment to probe **1**, these may include palmitoylated proteins. Haberkant *et al.* showed that in the absence of UV irradiation, probe **1** labelled numerous known palmitoylated proteins in CHO cells.[138] The additional proteins captured with UV irradiation, due to the formation of a covalent bond, would potentially be proteins that are hydrophobically or electrostatically interacting with probe **1** (e.g. integral membrane proteins). In the *MDA-MB-231* cells, both of these interactions (30 μM probe **1**±UV) were outcompeted upon co-treatment with palmitate (Figure 4.6), confirming that probe **1** mimics endogenous palmitic acid and labelled proteins are palmitate interactors. A further utilisation of photoaffinity probes is the visualisation of their subcellular localisation using fluorescent microscopy. Probe **1** was shown to be entering the cells and localising to both the cytoplasm and nucleus. Staining of Lamin A/C ensured that the entry of probe **1** into the nucleus was not due to membrane damage. Therefore, any nuclear protein interactions captured are natural FA interactions. This proved that altering the structure of palmitate to form probe **1** does not impede its transport across both the cell membrane and the nuclear membrane. To investigate if probe **1** was a substrate for mitochondrial metabolism, a protocol was developed to test the respiration levels of probe **1**. Palmitoyl-CoA resulted in respiration in isolated rat heart mitochondria. Palmitic acid was also oxidised by the mitochondria, following conversion to palmitoyl-CoA *in situ*, with a slightly lower oxygen consumption. This may result from the conversion to the acyl-CoA being a rate-

limiting step. However, probe **1** showed no increase in respiration compared to the malate baseline. As no significant mitochondrial fragmentation occurred in whole *MDA-MB-231* cells following probe **1** incubation, potential inhibition of the mitochondria was investigated. Probe **1** was shown not to inhibit respiration as the addition of palmitate, post-probe **1**, caused the mitochondria to enter state 3 respiration. The inability of probe **1** to induce state 3 respiration in mitochondria could be due to a number of factors. The chemical structure of the probe is slightly altered from palmitic acid, so therefore, the mitochondrial machinery (e.g. ACSL1 or CPT1) may not recognise probe **1** as a binding substrate and probe **1** may not be converted into the equivalent acyl-CoA or acyl-carnitine, required to shuttle FAs into the mitochondria for β-oxidation. The position of the photoreactive diazirine may also prevent or only allow partial β-oxidation to occur. Quantification of lipid droplets was performed to investigate lipid storage levels in the cells. The lipid droplet numbers increased in probe **1**-treated cells compared to palmitate-treated and control cells. This increase in lipid droplets may be due to preferential storage of probe **1** as it is not broken down through β-oxidation. This may mean that probe **1** is closer to mimicking lipid overload conditions, where cells accumulate excess lipids beyond their storage and metabolic capacity. Cell viability was not altered upon treatment with probe **1**, as measured by LDH release rates. Additionally, Probe **1** did not appear to change anaerobic glycolysis, as evidenced by lactate production and glucose consumption rates. High palmitate concentrations have previously been shown to cause both mitochondrial fragmentation and dysfunction through mitochondrial depolarisation, morphological fragmentation and impaired ATP synthesis.[176,179,180] Probe **1** did not show significant fragmentation in mitochondria, likely because it did not disrupt the mitochondrial dynamics or impair the processes of fission and fusion that regulate mitochondrial shape and integrity.[181] Finally, to analyse these protein interactors further using proteomic techniques, labelled proteins had to be purified using neutravidin-biotin affinity purification. Optimisation of pulldown conditions allowed for the enrichment of the biotinylated and probe **1**-labelled proteins to a satisfactory level for proteomic analysis. In conclusion, results described in this chapter have shown that probe **1** can be used as a chemical tool to label proteins *in vitro*, allowing for downstream analysis to identify the protein interactors in *MDA-MB-231* cells and other cell types.

Chapter 5

Identification of palmitic acid targets in *MDA-MB-231* cells using photoaffinity palmitate probe **1**

5.1 Abstract

PAL is a versatile and powerful technique for studying biomolecular interactions, enabling the precise identification of target molecules in complex biological systems. This chapter explores the use of a photoaffinity palmitic acid probe **1** as a powerful tool in breast cancer research, specifically focusing on their application in studying cancer cell biology through proteomics and transcriptomics. By integrating PAL with proteomic techniques such as mass spectrometry, the interaction networks of probe **1** with proteins can be mapped, uncovering potentially novel targets and pathways involved in cancer progression. Additionally, combining this approach with transcriptomic profiling allowed for a more comprehensive understanding of how the probe **1**-protein interactions influence gene expression patterns and biological pathways in cancer cells.

Proteomic analysis was performed on *MDA-MB-231* cells treated with probe **1** with or without UV irradiation, compared with control cells. Probe **1** was shown to interact with proteins involved in various biological pathways, including ribosomal biogenesis, organelle localisation, cell cycle progression, membrane trafficking, OXPHOS and intracellular transport. Transcriptomic analysis of cells treated with probe **1** showed an upregulation of genes involved in OXPHOS, cell cycle, organelle localisation, TGF-β signalling and mitochondrial gene expression. Genes involved in actin cytoskeleton organisation, Rho and VEGF signalling and metabolism of RNA were also downregulated. Confocal microscopy was used to show an increase in F-actin filaments after probe **1** incubation and also highlighted the colocalisation of probe **1** with a mitochondrial protein, MT-CO2, and lipid droplets.

In conclusion, probe **1** was used to identify protein interactors and changes in gene pathways due to these interactions in breast cancer cells. These changes were also accompanied by several phenotypic changes in the cells.

5.2 Introduction

Dysregulated FA metabolism plays a critical role in cancer progression, particularly in breast cancer, where obesity - often associated with lipid overload - has been strongly linked to an increased incidence of the disease.[182–186] This connection highlights the importance of understanding lipid-protein interactions within the cancerous environment, especially in breast cancer.

To determine whether probe **1** interacts similarly to endogenous palmitate, it is essential to use a lipid-naive cell line with the capacity to upregulate FA metabolism in response to appropriate lipid signals. *MDA-MB-231* cells, a well-established breast cancer model, provide an ideal system for these studies. By using these cells, we can first verify whether known lipid metabolism pathways, OXPHOS and mitochondrial proteins and genes are upregulated, serving as a positive control. Additionally, this model will enable us to identify novel lipid targets and pathways involved in cancer metabolism, potentially uncovering new therapeutic strategies and advancing our understanding of how lipid dynamics contribute to tumour growth and survival.

5.3 Chapter Aims:

FAs are known to be important in the development and metastasis of cancer, with dysregulated energy metabolism now recognised as a hallmark of the disease. Therefore, an investigation into the interactions of palmitic acid, one of the most abundant FAs in our diet, would be crucial in fully understanding its role in cancer development. This chapter, therefore, aimed to explore the protein interactions of the palmitic acid photoaffinity probe **1** in breast cancer (*MDA-MB-231*) cells. Furthermore, this chapter aimed to explore the downstream effects of these probe **1**-protein interactions, through gene expression and phenotypic changes. This was achieved through:

1. A proteomic analysis to investigate probe **1**-protein interactors in *MDA-MB-231* cells in the presence or absence of UV irradiation.
2. Confocal microscopy to explore changes in actin filaments and the colocalisation of probe **1** with mitochondria and lipid droplets.
3. A transcriptomic analysis of *MDA-MB-231* cells treated with probe **1**, to analyse changes in biological pathways.
4. A cell metabolism assay, using radioactive metabolic substrates to measure the metabolic state of *MDA-MB-231* cells post-probe **1** treatment.

5.4 Methods

5.4.1 Colocalisation of probe 1 with Mitochondrially Encoded Cytochrome C Oxidase II (MT-CO2)

Cells were seeded on fibronectin-coated glass coverslips in 24-well plates (10^5 cells per well) and allowed to adhere overnight. Cells were incubated with probe **1** for 16 h in low-glucose DMEM. The cells were washed twice with DPBS and fixed with 4% PFA for 10 min at RT. The cells were washed 3 times with DPBS, permeabilised with 0.5% Triton X-100 in DPBS for 10 min and rinsed twice with DPBS. The coverslips were then incubated with the Click reaction mixture (Cy5-azide (1.6 µL, 10 mM stock), $CuSO_4$ (3.2 µL 50 mM stock), TCEP (3.2 µL 50 mM stock) and TBTA (1.6 µL 10 mM stock)) in the dark for 1 h at RT. The cells were washed three times with DPBS, to remove excess Cy5-azide. Coverslips were then blocked at RT for 1 h using a blocking buffer (10% BSA in 0.1% Triton X-100 in DPBS) and incubated with anti-MTCO2 antibody diluted in blocking buffer overnight at 4 °C. The coverslips were then rinsed three times with 0.1% Triton X-100 in DPBS and incubated with a secondary antibody (1:200, Alexa Fluor™ 488, Invitrogen) in blocking buffer for 1 h at RT. The coverslips were then rinsed three times with 0.1% Triton X-100 in DPBS and then mounted on slides using Fluoromount-G™, with DAPI (Invitrogen) and allowed to set overnight at 4 °C. The cells were imaged using a Leica TCS SP5 confocal microscope (MTCO2: λ_{ex} 499/ λ_{em} 520 nm , Cy5: λ_{ex} 651/ λ_{em} 670 nm, DAPI: λ_{ex} 358/ λ_{em} 461 nm) and acquired images were processed using Fiji software.

5.4.2 F-actin staining

F-actin in cells was stained using an Alexa Fluor™ 488 Phalloidin stain (Invitrogen). The cells were washed twice with DPBS and fixed with 4% PFA for 10 min at RT. The cells were treated with Alexa Fluor™ 488 Phalloidin (1:200) in DPBS for 30 min at RT. The cells were washed 3 times with DPBS to remove excess stain. Coverslips were mounted on slides using Fluoromount-G™, with DAPI (Invitrogen) and allowed to set overnight at 4 °C. The cells were imaged using a Leica TCS SP5 confocal microscope (Phalloidin: λ_{ex} 495/ λ_{em} 518 nm, DAPI: λ_{ex} 358/ λ_{em} 461 nm) and acquired images were processed using Fiji software.

5.4.3 Measuring probe 1 colocalisation within lipid droplets

The cells were seeded on fibronectin-coated glass coverslips in 24-well plates (10^5 cells per well) and allowed to adhere overnight. Cells were incubated with probe **1** for 16 h in low-glucose DMEM. The cells were washed twice with DPBS and fixed with 4% PFA for 10 min at RT. The cells were washed 3 times with DPBS, permeabilised with 0.5% Triton X-100 in DPBS for 10 min and rinsed twice with DPBS. Lipid droplets in cells were stained using an HCS LipidTOX™ Green neutral lipid stain (Invitrogen) (1:200) in DPBS for 30 min at RT. The cells were washed 3 times with DPBS to remove excess stain. The coverslips were then incubated with the Click reaction mixture (Cy5-azide (1.6 µL), $CuSO_4$ (3.2 µL), TCEP (3.2 µL) and TBTA (1.6 µL)) in the dark for 1 h at RT. The cells were washed three times with DPBS, to remove excess Cy5-azide. The coverslips were then mounted on slides using Fluoromount-G™, with DAPI (Invitrogen) and allowed to set overnight at 4 °C. The cells were imaged using a Leica TCS SP5 confocal microscope (LipidTOX: λ_{ex} 495/ λ_{em} 505 nm, Cy5: λ_{ex} 651/ λ_{em} 670 nm, DAPI: λ_{ex} 358/ λ_{em} 461 nm) and acquired images were processed using Fiji software.

5.4.4 Assessing cell metabolism using radiolabelled compounds

All handling of radioactive material was performed by Claudia Montes Aparicio (Heather group).

(a) Measuring glycolysis

The rate of glycolysis in the *MDA-MB-231 cells* was measured using the rate of ^3H_2O production from 5-^{3}H-glucose. This well-established protocol was adapted from several previous publications.[187] At the enolase step of glycolysis, the ^{3}H is released in the form of ^3H_2O (Figure 5.1). *MDA-MB-231* cells were seeded in 24-well plates (10^5 cells per well) and allowed to grow to 80% confluency. Probe **1** (30 µM) was added and incubated for 16 h. Following this, cells were washed with DPBS and incubated with cell media containing 0.2 µCi/mL of glucose, D-[5-^{3}H(N)] (PerkinElmer) for 6 hours. After the incubation, the media was collected and frozen at -20 °C for subsequent extraction. The cells were lysed and stored at -20 °C for protein concentration measurements. The ^3H_2O was extracted from 5-^{3}H-glucose using anion exchange chromatography (Dowex) method. Dowex was prepared by mixing 250 g Dowex 1 x 4 chloride (100-200 mesh,

Sigma Aldrich) with NaOH (1.25 M) and boric acid (1.61 M). The solution was inverted several times, the aqueous phase removed and then repeatedly washed with dH_2O until the mixture reached pH 7.5. Pasteur pipettes were plugged with glass wool in the bottom and packed with Dowex. Cell media (200 µl) was added to the Dowex column and incubated for 15 mins at RT, allowing the 5-^{3}H-glucose to bind to the column. ^3H_2O was eluted into scintillation vials containing scintillation fluid, by rinsing the Dowex twice with dH_2O. Radioactivity was measured using Tri-Carb 2800TR liquid scintillation analyser (PerkinElmer). Cell media (200 µL) at time point 0 was used as a control to determine the specific activity of the buffer. Comparing ^3H_2O levels at time 0 and 6 h allowed the rate of glycolysis to be determined.

(b) Measuring fatty acid oxidation

Palmitate oxidation (Figure 5.2) was measured by determining the production of ^3H_2O from 9,10-^{3}H-palmitate via the electron transport chain.[187,188] *MDA-MB-231* cells were seeded in 24-well plates ($10^{5.5}$ cells per well) and allowed to grow to 80% confluency. Probe **1** (30 µM) was added and incubated for 16 h. Following this, cells were washed with DPBS and incubated with low-glucose DMEM containing 2% BSA and 0.2µCi/mL of palmitate, [9,10-3H(N)] (PerkinElmer) for 6 hours. After the incubation, the media was collected and frozen at -20 °C for subsequent extraction. The cells were lysed and stored at -20 °C for protein concentration measurements. ^3H_2O produced from the cells was separated using the Folch extraction method modified by Malandraki-Miller, S. et al. In a 15 mL falcon tube, chloroform:methanol (1.88 mL of a 1:2 v/v solution), chloroform (625 µL) and KCl:HCl solution (625 µL, 2 M KCl, 0.4 M HCl) was added to cell media (500 µL). The solution was then rotated on a laboratory Stuart rotator SB3 at 40 rpm for 1 h at RT before removing the top aqueous layer and discarding the organic layer. The top aqueous layer solution was added to a solution of chloroform (1 mL), methanol (1 mL) and KCl:HCl (0.9 mL, 2 M KCl, 0.4 M HCl) and rotated for 1 h at 40 rpm. The top aqueous layer (500 µL) was added to scintillation fluid and counted the radioactivity in a scintillation analyser. Cell media (500 µL) at time point 0 was used as a control to determine the specific activity of the buffer. The rate of FAO was the difference in ^3H_2O between time 0 and time 6 h, normalised to cell number and specific activity.

5.5 Results

5.5.1 Proteomic analysis in *MDA-MB-231* cells

To explore the interactions of probe **1** in *MDA-MB-231* cells, a proteomic analysis was performed on these groups: control cells, control cells with UV, 30 µM probe **1**, and 30 µM probe **1** with UV. Both principal component analysis and hierarchical clustering were performed (Figures 5.1 and 5.2), and it highlighted that sample 9 (control cell with UV) was very distinct from the rest of the samples. It was, therefore, decided to omit sample 9 for PCA analysis, revealing that principal component 1 (PC1) captured 30% of the variance, attributed to the UV irradiation step. Principal component 2 (PC2) captured 17% variance, which could be attributed to probe **1** treatment.

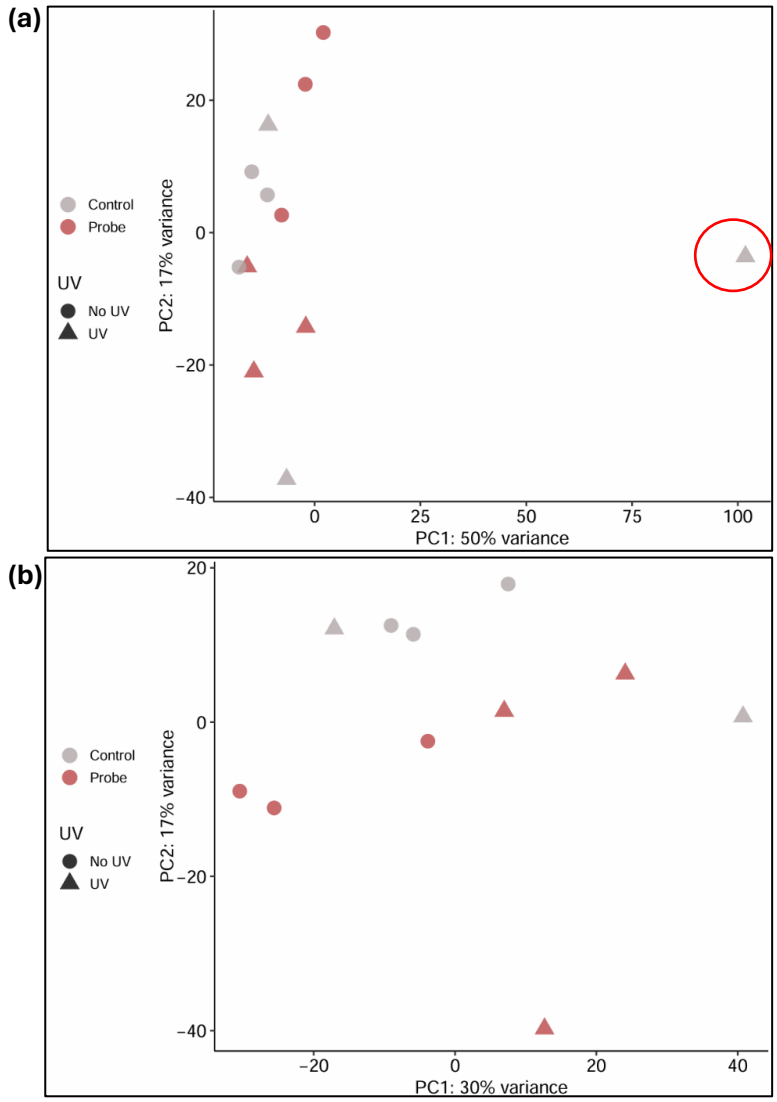

Figure 5.1: Principal component analysis (PCA) on proteomic samples of *MDA-MB-231* cells treated with 30 µM probe 1 (±UV). (a) PCA revealed sample 9 (circled in red) was very distinct from the other samples; (b) PCA, omitting sample 9, revealed principal component 1 (PC1) captured 30% variance, attributed to UV irradiation and principal component 2 (PC2) captured 17% variance, attribute to probe **1** treatment. Control = 0 µM probe **1**, Probe = 30 µM probe **1**, UV = 3 min UV irradiation, No UV = no UV irradiation.

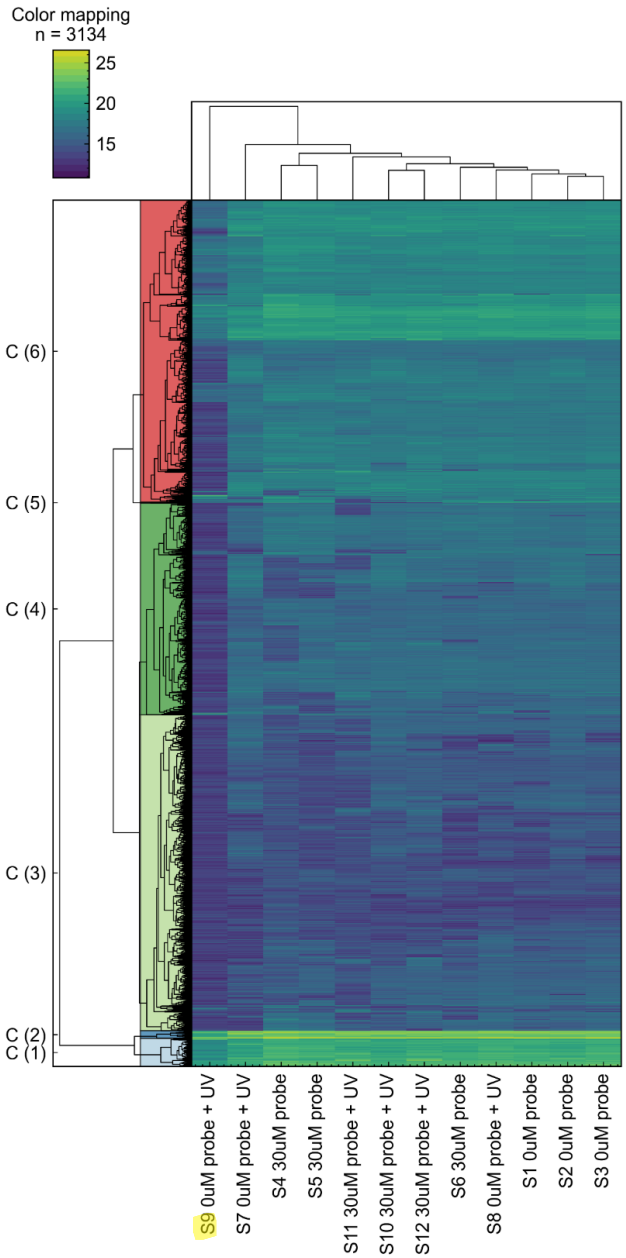

Figure 5.2: Hierachial clustering of proteomic samples from *MDA-MB-231* cells treated with 30 µM probe 1 (±UV). Sample 9 (highlighted) is very distinct from other samples.

5.5.1.1 Proteomic analysis in *MDA-MB-231* cells treated with 30 µM probe 1 (no UV)

Comparison of control cells with probe **1**-treated cells, in the absence of UV irradiation, identified proteins covalently modified by probe **1** (Figure 5.3). This revealed 1337 enriched proteins, of which, 213 were statistically significant ($p < 0.05$). STRING-database analysis of the significant proteins revealed that there were protein interactors in the membrane (purple), mitochondria (red) and also in vesicles (green) (Figure 5.4).

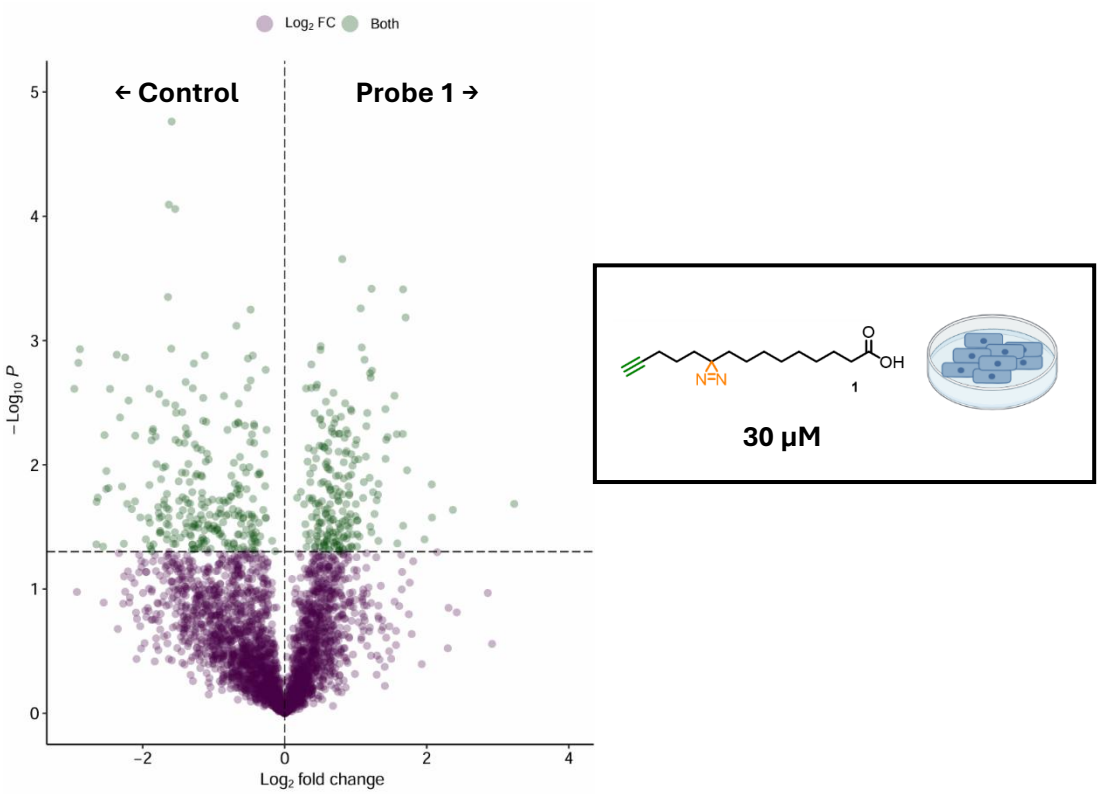

Figure 5.3: Proteomic analysis results of *MDA-MB-231* cells treated with 30 µM probe 1 (no UV). Volcano plot of proteins enriched by 30 µM probe **1** (16 h, no UV) compared with control cells.

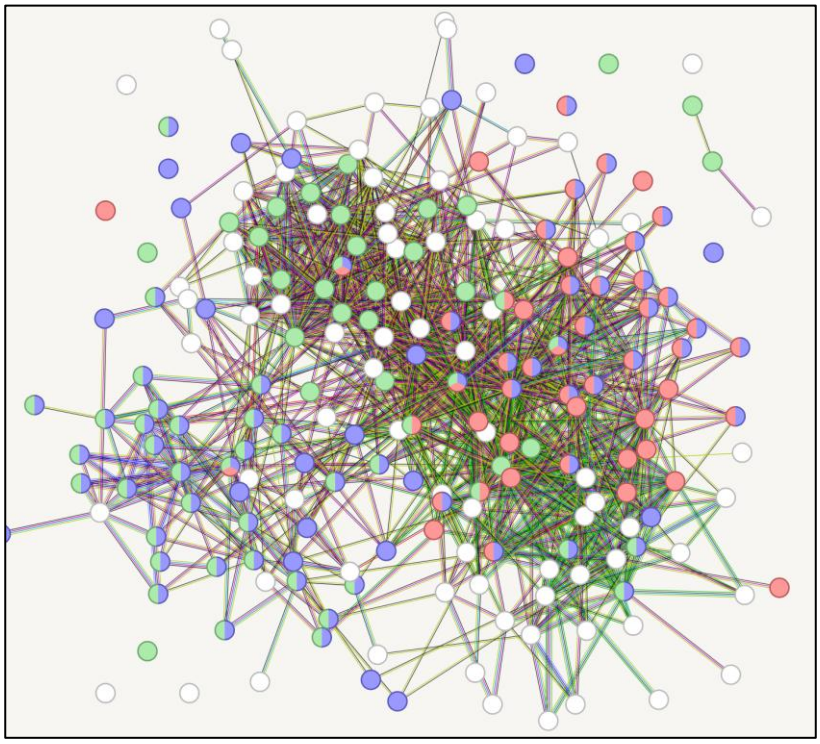

Figure 5.4: STRING analysis of significant proteins enriched by 30 µM probe 1 (no UV). Proteins in the membrane (purple), mitochondria (red) and in vesicles (green), with all other proteins (white).

The significantly enriched proteins were further analysed using Metascape for a pathway analysis to identify significantly enriched pathways associated with probe **1** treatment (Figure 5.5a). Among these significant pathways were 'Intracellular protein transport' and 'Membrane trafficking'. Proteins associated with these pathways included the Ras-Related Proteins 1A, 11A and 8B (RAB1A, RAB11A, RAB8B). Additionally, the 'Electron transport chain OXPHOS system in mitochondria' pathway was enriched upon treatment with probe **1**.

Next, an enrichment analysis of transcription factor (TF) targets was performed to investigate the gene regulation that occurred following the probe **1**-protein interactions. This analysis highlighted several protein interactors that are regulated by transcription factors of interest (Figure 5.5b). *PPARA* is a transcription factor that regulates lipid metabolism and energy homeostasis and was shown to have the most significantly enriched target genes. This interaction is of interest as FAs activate PPARs. Other TFs with enriched targets of interest were lysine methyltransferase 2D (KMT2D), histone deacetylase 4 (HDAC4) and DNA methyltransferase 3A (DNMT3A), all of which are involved in the regulation of epigenetics, through modifications that affect gene expression. Palmitoylation has been shown to be involved in the regulation of the localisation of histone acetyltransferases (HATs) and deacetylases (HDACs), with HDAC1 found to be palmitoylated using a variety of palmitoylation detection techniques.[189,190] Lastly, estrogen-related receptor 1 (ERR1), a TF heavily involved in regulating energy metabolism through mitochondrial biogenesis, OXPHOS and fatty acid oxidation.[191–193] This is of interest as ERR1 is often overexpressed in TNBC and associated with poor prognosis.[194,195]

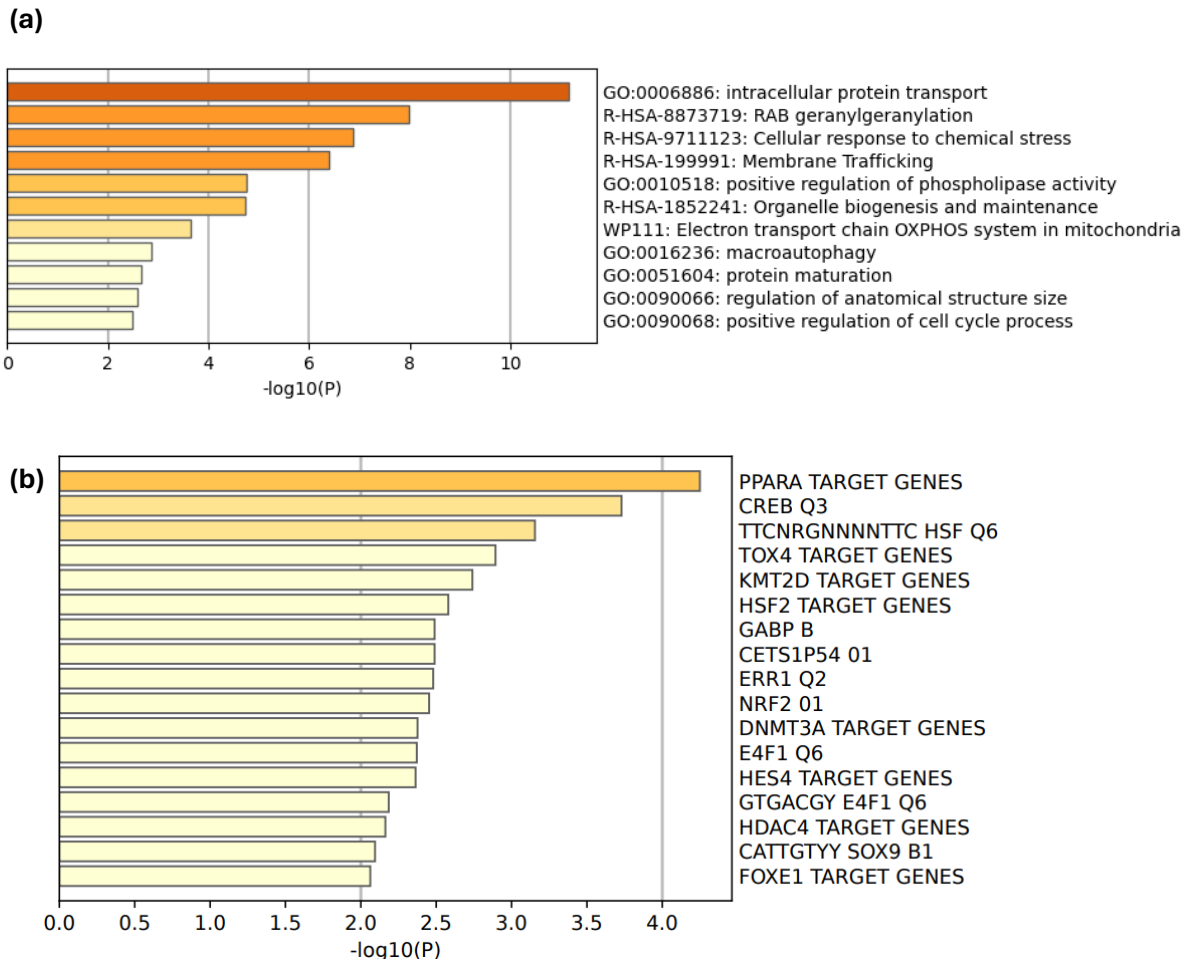

Figure 5.5: Pathway analysis of protein interactors following probe 1 (no UV) treatment): (a) Enriched terms across the input gene lists (proteins with an NSAF > 0) are coloured by p-values. (b) Enrichment analysis in transcription factor targets, coloured by p-values.

5.5.1.2 Proteomic analysis in *MDA-MB-231* cells treated with 30 µM probe 1 (with UV)

Comparison of control cells with probe **1**-treated (with UV) cells, identified proteins covalently modified by probe **1** (Figure 5.6). This revealed 2173 enriched proteins, of which, 196 were statistically significant ($p < 0.05$). STRING-database analysis of the significant proteins revealed that there were protein interactors in the nucleus (red), cytoskeleton (green) and membrane (purple) (Figure 5.7).

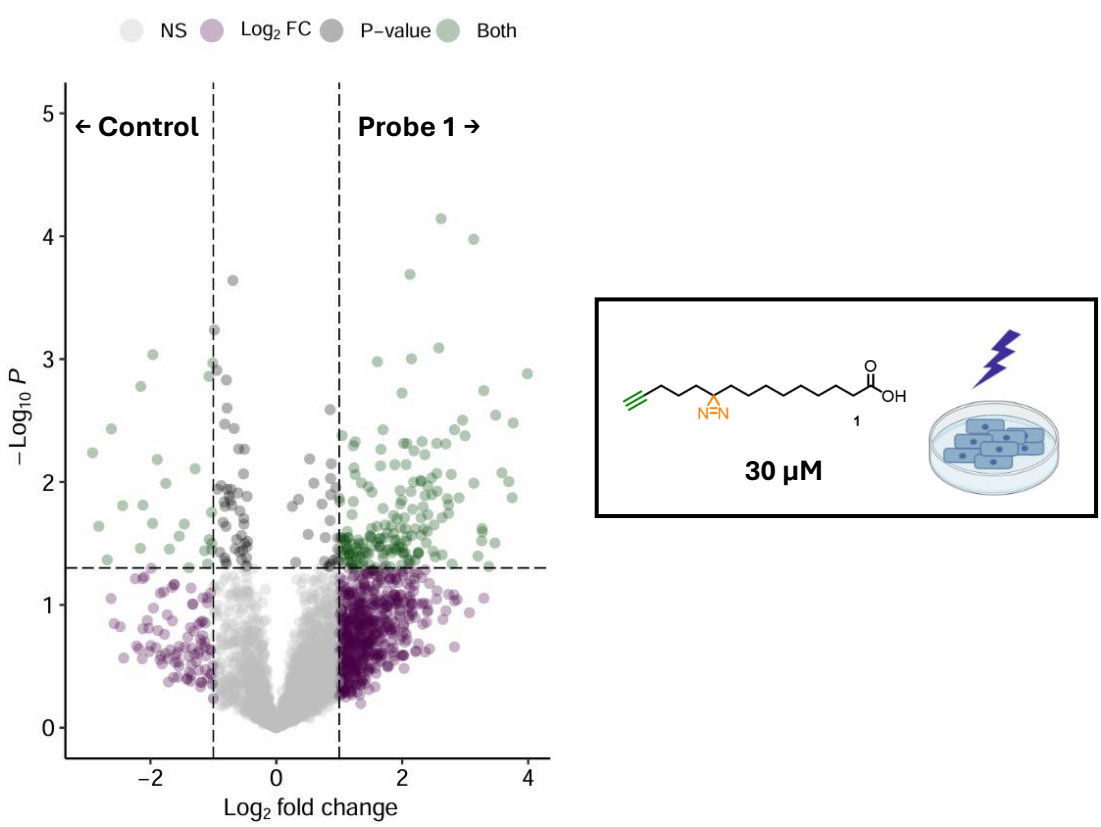

Figure 5.6: Proteomic analysis results of *MDA-MB-231* cells treated with 30 µM probe 1 (with UV). Volcano plot of proteins enriched by 30 µM probe **1** (16 h, with UV) compared with control cells.

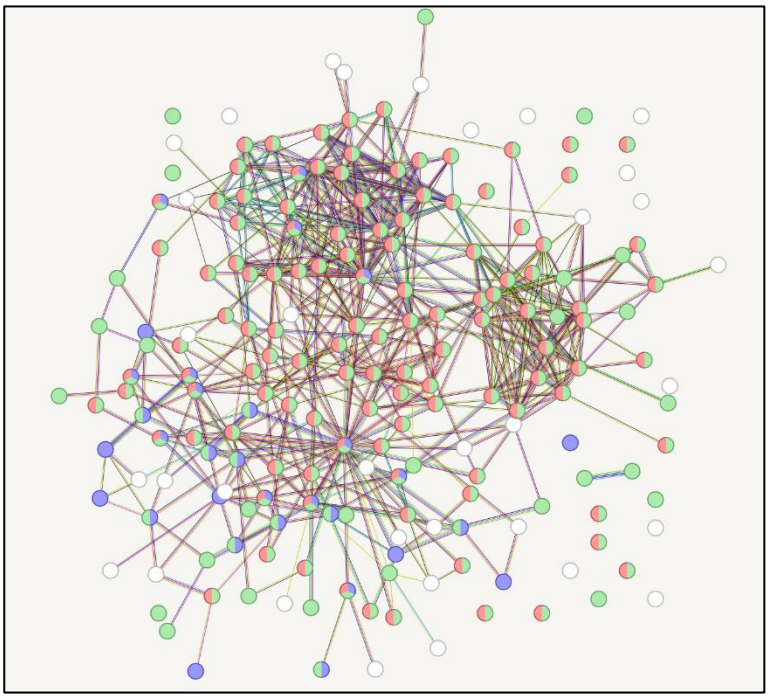

Figure 5.7: STRING analysis of significant proteins enriched by 30 µM probe 1 (with UV). Proteins in the nucleus (red), cytoskeleton (green) and membrane (purple) with all other proteins (white).

Next, an analysis of probe **1**-treated cells with UV irradiation was performed using Metascape and highlighted proteins that were non-covalent interactors of probe **1** (Figure 5.8a). Enriched pathways were involved in 'M Phase', 'Epigenetic regulation of gene expression' and 'Ribosomal large subunit biogenesis', suggesting that palmitate may be involved in the organisation and regulation of DNA and gene expression. Following enrichment of TF targets (Figure 5.8b), several TF of interest were involved in cancer progression. Myelocytomatosis oncogene (MYC) is involved in cell growth, proliferation and cell metabolism and its overexpression or dysregulation is linked to many cancers, including breast cancer.[53]

(a)

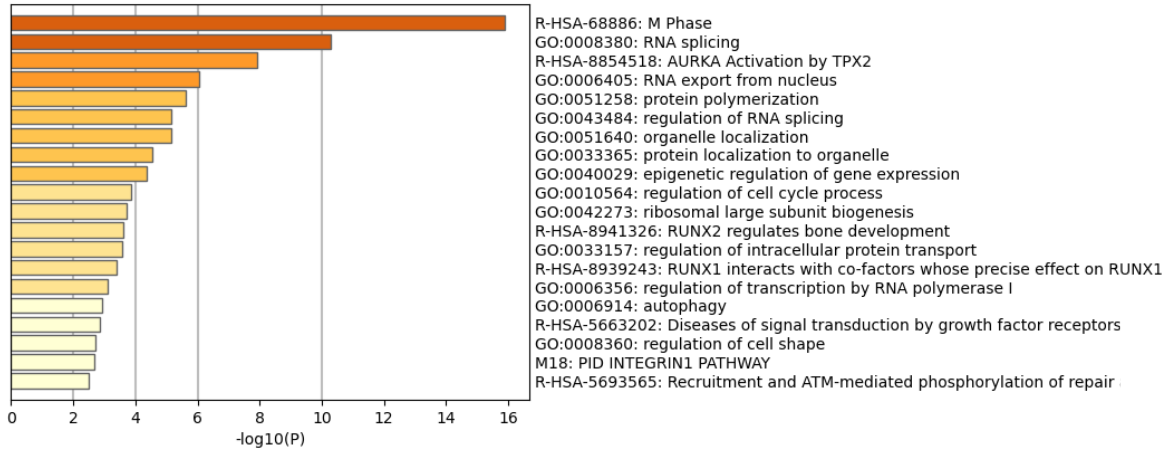

(b)

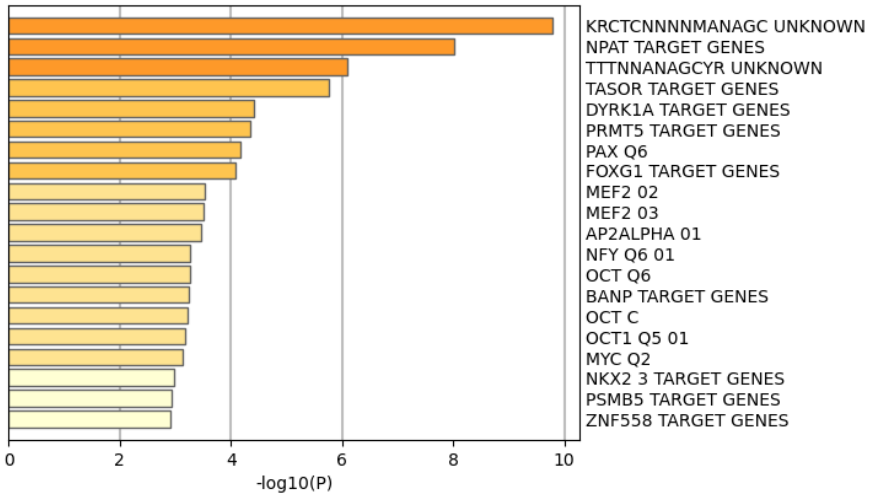

Figure 5.8: Pathway analysis of protein interactors following probe 1 (no UV) treatment): (a) Enriched terms across the input gene lists (proteins with an NSAF > 0) are coloured by p-values. (b) Enrichment analysis in transcription factor targets, coloured by p-values.

5.5.2 Validation of probe 1 protein targets in *MDA-MB-231* cells

Following pathway analysis of enriched proteins, experimental validation was performed to verify the authenticity of the identified probe **1** targets, without UV irradiation. Amongst these enriched proteins were examples of proteins that had previously been found in palmitoyl-proteomes, e.g., ATP5MG, RAB11B and MT-CO2 (Figure 5.8a).[196–198] ATP5MG and MT-CO2 are proteins involved in OXPHOS and RAB11B is heavily involved in protein transport. Validation of these proteins was performed by Western blot, and this demonstrated enrichment of all three proteins following neutravidin-biotin pulldown (Figure 5.9b).

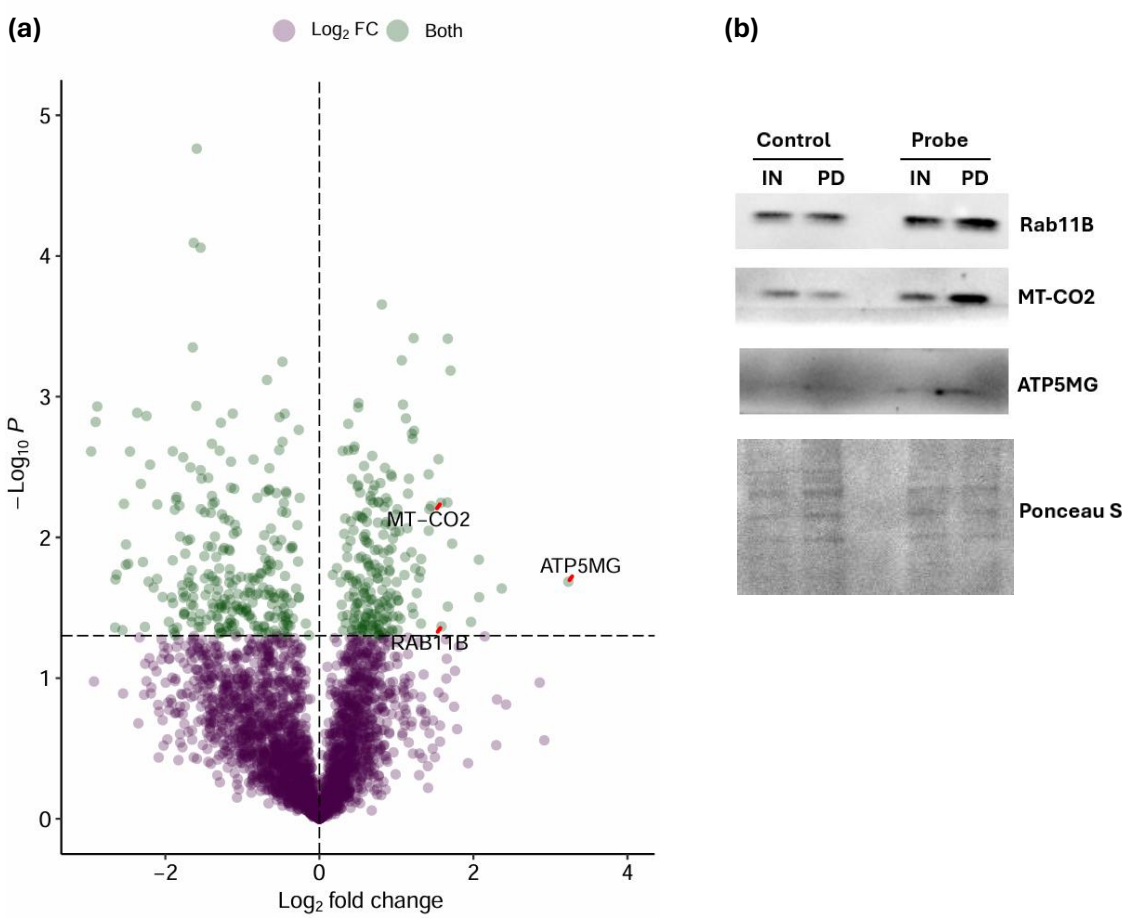

Figure 5.8: Validation of covalent protein interactors of probe 1: (a) Volcano plot of the differential abundance results for probe **1** treatment (16 h). (b) Validation of selected enriched proteins by Western blotting (IN = input, PD = pulldown). Increased enrichment following pulldown is shown when probe is present. Total protein stained using Ponceau S. Abbreviated proteins include RAB11B: Ras-Related Protein Rab-11B, MT-CO2: Mitochondrially Encoded Cytochrome C Oxidase II, ATP5MG: ATP Synthase Membrane Subunit G. For quantification of pulldown enriched targets in *MDA-MD-231* cells, see *Appendix B*.

Further confirmation of interaction between probe **1** and MT-CO2 was performed using confocal microscopy within cells. Cy5 was chosen as the fluorophore to be clicked onto probe **1** as the

fluorescence of TAMRA would have overlapped with the 488-channel (MT-CO2). The fluorescence signal from Cy5 demonstrated a strong overlap with the MT-CO2 antibody, indicating colocalisation of probe **1** with MT-CO2 (Figure 5.9). This colocalisation was quantified and showed a 2.5-fold increase when probe **1** was present compared with control cells. The observations that probe **1** accumulates in the mitochondria and interacts with proteins involved in OXPHOS suggest that the mitochondrial localisation may also directly influence the proteins involved in the OXPHOS pathway.

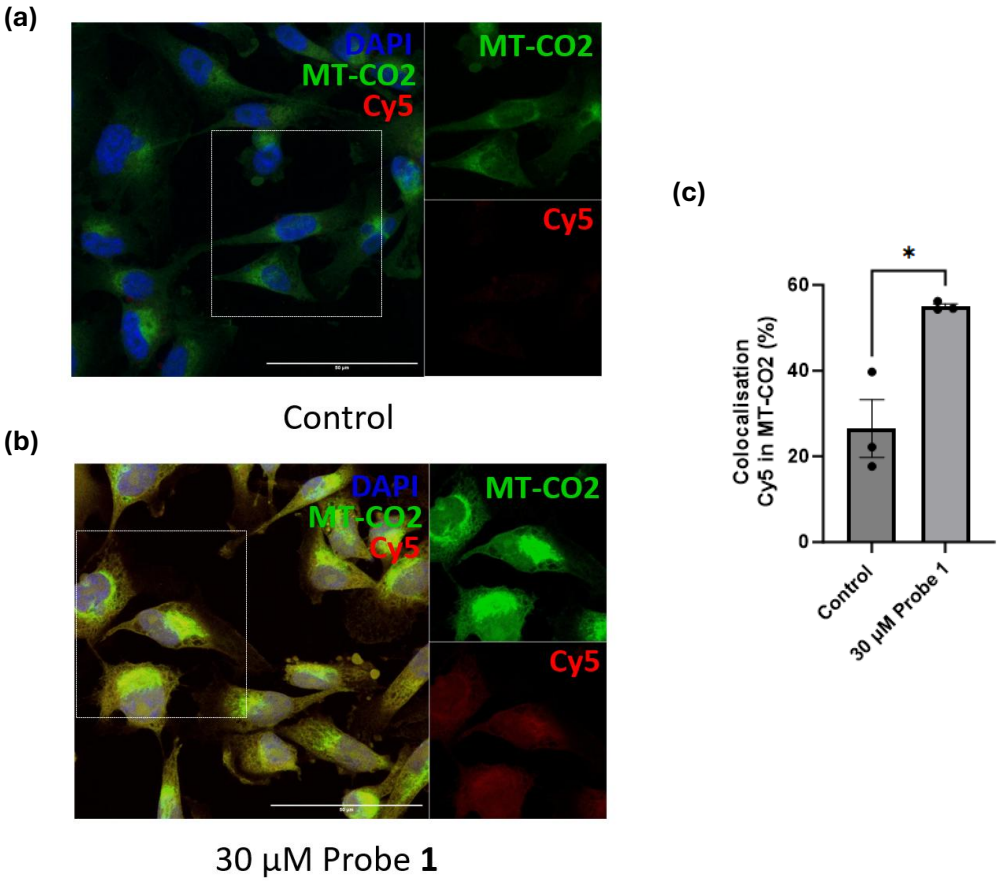

Figure 5.9: Colocalisation of probe 1 with MT-CO2: Imaging of colocalisation of probe **1** (Cy5) (green) with LipidTOX (red), as control (a) or after treatment for 16 h with (b) probe **1**. (c) Quantification of the probe 1(Cy5) colocalisation with MT-CO2. % = % volume.

Western blotting was also performed on selected proteins interacting with probe **1** in the presence of UV irradiation. Histone 3 (H3-3A) and beta-actin (ACTB) were validated by western blot, with both showing enrichment after neutravidin pulldown (Figure 5.10).

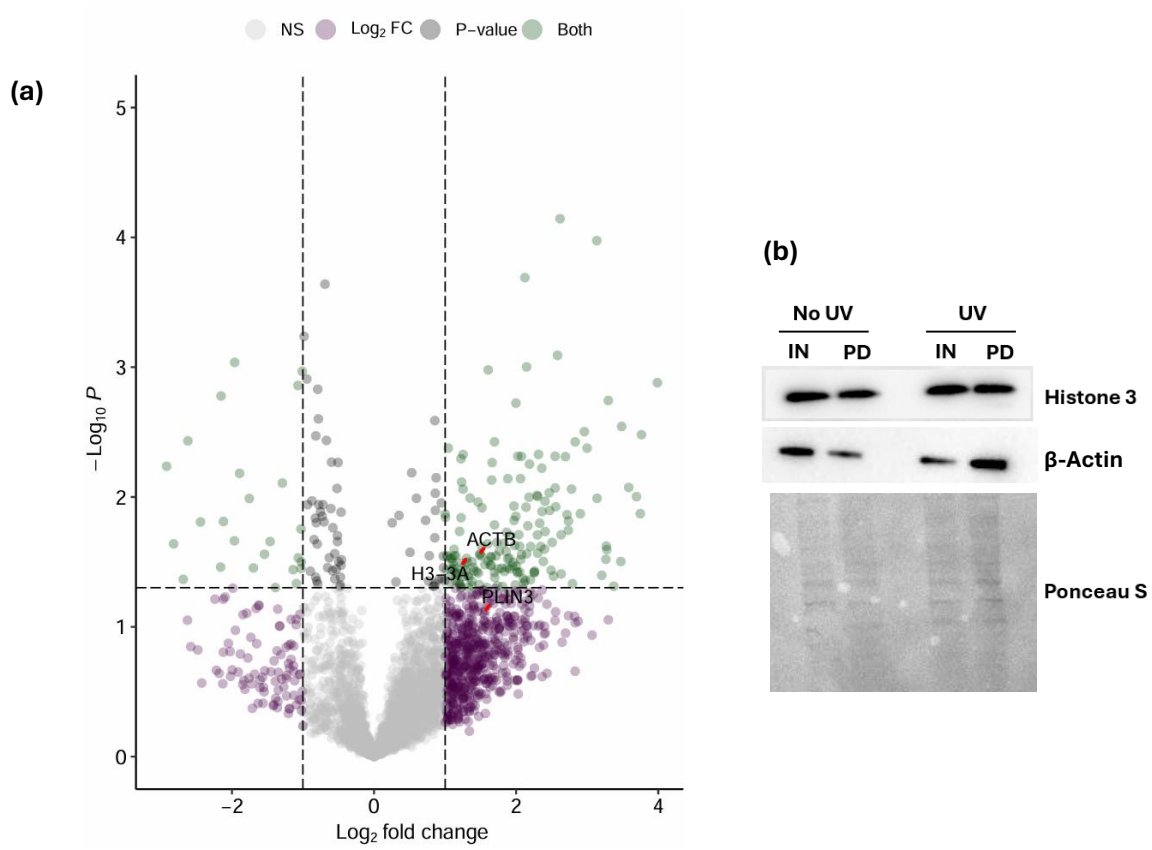

Figure 5.10: Validation of protein interactors of probe 1 (+UV): (a) Volcano plot of the differential abundance results for probe **1** treatment (16 h, +UV 3 min). (b) Validation of selected enriched proteins by Western blotting (IN = input, PD = post-pulldown). Increased enrichment following pulldown is shown with UV irradiation. Total protein stained using Ponceau S. For quantification of pulldown enriched targets in *MDA-MD-231* cells, see *Appendix B*.

FAs have been shown to be involved in actin remodelling as a consequence of insulin resistance.[199] Therefore, untreated, palmitate- and probe **1**-treated cells were stained with phalloidin to examine the F-actin filaments in the cells (Figure 5.11a-c). Comparing control with probe **1**-treated cells showed a statistically significant increase in the levels of F-actin when probe **1** was present (Figure 5.11d). However, there was no significant difference in levels when the cells were treated with 30 μM of palmitate. This suggests that probe **1** has a potential effect on actin remodelling in the cells.

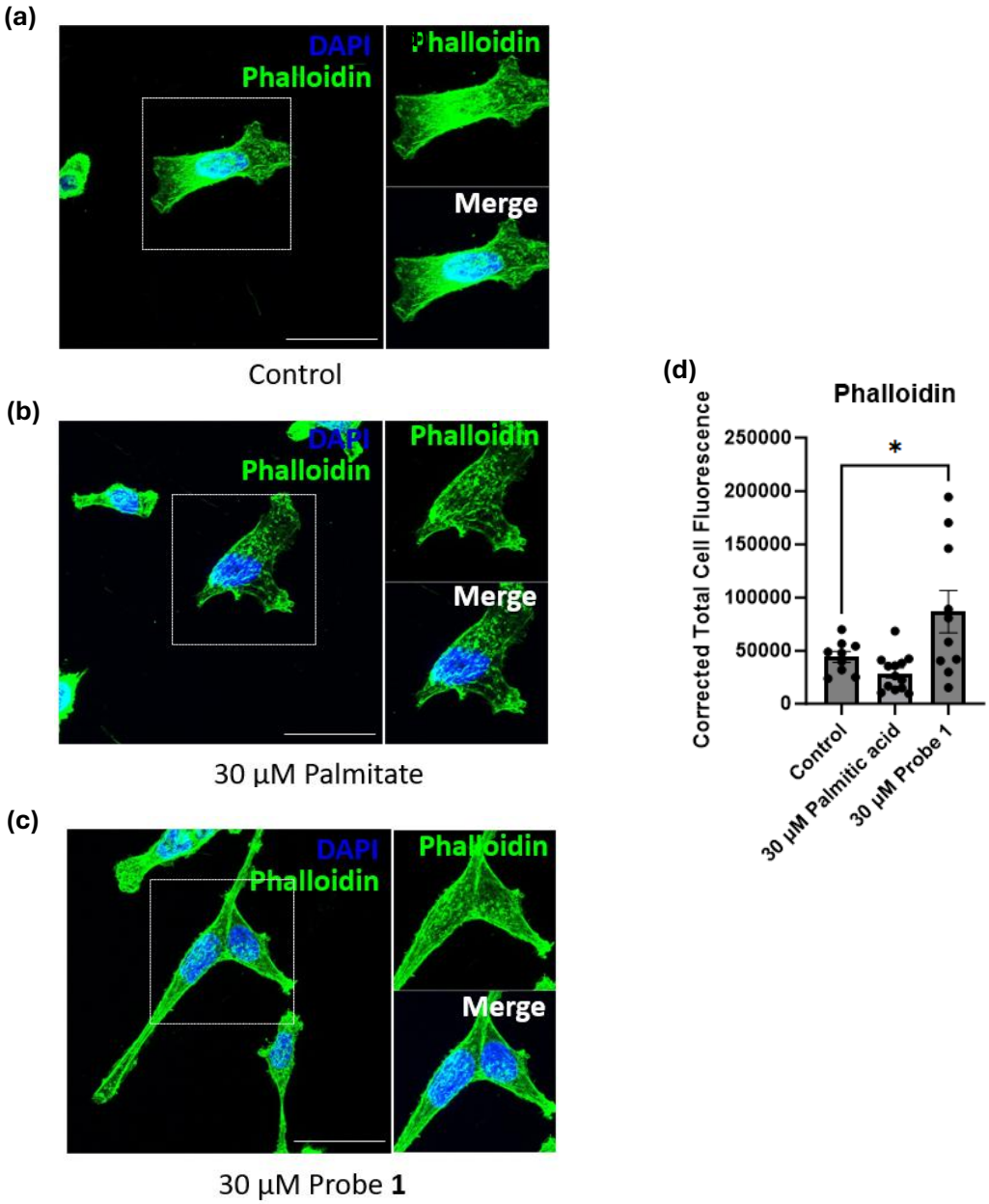

Figure 5.11: Probe 1 treatment is increasing F-actin filament levels: Imaging using Phalloidin (green) with DAPI (blue), as (a) control or after treatment for 16 h with (b) 30 µM palmitate or (c) 30 µM probe **1**; scale bar is 50 µM with ×2 zoom to the right and (d) quantified corrected total cell fluorescence. (e) Quantification of the colocalisation. % = % volume (n=10).

Perilipin 3 (PLIN3) is a protein involved in lipid storage, helping with the formation and stabilisation of lipid droplets within cells. Due to the borderline significance (p_{val} = 0.08) with 30 µM probe **1** (with UV) (Figure 5.10a) and its interest to the group, PLIN3 was explored further. Therefore, confocal imaging was performed to investigate the colocalisation of probe **1** and lipid droplets (Figure 5.12). The imaging revealed an overlap in the fluorescence signal between the Cy5 (probe

1) and the LipidTOX stain. This visualisation was quantified and showed a 1.5-fold increase in overlap when probe **1** was present versus control cells (Figure 5.12c). This quantification revealed that probe **1** was being localised to the lipid droplets and the specificity of the localisation suggested an affinity and potential esterification of probe **1** into the triglyceride pool.

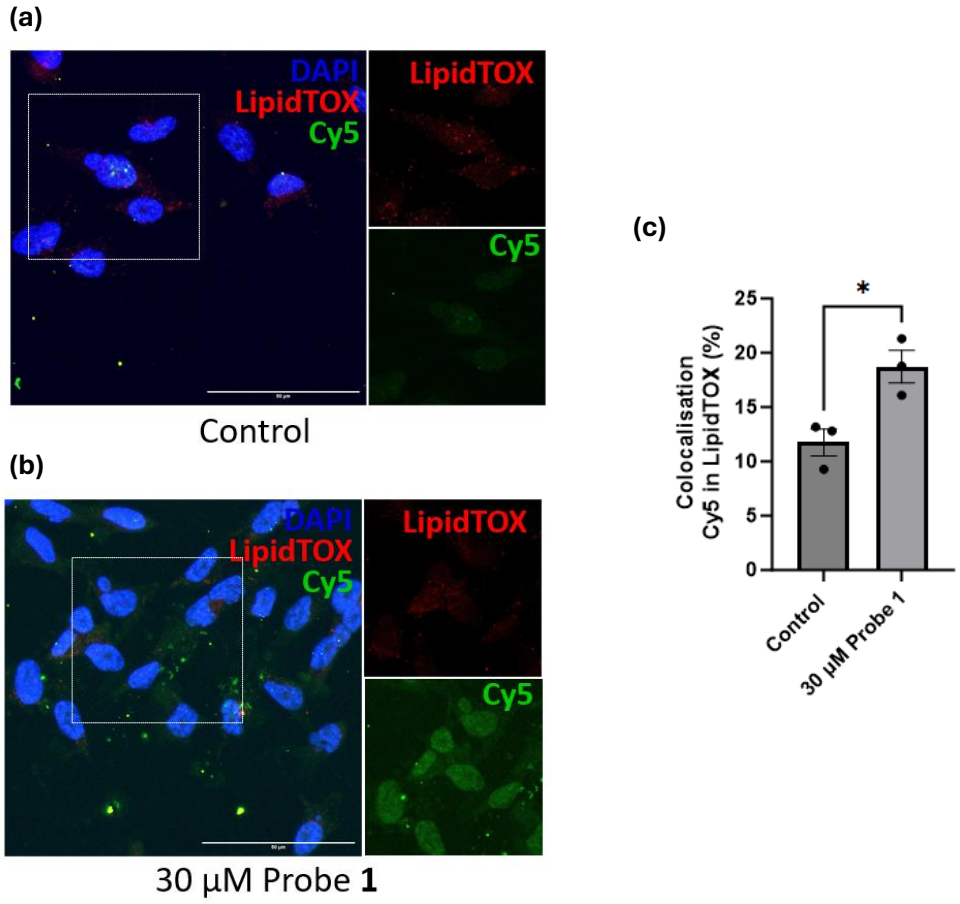

Figure 5.12: Probe 1 (Cy5) colocalises with lipid droplets (LipidTOX): Imaging of colocalisation of probe **1** (Cy5) (green) with LipidTOX (red), as (a) control cells or (b) cells treated for 16 h with probe **1**; (c) Quantification of the probe **1** (Cy5) colocalisation with LipidTOX. % = % volume.

5.5.3 Transcriptomic analysis of probe 1-treated *MDA-MB-231* cells

An investigation into the downstream consequences of the probe **1**-protein interactome was performed. To do this, *MDA-MB-231* cells were incubated with 30 µM probe **1** for 16 h (no UV), RNA was extracted and samples sent to Novogene for RNA sequencing. The rationale for this analysis was that if probe **1** was interacting with proteins – both covalently and non-covalently – this

would likely have an effect on cell function and gene transcription, allowing the identification of the downstream consequences of these interactions.

A transcriptomic analysis was conducted to allow for genome-wide analysis following probe **1** treatment. PCA demonstrated a clear separation between control and probe **1**-treated cells (16 h) (Figure 5.13). PC1 captured 75% variance due to probe **1** treatment. PC2 captured only 9% variance, likely due to variation unrelated to probe **1** treatment.

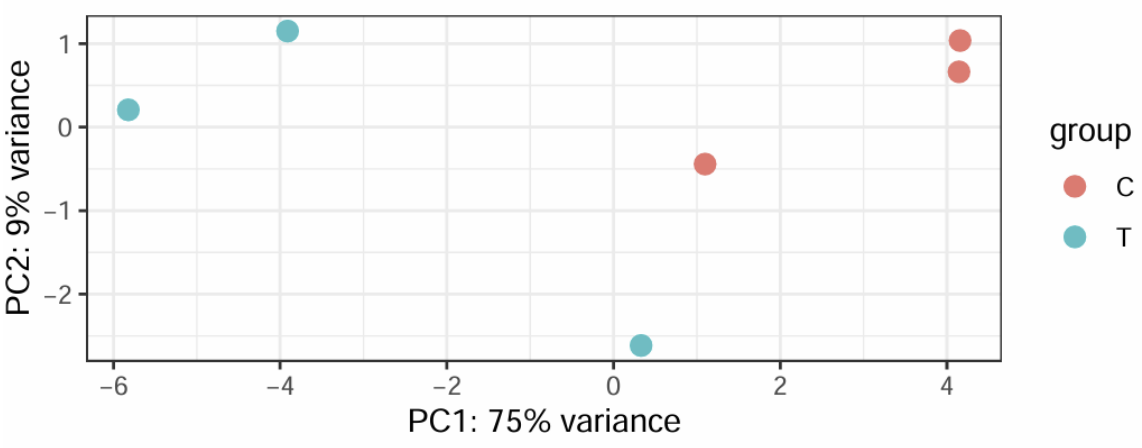

Figure 5.13: PCA plot of *MDA-MB-231* cell samples for transcriptomic analysis: Cell samples as controls (orange) or treated with: 30 µM Probe **1** (blue). PC1 captures 75% variance, attributed to probe **1** treatment. PC2 captures only 9% variance, attributed to variations unrelated to probe **1** treatment.

Differential gene expression (DEGs) analysis identified 10,531 genes changing with probe **1** treatment, of which, 5,410 were upregulated and 5,121 were downregulated (Figure 5.14). Further analysis gave 527 (9.7%) upregulated and 834 (16.2%) downregulated genes as statistically significant ($p_{val} < 0.05$). This demonstrated that the DEG analysis captured global gene changes caused by probe **1** treatment.

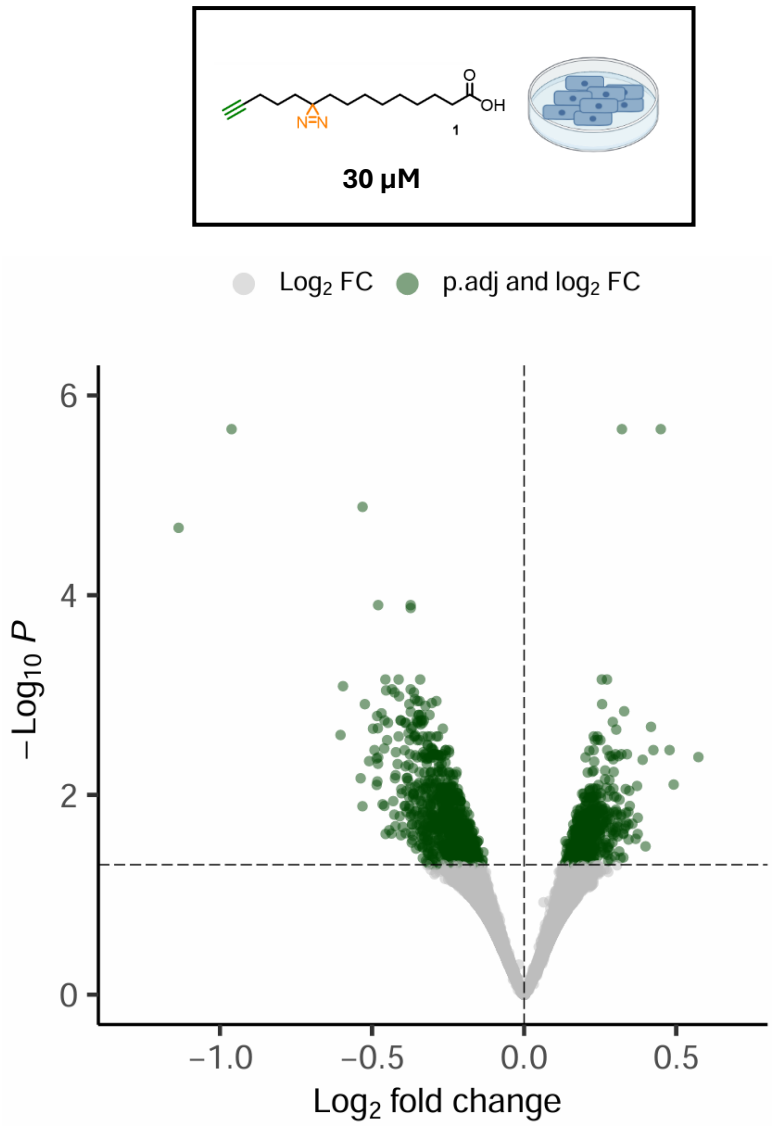

Figure 5.14: Transcriptomic analysis results of *MDA-MB-231* cells treated with 30 µM probe 1. Volcano plot of gene expression changes by 30 µM probe **1** (16 h) compared with control cell (16 h).

As these large-scale changes occurred in the transcriptome a pathway approach was adopted to reduce complexity and investigate broader biological function changes. According to Metascape, the highest upregulated GO biological process from the DEGs were 'Metabolic processes' (Figure 5.15a), meaning genes involved in cellular metabolism were upregulated following probe **1** treatment. Specifically, pathways of interest that were upregulated were: 'Oxidative phosphorylation', 'Mitotic cell cycle'; 'Organelle localisation'; and 'Mitochondrial gene expression' (Figure 5.15b).

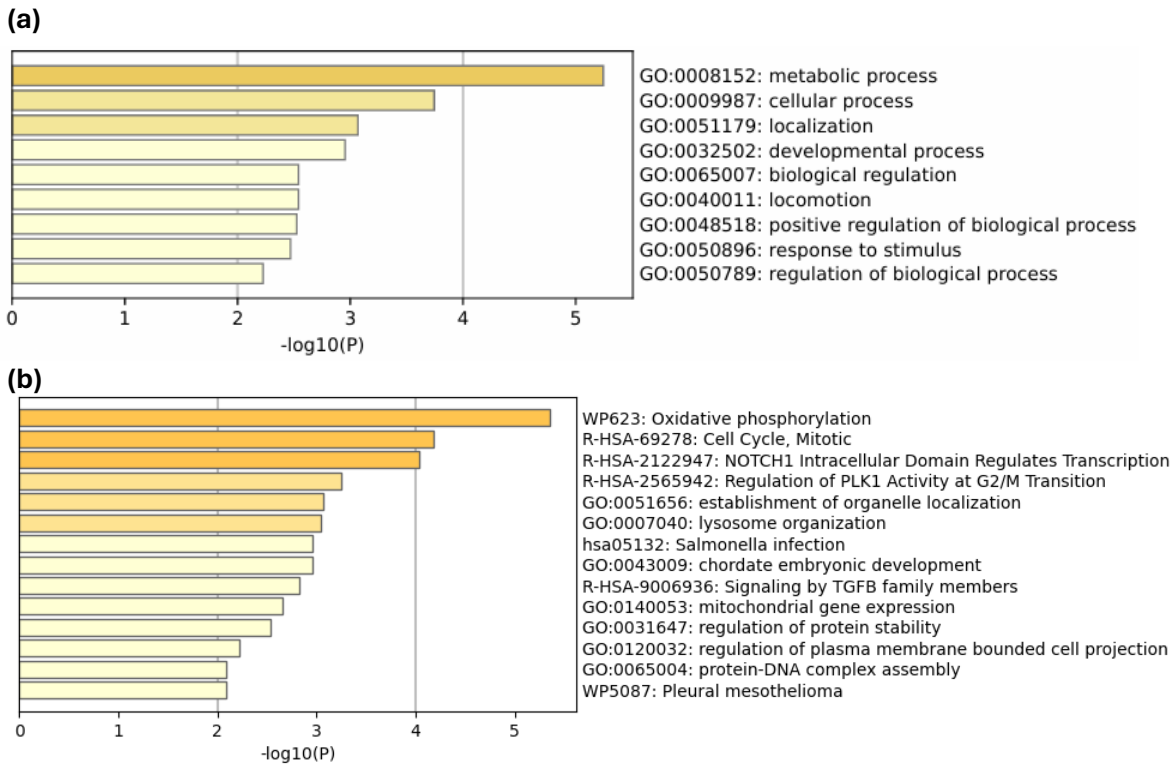

Figure 5.15: Pathway enrichment analysis of genes upregulated by probe 1: (a) Top-level GO biological processes coloured by p-values. (b) Top pathways enriched, coloured by p-values.

To gain further insight into affected upregulated biological pathways, a KEGG pathway analysis was also performed on the DEGs (Figure 5.16a). The analysis revealed significant upregulation in several key pathways. Notably, 'Oxidative phosphorylation' showed a substantial number of upregulated genes in the probe **1**-treated cells, suggesting enhanced OXPHOS as a response to treatment. The mTOR signalling pathway exhibited a significant upregulation, indicating a potential connection between probe **1** and mTOR signalling in cells.

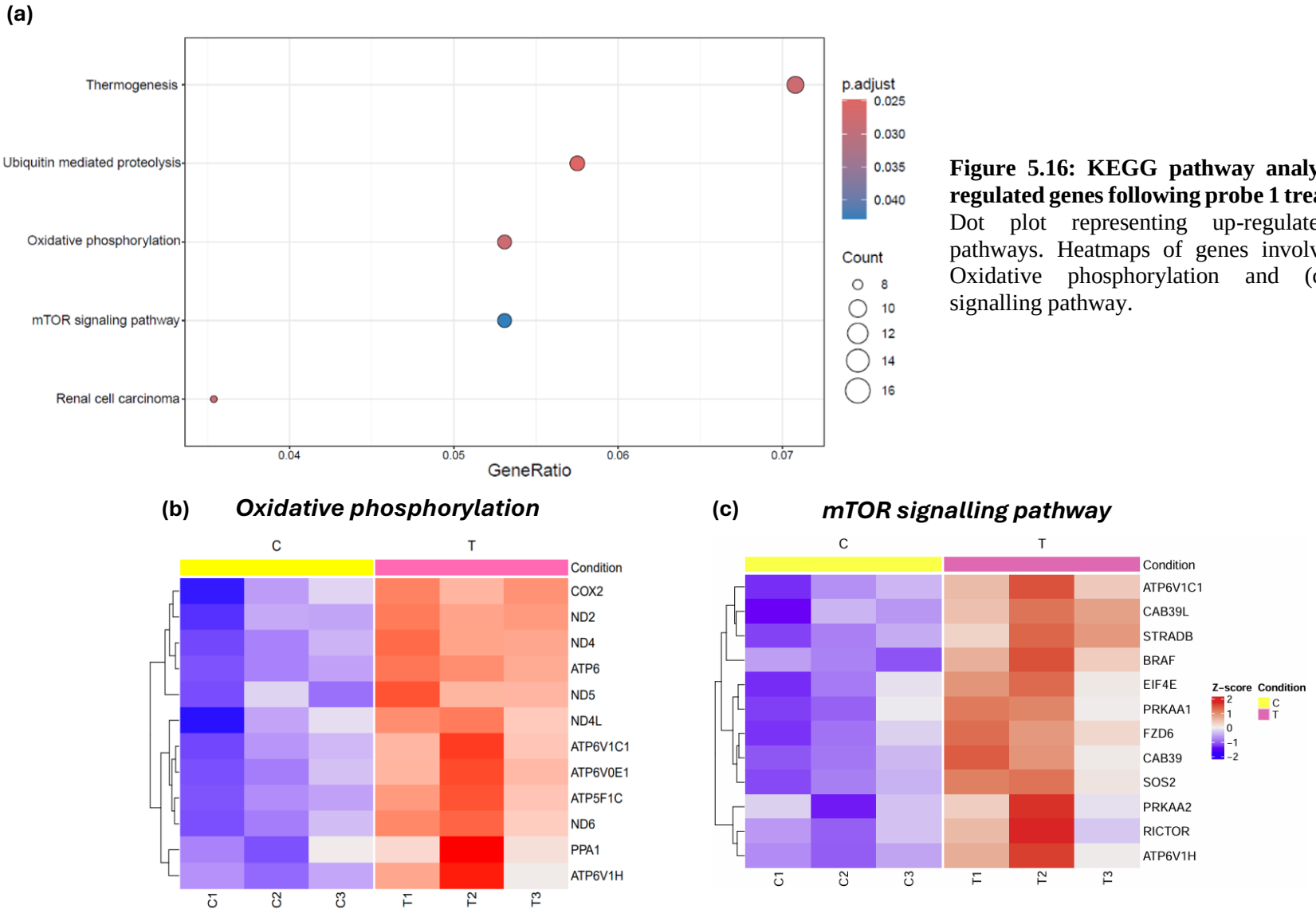

Figure 5.16: KEGG pathway analysis of up-regulated genes following probe 1 treatment: (a) Dot plot representing up-regulated KEGG pathways. Heatmaps of genes involved in: (b) Oxidative phosphorylation and (c) mTOR signalling pathway.

A Metascape analysis was performed to assess the biological implications of the downregulated genes following probe **1** treatment (Figure 5.14). 'Cellular processes' was the most enriched GO biological process, with 'localisation' and 'Metabolic processes' enriched too (Figure 5.17a). The results highlighted several significantly downregulated pathways and biological processes. The 'Actin Cytoskeleton Organisation' pathway was prominently downregulated, indicating suppression of actin-based cytoskeletal organisation (Figure 5.17b). Additionally, the 'Regulation of the Androgen Receptor (AR) Signalling' pathway was downregulated. This suggests that probe **1** treatment may potentially act as an inhibitor of androgen receptor signalling or lower androgen receptor levels in cells, or it may have a broader effect on multiple signalling pathways. Downregulation of the 'RNA metabolism' pathway following probe **1** treatment may suggest an interference with key processes involved in RNA processing, synthesis and stability (Figure 5.14a). Similarly to the upregulated genes, a KEGG analysis was performed and demonstrated that probe **1** treatment led to a significant downregulation of the 'Insulin Signalling' pathway, as observed in the KEGG pathway analysis (Figure 5.18). KEGG analysis also demonstrated a downregulation of the 'Regulation of Actin Cytoskeleton' pathway.

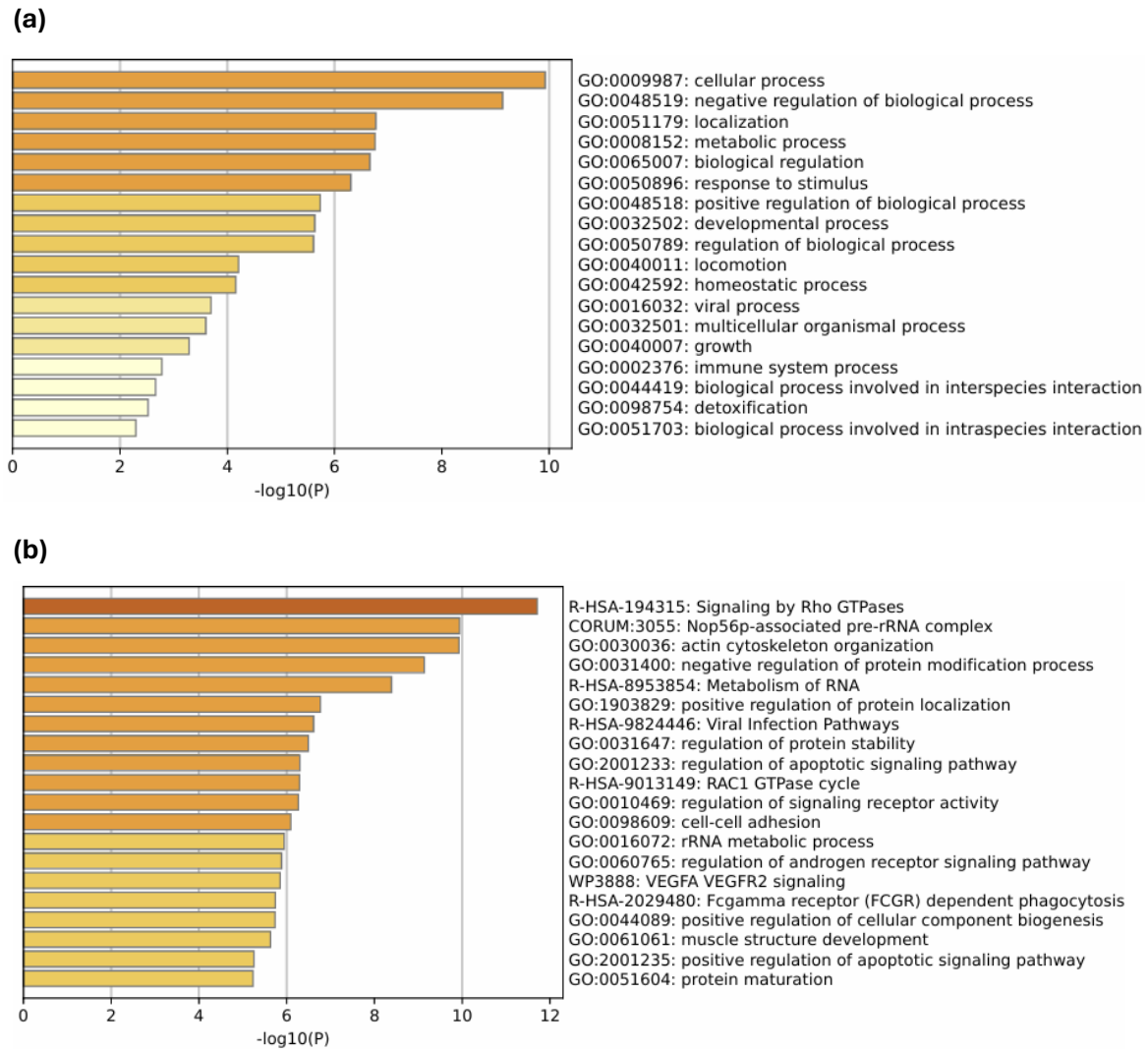

Figure 5.17: Pathway enrichment analysis of genes downregulated by probe 1: (a) Top-level GO biological processes, coloured by p-values; (b) Top pathways enriched, coloured by p-values

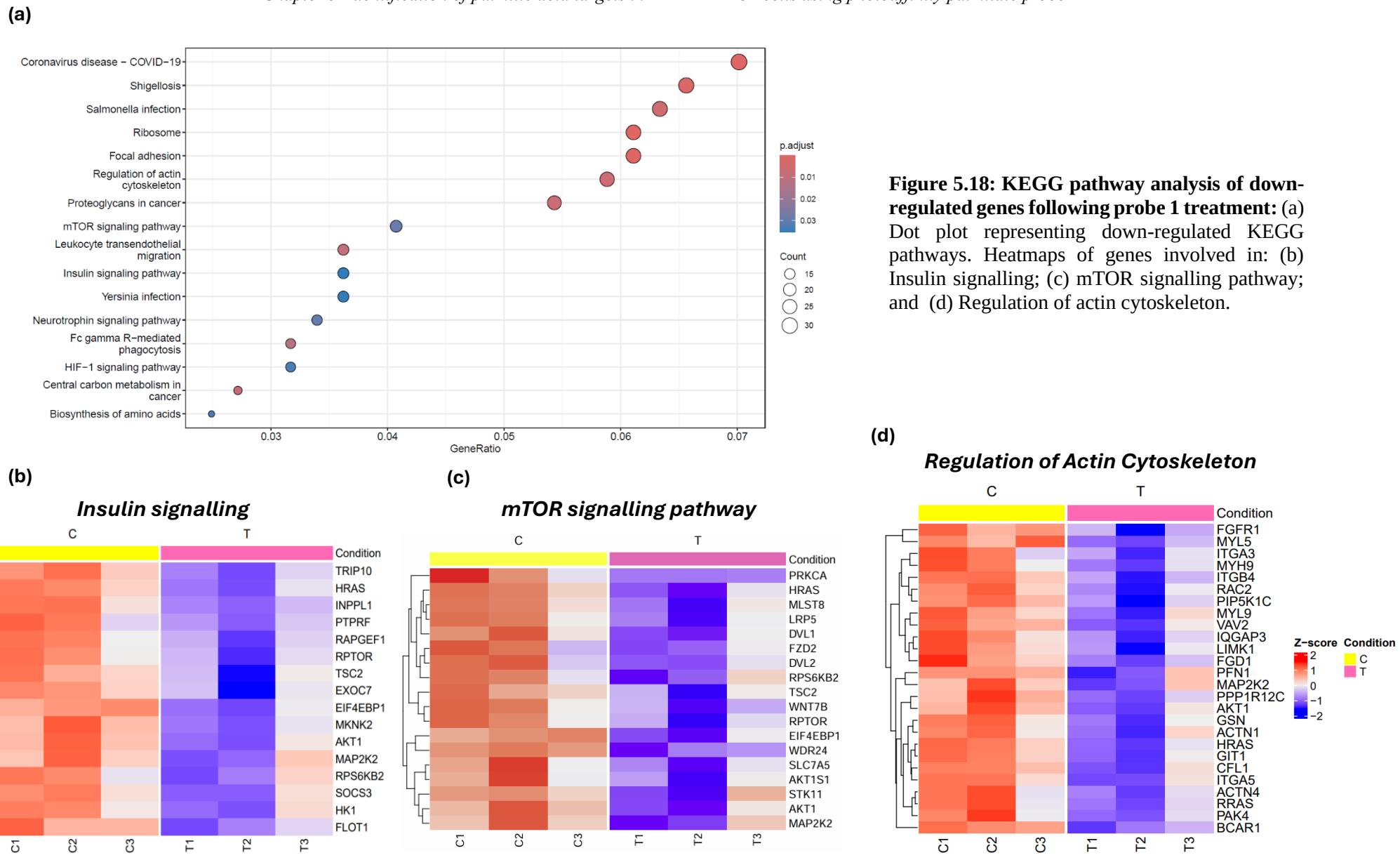

Figure 5.18: KEGG pathway analysis of down-regulated genes following probe 1 treatment: (a) Dot plot representing down-regulated KEGG pathways. Heatmaps of genes involved in: (b) Insulin signalling; (c) mTOR signalling pathway; and (d) Regulation of actin cytoskeleton.

Gene set enrichment analysis (GSEA) was performed as an alternative unbiased pathway approach to identify significant changes in pathway activities after probe **1** treatment (Figure 5.19). This analysis revealed a notable upregulation in the 'Energy Metabolism' pathway, suggesting an adaptive response to increased cellular energy demands or metabolic states. 'Synthesis of ceramides and deoxyceramides' was also a pathway of interest, as ceramides are involved in lipid storage processes, e.g. lipid droplet formation.

There was also a downregulation of several pathways of interest: 'Insulin Signalling', 'Glycolysis', 'Focal Adhesion' and 'Estrogen Early Response' pathways. The downregulation of the 'Insulin Signalling' pathway indicated an impaired insulin sensitivity or a shift away from insulin-dependent metabolic processes. The downregulation of the 'Glycolysis' pathway further corroborates a shift in cellular metabolism, as glycolysis is the primary glucose metabolism pathway. This is consistent with the upregulation in 'Energy Metabolism' pathways, suggesting reprogramming of energy stores. Additionally, the reduction in 'Focal Adhesion' pathways reflect altered cell-matrix interactions, which may affect cell motility and adhesion properties. Lastly, the downregulation in 'Estrogen Early Response' pathways indicates a diminished response to estrogen signalling, with a potential effect on processes like cell growth and proliferation.

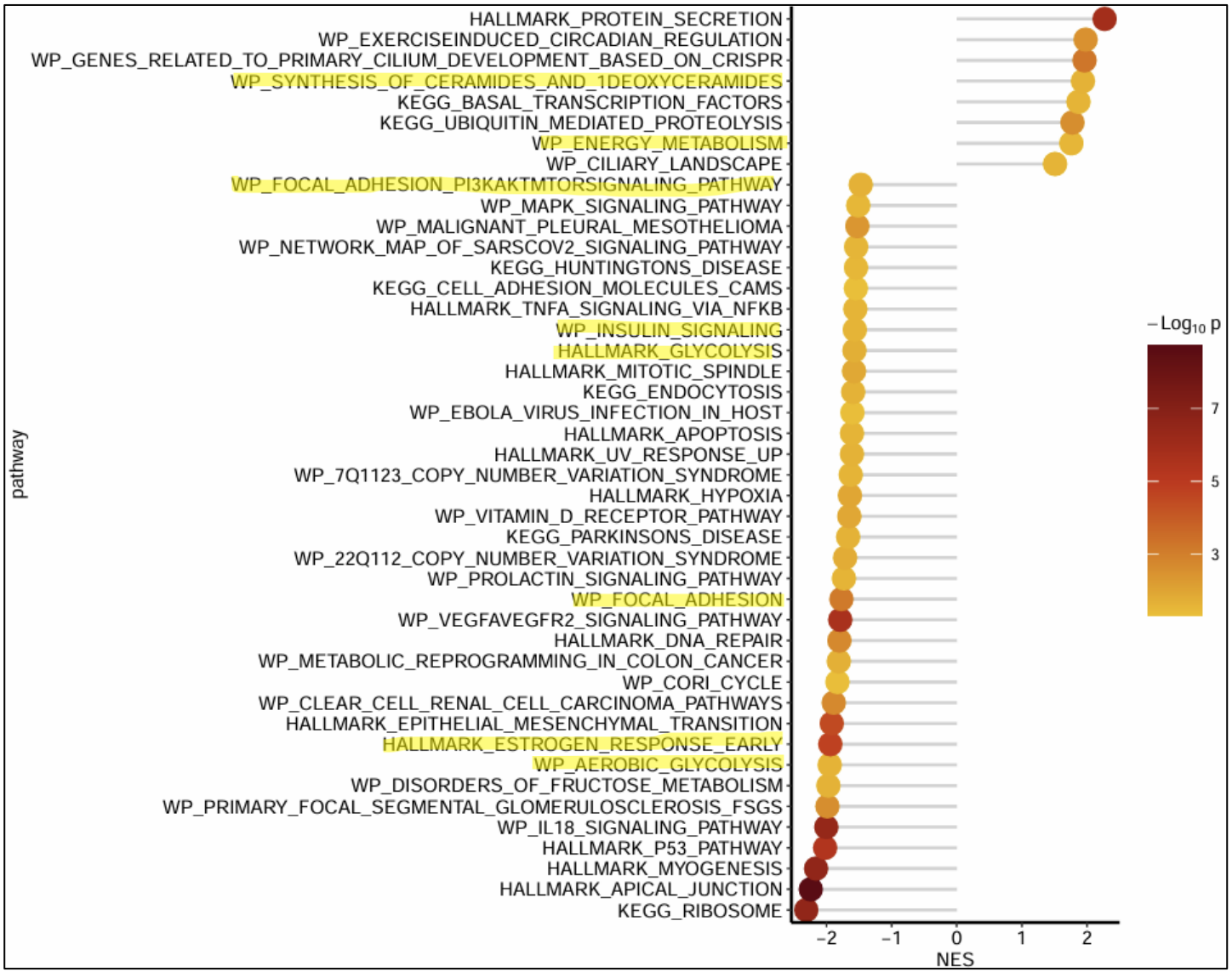

Figure 5.19: Gene Set Enrichment Analysis (GSEA) of transcriptomics: The results of a Gene Set Enrichment Analysis (GSEA) of transcriptomic data following 30 µM probe **1** treatment, identifying significantly enriched biological pathways and gene sets. The x-axis represents the normalized enrichment score (NES), with positive values indicating enrichment in the upregulated gene sets and negative values in the downregulated gene sets. The size and colour of the points correspond to the statistical significance of the enrichment, represented as the -Log_{10}(p-value), where warmer colours (red and orange) indicate higher significance levels. Highlighted pathways, such as , demonstrate significant metabolic and signalling changes in the dataset. This analysis provides insights into the molecular mechanisms underlying the transcriptomic profile.

5.5.4 Validation of transcriptomic targets in *MDA-MD-231* cells

To validate the transcriptomic results, qPCR was performed to confirm the expression levels of selected genes identified. A volcano plot of the enriched genes allowed for the selection of several statistically significant ($p_{val} > 0.05$) genes to validate (Figure 5.20).

Downregulated genes included *GPR89B, ACTN4* and *RAC2* and upregulated genes included *ND4* and *CXXC4*. Hypoxanthine phosphoribosyltransferase 1 (*HPRT*) was chosen as the housekeeper gene, as it had been previously used for *MDA-MB-231* cells[200] and showed no difference between probe **1**-treated and control cells (Figure 5.20). *GPR89B* was shown to be statistically decreased in probe **1**-treated samples (Figure 5.20). However, *ACTN4* and *RAC2* were not statistically significant. Two primers had been designed for *CXXC4* but did not pass the primer validation step of qPCR. As RNA sequencing is a more sensitive technique than qPCR, the fold changes for these genes may not have been sufficient to see by qPCR.

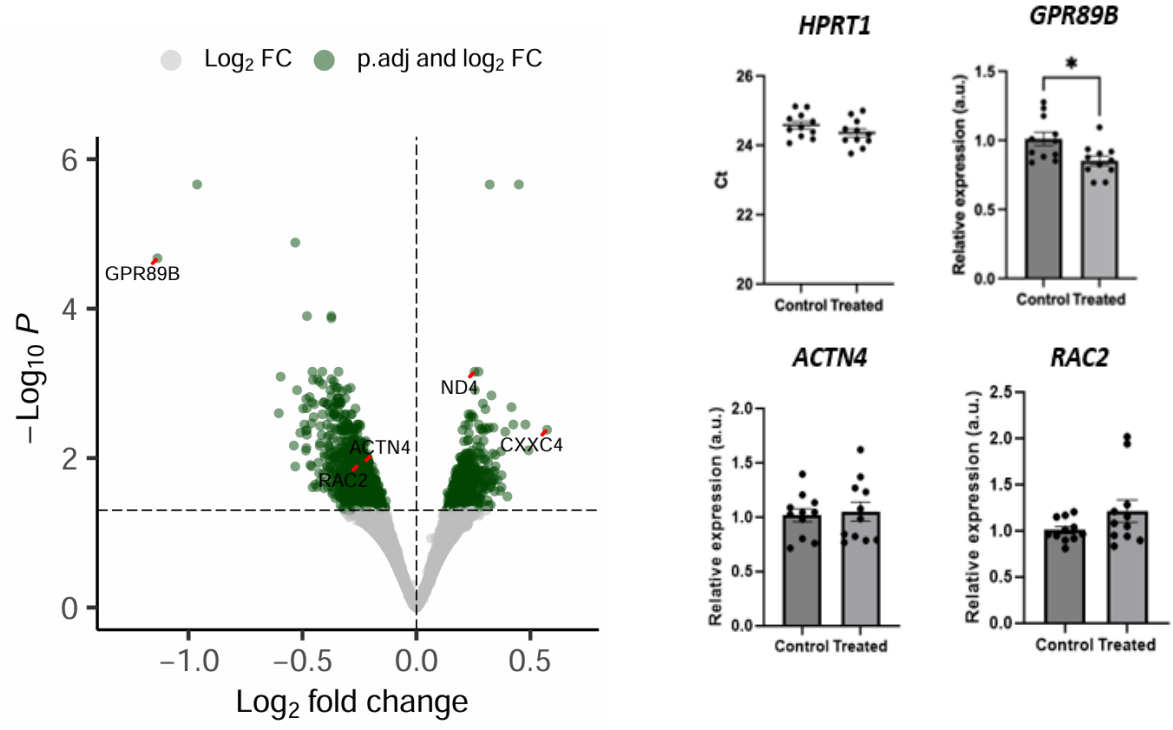

Figure 5.20: Validation of transcriptomic results for *MDA-MB-231* cells by qPCR: *HPRT* selected as housekeeper (n=11) with qPCR results of *GPR89B, ACTN4* and *RAC2* (n=11).

To further investigate the gene expression changes of the 'mTOR Signalling' pathway, as this pathway appeared in both the up- and down-regulated gene pathways, a mapping of gene expression levels to the signalling pathway was performed (Figure 5.21). Among the upregulated genes were serum/glucocorticoid regulated kinase 1 (*SGK1*), ras homolog family member A (*RHO*) and growth factor bound receptor 10 (*GRB10*), these are involved in cell survival, cytoskeleton organisation and lipolysis, respectively. Downregulated genes included autophagy-related 1 homolog (*ATG1*), lipin 1 (*LPIN1*) and cytoplasmic linker protein 170 (*CLIP1*), involved in autophagy, lipid synthesis and microtubule organisation. This suggests that incubation of the cells with probe **1**, a FA mimetic, is downregulating lipid synthesis, which is to be expected when cells are fed FAs.

A Western blot was performed to investigate if the gene expression changes in mTOR signalling caused downstream changes in protein and phosphorylation levels between control, 30 μM palmitate- and 30 μM probe **1**-treated groups (Figure 5.22). The total levels of mTOR trended towards an increase with palmitate and further increased with probe **1**. The protein levels of p-mTOR when normalised to total mTOR trended towards an increase with palmitate treatment, but probe **1** treatment did not exhibit the same degree of increase. This suggested that the overall abundance and activation status of mTOR remained stable. Whilst the total level of S6 RBP did not statistically change, the p-S6 RBP statistically increased with probe **1** when compared with control and palmitate groups. This may be due to increased activation of the mTOR target S6 RBP. Lastly, S6K protein levels statistically increased for probe **1** when compared to control and palmitate. However, p-S6K levels were not changed between groups. These results suggest that the increase in total S6K was not linked to an equivalent level of activation. These results show that probe **1** has similar effects to palmitate on certain mTOR targets and that these effects are selective and do not broadly activate the entire pathway.

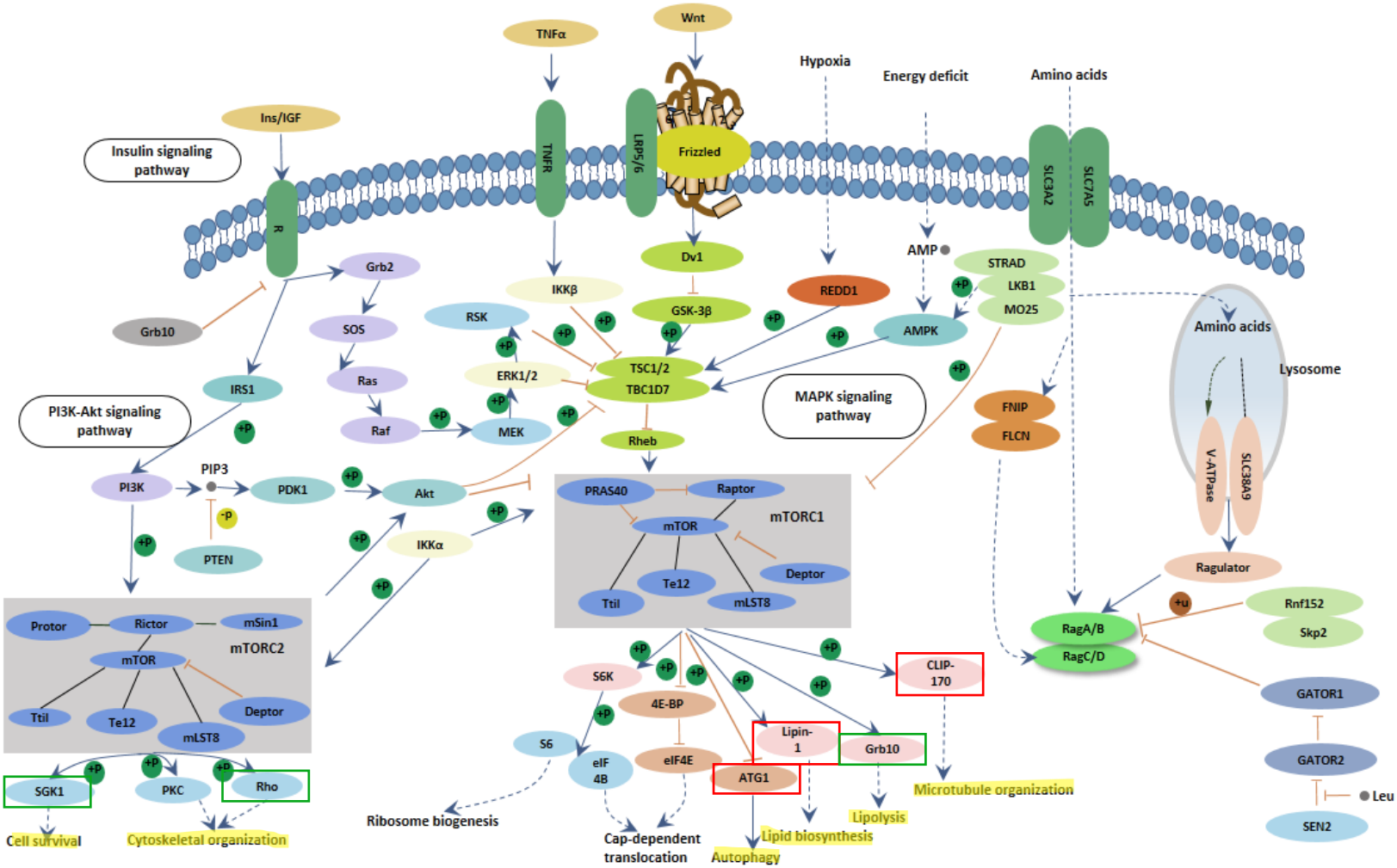

Figure 5.21: Overview of the mTOR signalling pathway. Proteins highlighted depending on the direction of their gene expression: upregulated (green box) or downregulated (red box).

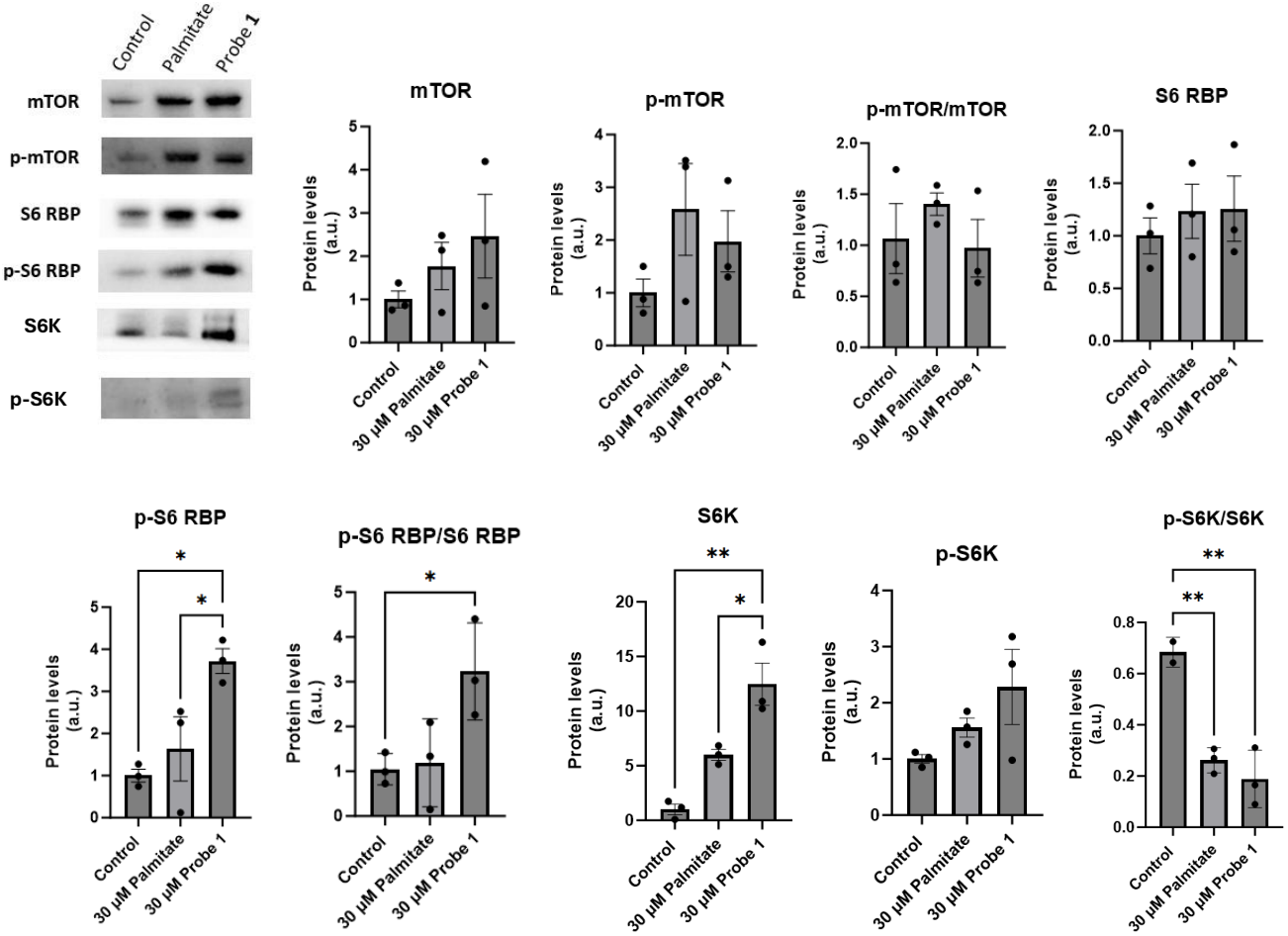

Figure 5.22: Probe 1 is causing changes in protein levels and activation of certain mTOR targets: Western blotting of mTOR targets in control cells, or 16 h treatment with 30 µM palmitate or probe **1**.

Considering the upregulation of 'Energy Metabolism' and the downregulation of 'Insulin Signalling' pathways, an assessment of the overall cell metabolism was performed using radioactive metabolic substrates. To measure FAO rates cells were incubated with probe **1** for 16 h, followed by treatment of 9,10-^{3}H-palmitate (5 h). This resulted in a trend towards an increase in β-oxidation, although not statistically significant, following probe **1** incubation (Figure 5.23a). To measure the rate of glycolysis in the cells, following incubation with probe **1**, 5-^{3}H-glucose was added (5 h). The levels of $^{3}H_2O$ were measured and demonstrated a trend towards a decrease in glycolysis following probe **1** treatment (Figure 5.23b). Although not statistically significant, these trends follow the same pattern as the transcriptomic analysis, whereby OXPHOS genes were increased, and glycolytic genes were down. Longer-term treatment may be necessary to see a change in total pathway flux, suggesting that changes in mRNA take time to impact overall pathway activity.

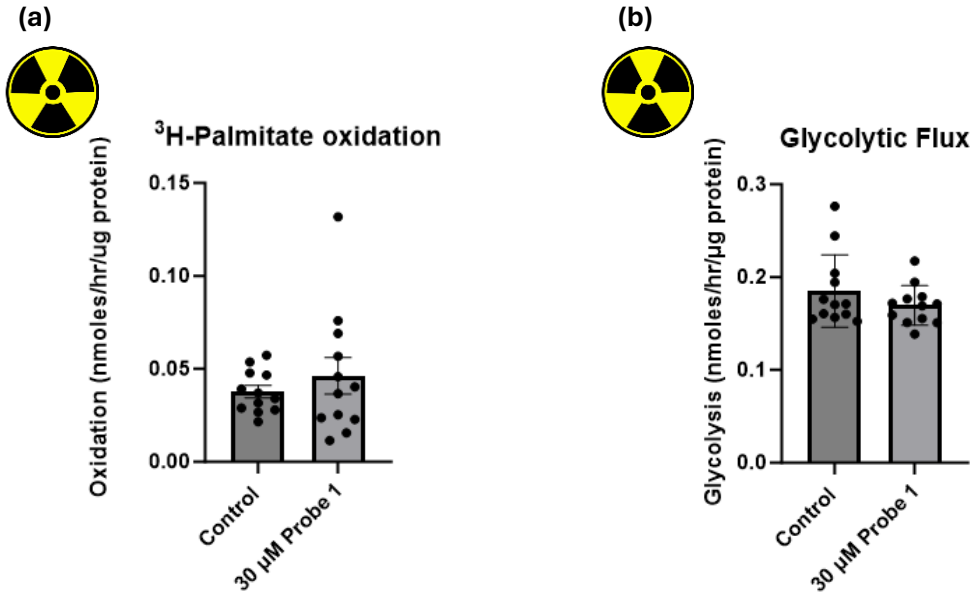

Figure 5.23: Measuring cell metabolism of radiolabelled compounds following probe 1 treatment: (a) Fatty acid oxidation rates of 9,10-^{3}H-palmitate. (b) Glycolytic flux of 5-^{3}H-glucose.

To further investigate the effects of probe **1** treatment on OXPHOS, western blotting using an OXPHOS antibody cocktail was performed on control and probe **1**-treated cells (16 h) (Figure 5.24). The antibody was raised for various subunits of the ETC. Comparing the two groups highlighted a

statistically significant decrease in the subunit of complex II and a trend towards an increase in the subunit of complex III. This demonstrated that probe **1** treatment affected protein levels of the ETC.

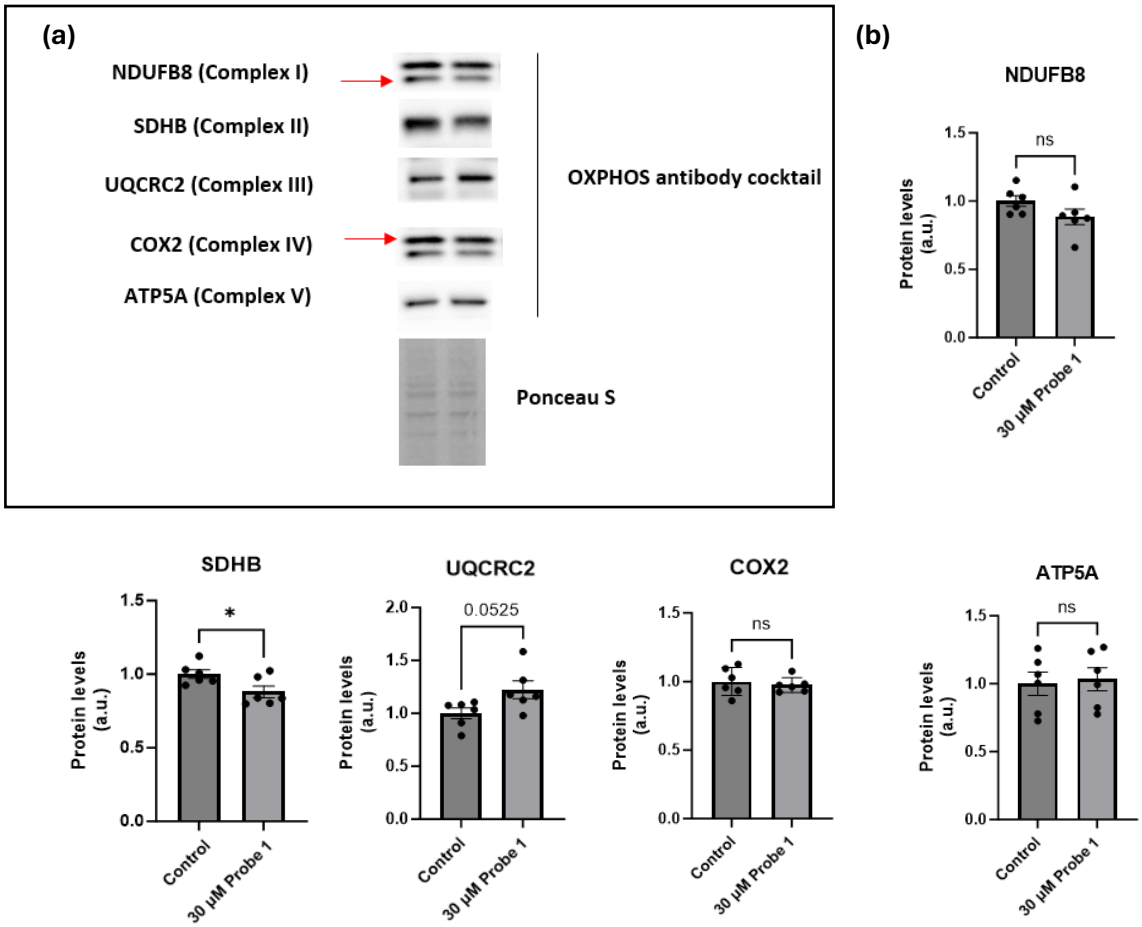

Figure 5.24: Probe 1 affects protein levels of subunits in the electron transport chain (ETC): (a) Western blots of various subunits of complexes in the ETC. Total protein stained with Ponceau S. (b) Quantification of blots (n=6).

5.5.5 Comparison of proteomic and transcriptomic analyses of probe 1 in *MDA-MB-231* cells

A comparison of the proteomic (30 µM probe 1+UV, 16 h) and transcriptomic (30 µM probe **1**, 16 h) results provided a deeper insight into the gene expression outcomes of the probe **1** interactions. Importantly, this is not a traditional approach, where transcriptomics looks at the gene changes and proteomics looks at the resulting protein level changes. This approach is looking at the proteomics first, to analyse binding/interaction and then looking at the gene expression outcome of these interactions. The probe **1**-protein interactions could be stimulatory or inhibitory of biological processes.

A Metascape analysis of enriched proteins compared to genes highlighted that similar pathways were enriched in both the proteomic and transcriptomic data (Figure 5.25 & 5.26). Pathways that had protein interactors and were upregulated on a gene level included: 'Rho GTPase signalling', 'Protein localisation to organelle', 'Membrane trafficking', 'Regulation of cell cycle process' and 'Metabolism of RNA' pathways (Figure 5.25). Pathways that had protein interactors and were downregulated on a gene level included: 'Positive regulation of protein localisation'; 'DNA damage response'; 'Regulation of cytoskeleton organisation'; 'Chromatin remodelling'; and 'VEGFA VEGF2 signalling' pathways (Figure 5.26). This could be explained by the potential binding of probe **1** to proteins causing downstream signalling effects or negative feedback loops to occur. This could also be explained by binding of probe **1** to proteins and either stimulating or inhibiting them causing downstream up- or down-regulation of these pathways.

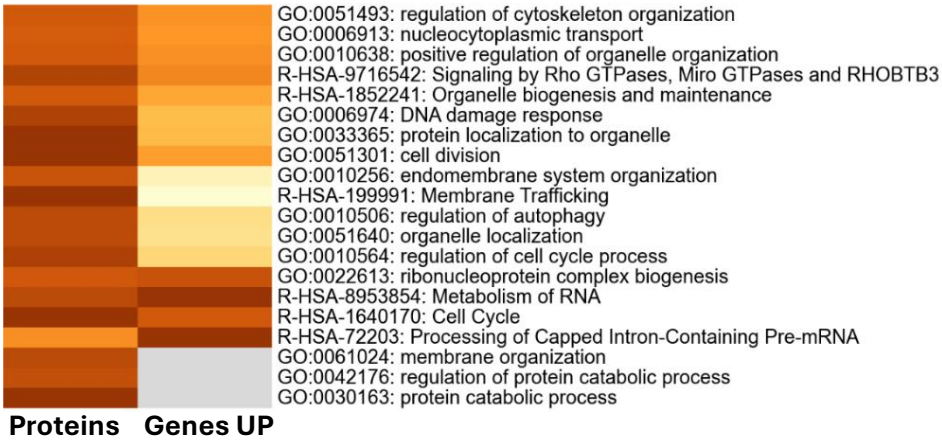

Figure 5.25: Comparison of protein interactors and upregulated transcriptomic targets: Heatmap of enriched terms in both transcriptomics and proteomic data (+UV), for 30 µM probe **1** coloured by p-values.

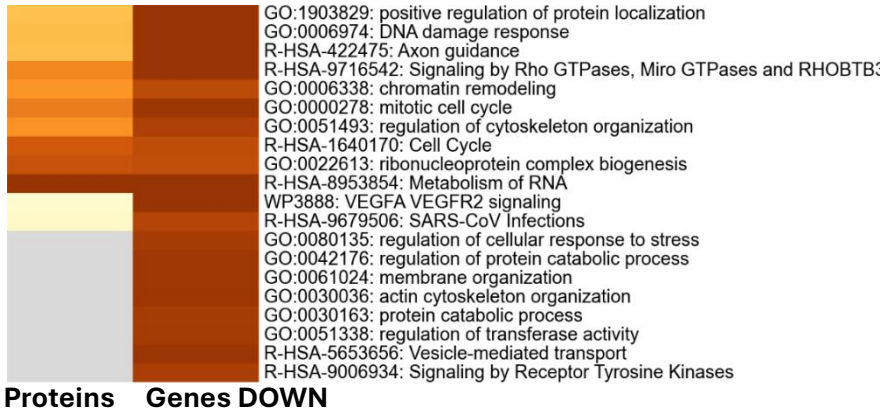

Figure 5.26: Comparison of protein interactors and downregulated transcriptomic targets: Heatmap of enriched terms in both transcriptomics and proteomic data (+UV), for 30 µM probe **1** coloured by p-values.

5.6 Discussion

Proteomic analysis allowed for investigation of protein interactors of probe-**1**and subsequently, an in-depth analysis of enriched pathways. In the absence of UV irradiation, probe **1** caused enrichment in 'Intracellular protein transport', 'Membrane trafficking' and 'Electron transport chain OXPHOS system in mitochondria' pathways. For both transport and trafficking, RAB proteins contributed the most. These proteins are a large family of small GTPases and are heavily involved in regulating membrane trafficking in cells, including processes like vesicle formation, movement and fusion with target membranes. RAB proteins are also essential in the precise control of the intracellular transport of proteins, including both endocytic and exocytic pathways.[201] Protein palmitoylation is a modification that has been shown to influence the localisation of proteins as the addition of a palmitate group can anchor proteins to cellular membranes and affect their interaction with other membrane-bound proteins.[90] However, palmitoylation can also influence signalling pathways involved in the regulation of intracellular transport and membrane trafficking, e.g. Ras GTPases involved in vesicle sorting and movement are regulated by palmitoylation.[202] Palmitoylation can also occur on mitochondrial proteins, affecting their localisation, stability and interactions with OXPHOS proteins.[203] Of interest were the proteins that were enriched under specific TFs: KMT2D and DNMT3A. These terms suggest that covalent interactions from palmitate may be involved in the regulation of DNA and histone modifications and therefore, in the regulation of DNA and gene expression. ERR1 was also enriched as a TF and has previously been shown to be overexpressed in TNBC cells.[195] This protein acts alongside peroxisome proliferator-activated receptor-γ-coactivator 1α (PGC-1α) in controlling the expression of genes involved in oxidative metabolism, the TCA cycle and mitochondrial biogenesis in tissues with higher energy demands.[194,195] Upon irradiation with UV, high enrichment of histones occurred (e.g. H3-3A, H2AC67, etc.). This result further supports a role for palmitate in the localisation of histones, during chromatin remodelling[204], and the potential regulation of their modifications. Importantly, in *Chapter* 4 confocal imaging of LaminA/C-stained cells that had been UV irradiated showed no loss of nuclear integrity, suggesting any probe **1** interactions with nuclear proteins are true interactions. Palmitic acid has been shown to induce

epigenetic changes: such as DNA methylation and histone methylation and acetylation.[205,206]Of interest was the presence of β-actin in the UV-enriched protein targets. Further investigation into the effects of probe **1** on the actin cytoskeleton highlighted a trend towards an increase in F-actin filaments following probe **1** treatment. Palmitoylation has previously been shown to be involved in the regulation of actin remodelling through Rac1, to control membrane organisation.[207,208] Therefore, palmitate could have a key role in the organisation and structure of the actin cytoskeleton in cells. Lastly, PLIN3 was also enriched with UV irradiation and staining of cells with LipidTOX demonstrated colocalisation of probe **1** in lipid droplets in the cells. Therefore, probe **1** is being recognised by the cell as a substrate for lipid storage. The proteomic analysis demonstrated potential pathways influenced by palmitate but also highlighted pathways and proteins previously known to interact with the endogenous fatty acid.

Transcriptomic analysis was performed to investigate the downstream consequences of the probe **1**-protein interactions. KEGG analysis highlighted global changes in several cellular and metabolic pathways. Upregulated pathways included both 'Oxidative phosphorylation' and 'mTOR signalling', with 'Insulin signalling', 'mTOR signalling' and 'Regulation of actin cytoskeleton' downregulated. Similar trends in pathways were observed after an unbiased GSEA, with 'Energy metabolism' upregulated and 'Glycolysis', 'Insulin signalling' and 'Focal adhesion' downregulated. A downregulation in insulin-dependent pathways and upregulation in genes involved in energy metabolism suggests that the cell is metabolically switching substrate usage. This indicates that probe **1** is a suitable fat mimetic, as OXPHOS is upregulated, and glycolysis is downregulated. The mTOR signalling pathway is known to respond to nutrient availability and is a central regulator of metabolism. Different genes involved in both mTORC1 and mTORC2 were up- and downregulated. Upregulated genes included: *SGK1; PPARA; HIF1A; PPARGC1A (PGC-1α);* and *PPARG*. These genes are involved in cell survival, lipid metabolism, angiogenesis, mitochondrial metabolism and adipogenesis, respectively.[209] Downregulated genes included: *PRKCA (PKC); TFEB; SREBF1; POLDIP3 (SKAR);* and *LPIN1.* These genes are involved in cytoskeletal organisation, autophagy, lipogenesis, mRNA splicing and lipid synthesis, respectively.[209] Protein levels of mTOR targets were

investigated, with mTOR and p-mTOR levels trending towards an increase when comparing control cells with palmitate- and probe **1**-treated cells. However, p-S6 RBP and p-S6K levels were statistically increased upon probe **1** treatment. These increases were not accompanied by an increase in the equivalent unphosphorylated proteins. This suggests that the increase in p-S6K, the kinase for S6 RBP, could be activating the kinase to phosphorylate S6 RBP and cause an increase in ribosomal biogenesis. This result further validates the enrichment of the 'Ribosomal large subunit biogenesis' pathway in the proteomic analysis of probe **1**. Protein level changes were similar in both the palmitate- and probe **1**-treated cells, suggesting the effect on mTOR is palmitate-dependent. These changes appeared to be specific, as there was no broad activation of the targets. Palmitate has previously been shown to activate the mTOR pathway, which regulates both protein synthesis but is also crucial for cell growth and proliferation through upregulation of cell cycle progression genes.[210] These changes in mTOR suggest the cells were switching on processes involved in the handling of fatty acids, such as mitochondrial and lipid metabolism and switching off lipid synthesis and cytoskeletal organisation. These changes in mTOR complement the changes in OXPHOS and actin cytoskeleton pathways.

Validation of the transcriptomic analysis further highlighted changes in various pathways. The gene with the greatest change following probe **1** treatment was *GPR89B.* This gene encodes for a protein located in the Golgi cisterna membrane and Golgi-associated vesicle membranes and is involved in the acidification of the Golgi. The protein of this has previously been shown to be palmitoylated by Click chemistry techniques, however, this protein was not enriched by probe **1**.[198] Measuring cell metabolism following probe **1** treatment using radioactive substrates demonstrated a trend towards an increase in β-oxidation and a trend towards a decrease in glycolysis. These trends follow the up-, and down-regulation of OXPHOS and glycolysis genes, respectively. These results suggest that the changes in gene expression happen during the treatment time, however, measuring metabolism at a longer time point may allow for changes in the pathway function to occur. However, there were changes in protein levels of some subunits of the ETC, with SDHB (subunit of complex II)

decreasing and UQCRC2 (subunit of complex III) trending towards an increase following probe **1** treatment.

In conclusion, the approach documented in this chapter utilised a multi-omics integrated approach to investigate the interactions and signalling outcomes of probe **1** treatment in *MDA-MB-231* cells. This approach has highlighted roles for probe **1** in protein transport, organelle localisation, actin remodelling, mitochondrial organisation and metabolic pathways in the cells. The integrated approach also demonstrated the importance of investigating both protein- and gene-level changes for a broader understanding of cellular outcomes following treatment with a molecule. This chapter also emphasises the effectiveness of probe **1** as a tool in exploring the interactions and cellular consequences of palmitate.

Chapter 6

Target identification in hiPSC cardiomyocytes using photoaffinity probe **1**

6.1 Abstract

FAs have a crucial role in the heart, providing 60-80% of its energetic needs. Palmitic acid is one of the most abundant FAs in the Western diet and is associated with lipotoxicity in the heart. However, an investigation of the direct interactions of palmitic acid with proteins in cardiomyocytes has not been performed. In this chapter, palmitic acid photoaffinity probe **1** was used to capture these interactions and the outcomes of these interactions were investigated.

Probe **1** was used for protein labelling in hiPSC-CMs at 30 μM and 100 μM concentrations, with or without UV irradiation. Probe **1** was interacting with proteins involved in RNA metabolism, chromatin organisation, glycolysis and gluconeogenesis, mitochondrial biogenesis and several signalling pathways (e.g. VEGFA and RHO GTPases). It was also shown that probe **1** directly interacted with proteins implicated in both mitochondrial diseases and various cardiomyopathies. Confocal microscopy showed an increase in mitochondrial number and fragmentation of the mitochondrial networks. The protein expression of subunits of ETC complexes was upregulated following probe **1** treatment, indicating increased mitochondrial biogenesis.

Transcriptomic analysis was performed to examine the effects of either probe **1** or palmitic acid on gene expression levels in the hiPSC-CMs. This showed an overlap between the pathways regulated by probe **1** and palmitate, but probe **1** had more significant changes in gene expression levels. The main pathways regulated by both treatments were extracellular matrix organisation, response to nutrients, regulation of actin cytoskeleton, response to hormones (androgen and estrogen) and regulation of NF-κB signal transduction.

These results demonstrate that probe **1** has revealed palmitate's multifaceted role in mature hiPSC-CMs, affecting diverse biological pathways, including metabolism, contractility, and signalling. It also interacted with pathways linked to cardiomyopathy, mitochondrial disease, and sex hormone signalling, underscoring its broad influence on cardiac cellular processes.

6.2 Introduction

6.2.1 Human-induced-pluripotent stem cell-derived cardiomyocytes (hiPSC-CM)

The discovery of human-induced-pluripotent stem cells (hiPSC) by the Yamanaka group allowed for the generation of stem cells that recapitulated human diseases.[211] hiPSCs are embryonic-like cells which are reprogrammed from adult cells (e.g., skin and blood).[212] Due to their pluripotency, hiPSCs can be differentiated into many different types of cells, including lung tissue, kidney, liver, and heart.[213–216] The heart model used for this chapter is the hiPSC cardiomyocytes (hiPSC-CMs), derived from lung tissue (IMR90 cells).[217] When matured, cells express key cardiac markers (e.g. troponin T and α-actinin) and exhibit characteristics of the adult heart, including spontaneous contraction, action potentials and calcium cycling. During their maturation as cardiomyocytes, these cells are exposed to 80 μM oleic acid, therefore they have been metabolically matured towards FA metabolism. This means probe **1** will be added to cells that preferentially utilise FAs, compared to the more glycolytic *MDA-MB-231* cells (*Chapter 5*).

The heart relies heavily on FAs for energy, with approximately 60% of its energy supply derived from FA metabolism. However, in conditions of lipid overload, such as in diabetic cardiomyopathy (DbCM)[218] and heart failure with preserved ejection fraction (HFpEF),[219] excessive accumulation of lipids can lead to lipotoxicity, contributing to cardiac dysfunction. Despite the known association between lipid overload and cardiac disease, our understanding of how FAs regulate normal heart function and how this regulation becomes disrupted in disease states remains limited. The use of probe **1** offers a valuable tool for investigating lipid-protein interactions in the heart, providing new insights into how FAs influence cardiac biology. This tool enables a more detailed exploration of how lipid signalling, and metabolism are modulated under physiological conditions and how these processes are hijacked in pathological settings.

6.3 Chapter Aims

This chapter aims to reveal what proteins and biological pathways are affected by probe **1** in the heart. The results from this analysis will begin to unravel the role of palmitic acid in an *in vitro* heart model: hiPSC-CMs, and potentially highlight pathways of therapeutic interest. This was achieved by the following:

1. A proteomics analysis of protein interactors of probe **1** at different concentrations and with or without UV irradiation in hiPSC-CMs, to identify both covalent and non-covalent interactor proteins.
2. Validation of various protein interactors of interest by western blotting.
3. A transcriptomic analysis and comparison of gene expression changes following either probe **1** or palmitic acid treatment.
4. Validation of genes of interest by qPCR, comparing probe **1** and palmitic acid treatment.
5. Validation of phenotypic changes in mitochondrial networks and protein levels of the ETC following probe **1** treatment, using both confocal and western blotting.

6.4 Methods

6.4.1 Human-induced-pluripotent stem cell-derived cardiomyocytes (hiPSC-CM)

IMR90 hiPSCs (fibroblast strain derived from the lungs of 16-week female foetus) were differentiated into hiPSC-CMs via the modulation of the Wnt signalling protocol (Figure 6.1).[217] Before differentiation, hiPSCs were grown to confluency in TeSR-E8 media on matrigel-coated culture plates, media was changed daily. Confluent hiPSCs were then differentiated into hiPSC-CMs, as previously described, over 15 days.[220] For days one to eleven, cells were cultured in RPMI media supplemented with 1% B27 minus insulin (RB-), with the addition of the GSK3 inhibitor CHIR99021 (6 μM) on days one and two and Wnt-C59 (2.5 μM) on day four. On day eleven, the culture will contain hiPSC-CMs with some evidence of contraction in the plate. Metabolic selections of CMs over adjacent lineages, such as fibroblasts, was performed by culturing with RB- (no glucose) on days eleven to fourteen. Finally, on day fifteen, the media is replaced with RPMI supplemented with 1% B27 complete (RB+). Maturation of the hiPSC-CMs was performed for seven days, with maturation media comprising of DMEM (1 g/L glucose) supplemented with 10% horse serum, 5 μg/mL vitamin B12, 0.5 mM ascorbic acid, 0.82 μM biotin, 50 nM insulin, 80 μM oleic acid: BSA (2:1), 1x MEM non-essential amino acids, and 20 U/mL penicillin-streptomycin.

6.5 Results

6.5.1 Labelling of hiPSC-CMs with probe 1

The concentration dependence of protein labelling by probe **1** in human induced pluripotent stem cell-derived cardiomyocytes (hiPSC-CMs) was examined. Cells were incubated with either 30 or 100 μM of probe **1** for 16 hours, then lysed and subjected to a Click reaction with TAMRA-azide (Figure 6.2). Comparing 30 μM probe **1**-treated cells with control cells highlighted an increase in protein labelling in the 30 μM probe **1**-treated cells. However, a concentration-dependent increase in protein labelling was not evident when increasing from 30 to 100 μM, but as hiPSC-CMs are matured in 80 μM of FFA, 100 μM of probe **1** was chosen as the optimal labelling concentration, to keep probe **1** concentration as close to the maturation concentration. No non-specific labelling was observed in the negative control lanes.

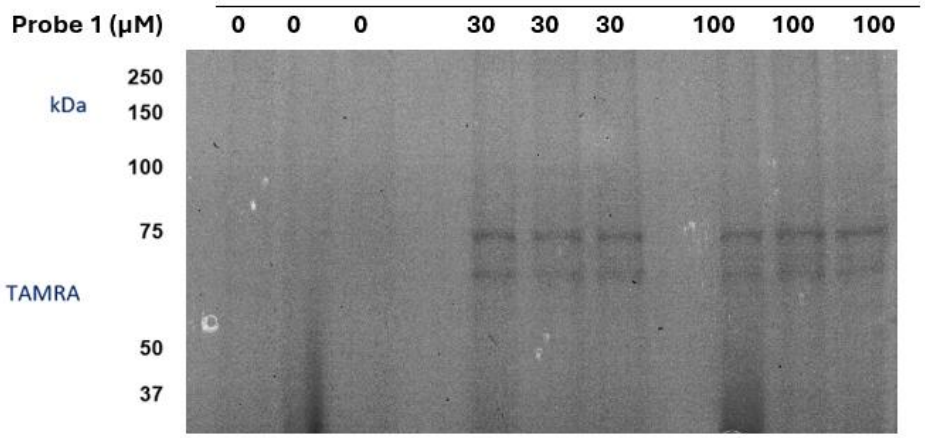

Figure 6.2: Covalent incorporation of probe 1 *in vitro*: In-gel fluorescence highlights protein labelling by probe **1** (16 h) at 30 or 100 μM in the absence of UV irradiation (n=3).

The use of the photoaffinity diazirine group was then employed to investigate non-covalent labelling with probe **1** (Figure 6.3). Cells were treated with 100 μM of probe **1** for 16 hours, then exposed to UV irradiation for 3 min, lysed, and subjected to a Click reaction with TAMRA-azide. A comparison between non-irradiated and irradiated cells revealed an increase in protein labelling following UV

exposure. This increase is again due to non-covalent interactions captured by the crosslinking of probe **1** to neighbouring proteins via diazirine photoactivation.

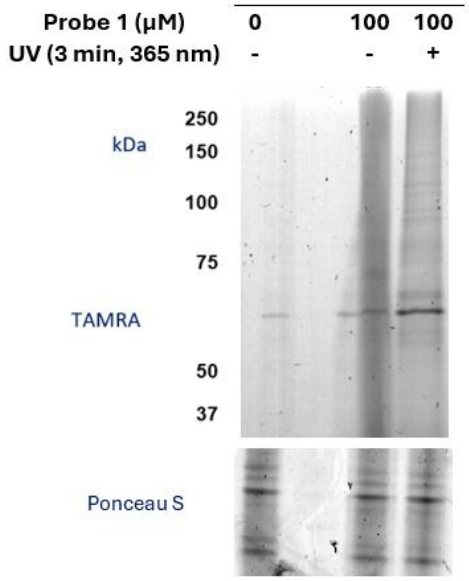

Figure 6.3: Non-covalent incorporation of probe 1 in hiPSC-CMs: In-gel fluorescence shows increased protein labelling by probe **1** (100 µM, 16 h) following UV irradiation.

To confirm that hiPSC-CM were taking up the probe, cells were incubated with 100 µM of probe **1** for 16 h and UV-irradiated, followed by fixation and the Click reaction was performed with the TAMRA fluorophore, allowing for imaging using confocal microscope. This demonstrated the localisation of probe **1** in the cells, in the cytoplasm and, additionally, in the nucleus (Figure 6.4).

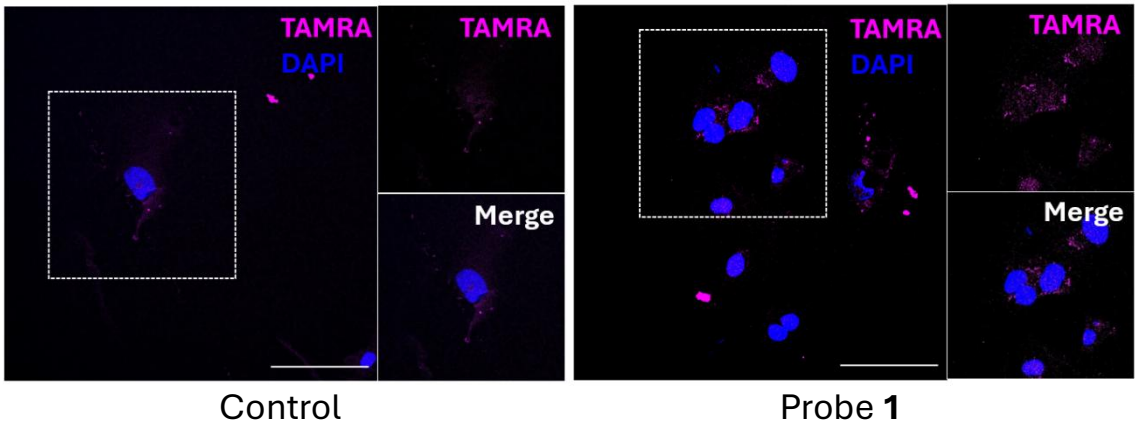

Figure 6.4: Confocal microscopy images of probe 1 using CuAAC reaction in hiPSC-CMs: Imaging for TAMRA (magenta) with DAPI (blue) as a nuclear stain, as (a) control or after treatment for 16 h with (b) 100 μM probe **1**; scale bar is 50 μm with ×2 zoom to the right.

6.5.2 Cell viability of hiPSC-CMs following probe 1 treatment

hiPSC-CMs were treated with 100 μM of either palmitic acid or probe **1** for 16 hours, after which LDH release into the media, lactate production and glucose consumption rates were measured using a Pentra C400 clinical chemistry analyser (Figure 6.5). As previously discussed, LDH, is released into the extracellular space following cell toxicity and damage. The results showed no significant difference in the LDH release rate for both the palmitic acid and probe **1**-treated cells compared to control cells (Figure 6.4a), indicating that both the concentration and time of incubation were non-toxic to the cells.

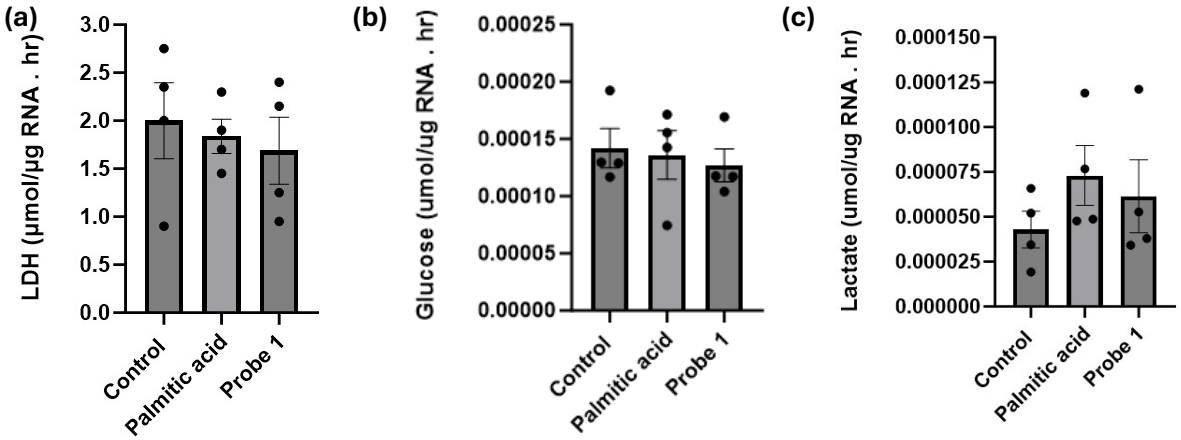

Figure 6.5: LDH release, glucose consumption and lactate production rates of hiPSC-CMs following palmitic acid or probe 1 treatment: (a) LDH release, (b) glucose consumption and (c) lactate production rates in cell media were measured (n=4).

To measure if the cells were becoming more glycolytic in response to palmitic acid or probe **1** treatment, both glucose consumption and lactate production rates were measured. The analysis revealed no significant differences in lactate production or glucose consumption (Figure 6.4b,c), suggesting both palmitic acid and probe **1** treatment were not inducing a shift towards anaerobic glycolysis in the cells.

6.5.3 Proteomic analysis of hiPSC-CMs treated with probe 1

hiPSC-CM cells were treated with probe **1** (16 h), either with or without subsequent UV irradiation. These samples were then enriched using a Neutravidin pulldown and subjected to trypsin digest and quality control (QC) analysis for protein mass spectrometry. The groups that were analysed are summarised in Table 6.1. The QC analysis revealed a very broad peak in the total ion chromatogram (TIC) across some of the mass spectrums, potentially due to a contaminant (Figure 6.6). This was not consistently seen across groups (despite all samples being generated at the same time), and this had not been present in the *MDA-MB-231* samples. Enrichment was performed on three separate attempts on all samples but did not improve the QC outcome for some groups. A hypothesis was drawn that it may be due to the Matrigel matrix that the cells are grown on during culturing. Some groups of samples were not passed for injection onto the mass spectrometer due to this contaminant, and due to time constraints these groups could not be repeated.

Table 6.1 QC analysis results of samples for proteomic analysis. (n=3 per group)

Sample	**QC analysis (pass or fail)**
Control (1 h) – UV	Failed
Control (16 h) – UV	Passed
Control (16 h) + UV	Failed
30 μM probe **1** (1h)	Failed
30 μM probe **1** (16 h) + UV	Passed
100 μM probe **1** (16 h) – UV	Passed
100 μM probe **1** (16 h) + UV	Passed

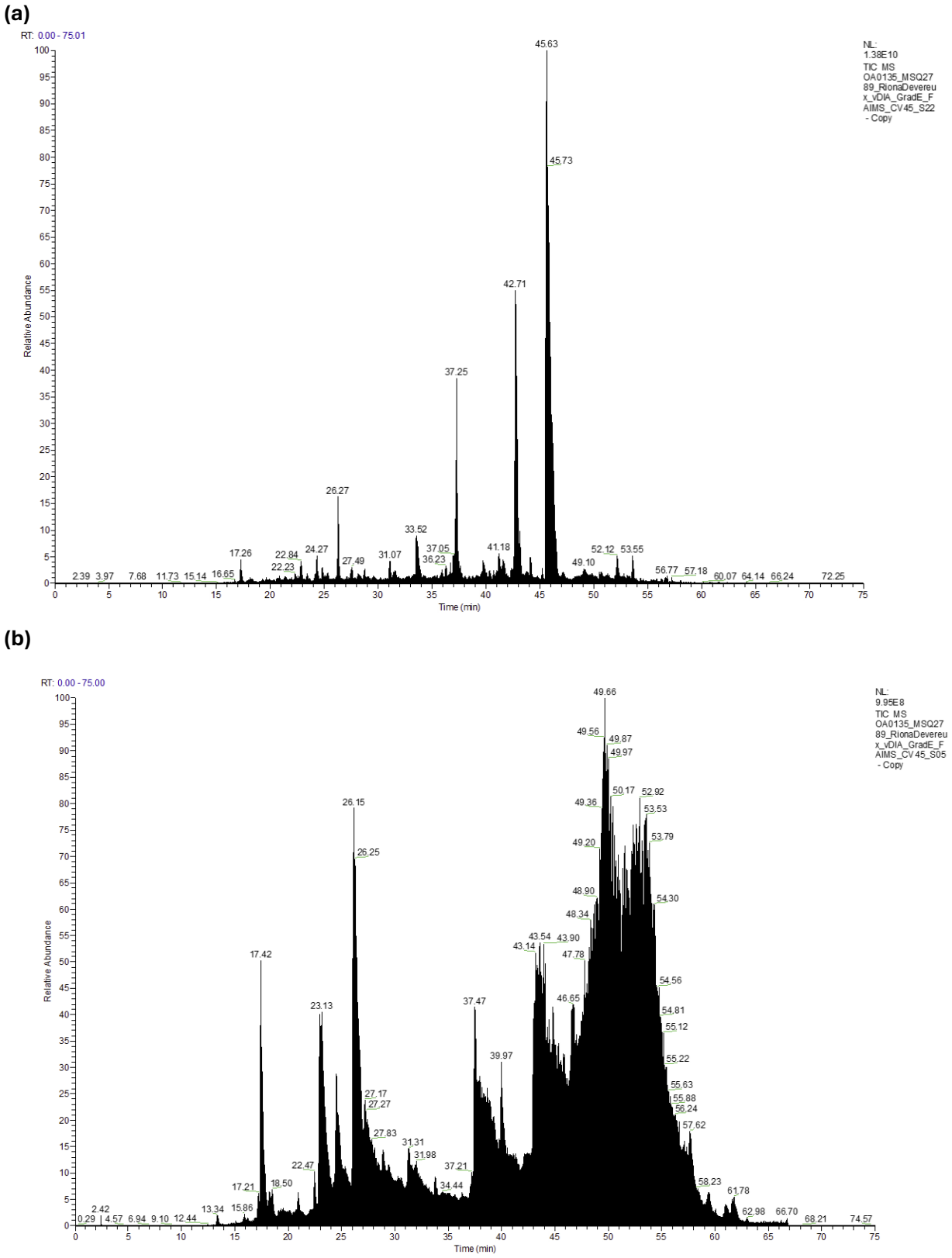

Figure 6.6: Quality control Totale Ion Chromatogram (TIC) of hiPSC-CMs treated with probe 1: (a) Example of a sample that passed QC analysis; (b) Example of a sample that failed QC, due to the broad peak covering the spectrum.

As a consequence, only a comparison between 4 groups could be performed: control; 30 µM probe **1** with UV; 100 µM probe **1** with UV; and 100 µM probe **1** no UV irradiation. The 30 µM probe **1** group would be directly comparable with the *MDA-MB-231* cell proteomic analysis from *Chapter 5*. Principal component analysis (PCA) showed a distinct separation between the groups (Figure 6.7) with PC1 accounting for 46% of the variance attributable to probe **1** treatment, primarily distinguishing the control from the probe **1**-treated cells, while PC2 accounted only 15% of the variance, potentially due to variability not attributable to compound treatment.

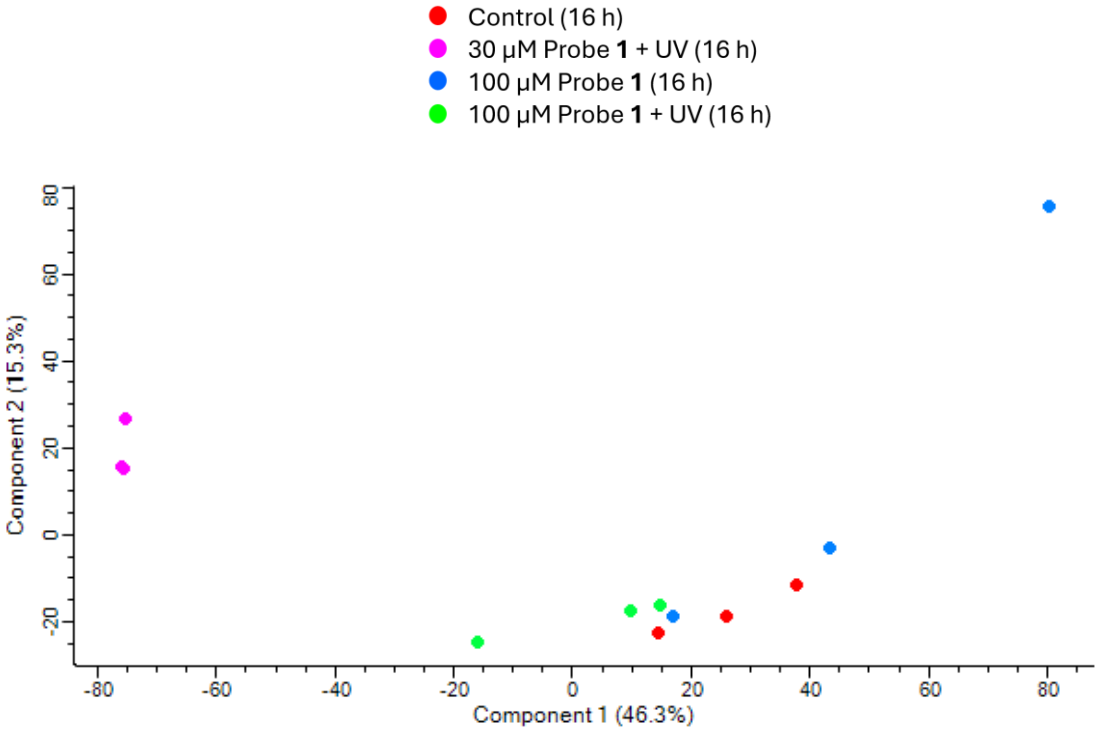

Figure 6.7: PCA plot of hiPSC-CM samples: Cell samples as controls (red) or treated with: 30 µM Probe **1** + UV (magenta); 100 µM Probe **1** (blue); or 100 µM Probe **1** + UV (green).

Following PCA, a linear correlation was performed on the samples, to investigate the heterogeneity of the samples (Figure 6.8). Hierarchical clustering using a Pearson correlation revealed differences in samples in the same groups. The 100 (100 µM no UV) and control groups both had one outlying sample that did not cluster with the others of the same group. This suggested differences in the protein enrichment in these samples, but this is to be expected when carrying out a pulldown enrichment.

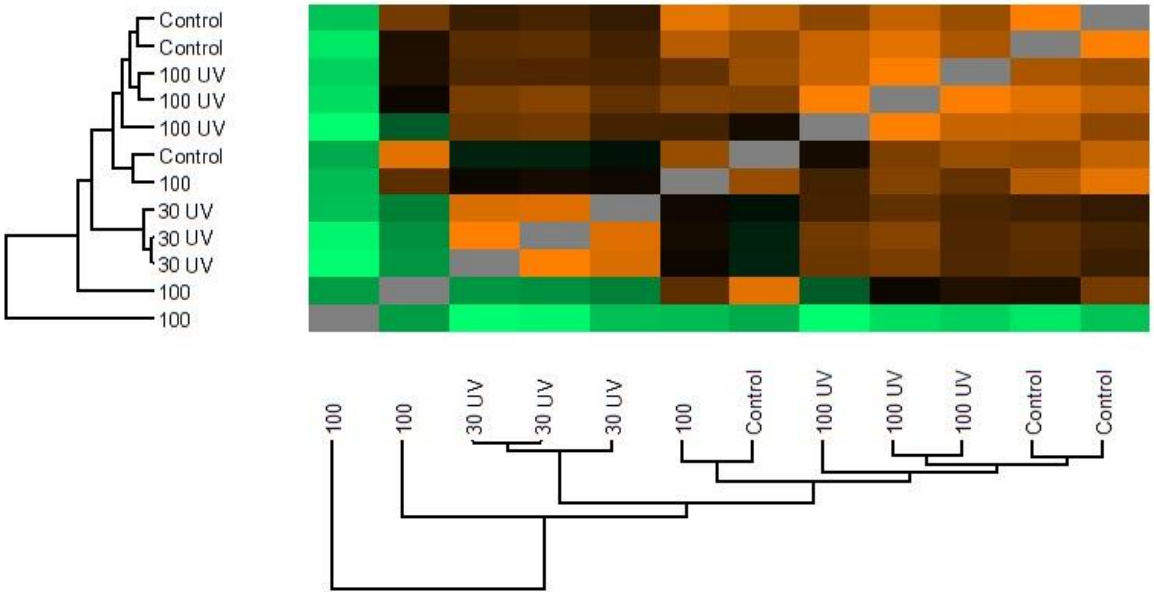

Figure 6.8: Hierarchical clustering using Pearson correlation of hiPSC-CM samples: Samples were run in an n = 3. Control = control cells 16 h, 30 UV = 30 µM probe **1** + UV, 100 = 100 µM probe **1**, 100 UV = 100 µM probe **1** + UV. Colours represent the expression levels of proteins compared with the mean expression. Green = low expression, orange = high expression and black = similar to the mean.

6.5.3.1 Proteins interactors of 30 µM probe 1 (with UV)

The first comparison was performed between the control and 30 µM probe **1**-treated cells (+ UV). This resulted in a total of 1503 proteins unique to 30 µM probe **1** (+ UV) treatment, and of these, 545 proteins were significant ($p < 0.05$) (Figure 6.9). Statistically significantly enriched proteins were input into the STRING database, and a mapping of the protein interactions was performed. Further analysis enabled the identification and highlighting of the subcellular localisation of these proteins (Figure 6.10). Enriched proteins were found in the nucleus (purple), membrane (green), mitochondria (red) and actin cytoskeleton (yellow).

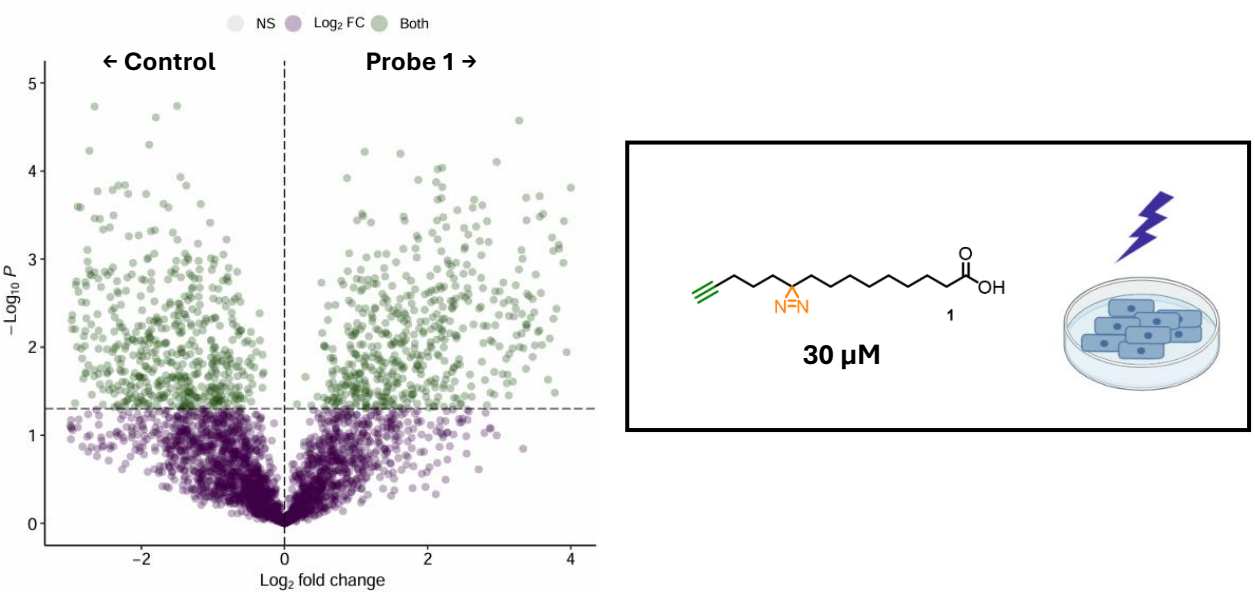

Figure 6.9: Proteomic analysis results of hiPSC-CMs treated with 30 µM probe 1 (with UV). Volcano plot of proteins enriched by 30 µM probe **1** (16 h, 3 min UV) compared with control cell (16 h, no UV).

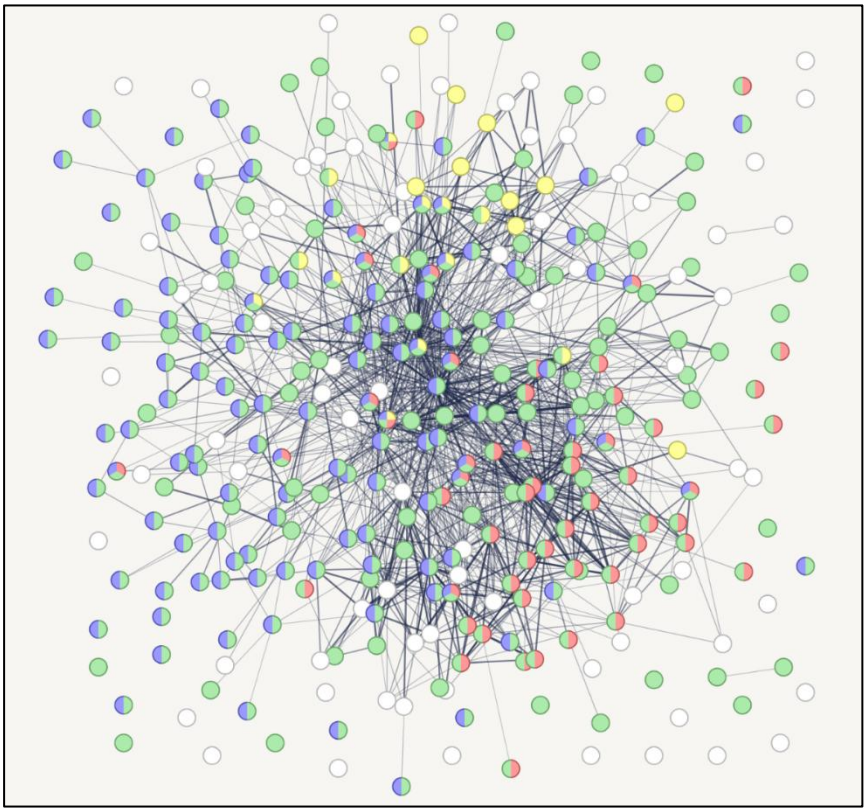

Figure 6.10: STRING network mapping of proteins enriched by 30 µM probe 1 (with UV). Protein localisation is coloured: nucleus (purple), membrane (green), mitochondria (red), actin cytoskeleton (yellow) and all other proteins (white).

Proteins significantly enriched (upper right quadrant of volcano plot) were then used for a Metascape pathway analysis (Figures 6.11 & 6.12). This pathway approach revealed that the top enriched parent GO term was 'Cellular process', with 'Metabolic process' and 'Localisation' being GO terms that were also enriched (Figure 6.11). Further analysis into these processes allowed for the identification of more specific pathways (Figure 6.12a). The top enriched term was 'Cytoskeleton in muscle cells', yet again indicating a role of probe **1** in cytoskeletal processes. Other pathways of interest were: 'Metabolism of RNA'; 'Diabetic cardiomyopathy'; and 'Chromatin organisation'. Several signalling pathways were also enriched: 'Signalling by Rho GTPases, Miro GTPases and RHOBTB3'; and 'VEGFA VEGF2 signalling'. Metascape analysis using the DisGeNet database to map gene names to diseases was performed (Figure 6.12b). This revealed that several cardiomyopathy disease terms were enriched, including: 'Cardiomyopathy, Dilated'; 'Hypertrophic cardiomyopathy'; and 'Familial dilated cardiomyopathy'; '

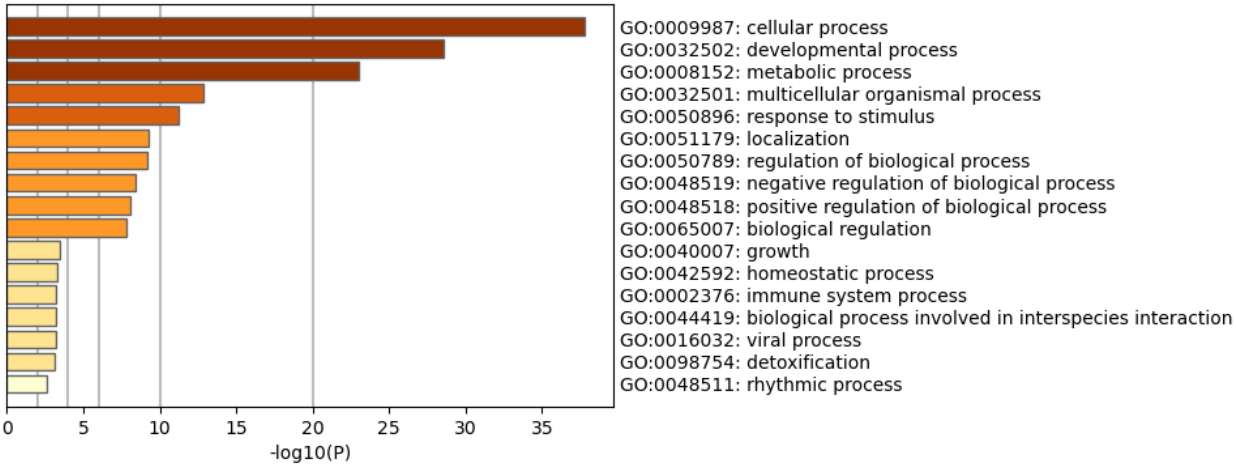

Figure 6.11: Metascape analysis of the enriched proteins with 30 µM probe 1 (with UV). Top level GO terms coloured by p-values.

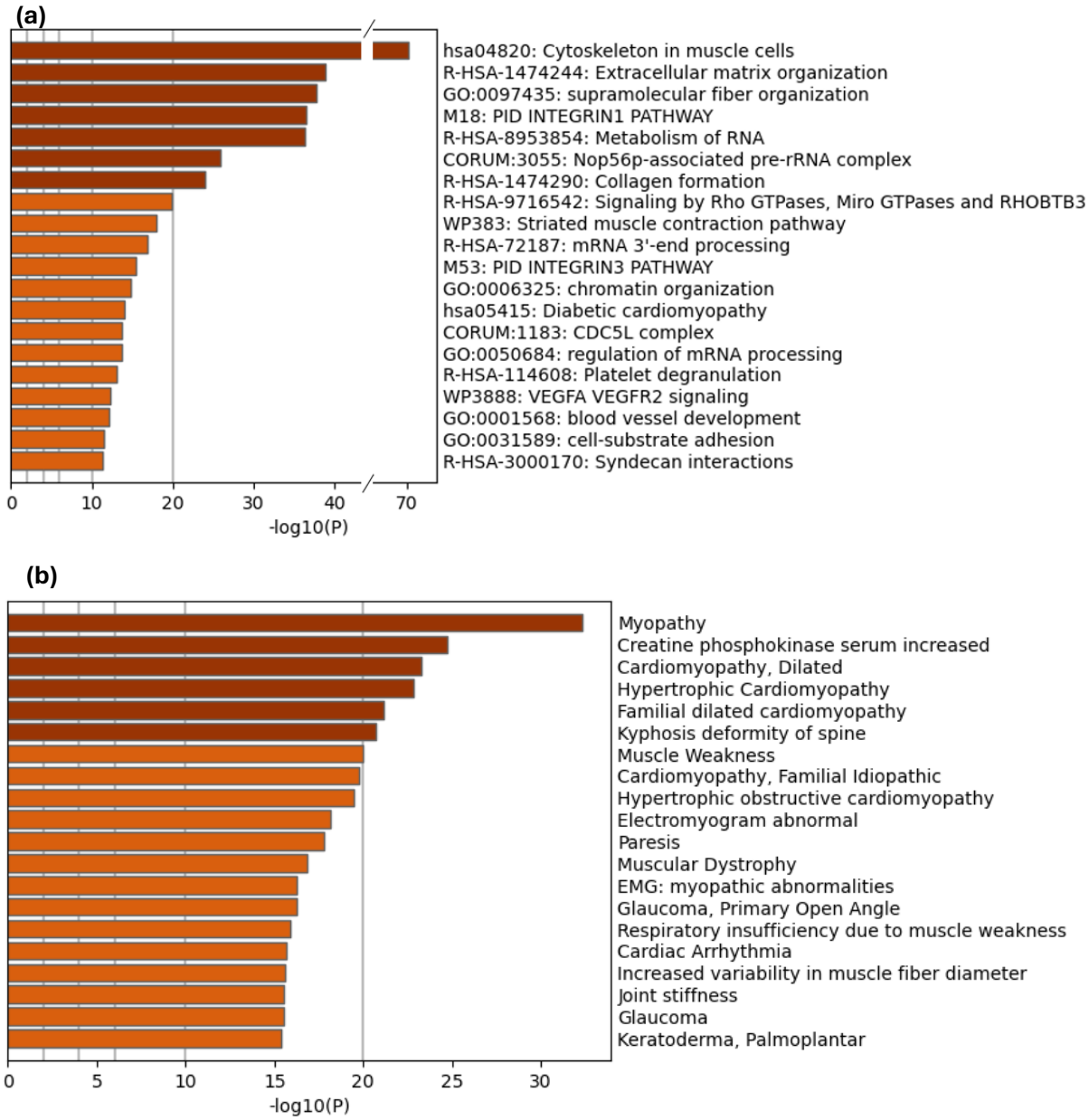

Figure 6.12: Metascape analysis of the enriched proteins with 30 µM probe 1 (with UV). (a) Enriched terms across the input gene lists (proteins with an NSAF > 0) are coloured by p-values; (b) Summary of enrichment analysis in DisGeNET – showing enrichment of disease pathways.

Transcription factor mining was performed to look at the transcription factors that regulate the probe **1**-enriched proteins, with several TFs of interest significantly enriched (Figure 6.13). Serum response factor (SRF) is a TF that regulates muscle differentiation and cytoskeletal organisation. Abnormalities in this TF can contribute to cardiovascular diseases.[221] Upstream transcription factor 1 (USF1) regulates lipid metabolism, glucose homeostasis and stress responses and has been linked

to metabolic diseases such as T2D and cardiovascular disorders.[222] Androgen receptor (AR) regulates genes involved in both male and female sexual development.[223]

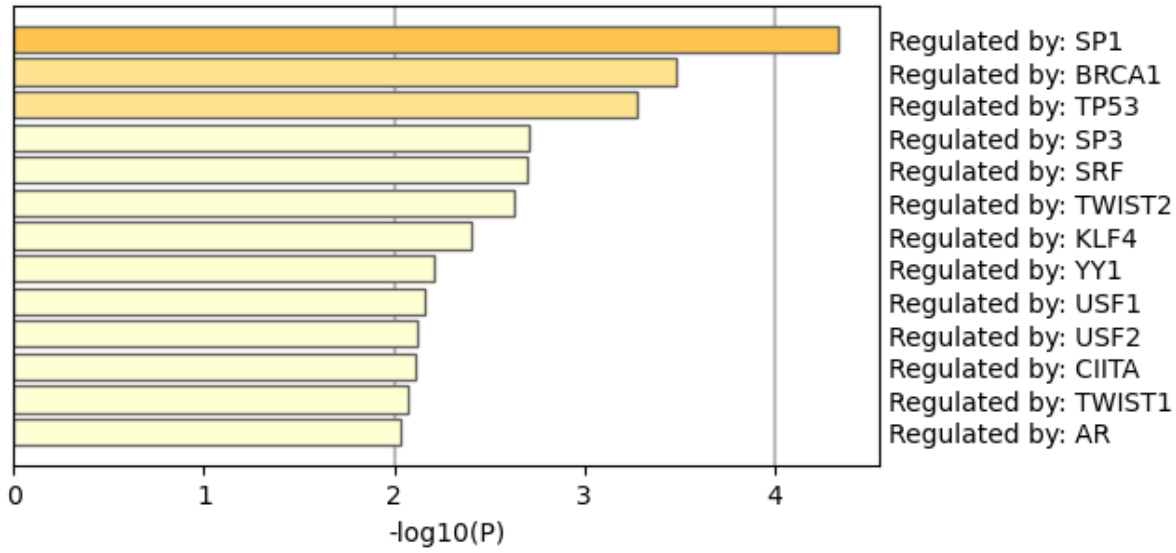

Figure 6.13: Transcription factors regulating proteins enriched by 30 µM probe 1 (with UV).

6.5.3.2 Proteins interactors of 100 µM probe 1 (no UV)

The next comparison was performed between the control and 100 µM probe **1**-treated (no UV) cells. This resulted in a total of 1751 proteins unique to 100 µM probe **1** (no UV) treatment, with 69 of these proteins being statistically significant ($p < 0.05$) (Figure 6.14). A significantly lower number of proteins were enriched in the absence of UV irradiation, potentially due to the lability of the thioester covalent linkage (e.g. palmitoylated proteins). STRING mapping of the protein interactions showed the interactions and subcellular localisation of the protein interactors (Figure 6.15). Enriched proteins were found in the nucleus (red), membrane (purple) and mitochondria (green).

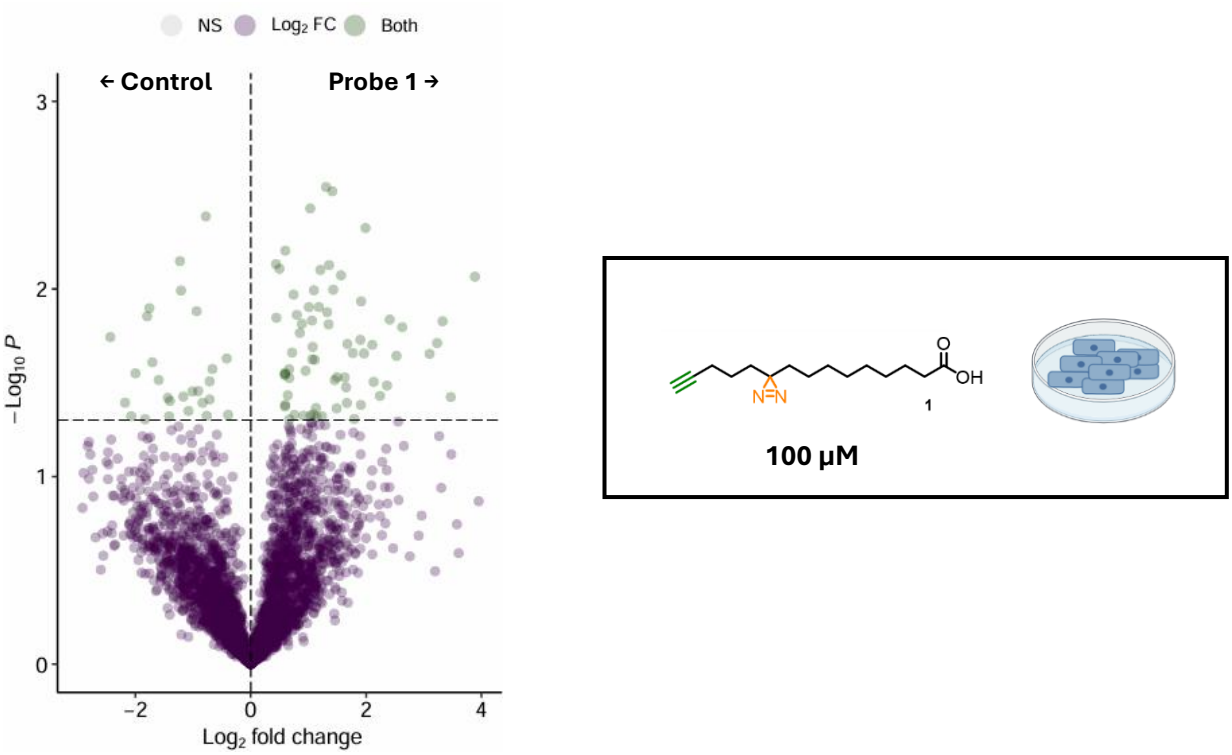

Figure 6.14: Proteomic analysis results of hiPSC-CMs treated with 100 µM probe 1 (no UV). Volcano plot of proteins enriched by 100 µM probe **1** (16 h, no UV) compared with control cell (16 h, no UV).

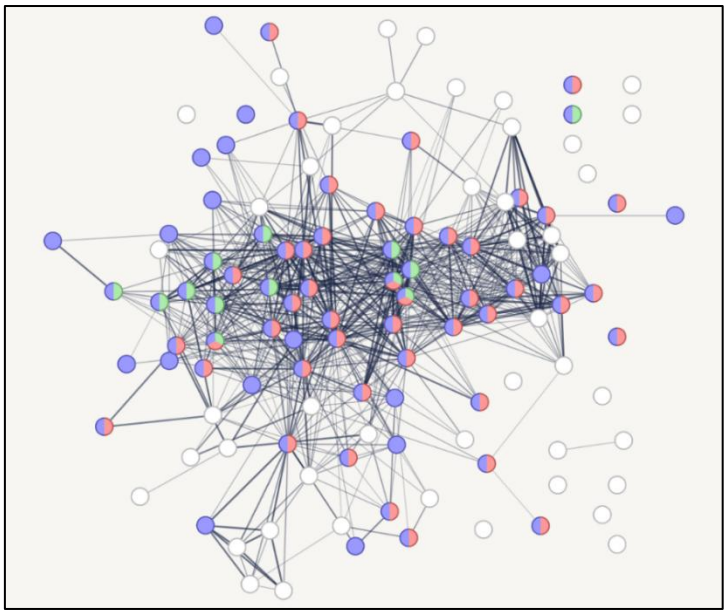

Figure 6.15: STRING network mapping of proteins enriched by 100 µM probe 1 (no UV). Protein localisation is coloured: nucleus (red), membrane (purple), mitochondria (green) and all other proteins (white).

Metascape was used to perform a pathway analysis of the probe **1**-enriched proteins (Figure 6.16).

This revealed that the top enriched parent GO term was ‘Metabolic process’, with ‘Localisation’

being a GO term of interest too (Figure 6.16a). Further analysis into these processes allowed for the identification of more specific pathways (Figure 6.16b) with the top enriched term 'Protein catabolic process', yet again indicating a role of probe **1** in protein metabolism processes. Other pathways of interest were: 'DNA metabolic process'; 'Membrane trafficking'; and 'Signalling pathway'.

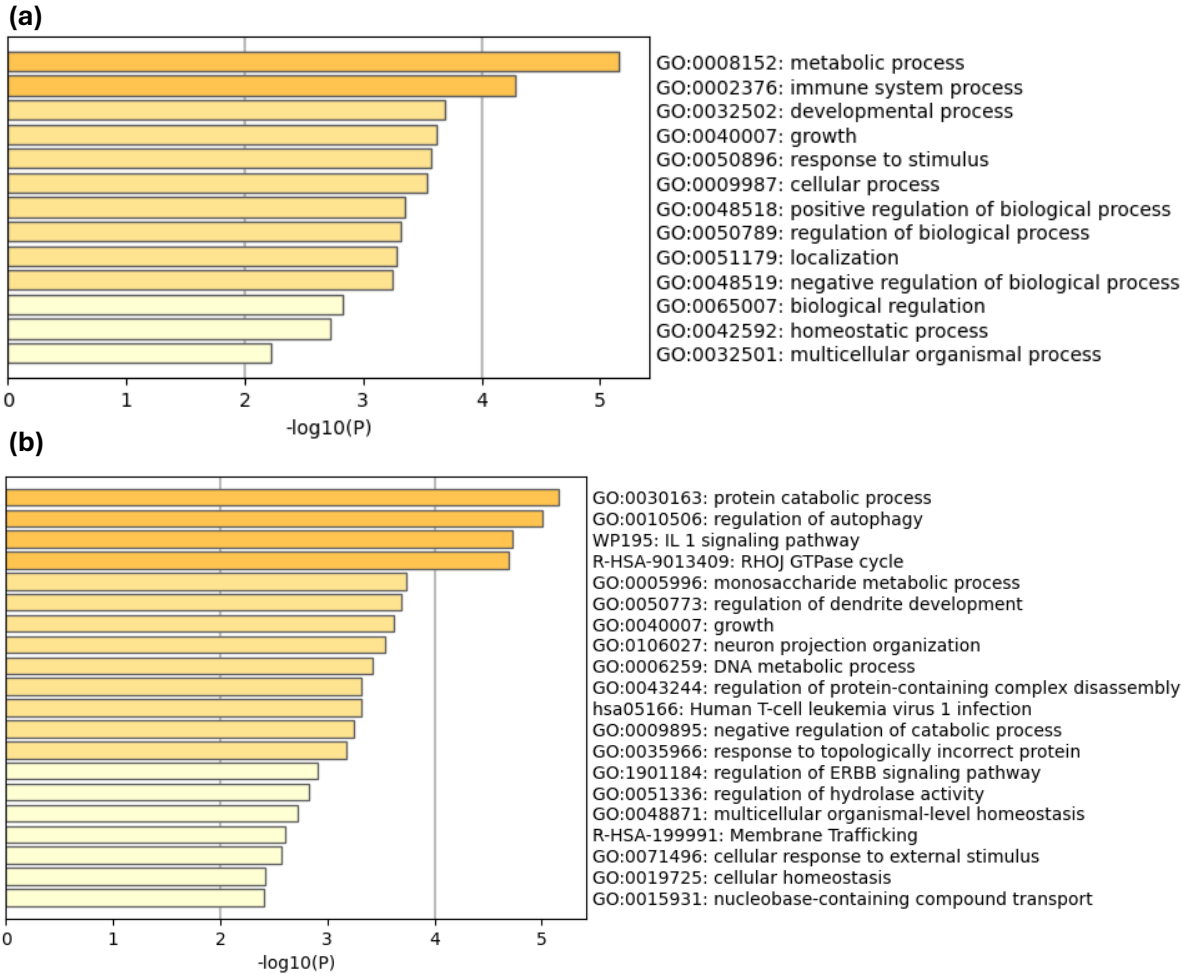

Figure 6.16: Metascape analysis of the enriched proteins with 100 µM probe 1 (no UV). (a) The top-level Gene Ontology (GO) biological processes are coloured by p-values; (b) Enriched terms across the input gene lists (proteins with an NSAF > 0) are coloured by p-values

Transcription factor mining was performed to look at the transcription factors that regulate the probe **1**-enriched proteins (Figure 6.17). Specificity protein 1 (SP1) is involved in the regulation of genes related to cell cycle, growth, DNA repair and apoptosis.[224] Minichromosome maintenance complex component 2 (MCM2) is also involved in the regulation of the cell cycle.[225] PR domain zinc finger

protein 4 (PRDM4) is a regulator involved in cell differentiation and chromatin modifications.[226] Farnesoid X receptor (FXR) is a nuclear receptor involved in the regulation of bile acid metabolism and plays a role in lipid and glucose homeostasis and its dysregulation is linked to T2D and obesity.[227]

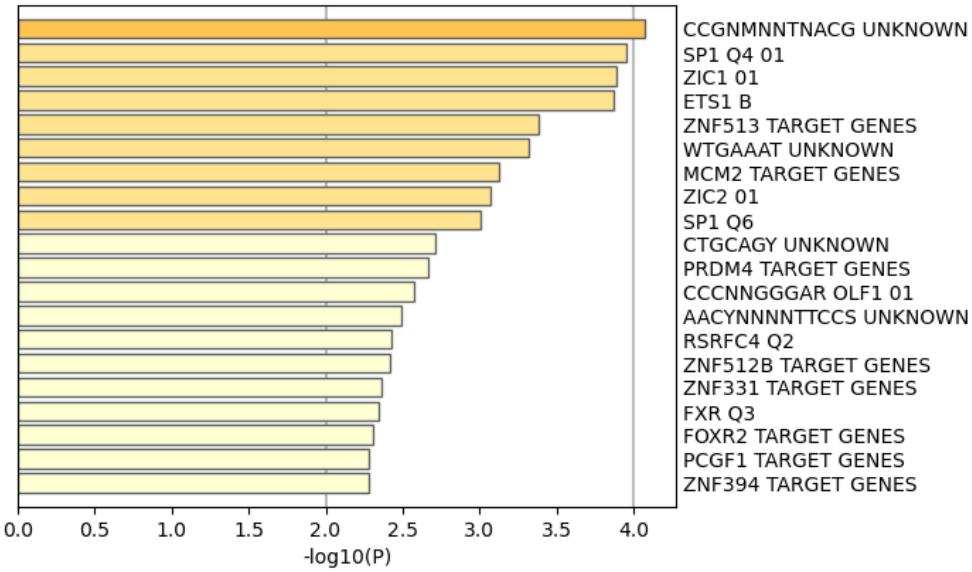

Figure 6.17: Transcription factors regulating proteins enriched by 100 µM probe 1 (no UV).

6.5.3.3 Proteins interactors of 100 µM probe 1 (with UV)

A comparison between the control and 100 µM probe **1**-treated cells (with UV) was performed. This resulted in a total of 1765 proteins unique to 100 µM probe **1**-treatment (with UV), of which 342 proteins were significant ($p < 0.05$) (Figure 6.18). This was significantly more protein interactors than 100 µM without UV due to the capture of covalently and non-covalently interacting proteins. STRING mapping of the protein interactions was performed, and further analysis allowed for subcellular localisation of the protein interactors (Figure 6.19). Enriched proteins were found in the nucleus (red), membrane (purple), mitochondria (green) and actin cytoskeleton (yellow).

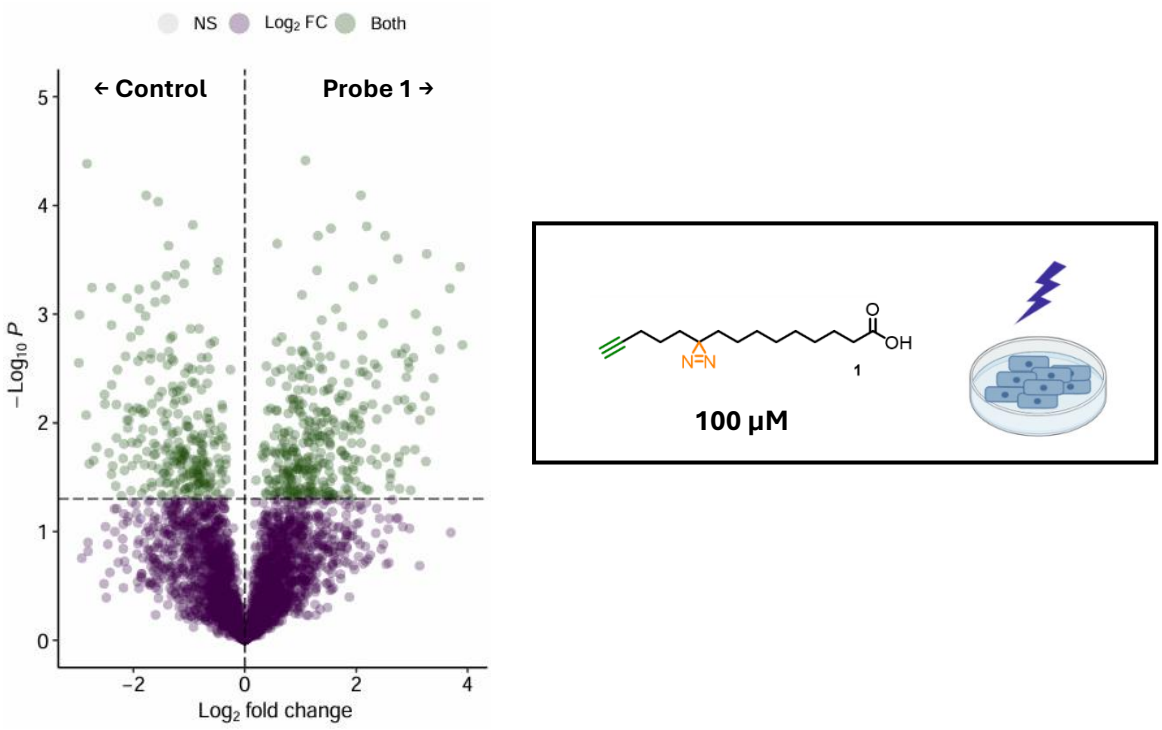

Figure 6.18: Proteomic analysis results of hiPSC-CMs treated with 100 µM probe 1 (with UV). Volcano plot of proteins enriched by 100 µM probe **1** (16 h, 3 min UV) compared with control cell (16 h, no UV.

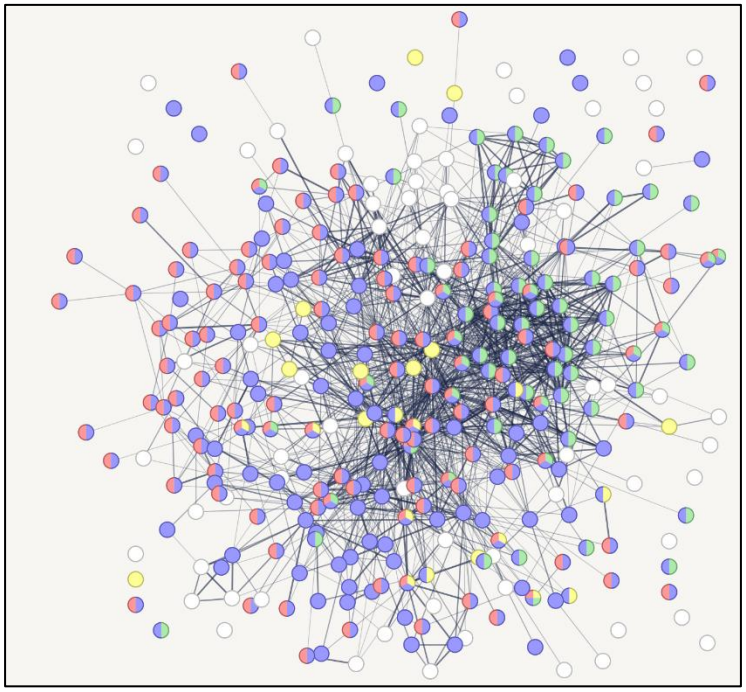

Figure 6.19: STRING network mapping of proteins enriched by 100 µM probe 1 (with UV). Protein localisation is coloured: nucleus (red), membrane (purple), mitochondria (green), actin cytoskeleton (yellow) and all other proteins (white).

Proteins significantly enriched (upper right quadrant of volcano plot) were again used for a Metascape pathway analysis (Figure 6.20). This revealed that the top enriched parent GO term was 'Cellular process', with 'Localisation' and 'Metabolism process' being GO terms of interest too. Further analysis of these processes allowed for the identification of more specific pathways (Figure 6.21) including 'Cytoskeleton in muscle cells', which was accompanied by 'Actin filament-based process', 'Smooth muscle contraction' and 'Actin filament-based movement'. Some mitochondrial pathways that were enriched were: 'Mitochondrial genome maintenance'; 'Regulation of mitochondrion organisation'; 'Transcriptional activation of mitochondrion biogenesis'. Other pathways of interest were: 'Chromatin organisation'; Glycolysis and Gluconeogenesis'; 'Ribosome'; and 'Unfolded protein response (UPR)'.

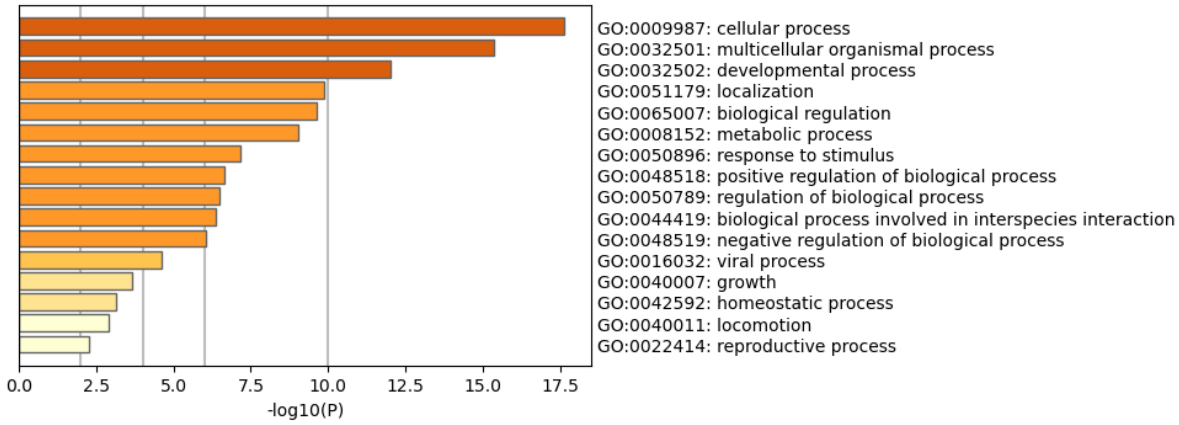

Figure 6.20: Metascape analysis of the enriched proteins with 100 µM probe 1 (with UV). The top-level Gene Ontology (GO) biological processes are coloured by p-values

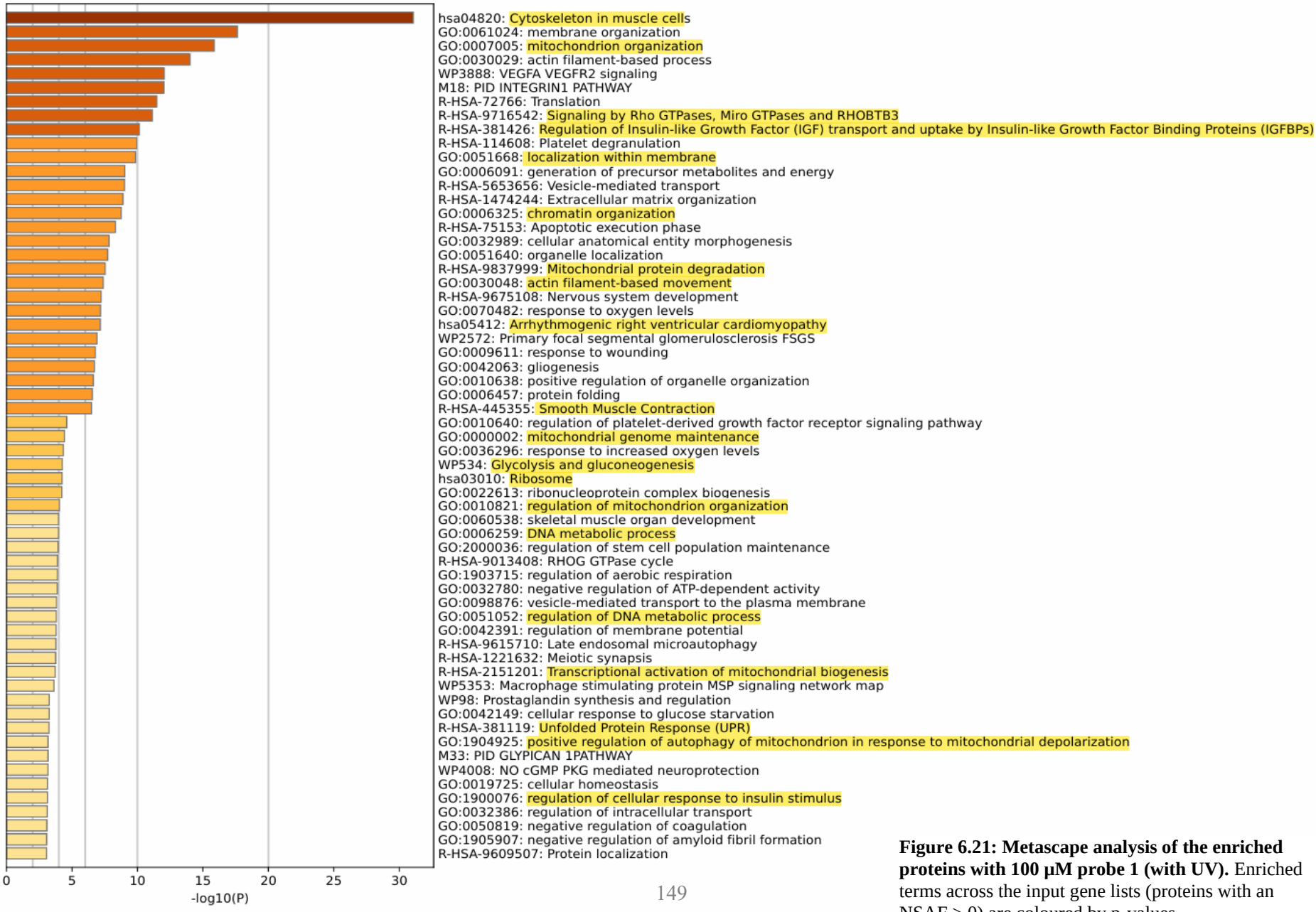

Figure 6.21: Metascape analysis of the enriched proteins with 100 µM probe 1 (with UV). Enriched terms across the input gene lists (proteins with an NSAF > 0) are coloured by p-values

Metascape analysis using the DisGeNet database to map gene names to diseases was performed (Figure 6.22a) and identified various cardiomyopathies (e.g. 'Cardiomyopathy, Dilated'); 'Lipodystrophy', 'Muscular dystrophy' and 'Mitochondrial diseases'. Transcription factor mining highlighted the interaction of probe **1** with proteins regulated by several transcription factors of interest (Figure 6.22b). Firstly, Peroxisome proliferator-activated receptor gamma (PPARG) is involved in the regulation of genes involved in lipid metabolism, glucose homeostasis and inflammation.[228] This acts as a positive control for probe **1** indicating it is interacting with proteins involved in these processes. Other TFs of interest were androgen receptor (AR) and hypoxia-induced factor 1 alpha (HIF1A).

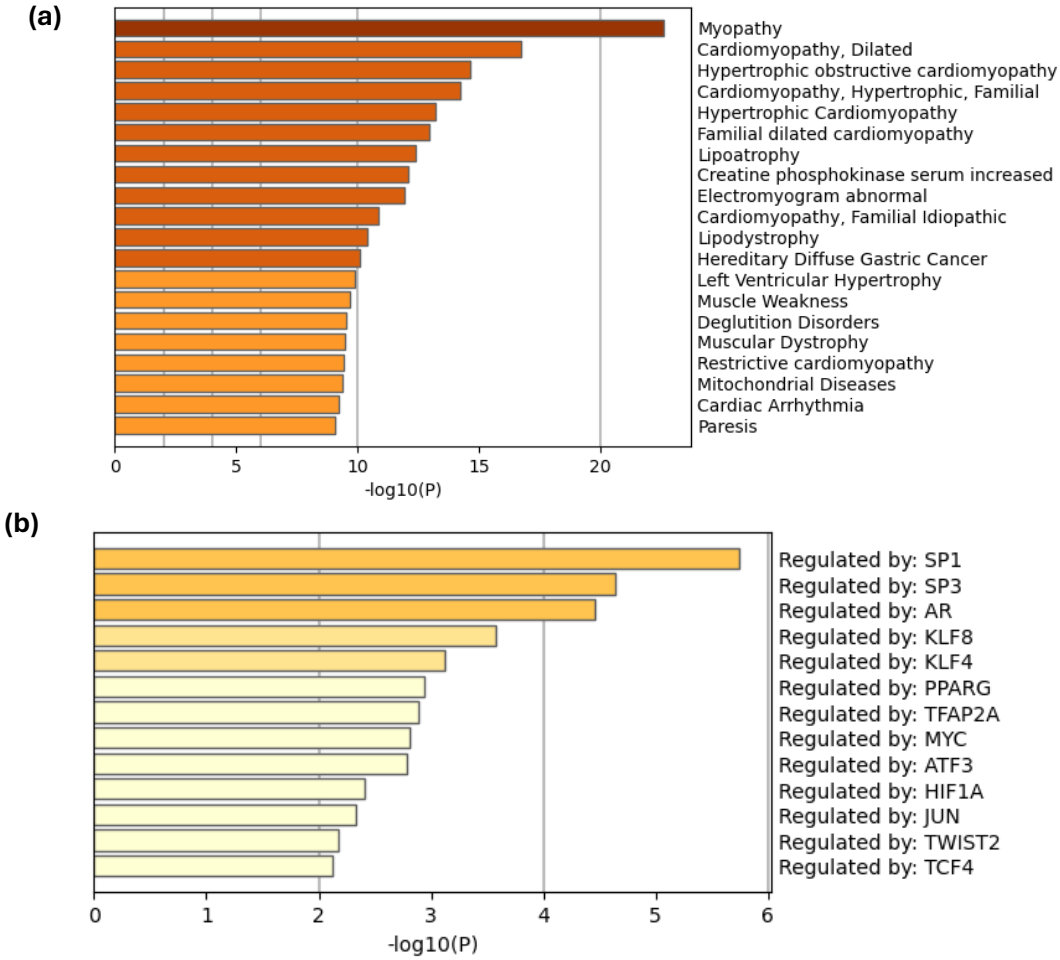

Figure 6.22: Metascape analysis of the enriched proteins with 100 µM probe 1 (with UV) (contd.) (a) Summary of enrichment analysis in DisGeNET for 100 µM probe **1** - showing enrichment of disease pathways. (b) Transcription factors regulating proteins enriched by 100 µM probe **1.**

6.5.4 Validation of identified targets from proteomic analysis

6.5.4.1 Validation of protein interactors of probe 1

To validate the proteomic analysis, several enriched protein targets from each treatment group were validated by western blot. For the cells treated with 30 µM probe **1** (16 h, + UV) two targets were validated: β-Actin (ACTB) and Lamin A (LMNA) (Figure 6.23). Western blot showed enrichment of the proteins following Neutravidin pulldown and therefore confirmed them as probe **1** protein targets (Figure 6.23b). Further analysis of the proteins using STRING highlighted the central role of β-Actin in the 'Actin cytoskeleton' network (Figure 6.24).

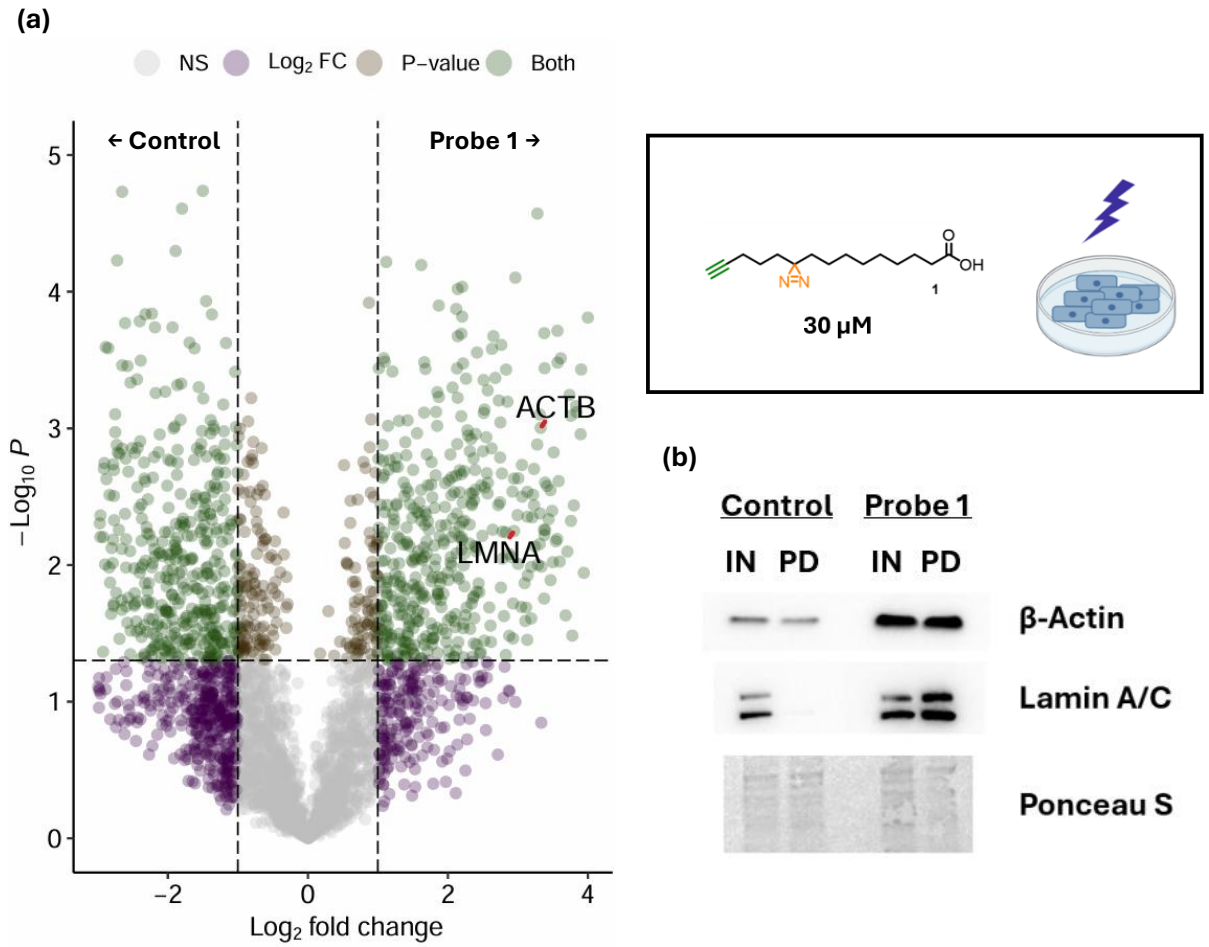

Figure 6.23: Validation of proteomic analysis results for hiPSC-CMs treated with 30 µM probe 1 (with UV). (a) Volcano plot of proteins enriched by 30 µM probe **1** (16 h, 3 min UV) compared with control cell (16 h, no UV). Proteins for validation highlighted; (b) Western blot analysis of neutravidin pulldown, blotting for ACTB and LMNA (IN=input, PD=postpulldown). For quantification of pulldown enriched targets in hiPSC cardiomyocytes, see *Appendix C*.

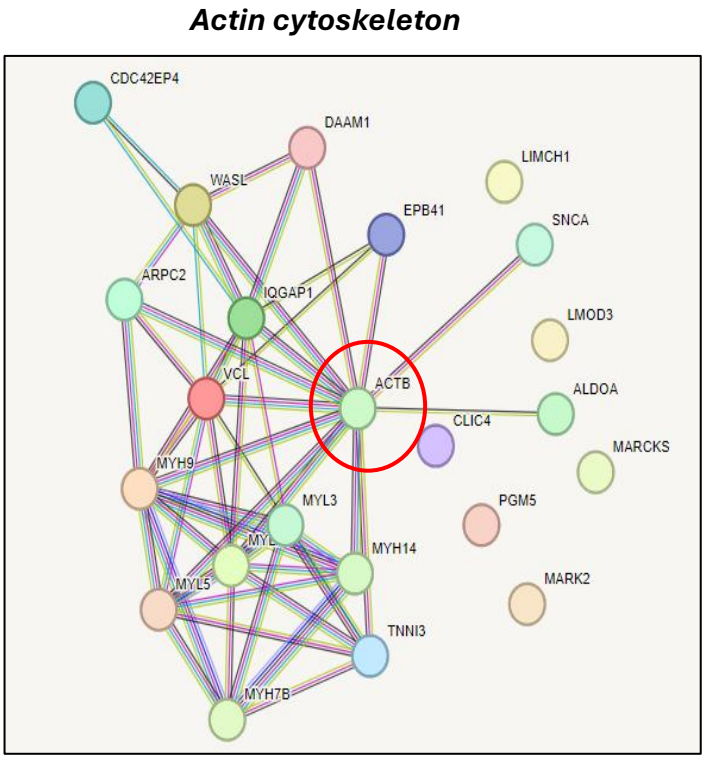

Figure 6.24: STRING network mapping of proteins enriched by 30 µM probe 1 (with UV). (a) actin cytoskeleton network map with ACTB (red) highlighted as a central protein.

Cells treated with 100 µM of probe **1** (16 h, no UV) had fewer proteins enriched, but some proteins of interest were: ribosomal protein L5 (RPL5) and hydroxyacyl-CoA dehydrogenase trifunctional multienzyme complex (HADHA) (Figure 6.25). Western blot showed enrichment of both these proteins following biotin pulldown, validating them as probe **1** targets. STRING network analysis showed that RPL5 was a component of the 'Proteolysis' network and HADHA was part of the 'Mitochondrion' network.

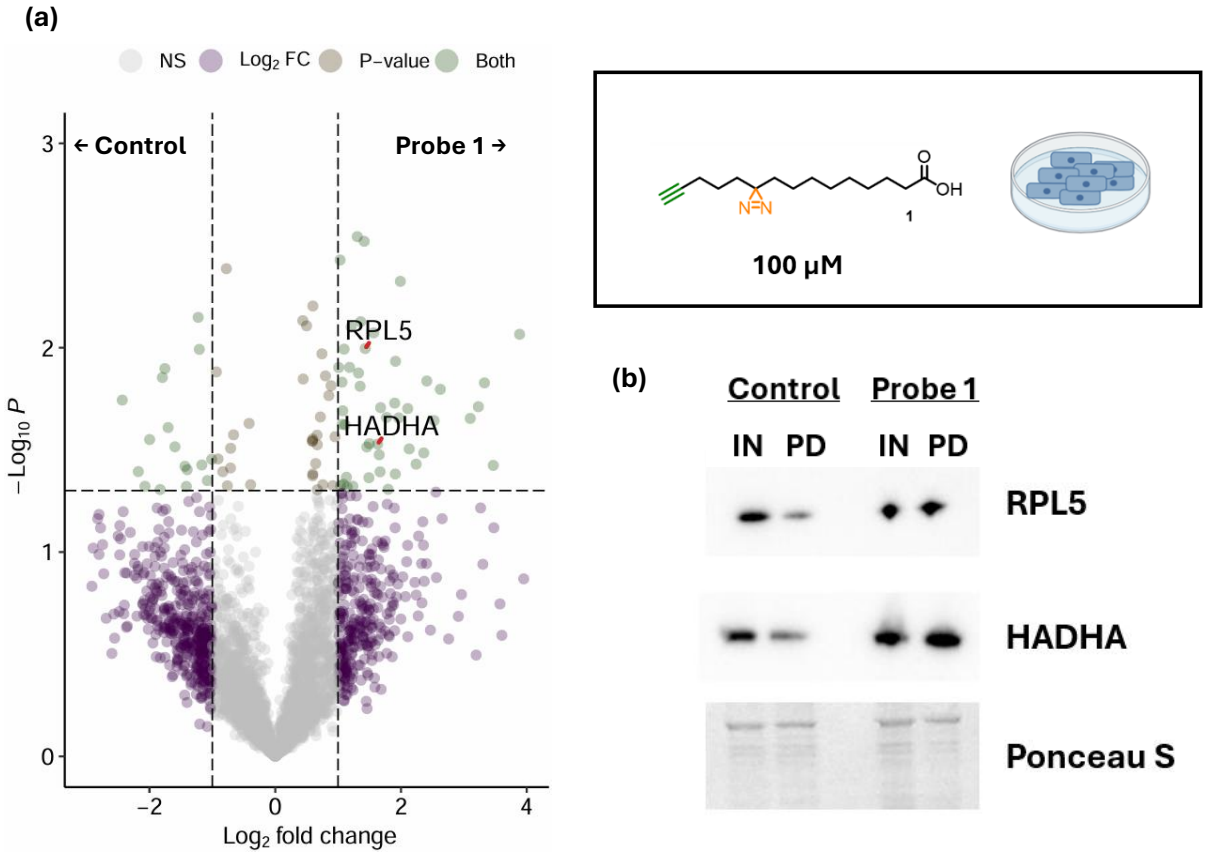

Figure 6.25: Validation of proteomic analysis results for hiPSC-CMs treated with 100 µM probe 1 (no UV). (a) Volcano plot of proteins enriched by 100 µM probe **1** (16 h, no UV) compared with control cell (16 h, no UV). Proteins for validation highlighted; (b) Western blot analysis of neutravidin pulldown, blotting for RPL5 and HADHA (IN=input, PD=postpulldown). For quantification of pulldown enriched targets in hiPSC cardiomyocytes, see *Appendix C*.

Cells treated with 100 µM probe **1** (16 h, + UV) had an increased number of proteins compared with the no UV group (Figure 6.27). Again, ACTB and LMNA were enriched as protein interactors and validated by Western blot. Other enriched proteins of interest were phosphodiesterase 3A (PDE3A), perilipin 3 (PLIN3), vascular endothelial growth factor A (VEGFA) and enolase 2 (ENO2). These were also validated by western blot, and all showed enrichment following pulldown. PLIN3 and PDE3A were shown to be involved in the 'Signal transduction' network on STRING, PLIN3 was also present in the 'Lipid storage' network, whereas ENO2 was shown to be part of the 'Glucose metabolic network'.

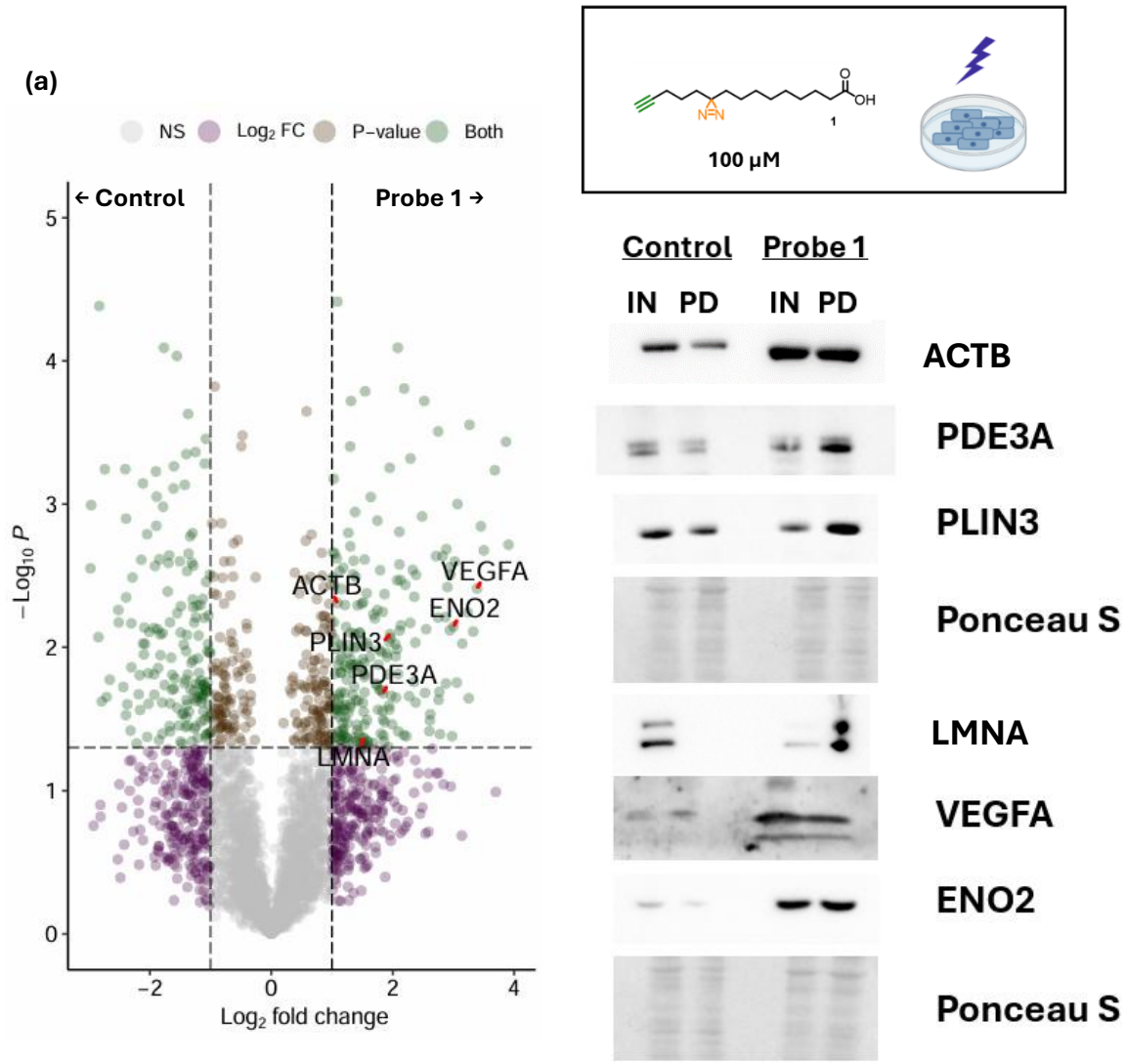

Figure 6.27: Validation of proteomic analysis results for hiPSC-CMs treated with 100 µM probe 1 (with UV). (a) Volcano plot of proteins enriched by 100 µM probe **1** (16 h, with UV) compared with control cell (16 h, no UV). Proteins for validation highlighted; (b) Western blot analysis of neutravidin pulldown, blotting for ACTB, PDE3A, PLIN3, LMNA, VEGF and ENO2 (IN=input, PD=postpulldown). For quantification of pulldown enriched targets in hiPSC cardiomyocytes, see *Appendix C*.

6.5.4.2 Effects of probe 1 on mitochondrial networks in hiPSC-CMs

As proteins involved in 'Mitochondrion' networks were enriched by probe **1**, an analysis of the phenotypic outcome of these interactions was performed. Control and probe **1**-treated hiPSC-CM cells (16 h) were stained using MitoTracker™ Red CMXRos, (Figure 6.29a,b). Quantification using the MitoAnalyzer plugin for ImageJ (version 1.54d) revealed that probe **1** resulted in a statistically significant increase in individual mitochondrial count (mitochondrial number) (Figure 6.29c). However, this increase did not result in a significant change in mitochondrial network area after

probe **1** treatment. Mitochondrial network branch number and junctions were both statistically decreased in probe **1**-treated cells when compared with control cells. These results suggest a shift in mitochondrial networks towards biogenesis and potentially fragmentation.

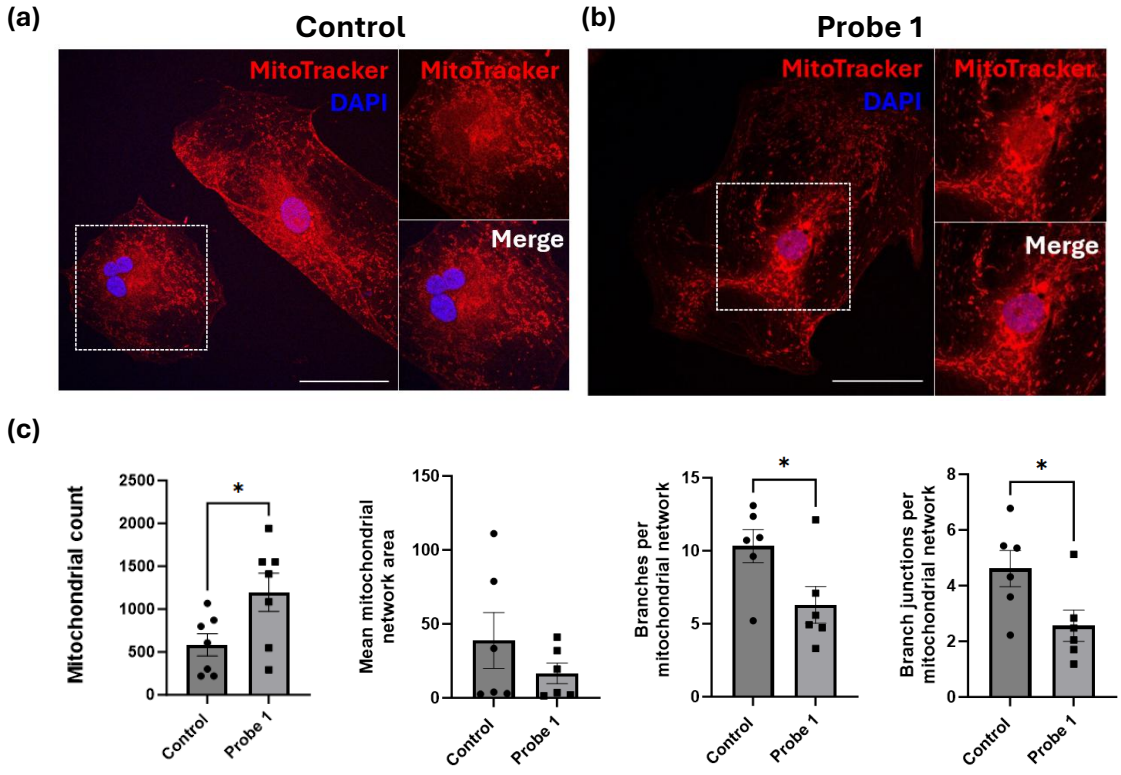

Figure 6.29: Confocal microscopy highlights mitochondrial fragmentation following 100 µM probe 1 treatment: Immunostaining using MitoTracker CMXRos (red) with DAPI (blue), as (a) control or after treatment for 16 h with (b) 100 µM probe **1**; scale bar is 50 µM with ×2 zoom to the right; (c) Quantification of mitochondrial count, area, branches per mitochondria and branch junctions per mitochondria (n = 6).

6.5.4.3 Effects of probe 1 on OXPHOS protein levels

As probe **1** was shown to be causing changes to mitochondrial networks, an OXPHOS antibody cocktail was used to investigate if there were any changes in OXPHOS whole protein levels (Figure 6.30) following control, 30 µM probe **1** or 100 µM probe **1** treatment for 16 h treatments. Statistically significant changes occurred in some of the subunits of oxidative phosphorylation, with increased levels of subunits of complex I, II and IV. This demonstrated that probe **1** was upregulating levels of proteins involved in OXPHOS.

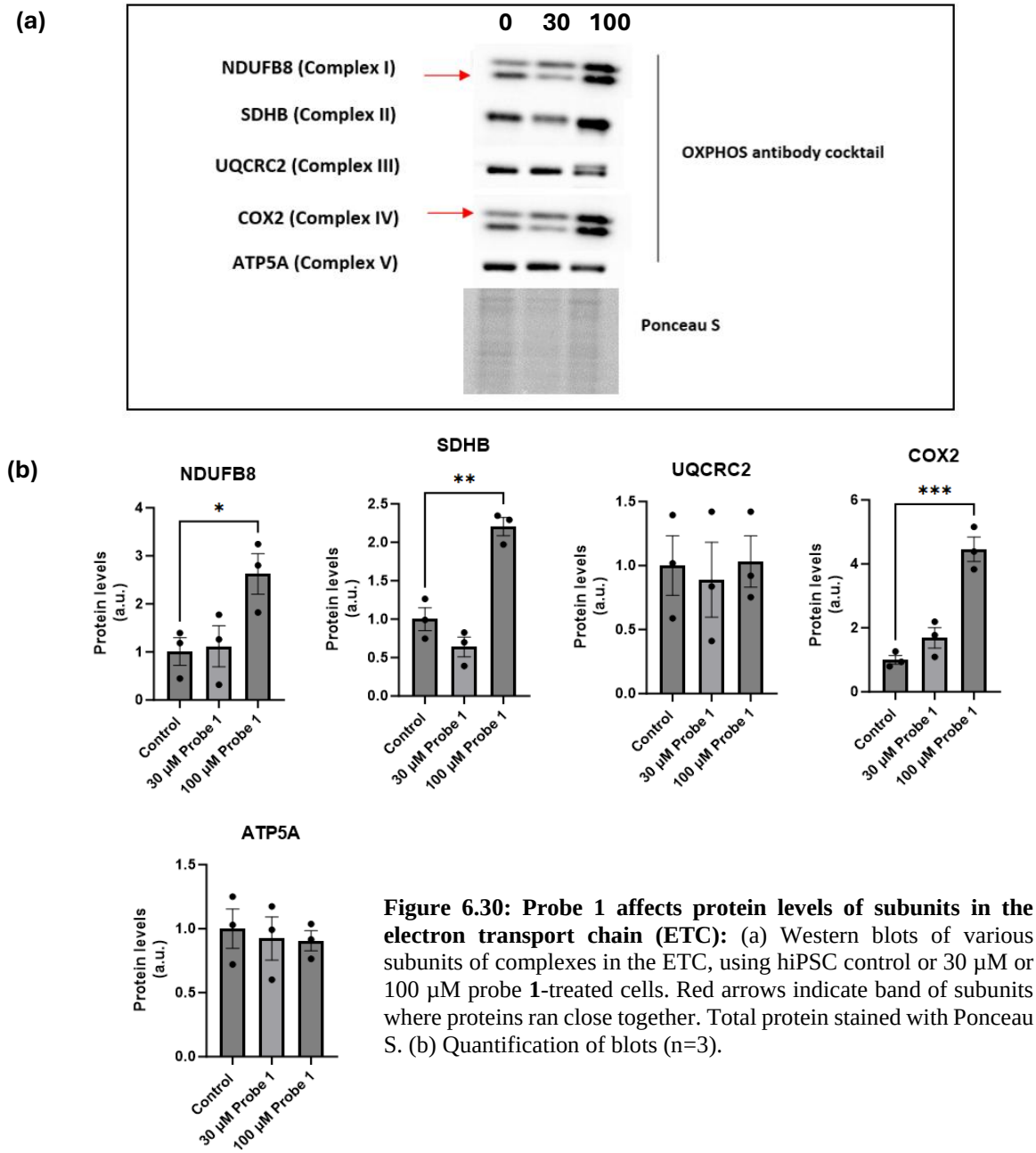

Figure 6.30: Probe 1 affects protein levels of subunits in the electron transport chain (ETC): (a) Western blots of various subunits of complexes in the ETC, using hiPSC control or 30 µM or 100 µM probe **1**-treated cells. Red arrows indicate band of subunits where proteins ran close together. Total protein stained with Ponceau S. (b) Quantification of blots (n=3).

6.5.4 Transcriptomics captures changes in gene expression induced by probe 1 or palmitate treatment

To understand the downstream consequences of the probe-protein interactions in hiPSC-CM, we performed a transcriptomic analysis to enable a comprehensive genome-wide assessment following 100 µM probe **1** treatment (16 h) or 100 µM palmitate. Principal component analysis (PCA) showed a distinct separation between the groups: control (C); palmitate (F); and probe **1** (T)-treated cells (Figure 6.31). PC1 accounted for 38% of the variance attributable to compound treatment, primarily distinguishing the probe **1** group from the control and palmitate-treated cells, while PC2 accounted

for 28% of the variance, further separating control and palmitate-treated cells from probe **1**-treated cells. These results highlight that probe **1**-treatment is causing more variance than palmitate treatment. It is important to note that due to the differences in chemical structure of the two compounds, some variation in biological effects is expected.

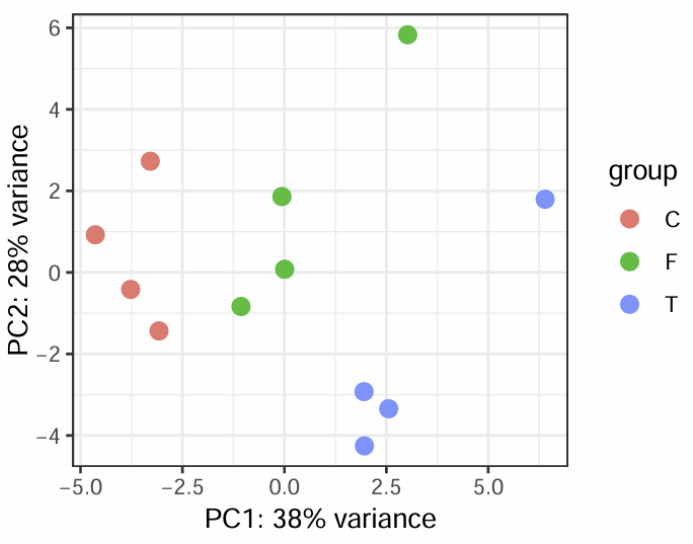

Figure 6.31: Principal component analysis (PCA) plot of transcriptomic samples for hiPSC-CMs. hiPSC-CM cells as controls (C) or treated with 100 µM palmitate (F) or 100 µM probe **1** (T).

6.5.5 Transcriptomic analysis of probe 1 treatment

Differential gene expression (DEG) analysis identified 14,993 genes affected by probe **1** treatment compared to control cells, with 7,266 upregulated and 6,379 downregulated (Figure 6.33). Of these, 473 (3.2%) upregulated and 875 (5.8%) downregulated genes were found to be statistically significant ($p < 0.05$).

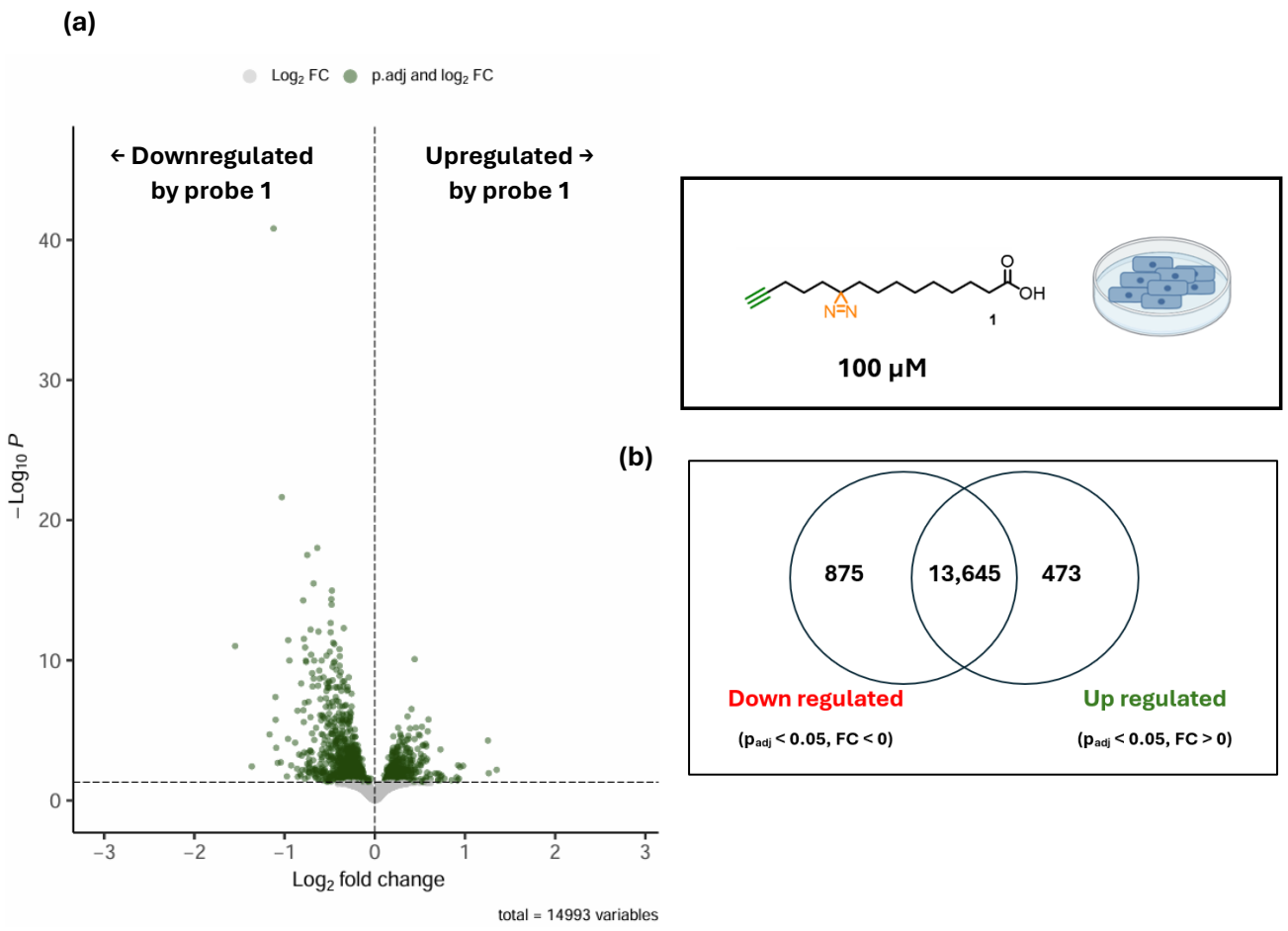

Figure 6.33: Transcriptomic analysis results of hiPSC-CMs treated with 100 µM probe 1. (a) Volcano plot of gene expression changes by 100 µM probe **1** (16 h) compared with control cell (16 h); (b) Venn diagram genes upregulated and downregulated by probe **1**.

6.5.5.1 Analysis of upregulated genes following probe 1 treatment

As large-scale changes occurred in the transcriptome a pathway approach was adopted, again to reduce complexity and investigate the broader biological function changes following probe **1** treatment. Statistically significant genes were then inputted into Metascape to facilitate a more comprehensive analysis. From this analysis, the highest upregulated GO biological process from the DEGs was the 'Regulation of biological process' (Figure 6.35a). Some other upregulated GO processes are 'Metabolic processes' and 'Localisation' (Figure 6.35a). Specifically, pathways that were upregulated included: 'Regulation of mitotic cell cycle', 'Chromatin organisation', 'Integration of energy metabolism', 'Metabolism of lipids', and 'Insulin signalling' (Figure 6.35b).

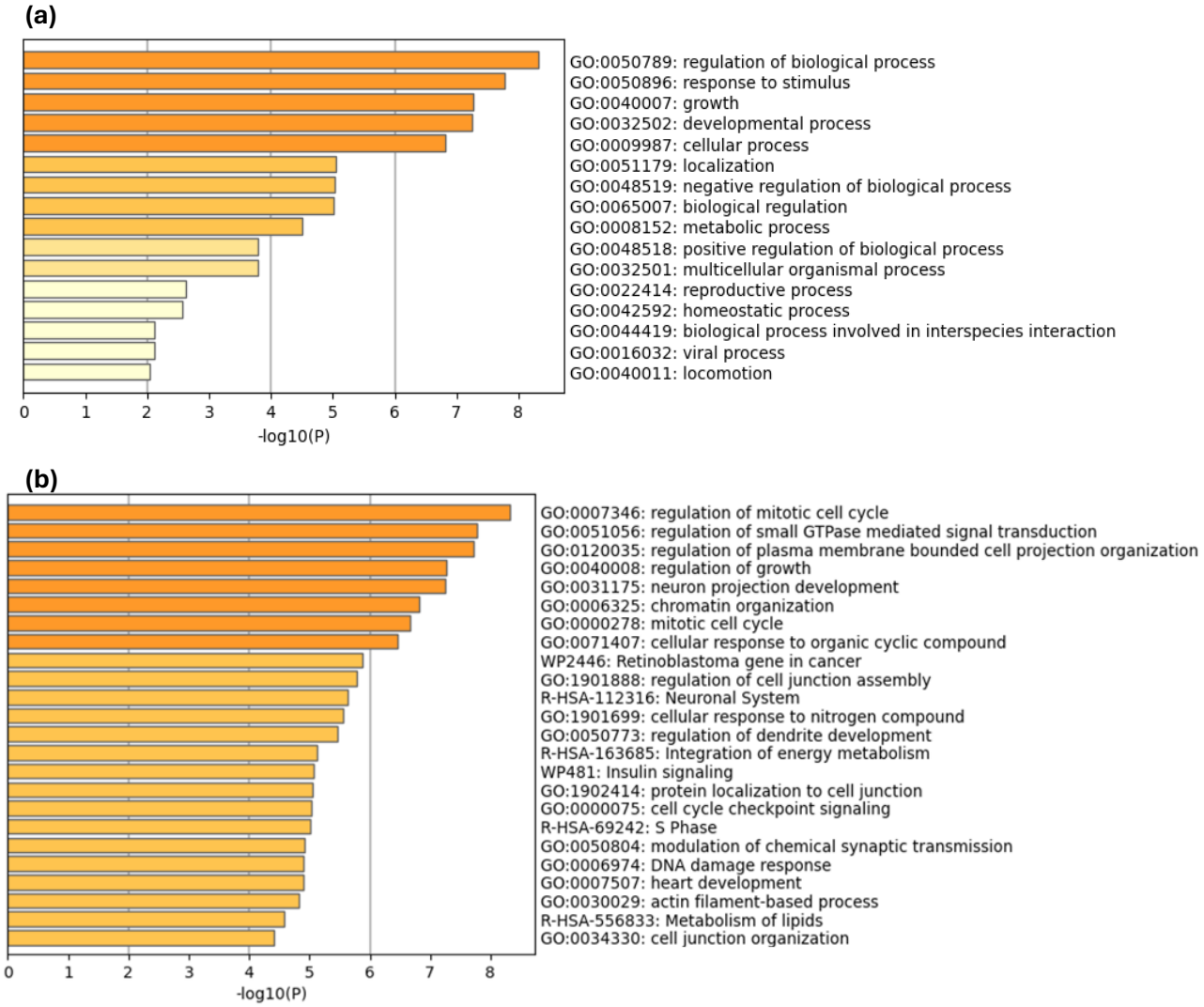

Figure 6.35: Metascape analysis of the upregulated genes with 100 µM probe 1. (a) The top-level Gene Ontology (GO) biological processes are coloured by p-values; (b) Enriched terms across the input gene lists (proteins with an NSAF > 0) are coloured by p-values.

Transcription factor mining revealed that several of the genes upregulated by probe **1** were regulated by transcription factors of interest (Figure 6.36). NPM1 (Nucleophosmin) is a nucleolar protein involved in ribosome biogenesis, regulation of cell cycle and DNA repair.[229] RELA is a component of the NF-κB complex and regulates genes involved in immune response, inflammation and cell survival.[230] PGR (progesterone receptor) regulates various physiological processes, including reproductive functions, menstrual cycle and pregnancy.[231] This suggests that probe **1** is upregulating genes involved in ribosome biogenesis, inflammation and reproduction.

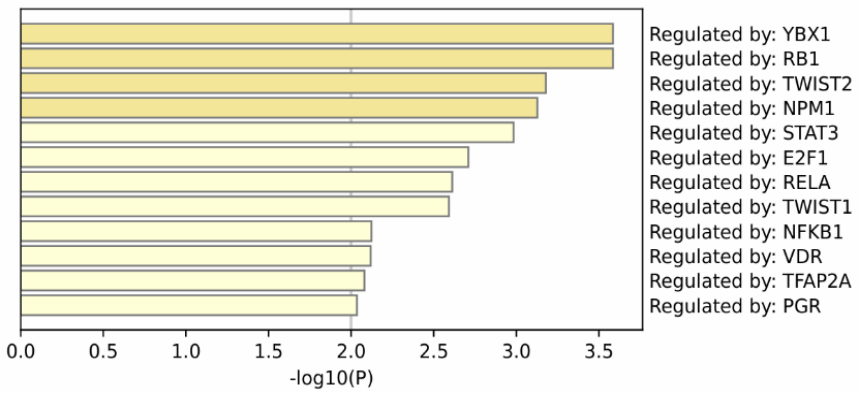

Figure 6.36: Transcription factors regulating proteins upregulated by 100 µM probe 1.

To gain further insight into affected upregulated biological pathways, a KEGG pathway analysis was also performed on the DEGs (Figure 6.37). The analysis revealed significant upregulation in several key pathways. Notably, 'Insulin signalling pathway' showed upregulated genes in the probe **1**-treated cells, additionally 'Cell cycle' and 'DNA replication' pathways also exhibited a significant upregulation, indicating a potential connection between probe **1** and cell cycle progression.

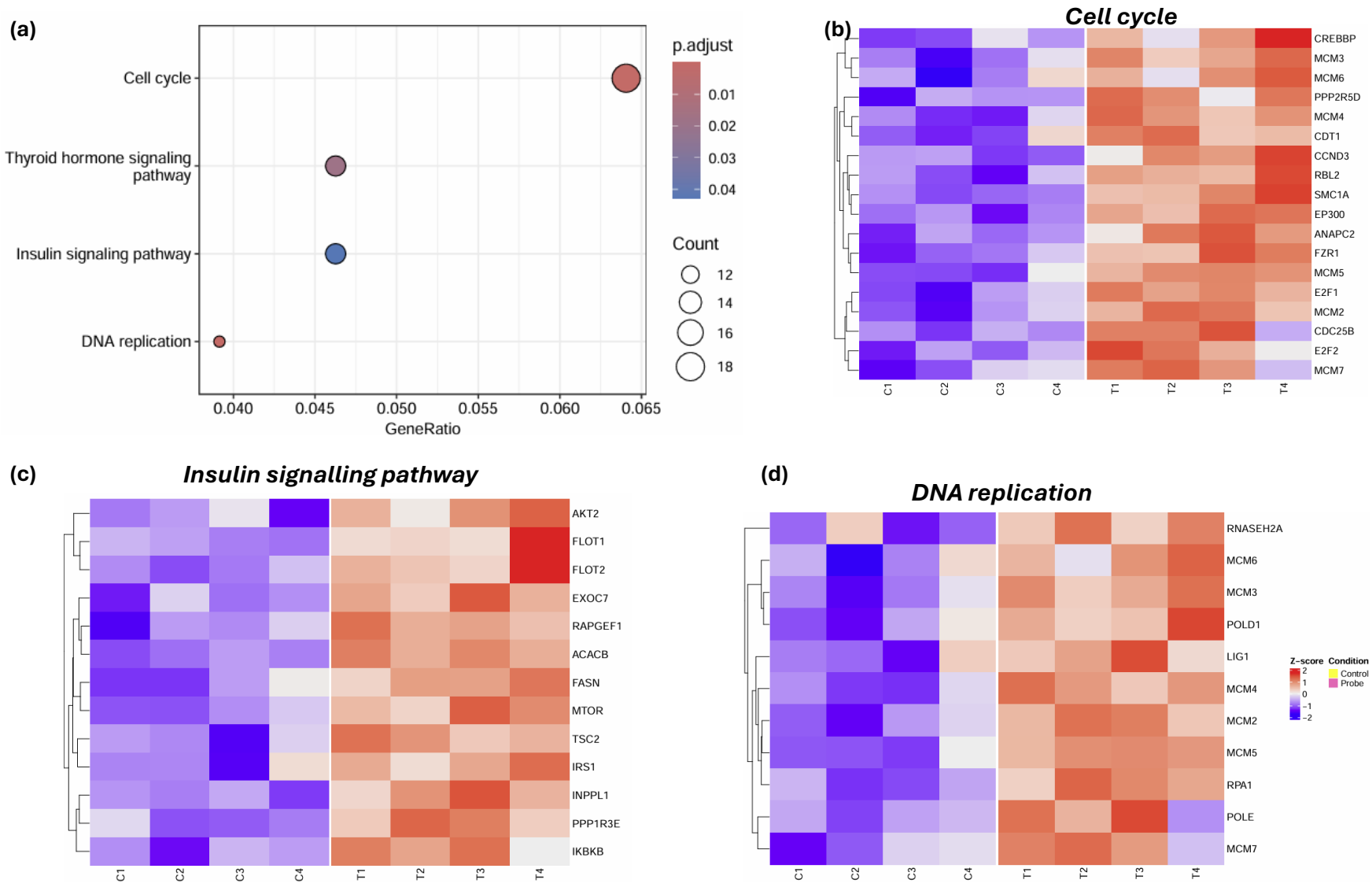

Figure 6.37: KEGG pathway analysis of up-regulated genes following 100 µM probe 1 treatment: (a) Dot plot representing up-regulated KEGG pathways. Heatmaps of genes involved in: (b) Cell-cycle; (c) Insulin signalling pathway and (d) DNA replication. C = control, T = 100 µM probe **1**.

6.5.5.2 Analysis of downregulated genes following probe 1 treatment

A Metascape analysis was then performed to assess the biological implications of the 875 significantly downregulated genes following probe **1** treatment (Figure 6.39). From this analysis, the highest downregulated GO parent biological process from the DEGs was the 'Cellular process' (Figure 6.39a). More specific annotation of the downregulated pathways revealed 'Actin filament-based process' as the most significant pathway (Figure 6.39b). This was also accompanied by other biological GO terms from similar processes: 'Muscle structure development'; 'Cytoskeleton in muscle cells'; 'Muscle cell differentiation'; and 'Regulation of actin filament-based processes'. Transcription factor mining revealed that several of the genes downregulated by probe **1** were regulated by transcription factors of interest (Figure 6.39c). PPARG and HIF1A are involved in responses to substate availability: glucose and lipids; and oxygen, respectively.[228,232] HDAC1 is an enzyme involved in the removal of acetyl groups from histones.[233] GATA6 is involved in the formation of the heart and other tissues.[234] NFKB1 is a subunit of the NF-κB complex, which regulates immune responses and can be dysregulated in several diseases, including cardiovascular diseases.[235] Using DisGeNet, a comprehensive database focusing on the relationship between genes and diseases, several cardiomyopathy and vascular diseases were highlighted as significantly enriched following probe **1** treatment (Figure 6.39d).

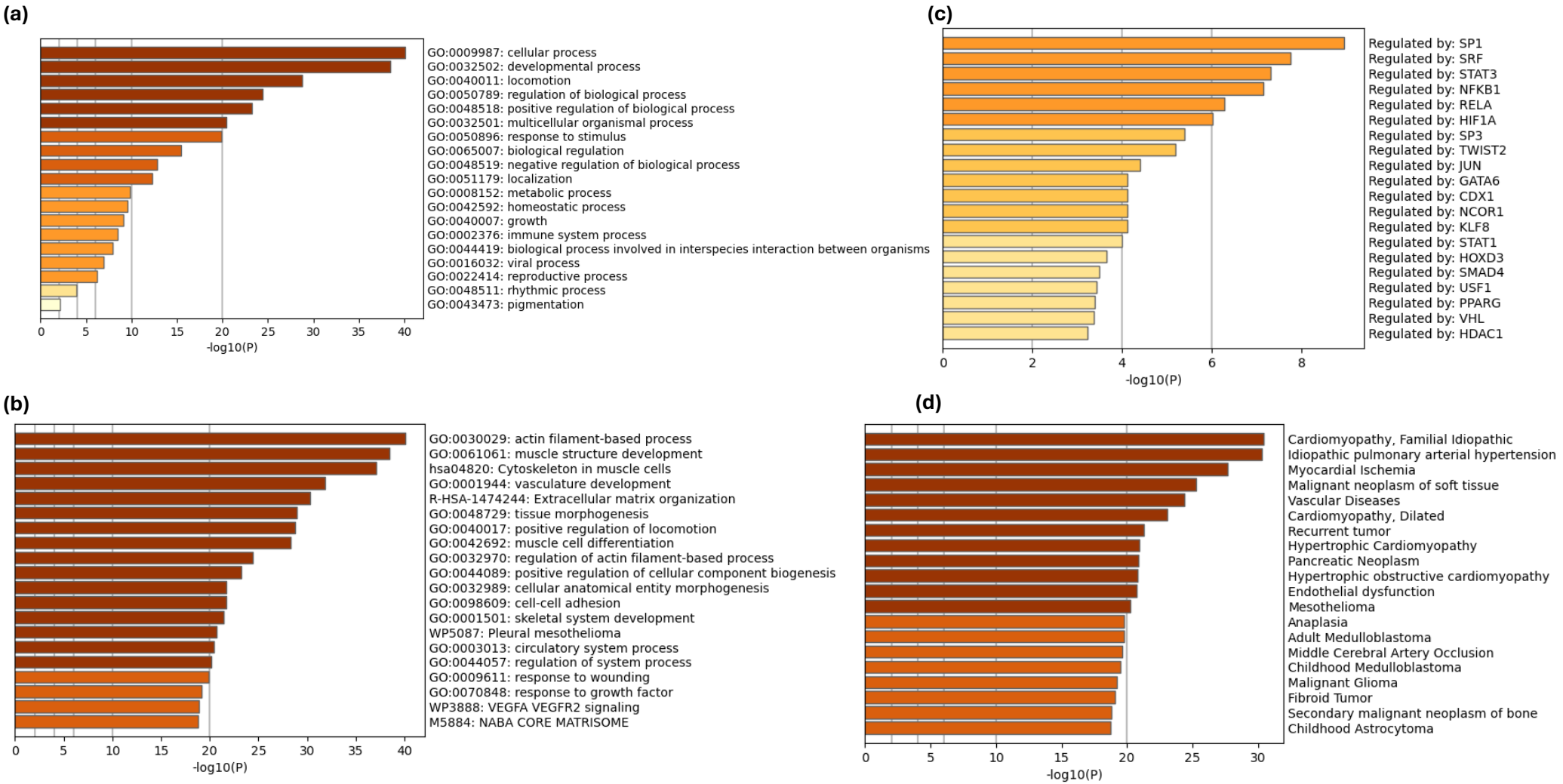

Figure 6.39: Metascape analysis of the downregulated genes with 100 µM probe 1. (a) The top-level Gene Ontology (GO) biological processes are coloured by p-values; (b) Enriched terms across the input gene lists (proteins with an NSAF > 0) are coloured by p-values; (c) Summary of enrichment analysis in DisGeNET for 100 µM probe **1** - showing enrichment of disease pathways; (d)Transcription factors regulating proteins enriched by 100 µM probe **1**.

To gain further insight into affected downregulated biological pathways, a KEGG pathway analysis was also performed on the DEGs (Figures 6.40 & 6.41). The analysis revealed significant downregulation in several key pathways. Notably, 'Cytoskeleton in muscle cells' and 'Regulation of cytoskeleton' were significantly downregulated pathways in the probe **1**-treated cells. "PI3K-Akt signalling pathway" was downregulated, which is implicated in both insulin and mTOR signalling in the cardiomyocyte. Finally, both "cAMP signalling" and "Adrenergic signalling" were decreased, of interest given the protein interaction with PDE3.

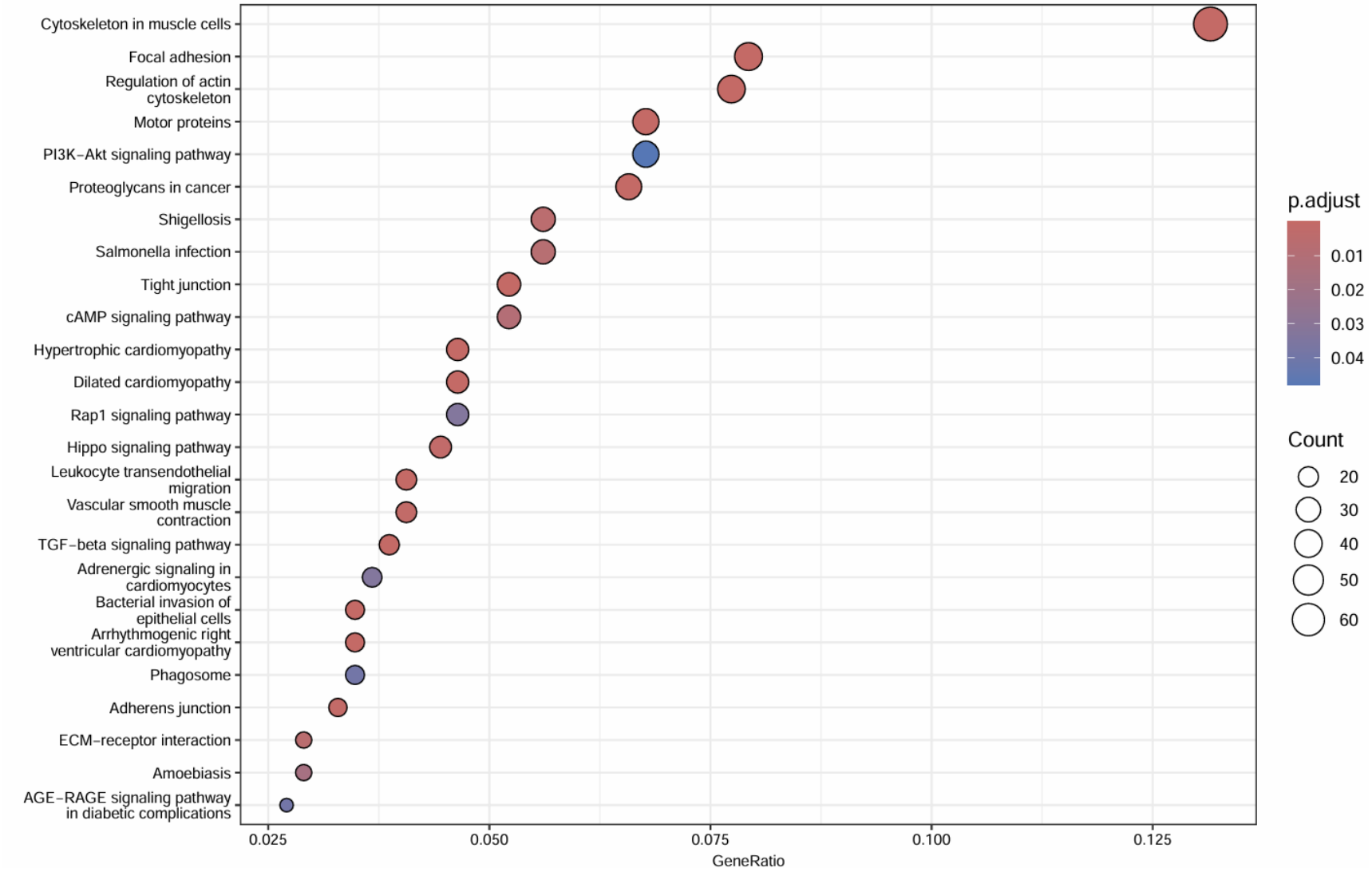

Figure 6.40: KEGG pathway analysis of down-regulated genes following 100 µM probe 1 treatment: Dot plot representing down-regulated KEGG pathways.

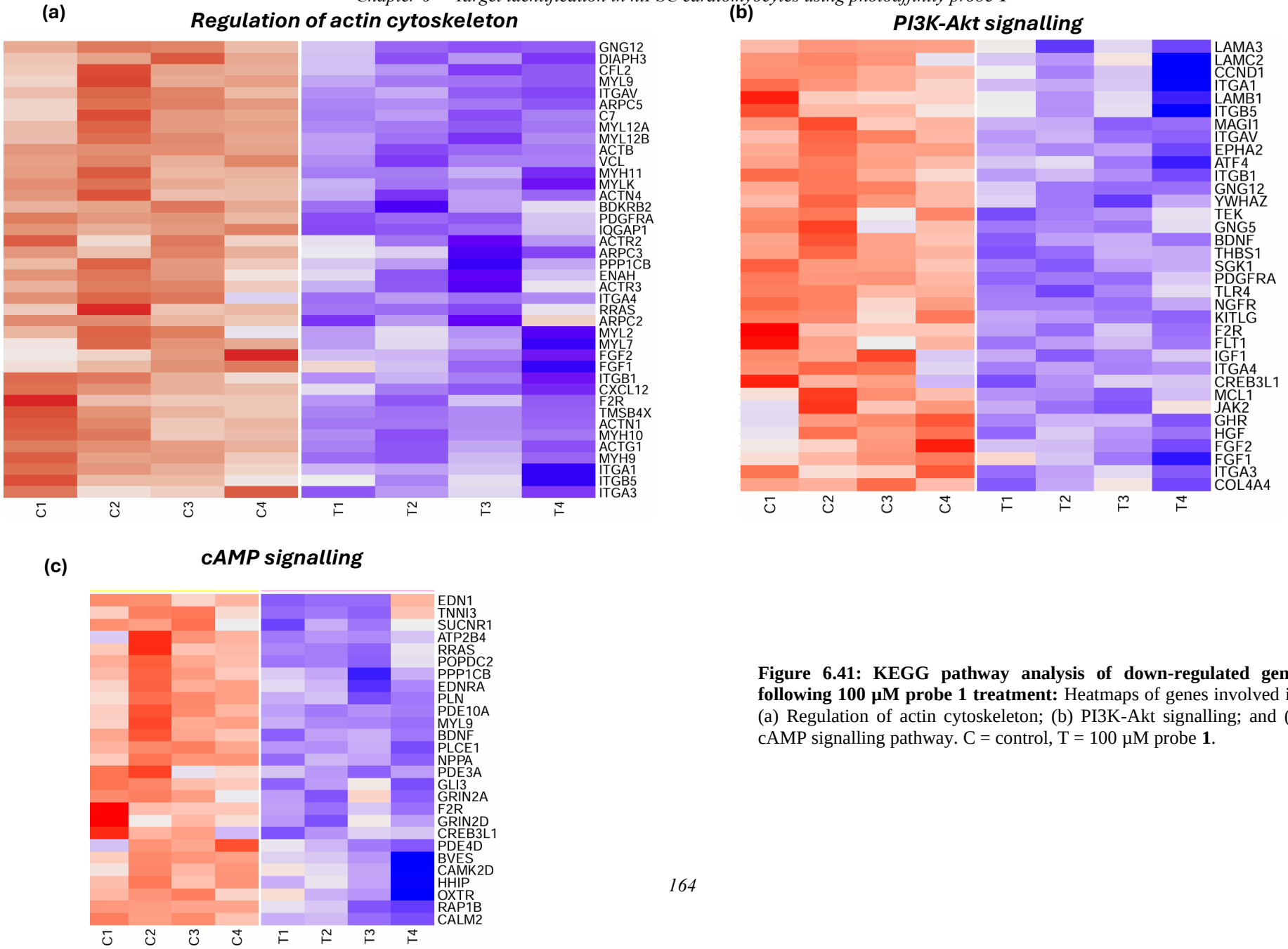

Figure 6.41: KEGG pathway analysis of down-regulated genes following 100 µM probe 1 treatment: Heatmaps of genes involved in: (a) Regulation of actin cytoskeleton; (b) PI3K-Akt signalling; and (c) cAMP signalling pathway. C = control, T = 100 µM probe **1**.

6.5.5.3 GSEA analysis following probe 1 treatment

Gene set enrichment analysis (GSEA) was performed as an unbiased approach to identify significant changes in pathway activities after probe **1** treatment (Figure 6.42). This analysis revealed a notable upregulation in the 'DNA replication' pathway, suggesting a link between probe **1** and cell cycle progression. There was also downregulation of several pathways of interest: 'Proteasome degradation'; 'Ribosome'; 'Regulation of actin cytoskeleton'; 'Glycolysis'; 'Citrate/TCA cycle'; 'MTORC1 signalling'; 'PI3AKT signalling'; 'Estrogen response early'; 'Androgen receptor'; and 'VEGFA/VEGFR2 signalling'.

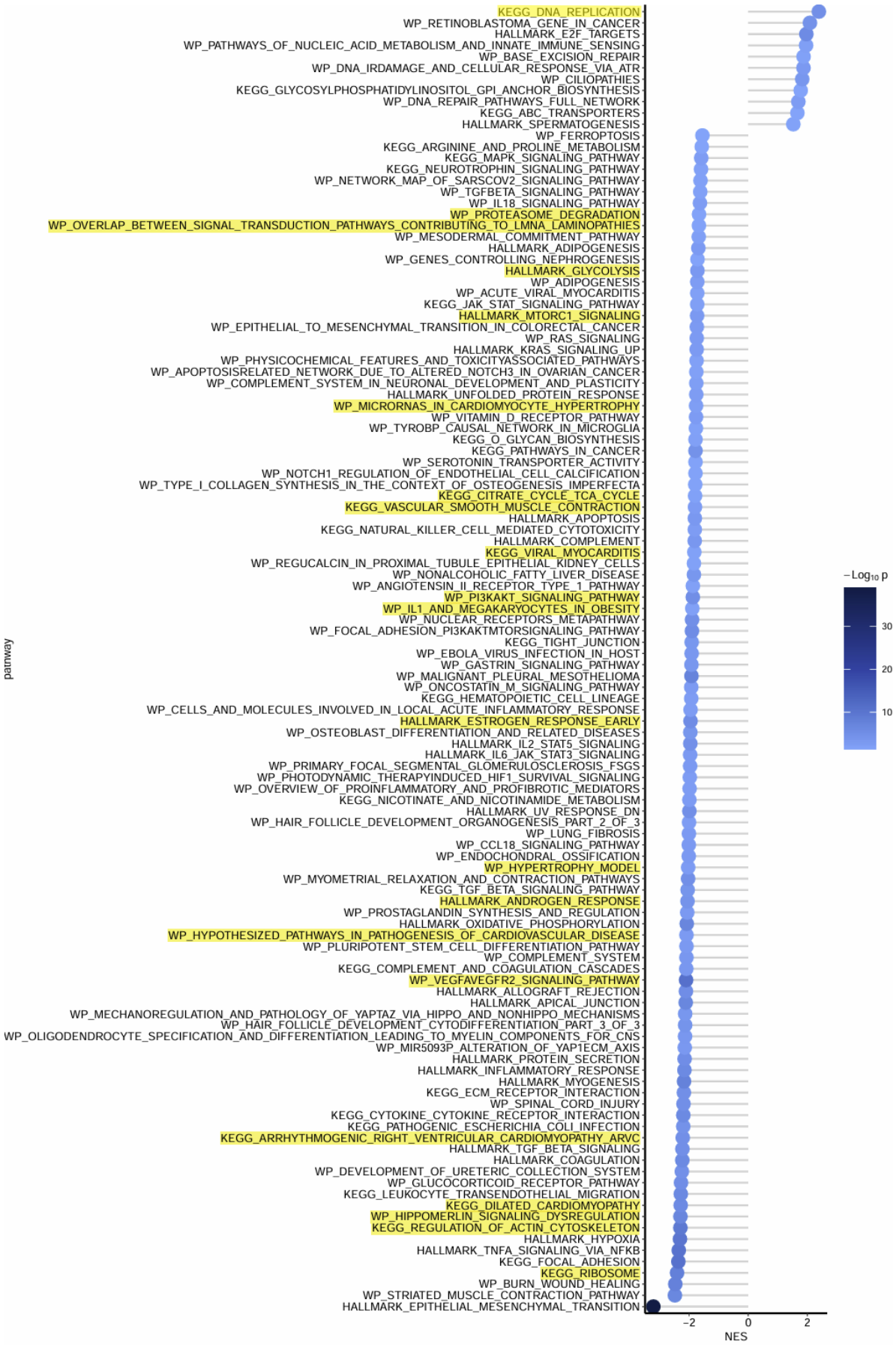

Figure 6.42: Gene Set Enrichment Analysis (GSEA) of transcriptomics results for 100 µM probe 1. Pathways of interest are highlighted.

6.5.6 Transcriptomic analysis of changes in gene expression following palmitate treatment

Transcriptomic analysis was also performed on hiPSC-CMs treated with 100 µM palmitic acid and compared with control cells. This data would act as a comparator for probe **1**, with key findings summarised here and the comparison with probe **1** in section 6.5.8 below. Differential expressed gene (DEG) analysis identified 13,144 genes affected by palmitate treatment (100 µM, 16 h), with 6,291 upregulated and 6,641 downregulated (Figure 6.43). Of these, 88 (0.5%) upregulated and 124 (0.9%) downregulated genes were found to be statistically significant ($p < 0.05$). These cells had previously been matured with 80 µM oleate, therefore, changes in gene expression were likely to be smaller than in the probe **1**-treated *MDA-MB-231* cells. Gene expression changes were smaller with palmitate treatment than for the probe treatment despite equimolar concentrations being used.

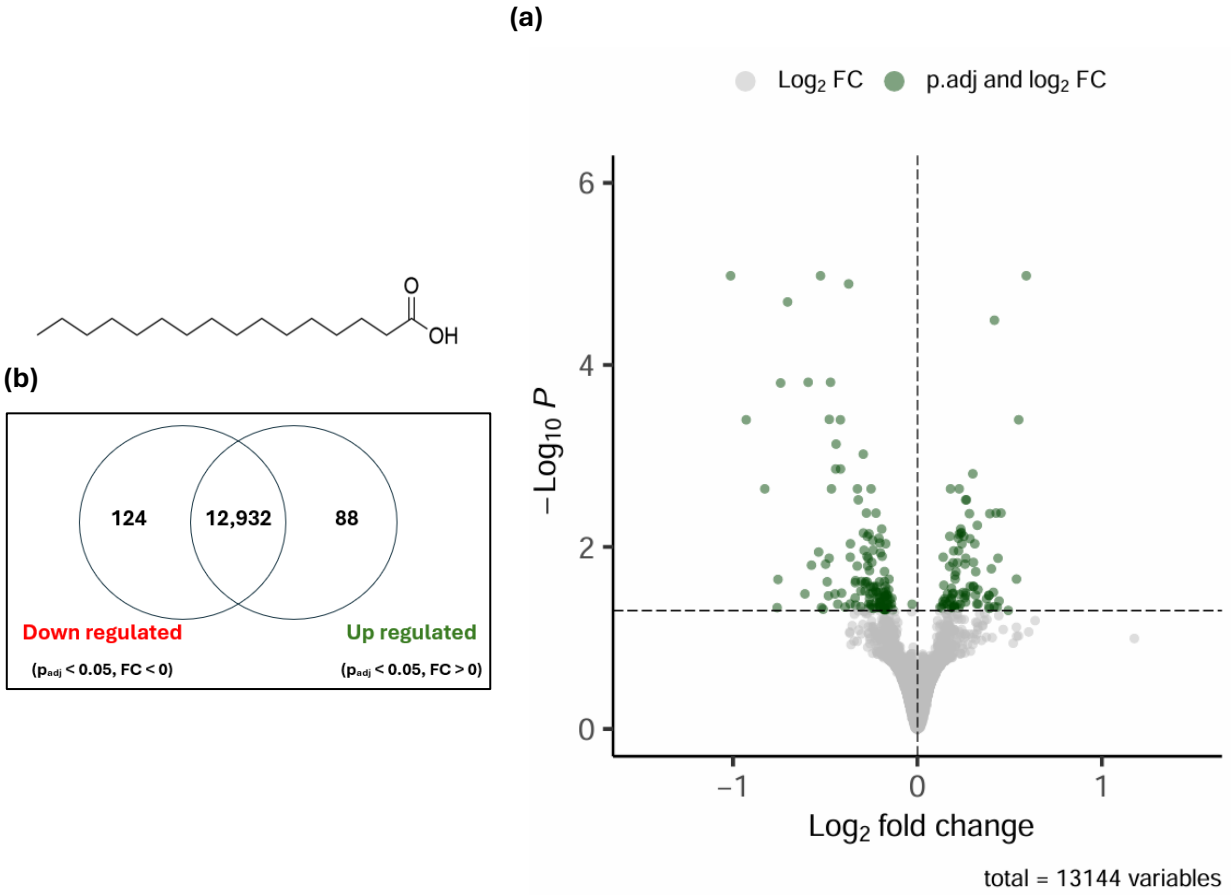

Figure 6.43: Transcriptomic analysis results of hiPSC-CMs treated with 100 µM palmitate. (a) Volcano plot of gene expression changes by 100 µM palmitate (16 h) compared with control cell (16 h); (b) Venn diagram genes upregulated and downregulated by palmitate.

6.5.6.1 Analysis of the upregulated genes following palmitate treatment

As large-scale changes occurred in the transcriptome a pathway approach was adopted, again to reduce complexity and investigate the broader biological function changes following palmitate treatment. Metascape analysis highlighted the highest upregulated GO biological process from the DEGs was the 'developmental process' (Figure 6.44a). This GO term, according to the Gene Ontology database, has the specific outcome of enhancing the progression of an integrated living unit. Another upregulated GO process to note is the 'Metabolic processes' (Figure 6.44a). Pathways that were specifically upregulated by palmitate included: 'Mitochondrial protein degradation', 'Adipogenesis', 'Tissue remodelling, 'Regulation of DNA-templated transcription elongation' and 'Transport of small molecules' (Figure 6.44b). Transcription factor mining revealed that several of the genes upregulated by palmitate were regulated by transcription factors of interest (6.45a).

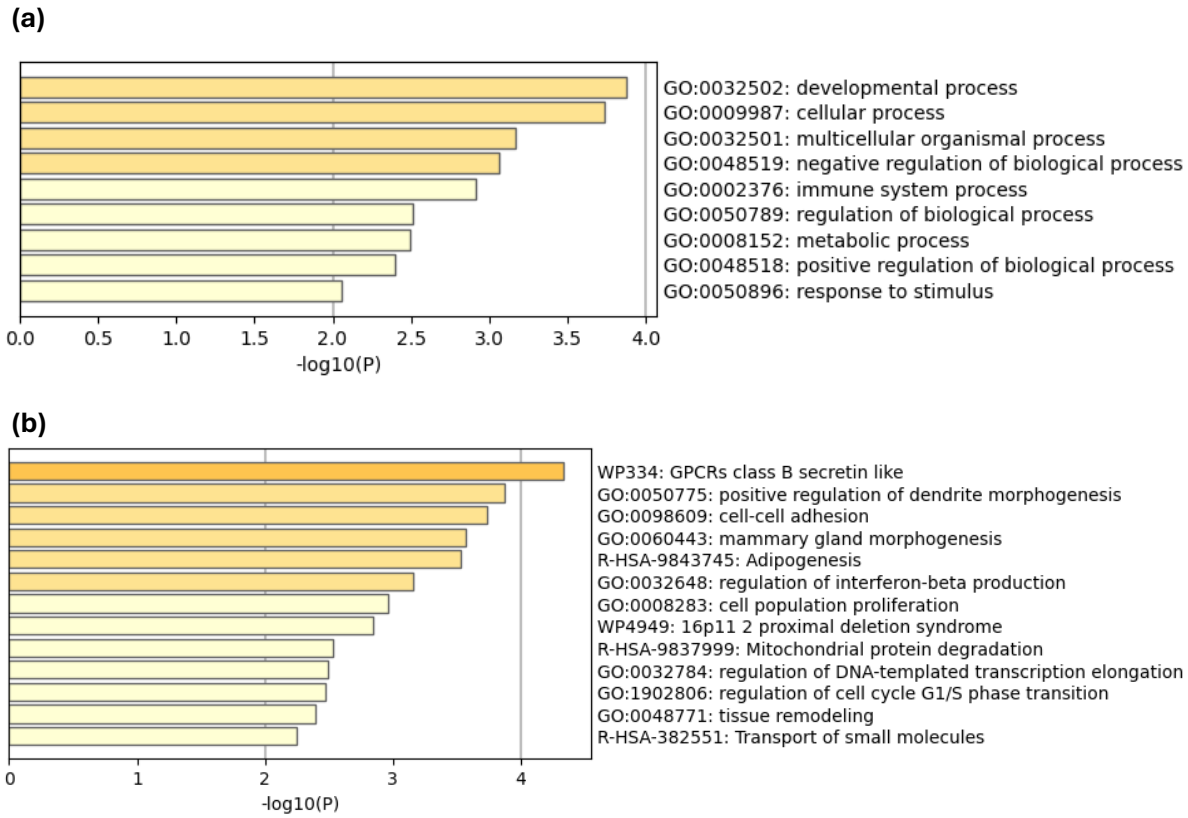

Figure 6.44: Metascape analysis of the upregulated genes with 100 µM palmitate. (a) The top-level Gene Ontology (GO) biological processes are coloured by p-values; and (b) Enriched terms across the input gene lists (proteins with an NSAF > 0) are coloured by p-values.

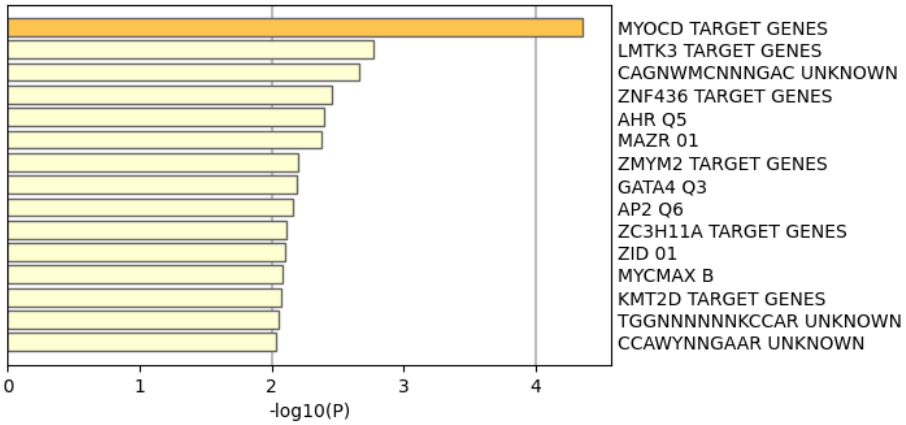

Figure 6.36: Transcription factors regulating proteins upregulated by 100 µM palmitic acid.

To gain further insight into affected upregulated biological pathways, a KEGG pathway analysis was also performed on the DEGs (Figures 6.46 & 6.47). The analysis revealed significant upregulation in several key pathways. Notably, some upregulated pathways of interest were: 'Diabetic cardiomyopathy', 'Protein processing in the endoplasmic reticulum'; 'Oxidative phosphorylation'; and 'Fatty acid metabolism'.

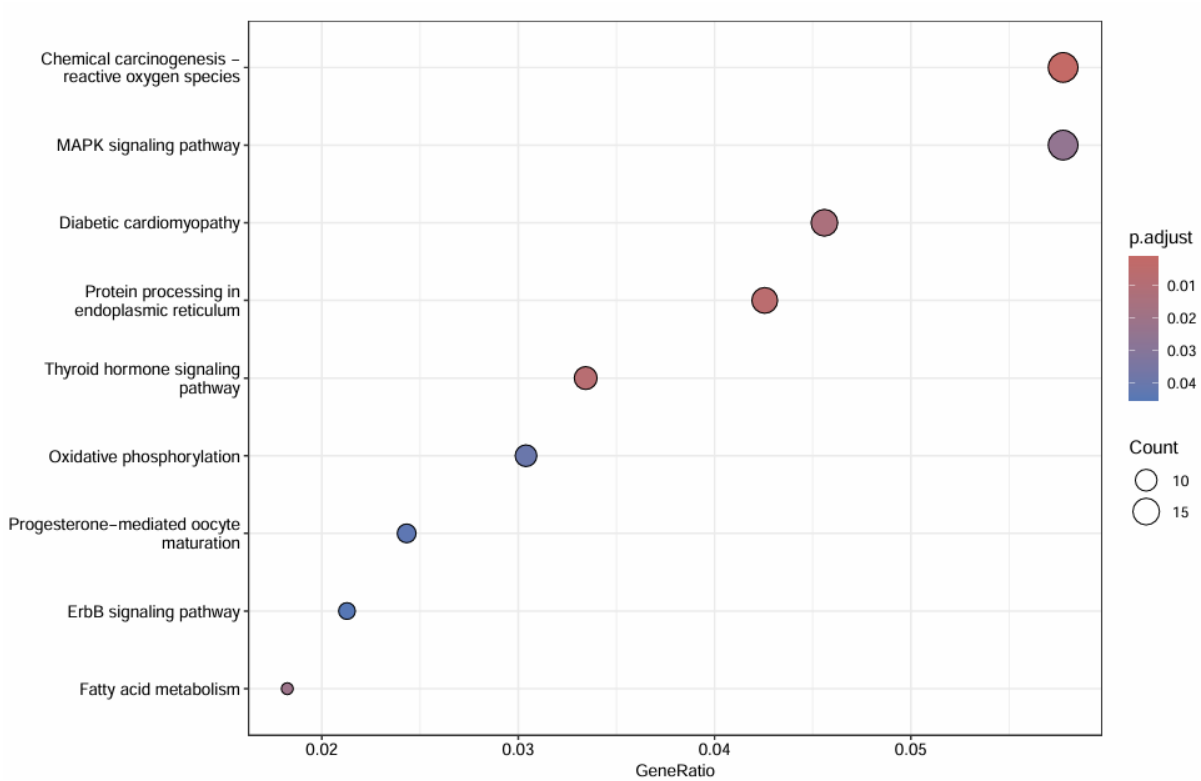

Figure 6.46: KEGG pathway analysis of up-regulated genes following 100 µM palmitate treatment: Dot plot representing up-regulated KEGG pathways.

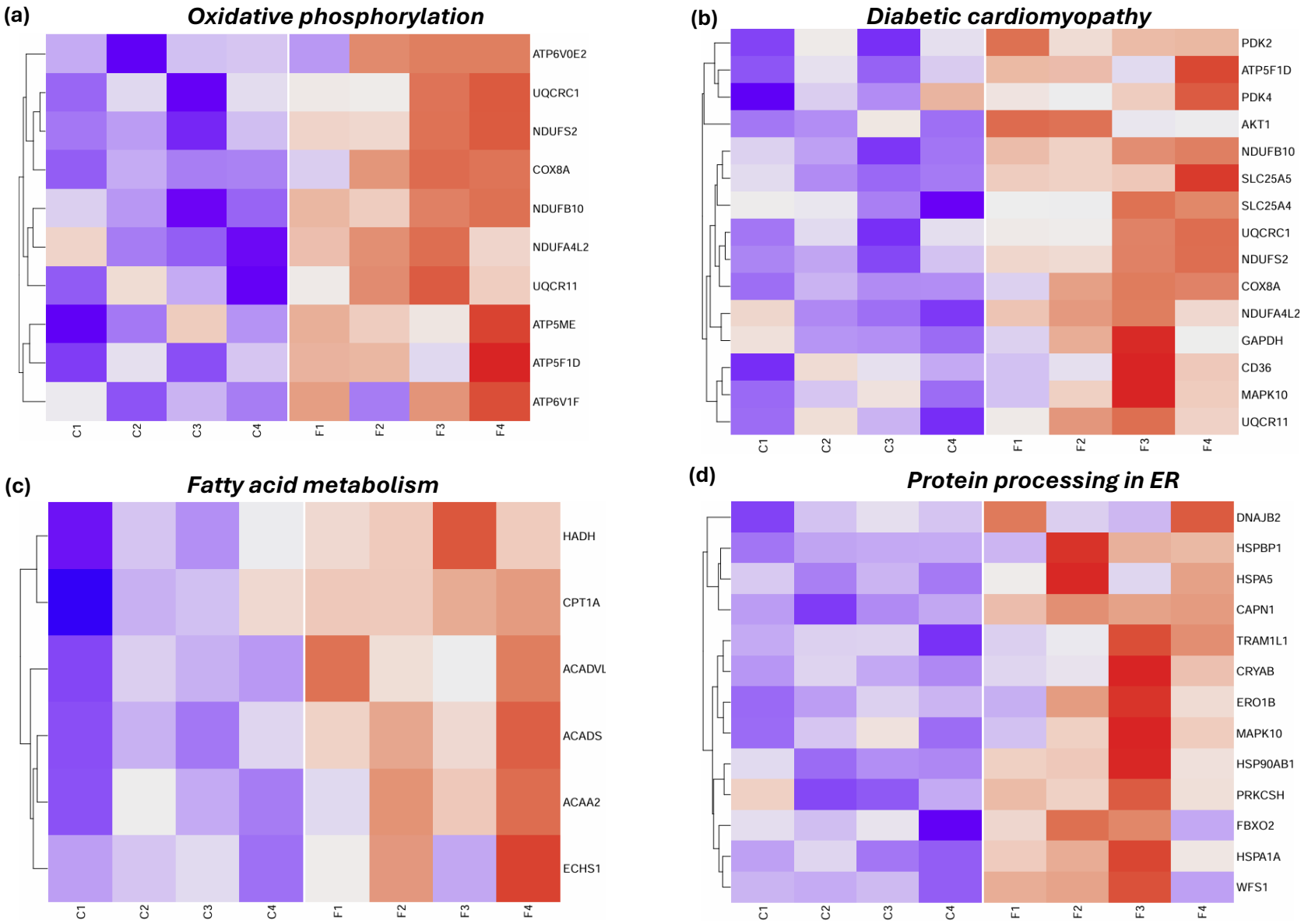

Figure 6.47: KEGG pathway analysis of up-regulated genes following 100 µM palmitate treatment: Heatmaps of genes involved in: (a) Oxidative phosphorylation; (b) Diabetic cardiomyopathy; (c) Fatty acid metabolism and (d) Protein processing in the ER.

6.5.6.2 Analysis of the downregulated genes following palmitate treatment

Metascape analysis of the 124 downregulated genes highlighted the highest downregulated GO parent biological process from the DEGs was the 'Response to stimulus' (Figure 6.48a). Other GO biological parent processes that were of interest were: ' Localisation'; and 'Metabolic process'. More specific annotation of the downregulated pathways revealed 'Response to growth factor' as the most significant pathway (Figure 6.48b). Other processes of interest were 'Muscle tissue morphogenesis'; 'Extracellular matrix organisation'; 'NABA matrisome associated'; 'MAPK signalling pathway'; and 'Regulation of angiogenesis' indicating palmitate may be affecting ECM and angiogenesis. Transcription factor mining revealed that several of the genes downregulated by palmitate were regulated by transcription factors of interest (Figure 6.48c). TP53 (Tumour protein 53) is a tumour suppressor and regulated the cell cycle, promotes DNA repair and helps maintain genome stability.[236] MYC is involved in cell proliferation, growth, apoptosis and metabolism.[237] ATF4 is a TF that responds to cellular stress, apoptosis and metabolism.[238] RELA and NFKB1, which also regulate genes downregulated by probe **1**, are involved in inflammation.[230,235] Using DisGeNet, the relationship between the downregulated genes and diseases was mapped, with 'Acute myocardial infarction', and 'Estrogen receptor-positive breast cancer' significantly enriched following palmitate treatment (Figure 6.48d).

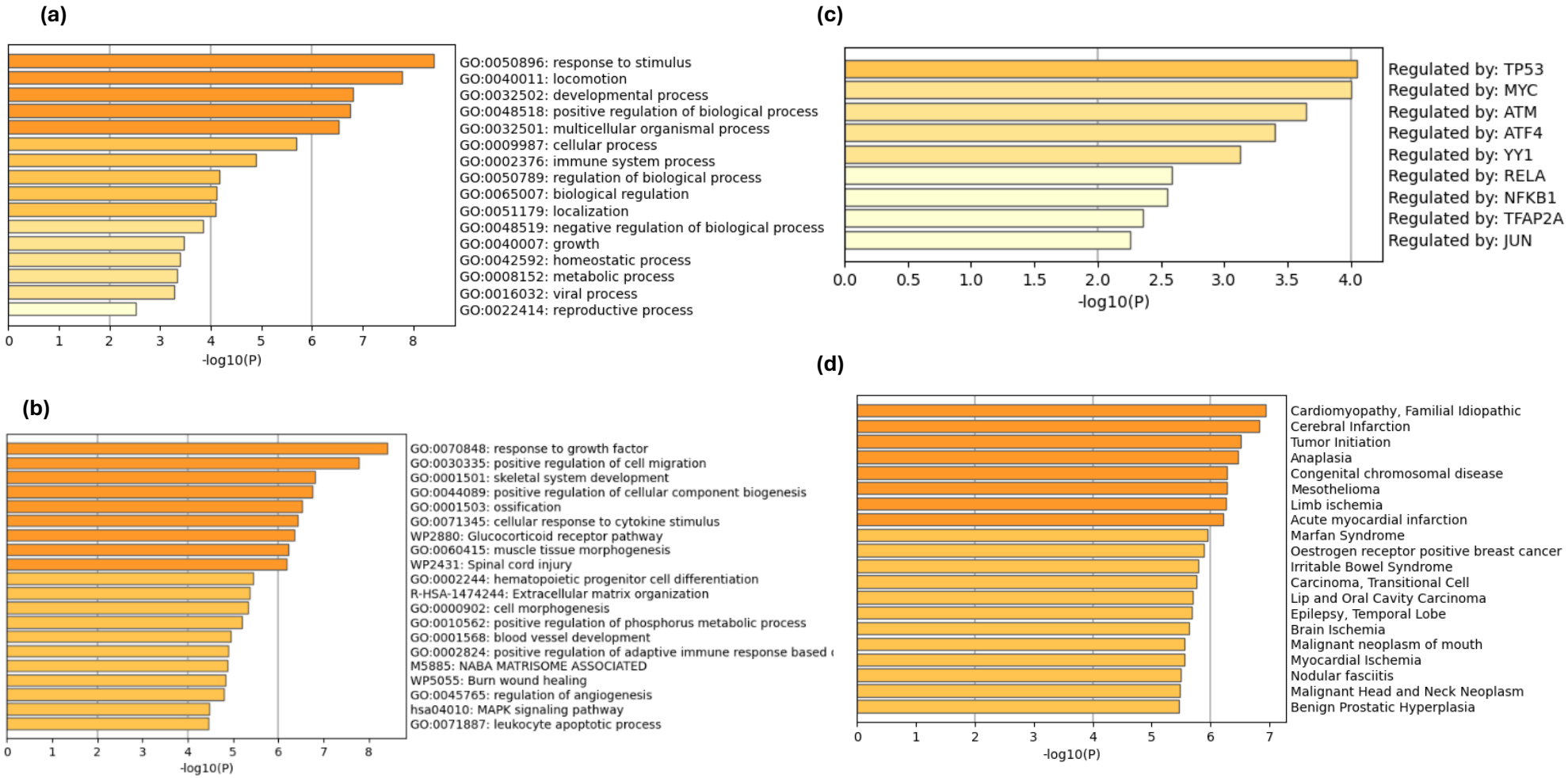

Figure 6.48: Metascape analysis of the downregulated genes with 100 µM palmitate. (a) The top-level Gene Ontology (GO) biological processes are coloured by p-values; (b) Enriched terms across the input gene lists (proteins with an NSAF > 0) are coloured by p-values; (c) Transcription factors regulating proteins downregulated by palmitate; (d) Summary of enrichment analysis in DisGeNET- showing enrichment of disease pathways.

KEGG pathway analysis revealed significant downregulation in several key pathways (Figures 6.49-51). Notably, some downregulated pathways of interest were: 'Regulation of actin cytoskeleton' and PI3k-Akt signalling pathway'.

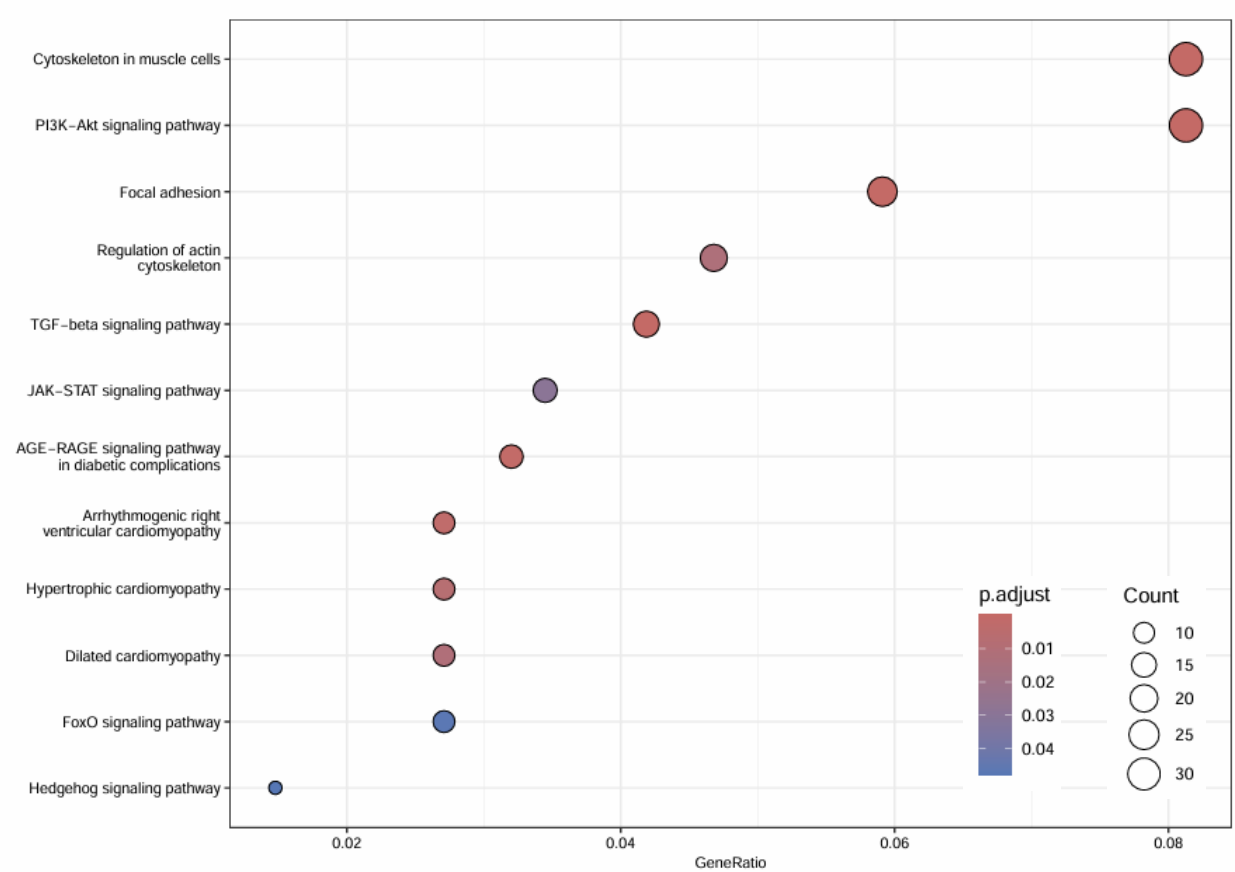

Figure 6.49: KEGG pathway analysis of down-regulated genes following 100 µM palmitate treatment: Dot plot representing down-regulated KEGG pathways.

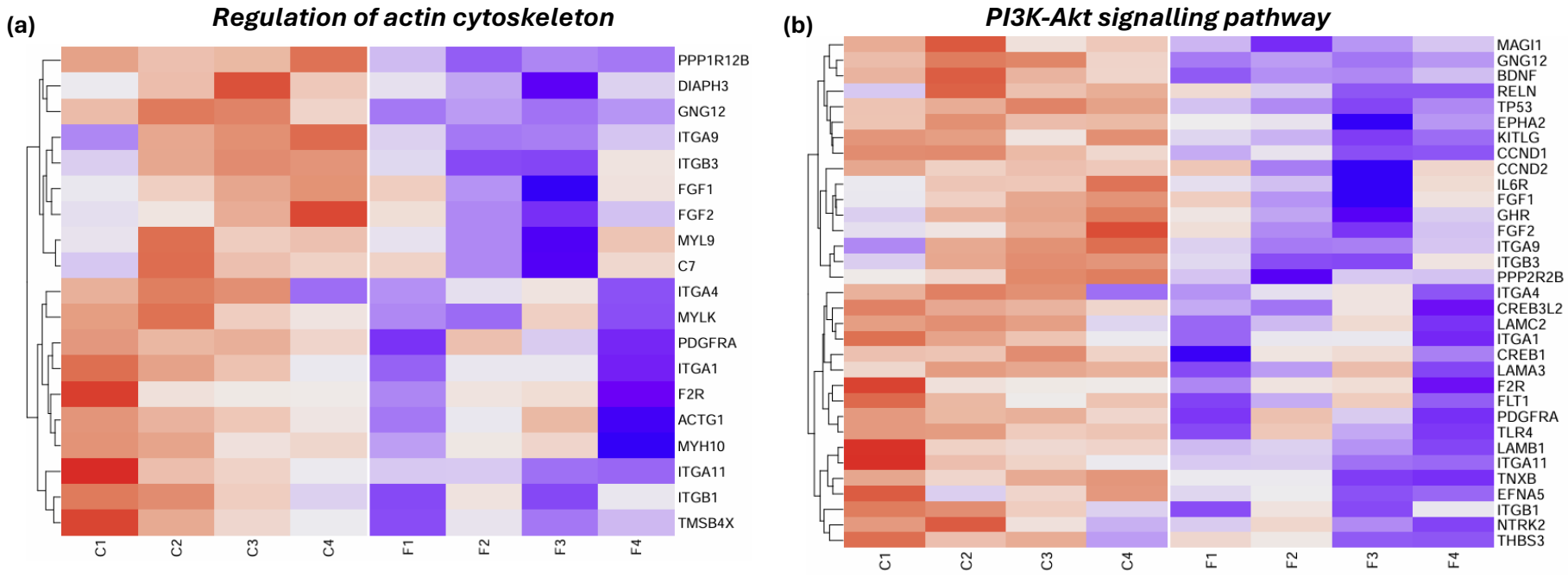

Figure 6.50: KEGG pathway analysis of down-regulated genes following 100 µM palmitate treatment: Heatmaps of genes involved in: (a) Regulation of actin cytoskeleton; (b) PI3K-Akt signalling. C = Control, F = 100 µM palmitate.

6.5.6.3 GSEA analysis following palmitate treatment

Gene set enrichment analysis (GSEA) was performed as an unbiased approach to identify significant changes in pathway activities after palmitate treatment (Figure 6.52). This analysis revealed a notable upregulation in the 'Oxidative phosphorylation', 'Fatty acid beta-oxidation', Glycolysis and gluconeogenesis' and 'Fatty acid metabolism'. This indicates that palmitate treatment was causing an upregulation effect on metabolism in the cell. This upregulation of metabolic pathways did not occur following probe **1** treatment. There was also downregulation of several pathways of interest: 'Regulation of actin cytoskeleton'; 'Dilated cardiomyopathy'; 'MTORC1 signalling'; 'Androgen response'; 'Androgen receptor signalling'; 'Estrogen response early'; 'Hypothesised pathways in pathogenesis of cardiovascular disease' and 'VEGFA/VEGFR2 signalling'. These suggest the downregulation of some contraction, signalling and hormonal pathways in response to palmitate treatment. Several of the downregulated pathways were also downregulated in probe **1** treated cells: 'Regulation of actin cytoskeleton'; 'Dilated cardiomyopathy'; 'MTORC1 signalling'; 'Estrogen response early'; 'Hypothesised pathways in pathogenesis of cardiovascular disease' and 'VEGFA/VEGFR2 signalling'.

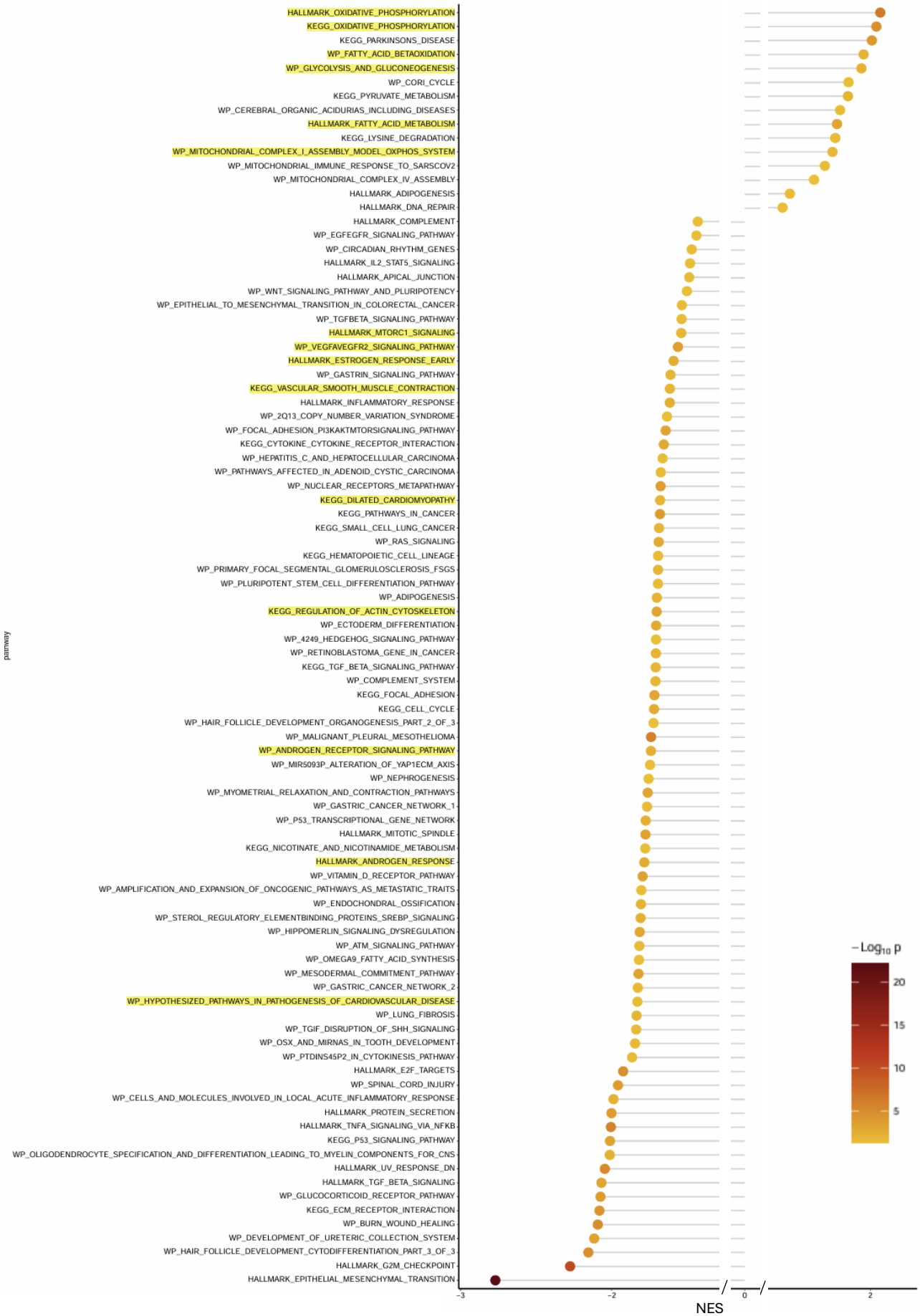

Figure 6.52: Gene Set Enrichment Analysis (GSEA) of transcriptomics results for 100 µM palmitate. Pathways of interest are highlighted.

6.5.7 Comparison of the pathway changes following probe 1 or palmitate treatment

Comparison of both palmitic acid and probe **1** up- and down-regulated genes highlighted some overlap between the two treatments (Figure 6.53). Both treatments had 44 upregulated genes and 91 downregulated genes in common. Probe **1** had a much greater change in gene expression compared with palmitic acid; this could be due to the differences in the chemical structure of the two molecules or that probe **1** is not metabolised making it likely that the concentration of probe **1** does not decrease over the 16 h incubation.

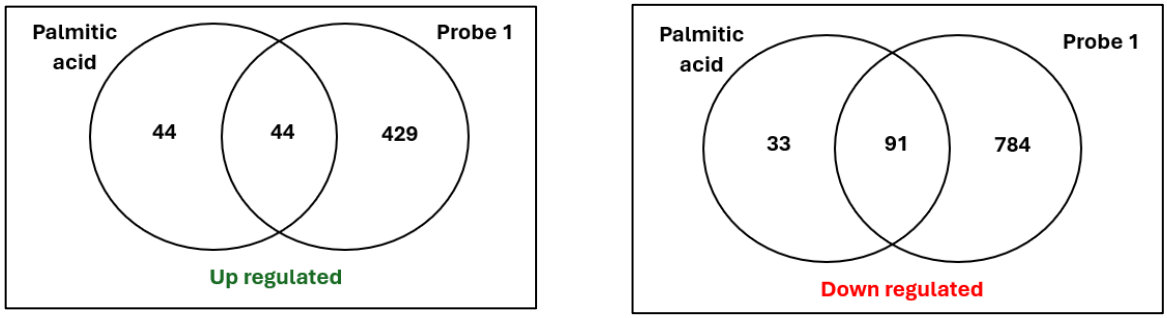

Figure 6.53: Venn diagrams comparing up- and down-regulated genes in probe 1 and palmitate treated cells.

6.5.7.1 Analysis of the upregulated pathways

Following the comparison of the effects of both probe **1** and palmitate treatment, upregulated significant genes were analysed using Metascape (Figure 6.54). It was observed that both treatments resulted in upregulation of 'Regulation of plasma membrane bounded cell projection organisation'; and 'Regulation of mitotic cell cycle'. Palmitate treatment-only (left column) resulted in the upregulation of 'Adipogenesis', 'Negative regulation of canonical NF-κB signal transduction' and 'GPCRs class B secretin like'. Probe **1** treatment-only (right column) resulted in upregulation of 'Insulin signalling', 'Protein localisation to cell junction', 'heart development', Integration of energy metabolism', 'Regulation of small GTPase mediated signal transduction' and 'Chromatin organisation'.

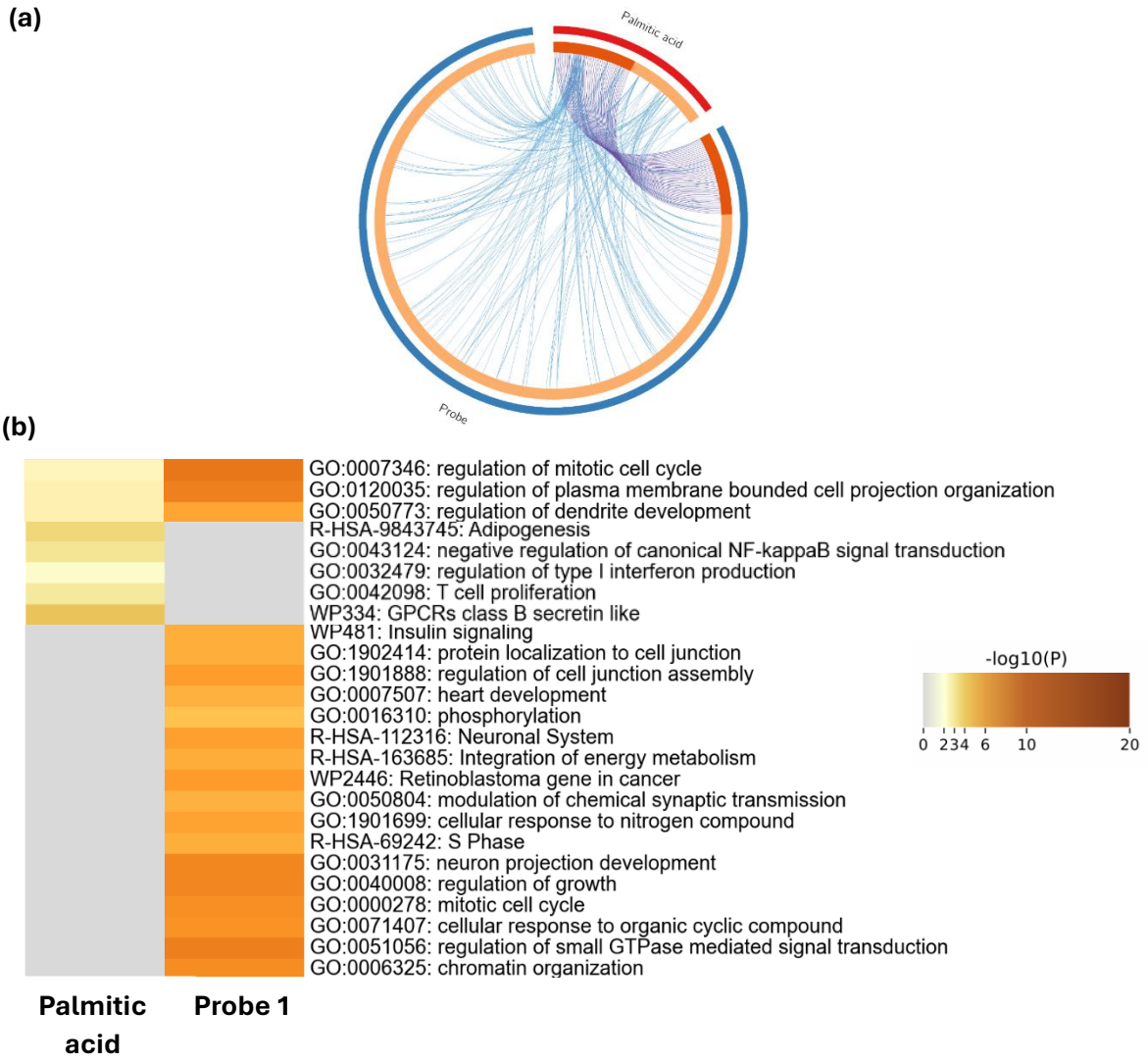

Figure 6.54: Metascape analysis to compare the upregulated genes in the 100 µM probe 1 and 100 µM palmitate treated cells. (a) Overlap between genes lists (Palmitate = blue, Probe **1** = red): where purple curves link identical genes and the light blue curves link genes that belong to the same enriched ontology term; (b) Heatmap of enriched terms across gene lists, coloured by p-values.

6.5.7.2 Analysis of the downregulated pathways

Down-regulation of genes appeared to occur to a greater extent and more pathways were shared between treatments. (Figure 6.55): ‘Extracellular matrix organisation’; ‘Regulation of Insulin-like growth factor transport and uptake’; ‘Response to nutrients’; ‘Response to hormone’; ‘Signalling by Rho GTPases, Miro GTPases and RhoBTB3’; ‘Positive regulation of canonical NF-κB signal transduction’; and ‘Cytoskeleton in muscle cells’. This overlap highlighted that both palmitate and probe **1** are causing a shared downregulation in pathways involved in cytoskeletal organisation, responses to both nutrients and hormones and several signal transduction pathways.

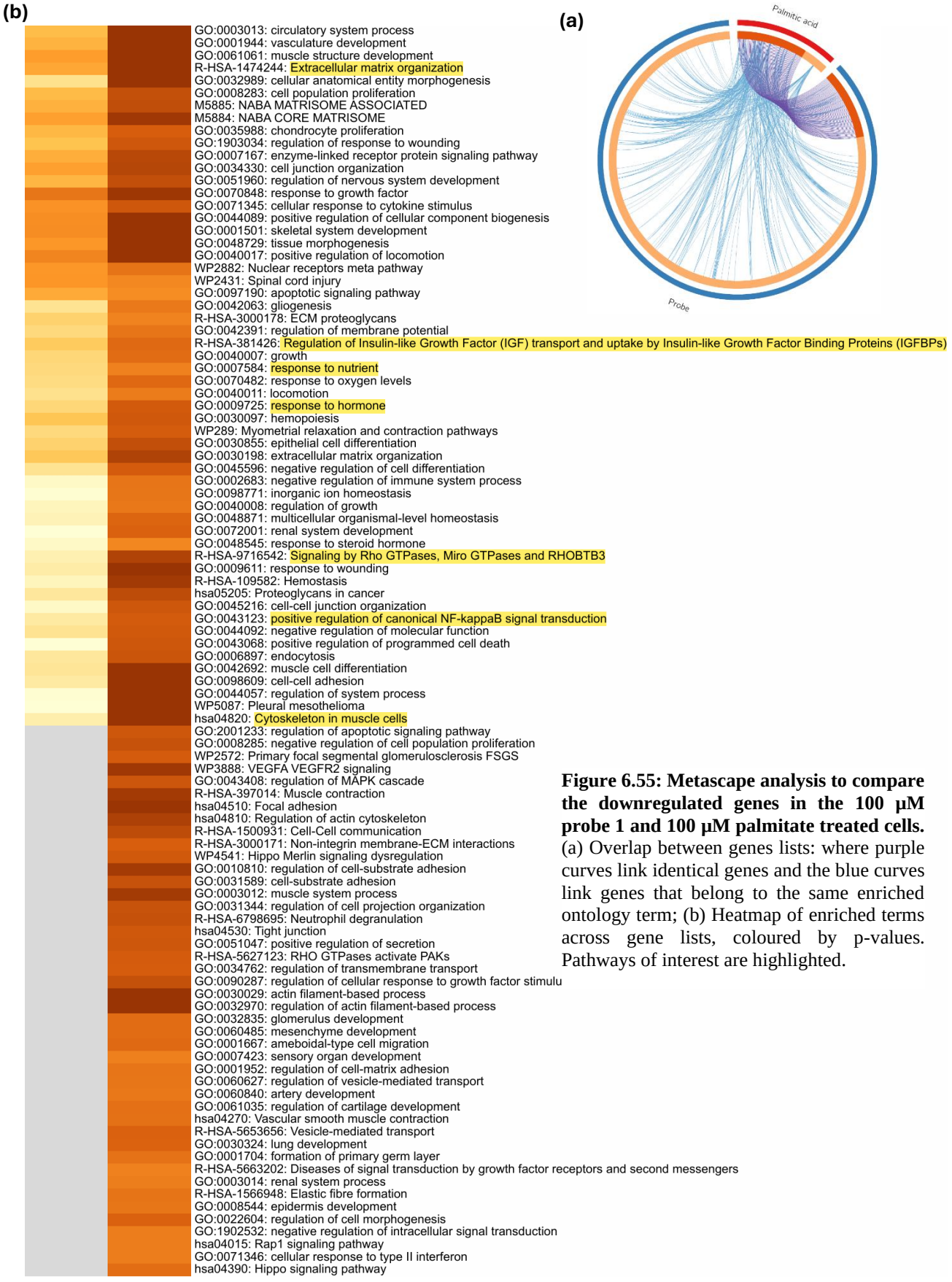

Figure 6.55: Metascape analysis to compare the downregulated genes in the 100 µM probe 1 and 100 µM palmitate treated cells. (a) Overlap between genes lists: where purple curves link identical genes and the blue curves link genes that belong to the same enriched ontology term; (b) Heatmap of enriched terms across gene lists, coloured by p-values. Pathways of interest are highlighted.

Comparison of both the palmitic acid and probe **1** treated cells allowed for the identification of biological pathways that are regulated by both molecules. This confirms that probe **1** is having an effect on similar pathways to palmitic acid, but also highlights that probe **1** is causing changes in different pathways too.

6.5.8 Validation of transcriptomic targets in hiPSC cardiomyocytes

To confirm that the targets identified using transcriptomics were legitimate probe **1** and palmitate targets, qPCR analysis was performed to validate the genes (Figure 6.56). *HRPT1* was used as the housekeeping gene and showed no differences between groups.

Upregulated genes were validated first (Figure 6.56b). Sodium voltage-gated channel alpha subunit 1 (*SCN1A*) was shown to be significantly upregulated (100% increase) in the probe **1** treated cells, with no statistical change in the palmitic acid treated cells. The second gene was cadherin-related family member 5 (*CDHR5*), but unfortunately two primers were designed for this gene, but neither worked during the primer validation step.

Numerous downregulated genes were validated (Figure 6.56b): ankyrin repeat domain 1 (*ANKRD1*), succinate receptor 1 (*SUCNR1*), natriuretic peptide B (*NPPB*), sulfotransferase family 1E member 1 (*SULT1E1*) and insulin-like growth factor 1 (*IGF1*). Of these *ANKRD1, NPPB, SULT1E1* and *IGF1* were shown to be significantly downregulated in both treatment groups. *ANKRD1*, encodes for a protein that regulates muscle function and cardiovascular health,[239] was decreased by 64% with probe **1** treatment and 40% decreased following palmitate treatment. *NPPB,* encodes for a cardiac hormone,[240] decreased by 71% with probe **1** and 37% with palmitate treatment. *SULT1E1,* involved in the metabolism of estrogens and related compounds (e.g. estradiol or estrone),[241] had a 60% decrease in expression with probe **1** and a 55% decrease with palmitate. Lastly, *IGF1,* encodes for a hormone and growth factor,[242,243] was down 49% and 32%, after probe **1** and palmitate treatment, respectively. *SUCNR1* was only significantly downregulated (40% decrease) in probe **1**-treated cells. For all gene targets changing in probe **1** and palmitic acid treated cells, the degree of change was greater in the probe **1** group.

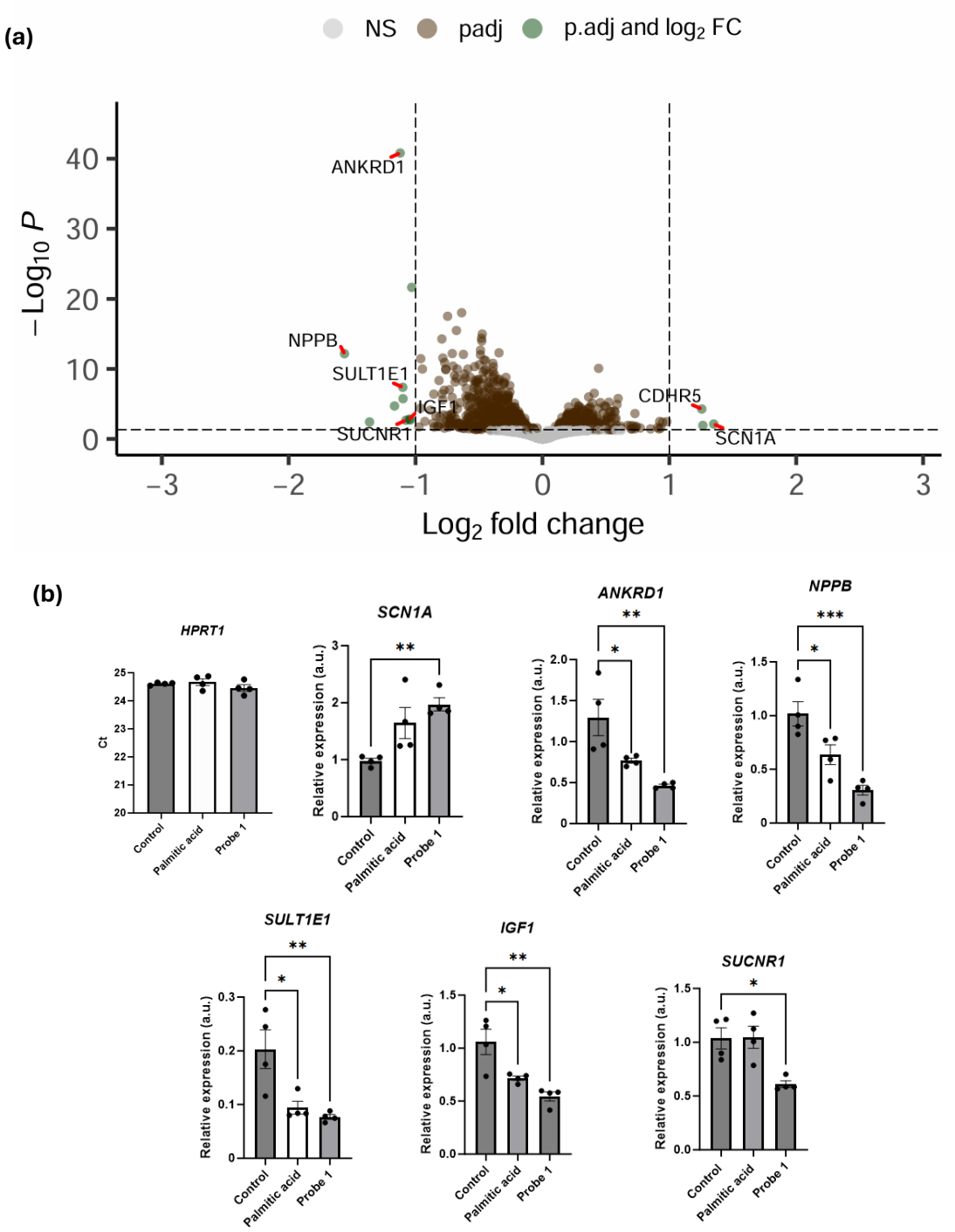

Figure 6.56: Validation of transcriptomic results for hiPSC-CM cells treated with 100 µM probe 1 by qPCR: (a) Volcano plot of transcriptomic analysis of probe **1**. (b) qPCR results for *ANKRD1*, *SUCNR1* and *NPPB* using *HRPT* as a housekeeping gene (n=4). Data represents the mean ± SEM and statistical significance was assessed by one-way ANOVA followed by Dunnett's test with *, **, *** $p < 0.05, 0.01, 0.001$, compared with control *MDA-MB-231* cells (n=4)

6.6 Discussion

6.6.1 Protein labelling with probe 1 in hiPSC-CMs

Using probe **1** in hiPSC-CMs required optimisation on the concentration for protein labelling. As the hiPSC-CMs are matured using 80 μM of FFA, it was hypothesised that a concentration of probe **1** higher than that of maturation was needed for labelling under these FA-abundant conditions. Using 100 μM probe **1** resulted in protein labelling as shown by in-gel fluorescence. There was no evidence of cytotoxicity in the hiPSC-CMs following 16 h treatment with 100 μM probe **1**. However, 30 μM probe **1** treatment was also performed and would allow for the direct comparison between the *MDA-MB*-231 cells (*Chapter* 5)and hiPSC-CMs.

6.6.2 Protein target identification with probe 1

Proteomic analysis of the various treatments allowed for the identification of protein and pathway targets of probe **1**. Comparison of the 30 μM probe **1** (30+UV) and 100 μM probe **1** (100+UV) groups highlighted the difference in the levels of protein capture and specificity at different concentrations of probe **1**. In the 30+UV cells, 545 proteins were enriched, compared to 342 proteins in the 100+UV cells. This could be due to higher protein labelling efficiency in the 30+UV group but could also be due to increased non-specific binding on the neutravidin beads at the lower probe **1** concentration. The 30+UV group interacted with cytoskeletal, RNA metabolism, chromatin organisation, VEGFA signalling and RHO GTPase signalling pathways. The 100+UV group interacted with more metabolic (e.g. glycolysis and gluconeogenesis) and mitochondrial pathways but also interacted with chromatin and cytoskeletal pathways which supports the hypothesis that these cells would need more probe **1** as they are more metabolically conditioned. In both groups proteins involved in cardiomyopathies (e.g. diabetic cardiomyopathy (DbCM)) were enriched. Palmitate-induced ER stress has been shown to be involved in DbCM, as it leads to an accumulation of unfolded proteins (unfolded protein response (UPR)).[244,245] The 100+UV group also showed interactions with UPR pathways. The 100+UV group also enriched proteins involved in mitochondrial diseases. It is known that palmitate can impair mitochondrial function by disrupting energy production, increasing oxidative stress and compromising mitochondrial membrane

integrity.[246,247]. Confocal microscopy demonstrated that probe **1** was inducing both mitochondrial biogenesis and fragmentation, and was also increasing the protein levels of subunits of complexes I, II and IV of the ETC. These results suggest that probe **1** is causing an increase in mitochondrial biogenesis, but the new networks are more fragmented. Alongside this, the interaction of probe **1** with proteins linked to various mitochondrial processes highlights its significant role in modulating mitochondrial function and overall cellular metabolism. Specifically, probe **1** interacted with proteins involved in mitochondrial protein degradation, mitochondrial genome maintenance, mitochondrial organisation, and the transcriptional activation of mitochondrial biogenesis. These processes are essential for maintaining mitochondrial integrity and function, suggesting that probe **1** may have an influence on mitochondrial dynamics and bioenergetics. Proteins such as ENO2 and PLIN3, which are involved in energy production and lipid metabolism, exemplify how probe **1** may influence the regulation of metabolic substrates and the coordination of energy utilisation. The upregulation of these genes suggests that probe **1** not only affects mitochondrial health but also contributes to the broader integration of metabolic processes within the cell, with potential implications for metabolic diseases such as diabetes and mitochondrial disorders.

6.6.3 Gene expression changes following treatment of hiPSC-CMs with probe 1

Gene expression analysis allowed for the direct comparison of gene levels following probe **1** (100 μM, 16 h) or palmitate treatment (100 μM, 16 h). This analysis highlighted biological pathways that were affected by both treatments. Both probe **1** and palmitate exhibited common regulatory effects, particularly in their ability to influence key cellular pathways. Both upregulated processes related to energy metabolism and insulin signalling, with probe **1** enhancing chromatin organization and cell cycle progression, thereby promoting cellular functions and growth. Similarly, both compounds downregulated pathways associated with muscle function, actin, and cardiomyopathies, as well as the TGFβ pathway, which could have implications for muscle integrity and fibrotic responses. However, there were notable divergences in their regulatory profiles. Probe **1** specifically targeted pathways involved in chromatin organisation and the cell cycle, whereas palmitate uniquely upregulated mitochondrial degradation, transcription, fatty acid metabolism, oxidative phosphorylation, and diabetic cardiomyopathy, indicating an increased metabolic stress and

disrupted cardiac function. Palmitate also exhibited distinct downregulation of extracellular matrix (ECM) pathways, MAPK signalling, FOXO signalling, and additional metabolic and stress responses, further highlighting its role in altering muscle function and overall cardiac health.[244,248–250] While on a gene level probe **1** supports key cellular functions and mitigates certain stress-related pathways, palmitate drives mitochondrial and metabolic changes, with potentially significant implications for cardiac health and stress responses. These differences between compounds could be due to several reasons. The chemical structure of probe **1** was designed as close to the structure of palmitate as possible, however, the diazirine group introduces areas of electron density that are not present in the hydrophobic tail of palmitate (*Chapter 7*). This could be causing non-specific interactions of probe **1** with some biological pathways. These chemical differences could also affect the outcome of the interactions and whether they are inhibitory or stimulatory. Probe **1** was also shown not to be metabolised by isolated mitochondria (*Chapter 4*), and so, therefore, the initial concentration of probe **1** may not be changing compared with palmitate, a metabolic substrate. This could lead to differences in the concentrations of the compounds and therefore, the increased pathways affected by probe **1**, compared with palmitate.

6.6.4 Novel mechanisms of lipid-induced cardiac dysfunction: downregulation of actin cytoskeletal organisation and hormone signalling by probe 1 and palmitate

The downregulation of actin cytoskeletal organisation and both estrogen and androgen responses by probe **1** and palmitate presents a novel and intriguing finding in the context of cardiac biology. The actin cytoskeleton is essential in the heart for maintaining the structural integrity of cardiomyocytes, enabling proper contraction, and facilitating intracellular signalling pathways. Disruption of cytoskeletal organisation in the heart can impair these pathways and overall cardiac function, potentially contributing to conditions such as heart failure and cardiomyopathies. What makes this finding particularly interesting is the intersection of cytoskeletal dynamics and hormone signalling in the heart. Estrogen and androgen pathways have been shown to have protective and regulatory roles in cardiac function. Estrogen, for instance, has been shown to provide cardioprotective effects, influencing heart muscle repair, reducing inflammation, and modulating lipid metabolism.[251,252] Androgens, similarly, affect cardiovascular physiology, particularly influencing cardiac hypertrophy

and the regulation of myocardial contractility.[253,254] The suppression of both hormone pathways by palmitate and probe **1** suggests that lipids in the heart could directly interfere with these protective hormone signals. This dual downregulation could represent a novel mechanism by which high levels of FAs, such as palmitate, contribute to cardiac dysfunction. In metabolic disorders like diabetes and obesity, elevated FFAs are often observed, which can accumulate in the heart and lead to lipotoxicity. The downregulation of actin cytoskeletal organisation combined with hormone signalling suppression might impair cardiomyocyte contractility and exacerbate this metabolic stress on the heart. Moreover, the hormonal aspect is particularly noteworthy given the gender differences observed in cardiovascular disease and the implications for sex differences in fat metabolism and lipotoxic cardiac diseases. Women generally tend to be more protected from lipotoxicity than men, as estrogen promotes healthier fat distribution and enhances fat oxidation, reducing the risk of lipid accumulation in organs. Estrogen has also been shown to play a protective role in women, helping to regulate vascular function, reduce inflammation, and protect against atherosclerosis.[251,252] However, post-menopause, as estrogen decreases, this protection also decreases, leading to an increased risk of lipotoxic effects and heart disease. Conversely, men tend to develop heart disease at an earlier age, as they are more prone to visceral fat accumulation, which is linked to higher lipotoxicity risk, increased insulin resistance, and cardiovascular disease.[253,254] These sex-based variations in lipid metabolism and storage underscore the importance of considering sex differences in the development and treatment of metabolic diseases associated with lipotoxicity, such as type 2 diabetes, non-alcoholic fatty liver disease (NAFLD), and cardiovascular disease.

Altogether, taking both the protein interactions and gene expression changes, probe **1** has demonstrated that palmitate plays a multifaceted role in mature hiPSC-CMs, influencing a wide range of biological pathways through both direct interactions and induced changes in gene expression. Probe **1** was involved in key cellular functions, including metabolism, contractility, chromatin organization, protein trafficking, and various signalling pathways. Additionally, it interacted with pathways related to cardiomyopathy, mitochondrial disease, and sex hormone signalling, highlighting its broad impact on cellular processes in these cardiomyocytes.

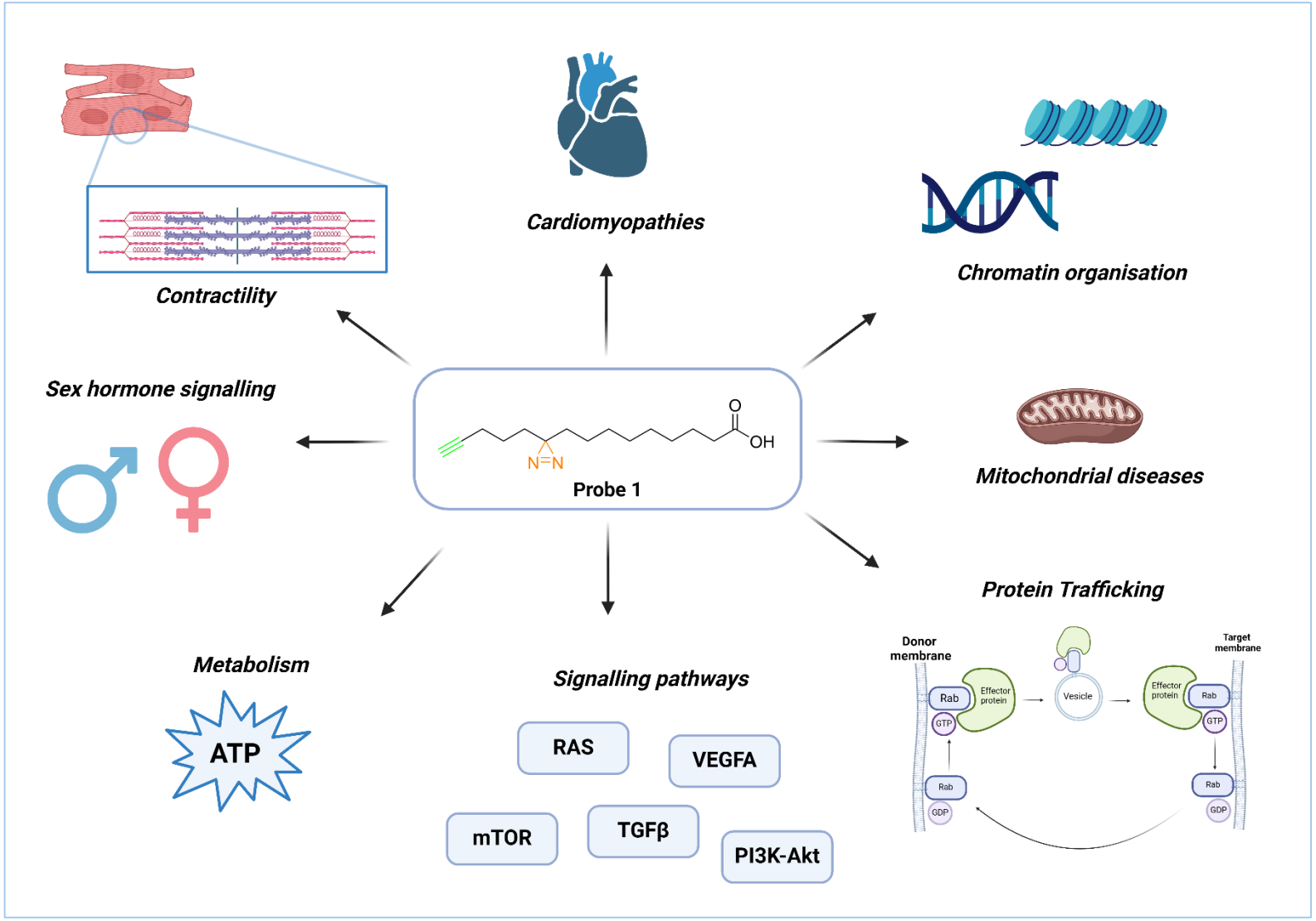

Figure 6.57: Summary of the pathways that probe 1 interacts with in hiPSC-CMs

Chapter 7

Optimisation and development of further palmitate and palmitate metabolite probes

7.1 Abstract

Photocatalytic labelling is a more recent advancement in the area of proximity labelling and offers advantages over other techniques, such as PAL. This new technique allows for increased labelling (a catalytic mechanism) of low-abundance proteins and labelling of protein complexes (microenvironment). The use of a photocatalytic palmitic acid probe would be beneficial to compare the lipid-protein labelling patterns of both PAL and photocatalytic labelling to investigate if the later can capture more protein indicators. However, since biological outcomes in cells may arise from palmitic acid or its metabolites, additional probes for palmitoyl-CoA (**2**) and palmitoyl-carnitine (**3**) were also developed. These probes are essential for dissecting the role of both the parent compound and its metabolites in cellular processes.

The proteomic interactions of the photocatalytic palmitic acid probe **4** were analysed in MDA-MB-231 cells, and it was found that interactor proteins were involved in various pathways, including the metabolism of RNA, chromatin remodelling, localisation within the membrane, actin cytoskeleton organisation and Rho, VEGF, RAC1 and TGF-β signalling. A comparison of the biological pathways enriched by both the PAL (probe **1**) and photocatalytic (probe **4**) palmitic acid probes found that there was an overlap between the two probes, but the photocatalytic probe interacted with more proteins and pathways due to its catalytic mechanism. *In-silico* alignment analyses of all synthesised probes with their respective parent molecules were performed, and the similarities and differences between the various probes were highlighted.

In conclusion, probe **4** labelled more proteins in *MDA-MB—231* cells, but had an increased cell toxicity compared with probe **1**. Probe **4** also interacted with an increased number of nuclear proteins and pathways. *In silico* alignment demonstrated that probes **1** and **3** were structurally similar to parent compounds, and probes **3** and **4** deviated somewhat.

7.2 Introduction

7.2.1 PAL versus photocatalytic labelling

PAL and photocatalytic labelling are two powerful techniques used to study biomolecular interactions *in vitro*, but they differ fundamentally in their mechanisms and applications (Figure 7.1). PAL relies on using a photoactivatable group, which forms a covalent bond with nearby proteins or biomolecules upon exposure to UV light. However, PAL is generally limited to stoichiometric protein labelling of interactions at or near the probe's binding site. Therefore, only direct interactors are captured. On the other hand, photocatalytic labelling employs light-activated catalysts, typically small-molecule photosensitisers, to induce broad labelling of proximal proteins without the need for a direct probe-target interaction (Figure 7.1). This results in a more unbiased and comprehensive mapping of the protein environment, capturing a wide array of proteins in the vicinity of the photocatalyst. Therefore, the generation and utilisation of a photocatalytic palmitic acid probe may identify more palmitate-protein interactions within the cell.

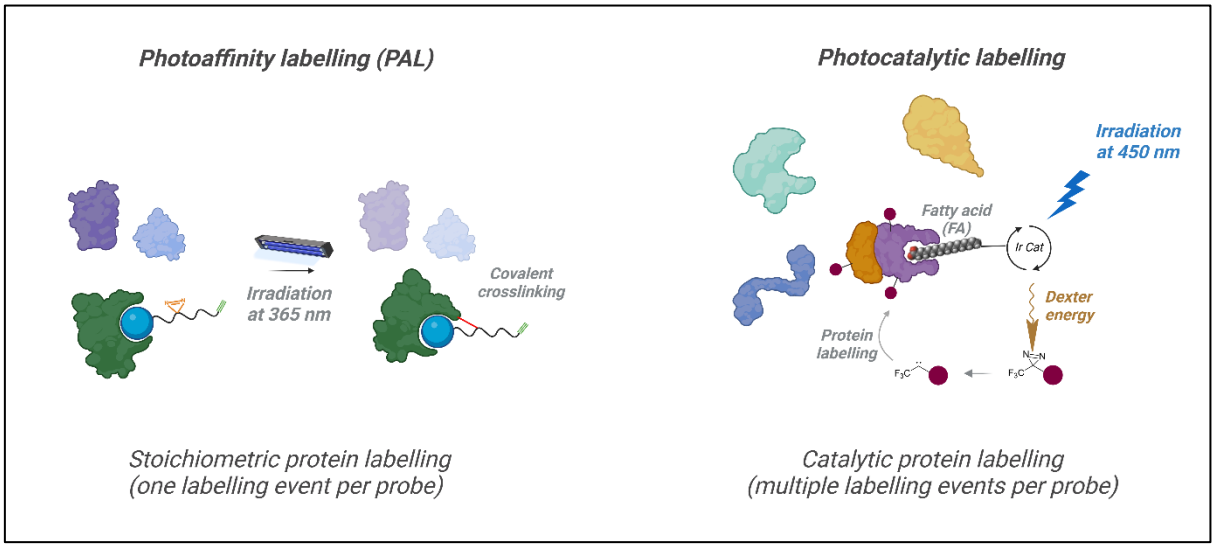

Figure 7.1: Mechanisms of protein labelling for both photoaffinity labelling (PAL) and photocatalytic labelling techniques.

7.2.2 Palmitic acid and metabolite probes

Following palmitic acid uptake in cells, it is metabolised via various palmitate intermediates, including palmitoyl-CoA and palmitoyl-carnitine. These intermediates can accumulate in the cell and have been implicated in contributing to lipotoxicity. We do not know whether it is palmitic acid itself or its downstream metabolites that are most relevant to regulating signalling processes. Therefore, various palmitic acid and metabolite probes were synthesised for *in vitro* testing, these included the palmitic acid photoaffinity probe **1** (used in *Chapter 4,5,& 6*), a photocatalytic palmitic acid probe **4**, a palmitoyl-CoA photoaffinity probe **2** and a palmitoyl-carnitine probe **3** (Figure 7.2). Testing of these probes in parallel would allow for a comprehensive analysis of the protein interactome of both palmitic acid and its key metabolites in cell lines of interest. Due to time constraints, probes **2** and **3** were synthesised but were not biologically tested.

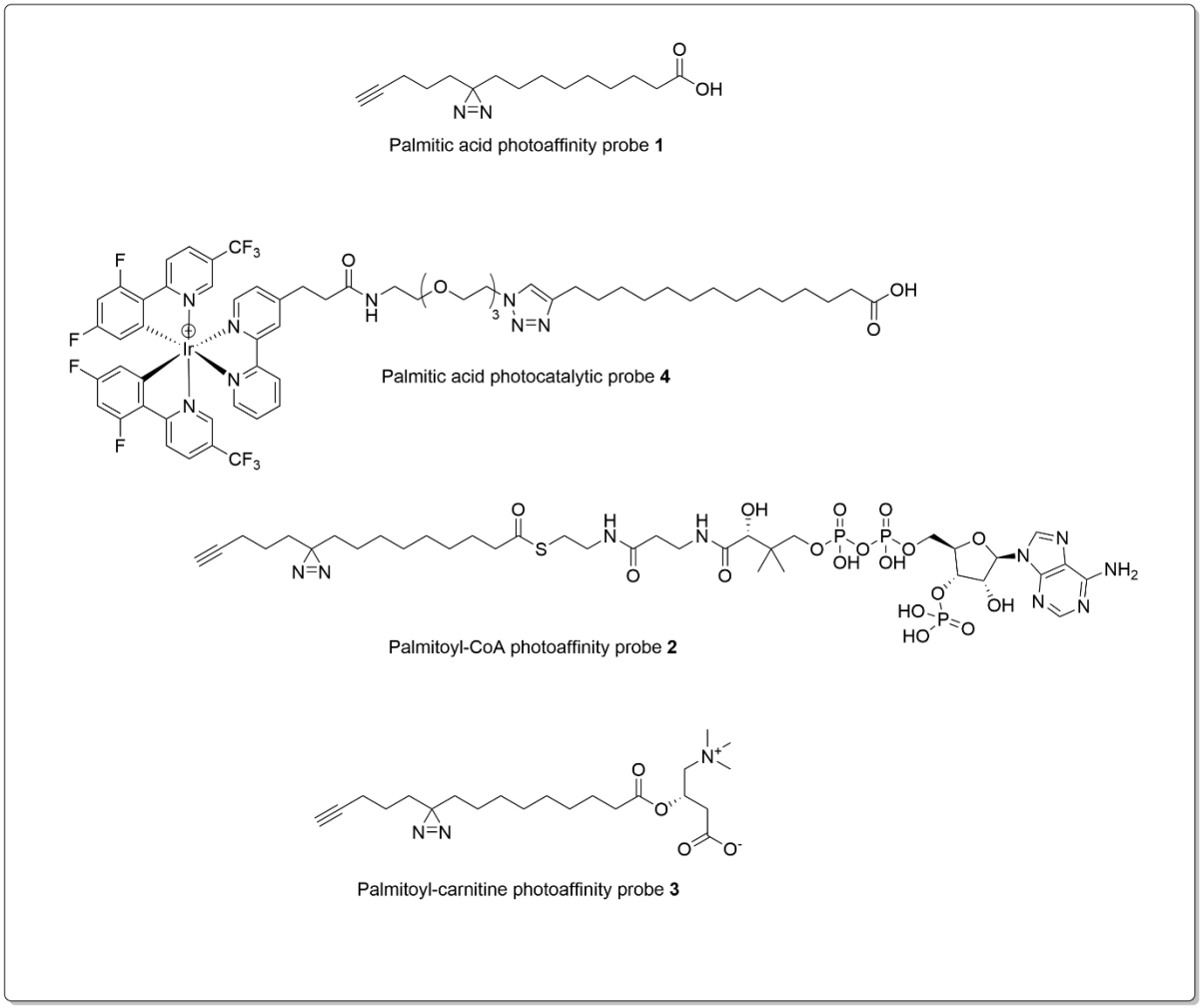

Figure 7.2: Chemical structures and names of probes 1, 4, 2 and 3.

The chemical structures of these probes (**1**, **2**, **3** and **4**) were designed to minimally perturb any protein interactions, which could be confirmed using computational modelling to compare the chemical structures of the probes with the endogenous molecules. *In-silico* alignments are a computational technique used to compare, through alignment, the structures or conformations of small molecules.[255] This technique allows for the identification of shared functional groups, binding motifs or structural features of different molecules. 3D alignment methods compare the spatial arrangement of the atoms in a molecule and can be helpful in understanding how molecules will interact with biological targets.[256] Root mean squared deviation (RMSD) is used as a metric for measuring the alignment of molecules and how their atoms are positioned, the lower the RMSD, the higher the spatial arrangement similarity.[257]

7.3 Chapter Aims:

Developing a range of probes for palmitic acid, but also its metabolites, is critical to fully understand the biological impact of palmitic acid. Having both PAL and photocatalytic palmitic acid probes would also be of benefit as PAL captures direct interactions, and photocatalytic labelling causes broader labelling of proximal proteins, providing a more unbiased mapping of palmitic acid-protein interactions *in vitro*. Outcomes in the cell may be due to palmitic acid, but it may be the case that palmitic acid metabolites are responsible for some of the biological effects, therefore, the palmitoyl-CoA and palmitoyl-carnitine probes were synthesised. However, developing probes can require optimisation of structure for binding and activity. Therefore, a computational analysis of the probe structures compared to endogenous compounds should be conducted. The aims of this chapter were to analyse the photocatalytic palmitic acid probe in cells and to compare it with the PAL probe, but also to carry out an *in-silico* alignment analysis of all the synthesised probes with parent compounds. This was achieved through:

1. A proteomic analysis of the photocatalytic palmitic acid in *MDA-MB-231* cells compared with control cells.
2. A comparison of the pathways enriched by the palmitic acid PAL probe **1** and the photocatalytic probe **4**.
3. An *in-silico* alignment analysis of probes **1**, **2**, **3** and **4** with the parent molecules: palmitic acid, palmitoyl-CoA and palmitoyl-carnitine.

7.4 Materials & Methods

7.4.1 Chemical synthesis

The chemical syntheses and characterisation of probes **1**, **2**, **3** and **4** and the biotin labelling reagent can be found in *Chapter 3* and *Chapter 9*, respectively.

7.4.2 Metabolic incorporation of probe 4 in *MDA-MB-231* cells

MDA-MB-231 cells were cultured in low glucose DMEM supplemented with 10% fetal bovine serum (FBS) and maintained in a humidified incubator at 37°C with 5% CO_2. For metabolic labelling, cells were seeded in 6 well plates and grown to 80% confluency. Cells were then incubated with probe **4** for 4 h at 37°C. The media was removed, and cells were washed gently with DPBS. The cells were then incubated with 250 μM of the biotin labelling reagent in DMEM at 37°C. The media was removed, and the cells were gently washed with DPBS and then irradiated for 3 min in the dark with an EvoluChem™ PhotoRedOx box light source (450 nm, 18 W, 110V, Strem Chemicals Inc). Cells were lysed at 4 °C with 200 μL of a buffer containing 1% SDS, 1% triton X-100 and protease inhibitors in DPBS. The cells were scraped to collect the lysate, stored at -80°C, and the total protein concentration was determined by a bicinchoninic acid protein assay (Thermo Scientific Pierce).

7.4.3 Live Cell Imaging of Blue Light-Sensitive Fluorescent Compound Using Fluorescence Microscopy

MDA-MB-231 cells were incubated with probe **4** for 4 h at 37°C, allowing sufficient time for the compound to enter the cells and fluoresce upon excitation. After incubation, the compound-containing medium was replaced with PBS to eliminate background fluorescence during imaging. Cell imaging was performed using a bright field microscope equipped with a blue light excitation source (e.g., 460 nm LED). Control experiments were performed to ensure the observed fluorescence was specifically due to probe **4**. Cells were treated with the same volume of DMSO without the compound, and fluorescence was assessed under identical conditions.

7.4.4 Ab Initio Computational Methods for Structural Behaviour Analysis of Probes 1 and 3 and Native Molecules

An ab initio computational study was conducted by *Dr. Jack Miller* on probes **1** and **3** to quantitatively understand how the different probes might behave structurally in solution compared

to native molecules (palmitic acid and palmitoyl carnitine). A Boltzmann-weighted conformer search aimed to account for molecular flexibility by generating a variety of conformers and analysing them using a more efficient level of theory. A conformer search was conducted using the CREST program at the GFN2-xTB level of theory, with a solvation model for water. Conformers within 3 kcal/mol of the lowest energy structure were retained. These structures were then optimized at the Hartree-Fock (HF) level using a smaller 6-31G(d) basis set, with solvent effects modelled by the self-consistent reaction field (SCRF) approach.[258,259] After optimization, frequency calculations confirmed that the structures represented energy minima. A Boltzmann-weighted conformer analysis was performed using the GoodVibes package to estimate the bulk properties of the molecules.[260] The most prevalent conformers were extracted and aligned using BCL::MolAlign, a tool designed for the 3D alignment of small molecules.[256] All computations were run on the Arcus-C supercomputer, using 48 worker nodes and 12 GB of RAM per node for parallel execution.[261] Some methods and basis sets were excluded due to excessive computation times or unstable results.

7.4.5 Energy Minimisation of Small Molecules Using MOE and Structural Alignment via PyMOL for Comparative Analysis

Due to the vast number of potential conformers of probe **2** and probe **4**, these molecules were energy minimised and aligned using the Molecular Operating Environment (MOE) software and PyMol, to avoid long computation time on the Arcus-C supercomputer. The energy minimization of molecular structures was performed using the MOE software suite.[262] The input structures were imported into MOE in their respective file formats (.sdf). Hydrogen atoms were added to the structures if not already present, and partial charges were assigned using the default parameters in MOE. The structures were protonated using the Protonate 3D tool to assign the appropriate protonation states at physiological pH (7.0). The Amber10: EHT force field was selected for the energy minimisation process. This force field is well-suited for small molecules. Solvent effects were modelled using an implicit solvation model (Reaction Field method). The energy minimization was initiated using the Steepest Descent algorithm followed by the Conjugate Gradient algorithm for greater convergence accuracy. The maximum number of iterations was set to 10,000 or until the root-mean-square (RMS) gradient fell below 0.01 kcal/mol Å, ensuring convergence to a local minimum and the minimised

structure was saved for subsequent steps. Following energy minimisation, a solvent-accessible surface map was generated for each molecule within MOE. This visualisation was created based on the calculated electrostatic potential, providing insight into the surface properties of the molecule, such as charge distribution and solvent interactions. The surface map was exported and analysed for comparison with other structural features. Once energy minimisation was complete, the two molecular structures were aligned using PyMOL to evaluate their structural similarity.[263] The energy-minimized structures were imported into PyMOL as separate objects. PyMOL's align command was used to align the two molecules based on their atomic coordinates. The align command uses a least-squares fitting algorithm to superimpose the structures, minimizing the root-mean-square deviation (RMSD) between the corresponding atoms. Following the alignment, PyMOL automatically calculated the RMSD between the two structures, providing a quantitative measure of their similarity. This value was recorded for analysis. The final minimized and aligned structures were exported for reporting. The energy minimization and RMSD values were used to assess structural differences and similarities between the two molecules.

7.5 Results

7.5.1 Cell viability of MDA-MB-231 cells with photocatalytic probe 4

MDA-MB-231 cells were treated with various concentrations of photocatalytic palmitic acid probe **4** (Figure 7.3) for 4 hours. The shorter time course of treatment was due to the potential cytotoxic effect of the iridium complex after this time, as Geri *et al.* mentioned this cytotoxicity in the original work.[120] Using a blue light microscope, the cells were imaged, and this demonstrated that the cells were alive at 10 µM and 30 µM of probe **4** but were dying at 100 µM (Figure 7.4). It was, therefore, decided to use 30 µM probe **4** for cell labelling experiments as this concentration would also allow for direct comparison with the results from probe **1** in the same cells (Chapters 4 & 5).

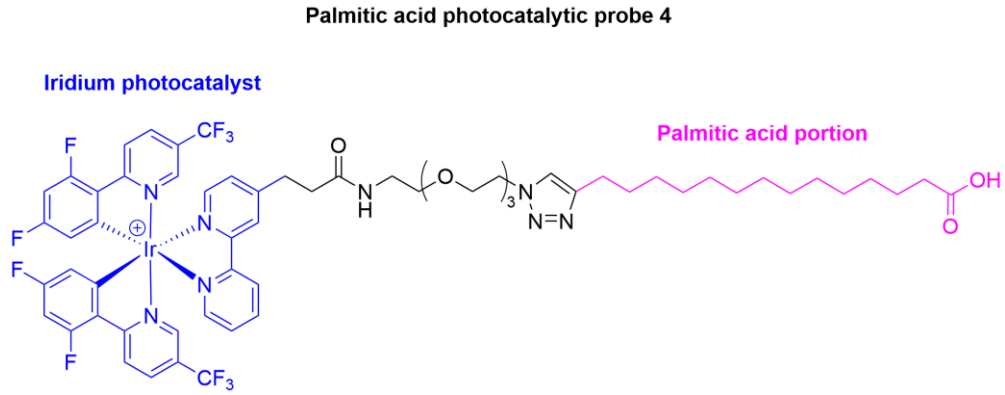

Figure 7.3: Chemical structure of photocatalytic palmitic acid probe 4

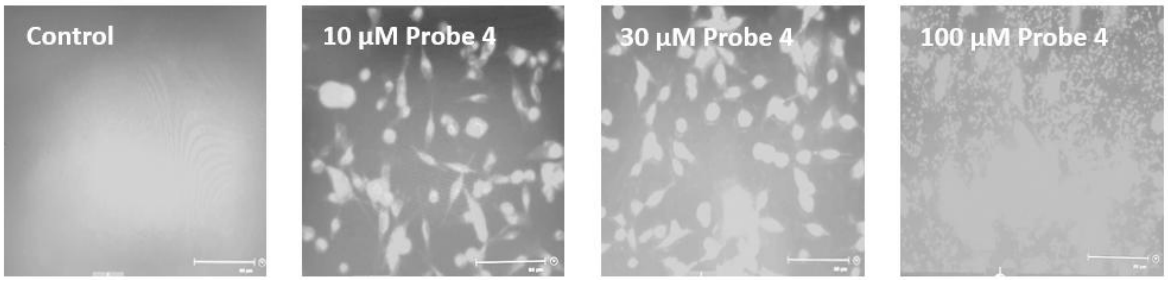

Figure 7.4: Blue light images of *MDA-MB-231* cells following probe 4 treatment at various concentrations.

The cell culture media from cells treated as controls or with 30 µM probe **4** was used to measure LDH release, lactate production, and glucose consumption rates (Results shown in Figure 7.5). The results showed a trend towards a significant increase in LDH release rates for the probe **4**-treated

cells compared to control cells. To measure if the cells were becoming more glycolytic in response to probe **4** treatment, both glucose consumption and lactate production rates were measured. The 60% increase in lactate production following probe **4** treatment suggests a metabolic switch is being induced in the cells, leading to a reliance on anaerobic glycolysis. This could be due to mitochondrial dysfunction or metabolic stress.

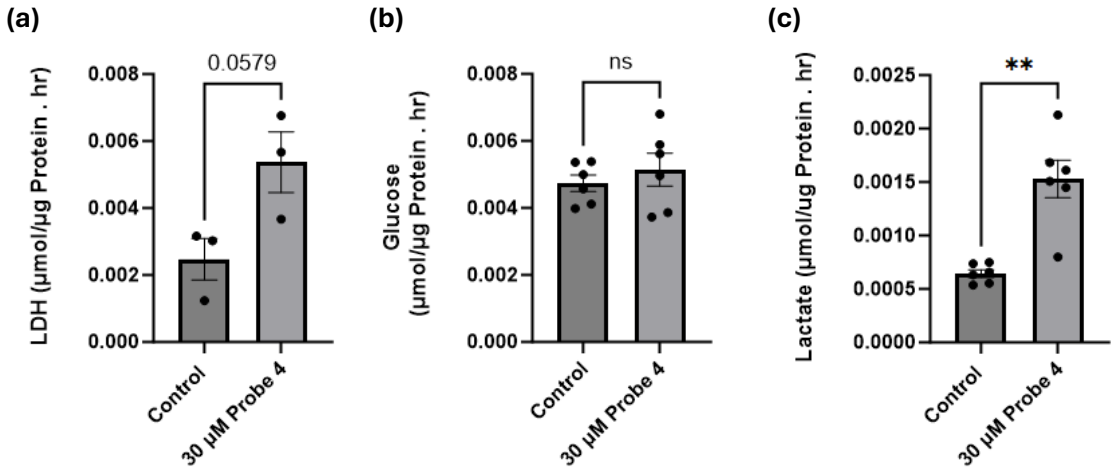

Figure 7.5: Lactate dehydrogenase (LDH) release, glucose consumption and lactate production rates of *MDA-MB-231* cells following probe 4 treatment: (a) LDH release, (b) glucose consumption and (c) lactate production rates in cell media were measured (4 h treatment) (n=3 or 6).

7.5.2 Protein labelling of MDA-MB-231 cells with photocatalytic probe

The concentration dependence of protein labelling by probe **4** in *MDA-MB-231* cells was examined. Cells were incubated with either 10 or 30 µM of probe **4** for 4 hours. The cells were then dosed with the biotin labelling reagent and irradiated with 450 nm for 3 min. Following cell lysis, the samples were analysed by western blot, using a streptavidin fluorescent antibody for imaging (Figure 7.6a). A concentration-dependent increase in protein labelling was evident when increasing from 10 to 30 µM of probe **4**. Therefore, 30 µM was the optimal labelling concentration. There was some labelling in the negative control lane, but as a streptavidin dye was used, all endogenous biotinylated proteins in the cells were also stained. Probe **4** was shown to be entering into the cells, as imaging washed cells under blue light demonstrated fluorescence of the iridium probe **4**, which was not present in the control cells (Figure 7.6b).

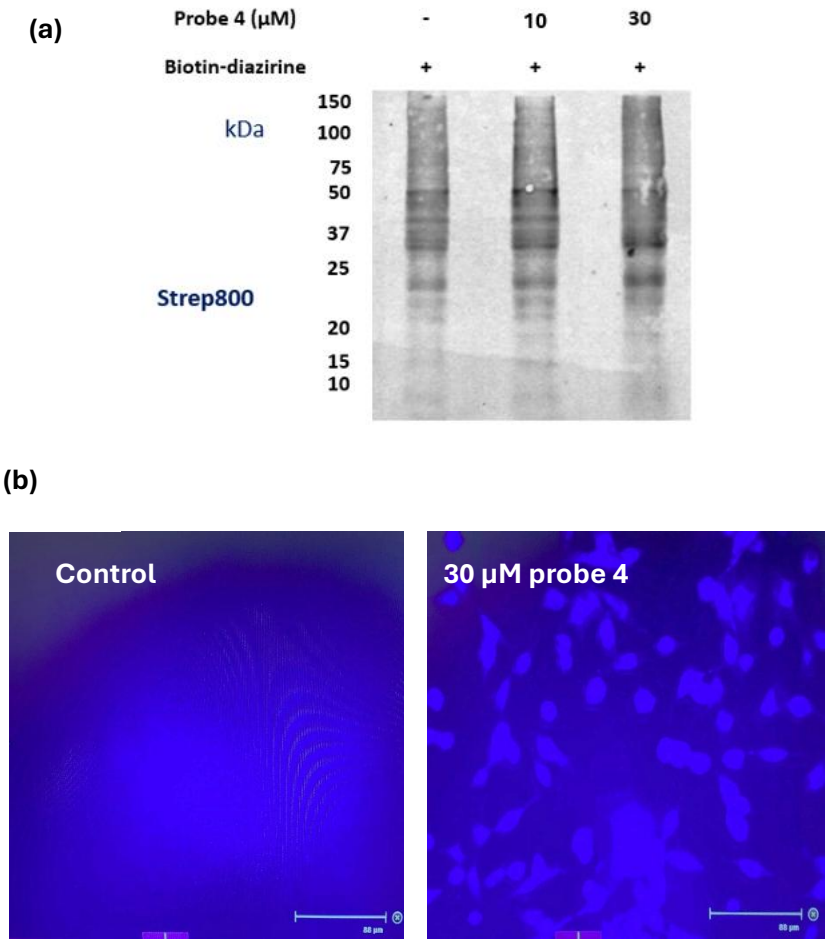

Figure 7.6: In-cell labelling using probe 4 in *MDA-MB-231* cells. (a) Western blot with a Strep800 dye highlights protein labelling by probe **4** (4 h) at 10 or 30 μM; (b) Imaging of washed control or 30 μM probe **4**-treated cells using a blue light microscope. Fluorescence is only seen in the probe **4**-treated cells.

7.5.3 Proteomic analysis of *MDA-MB-231* cells treated with probe 4

Proteomic analysis was performed on control cells and cells treated with 30 μM probe **4** (4 h). Principal component analysis (PCA) showed a distinct separation between the groups (Figure 7.7), however one of the probe samples was an outlier. PC1 accounted for 50% of the variance, while PC2 accounted for only 25% of the variance, potentially due to variability not attributable to compound treatment. Following PCA, a linear correlation was performed on the samples, looking at the heterogeneity of the samples (Figure 7.8). Hierarchical clustering using a Pearson correlation revealed differences in samples in the probe **4** group, with one outlier. Again, this suggested differences in the protein enrichment in samples from the same group, but this is to be expected when carrying out a pulldown enrichment.

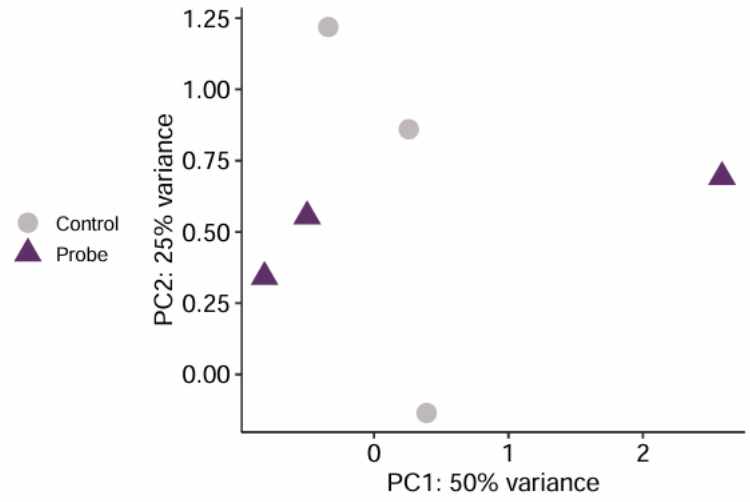

Figure 7.7: PCA plot of *MDA-MB-231* proteomic samples: Cell samples as controls (grey) or treated with 30 µM Probe **4** (purple) (n=3).

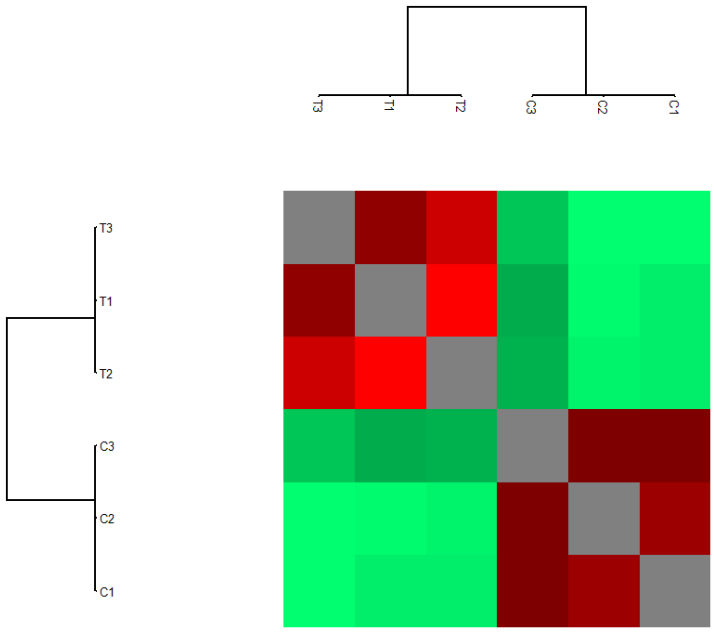

Figure 7.8: Hierarchical clustering using Pearson correlation of *MDA-MB-231* proteomic samples. Samples were run in an n = 3, with C = Control and T = 30 µM probe **4**. Colours represent expression of proteins compared with the mean expression. Green = low expression and red = high expression.

A proteomic comparison was performed between the control and 30 µM probe **4**-treated cells (4 h). This resulted in 1881 interactor proteins total, with 915 of these significantly ($p < 0.05$) enriched by 30 µM probe **4**, compared with controls (Figure 7.9). Statistically significantly enriched proteins (top right quadrant of volcano plot) were fed into the STRING database, and mapping of the protein interactions was performed, highlighting the subcellular localisation of the enriched proteins (Figure

7.10). Proteins were found in the nucleus (red), actin cytoskeleton (purple), chromatin (green) and ATPase complex (yellow).

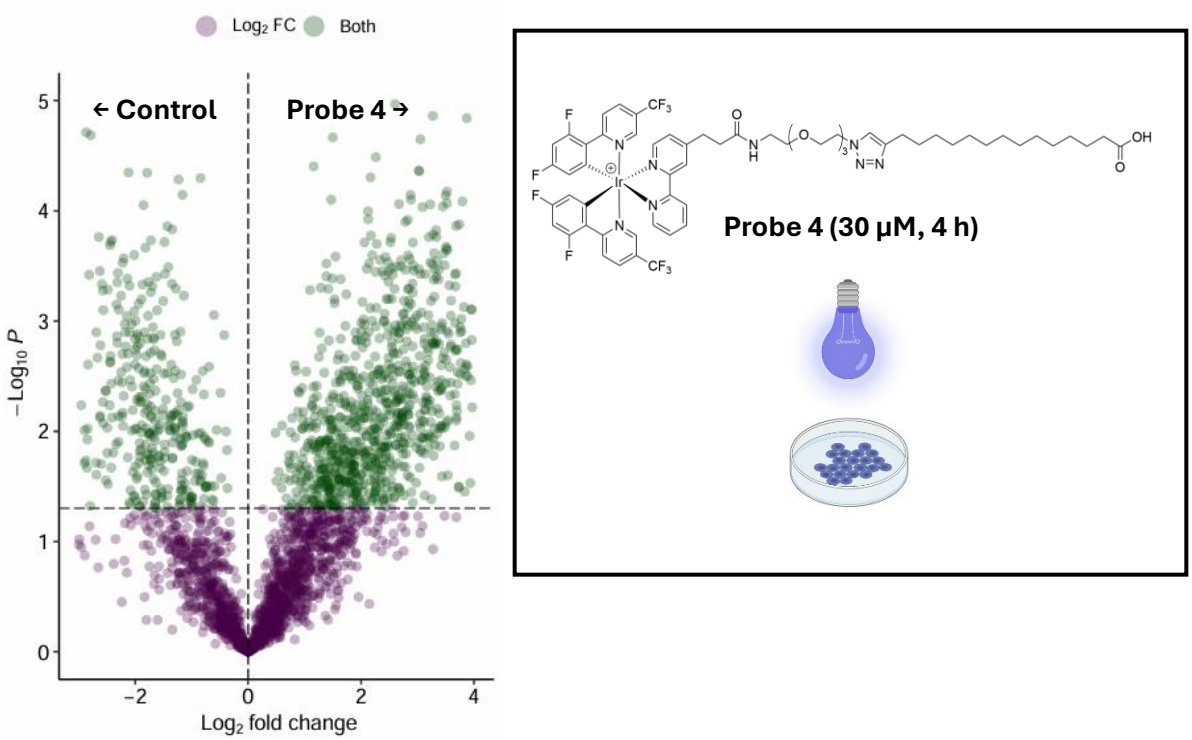

Figure 7.9: Proteomic analysis results of *MDA-MB-231* cells treated with 30 μM probe 4. Volcano plot of proteins enriched by 30 μM probe **4** (4 h, 3 min 450 nm) compared with control cell (4 h, 3 min 450 nm)

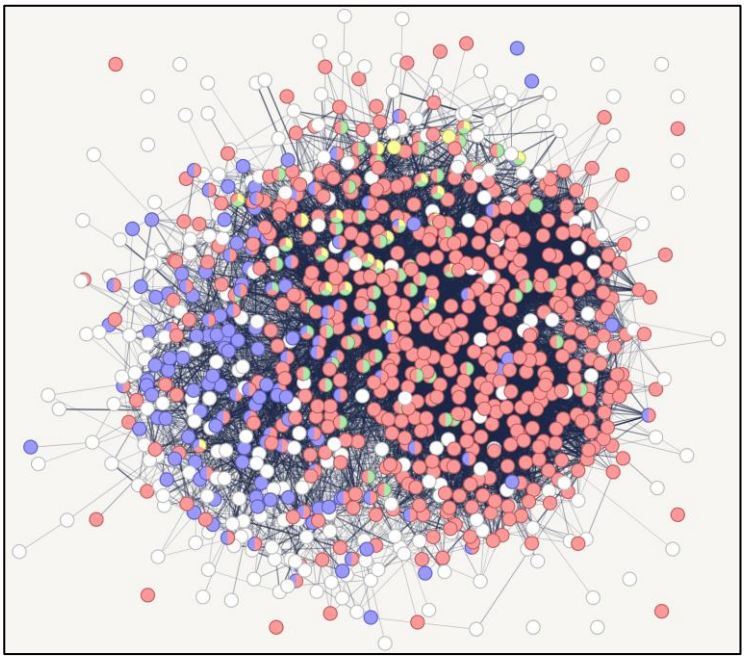

Figure 7.10: STRING network mapping of proteins enriched by 30 μM probe 4. Protein localisation is coloured: nucleus (red), actin cytoskeleton (purple), chromatin (green) and ATPase complex (yellow).

Significantly enriched proteins were then used for a Metascape pathway analysis (Figures 7.11 & 7.12). This pathway approach revealed that the top enriched parent GO term was 'Metabolic process', with 'Localisation' and 'Homeostatic process' being GO terms of interest too (Figure 7.11a). Metascape analysis using the DisGeNet database mapped protein names to diseases and revealed that probe **4** was not having an effect on diseases of interest, as most of the diseases were related to craniofacial abnormalities, developmental disorders, and neurological conditions (Figure 7.11b). Transcription factor mining revealed that the probe **4** enriched proteins were regulated by transcription factors of interest, including transcription factors involved in cell cycle progression, hormone response, cytoskeletal processes and chromatin remodelling (Figure 7.11c), including TP53 (Tumor Protein 53or p53), MYC (c-Myc), E2F family and ESR1 (Estrogen Receptor 1).

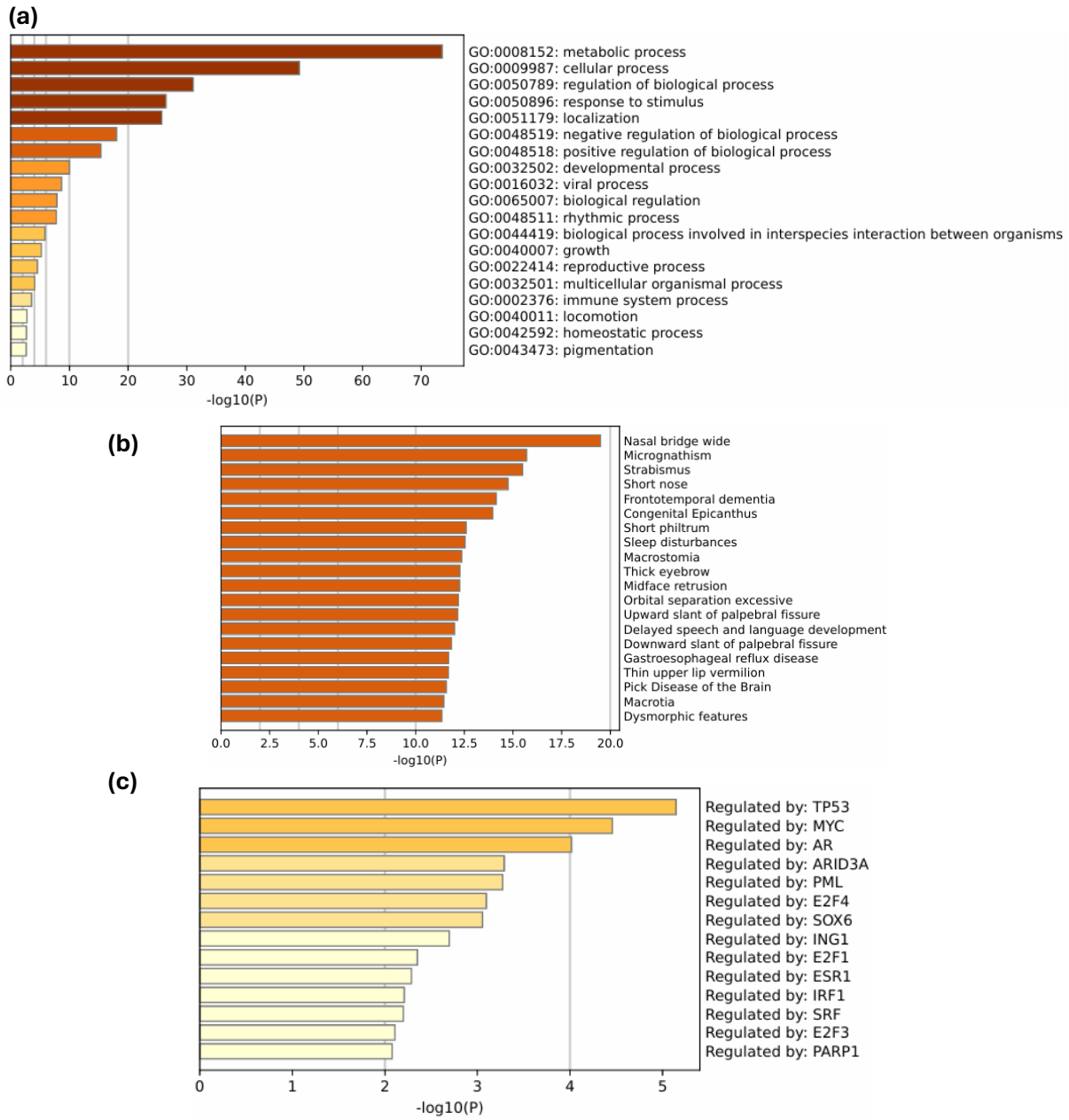

Figure 7.11: Metascape analysis of the enriched proteins with 30 µM probe 4. (a) The top-level Gene Ontology (GO) biological processes; (b) Summary of enrichment analysis in DisGeNET – showing enrichment of disease pathways; (c) Transcription factors regulating proteins enriched by 30 µM probe 1. All graphs are coloured by p-values.

Further analysis of these processes allowed for the identification of more specific pathways (Figure 7.12). The top enriched term was 'Metabolism of RNA, yet again indicating the role of probe **4** in RNA metabolic processes. Other pathways of interest were: 'Chromatin remodelling', 'Actin cytoskeleton organisation', 'VEGFA-VEGFR2 signalling', 'Membrane trafficking', 'RHOA GTPase cycle', 'Rac1 GTPase cycle', 'TGF beta signalling' and 'Localisation within the membrane'. This demonstrated a role for probe **4** in gene expression, structural, signalling and localisation processes

within the *MDA-MB-231* cells. Many of these pathways were also enriched with photoaffinity palmitic acid probe **1** in this cell line.

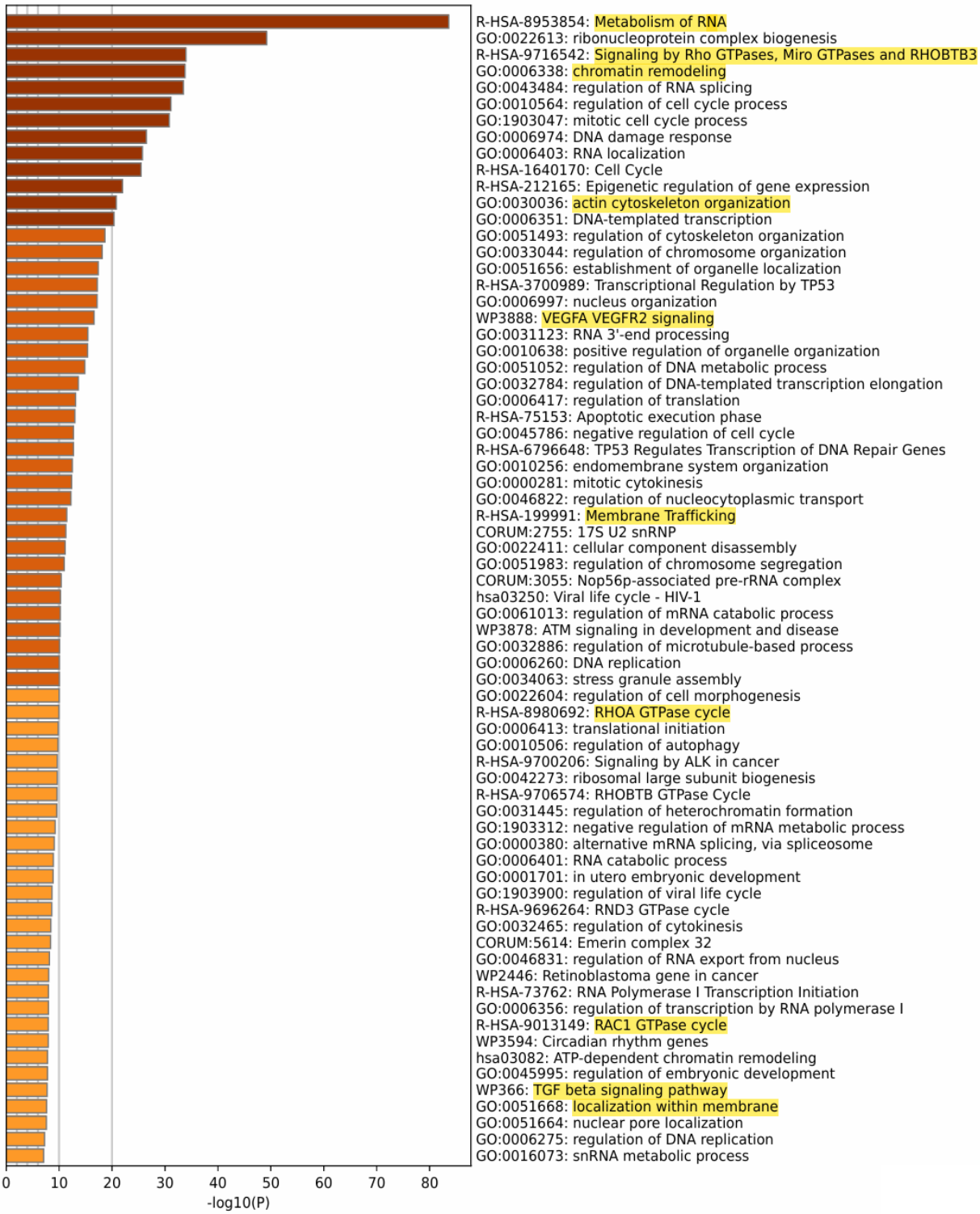

Figure 7.12: Metascape analysis of the enriched proteins with 30 µM probe 4 (contd.). Enriched terms across the input gene lists (proteins with an NSAF > 0) are coloured by p-values. Pathways of interest are highlighted.

A network of enriched terms following probe **4** treatment was constructed and depicts the interconnected biological processes and pathways based on a functional gene enrichment analysis

(Figure 7.13). Each node represents a distinct biological term or pathway, and the lines (edges) connecting the nodes indicate shared or related functions among them. Clusters of densely connected nodes suggest highly interrelated processes. For example, processes like 'RNA splicing', 'RNA localisation', and 'Ribonucleoprotein complex biogenesis' are closely related, reflecting their roles in RNA processing and gene expression regulation. Similarly, 'Cell cycle processes', including mitotic regulation and DNA damage response, form another distinct cluster, emphasising their coordination in cellular proliferation and genomic integrity. 'Actin cytoskeleton organisation' and 'Regulation of cytoskeleton organisation' form a completely distinct cluster, closely connected with one another. This network illustrates how diverse cellular functions enriched by the probe are interlinked, with multiple pathways contributing to complex biological responses.

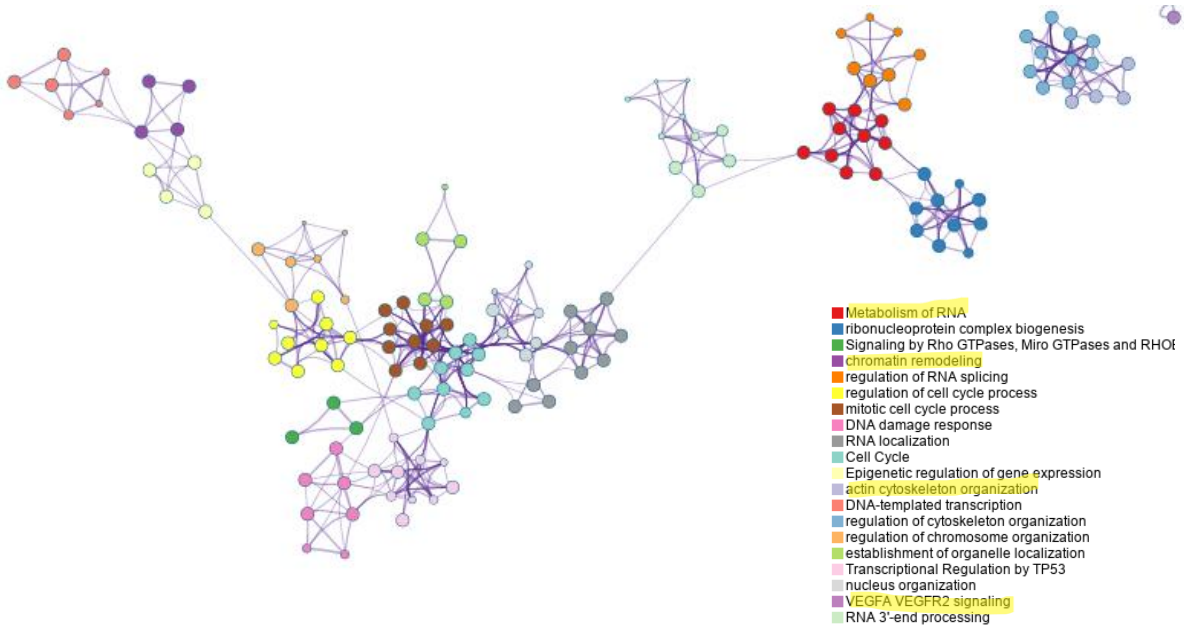

Figure 7.13: Network of enriched terms from probe 4 treated cells. Coloured by cluster ID, where nodes that share the same cluster-ID are typically close to each other. Pathways of interest are highlighted.

A STRING protein-protein interaction network was created using the statistically significant enriched proteins after probe **4** treatment (Figure 7.14 & 7.15). Some biological processes of interest were mapped including: 'Membrane trafficking', 'Actin cytoskeleton organisation', 'Chromatin organisation', and 'mRNA metabolism'. Each node represents a protein, and the lines connecting them indicate interactions, including physical and functional associations. Some networks are highly

interconnected, such as chromatin organisation and RNA metabolism suggesting a complex interaction system among these proteins. Various colours of nodes and edges represent different clusters and types of interactions, indicating that multiple proteins work together in the processes.

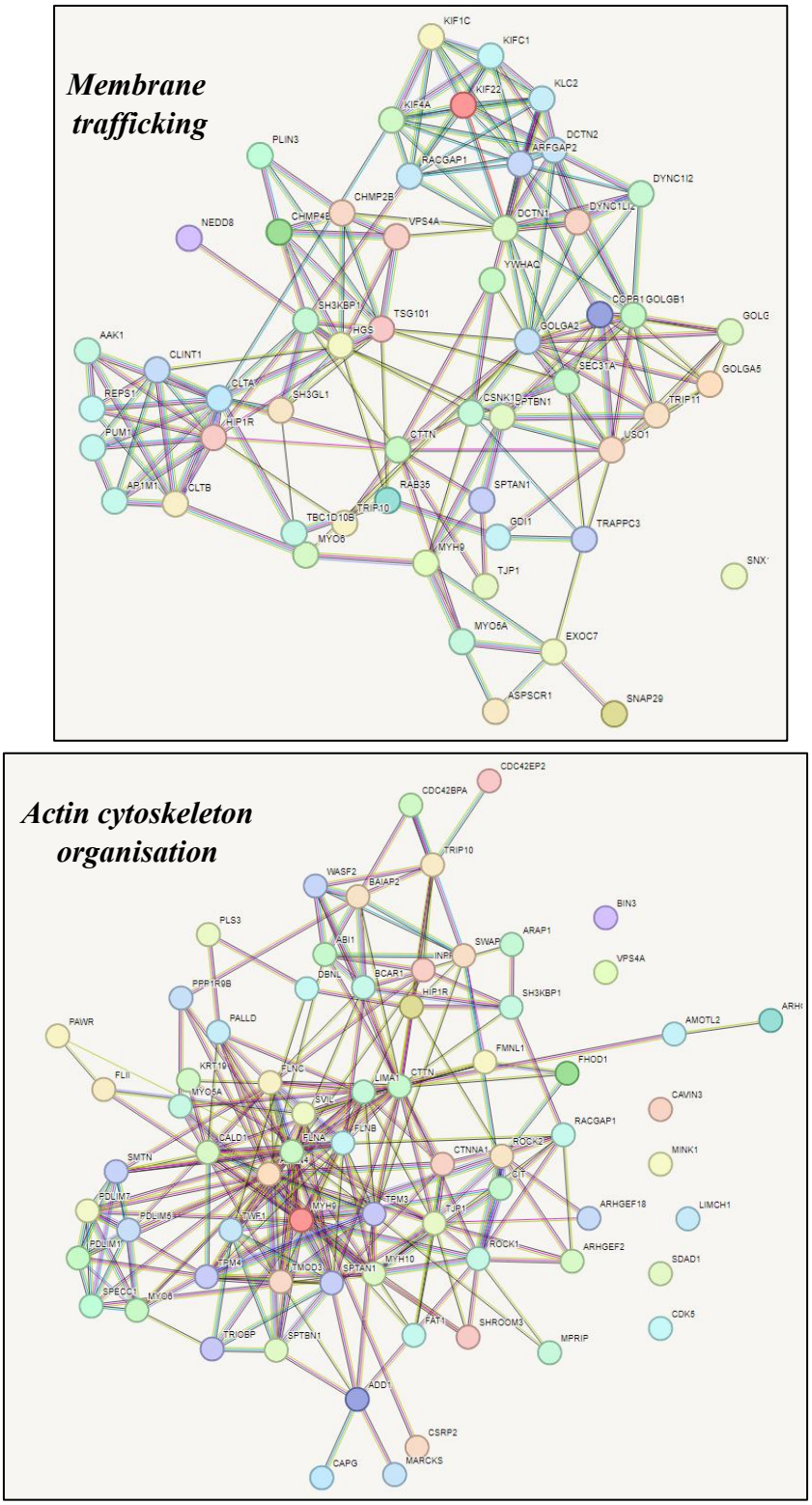

Figure 7.14 STRING protein-protein networks for probe 4

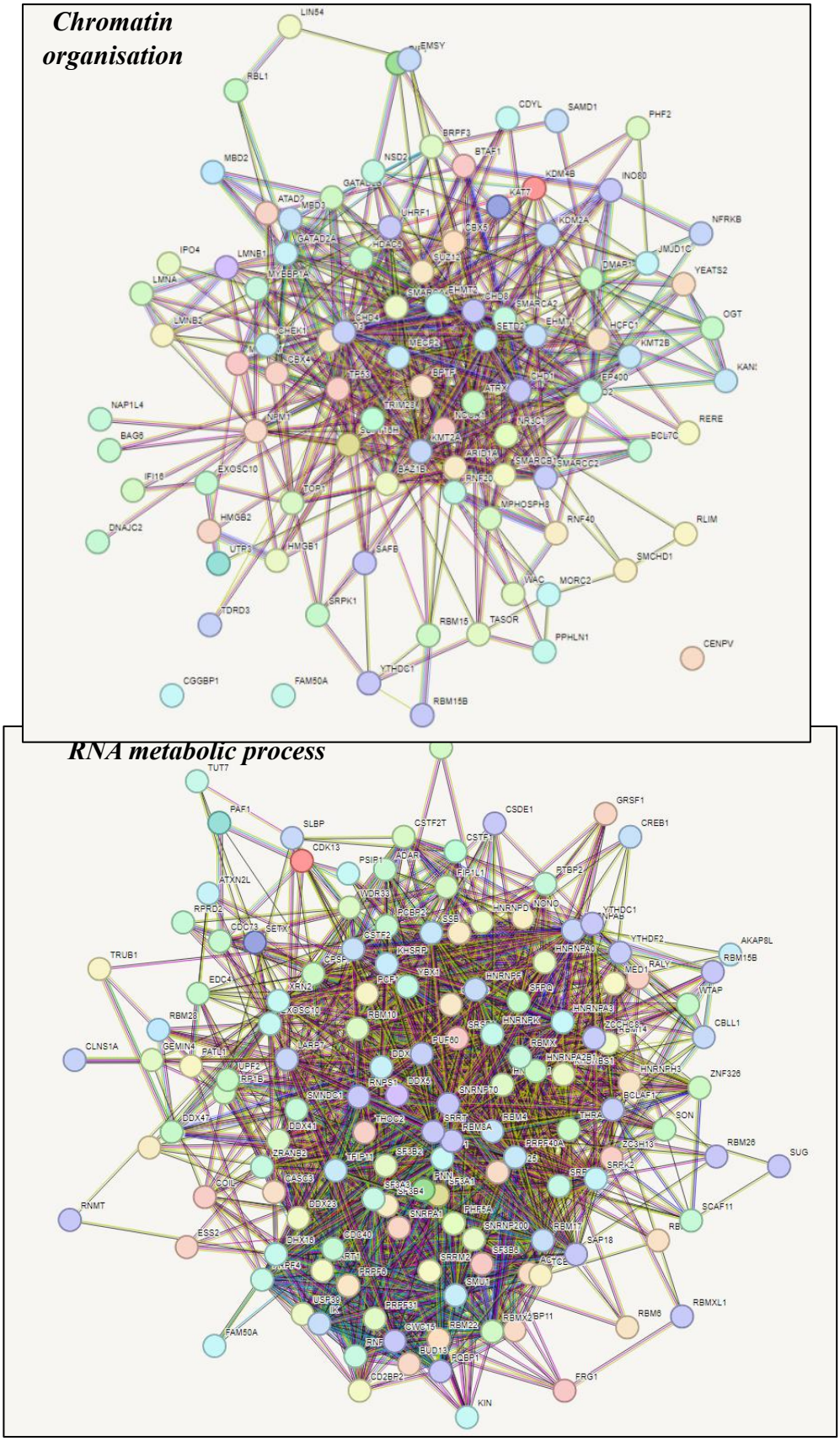

Figure 7.15 STRING protein-protein networks for probe 4 (contd.)

7.5.4 Comparison of proteins and pathways enriched by probe 4 with probe 1

A comparison of the enriched proteins by both probe **4** and probe **1** in *MDA-MB-231* cells found that only 16 proteins were commonly enriched between the probes (Figure 7.18). These proteins are described in Table 7.1. Overlap in proteins involved in actin cytoskeleton organisation, membrane trafficking, cell cycle control, RNA binding and protein processing suggest a role for palmitate in these biological processes. An increased number of proteins are enriched by probe **4**, which is to be expected due to the photocatalytic labelling mechanism of this probe. The small number of overlapping proteins may be due to the distinct difference in chemical structures of the probes, with probe **4** being much more polar compared to the more hydrophobic probe **1**. This small overlap may also be due to the difference in incubation time of the probes and the protein labelling efficiency of the probes, with probe **1** having stoichiometric labelling and probe **4** causing catalytic labelling.

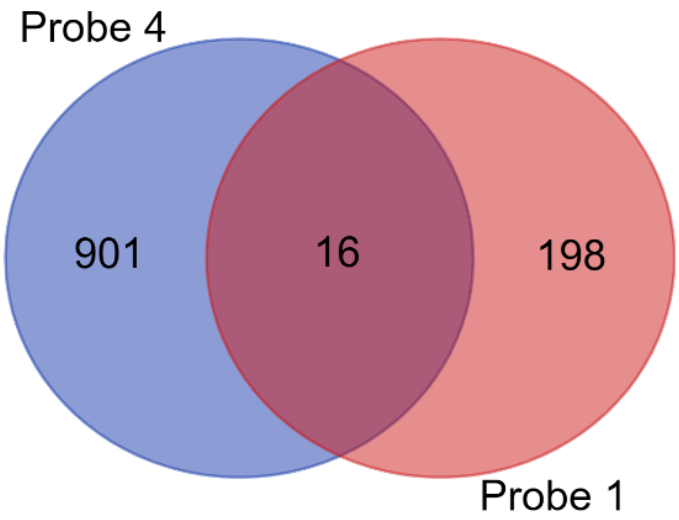

Figure 7.18 Overlap of proteins enriched my probe 4 and probe 1

Table 7.1: Proteins enriched by both probe 1 and 4 in *MDA-MB-231* cells.

Protein	Name	Function
CLTA	Clathrin Light Chain A	*Involved in clathrin-mediated endocytosis*
CDK1	Cyclin-Dependent Kinase 1	*A key regulator of cell cycle progression, specifically involved in the transition from G2 phase to M phase*
YWHAQ	14-3-3 Theta	*Part of the 14-3-3 protein family that regulates many cellular processes, including signal transduction, cell cycle control, and apoptosis*
RAB35	Ras-Related Protein Rab-35	*A small GTPase involved in the regulation of membrane trafficking, specifically endocytic recycling and cytokinesis*
GDI1	Rab GDP Dissociation Inhibitor Alpha	*Regulates the GDP-GTP exchange reaction of Rab proteins, which are involved in vesicle trafficking*
ARMC6	Armadillo Repeat-Containing Protein 6	*The specific function is not well- characterised, but armadillo repeat-containing proteins are often involved in protein-protein interactions and can play roles in signalling pathways and cellular structure.*
ZNF324	Zinc Finger Protein 324	*Part of the zinc finger protein family, which typically functions as transcription factors that bind DNA and regulate gene expression.*
PCBP1	Poly(RC) Binding Protein 1	*Functions in RNA binding and is involved in various aspects of RNA metabolism, including mRNA stabilisation, splicing, and translation. It also binds single-stranded DNA and RNA with high affinity.*
CAPG	Capping Actin Protein, Gelsolin Like	*A member of the gelsolin/villin family of actin-regulatory proteins. It binds to actin filaments and caps their barbed ends, regulating actin polymerization and dynamics important for cell motility and structure.*
NUDCD2	NudC Domain-Containing 2	*The exact function is not well-characterized, but NUDC domain-containing proteins are often involved in cellular processes like cell division and intracellular transport.*
FMNL1	Formin-Like 1	*An actin-binding protein that plays a role in cytoskeletal organization, cell shape, and movement. It is involved in the nucleation and elongation of actin filaments.*
HEBP1	Heme Binding Protein 1	*Binds heme and may be involved in heme metabolism and transport. It has also been implicated in regulating apoptosis.*
API5	Apoptosis Inhibitor 5	*An anti-apoptotic protein that inhibits programmed cell death. It interacts with other proteins to protect cells from apoptosis induced by various stimuli.*
KRT18	Keratin 18	*A type I intermediate filament protein found in epithelial cells. It provides structural stability to cells and is involved in protecting cells from stress.*
PCBP2	Poly(RC) Binding Protein 2	*Similar to PCBP1, it is involved in RNA binding and regulation. It has roles in mRNA stabilization and translation, as well as in the regulation of RNA viruses.*
NCLN	Nicalin	*Part of a complex involved in the regulation of Nodal signalling, which is important for embryonic development. It has a role in the endoplasmic reticulum and may be involved in protein processing or trafficking.*

A comparison of the results from the proteomic analysis of probe **4** and probe **1** in *MDA-MB-231* cells was performed using Metascape. A circos plot, illustrating the relationships or interactions between probes **1** and **4** allows for a clear visualization of the connections between different elements within these groups (Figure 7.19). Each segment around the circle represents a probe and the purple lines within the circle link identical proteins and the blue lines link proteins that belong to a shared enriched ontology term. There is a substantial number of interactions, indicating a significant level of connectivity or shared features between the two probes. A heatmap illustrating the enrichment of various Gene Ontology (GO) biological processes across the two probes shows patterns of similarity in their enrichment profiles (Figure 7.20). Notably, several processes, including 'Metabolic process', 'Localisation' and 'Homeostatic process' exhibit highly significant associations across the probes. In contrast, some processes like "rhythmic process" and "growth" are enriched by probe **4** but are absent for probe **1**. This suggests that the probes may be influencing distinct sets of biological processes, potentially due to their differing chemical structures, but also differences in incubation time and labelling efficiency.

A comparison of the enrichment analysis for both probes was also performed (Figure 7.21) and allowed for highlighting of similarities and differences in the enrichment of various biological processes and pathways by both probes. Probe **4** shows significant enrichment in pathways related to small GTPase-mediated signal transduction, protein folding, DNA and RNA metabolic processes and protein stability. There is also a notable enrichment in processes associated with membrane organisation, endosomal transport, and the cell cycle, particularly the G2/M transition. The presence of signalling pathways like TGF-beta signalling and Rho GTPase signalling suggests that probe **4** may be involved in cellular responses to external stimuli or stress. In comparison to probe **4**, probe **1** appears to have lower enrichment in signal transduction processes, indicating it may not be as actively involved in signalling pathways. However, similarly, to probe **4**, probe **1** also shows enrichment in cell cycle regulation, DNA replication, and chromatin remodelling, indicating a role in maintaining cellular proliferation and genomic stability. Probe **1** is associated with mitochondrial

metabolic processes and organelle organization, indicating that probe **1** may be involved in cellular metabolism and the maintenance of organelle function.

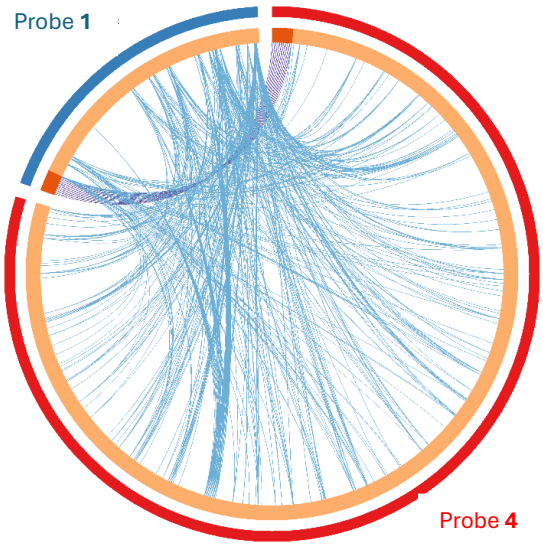

Figure 7.19: Circos plot of the overlap between probe 1 (blue) and probe 4 (red) enriched proteins: Blue curves link genes that belong to the same enriched ontology term. The inner circle represents gene lists, where hits are arranged along the arc. Genes that hit multiple lists are coloured in dark orange, and genes unique to a list are shown in light orange.

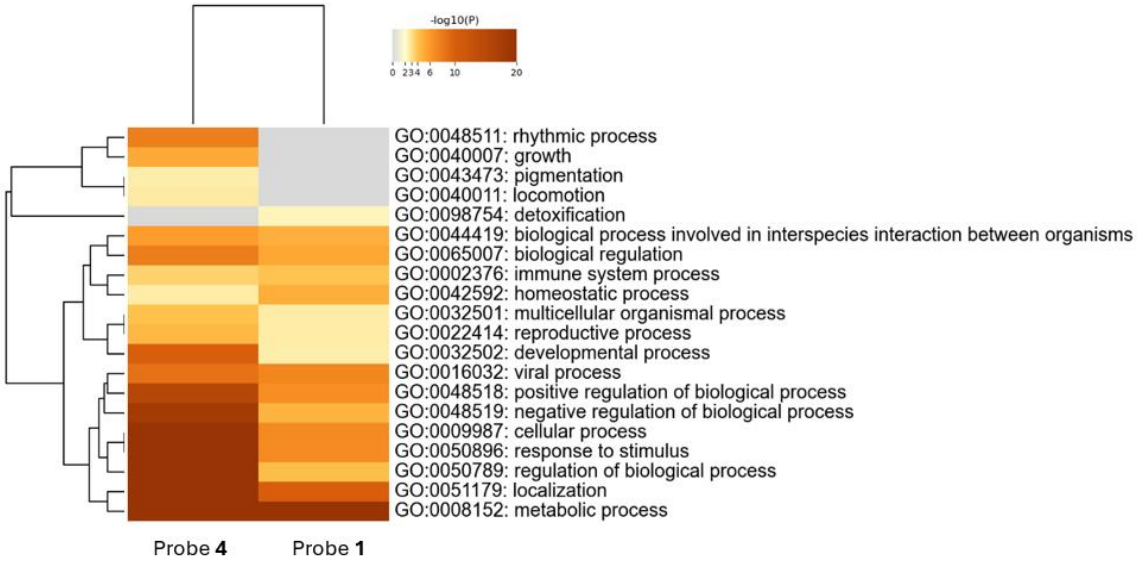

Figure 7.20: A comparison of the top-level Gene Ontology (GO) biological processes enriched by both probe 1 and probe 4. Coloured by p-values.



Figure 7.21: A heatmap comparing the enriched terms by probe 4 and probe 1. Coloured by p-values.

7.5.5 Computational methods to analyse probe structures

In collaboration with Dr. Jack Miller (RDM, Oxford & Department of Physics, Oxford), an *ab initio* computational approach was used to investigate the chemical structures of the various palmitate or palmitate metabolite probes in comparison to the parent compounds. This was performed by Dr. Miller on the Arcus-C supercomputer in the Department of Physics (University of Oxford).[261]

Energy minimisation was performed using a Boltzmann-weight conformer search and conformers were then optimised at a Hartree-Fock level (basis 6-31G(d)) using water as a solvent. The results for the palmitic acid photoaffinity probe **1** where 643 conformers were run, was 'Conformer 1' populating 0.366 of the Boltzmann distribution (Table 7.2). The Boltzmann population refers to the relative population of different molecular conformers at thermal equilibrium. It is based on the Boltzmann distribution, which describes how particles (in this case, different conformers of a molecule) are distributed among various energy states at a given temperature. Therefore, 36.6% of the molecules of probe **1** exist as conformer 1 at thermal equilibrium, meaning conformer 1 is one of the dominant conformers of probe **1**.

Table 7.2: Table showing the thermodynamic properties of various conformers of the probe 1 at 298.15 K.

Structure	E	ZPE	H	T.S	T.qh-S	G(T)	qh-G(T)	Boltz
Palmitate probe_rdkit_conf_374	-840.519964	0.363826	-840.133017	0.078910	0.071029	-840.211927	-840.204046	0.001
Palmitate probe_rdkit_conf_1	-840.525627	0.363200	-840.139121	0.077532	0.071018	-840.216653	-840.210139	0.366
Palmitate probe_rdkit_conf_250	-840.519172	0.363811	-840.132391	0.077976	0.070352	-840.210367	-840.202744	0.000
Palmitate probe_rdkit_conf_147	-840.521028	0.363822	-840.134163	0.077475	0.070292	-840.211638	-840.204455	0.001
Palmitate probe_rdkit_conf_281	-840.520510	0.363926	-840.133710	0.076637	0.069804	-840.210347	-840.203514	0.000
Palmitate probe_rdkit_conf_526	-840.515594	0.364139	-840.128514	0.077217	0.069998	-840.205731	-840.198513	0.000
Palmitate probe_rdkit_conf_479	-840.517784	0.364155	-840.130856	0.076069	0.069287	-840.206925	-840.200143	0.000
Palmitate probe_rdkit_conf_636	-840.516410	0.363732	-840.129605	0.077875	0.070515	-840.207480	-840.200120	0.000

The data includes electronic energy (E), zero-point energy (ZPE), enthalpy (H), entropy contributions (T.S and T.qh-S), Gibbs free energy (G(T) and qh-G(T)), and the Boltzmann population. Conformer 1 exhibits the lowest electronic and Gibbs free energy, resulting in the highest Boltzmann population (0.366), indicating it is the most stable and predominant conformer under the given conditions.

For the palmitoyl-carnitine photoaffinity probe **3**, conformer 10 was the most stable and predominant conformer at 298.15 K, as indicated by its high Boltzmann population of 0.987 (98.7%) (Table 7.3). This suggests that under the given conditions, nearly all the molecules of the palmitoyl carnitine probe will adopt this conformation. This conformer's dominance is due to its very low Gibbs free

energy (-1316.8 Hartree), which ensures it is the thermodynamically preferred state in the sample of possible conformations.

Table 7.3: Table showing the thermodynamic properties of various conformers of the probe 3 at 298.15 K.

Structure	E	ZPE	H	T.S	T.qh-S	G(T)	qh-G(T)	Boltz
Palmitoyl carnitine probe_rdkit_conf_9	-1317.307310	0.565212	-1316.708016	0.100763	0.091518	-1316.808780	-1316.799535	0.000
Palmitoyl carnitine probe_rdkit_conf_21	-1317.312569	0.564762	-1316.713507	0.103796	0.092937	-1316.817303	-1316.806444	0.007
Palmitoyl carnitine probe_rdkit_conf_1	-1317.309995	0.564721	-1316.710995	0.102970	0.092579	-1316.813965	-1316.803574	0.000
Palmitoyl carnitine probe_rdkit_conf_12	-1317.309800	0.564525	-1316.710795	0.104464	0.093675	-1316.815259	-1316.804470	0.001
Palmitoyl carnitine probe_rdkit_conf_8	-1317.307762	0.564404	-1316.709037	0.102523	0.092532	-1316.811560	-1316.801569	0.000
Palmitoyl carnitine probe_rdkit_conf_23	-1317.302212	0.566310	-1316.702248	0.097927	0.089728	-1316.800174	-1316.791975	0.000
Palmitoyl carnitine probe_rdkit_conf_18	-1317.311577	0.564343	-1316.712719	0.103602	0.093421	-1316.816321	-1316.806141	0.005
Palmitoyl carnitine probe_rdkit_conf_10	-1317.317805	0.564348	-1316.719112	0.100785	0.092058	-1316.819897	-1316.811170	0.987
Palmitoyl carnitine probe_rdkit_conf_4	-1317.310148	0.564830	-1316.711109	0.100709	0.091746	-1316.811818	-1316.802855	0.000

The data includes electronic energy (E), zero-point energy (ZPE), enthalpy (H), entropy contributions (T.S and T.qh-S), Gibbs free energy (G(T) and qh-G(T)), and the Boltzmann population. Conformer 10 exhibits the lowest electronic and Gibbs free energy, resulting in the highest Boltzmann population (0.987), indicating it is the most stable and predominant conformer under the given conditions.

The Molecular Operating Environment (MOE) was used to energy minimise probes **2**, probe **4** and palmitoyl-CoA due to time constraints, as using HF methods would have taken weeks of supercomputer time due to the high number of potential conformers. The MOE-minimised and the HF energy-minimised conformers of palmitic acid, palmitoyl-carnitine and probes **1** and **3** (Table 7.2 & 7.3) were used to generate molecular surfaces using the software MOE. The surface representations provide insights into the ligand's shape, size, and potential interaction regions. Comparing probe surfaces with parent compound surfaces reveals similar areas of surface properties, but also some differences. In the surfaces of palmitic acid and probe **1**, both are elongated ligands with a similar overall shape, suggesting they share a common scaffold (hydrophobic tail) (Figure 7.22). However, there are notable differences in their surface properties, indicated by the presence of an additional polar region (diazirine) in probe **1**. This difference in surface properties may introduce more complex binding interactions with target proteins. These differences in probe **1** are conserved across probes **2** and **3**, which all contain the extra polar diazirine group compared to parent compounds (Figure 7.22). Probe **4**, the photocatalytic probe, has the added bulky iridium photocatalyst. This introduces an additional large polar region compared with palmitic acid, and again, this could cause changes in the binding properties of probe **4**.

Figure 7.22: Molecular surface comparison of palmitic acid and metabolite probes with parent compounds: Surface properties of parent compounds (left) show a mostly hydrophobic region (grey) with polar head groups (coloured), whereas the probe structures (right) have an additional polar region (coloured) due to the introduction of a diazirine group or a photocatalytic group. Probes **1** and **3** and palmitic acid and palmitoyl-carnitine are based on Hartree-Fock minimised conformers (Tables 7.2 & 7.3).

Parent compound	**Probe**
Palmitic acid 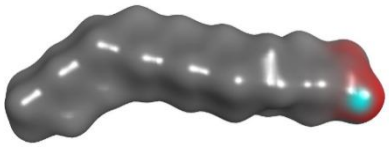	**1** (conf. 1) 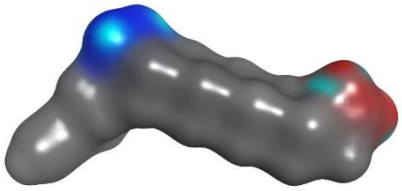
Palmitoyl-CoA 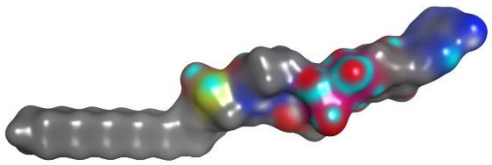	**2** 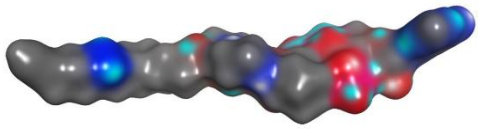
Palmitoyl-Carnitine 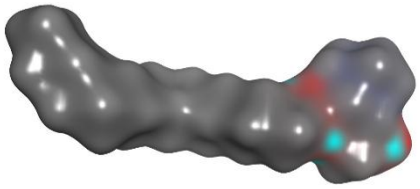	**3** (conf. 10) 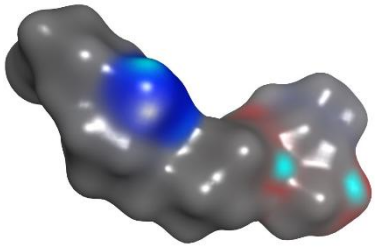
Palmitic acid 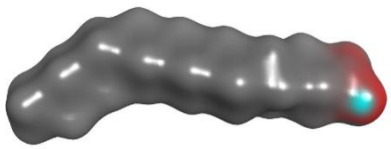	**4** 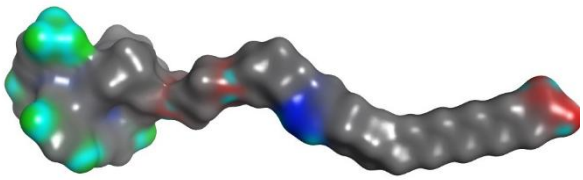

Using the same energy-minimised ligands, an alignment was performed in MOE to compare all palmitic acid or metabolite probes with their parent compounds (Table 7.4). The resulting alignment indicates that probes **1** and **3** are structurally very similar to their parent compounds, palmitic acid and palmitoyl-CoA, respectively. This is due to their alignments having a root mean squared deviation (RMSD) of 0.84 and 0.68 Å, respectively. An RMSD of < 1 Å indicates high structural

similarity, and an RMSD > 2 Å suggests differences between the two structures.[264] The diazirine group appears to introduce a kink into both probe molecules, compared to the parent compounds.

Next, a comparison between the structures of palmitoyl-CoA and probe **2** was performed (Table 7.4). The alignment of the two molecules, with an RMSD of 1.08 Å, suggests that both share a common backbone structure, particularly in the long FA chain and the coenzyme A (CoA) moiety, as evidenced by the close overlap of the green and blue regions. The differences in the alignment, marked by the presence of the additional diazirine group in probe **2**, result in slight deviations around this region.

Lastly, a comparison between palmitic acid and the photocatalytic probe **4** was performed (Table 7.4). The alignment gave an RMSD of 2.8 Å, indicating differences between the molecules. Probe **4** contains significant modifications, including a large photocatalytic group, PEG-linker and a triazole ring. The added moieties, especially the photocatalytic group, add rigidity and steric bulk compared to palmitic acid. The molecular surface illustrates a more complex shape with additional electronic features due to the photocatalytic group. The modifications in probe **4** therefore make it significantly different in terms of chemical properties and potential interactions.

Table 7.4: Alignment analysis of palmitic acid and metabolite probes with parent FAs

Probe	Parent compound	Alignment	RMSD (Å)
1 	Palmitic acid 	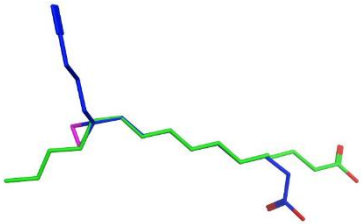	0.84
2 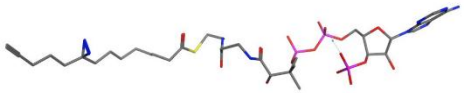	Palmitoyl-CoA 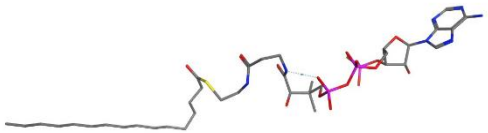		1.08
3 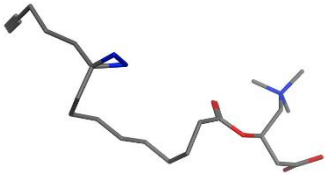	Palmitoyl-Carnitine 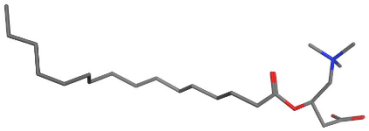	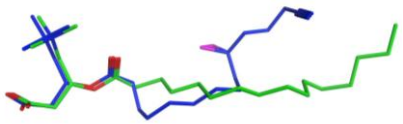	0.68
4 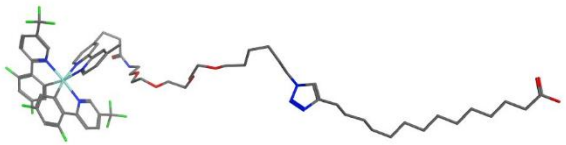	Palmitic acid 	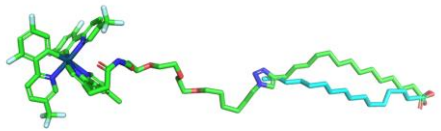	2.8

3D chemical structures of palmitic acid and metabolite probes **1**-**4** and parent compounds, followed by aligned structures (MOE software) and root mean squared deviation (RMSD) of alignments. RMSD < 1 suggests high structural similarity. Probes **1** and **3** and palmitic acid and palmitoyl-carnitine are based on Hartree-Fock minimised conformers (Tables 7.2 & 7.3).

7.6 Discussion

Probe **4** is an iridium-based photocatalytic palmitic acid probe, which can be used for the catalytic labelling of protein interactors of palmitic acid. The catalytic mechanism of protein labelling should cause increased labelling compared to the PAL approach (palmitic acid photoaffinity probe **1**), potentially identifying more interacting partners.

Probe **4** exhibits cytotoxic effects at higher concentrations, specifically at 100 μM, but not at 30 μM. At the 30 μM concentration, there is a trend toward increased levels of lactate dehydrogenase (LDH) release rates into the cell culture media, which suggests a possible rise in cell membrane permeability or early signs of cytotoxicity. However, these changes do not reach statistical significance. Interestingly, lactate production rates in the media were significantly increased at 30 μM, indicating a shift towards anaerobic glycolysis or increased metabolic stress within the cells, whilst glucose consumption remains unchanged, suggesting that glucose uptake or metabolism might not be the limiting factor. This suggests that while 30 μM is not overtly cytotoxic, probe **4** does exert metabolic stress on the cells.

Proteomic enrichment studies reveal that probe **4** significantly enriches 915 proteins. In theory, these proteins include not only those that directly interact with the compound but also those in a complex with the direct interactors, due to the mechanism of labelling by the photocatalytic probe. It was, therefore, shown that probe **4** labelled a more significant number of proteins than probe **1** (915 and 214, respectively). The compound was particularly effective in enriching proteins localised to the nucleus and the actin cytoskeleton. Among the biological pathways that these proteins are involved in, several key cellular processes are impacted, including membrane trafficking, chromatin remodelling, RNA metabolism, and subcellular localisation within membranes. The enrichment also spans important signalling pathways such as TGF-β signalling, VEGFA-VEGFR2 signalling, Rac1 GTPase signalling, RHO GTPase signalling, and pathways related to histone modifications and estrogen-dependent gene expression.

Due to the bulky iridium photocatalyst attached to probe **4** it is unlikely that the enzymes required to transfer palmitic acid to proteins (e.g. DHHCs), via palmitoylation, would bind this molecule. And

as all labelling occurs via photo-crosslinking it is more difficult to distinguish which proteins are covalently or non-covalently interacting with probe **4**. The increased toxicity of probe **4**, potentially due to the charged iridium photocatalyst, makes it difficult to conclude which interactions are due to endogenous interactions and which are due to toxicity. A competition experiment with palmitic acid may help to tease out endogenous interactions.

One of the most significant and novel findings of this study is the strong nuclear involvement of probe **4**. Analysis using the STRING database revealed that most of the protein interactors of probe **4** are localised within the nucleus. Building on this, pathway analysis further confirmed the upregulation of several nuclear processes, which are crucial for maintaining the structural and functional integrity of the nucleus - essential for proper gene expression, DNA replication, and cell cycle progression. In the context of cancer cells, this nuclear involvement could be particularly significant, as these interactions may also contribute to cellular toxicity (increased LDH release). Cancer cells are highly sensitive to disruptions in nuclear processes, and the upregulation or dysregulation of nuclear pathways by probe **4** may exacerbate genomic instability - a hallmark of cancer progression.[265,266] Aberrant nuclear signalling driven by lipid-protein interactions could further disrupt the balance of growth, differentiation, and apoptosis of the cancer cells.

A comparison of the enrichment profiles of the two compounds, probe **4** and probe **1** in *MDA-MB-231* cells, highlighted distinct biological pathways, yet showed some areas of overlap in fundamental cellular processes. Probe **1** predominantly enriches proteins involved in metabolic processes and developmental pathways, suggesting its interaction with proteins that play roles in energy production, biosynthesis, and cell differentiation. In contrast, probe **4** preferentially enriched proteins are associated with signal transduction and protein degradation, implying its involvement in regulating cellular communication and the controlled breakdown of proteins. Despite these differences, both probes share an enrichment of proteins involved in key cellular functions, including GTPase signalling, protein stability, membrane trafficking, cell cycle regulation, RNA metabolism, and ribosome biogenesis. The direct protein overlap (enriched proteins common to both probes) is particularly notable in governing the cell cycle, vesicle and endocytotic processes, RNA binding,

cytoskeletal organisation, and heme metabolism, underscoring their common impact on fundamental cellular infrastructure (Table 7.1). The divergent enrichment patterns between the two probes may stem from their chemical structural differences, which could influence their interaction with specific protein networks. Additionally, probe **4** may not be recognised by metabolic machinery and, therefore, could explain its focus on non-metabolic processes, such as signalling and degradation, further contributing to the differential protein enrichment profiles between the two probes.

In a collaborative computational study, a comparison of the structural and electronic properties of the various palmitic acid and metabolite probes (probes **1**, **2**, **3** and **4**) against their native FAs to assess the impact of introducing additional functional groups into their structures. When comparing palmitic acid with probe **1**, differences were observed due to the introduction of a photoreactive diazirine group, which altered the electron density and introduced a slight kink in the structure of probe **1**, which was also observed in probes **2** and **3**. Probes **1** and **3** were shown to be structurally similar to palmitic acid and palmitoyl-carnitine, respectively. However, probes **2** and **4** were structurally different, due to the kink from the diazirine and the bulky photocatalyst, respectively. These findings suggest that the incorporation of diazirine groups does not significantly alter the overall molecular shape, supporting the notion that biological interactions of the probes are likely to be endogenous. However, the photocatalyst modification does drastically change both the structure and electron density of palmitic acid, potentially blocking endogenous protein interactions. The slight structural deviation in the probes underscores the importance of including appropriate controls to account for potential alterations in biomolecular interactions.

Chapter 8

General Discussion

8.1 General Discussion

Despite the acknowledged importance of FAs in both health and disease, relatively little research has been conducted on the direct interactions between FAs and proteins, especially in the context of breast cancer and cardiovascular health. Identifying how specific FAs bind to and modulate protein function in these diseases could improve our understanding of how lipid metabolism contributes to disease progression and reveal novel therapeutic targets. Therefore, this thesis investigated the molecular interactions of FAs *in vitro*, in the context of both breast cancer and the heart, using various chemical FA probes. This revealed complex interactions between the probes and several cellular pathways. While these two cell types differ significantly in function, there are notable parallels in how the probe modulates key cellular pathways in both.

Metabolism and Energy Production

In *Chapters 5* and *6*, probe **1** caused significant changes in metabolic pathways in both *MDA-MB-231* cells and hiPSC-CMs. However, the outcomes of these changes differed based on the inherent metabolic characteristics of each cell type. Cancer cell metabolism is influenced by the Warburg effect, relying predominantly on glycolysis for rapid ATP generation, supporting their high proliferation rates[47]. In contrast, cardiomyocytes primarily rely on FA and OXPHOS due to their high energy demands for sustained contractility[67]. In cancer cells, probe **1** caused a shift from anaerobic to aerobic metabolism, by upregulating OXPHOS and downregulating glycolysis and insulin signalling pathways. This metabolic shift could reduce the cancer cell's ability to proliferate rapidly, as OXPHOS is a more efficient but slower process compared to glycolysis. This shift is also similar to the metabolic shift that occurs in heart metabolism post-birth in response to the mother's lipid-rich milk, where the prenatal heart relies on glycolysis, and the postnatal heart shifts dependence to more FAO[267–269]. Interestingly, a similar upregulation of energy metabolism pathways was observed in cardiomyocytes, where probe **1** increased mitochondrial numbers and upregulated the expression of genes related to lipid metabolism. In this context, the shift toward enhanced mitochondrial energy production supports the high energy needs of cardiomyocytes. This same

process is also seen post-weaning in the heart and has been linked to lipid-mediated activation of PGC1α.[267]

Cytoskeletal Organisation and Cell Motility

The cytoskeleton is crucial for maintaining cell shape, enabling intracellular transport, facilitating cell division, and supporting cell movement and structural integrity, making it essential for virtually all cellular processes. Cytoskeletal organisation was a cellular pathway affected by probe **1** in both cell types. In *Chapter 5*, probe **1** downregulated RHO GTPase and RAC1 signalling pathways in *MDA-MB-231* cells, both of which are crucial for actin cytoskeleton function, cell movement, and metastasis, suggesting that the probe may inhibit cancer cell migration, thereby reducing metastatic potential[208,270]. Similarly, in *Chapter 6*, probe **1** interacted with proteins involved in cytoskeletal and extracellular matrix (ECM) organisation in hiPSC-CMs, which are vital pathways critical for maintaining the structural integrity and function of heart muscle cells. RHO GTPase signalling is also essential in cardiomyocytes for controlling cell shape and contractility and the downregulation of this pathway could have detrimental effects, potentially impairing the cells' ability to contract and respond to mechanical forces, leading to reduced contractility and structural defects[270].

Signalling Pathways and Hormone Responses

FAs play a key role in cellular signalling and hormone responses by serving as signalling molecules themselves, modulating membrane fluidity, and influencing the activation of receptors and transcription factors involved in metabolic, inflammatory, and hormonal pathways. Probe **1** interacted with key signalling pathways in both cell types.

In *Chapter 5*, probe **1** demonstrated broad effects on key signalling pathways, influencing cell growth, survival, metabolism, and hormone responses. By downregulating mTORC1 and upregulating mTORC2 in *MDA-MB-231* cells, probe **1** altered the balance between anabolic growth and survival pathways, potentially reducing protein synthesis while promoting cell migration, invasion, and survival.[209] This shift in signalling, coupled with the upregulation of TGF-β signalling,

a pathway associated with epithelial-to-mesenchymal transition (EMT), suggests that probe **1** may enhance cancer metastasis and immune evasion.[250,271,272]

In *Chapter 6*, probe **1** interacted significantly with hormone-related pathways, particularly estrogen, androgen, and insulin signalling in hiPSC-CMs. The downregulation of insulin signalling in both cell types of points to an overarching influence on glucose metabolism and energy homeostasis. Interestingly, the suppression of estrogen and androgen signalling in cardiomyocytes may have mixed consequences. While estrogen typically exerts cardioprotective, androgens also play a role in cardiovascular regulation, including muscle mass and blood pressure control.[223,251,252] The inhibition of these hormone pathways by probe **1** could limit hypertrophic growth, which may be beneficial in preventing heart disease, but it could also impair the heart's ability to manage stress and maintain homeostasis, suggesting complex effects on cardiac function. Overall, the ability of probe **1** to modulate these critical pathways points to its potential impact on both cancer progression and cardiovascular health.

In *Chapter 7,* probe **4** also interacted with multiple signalling pathways in *MDA-MB-231* cells suggesting a broad, overarching effect on key cellular functions related to growth, survival, and structural dynamics. Its involvement in TGF-β signalling points to a potential role in driving EMT, a crucial process in cancer metastasis and tissue remodelling.[250,271,272] Similarly, its impact on VEGFA-VEGFR2 signalling indicates that probe **4** may enhance angiogenesis, supporting the development of new blood vessels vital for sustaining tumour growth and survival.[273,274] Additionally, the modulation of Rac1 and Rho GTPase signalling pathways reflects probe **4** effect on cytoskeletal reorganisation, which is comparable to probe **1**.

Unexpected pathways regulated by palmitic acid

The purpose of this thesis was to uncover novel proteins or pathways affected by FAs. Across *Chapters 5, 6* and *7*, several unexpected biological pathways were highlighted by probes **1** and **4**. These palmitic acid-mimetic probes interacted with proteins involved in RNA metabolism, nuclear and chromatin organisation, and actin cytoskeleton regulation. The typical role of FAs in cells centres around their function as metabolic fuels or membrane components, making these findings

particularly surprising. The involvement of the probes in RNA metabolism suggests a previously unrecognised connection between FA signalling and gene regulation at the post-transcriptional level, impacting processes like RNA synthesis, splicing, and degradation. Furthermore, interactions with proteins involved in nuclear and chromatin organisation suggest a potential role for lipid interactions in regulating chromatin architecture and gene accessibility, which are both critical for transcriptional control. The regulation of the actin cytoskeleton by both probes also extends beyond its expected metabolic function, suggesting that lipids may have a broader influence on the dynamics of the cytoskeleton and cellular structure. This novel intersection of lipid metabolism with RNA, nuclear, and cytoskeletal regulation requires further validation but may potentially open up new avenues for exploring how lipid signals interact with essential cellular processes and potentially influence disease pathways such as cancer or heart disease.

8.2 Research Limitations

Further Validation of Probe Conditions

This study did not fully explore a broader range of conditions for probe **1** validation, including variations in concentration and competition assays with palmitic acid. While the experimental conditions provided valuable insights, additional validation across a range of conditions could increase confidence in probe **1**'s specificity and functionality. In particular, further optimisation is required for hiPSC CMs (*Chapter 6*), as an assumption was made that the conditions optimal for labelling in *MDA-MB-231* cells (*Chapter 5*) would also be suitable for cardiomyocytes due to time constraints. However, this assumption requires further validation given the cellular architecture, metabolism, and lipid handling differences between these cell types.

Time Course for Probe Treatment

The study did not include an extensive time-course analysis to investigate the dynamics of probe **1**'s effects over different treatment durations, as only a single time point of 16 h was examined.

Exploring earlier time points may capture potential time-dependent differences in covalent and non-covalent interactions, providing a more comprehensive understanding of any temporal effects of probe **1**.

Probe Metabolism and Stability

The differential metabolism and half-life of palmitate or probe **1** in cells were not directly quantified. Preliminary observations in *Chapter 4* suggested that probe **1** was not metabolised by isolated mitochondria, indicating that it may not serve as a metabolic substrate. This was further supported by observations such as increased lipid droplet formation with probe **1** treatment, potentially indicating its preference for storage over metabolism. As a result, probe **1** could accumulate in the cell over time, allowing for prolonged interaction with cellular components. This potential difference in intracellular concentration, driven by reduced metabolism, may contribute to probe **1**'s extended activity and effects within the cell. However, more detailed studies are needed to confirm these findings.

Additional Controls for Photocatalytic Probe 4

The photocatalytic labelling study in *Chapter 7* lacked certain controls that could help distinguish the specific effects of probe **4**. Assessing the influence of the iridium catalyst (unconjugated to palmitate) on cellular uptake and localisation could elucidate whether the metal catalyst directs probe **4** localisation or affects cellular behaviour in unintended ways.

8.3 Future work

Future research should focus on expanding the utility and application of the palmitic acid probe **1** and its derivatives in diverse biological systems. One key avenue involves exploring the potential of metabolic intermediate probes, such as palmitoyl-CoA probe **5** and palmitoyl-carnitine probe **6**, for in-cell studies. Directly comparing their interactomes with probe **1** would provide valuable insights into how structural differences influence cellular interactions, metabolic pathways, and lipid storage

or utilisation. Such comparative studies could uncover new roles for these lipids in cellular biology and help design probes for specific applications.

Additionally, investigating probe **1**'s stability and metabolic fate at a deeper level could enhance its utility in biological research. Incorporating technologies like high-resolution mass spectrometry could provide finer detail on probe-derived metabolites and their distribution within cellular compartments. This analysis would be valuable in clarifying probe **1**'s metabolic fate and potential to influence cellular processes differently from the parent fatty acid palmitate.

Integrating molecular biology approaches to validate proteomic and transcriptomic findings represents another critical direction for future work. Techniques such as RNA interference (RNAi), CRISPR-Cas9 gene editing, and overexpression systems can be employed to validate specific targets identified through interactome analysis. Importantly, the targets selected for validation should undergo a robust preliminary evaluation to ensure their relevance as valid palmitate targets. This could include competition assays with palmitic acid to confirm the specificity of probe **1** binding and to distinguish genuine interactions from off-target effects. These validation steps would ensure that subsequent molecular techniques are applied to the most relevant and biologically significant targets, facilitating a deeper mechanistic understanding of palmitate-associated pathways and cellular processes.

Further investigation into the multi-omic approach used in this study could significantly enhance its utility for uncovering biologically relevant pathways and targets. While pathway analysis was employed to integrate proteomic targets and gene expression changes, questions remain about whether this method is too general for highlighting specific biological mechanisms of interest. Alternative approaches, such as network analysis, machine learning-based clustering, or systems biology models, may provide a greater understanding of the interplay between different omics layers. Collaborating with bioinformaticians could be invaluable for implementing these advanced methods and identifying more targeted, pathway-specific insights.

8.4 Conclusion

Therefore, in this thesis, the molecular interactions of palmitic acid have been investigated using two metabolically different cell lines and a multi-omics approach. Collectively, this thesis demonstrated that using chemical probes to investigate the role of palmitic acid in vitro highlighted its involvement in various cellular processes critical to function, metabolism and survival. This thesis has designed, synthesised, and utilised *in vitro* a number of chemical probes of palmitate to identify novel protein binding partners for FAs and their downstream effects regulating cell function and signalling (Figure 8.1). The findings from this work, particularly in relation to cancer and cardiomyopathies, may potentially guide future therapeutic strategies.

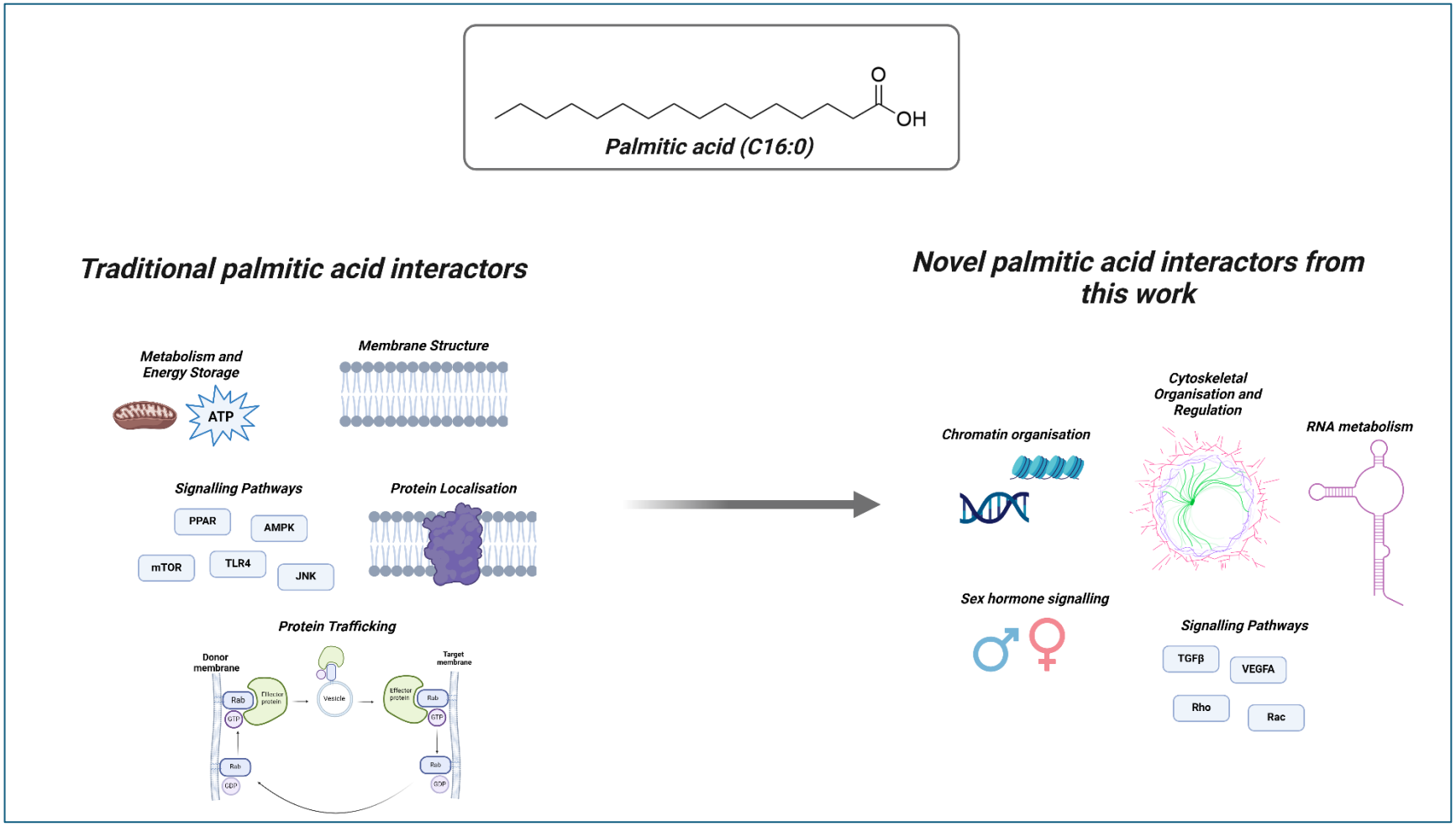

Figure 8.1: Pathway interactors of palmitic acid that this work has added.

Chapter 9

Chemistry Experimental

9.1 General Experimental

All reactions involving organometallic or other moisture-sensitive reagents were performed under a nitrogen or argon atmosphere using standard vacuum line techniques and glassware that was flame-dried and cooled under nitrogen before use. Anhydrous solvents were dried by passing over an activated alumina column, under an inert atmosphere, using a solvent purification system. Water was purified by an Elix® UV-10 system. All other reagents were used as supplied (analytical or HPLC grade) without prior purification. Organic layers were dried over Na_2SO_4. Thin-layer chromatography was performed on aluminium plates coated with 60 F254 silica. Plates were visualised using UV light (254 nm), $KMnO_4$ (1% aq.), 10% ethanolic phosphomolybdic acid, and 10% ethanolic p-anisaldehyde. Flash column chromatography was performed either on Kieselgel 60 silica in a glass column or on a Biotage Isolera Four automated flash column chromatography platform. Melting points were recorded on SRS MPA120 EZ-Melt Melting Point Apparatus and are uncorrected. IR spectra were recorded on a Bruker Tensor 27 FT-IR spectrometer as a thin film. Selected characteristic peaks are reported in cm^{-1}. NMR spectra were recorded on Bruker Avance spectrometers in the deuterated solvent stated. Spectra were recorded at RT unless otherwise stated. The field was locked by external referencing to the relevant deuterium resonance. Low-resolution mass spectra were recorded on either an Agilent 6120 Single Quadrupole or a Waters LCT Premier spectrometer. Accurate mass measurements were run on either a Bruker MicroTOF internally calibrated with polyalanine, or a Micromass GCT instrument fitted with a 162 Scientific Glass Instruments BPX5 column (15 m × 0.25 mm) using amyl acetate as a lock mass.

9.2General Procedures:

General procedure 1: Grignard formation

Magnesium turnings (4.0 eq.) were etched with a pestle and mortar and placed in a flame-dried microwave vial. A small bead of I_2 (~3 mg/mL) was added, and the reaction vessel was sealed and purged with argon three times. The magnesium and I_2 were then covered with anhydrous THF (2 M). The mixture was stirred for 15 min at RT. 1,2-Dibromoethane (10 %v/v) and a few drops of (5-chloropent-1-yn-1-yl)trimethylsilane were added to the reaction, whichwas allowed to heat to reflux. At reflux, a solution of (5 chloropent-1-yn-1-yl)trimethylsilane (4.0 eq.) in anhydrous THF (3 M) was added dropwise over 30 min. The reaction mixture was stirred at reflux for 3 h and then cooled to −78 °C. A solution of the appropriate Weinreb amide or aldehyde (1.0 eq.) in anhydrous THF (1.5 M) was added dropwise and the mixture was allowed to warm to RT and stirred overnight. The reaction was then quenched with NH_4Cl (satd. aq.) and the layers were then separated and extracted with EtOAc. The combined organics were then washed with brine, dried over Na_2SO_4 and concentrated *in vacuo*.

General procedure 2: Swern oxidation

A solution of DMSO (3.0 eq.) in anhydrous CH_2Cl_2 (0.6 M) was cooled to -78 °C in a flame-dried flask under N_2 and was slowlr added to a solution of oxalyl chloride (1.5 eq.) in CH_2Cl_2 (0.7 M) and stirred for 10 mins. A solution of the appropriate alcohol (1.0 eq.) in CH_2Cl_2 (0.5 M) was then slowly added and the reaction was stirred for 1h at -78 °C. NEt_3 (4.7 eq.) was added, and the mixture was then warmed gradually to RT. After 1 h the reaction was quenched with satd. aq. NH_4Cl. The organic layers were extracted using Et_2O, washed with brine, dried over Na_2SO_4 and concentrated *in vacuo*.

General procedure 3: TMS deprotection

K_2CO_3 (2.5 eq.) was added to a solution of the appropriate alkyne (1.0 eq.) in MeOH (0.1 M). The reaction was stirred at RT for 20 h before the solvent was evaporated *in vacuo*. The residue was dissolved in EtOAc and aq. HCl (1.0 M) added. The layers were separated, and the aqueous phase was extracted with EtOAc. The combined organics were washed with brine, dried over Na_2SO_4, filtered and concentrated *in vacuo*.

General procedure 4: Jones oxidation

Jones reagent (4.0 eq., 2.0 M CrO_3 in aq. H_2SO_4) was added dropwise to a solution of the appropriate alcohol (1.0 eq.) in acetone (0.4 M). The reaction was stirred at RT for 20 h before H_2O and CH_2Cl_2 were added. The layers were separated, and the aqueous phase was extracted with CH_2Cl_2. The combined organics were washed with brine, dried over Na_2SO_4, filtered, and concentrated *in vacuo*.

9.3 Compound preparations

9-(3-(Pent-4-yn-1-yl)-3*H*-diazirin-3-yl)nonanoic acid – Palmitic acid photoaffinity probe (1)

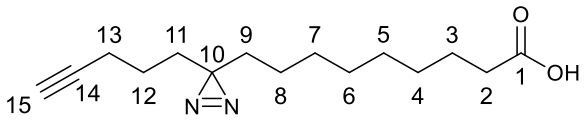

Ketone **28** (217 mg, 0.861 mmol) was dissolved in anhydrous MeOH (2 mL) and the mixture was cooled to 4 °C. Ammonia (g) was condensed into the reaction until it was fully saturated, and the mixture was stirred at 4 °C for 3 h. A solution of hydroxylamine-*O*-sulfonic acid (214 mg, 1.89 mmol) in anhydrous MeOH (1 mL) was added and the mixture was stirred for 30 min at 4 °C and overnight at room temperature. The solution was filtered and washed with MeOH (5 mL). NEt_3 (1.6 mL, 1.7 mmol) was added to the filtrate and the solvent was evaporated to a minimum volume. The residue was redissolved in MeOH (5 mL) and NEt_3 (1.6 mL, 1.7 mmol) and I_2 (~500 mg) were added in portions untilto give a persistent brown colour. The solvent was evaporated, and H_2O was added. The mixture was acidified with aq. HCl (1 mL, 1.0 M) and diluted with EtOAc. The layers were separated, and the aqueous phase extracted with EtOAc. The combined organics were washed with brine, dried over Na_2SO_4, filtered and concentrated *in vacuo*. Purification via flash column chromatography (eluent EtOAc/Pentane/AcOH, 9:1:0.1) gave probe **1** (45.4 mg, 20%) as a white solid. **^{1}H NMR** (500 MHz, $CDCl_3$) δ 2.28 (m, 4H, H_2 and H_{11}), 2.09 (td, J = 6.9, 2.6 Hz, 2H, H_{13}), 1.88 (t, J = 2.6 Hz, 1H, H_{15}), 1.54-range (m, 4H, H_9 and H_{12}), 1.47 – 1.39 (m, 2H, H_3), 1.32 – 1.13 (m, 8H, H_4, H_5, H_6 and H_7), 1.07 – 0.94 (m, 2H, H_8); **^{13}C NMR** (125 MHz, $CDCl_3$) δ 180.1 (C_1), 83.6 (C_{14}), 77.4 (C_{10}), 69.0 (C_{15}), 34.2 (C_{11}), 33.0 (C_9), 32.0 (C_2), 29.3 (C_4), 29.2 (C_6), 29.1 (C_5), 28.6 (C_7), 24.8 (C_3), 23.9 (C_8), 22.9 (C_{12}), 18.1 (C_{13}); **LRMS** (ESI$^+$) $C_{15}H_{24}N_2O_2$ $[M+H]^+$ 265.19, found 265.21. Characterisation data is consistent with the literature.[138]

Palmitoyl-CoA photoaffinity probe (2)

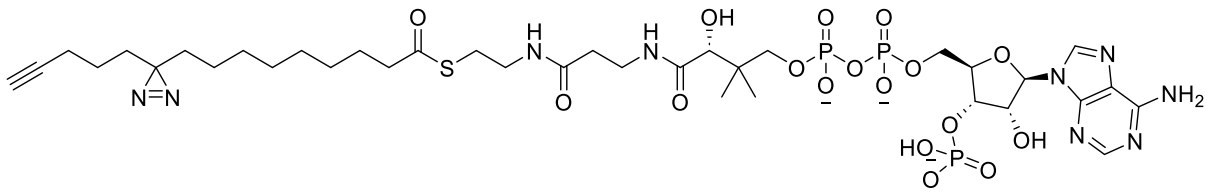

A solution of CDI (22 mg, 0.136 mmol) in CH_2Cl_2 (1 mL) was added to a stirring solution of **1** (32.8 mg, 0.124 mmol) in anhydrous THF (2 mL). the reaction as allowed to stir for 30 min. The solvent was removed *in vacuo* and the solids were resuspended in anhydrous THF (2 mL) under N_2 and added to a degassed solution of coenzyme A (98 mg, 0.124 mmol) in aq. $NaHCO_3$ (4 mL, 0.5 M). The reaction was stirred for 4 h at RT. Solvents were removed *in vacuo*. Purification via reverse phase column chromatography (eluent 0-30% MeCN in H_2O) afforded **2** (25 mg, 20%) as a white solid. **mp** ($CHCl_3$) 143-146 °C; **^{1}H NMR** (600 MHz, DMSO-d_6) δ 7.58 (ddd, J = 5.7, 3.5, 1.1 Hz, 1H), 7.48 – 7.41 (m, 1H), 7.09 – 6.99 (m, 4H), 5.91 (t, J = 6.3 Hz, 1H), 4.88 – 4.59 (m, 3H), 4.25 (t, J = 25.3 Hz, 2H), 4.02 (m, 6H), 3.88 – 3.74 (m, 4H), 3.49 – 3.12 (m, 8H), 2.76 (d, J = 7.9 Hz, 2H), 2.33 – 2.24 (m, 2H), 1.87 (m, 13H), 0.99 – 0.90 (m, 3H), 0.74 – 0.65 (m, 3H); **^{13}C NMR** (151 MHz, DMSO-d_6) δ 200.37, 172.23, 170.66, 155.99, 152.67, 149.71, 142.85, 139.24, 127.18, 122.04, 121.42, 121.38, 118.85, 117.82, 111.67, 79.17, 79.16, 78.95, 78.73, 42.13, 40.06, 39.94, 39.80, 39.66, 39.52, 39.38, 39.24, 39.10, 38.62, 36.34, 35.21, 34.88, 23.37, 21.55, 18.97; **LRMS** (ESI^-) $[M-H]^-$ 1010.8, found 1010.8 ; **HRMS** calc. for $C_{36}H_{55}N_9O_{17}P_3S^{-3}$ requires 1010.7555, found 1010.7553.

3-((9-(3-(pent-4-yn-1-yl)-3H-diazirin-3-yl)nonanoyl)oxy)-4-(trimethylammonio)butanoate - Palmitoyl-carnitine photoaffinity probe (3)

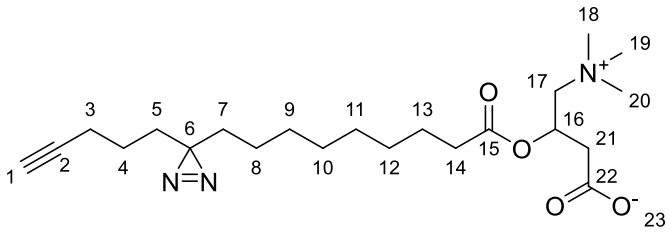

Oxalyl chloride (380 µL, 10.5 mmol) and DMF (10 µL) were added to probe **1** (100 mg, 0.376 mmol) and the reaction was stirred for 1 h at RT. Excess oxalyl chloride was removed *in vacuo* and the acid chloride was added dropwise to a solution of *L*-carnitine (60 mg, 0.37 mmol) in TFA (635 µL). The mixture was stirred in the dark at RT overnight. The reaction was quenched with H_2O (100 µL) and concentrated *in vacuo*. Purification via reverse phase column chromatography (eluent 0-30% MeCN in H_2O) afforded probe **3** (65.9 mg, 43%) as a white solid. **mp** ($CHCl_3$) 113-116 °C; **^{1}H NMR** (600 MHz, DMSO-d_6) δ 4.79-range (m, 1H, H_{16}), 3.01 – 2.84 (m, 2H, H_{17}), 2.37 (s, 9H, H_{18}, H_{19}, H_{20}), 1.81 (dd, *J* = 15.8, 4.4 Hz, 1H, $H_{21'}$), 1.63 – 1.51 (m, 3H, $H_{21''}$, H_3), 1.41 (t, *J* = 2.7 Hz, 1H, H_1), 1.34 (td, *J* = 6.9, 2.7 Hz, 2H, H_5), 0.81 (p, *J* = 7.2 Hz, 2H, H_4), 0.70 – 0.65 (m, 2H, H_7), 0.59 – 0.54 (m, 2H, H_{14}), 0.53 – 0.44 (m, 10H, H_9, H_{10}, H_{11}, H_{12}, H_{13}), 0.30 (t, *J* = 7.3 Hz, 2H, H_8); **^{13}C NMR** (151 MHz, DMSO-d_6) δ 166.6 (C_{15}), 164.8 (C_{22}), 74.7 (C_6), 60.6 (C_1), 60.6 (C_{17}), 58.5 (C_{16}), 45.1 (C_{18}, C_{19}, C_{20}), 31.9 (C_{21}), 25.7 (C_7), 24.3 (C_{14}), 23.3 (C_5), 20.8 (C_9), 20.7 (C_{10}), 20.7 (C_{11}), 20.6 (C_{12}), 19.8 (C_{13}), 16.2 (C_8), 15.3 (C_4), 9.0 (C_3); **LRMS** (ESI^+) $[M+H]^+$ 408.2, found 408.3; **HRMS** calc. for $C_{22}H_{37}N_3O_4^+$ $[M+H]^+$ requires 407.2784, found 407.2801.

Palmitic acid photocatalytic probe (4)

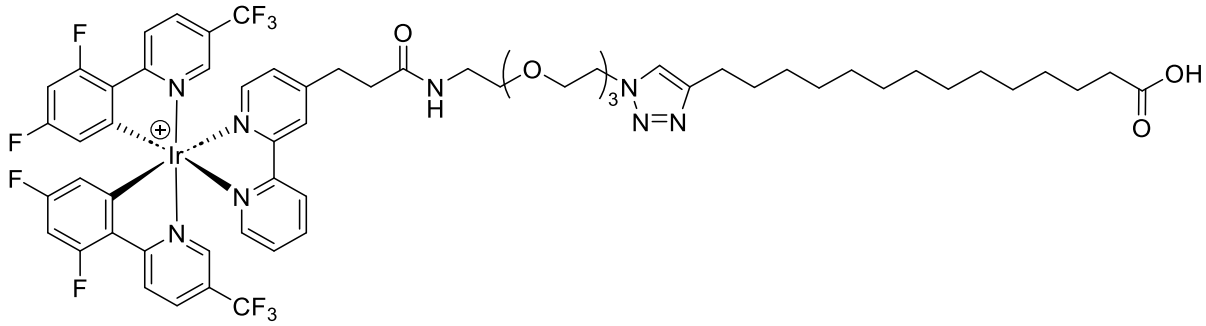

Azide **34** (97.5 mg, 0.075 mmol), alkyne **33** (18.93 mg, 0.08 mmol) and DIPEA (60 µL, 0.38 mmol) were combined in MeCN (0.75 mL). To this mixture was added a freshly prepared suspension of copper (II) sulfate (47 mg, 0.19 mmol) and sodium ascorbate (149 mg, 0.750 mmol) in water (1.5 mL) which instantly resulted in a yellow solution. This reaction mixture was stirred at RT for 16 h. The solvent was removed *in vacuo*. Purification via flash column chromatography (eluent CH_2Cl_2/MeOH, 7:3) gave **4** (42.3 mg, 40%) as a yellow oil. $\boldsymbol{\nu_{max}}$ (film) 3283 (N−H), 2867, 2851, 1695 (C=O), 1472, 1410 (C−O−H), 1330; **^{1}H NMR** (500 MHz, DMSO-d_6) δ 9.45 – 9.27 (m, 2H), 8.51 – 8.43 (m, 3H), 8.04 (m, 3H), 7.71 (dd, *J* = 9.4, 5.6 Hz, 3H), 7.61 (s, 1H), 7.52 (d, *J* = 8.7 Hz, 2H), 7.47 (d, *J* = 5.7 Hz, 1H), 7.30 (d, *J* = 5.7 Hz, 1H), 6.64 (td, *J* = 9.1, 2.8 Hz, 3H), 5.63 (ddd, *J* = 7.5, 4.9, 2.2 Hz, 3H), 4.50 (dt, *J* = 10.0, 5.1 Hz, 4H), 3.84 (dt, *J* = 6.9, 5.0 Hz, 4H), 3.64 – 3.51 (m, 16H), 3.23 (t, *J* = 7.3 Hz, 3H), 2.70 (q, *J* = 6.3 Hz, 8H), 2.36 – 2.26 (m, 4H), 1.64 – 1.55 (m, 4H), 1.28 (m, 20H); **^{13}C NMR** (125 MHz, DMSO-d_6) δ 178.2, 176.6, 172.6, 168.3, 166.2, 164.4, 163.9, 162.1, 157.9, 155.9, 155.5, 155.2, 155.0, 149.7, 149.2, 145.3, 136.8, 129.7, 128.7, 127.2, 126.7, 126.4, 126.2, 124.0, 122.8, 122.4, 122.1, 120.9, 114.4, 100.4, 70.9, 70.8, 70.8, 70.6, 70.0, 69.9, 50.5, 39.5, 35.6, 32.3, 31.9, 30.0, 29.4, 26.0, 25.3, 25.1, 23.0, 21.9; **^{19}F NMR** (376 MHz, DMSO-d6) δ −62.68 (d, *J* = 41.0 Hz), –71.87 (d, *J* = 714.1 Hz), –101.42 (ddt, *J* = 46.8, 12.6, 8.4 Hz), –105.88 (m); **LRMS** (ESI$^+$) $[M+H]^+$ 1390.34, found 1390.46.

Methyl 10-(methoxy(methyl)amino)-10-oxodecanoate (14)

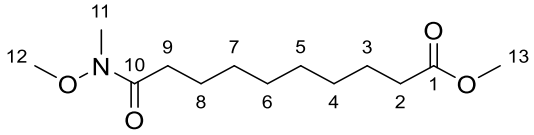

NEt_3 (8.0 mL, 55 mmol) and HATU (10.5 g, 27.7 mmol) were added to a solution of monomethyl sebacate (3.0 g, 13 mmol) and *N,O*-dimethylhydroxylamine hydrochloride (1.62 g, 16.6 mmol) in anhydrous CH_2Cl_2 (50 mL) at 0 °C and stirred for 1 h at 0 °C. The reaction was warmed to room temperature and stirred overnight. The reaction was diluted with EtOAc, and the combined organics were washed with aq. HCl (1.0 M), satd aq. brine, dried over Na_2SO_4 and concentrated *in vacuo*. Purification via flash column chromatography (eluent EtOAc/Pentane, 9:1) gave amide **14** (3.122 g, 87%) as a colourless oil. $\boldsymbol{\nu_{max}}$ (film) 2932, 1775, 1740 (C=O ester), 1463, 1417, 1384, 1321, 1195 (C-O), 1174, 1114; **^{1}H NMR** (500 MHz, $CDCl_3$) δ 3.62 (s, 3H, H_{12}), 3.58 (s, 3H, H_{13}), 3.12 (s, 3H, H_{11}), 2.35 (t, J = 7.6 Hz, 2H, H_9), 2.24 (s, 3H, H_2), 1.62 – 1.50 (m, 4H, H_3 and H_8), 1.29 – 1.21 (m, 8H, H_4, H_5, H_6 and H_7); **^{13}C NMR** (151 MHz, $CDCl_3$) δ 175.2 (C_{10}), 174.7 (C_1), 61.5 (C_{12}), 51.8 (C_{13}), 34.4 (C_2), 32.5 (C_{11}), 32.2 (C_9), 29.7 (C_4, C_7), 29.6 (C_5/C_6), 29.4 (C_5/C_6), 25.3 (C_3), 25.0 (C_8); **LRMS** (ESI$^+$) $[M+Na]^+$ 282.2, found 282.2; **HRMS** (ESI+) $[M+H]^+$ requires 260.1856; found 260.1854.

10-(Methoxy(methyl)amino)-10-oxodecanoic acid (15)

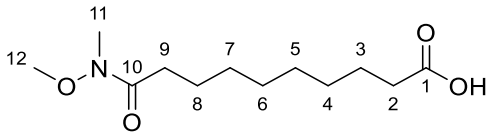

A solution of aq. NaOH (1.0 M, 16 mL) was added to a solution of ester **14** (3.122 g, 12.04 mmol) in MeOH (100 mL) and the mixture was stirred at room temperature for 16 h. Upon completion, the solvent was removed in vacuo and the resulting residue resuspended in EtOAc. The reaction mixture

was acidified to pH 3 and extracted using EtOAc, washed with brine, dried over Na_2SO_4 and concentrated *in vacuo*. Purification via flash column chromatography (eluent EtOAc/Pentane, 9:1) gave carboxylic acid **15** (1.6483 g, 56%) as a yellow oil. $\boldsymbol{\nu_{max}}$ (film) 3018 (O−H), 2855, 1729 (C=O amide), 1709, 1626, 1463, 1417, 1390, 1181 (C−O), 1114; **^{1}H NMR** (500 MHz, $CDCl_3$) δ 3.64 (s, 3H, H_{12}), 3.14 (s, 3H, H_{11}), 2.37 (t, J = 7.6 Hz, 2H, H_9), 2.28 (t, J = 7.5 Hz, 3H, H_2), 1.61 – 1.56 (m, 4H, H_3 and H_8), 1.31 – 1.27 (m, 8H, H_4, H_5, H_6, H_7); **^{13}C NMR** (125 MHz, $CDCl_3$) δ 179.3 (C_1), 175.3 (C_{10}), 61.6 (C_{12}), 34.3 (C_2), 32.5 (C_{11}), 32.2 (C_9), 29.7 (C_4), 29.5 (C_7), 29.4 (C_5/C_6), 29.3 (C_5/C_6), 25.0 (C_3), 24.9 (C_8); **LRMS** (ESI^-) $[M\text{-}H]^-$ 244.2, found 244.3; **HRMS** (ESI^+) $C_{12}H_{23}NO_4^+$ $[M+H]^+$ requires 246.1627, found 246.1702.

10-Oxopentadecanoic acid (16)

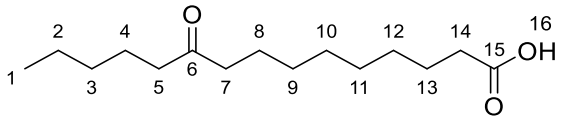

Pentyl magnesium bromide (250 μL, 0.504 mmol, 2.0 M in THF) was added to a solution of amide **15** (51 mg, 0.210 mmol) in anhydrous THF (1 mL) at –78 °C under an argon atmosphere. The mixture was allowed to warm back up to RT and stirred overnight. The reaction was quenched with satd. NH_4Cl and extracted with EtOAc. The combined organic layers were dried over Na_2SO_4, filtered and concentrated *in vacuo*. Purification via flash column chromatography (eluent Pentane/EtOAc, 95:5) afforded ketone **16** (39.3 mg, 73%) as a colourless oil. **^{1}H NMR** (400 MHz, $CDCl_3$) δ 2.36 (m, 6H, H_5, H_7, H_{14}), 1.69 – 1.49 (m, 6H, H_4, H_8, H_{13}), 1.33 – 1.25 (m, 12H, H_2, H_3, H_9, H_{10}, H_{11}, H_{12}), 0.90 – 0.87 (m, 3H, H_1); **LRMS** (ESI^-) $[M\text{-}H]^-$ 255.2, found 255.1; **HRMS** (ESI^-) $C_{15}H_{27}O_3^-$ $[M\text{-}H]^-$ requires 255.3860, found 255.3858.

10-Oxo-15-(trimethylsilyl)pentadec-14-ynoic acid (17)

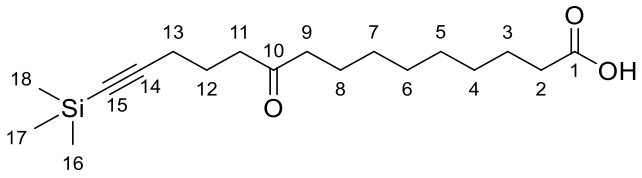

Following general procedure 1, magnesium (250 mg, 10.3 mmol), I_2 (10 mg), 1,2-dibromoethane (0.3 mL) and (5 chloropent-1-yn-1-yl)trimethylsilane (1.0 mL, 5.7 mmol) were reacted in anhydrous THF (5 mL) to form the Grignard reagent. This solution was then cooled to –78 °C and reacted with amide **15** (368 mg, 1.50 mmol) in anhydrous THF (1 mL). Purification via flash column chromatography (eluent EtOAc/Pentane, 9:1) gave **17** (435.2 mg, 89%) as a yellow oil. $\boldsymbol{\nu_{max}}$ (film) 3275, 3056 (O-H), 2936, 2857, 2174, 1764 (C=O acid), 1639, 1541, 1410; **^{1}H NMR** (500 MHz, $CDCl_3$) δ 2.52 (t, *J* = 7.2 Hz, 2H, H_{11}), 2.39 (t, *J* = 7.5 Hz, 2H, H_9), 2.33 (t, *J* = 7.5 Hz, 2H, H_2), 2.24 (t, *J* = 6.9 Hz, 2H, H_{13}), 1.75 (p, *J* = 7.1 Hz, 2H, H_{12}), 1.67 – 1.50 (m, 4H, H_3 and H_8), 1.36 – 1.20 (m, 8H, H_4, H_5, H_6 and H_7), 0.13 (s, 9H, H_{16}, H_{17} and H_{18}); **^{13}C NMR** (125 MHz, $CDCl_3$) δ 211.0 (C_{10}), 180.0 (C_1), 106.5 (C_{15}), 85.5 (C_{14}), 43.1 (C_{11}), 41.2 (C_9), 34.1 (C_2), 29.3 (C_4), 29.3 (C_6), 29.2 (C_5), 29.1 (C_7), 24.8 (C_3), 24.0 (C_8), 22.5 (C_{12}), 19.3 (C_{13}), -0.0 (C_{16}, C_{17}, C_{18}); **LRMS** (ESI^-) $[M-H]^-$ 323.2, found 323.2; **HRMS** (ESI^-) calc. for $C_{18}H_{31}O_3Si^-$ $[M-H]^-$ requires 323.2048, found 323.2047.

10-((*Tert*-butyldimethylsilyl)oxy)decanoic acid (19)

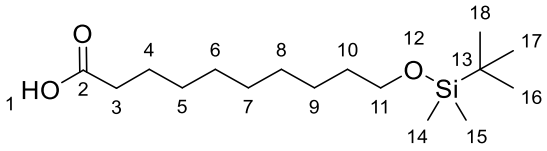

Tert-butyldimethylsilyl chloride (442 mg, 2.93 mmol) was added to a solution of 10-hydroxydecanoic acid (500 mg, 2.66 mmol) and imidazole (397 mg, 5.84 mmol) in DMF (5 mL) at 0 °C and stirred for 1 h, under argon. The reaction was quenched with satd. aq. NH_4Cl and the mixture

was extracted using Et_2O. The combined organic layers were washed with brine, dried over Na_2SO_4 and concentrated *in vacuo*. Purification via flash column chromatography (eluent Pentane/EtOAc, 5:95) gave acid **19** (482.8 mg, 60%) as a colourless oil. **^{1}H NMR** (400 MHz, $CDCl_3$) δ 3.55 (t, *J* = 6.6 Hz, 2H, H_{11}), 2.26 (q, *J* = 7.1 Hz, 2H, H_3), 1.57 (p, *J* = 7.5 Hz, 2H, H_4), 1.44 (q, *J* = 6.7 Hz, 2H, H_{10}), 1.24 (m, 10H, H_5, H_6, H_7, H_8, H_9), 0.84 (s, 9H, H_{16}, H_{17}, H_{18}), -0.01 (s, 6H, H_{14}, H_{15}); **^{13}C NMR** (101 MHz, $CDCl_3$) δ 178.4 (C_2), 63.3 (C_{11}), 34.3 (C_3), 31.6 (C_{10}), 29.5 (C_5), 29.4 (C_7), 29.3 (C_8), 29.2 (C_6), 26.0 (C_{16},C_{17},C_{18}) 25.8 (C_9), 24.9 (C_4), 18.4 (C_{13}), -5.2 (C_{12},C_{14}); **LRMS** (ESI$^-$) $[M-H]^-$ 301.2, found 301.3. Characterisation data is consistent with the literature.[145,146]

10-((*Tert*-butyldimethylsilyl)oxy)decan-1-ol (20)

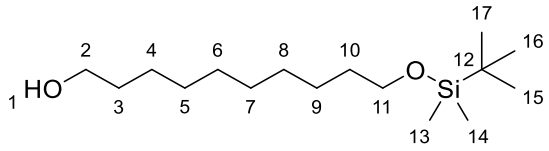

$LiAlH_4$ (1.94 mL, 1.94 mmol, 1.0 M in THF) was slowly added to a solution of acid **19** (36 mg, 1.48 mmol) in anhydrous THF (3 mL) at 0 °C. The reaction was allowed to warm to RT and stirred for 4 h. Upon completion, the reaction mixture cooled to 0 °C and quenched with H_2O (5 mL). Sulphuric acid (10 M) was added slowly until the precipitated solid was dissolved. The mixture was then extracted using EtOAc, washed with brine, filtered and concentrated *in vacuo* to afford **20** (338.9 mg, 93%) as a colourless oil. **^{1}H NMR** (400 MHz, $CDCl_3$) δ 3.61 (dt, *J* = 17.6, 6.7 Hz, 4H, H_2, H_{11}), 1.60 – 1.52 (m, 4H, H_3, H_{10}), 1.38 – 1.26 (m, 12H, H_4, H_5, H_6, H_7, H_8, H_9), 0.89 (s, 9H, H_{15}, H_{16}, H_{17}), 0.04 (s, 6H, H_{13}, H_{14}); **^{13}C NMR** (101 MHz, $CDCl_3$) δ 63.5 (C_2/C_{11}), 63.2 (C_2/C_{11}), 33.0 (C_3), 32.9 (C_{10}), 29.7 (C_5), 29.7 (C_7), 29.6 (C_6), 29.5 (C_8), 26.1 (C_{15},C_{16},C_{17}), 25.9 (C_9), 25.8 (C_4), -5.1 (C_{13},C_{14}); **LRMS** (ESI$^+$) $[M+H]^+$ 289.3, found 289.3. Characterisation data is consistent with the literature.[147,148]

10-((*Tert*-butyldimethylsilyl)oxy)decyl 4-methylbenzenesulfonate (21)

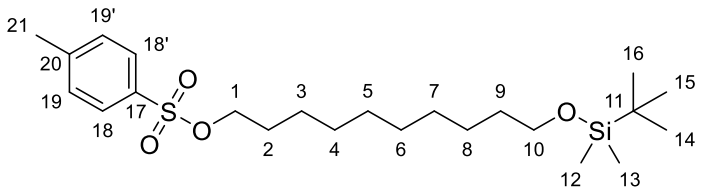

NEt_3 (466 µL, 3.36 mmol) and tosyl chloride (320 mg, 1.68 mmol) were added to a solution of alcohol **20** (338 mg, 1.12 mmol) in CH_2Cl_2 (5 mL) at 0 °C. The mixture was stirred for 12 h, quenched with $NaHCO_3$ (5 mL), and extracted with EtOAc. The combined organics were dried over $MgSO_4$, filtered and concentrated *in vacuo.* Purification via flash column chromatography (eluent Pentane/EtOAc, 95:5) afforded tosylate **21** (431.4 mg, 87%) as a white solid. **^{1}H NMR** (400 MHz, $CDCl_3$) δ_H 7.96 – 7.70 (m, 2H, H_{18}, $H_{18'}$), 7.39 (m, 2H, H_{19}, $H_{19'}$), 4.00 (m, 2H, H_1), 3.59-range (m, 2H, H_{10}), 2.53 – 2.36 (s, 3H, H_{21}), 2.12 – 1.92 (m, 2H, H_2), 1.68 – 1.41 (m, 2H, H_9), 1.36 – 1.11 (m, 12H, H_3, H_4, H_5, H_6, H_7, H_8), 0.98 (s, 9H, H_{14}, H_{15}, H_{16}), 0.19 (s, 6H, H_{12}, H_{13}); **LRMS** (ESI^+) $[M+H]^+$ 443.3, found 443.2; **HRMS** (ESI^+) calc. for $C_{23}H_{43}O_4SSi^+$ $[M+H]^+$ requires 442.2573, found 442.2577. Characterisation data is consistent with the literature.[275]

(5-Iodopent-1-yn-1-yl)trimethylsilane (23)

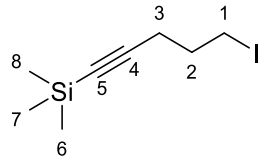

I_2 (2.08 g, 8.18 mmol) was added to a solution of triphenylphosphine (2.15 mg, 8.18 mmol), imidazole (557 mg, 8.18 mmol) and 5-(trimethylsilyl)pent-4-yn-1-ol (1.0 mL, 5.5 mmol) in anhydrous THF (10 mL) at 0 °C. The reaction was stirred at RT overnight. The mixture was extracted

with Et_2O and washed with satd. $Na_2S_2O_3$ and brine. The combined organics were dried over $MgSO_4$, filtered and concentrated *in vacuo*. Iodide **23** (1.182 g, 82%) was obtained as a colourless oil and used without further purification. **^{1}H NMR** (400 MHz, $CDCl_3$) δ 3.16 (t, *J* = 6.8 Hz, 2H, H_1), 2.23 (td, *J* = 6.9, 2.0 Hz, 2H, H_3), 1.87 (t, *J* = 6.8 Hz, 2H, H_2), 0.00 (s, 9H, H_6, H_7, H_8); **^{13}C NMR** (101 MHz, $CDCl_3$) δ 118.8 (C_4), 105.6 (C_5), 32.5 (C_2), 21.3 (C_3), 5.5 (C_1), 0.5 (C_6,C_7,C_8); **LRMS** (ESI^+) $[M+H]^+$ 266.0, found 266.1. Characterisation data is consistent with the literature.[151,152]

(5-(1,3-Dithian-2-yl)pent-1-yn-1-yl)trimethylsilane (24)

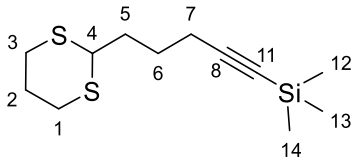

n-BuLi (730 µL, 1.83 mmol, 2.5 M in hexanes) was added dropwise to a solution of 1,3-dithiane (200 mg, 1.66 mmol) in anhydrous THF (3 mL) at −78 °C and stirred for 30 min. A solution of iodide **23** (mg, mmol) in anhydrous THF (2 mL) was added and the reaction was stirred at −78 °C for 3 h. The reaction was quenched with H_2O (5 mL) and extracted with CH_2Cl_2. The combined organics were dried over Na_2SO_4, filtered and concentrated *in vacuo* purification via flash column chromatography (eluent Pentane/Et_2O, 95:5) afforded dithiane **24** (171.65 mg, 40%) as a yellow oil. **ν_{max}** (film) 3047, 2317 (C≡C), 1377, 1261, 1077, 954, 941, 859, 793 (C−S), 739; **^{1}H NMR** (400 MHz, $CDCl_3$) δ 4.05 (t, *J* = 6.9 Hz, 1H, H_4), 2.93 – 2.77 (m, 4H, H_1,H_3), 2.25 (t, *J* = 7.0 Hz, 2H, H_7), 1.93 – 1.66 (m, 6H, H_2,H_5,H_6), 0.13 (s, 9H, H_{12},H_{13},H_{14}); **^{13}C NMR** (101 MHz, $CDCl_3$) δ 106.56 (C_8), 85.30 (C_{11}), 47.14 (C_4), 34.52 (C_5), 30.47 (C_1,C_3), 26.11 (C_2), 25.76 (C_6), 19.60 (C_7), 0.30 (C_{12},C_{13},C_{14}); **LRMS** (ESI^+) $[M+H]^+$ 259.1, found 259.0, **HRMS** (ESI^+) calc. for $C_{12}H_{22}S_2Si^+$ requires 258.0932, found 258.0948.

((9-(1,3-Dithian-2-yl)nonyl)oxy)(*tert*-butyl)dimethylsilane (27)

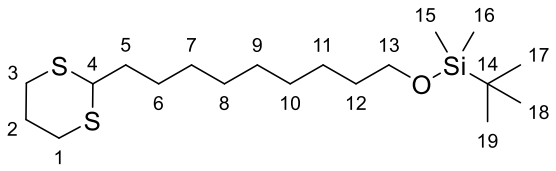

n-BuLi (368 µL, 0.92 mmol, 2.5 M in hexanes) was added dropwise to a solution of 1,3-dithiane (100 mg, 0.83 mmol) in anhydrous THF (1.5 mL) at −78 °C and stirred for 30 min. A solution of tosylate **21** (275 µL, 0.83 mmol) in anhydrous THF (1 mL) was added and the reaction was stirred at −78 °C for 3 h. The reaction was quenched with H_2O (2.5 mL) and extracted with CH_2Cl_2. The combined organics were dried over Na_2SO_4, filtered and concentrated *in vacuo* purification via flash column chromatography (eluent Pentane/Et_2O, 95:5) afforded dithiane **27** (54.2 mg, 17%) as a white solid. **mp** ($CHCl_3$) 52-54 °C; $\mathbf{\nu_{max}}$ (film) 3120, 3001, 2370, 2105, 1298, 1233 (C−O), 1111 (Si−O), 969, 870, 775 (C−S); **^{1}H NMR** (400 MHz, $CDCl_3$) δ 4.00 (t, *J* = 6.9 Hz, 1H, H_4), 3.55 (t, *J* = 6.7 Hz, 2H, H_{13}), 2.89 – 2.72 (m, 4H, H_1, H_3), 1.88 – 1.61 (m, 4H, H_2, H_5), 1.49 – 1.41 (m, 4H, H_6, H_{12}), 1.29 – 1.16 (m, 10H, H_7, H_8, H_9, H_{10}, H_{11}), 0.85 (s, 9H, H_{17}, H_{17}, H_{18}), 0.00 (s, 6H, H_{15}, H_{16}); **LRMS** (ESI^+) $[M+H]^+$ 376.2, found 376.2; **HRMS (**ESI^+) calc. for $C_{19}H_{40}OS_2Si$ $[M+H]^+$ requires 376.2290, found 376.2301.

10-Oxopentadec-14-ynoic acid (28)

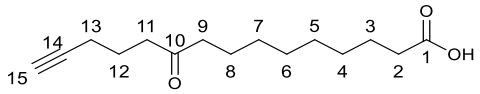

K_2CO_3 (426 mg, 3.28 mmol) was added to a solution of acid **17** (435.2 mg, 1.310 mmol) in MeOH (12 mL). The reaction was stirred at RT for 20 h before the solvent was evaporated *in vacuo*. The residue was dissolved in EtOAc and aq. HCl (1.0 M) added. The layers were separated, and the

aqueous phase was extracted with EtOAc. The combined organics were washed with brine, dried over Na_2SO_4, filtered and concentrated *in vacuo*. Purification via flash column chromatography (eluent EtOAc/Pentane, 9:1) gave ketone **28** (303.7 mg, 92%) as an off-white solid. **^{1}H NMR** (600 MHz, $CDCl_3$) δ 2.55 (t, *J* = 7.2 Hz, 2H, H_{11}), 2.40 (t, *J* = 7.4 Hz, 2H, H_9), 2.34 (t, *J* = 7.5 Hz, 2H, H_2), 2.23 (td, *J* = 6.8, 2.6 Hz, 2H, H_{13}), 1.96 (t, *J* = 2.7 Hz, 1H, H_{15}), 1.79 (p, *J* = 7.1 Hz, 2H, H_{12}), 1.66 – 1.53 (m, 4H, H_3 and H_8), 1.32 – 1.28 (m, 8H, H_4, H_5, H_6 and H_7); **^{13}C NMR** (151 MHz, $CDCl_3$) δ 210.7 (C_{10}), 178.5 (C_1), 83.7 (C_{14}), 69.0 (C_{15}), 43.0 (C_{11}), 41.0 (C_9), 33.8 (C_2), 29.2 (C_4), 29.1 (C_6), 29.0 (C_5), 29.0 (C_7), 24.7 (C_3), 23.8 (C_8), 22.3 (C_{12}), 17.8 (C_{13}); **LRMS** (ESI^-) $[M-H]^-$ 251.2 , found 251.2. Characterisation data is consistent with the literature.[138]

Ethyl 3-(4'-methyl-[2,2'-bipyridin]-4-yl)propanoate (33)

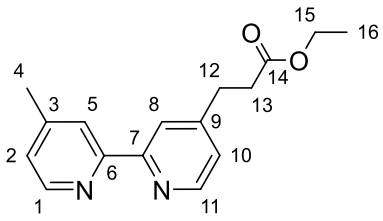

4,4'-Dimethyl-2,2'-bipyridyl (1.0 g, 5.4 mmol) was dissolved in anhydrous THF (15 mL) under N_2 in a flame-dried flask. The solution was cooled to −78 °C, and a solution of lithium diisopropylamide (5.97 mL, 5.97 mmol, 1.0 M in THF/Hexanes) was added. The reaction mixture was allowed to warm to RT for 1.5 h. This solution was cannulated into a solution of ethyl 2-bromoacetate (722 µL, 6.51 mmol) in anhydrous THF (5 ml) at – 78 °C under N_2. The reaction mixture was allowed to reach RT slowly overnight and quenched upon the addition of satd. aq. $NaHCO_3$. The mixture was extracted using EtOAc, dried over Na_2SO_4 and concentrated *in vacuo*. Purification via flash column chromatography (eluent CH_2Cl_2/MeOH, 95:5) to give bipyridine **33** (805.9 mg, 55%) as a yellow oil. **^{1}H NMR** (500 MHz, $CDCl_3$) δ 8.49 (dd, *J* = 5.0, 0.8 Hz, 1H, H_{11}), 8.45 (dd, *J* = 4.9, 0.8 Hz, 1H, H_1), 8.19 (dd, *J* = 1.7, 0.8 Hz, 1H, H_5), 8.15 (dt, *J* = 1.6, 0.8 Hz, 1H, H_8), 7.09 (dd, *J* = 5.0, 1.8 Hz,

1H, H_2), 7.06 (ddd, *J* = 5.0, 1.7, 0.9 Hz, 1H, H_{10}), 4.06 (q, *J* = 7.1 Hz, 2H, H_{15}), 2.96 (t, *J* = 7.7 Hz, 2H, H_{12}), 2.64 (t, *J* = 7.7 Hz, 2H, H_{13}), 2.36 (s, 3H, H_4), 1.16 (t, *J* = 7.2 Hz, 3H, H_{16}); **^{13}C NMR** (125 MHz, $CDCl_3$) δ 172.3 (C_{14}), 156.4 (C_7), 155.9 (C_6), 150.5 (C_9), 149.2 (C_{11}), 148.9 (C_1), 148.1 (C_3), 124.7 (C_2), 123.7 (C_{10}), 122.0 (C_8), 121.1 (C_5), 60.6 (C_{15}), 34.6 (C_{13}), 30.4 (C_{12}), 21.2 (C_4), 14.2 (C_{16}); **LRMS** (ESI^+) $[M+H]^+$ 271.1 , found 271.1. Characterisation data is consistent with the literature.[124]

5-(4'-Methyl-[2,2]bipyridinyl-4-yl)-pent-4-enoic acid (34)

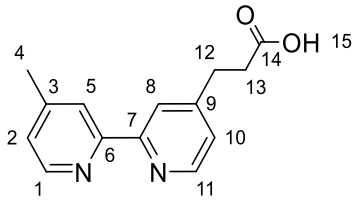

Ester **33** (282.6 mg, 1.045 mmol) was dissolved in THF (1.5 mL) before the addition of $LiOH.H_2O$ (90 mg, 2.091 mmol). The reaction mixture was stirred at RT for 16 h. Upon completion, the reaction was quenched upon the addition of satd. NH_4Cl (until pH 5-6). The mixture was extracted with EtOAc, dried over Na_2SO_4, and concentrated *in vacuo*. Purification via flash column chromatography (eluent CH_2Cl_2/MeOH, 80:20) afforded acid **34** (223.8 mg, 85%) as an off-white powder. $\boldsymbol{\nu_{max}}$ (film) 2922 (O−H), 2849, 2397, 1698 (C=O), 1597, 1558; **^{1}H NMR** (500 MHz, $CDCl_3$) δ 8.59 (dd, *J* = 9.1, 3.7 Hz, 2H, H_1 and H_{11}), 8.24 – 8.19 (m, 2H, H_5 and H_8), 7.24 – 7.16 (m, 2H, H_2 and H_{10}), 3.07 (t, *J* = 7.7 Hz, 2H, H_{12}), 2.85 (t, *J* = 7.9 Hz, 2H, H_{13}), 2.46 (s, 3H, H_4); **LRMS** (ESI^-) $[M-H]^-$ 241.1, found 241.3. Characterisation data is consistent with the literature.[124]

2-(2,4-Difluorophenyl)-5-(trifluoromethyl)pyridine (35)

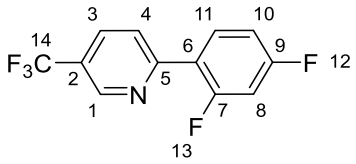

To a flame-dried microwave vial charged with a magnetic stir bar was added 2-bromo-5 (trifluoromethyl)pyridine (500 mg, 2.21 mmol) and (2,4-difluorophenyl)boronic acid (419 mg, 2.65 mmol) in 1,4-dioxane (6.7 mL) and the reaction was degassed with N_2 for 10 min. $Pd(dppf)Cl_2.CH_2Cl_2$ (33 mg, 0.044 mmol) was added, and the reaction was degassed for a further 10 min. A degassed solution of Cs_2CO_3 (2.522 g, 7.742 mmol) in H_2O (2.2 mL) was added and the reaction was sealed and heated to 100 °C for 20 h. Upon completion, the solvent was evaporated *in vacuo* and the resulting residue re-dissolved in EtOAc (8 mL), dried over Na_2SO_4, filtered, and concentrated *in vacuo*. Purification via flash column chromatography (eluent pentane/EtOAc, 95:5) gave ligand **35** (362.85 mg, 63%) as a light-yellow solid. **^{1}H NMR** (500 MHz, $CDCl_3$) δ 8.96 (dq, *J* = 2.5, 0.8 Hz, 1H, H_1), 8.09 (td, *J* = 8.9, 6.6 Hz, 1H, H_3), 8.03 – 7.96 (m, 1H, H_7), 7.91 (ddt, *J* = 8.3, 1.8, 0.8 Hz, 1H, H_4), 7.04 (dddd, *J* = 10.0, 7.7, 2.5, 1.0 Hz, 1H, H_{10}), 6.95 (ddd, *J* = 11.3, 8.7, 2.5 Hz, 1H, H_8); **^{13}C NMR** (125 MHz, $CDCl_3$) δ 164.1 (dd, *J* = 252.9, 12.1 Hz, C_9), 161.1 (dd, *J* = 253.6, 12.0 Hz, C_{11}), 156.0 (C_5), 146.7 (q, *J* = 4.2 Hz, C_1), 133.9 (q, *J* = 3.4 Hz, C_3), 132.6 (dd, *J* = 9.9, 4.1 Hz, C_7), 123.4 (q, *J* = 273.1 Hz, C_{14}), 125.3 (q, *J* = 33.2 Hz, C_2), 123.8 (d, *J* = 10.9 Hz, C_4), 122.6 (dd, *J* = 11.1, 3.9 Hz, C_6), 112.4 (dd, *J* = 21.2, 3.4 Hz, C_8), 104.6 (dd, *J* = 25.5, 1.0 Hz, C_{10}); **HRMS** (ESI+) calc. for $C_{12}H_7F_5N^+$ $[M+H]^+$ requires 260.0493, found 260.0492. Characterisation data is consistent with the literature.[154,155]

Tetradecane-1,14-diol (37)

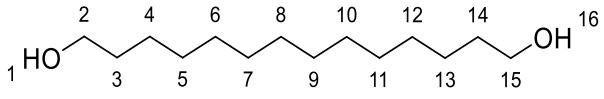

$LiAlH_4$ (1.0 M, 38 mL, 38.7 mmol) was added to a solution of 1,14-tetradecanedioic acid (5.0 g, 19 mmol) in anhydrous THF (195 mL) at 0 °C. The reaction was allowed to warm to RT and stirred for 20 h. Upon completion, the reaction mixture was diluted with Et_2O (100 mL) and cooled to 0 °C. H_2O (1.5 mL) was added slowly, followed by 15% aq. NaOH (1.5 mL) and H_2O (4.5 mL). The mixture was warmed back up to RT and stirred for 15 min. $MgSO_4$ was added and the mixture was stirred for a further 15 min. The mixture was filtered and concentrated *in vacuo* to afford alcohol **37** (3.783 g, 85%) as a white solid. The product was used without further purification. **^{1}H NMR** (500 MHz, $CDCl_3$) δ_H 4.30 (t, *J* = 5.2 Hz, 2H, H_1 and H_{16}), 3.36 (td, *J* = 6.6, 5.1 Hz, 4H, H_2 and H_{15}), 1.39 (p, *J* = 7.0 Hz, 4H, H_3 and H_{14}), 1.24 (s, 20H, H_4, H_5, H_6, H_7, H_8, H_9, H_{10}, H_{11}, H_{12} and H_{13}); **^{13}C NMR** (125 MHz, $CDCl_3$) δ 60.7 (C_2, C_{15}), 32.5 (C_3, C_{14}), 29.1 (C_8, C_9), 29.0 (C_7, C_{10}), 29.0 (C_6, C_{11}), 28.9 (C_5, C_{12}), 25.5 (C_4, C_{13}); **HRMS** (ESI^+) calc. for $C_{14}H_{31}O_2^+$ $[M+H]^+$ requires 231.2318, found 231.2319. Characterisation data is consistent with the literature.[156,157]

14-Bromotetradecan-1-ol (38)

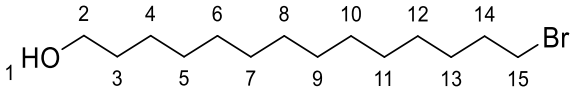

HBr (48% in H_2O, 5.5 mL) was added to a suspension of alcohol **37** (500 mg, 2.17 mmol) in C_6H_{12} (6 mL). The biphasic mixture was heated to reflux for 10 h and then cooled to RT. The layers were separated, and the aqueous phase was extracted with CH_2Cl_2. The combined organic layers were washed with sat. aq. $NaHCO_3$, brine, dried over Na_2SO_4, filtered, and concentrated *in vacuo*. Purification via flash column chromatography (eluent Pentane/EtOAc, 95:5 then Pentane/EtOAc, 70:30) gave bromide **38** (329.5 mg, 52%) as a pale-yellow solid. **^{1}H NMR** (500 MHz, $CDCl_3$) δ 3.63 (2H, t, *J* = 6.6 Hz, H_2), 3.40 (2H, t, *J* = 6.9 Hz, H_{15}), 1.91 – 1.79 (2H, m, H_{14}), 1.56 (2H, dq, *J* = 7.9, 6.5 Hz, H_3), 1.45 – 1.25 (20H, m, H_4, H_5, H_6, H_7, H_8, H_9, H_{10}, H_{11}, H_{12} and H_{13}); **^{13}C NMR** (125

MHz, $CDCl_3$) δ 63.2 (C_2), 34.2 (C_{15}), 33.0 (C_3), 33.0 (C_{14}), 29.7 (C_7), 29.7 (C_{11}), 29.7 (C_9), 29.6 (C_5), 28.9 (C_6), 28.3 (C_{13}), 25.9 (C_4); **HRMS** (ESI^+) calc. for $C_{14}H_{30}BrO^+$ $[M+H]^+$ requires 293.2890, found 293.1783. Characterisation data is consistent with the literature.[156,158]

14-Bromotetradecanoic acid (39)

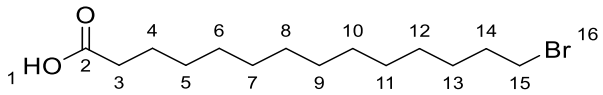

Following general procedure 2, Jones reagent (2.52 mL, 5.05 mmol, 2.0 M CrO_3 in aq. H_2SO_4) was added dropwise to a solution of alcohol **38** (370 mg, 1.26 mmol) in acetone (29 mL). Purification via column chromatography (eluent Pentane/EtOAc /AcOH, 90:10:0.1) gave acid **39** (301.2 mg, 78%) as a white solid. $\boldsymbol{\nu_{max}}$ (film) 3048 (O−H), 2851, 2798, 1677 (C=O); **^{1}H NMR** (500 MHz, $CDCl_3$) δ 3.41 (t, *J* = 6.9 Hz, 2H, H_{15}), 2.35 (t, *J* = 7.5 Hz, 2H, H_3), 1.85 (p, *J* = 7.0 Hz, 2H, H_{14}), 1.63 (p, *J* = 7.4 Hz, 2H, H_4), 1.42 (p, *J* = 7.2 Hz, 2H, H_{13}), 1.37 – 1.21 (m, 16H, H_5, H_6, H_7, H_8, H_9, H_{10}, H_{11} and H_{12}); **^{13}C NMR** (125 MHz, $CDCl_3$) δ 178.2 (C_2), 34.0 (C_{15}), 33.7 (C_3), 32.8 (C_{14}), 29.5 (C_{10}), 29.5 (C_8), 29.5 (C_{11}), 29.4 (C_5), 29.4 (C_9), 29.2 (C_6), 29.0 (C_7), 28.7 (C_{12}), 28.1 (C_{13}), 24.6 (C_4). Characterisation data is consistent with the literature.[159]

16-(*tert*-Butyldimethylsilyl)hexadec-15-ynoic acid (40)

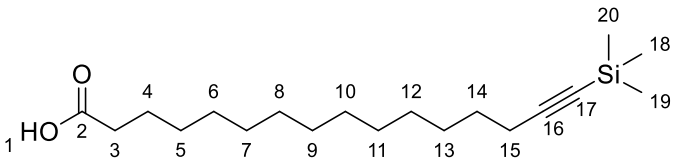

n-BuLi (5.05 mL, 8.079 mmol, 1.6 M) was added dropwise to a solution of (trimethylsilyl)acetylene (0.793 mL, 8.079 mmol) in anhydrous THF (5 mL) at −78 °C. The reaction was stirred at −78 °C for 1 h before HMPA (8 mL) was added and the reaction stirred for a further 30 min. A solution of

acid **39** (247.3 mg, 0.8079 mmol) in anhydrous THF (18 mL) was added dropwise and the reaction stirred at RT for 48 h. Upon completion, the reaction was quenched with aq. HCl (1.0 M, 10 mL). The layers were separated, and the aqueous phase was extracted with Et_2O and concentrated *in vacuo*. Purification via flash column chromatography (eluent Pentane/EtOAc/AcOH, 90:10:0.1) gave acid **40** (130.9 mg, 50%) as a white solid. **^{1}H NMR** (500 MHz, $CDCl_3$) δ 2.34 (d, *J* = 7.5 Hz, 2H, H_3), 2.21 (t, *J* = 7.2 Hz, 2H, H_{15}), 1.64 (q, *J* = 7.4 Hz, 2H, H_4), 1.55 – 1.43 (m, 2H, H_{14}), 1.29 – 1.25 (m, 18H, H_5, H_6, H_7, H_8, H_9, H_{10}, H_{11}, H_{12} and H_{13}), 0.14 (s, 6H, H_{18}, H_{19} and H_{20}); **^{13}C NMR** (125 MHz, $CDCl_3$) δ 177.9 (C_2), 108.0 (C_{17}), 90.3 (C_{16}), 84.4, 33.8 (C_3), 29.9 (C_9), 29.6 (C_8), 29.6 (C_5), 29.4 (C_{10}), 29.2 (C_6), 29.0 (C_7), 28.8 (C_{11}), 24.9 (C_4), 20.0 (C_{15}), 0.3 (C_{18}, C_{19}, C_{20}); **LRMS** (ESI^-) $[M\text{-}H]^-$ 323.3, found 323.2. Characterisation data is consistent with the literature.[159]

Hexadec-15-ynoic acid (31)

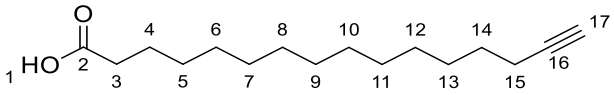

Following general procedure 3, K_2CO_3 (168 mg, 1.21 mmol) was added to a solution of acid **40** (151 mg, 0.487 mmol) in MeOH (4 mL). Purification via flash column chromatography (eluent Pentane/EtOAc/AcOH, 90:10:0.1) afforded alkyne **31** (85.8 mg, 70%) as a white solid. **^{1}H NMR** (500 MHz, $CDCl_3$) δ 2.35 (t, *J* = 7.5 Hz, 2H, H_3), 2.20 – 2.16 (m, 2H, H_{15}), 1.93 (t, *J* = 2.6 Hz, 1H, H_{17}), 1.67 – 1.60 (m, 2H, H_4), 1.57 – 1.48 (m, 2H, H_{14}), 1.27 (m, 18H, H_5, H_6, H_7, H_8, H_9, H_{10}, H_{11}, H_{12} and H_{13}); **^{13}C NMR** (125 MHz, $CDCl_3$) δ 180.7 (C_2), 84.8 (C_{16}), 68.2 (C_{17}), 34.3 (C_3), 29.7 (C_{10}), 29.6 (C_8), 29.5 (C_5), 29.4 (C_6, C_9, C_{11}), 29.2 (C_7), 29.2 (C_{12}), 28.9 (C_{13}), 28.6 (C_{14}), 24.8 (C_4), 18.8 (C_{15}); **HRMS** (ESI^-) calc. for $C_{15}H_{28}O_2^-$ $[M\text{-}H]^-$ requires 251.2017, found 251.2016. Characterisation data is consistent with the literature.[159]

Ir(dF-CF$_3$-ppy)$_2$Cl]$_2$-dimer (41)

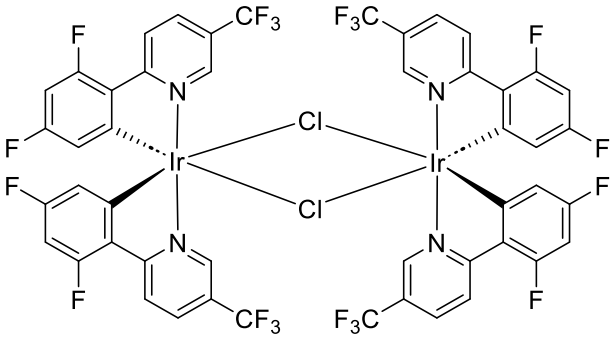

$IrCl_3.H_2O$ (190 mg, 0.683 mmol) and bipyridine **35** (362 mg, 1.40 mmol) were added to a flame-dried microwave vial, charged with a magnetic stir bar. The vial was evacuated and backfilled with argon three times. 2-Ethoxyethanol (8 mL) and H_2O (4 mL) were added, and the reaction solution was degassed for 30 min. The reaction was heated to 135 °C and stirred overnight. Upon completion, the reaction was cooled to RT and precipitation was observed. The precipitate was filtered and washed with H_2O. The yellow solid complex **41** (353.3 mg, 71%) was dried under airflow and used without further purification. **^{1}H NMR** (500 MHz, $CDCl_3$) δ 9.51 (d, *J* = 2.1 Hz, 4H), 8.46 (dd, *J* = 8.7, 3.0 Hz, 4H), 8.04 (dd, *J* = 8.5, 2.2 Hz, 4H), 6.43 (td, *J* = 8.9, 2.3 Hz, 4H), 5.07 (dd, *J* = 8.8, 2.3 Hz, 4H); **^{19}F NMR** (377 MHz, $CDCl_3$) δ -62.03, -103.48 (dt, *J* = 11.9, 8.8 Hz), -107.64 (td, *J* = 12.1, 3.2 Hz); **LRMS** (ESI^+) $[M+H]^+$ 1491.1, found 1491.0 Characterisation data is consistent with the literature.[124,276]

$[Ir(dF\text{-}CF_3\text{-}ppy)_2(NCMe)_2]^+PF_6$ (42)

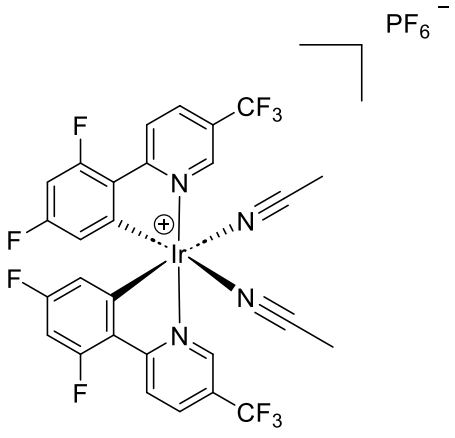

$AgPF_6$ (69.7 mg, 0.276 mmol) and complex **41** (200 mg, 0.1344 mmol) were added to a flame-dried microwave vial, charged with a magnetic stir bar. The vial was evacuated and backfilled with argon three times. Anhydrous and degassed CH_2Cl_2 (5 mL) and MeCN (1.7 mL) were added to the reaction mixture. The reaction mixture was heated at 55 °C for 20 h. Upon completion, the reaction mixture was cooled to room temperature and filtered through celite, to remove the AgCl. The solution was concentrated to give a yellow solid, which was partially dissolved in 1:1 CH_2Cl_2/Acetone. Pentane was added dropwise to afford a yellow precipitate. Complex **42** (146.5 mg, 58%) was obtained by filtration, as a yellow solid and used without further purification. **^{1}H NMR** (500 MHz, $CDCl_3$) δ 9.20 (d, J = 2.0 Hz, 2H), 8.46 (dd, *J* = 8.8, 3.1 Hz, 2H), 8.22 (dd, *J* = 8.7, 2.1 Hz, 2H), 6.51 (ddd, *J* = 12.4, 8.9, 2.3 Hz, 2H), 5.42 (dd, *J* = 8.3, 2.3 Hz, 2H), 2.45 (s, 6H); **^{19}F NMR** (377 MHz, $CDCl_3$) δ -62.35, -72.61 (d, *J* = 707.7 Hz), -102.57 (dt, *J* = 12.0, 8.5 Hz), -107.01 (td, *J* = 11.5, 6.4 Hz); **HRMS** (ESI^+) calc. for $C_{28}H_{16}F_{10}IrN_4^+$ $[M+H]^+$ requires 791.0840, found 791.0820. Characterisation data is consistent with the literature.[124]

Gen 2 Iridium catalyst (29)

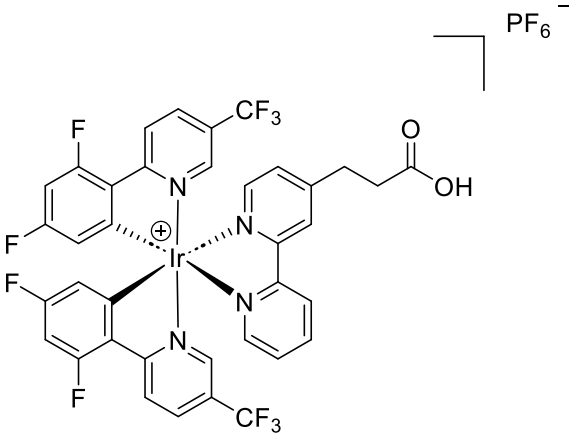

Reaction performed under N_2. Complex **42** (140 mg, 0.400 mmol) and bipyridine **34** (44.5 mg, 0.492 mmol) were dissolved in degassed CH_2Cl_2/EtOH (3:1) (2 mL). The reaction was stirred at 30 °C for 16 h in the dark, under N_2. The resulting solution was concentrated *in vacuo* onto silica.

Purification via flash column chromatography (eluent CH_2Cl_2/MeOH, 90:10) afforded complex **29** (161.2 mg, 95%) as a yellow oil. **^{1}H NMR** (500 MHz, DMSO-d_6) δ 8.86 – 8.81 (m, 2H), 8.52 – 8.40 (m, 4H), 7.83 (dd, *J* = 26.0, 5.7 Hz, 2H), 7.68 (s, 1H), 7.64 (dd, *J* = 5.8, 1.7 Hz, 1H), 7.58 (dd, 1H), 7.51 (s, 1H), 7.07 (ddd, *J* = 12.7, 9.4, 2.3 Hz, 2H), 5.78 (td, *J* = 8.5, 2.3 Hz, 2H), 3.07 (t, *J* = 7.5 Hz, 2H), 2.74 (t, *J* = 7.5 Hz, 2H), 2.58 (m, 2H); **LRMS** (ESI^+) $[M+H]^+$ 937.1, found 937.1; **HRMS** (ESI^-) calc. for $C_{45}H_{38}F_{10}IrN_8O_4^+$ $[M]^+$ requires 935.1184, found 935.1181. Characterisation data is consistent with the literature.[124]

Iridium-linker conjugate (43)

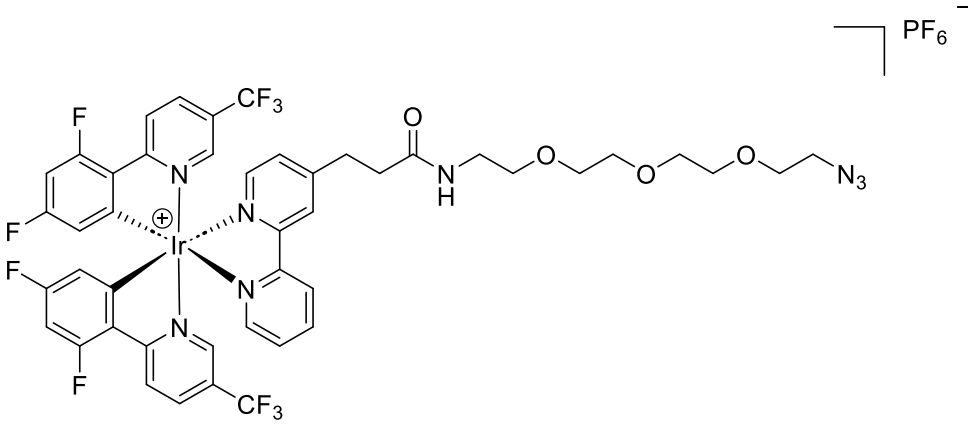

Complex **29** (161.2 mg, 0.1695 mmol) was dissolved in anhydrous MeCN (2 mL) followed by the addition of DMAP (5 mg, 0.03 mmol), 1-ethyl-3-(3-dimethylaminopropyl)carbodiimide hydrochloride (40 mg, 0.2034 mmol), NEt_3 (100 µL, 0.678 mmol), and 11-azido-3,6,9 trioxaundecan-1-amine (40 µL, 0.20 mmol). The reaction mixture was stirred overnight under N_2. The reaction mixture was diluted with EtOAc and the organic layers were washed with satd. aq. $NaHCO_3$, 0.1 M aq. HCl, brine, and dried over Na_2SO_4, then dried and concentrated *in vacuo*. Purification via flash column chromatography (eluent CH_2Cl_2/MeOH, 9:1) gave azide **43** (152.2 mg, 67%) as a yellow oil. **ν_{max}** (film) 3339 (N−H), 2155 (N=N=N), 1772 (C=O), 1265, 1204, 1107

(C−O); **^{1}H NMR** (500 MHz, DMSO-d_6) δ 8.74 – 8.70 (m, 1H), 8.68 (d, *J* = 1.7 Hz, 1H), 8.48 (ddd, *J* = 12.2, 8.7, 3.2 Hz, 1H), 8.10 – 8.01 (m, 1H), 7.74 (dd, *J* = 8.3, 5.6 Hz, 1H), 7.59 (dt, *J* = 1.9, 0.9 Hz, 1H), 7.52 – 7.48 (m, 1H), 7.34 (ddd, *J* = 5.6, 1.8, 0.8 Hz, 1H), 6.71 – 6.60 (m, 2H), 5.63 (ddd, *J* = 8.0, 4.1, 2.3 Hz, 1H), 3.71 – 3.60 (m, 13H), 3.52 (t, *J* = 5.5 Hz, 1H), 3.43 – 3.32 (m, 4H), 3.21 (td, *J* = 7.3, 2.6 Hz, 1H), 2.79 (h, *J* = 7.9 Hz, 1H), 2.69 (s, 2H), 1.61 (s, 5H); **^{13}C NMR** (125 MHz, DMSO-d_6) δ 175.1, 168.1 (d, *J* = 16.9 Hz), 165.0 (dd, *J* = 261.8, 12.4 Hz), 161.9 (d, *J* = 14.6 Hz), 155.4, 155.2, 149.9 (d, *J* = 13.5 Hz), 149.3, 148.4, 145.0, 136.7, 130.0 – 129.5 (m), 128.7, 127.3, 126.3 (d, *J* = 30.8 Hz), 126.0, 123.9 (d, *J* = 24.5 Hz), 122.6, 114.5 – 114.0 (m), 100.4 – 99.8 (m), 73.5, 70.6 (d, *J* = 5.7 Hz), 69.5 (d, *J* = 17.8 Hz), 69.2, 67.7, 50.3, 43.4, 37.9, 34.1, 32.1, 21.6; **LRMS** (ESI$^+$) $[M+H]^+$ 1151; **HRMS** (ESI$^+$) calc. for $C_{45}H_{38}F_{10}IrN_8O_4^+$ $[M]^+$ requires 1137.2481, found 1137.2483.

N-(3-Oxo-1-(4-(3-(trifluoromethyl)-3*H*-diazirin-3-yl)phenyl)-6,9,12-trioxa-2-azatetradecan-14-yl)-5-((3a*S*,4*S*,6a*R*)-2-oxohexahydro-1*H*-thieno[3,4-*d*]imidazol-4-yl)pentanamide (44)

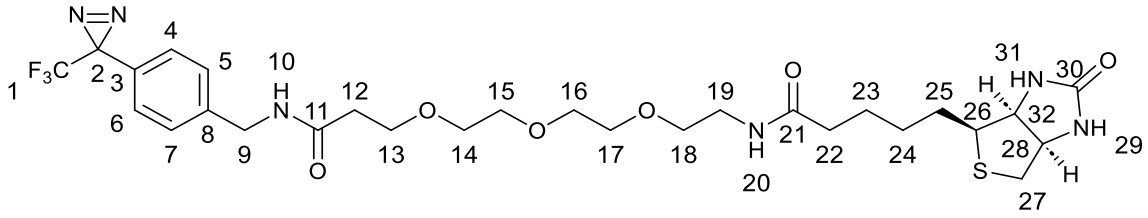

To a solution of (4-(3-(trifluoromethyl)-3*H*-diazirin-3-yl)phenyl)methanamine hydrochloride (100 mg, 0.397 mmol) in anhydrous DMF (2 mL) was added biotin-PEG3-NHS ester (216 mg, 0.397 mmol) and diisopropylethylamine (0.138 mL, 0.795 mmol). The mixture was stirred at RT overnight. The mixture was diluted with EtOAc and the combined organics were washed with brine, dried over Na_2SO_4 and concentrated *in vacuo*. Purification via flash column chromatography (eluent CH_2Cl_2/MeOH, 5:5) gave **44** (153.41 mg, 60%) as a white solid. $\boldsymbol{\nu_{max}}$ (film) 2964 (N-H), 2348, 1662

(C=O), 1032 (C-F); **^{1}H NMR** (500 MHz, $CDCl_3$) δ 8.41 (t, *J* = 6.0 Hz, 1H, H_{10}), 7.81 (t, *J* = 5.7 Hz, 1H, H_{20}), 7.40 – 7.36 (m, 2H, H_4 and H_6), 7.23 (m, 2H, H_5 and H_7), 6.40 (m, 1H, H_{29}/H_{31}), 6.34 (m, 1H, H_{29}/H_{31}), 4.30 (m, 3H, H_9 and H_{28}), 4.15 – 4.10 (m, 1H, H_{32}), 3.63 (t, *J* = 6.3 Hz, 2H, H_{13}), 3.53 – 3.46 (m, 8H, H_{14}, H_{15}, H_{16} and H_{17}), 3.38 (t, *J* = 6.0 Hz, 3H, H_{18}), 3.21 – 3.15 (m, 2H, H_{19}), 3.09 (ddd, *J* = 8.5, 6.1, 4.4 Hz, 1H, H_{26}), 2.81 (dd, *J* = 12.4, 5.1 Hz, 1H, H_{27}), 2.58 (d, *J* = 12.4 Hz, 1H, $H_{27f'}$), 2.38 (t, *J* = 6.3 Hz, 2H, H_{12}), 2.06 (t, *J* = 7.5 Hz, 2H, H_{22}), 1.65 – 1.56 (m, 1H, H_{23}), 1.55 – 1.41 (m, 3H, H_{23} and H_{24}, 1.35 – 1.25 (m, 2H, H_{25}); **^{13}C NMR** (125 MHz, $CDCl_3$) δ 172.1 (C_{21}), 170.3 (C_{11}), 162.7 (C_{30}), 142.2 (C_8), 128.0 (C_4 and C_6), 126.6 (C_5 and C_7), 121.9 (q, J = 275.4 Hz, C_1), 69.8 (C_{17}), 69.7 (C_{18}), 69.5 (C_{14}), 69.2 (C_{15} and C_{16}), 66.8 (C_{13}), 61.1 (C_{32}), 59.2 (C_{28}), 55.4 (C_{26}), 41.5 (C_9), 38.4 (C_{13} and C_{17}), 36.1 (C_{12}), 35.1 (C_{22}), 28.2 (C_{25}), 28.0 (C_{24}), 25.2 (C_{23}) – C_2 is masked by the $CDCl_3$ peak at ~77 ppm. Characterisation data is consistent with the literature.[124]

4-((*tert*-Butyldimethylsilyl)oxy)butan-1-ol (45)

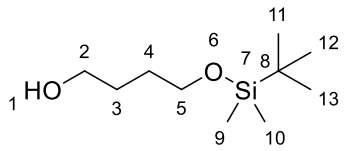

A solution of *tert*-butyldimethylsilyl chloride (428 mg, 2.62 mmol) was added to a solution of 1,4-butanediol (1.5 mL, 5.6 mmol) and imidazole (211 mg, 3.10 mmol) in anhydrous DMF (5 mL) at 0 °C and stirred for 1 h, under argon. The reaction was quenched with satd. aq. NH_4Cl and the mixture was extracted using EtOAc. The combined organics were washed with brine, dried over Na_2SO_4 and concentrated *in vacuo*. Purification via flash column chromatography (eluent Pentane/EtOAc, 1:1) gave alcohol **45** (717.1 mg, 62%) as a white solid. **^{1}H NMR** (400 MHz, $CDCl_3$) δ 3.64 – 3.50 (m, 4H, H_2,H_5), 3.25 (s, 1H, H_1), 1.62 – 1.50 (m, 4H, H_4, H_3), 0.84 (s, 9H, H_{11}, H_{12}, H_{13}), 0.00 (s, 6H, H_9, H_{10}); **^{13}C NMR** (101 MHz, $CDCl_3$) δ 63.2 (C_5), 62.4 (C_2), 29.8 (C_3), 29.7 (C_4), 25.9 (C_{11},C_{12},C_{13}),

18.2 (C_8), −5.5 (C_9,C_{10}); **LRMS** (ESI^+) $[M+H]^+$ 205.2, found 205.2. Characterisation data is consistent with the literature.[161]

4-((*tert*-Butyldimethylsilyl)oxy)butanal (46)

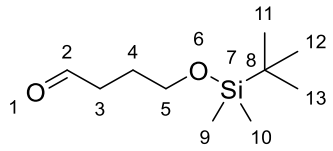

A solution of DMSO (213 µL, 3.01 mmol) in anhydrous CH_2Cl_2 (2 mL) was cooled to −78 °C in a flame-dried flask under N_2 and to this a solution of oxalyl chloride (186 µL, 1.46 mmol) in CH_2Cl_2 (2 mL) was slowly added and stirred for 10 mins. A solution of alcohol **45** (200 mg, 0.979 mmol) in CH_2Cl_2 (2 mL) was then slowly added, and the reaction was stirred for 1h at −78 °C. NEt_3 (641 µL, 4.60 mmol) was added and the mixture was then warmed gradually to RT. After 1 h the reaction was quenched with satd. aq. NH_4Cl. The organic layers were extracted using Et_2O, washed with brine, dried over Na_2SO_4 and concentrated *in vacuo*. Purification via flash column chromatography (eluent pentane/EtOAc, 95:5) gave aldehyde **46** (53.2 mg, 27%) as a white solid. **^{1}H NMR** (400 MHz, $CDCl_3$) δ 9.74 (t, *J* = 1.7 Hz, 1H, H_2), 3.62 (d, *J* = 6.0 Hz, 2H, H_5), 2.46 (td, *J* = 7.1, 1.7 Hz, 2H, H_3), 1.82 (tt, *J* = 7.1, 5.9 Hz, 2H, H_4), 0.85 (s, 9H, H_{11}, H_{12}, H_{13}), 0.00 (s, 6H, H_9, H_{10}); **^{13}C NMR** (101 MHz, $CDCl_3$) δ 202.5 (C_2), 62.0 (C_5), 40.7 (C_3), 25.9 (C_{11}, C_{12}, C_{13}), 25.5 (C_4), 18.2 (C_8), −5.5 (C_9, C_{10}); **LRMS** $(ESI)^+$ $[M+H]^+$ 203.1, found 203.1. Characterisation data is consistent with the literature.[162]

1-((*tert*-Butyldimethylsilyl)oxy)-9-(trimethylsilyl)non-8-yn-4-ol (47)

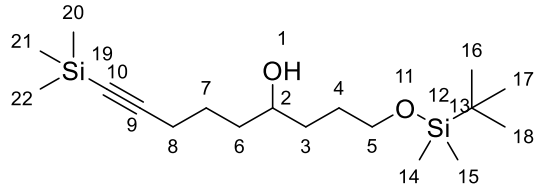

Following general procedure 2, aldehyde **46** (1.15 g, 5.72 mmol) in anhydrous THF (5 mL) was reacted with (5-(trimethylsilyl)pent-4-yn-1-yl)magnesium chloride (5.72 mmol) in anhydrous THF (5 mL). Purification via flash column chromatography (eluent pentane/EtOAc, 90:10) gave alcohol **47** as a colourless oil (1.019 g, 52%). **^{1}H NMR** (400 MHz, $CDCl_3$) δ 3.46 (m, 3H, H_2, H_5), 2.13 – 2.05 (m, 2H, H_8), 1.62 – 1.27 (m, 6H, H_3, H_4, H_6, H_7), 0.75 (s, 9H, H_{16}, H_{17}, H_{18}), 0.00 (s, 9H, H_{19}, H_{20}, H_{21}), −0.10 (s, 6H, H_{14}, H_{15}); **LRMS** (ESI^+) $[M+H]^+$ 343.2, found 343.3, **HRMS** (ESI+) calc. for $C_{18}H_{39}O_2Si_2^+$ $[M+H]^+$ 343.2410, found 343.2407. Characterisation data is consistent with the literature.[139]

Non-8-yne-1,4-diol (48)

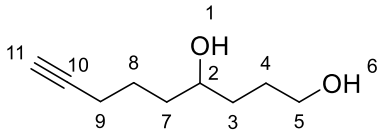

Alcohol **47** (331.9 mg, 0.968 mmol) was dissolved in anhydrous THF (5 mL) and cooled to 0 ºC under N_2 before the addition of TBAF (3.9 mL, 3.9 mmol, 1.0 M in THF) dropwise. The reaction was stirred for 2 h at RT before $CaCO_3$ (308 g, 5.05 mmol), Dowex 50WX8 (200-400 mesh, 1.5 g) and MeOH (4 mL) were added. The suspension was stirred for 1 h under N_2. The resulting mixture was filtered through a celite pad with MeOH (15 mL) as the eluent. The filtrate was then concentrated *in vacuo*. Purification via flash column chromatography (eluent Pentane/EtoAc, 1:4) gave alcohol **48** (113.9 mg, 74%) as a colourless oil. **^{1}H NMR** (400 MHz, $CDCl_3$) δ 3.74 – 3.55 (m, 3H, H_2, H_5),

2.21 (td, *J* = 6.4, 2.7 Hz, 2H, H_9), 1.94 (t, *J* = 2.6 Hz, 1H, H_{11}), 1.75 – 1.39 (m, 8H, H_3, H_4, H_7, H_8); **^{13}C NMR** (101 MHz, $CDCl_3$) δ 84.5 (C_{10}), 71.4 (C_2), 68.7 (C_{11}), 62.9 (C_5), 36.7 (C_7), 34.6 (C_3), 29.1 (C_4), 24.8 (C_8), 18.5 (C_9); **LRMS** $(ESI)^+$ $[M+H]^+$ 157.1, found 157.2. Characterisation data is consistent with the literature.[139]

4-Oxonon-8-ynal (49)

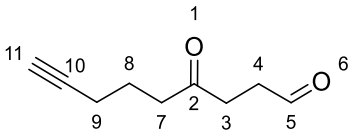

Following general procedure 4, DMSO (628 µL, 8.84 mmol) in CH_2Cl_2 (5 mL) was reacted with oxalyl chloride (852 µL, 9.92 mmol) in CH_2Cl_2 (5 mL) at −78 °C for 30 min. This was then reacted with a solution of alcohol **48** (418 mg, 2.997 mmol) in CH_2Cl_2 (5 mL). Aldehyde **49** (230.5 mg, 50%) was obtained as a colourless oil and used without further purification. **^{1}H NMR** (400 MHz, $CDCl_3$) δ 9.64 (s, 1H, H_5), 2.61 (s, 4H, H_3, H_4), 2.49 (t, *J* = 7.3 Hz, 2H, H_7), 2.09 (td, *J* = 6.9, 2.7 Hz, 2H, H_9), 1.92 – 1.83 (m, 1H, H_{11}), 1.66 (p, *J* = 7.1 Hz, 2H, H_8); **LRMS** $(ESI)^+$ $[M+H]^+$ 153.1, found 153.1; **HRMS** (ESI+) calc. for $C_9H_{13}O_2^+$ $[M+H]^+$ requires 152.0837, found 152.0835. Characterisation data is consistent with the literature.[139]

9-Bromononanoic acid (50)

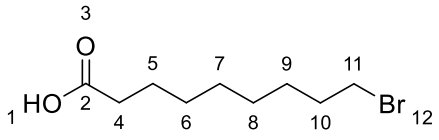

Following general procedure 2, Jones reagent (7.2 mL, 14 mmol, 2.0 M CrO_3 in aq. H_2SO_4) was reacted with a solution of 10-bromononan-1-ol (1.00 g, 4.48 mmol) in acetone (80 mL). Purification via flash column chromatography (eluent Pentane/EtOAc, 1:1) gave bromide **50** (747.1 mg, 70%) as a white solid. **^{1}H NMR** (400 MHz, $CDCl_3$) δ 3.37 (t, *J* = 6.8 Hz, 2H, H_{11}), 2.32 (t, *J* = 7.5 Hz, 2H, H_4), 1.88 – 1.76 (m, 2H, H_{10}), 1.66 – 1.53 (m, 2H, H_5), 1.47 – 1.34 (m, 2H, H_9), 1.35 – 1.27 (m, 6H, H_6, H_7, H_8); **^{13}C NMR** (101 MHz, $CDCl_3$) δ 180.6 (C_2), 34.1 (C_{11}), 33.9 (C_4), 32.8 (C_{10}), 29.1 (C_6), 29.0 (C_8), 28.6 (C_7), 28.1 (C_9), 24.6 (C_5); **LRMS** (ESI^-) $[M-H]^-$ 236.1, found 236.0. Characterisation data is consistent with the literature.[163]

(8-Carboxyoctyl)triphenylphosphonium bromide (51)

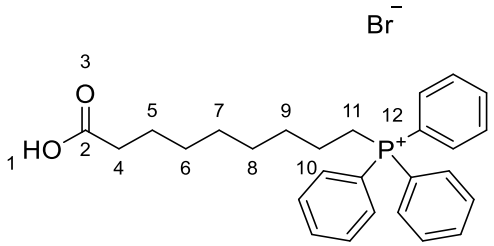

To a solution of triphenylphosphine (2.297 g, 8.570 mmol) in MeCN (5 mL) was slowly added bromide **50** (2.087 g, 8.570 mmol) in MeCN (5 mL). The mixture was heated to reflux and stirred for 48 h under argon. The reaction mixture was then cooled to RT and the solvent was removed *in vacuo* to afford phosphonium **51** (3.128 g, 87%) as a yellow oil and was used without further purification. **^{1}H NMR** (400 MHz, $CDCl_3$) δ 7.84 – 7.64 (m, 15H, H_{Ph}), 3.67 – 3.51 (m, 2H, H_{11}), 2.34 (td, *J* = 7.4, 5.0 Hz, 2H, H_4), 1.67 – 1.49 (m, 6H, H_5, H_9, H_{10}), 1.37 – 1.17 (m, 6H, H_6, H_7, H_8); **^{13}C NMR** (101 MHz, $CDCl_3$) δ 177.0 (C_2), 135.2 (C_{Ph}), 133.8 (C_{Ph}), 130.7 (C_{Ph}), 128.8 (C_{Ph}), 128.5 (C_{Ph}), 118.8 (C_4), 117.9 (C_7), 34.4 (C_6), 30.0 (C_{10}), 29.9 (C_8), 28.9 (C_5), 28.5 (C_9), 22.4 (C_{11}); **LRMS** (ESI^-) $[M-H]^-$ 418.2, found 418.2. Characterisation data is consistent with the literature.[164]

Dec-9-ynal (54)

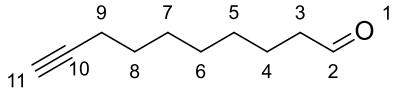

To a stirring solution of PCC (10 g, 47 mmol) and heat-activated molecular sieves (4Å, 15 g) in CH_2Cl_2 (100 mL) was slowly added dec-9-yn-1-ol (5 g, 32 mmol). The reaction was stirred at RT for 30 min. The solvent was evaporated *in vacuo* and the crude residue was resuspended in hexane/EtOAc (3:1, 50 mL) and filtered through a silica bed. The filtrate was concentrated *in vacuo* and aldehyde **54** (4.238 g, 87%) was obtained as a colourless oil and used without further purification. **^{1}H NMR** (400 MHz, $CDCl_3$) δ 9.71 (t, *J* = 1.6 Hz, 1H, H_2), 2.34 – 2.21 (m, 2H, H_3), 2.13 (dddd, *J* = 8.3, 7.1, 2.7, 1.2 Hz, 2H, H_9), 1.90 (t, *J* = 2.6 Hz, 1H, H_{11}), 1.59 (p, *J* = 7.3 Hz, 2H, H_6), 1.47 (p, *J* = 7.0 Hz, 2H, H_2), 1.40 – 1.27 (m, 6H, H_3, H_4, H_5); **LRMS** (ESI^+) $[M+H]^+$ 153.1, found 153.2; **HRMS** (ESI+) calc. for $C_{10}H_{17}O^+$ $[M+H]^+$ requires 152.1201, found 152.1206. Characterisation data is consistent with the literature.[166]

Appendix:

NMRs for compound **1**:

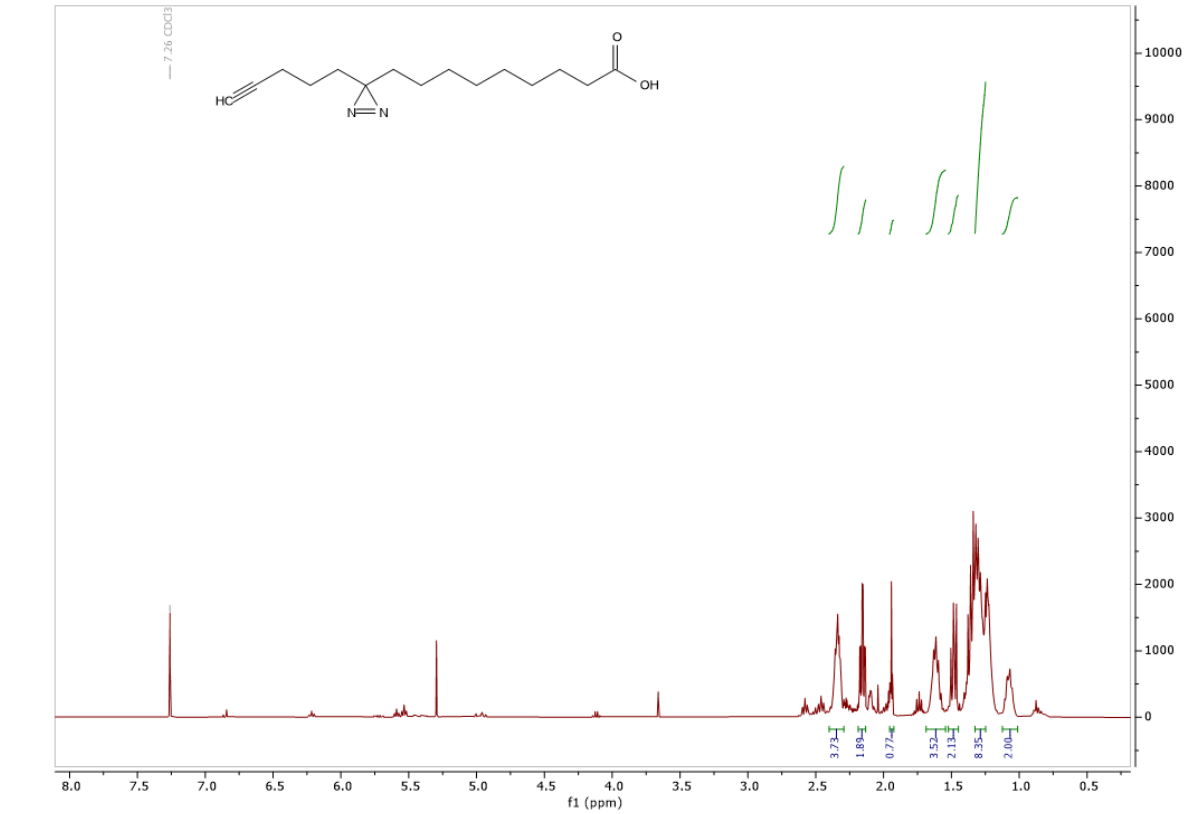

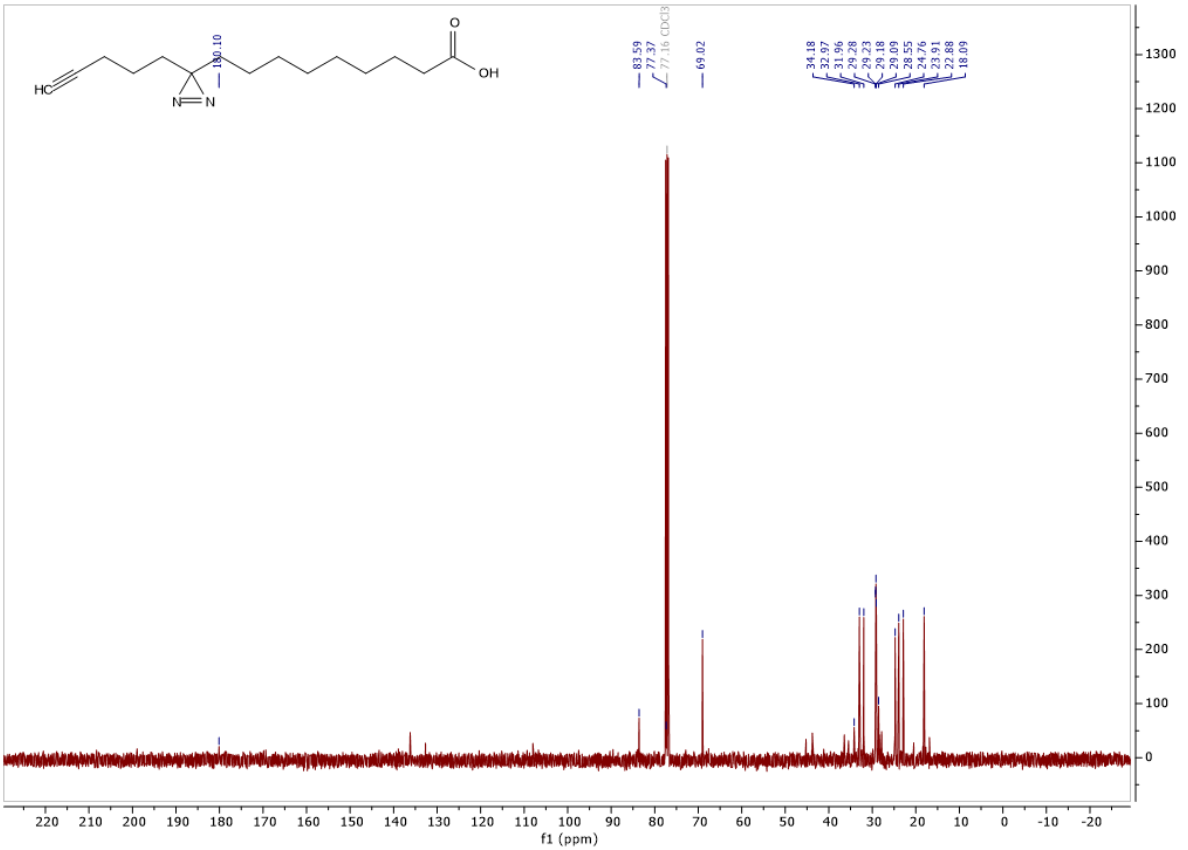

NMRs for compound **2**:

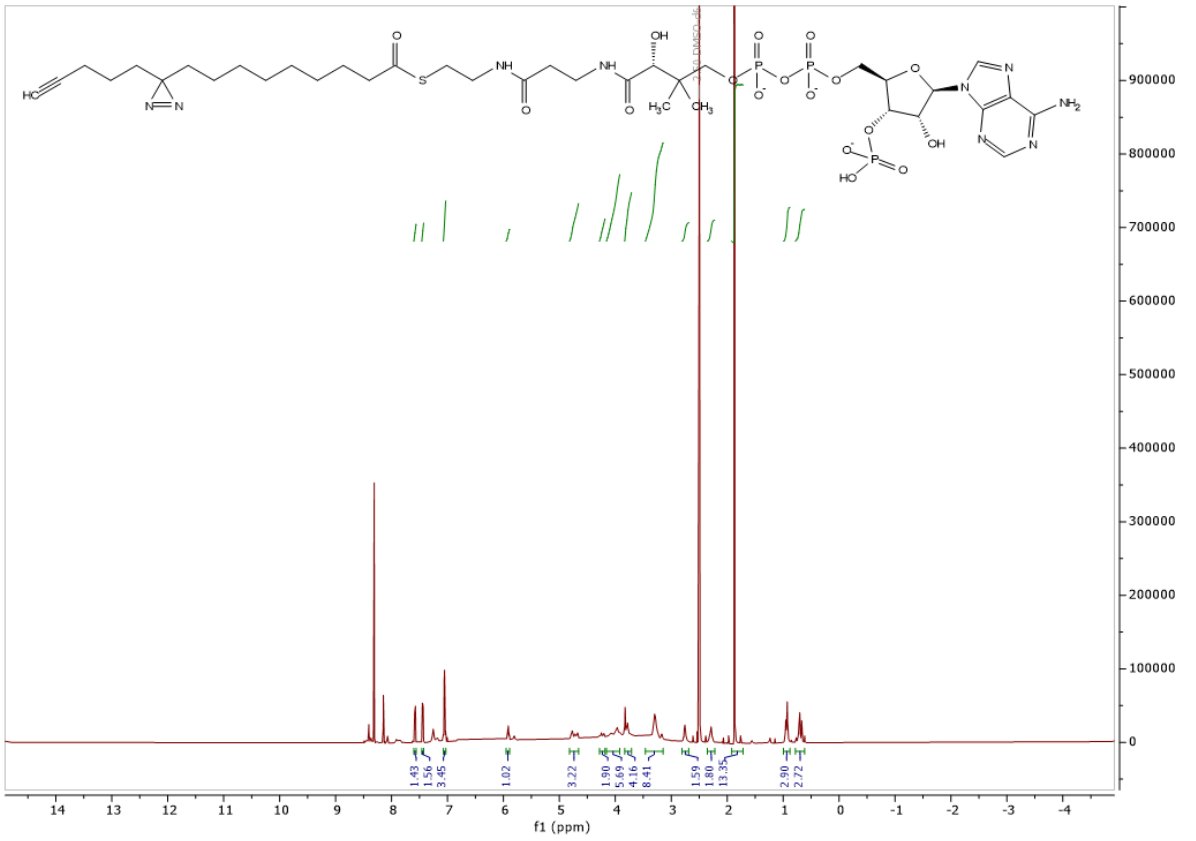

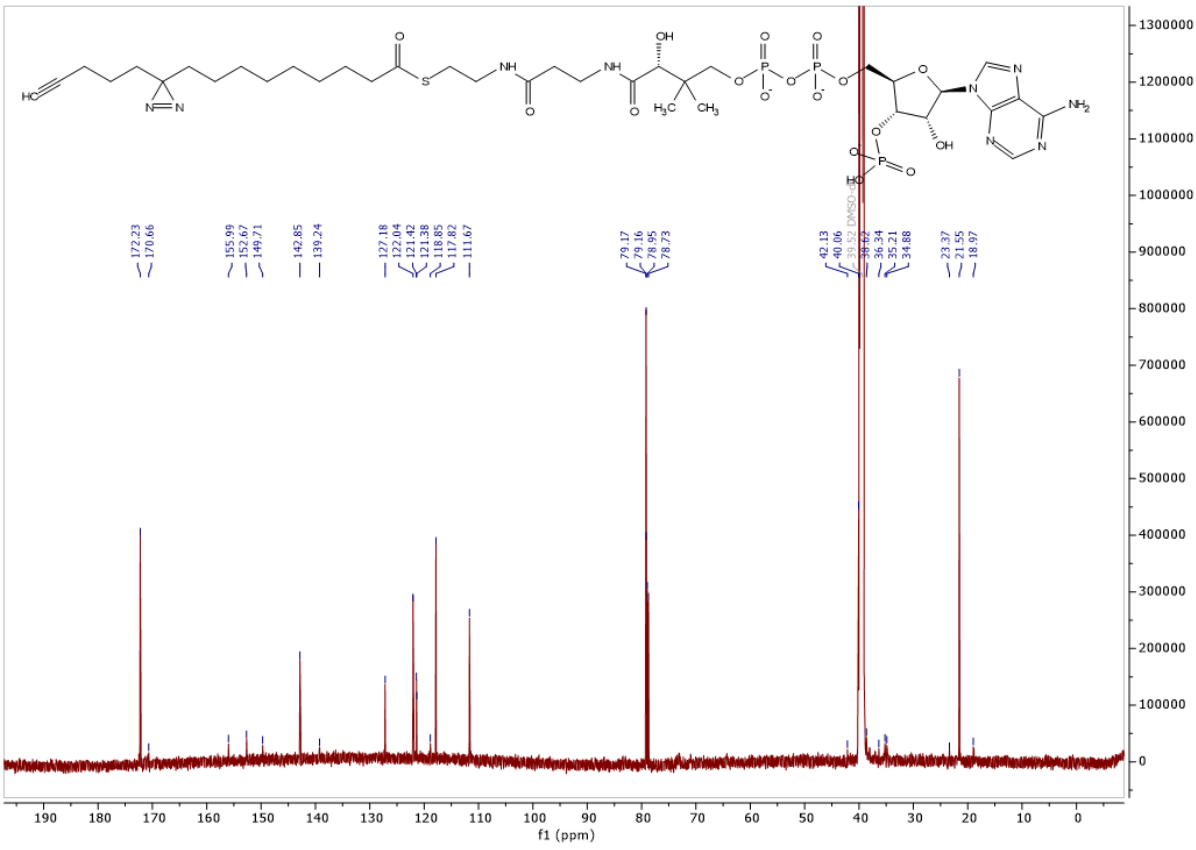

NMRs for compound **3**:

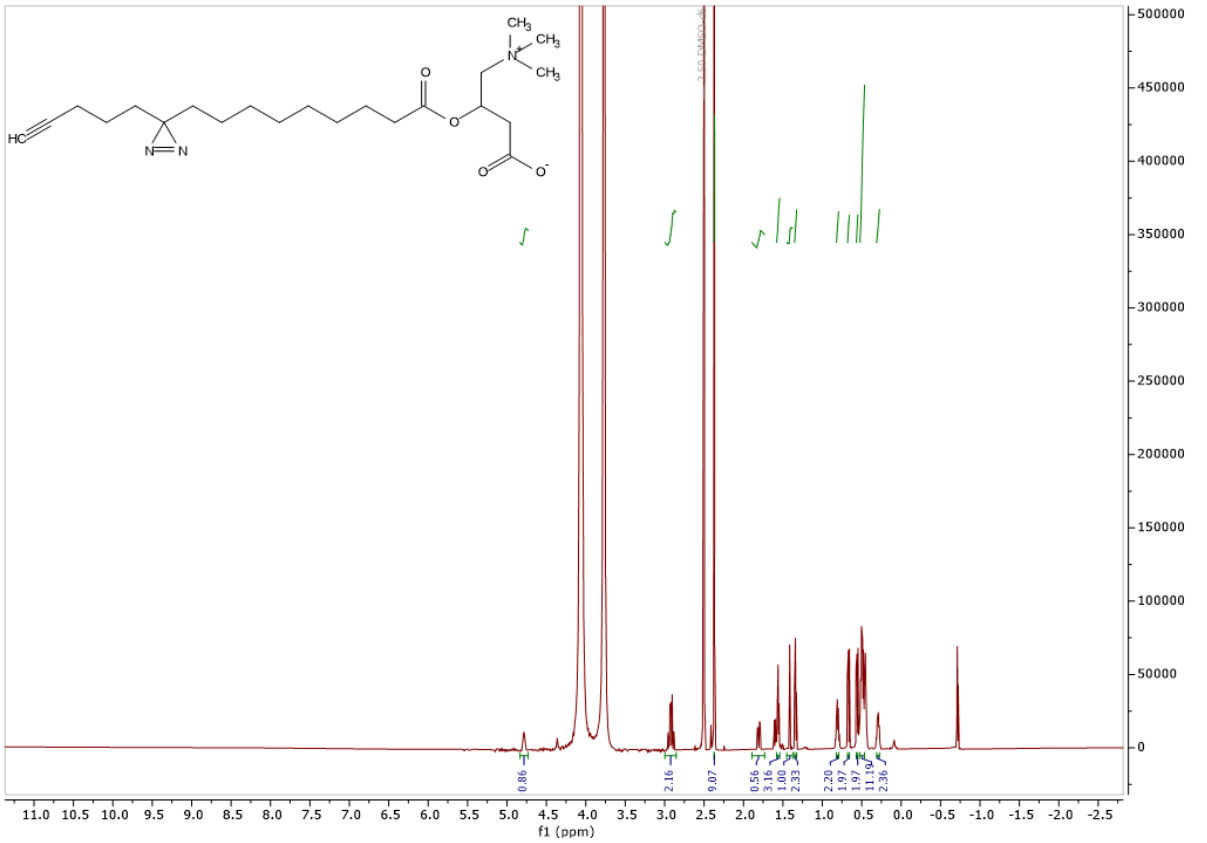

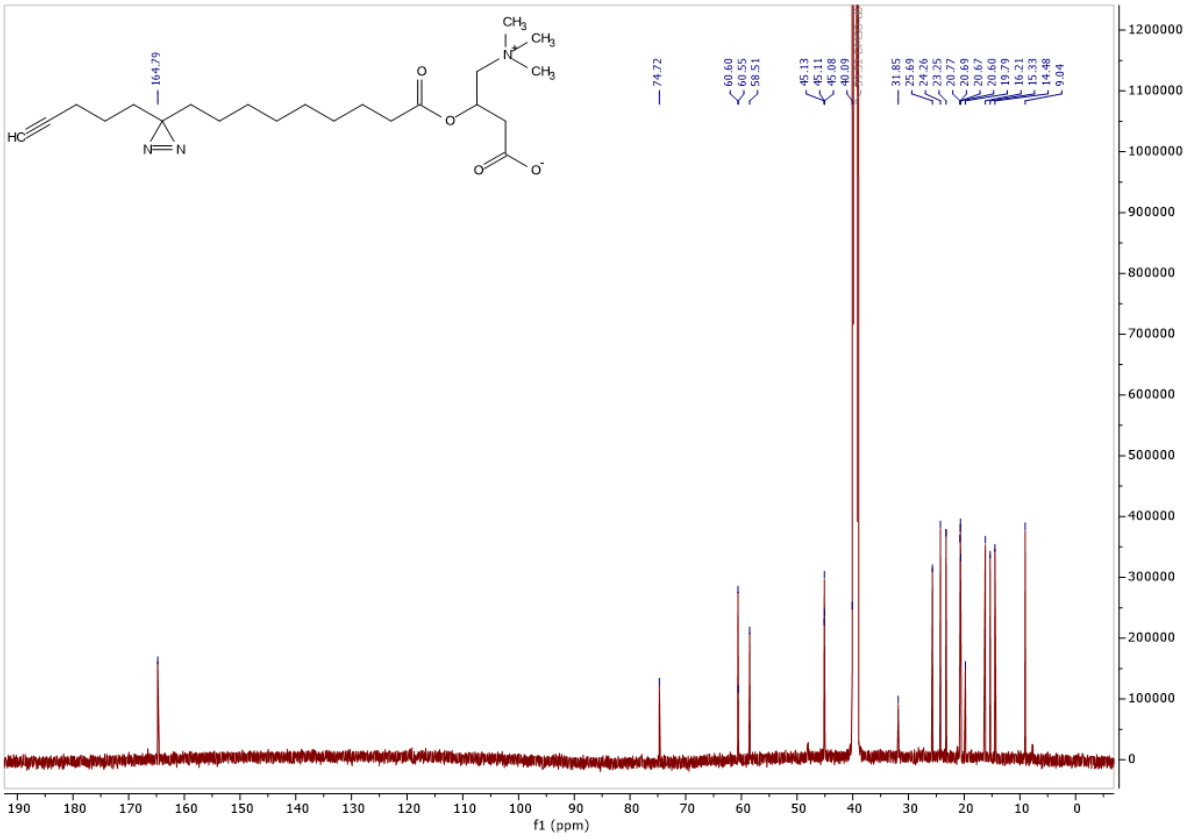

NMRs for compound **4**:

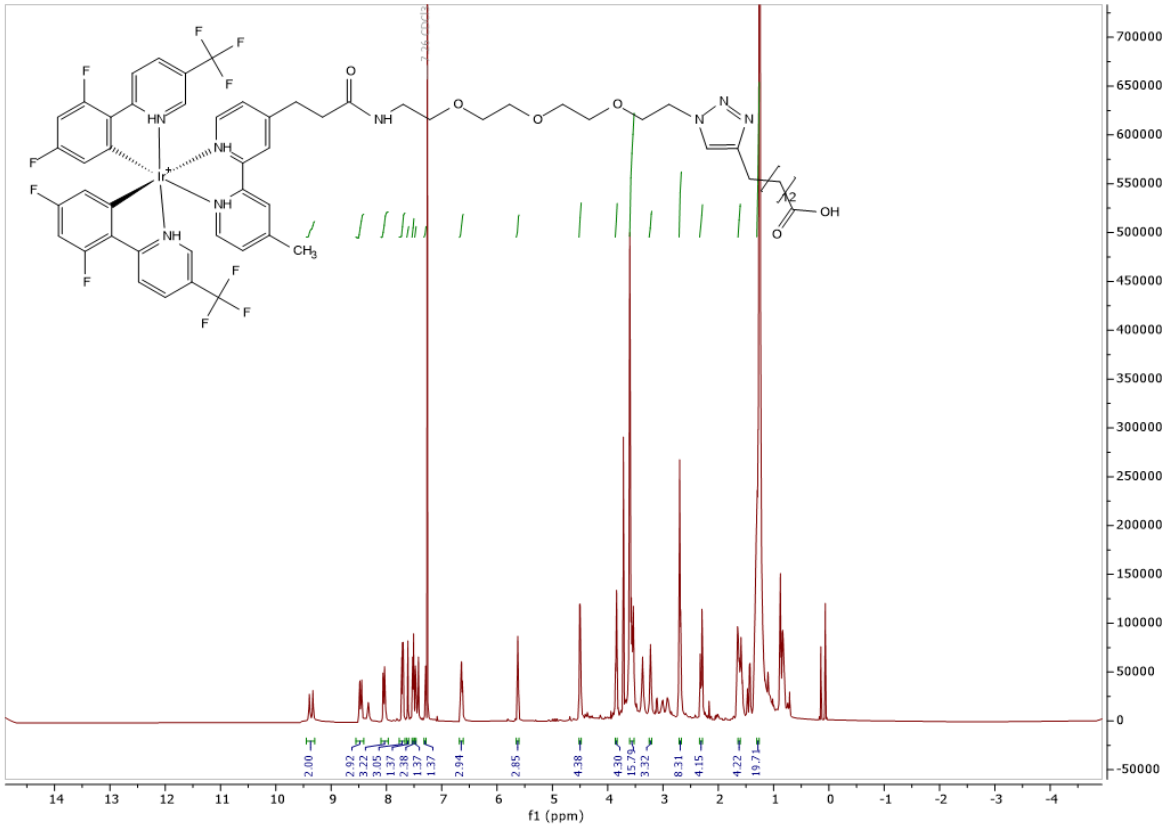

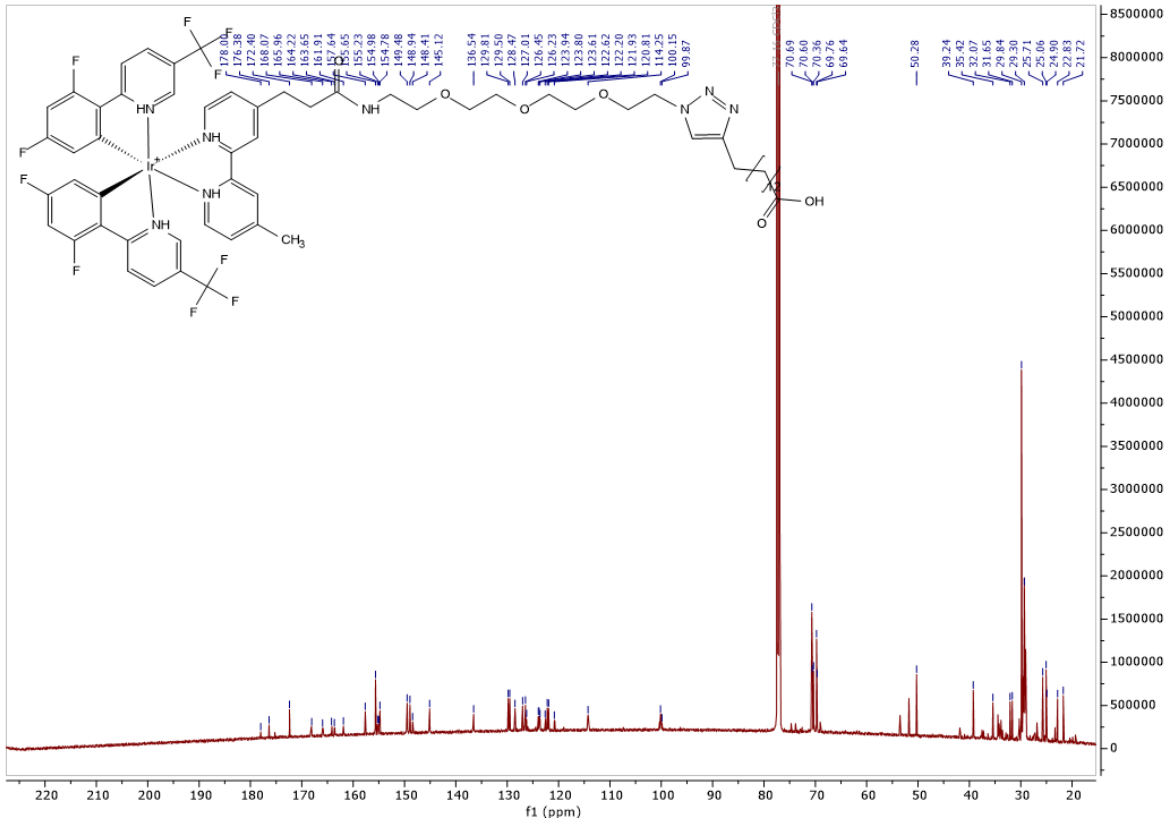

Bibliography

Bibliography

(1) Cockcroft, S. Mammalian Lipids: Structure, Synthesis and Function. *Essays Biochem* **2021**, *65* (5), 813–845. https://doi.org/10.1042/EBC20200067.

(2) Fahy, E.; Subramaniam, S.; Brown, H. A.; Glass, C. K.; Merrill, A. H.; Murphy, R. C.; Raetz, C. R. H.; Russell, D. W.; Seyama, Y.; Shaw, W.; Shimizu, T.; Spener, F.; Van Meer, G.; VanNieuwenhze, M. S.; White, S. H.; Witztum, J. L.; Dennis, E. A. A Comprehensive Classification System for Lipids. *J Lipid Res* **2005**, *46* (5), 839–861. https://doi.org/10.1194/jlr.E400004-JLR200.

(3) Acevedo, N.; Alhamwe, B. A.; Caraballo, L.; Ding, M.; Ferrante, A.; Garn, H.; Garssen, J.; Hii, C. S.; Irvine, J.; Llinás-Caballero, K.; López, J. F.; Miethe, S.; Perveen, K.; von Strandmann, E. P.; Sokolowska, M.; Potaczek, D. P.; van Esch, B. C. A. M. Perinatal and Early-Life Nutrition, Epigenetics, and Allergy. *Nutrients* **2021**, *13* (3), 1–53. https://doi.org/10.3390/nu13030724.

(4) Xu, E.; Chen, C.; Fu, J.; Zhu, L.; Shu, J.; Jin, M.; Wang, Y.; Zong, X. Dietary Fatty Acids in Gut Health: Absorption, Metabolism and Function. *Animal Nutrition* **2021**, *7* (4), 1337–1344. https://doi.org/10.1016/j.aninu.2021.09.010.

(5) Wang, T. Y.; Liu, M.; Portincasa, P.; Wang, D. Q. H. New Insights into the Molecular Mechanism of Intestinal Fatty Acid Absorption. *Eur J Clin Invest* **2013**, *43* (11), 1203–1223. https://doi.org/10.1111/eci.12161.

(6) Glatz, J. F. C.; Luiken, J. J. F. P. Fatty Acids in Cell Signaling: Historical Perspective and Future Outlook. *Prostaglandins Leukot Essent Fatty Acids* **2015**, *92*, 57–62. https://doi.org/10.1016/j.plefa.2014.02.007.

(7) Murru, E.; Manca, C.; Carta, G.; Banni, S. Impact of Dietary Palmitic Acid on Lipid Metabolism. *Front Nutr* **2022**, *9*. https://doi.org/10.3389/fnut.2022.861664.

(8) Carta, G.; Murru, E.; Banni, S.; Manca, C. Palmitic Acid: Physiological Role, Metabolism and Nutritional Implications. *Front Physiol* **2017**, *8*. https://doi.org/10.3389/fphys.2017.00902.

(9) Kakimoto, P. A.; Serna, J. D. C.; de Miranda Ramos, V.; Zorzano, A.; Kowaltowski, A. J. Increased Glycolysis Is an Early Consequence of Palmitate Lipotoxicity Mediated by Redox Signaling. *Redox Biol* **2021**, *45*. https://doi.org/10.1016/j.redox.2021.102026.

(10) Ertunc, M. E.; Hotamisligil, G. S. Lipid Signaling and Lipotoxicity in Metaflammation: Indications for Metabolic Disease Pathogenesis and Treatment. *J Lipid Res* **2016**, *57* (12), 2099–2114. https://doi.org/10.1194/jlr.R066514.

(11) Ly, L. D.; Xu, S.; Choi, S.-K.; Ha, C.-M.; Thoudam, T.; Cha, S.-K.; Wiederkehr, A.; Wollheim, C. B.; Lee, I.-K.; Park, K.-S. Oxidative Stress and Calcium Dysregulation by Palmitate in Type 2 Diabetes. *Exp Mol Med* **2017**, *49* (2). https://doi.org/10.1038/emm.2016.157.

(12) Owen, R. W.; Mier, W.; Giacosa, A.; Hull, W. E.; Spiegelhalder, B.; Bartsch, H. Phenolic Compounds and Squalene in Olive Oils: The Concentration and Antioxidant Potential of Total Phenols, Simple Phenols, Secoiridoids, Lignans and Squalene. *Food and Chemical Toxicology* **2000**, *38* (8), 647–659.

(13) Bester, D.; Esterhuyse, A. J.; Truter, E. J.; Van Rooyen, J. Cardiovascular Effects of Edible Oils: A Comparison between Four Popular Edible Oils. *Nutr Res Rev* **2010**, *23* (2), 334–348. https://doi.org/10.1017/S0954422410000223.

(14) Bermudez, B.; Lopez, S.; Ortega, A.; M. Varela, L.; M. Pacheco, Y.; Abia, R.; J.G. Muriana, F. Oleic Acid in Olive Oil: From a Metabolic Framework Toward a Clinical Perspective. *Curr Pharm Des* **2011**, *17* (8). https://doi.org/10.2174/138161211795428957.

(15) Drescher, S.; van Hoogevest, P. The Phospholipid Research Center: Current Research in Phospholipids and Their Use in Drug Delivery. *Pharmaceutics* **2020**, *12* (12), 1–36. https://doi.org/10.3390/pharmaceutics12121235.

(16) Dowhan, W. Understanding Phospholipid Function: Why Are There so Many Lipids? *Journal of Biological Chemistry* **2017**, *292* (26), 10755–10766. https://doi.org/10.1074/jbc.X117.794891.

(17) Lordan, R.; Tsoupras, A.; Zabetakis, I. Phospholipids of Animal and Marine Origin: Structure, Function, and Anti-Inflammatory Properties. *Molecules* **2017**, *22* (11), 1–32. https://doi.org/10.3390/molecules22111964.

(18) Sun, Q. The Hydrophobic Effects: Our Current Understanding. *Molecules* **2022**, *27* (20). https://doi.org/10.3390/molecules27207009.

(19) Luo, J.; Yang, H.; Song, B. L. Mechanisms and Regulation of Cholesterol Homeostasis. *Nat Rev Mol Cell Biol* **2020**, *21* (4), 225–245. https://doi.org/10.1038/s41580-019-0190-7.

(20) Paukner, K.; Lesná, I. K.; Poledne, R. Cholesterol in the Cell Membrane—An Emerging Player in Atherogenesis. *Int J Mol Sci* **2022**, *23* (1). https://doi.org/10.3390/ijms23010533.

(21) Yang, S. T.; Kreutzberger, A. J. B.; Lee, J.; Kiessling, V.; Tamm, L. K. The Role of Cholesterol in Membrane Fusion. *Chem Phys Lipids* **2016**, *199*, 136–143. https://doi.org/10.1016/j.chemphyslip.2016.05.003.

(22) Sebastian, T. T.; Baldridge, R. D.; Xu, P.; Graham, T. R. Phospholipid Flippases: Building Asymmetric Membranes and Transport Vesicles. *Biochim Biophys Acta Mol Cell Biol Lipids* **2012**, *1821* (8), 1068–1077. https://doi.org/10.1016/j.bbalip.2011.12.007.

(23) Kay, J. G.; Fairn, G. D. Distribution, Dynamics and Functional Roles of Phosphatidylserine within the Cell. *Cell Communication and Signaling* **2019**, *17* (1). https://doi.org/10.1186/s12964-019-0438-z.

(24) Anton, S. D.; Moehl, K.; Donahoo, W. T.; Marosi, K.; Lee, S. A.; Mainous, A. G.; Leeuwenburgh, C.; Mattson, M. P. Flipping the Metabolic Switch: Understanding and Applying the Health Benefits of Fasting. *Obesity* **2018**, *26* (2), 254–268. https://doi.org/10.1002/oby.22065.

(25) Palmer, B. F.; Clegg, D. J. Metabolic Flexibility and Its Impact on Health Outcomes. *Mayo Clin Proc* **2022**, *97* (4), 761–776. https://doi.org/10.1016/j.mayocp.2022.01.012.

(26) Longo, N.; Frigeni, M.; Pasquali, M. Carnitine Transport and Fatty Acid Oxidation. *Biochim Biophys Acta Mol Cell Res* **2016**, *1863* (10), 2422–2435. https://doi.org/10.1016/j.bbamcr.2016.01.023.

(27) Longo, N.; Frigeni, M.; Pasquali, M. Carnitine Transport and Fatty Acid Oxidation. *Biochim Biophys Acta Mol Cell Res* **2016**, *1863* (10), 2422–2435. https://doi.org/10.1016/j.bbamcr.2016.01.023.

(28) Houten, S. M.; Wanders, R. J. A. A General Introduction to the Biochemistry of Mitochondrial Fatty Acid β-Oxidation. *J Inherit Metab Dis* **2010**, *33* (5), 469–477. https://doi.org/10.1007/s10545-010-9061-2.

(29) Arnold, P. K.; Finley, L. W. S. Regulation and Function of the Mammalian Tricarboxylic Acid Cycle. *Journal of Biological Chemistry* **2023**, *299* (2). https://doi.org/10.1016/j.jbc.2022.102838.

(30) Martínez-Reyes, I.; Chandel, N. S. Mitochondrial TCA Cycle Metabolites Control Physiology and Disease. *Nat Commun* **2020**, *11* (1). https://doi.org/10.1038/s41467-019-13668-3.

(31) Vercellino, I.; Sazanov, L. A. The Assembly, Regulation and Function of the Mitochondrial Respiratory Chain. *Nat Rev Mol Cell Biol* **2022**, *23* (2), 141–161. https://doi.org/10.1038/s41580-021-00415-0.

(32) Wilson, D. F. Oxidative Phosphorylation: Regulation and Role in Cellular and Tissue Metabolism. *Journal of Physiology* **2017**, *595* (23), 7023–7038. https://doi.org/10.1113/JP273839.

(33) Nolfi-Donegan, D.; Braganza, A.; Shiva, S. Mitochondrial Electron Transport Chain: Oxidative Phosphorylation, Oxidant Production, and Methods of Measurement. *Redox Biol* **2020**, *37*. https://doi.org/10.1016/j.redox.2020.101674.

(34) Houten, S. M.; Violante, S.; Ventura, F. V.; Wanders, R. J. A. The Biochemistry and Physiology of Mitochondrial Fatty Acid β-Oxidation and Its Genetic Disorders. *Annu Rev Physiol* **2016**, *78*, 23–44. https://doi.org/10.1146/annurev-physiol-021115-105045.

(35) Houten, S. M.; Wanders, R. J. A. A General Introduction to the Biochemistry of Mitochondrial Fatty Acid β-Oxidation. *J Inherit Metab Dis* **2010**, *33* (5), 469–477. https://doi.org/10.1007/s10545-010-9061-2.

(36) Salih, K. J. The Major Pathways of Lipids (Triglyceride and Cholesterol) and Lipoprotein Metabolism. *Zanco J Pure Appl Sci* **2021**, *33* (4), 61–72. https://doi.org/10.21271/zjpas.

(37) Varga, T.; Czimmerer, Z.; Nagy, L. PPARs Are a Unique Set of Fatty Acid Regulated Transcription Factors Controlling Both Lipid Metabolism and Inflammation. *Biochim Biophys Acta Mol Basis Dis* **2011**, *1812* (8), 1007–1022. https://doi.org/10.1016/j.bbadis.2011.02.014.

(38) Berger, J.; Moller, D. E. The Mechanisms of Action of PPARs. *Annu Rev Med* **2002**, *53*, 409–435. https://doi.org/10.1146/annurev.med.53.082901.104018.

(39) Montaigne, D.; Butruille, L.; Staels, B. PPAR Control of Metabolism and Cardiovascular Functions. *Nat Rev Cardiol* **2021**, *18* (12), 809–823. https://doi.org/10.1038/s41569-021-00569-6.

(40) Lin, Y.; Wang, Y.; Li, P. F. PPARα: An Emerging Target of Metabolic Syndrome, Neurodegenerative and Cardiovascular Diseases. *Front Endocrinol (Lausanne)* **2022**, *13*. https://doi.org/10.3389/fendo.2022.1074911.

(41) Yamaguchi, A.; Botta, E.; Holinstat, M. Eicosanoids in Inflammation in the Blood and the Vessel. *Front Pharmacol* **2022**, *13*. https://doi.org/10.3389/fphar.2022.997403.

(42) Sheppe, A. E. F.; Edelmann, M. J. Roles of Eicosanoids in Regulating Inflammation and Neutrophil Migration as an Innate Host Response to Bacterial Infections. *Infect Immun* **2021**, *89* (8).

(43) Hammond, G. R. V.; Burke, J. E. Novel Roles of Phosphoinositides in Signaling, Lipid Transport, and Disease. *Curr Opin Cell Biol* **2020**, *63*, 57–67. https://doi.org/10.1016/j.ceb.2019.12.007.

(44) Dickson, E. J.; Hille, B. Understanding Phosphoinositides: Rare, Dynamic, and Essential Membrane Phospholipids. *Biochemical Journal* **2019**, *476* (1), 1–23. https://doi.org/10.1042/BCJ20180022.

(45) Miller, W. L.; Bose, H. S. Early Steps in Steroidogenesis: Intracellular Cholesterol Trafficking. *J Lipid Res* **2011**, *52* (12), 2111–2135. https://doi.org/10.1194/jlr.R016675.

(46) Atkovska, K.; Klingler, J.; Oberwinkler, J.; Keller, S.; Hub, J. S. Rationalizing Steroid Interactions with Lipid Membranes: Conformations, Partitioning, and Kinetics. *ACS Cent Sci* **2018**, *4* (9), 1155–1165. https://doi.org/10.1021/acscentsci.8b00332.

(47) Warburg, O. On the Origin of Cancer Cells. *Science (1979)* **1956**, *123*, 309–314.

(48) Koundouros, N.; Poulogiannis, G. Reprogramming of Fatty Acid Metabolism in Cancer. *Br J Cancer* **2020**, *122* (1), 4–22. https://doi.org/10.1038/s41416-019-0650-z.

(49) Santos, C. R.; Schulze, A. Lipid Metabolism in Cancer. *FEBS Journal* **2012**, *279* (15), 2610–2623. https://doi.org/10.1111/j.1742-4658.2012.08644.x.

(50) Currie, E.; Schulze, A.; Zechner, R.; Walther, T. C.; Farese, R. V. Cellular Fatty Acid Metabolism and Cancer. *Cell Metab* **2013**, *18* (2), 153–161. https://doi.org/10.1016/j.cmet.2013.05.017.

(51) Hanahan, D. Hallmarks of Cancer: New Dimensions. *Cancer Discov* **2022**, *12* (1), 31–46. https://doi.org/10.1158/2159-8290.CD-21-1059.

(52) Nath, A.; Chan, C. Genetic Alterations in Fatty Acid Transport and Metabolism Genes Are Associated with Metastatic Progression and Poor Prognosis of Human Cancers. *Sci Rep* **2016**, *6*. https://doi.org/10.1038/srep18669.

(53) Camarda, R.; Zhou, A. Y.; Kohnz, R. A.; Balakrishnan, S.; Mahieu, C.; Anderton, B.; Eyob, H.; Kajimura, S.; Tward, A.; Krings, G.; Nomura, D. K.; Goga, A. Inhibition of Fatty Acid Oxidation as a Therapy for MYC-Overexpressing Triple-Negative Breast Cancer. *Nat Med* **2016**, *22* (4), 427–432. https://doi.org/10.1038/nm.4055.

(54) Bennett, M. K.; Lopez, J. M.; Sanchez, H. B.; Osborne, T. F. Sterol Regulation of Fatty Acid Synthase Promoter. *J Biol Chem* **1995**, *270* (43), 25578–25583.

(55) Yokoyama, C.; Wang, X.; Briggs, M. R.; Admon, A.; Wu, J.; Hua, X.; Goldstein, J. L.; Brown, M. S. SREBP-1, a Basic-Helix-Loop-Helix-Leucine Zipper Protein That Controls Transcription of the Low Density Lipoprotein Receptor Gene. *Cell* **1993**, *75* (1). https://doi.org/10.1016/S0092-8674(05)80095-9.

(56) Xia, L.; Zhou, Z.; Chen, X.; Luo, W.; Ding, L.; Xie, H.; Zhuang, W.; Ni, K.; Li, G. Ligand-Dependent CD36 Functions in Cancer Progression, Metastasis, Immune Response, and Drug Resistance. *Biomedicine and Pharmacotherapy* **2023**, *168*. https://doi.org/10.1016/j.biopha.2023.115834.

(57) Feng, W. W.; Wilkins, O.; Bang, S.; Ung, M.; Li, J.; An, J.; del Genio, C.; Canfield, K.; DiRenzo, J.; Wells, W.; Gaur, A.; Robey, R. B.; Guo, J. Y.; Powles, R. L.; Sotiriou, C.; Pusztai, L.; Febbraio, M.; Cheng, C.; Kinlaw, W. B.; Kurokawa, M. CD36-Mediated Metabolic Rewiring of Breast Cancer Cells Promotes Resistance to HER2-Targeted Therapies. *Cell Rep* **2019**, *29* (11), 3405–3420. https://doi.org/10.1016/j.celrep.2019.11.008.

(58) Jarc, E.; Petan, T. Lipid Droplets and the Management of Cellular Stress. *Yale Journal of Biology and Medicine* **2019**, *92*, 435–452.

(59) Cairns, R. A.; Harris, I.; Mccracken, S.; Mak, T. W. Cancer Cell Metabolism. *Cold Spring Harb Symp Quant Biol* **2011**, *76*, 299–311. https://doi.org/10.1101/sqb.2011.76.012856.

(60) Rysman, E.; Brusselmans, K.; Scheys, K.; Timmermans, L.; Derua, R.; Munck, S.; Van Veldhoven, P. P.; Waltregny, D.; Daniëls, V. W.; Machiels, J.; Vanderhoydonc, F.; Smans, K.; Waelkens, E.; Verhoeven, G.; Swinnen, J. V. De Novo Lipogenesis Protects Cancer Cells from Free Radicals and Chemotherapeutics by Promoting Membrane Lipid Saturation. *Cancer Res* **2010**, *70* (20), 8117–8126. https://doi.org/10.1158/0008-5472.CAN-09-3871.

(61) Shin, I.; Yakes, F. M.; Rojo, F.; Shin, N. young; Bakin, A. V.; Baselga, J.; Arteaga, C. L. PKB/Akt Mediates Cell-Cycle Progression by Phosphorylation of P27Kip1 at Threonine 157 and Modulation of Its Cellular Localization. *Nat Med* **2002**, *8* (10), 1145–1152. https://doi.org/10.1038/nm759.

(62) Han, F.; Li, C. F.; Cai, Z.; Zhang, X.; Jin, G.; Zhang, W. N.; Xu, C.; Wang, C. Y.; Morrow, J.; Zhang, S.; Xu, D.; Wang, G.; Lin, H. K. The Critical Role of AMPK in Driving Akt Activation under Stress, Tumorigenesis and Drug Resistance. *Nat Commun* **2018**, *9* (1). https://doi.org/10.1038/s41467-018-07188-9.

(63) Khwairakpam, A.; Shyamananda, M.; Sailo, B.; Rathnakaram, S.; Padmavathi, G.; Kotoky, J.; Kunnumakkara, A. ATP Citrate Lyase (ACLY): A Promising Target for Cancer Prevention and Treatment. *Curr Drug Targets* **2015**, *16* (2). https://doi.org/10.2174/1389450115666141224125117.

(64) Hoxhaj, G.; Manning, B. D. The PI3K–AKT Network at the Interface of Oncogenic Signalling and Cancer Metabolism. *Nat Rev Cancer* **2020**, *20* (2), 74–88. https://doi.org/10.1038/s41568-019-0216-7.

(65) Casciano, J. C.; Perry, C.; Cohen-Nowak, A. J.; Miller, K. D.; Vande Voorde, J.; Zhang, Q.; Chalmers, S.; Sandison, M. E.; Liu, Q.; Hedley, A.; McBryan, T.; Tang, H. Y.; Gorman, N.; Beer, T.; Speicher, D. W.; Adams, P. D.; Liu, X.; Schlegel, R.; McCarron, J. G.; Wakelam, M. J. O.; Gottlieb, E.; Kossenkov, A. V.; Schug, Z. T. MYC Regulates Fatty Acid Metabolism through a Multigenic Program in Claudin-Low Triple Negative Breast Cancer. *Br J Cancer* **2020**, *122* (6), 868–884. https://doi.org/10.1038/s41416-019-0711-3.

(66) Singh, K. B.; Hahm, E. R.; Kim, S. H.; Wendell, S. G.; Singh, S. V. A Novel Metabolic Function of Myc in Regulation of Fatty Acid Synthesis in Prostate Cancer. *Oncogene* **2021**, *40* (3), 592–602. https://doi.org/10.1038/s41388-020-01553-z.

(67) Actis Dato, V.; Lange, S.; Cho, Y. Metabolic Flexibility of the Heart: The Role of Fatty Acid Metabolism in Health, Heart Failure, and Cardiometabolic Diseases. *Int J Mol Sci* **2024**, *25* (2). https://doi.org/10.3390/ijms25021211.

(68) Karwi, Q. G.; Uddin, G. M.; Ho, K. L.; Lopaschuk, G. D. Loss of Metabolic Flexibility in the Failing Heart. *Front Cardiovasc Med* **2018**, *5*. https://doi.org/10.3389/fcvm.2018.00068.

(69) Lopaschuk, G. D.; Karwi, Q. G.; Tian, R.; Wende, A. R.; Abel, E. D. Cardiac Energy Metabolism in Heart Failure. *Circ Res* **2021**, *128* (10), 1487–1513. https://doi.org/10.1161/CIRCRESAHA.121.318241.

(70) Lopaschuk, G. D.; Ussher, J. R.; Folmes, C. D. L.; Jaswal, J. S.; Stanley, W. C. Myocardial Fatty Acid Metabolism in Health and Disease. *Physiol Rev* **2010**, *90*, 207–258. https://doi.org/10.1152/physrev.00015.2009.-There.

(71) Chong, C. R.; Clarke, K.; Levelt, E. Metabolic Remodelling in Diabetic Cardiomyopathy. *Cardiovasc Res* **2017**, *113* (4), 422–430. https://doi.org/10.1093/cvr/cvx018.

(72) Athithan, L.; Gulsin, G. S.; McCann, G. P.; Levelt, E. Diabetic Cardiomyopathy: Pathophysiology, Theories and Evidence to Date. *World J Diabetes* **2019**, *10* (10), 490–510. https://doi.org/10.4239/wjd.v10.i10.490.

(73) An, D.; Rodrigues, B. Role of Changes in Cardiac Metabolism in Development of Diabetic Cardiomyopathy. *Am J Physiol Heart Circ Physiol* **2006**, *291*, 1489–1506. https://doi.org/10.1152/ajpheart.00278.2006.-In.

(74) Wende, A. R.; Abel, E. D. Lipotoxicity in the Heart. *Biochim Biophys Acta Mol Cell Biol Lipids* **2010**, *1801* (3), 311–319. https://doi.org/10.1016/j.bbalip.2009.09.023.

(75) Zhou, Y.-T.; Grayburn, P.; Karim, A.; Shimabukuro, M.; Higa, M.; Baetens, D.; Orci, L.; Unger, R. H. Lipotoxic Heart Disease in Obese Rats: Implications for Human Obesity. *Proc Natl Acad Sci U S A* **2000**, *97* (4), 1784–1789.

(76) Bosma, M.; Kersten, S.; Hesselink, M. K. C.; Schrauwen, P. Re-Evaluating Lipotoxic Triggers in Skeletal Muscle: Relating Intramyocellular Lipid Metabolism to Insulin Sensitivity. *Prog Lipid Res* **2012**, *51* (1), 36–49. https://doi.org/10.1016/j.plipres.2011.11.003.

(77) Yamamoto, T.; Sano, M. Deranged Myocardial Fatty Acid Metabolism in Heart Failure. *Int J Mol Sci* **2022**, *23* (2). https://doi.org/10.3390/ijms23020996.

(78) Li, X.; Bi, X. Integrated Control of Fatty Acid Metabolism in Heart Failure. *Metabolites* **2023**, *13* (5). https://doi.org/10.3390/metabo13050615.

(79) Van Wagoner, D. R.; Rennison, J. H. Impact of Dietary Fatty Acids on Cardiac Arrhythmogenesis. *Circ Arrhythm Electrophysiol* **2009**, *2* (4), 460–469. https://doi.org/10.1161/CIRCEP.109.880773.

(80) Gordon, G. B. Saturated Free Fatty Acid Toxicity II. Lipid Accumulation, Ultrastructural Alterations, and Toxicity in Mammalian Cells in Culture. *Exp Mol Pathol* **1977**, *27*, 262–276.

(81) Drosatos, K.; Schulze, P. C. Cardiac Lipotoxicity: Molecular Pathways and Therapeutic Implications. *Curr Heart Fail Rep* **2013**, *10* (2), 109–121. https://doi.org/10.1007/s11897-013-0133-0.

(82) Ebong, I. A.; Goff, D. C.; Rodriguez, C. J.; Chen, H.; Bertoni, A. G. Mechanisms of Heart Failure in Obesity. *Obes Res Clin Pract* **2014**, *8* (6), 540–548. https://doi.org/10.1016/j.orcp.2013.12.005.

(83) Penzo, D.; Tagliapietra, C.; Colonna, R.; Petronilli, V.; Bernardi, P. Effects of Fatty Acids on Mitochondria: Implications for Cell Death. *Biochimica et Biophysica Acta 1555* **2002**, 160–165.

(84) Korge, P.; Honda, H. M.; Weiss, J. N.; Korge, P. Effects of Fatty Acids in Isolated Mitochondria: Implications for Ischemic Injury and Cardioprotection. *Am J Physiol Heart Circ Physiol* **2003**, *285*, 259–269. https://doi.org/10.1152/ajpheart.01028.

(85) Tominaga, H.; Katoh, H.; Odagiri, K.; Takeuchi, Y.; Kawashima, H.; Saotome, M.; Urushida, T.; Satoh, H.; Hayashi, H. Different Effects of Palmitoyl-L-Carnitine and Palmitoyl-CoA on Mitochondrial Function in Rat Ventricular Myocytes. *Am J Physiol Heart Circ Physiol* **2008**, *295* (1). https://doi.org/10.1152/ajpheart.01307.2007.

(86) Sparagna, G. C.; Hickson-bick, D. L.; Maximilian Buja, L.; Mcmillin, J. B. A Metabolic Role for Mitochondria in Palmitate-Induced Cardiac Myocyte Apoptosis. *Am J Physiol Heart Circ Physiol* **2000**, *279* (5), 2124–2132.

(87) D'Souza, K.; Nzirorera, C.; Kienesberger, P. C. Lipid Metabolism and Signaling in Cardiac Lipotoxicity. *Biochim Biophys Acta Mol Cell Biol Lipids* **2016**, *1861* (10), 1513–1524. https://doi.org/10.1016/j.bbalip.2016.02.016.

(88) Linder, M. E.; Deschenes, R. J. Palmitoylation: Policing Protein Stability and Traffic. *Nat Rev Mol Cell Biol* **2007**, *8* (1), 74–84. https://doi.org/10.1038/nrm2084.

(89) Gao, X.; Hannoush, R. N. A Decade of Click Chemistry in Protein Palmitoylation: Impact on Discovery and New Biology. *Cell Chem Biol* **2018**, *25* (3), 236–246. https://doi.org/10.1016/j.chembiol.2017.12.002.

(90) Linder, M. E.; Deschenes, R. J. Palmitoylation: Policing Protein Stability and Traffic. *Nat Rev Mol Cell Biol* **2007**, *8* (1), 74–84. https://doi.org/10.1038/nrm2084.

(91) Jansen, M.; Beaumelle, B. How Palmitoylation Affects Trafficking and Signaling of Membrane Receptors. *Biol Cell* **2022**, *114* (2), 61–72. https://doi.org/10.1111/boc.202100052.

(92) Ahmadian, M.; Duncan, R. E.; Jaworski, K.; Sarkadi-Nagy, E.; Sul, H. S. Triacylglycerol Metabolism in Adipose Tissue. *Future Lipidol* **2007**, *2* (2), 229–237. https://doi.org/10.2217/17460875.2.2.229.

(93) Goldberg, I. J. Triglyceride: One Molecule at the Center of Health and Disease. *Biochim Biophys Acta Mol Cell Biol Lipids* **2012**, *1821* (5), 719–720. https://doi.org/10.1016/j.bbalip.2012.02.005.

(94) Saliba, A. E.; Vonkova, I.; Gavin, A. C. The Systematic Analysis of Protein-Lipid Interactions Comes of Age. *Nat Rev Mol Cell Biol* **2015**, *16* (12), 753–761. https://doi.org/10.1038/nrm4080.

(95) Mulgrew-Nesbitt, A.; Diraviyam, K.; Wang, J.; Singh, S.; Murray, P.; Li, Z.; Rogers, L.; Mirkovic, N.; Murray, D. The Role of Electrostatics in Protein-Membrane Interactions. *Biochim Biophys Acta Mol Cell Biol Lipids* **2006**, *1761* (8), 812–826. https://doi.org/10.1016/j.bbalip.2006.07.002.

(96) Morrow, M. R.; Singh, D.; Lu, D.; Grant, C. W. Glycosphingolipid Fatty Acid Arrangement in Phospholipid Bilayers: Cholesterol Effects. *Biophys J* **1995**, *68* (1), 179–186. https://doi.org/10.1016/S0006-3495(95)80173-6.

(97) Grassi, S.; Giussani, P.; Mauri, L.; Prioni, S.; Sonnino, S.; Prinetti, A. Lipid Rafts and Neurodegeneration: Structural and Functional Roles in Physiologic Aging and Neurodegenerative Diseases. *J Lipid Res* **2020**, *61* (5), 636–654. https://doi.org/10.1194/jlr.TR119000427.

(98) Curry, S.; Mandelkow, H.; Brick, P.; Franks, N. Crystal Structure of Human Serum Albumin Complexed with Fatty Acid Reveals an Asymmetric Distribution of Binding Sites. *Nat Struct Biol* **1998**, *5* (9). https://doi.org/10.1038/1869.

(99) Zechner, R.; Zimmermann, R.; Eichmann, T. O.; Kohlwein, S. D.; Haemmerle, G.; Lass, A.; Madeo, F. FAT SIGNALS - Lipases and Lipolysis in Lipid Metabolism and Signaling. *Cell Metab* **2012**, *15* (3). https://doi.org/10.1016/j.cmet.2011.12.018.

(100) Flores, J.; White, B. M.; Brea, R. J.; Baskin, J. M.; Devaraj, N. K. Lipids: Chemical Tools for Their Synthesis, Modification, and Analysis. *Chem Soc Rev* **2020**, *49* (14), 4602–4614. https://doi.org/10.1039/d0cs00154f.

(101) Wang, R.; Chen, Y. Q. Protein Lipidation Types: Current Strategies for Enrichment and Characterization. *Int J Mol Sci* **2022**, *23* (4). https://doi.org/10.3390/ijms23042365.

(102) Haldar, S.; Chattopadhyay, A. Application of NBD-Labeled Lipids in Membrane and Cell Biology. In *Application of NBD-Labeled Lipids in Membrane and Cell Biology. Fluorescent Methods to Study Biological Membranes.*; Springer, 2012; Vol. 13, pp 37–50. https://doi.org/10.1007/4243_2012_43.

(103) Bergelson, L. D.; Molotkovsky, J. G.; Manevich, Y. M. LIPID-SPECIFIC FLUORESCENT PROBES IN STUDIES OF BIOLOGICAL MEMBRANES. *Chem Phys Lipids* **1985**, *37*, 165–195.

(104) Maier, O.; Oberle, V.; Hoekstra, D. Fluorescent Lipid Probes: Some Properties and Applications (a Review). *Chem Phys Lipids* **2002**, *116*, 3–18.

(105) Kajiwara, K.; Osaki, H.; Greßies, S.; Kuwata, K.; Kim, J. H.; Gensch, T.; Sato, Y.; Glorius, F.; Yamaguchi, S.; Taki, M. A Negative-Solvatochromic Fluorescent Probe for Visualizing Intracellular Distributions of Fatty Acid Metabolites. *Nat Commun* **2022**, *13* (1). https://doi.org/10.1038/s41467-022-30153-6.

(106) Martin, D. D. O.; Vilas, G. L.; Prescher, J. A.; Rajaiah, G.; Falck, J. R.; Bertozzi, C. R.; Berthiaume, L. G. Rapid Detection, Discovery, and Identification of Post-translationally Myristoylated Proteins during Apoptosis Using a Bio-orthogonal Azidomyristate Analog. *The FASEB Journal* **2008**, *22* (3), 797–806. https://doi.org/10.1096/fj.07-9198com.

(107) Schlesinger, M. J.; Magee, A. I.; Schmidt3, M. F. G. Fatty Acid Acylation of Proteins in Cultured Cells. *J Biol Chem* **1980**, *255* (21), 10021–10024.

(108) Rostovtsev, V. V.; Green, L. G.; Fokin, V. V.; Sharpless, K. B. A Stepwise Huisgen Cycloaddition Process: Copper(I)-Catalyzed Regioselective "Ligation" of Azides and Terminal Alkynes. *Angewandte Chemie - International Edition* **2002**, *41* (14), 2596–2599. https://doi.org/10.1002/1521-3773(20020715)41:14<2596::AID-ANIE2596>3.0.CO;2-4.

(109) Tornøe, C. W.; Christensen, C.; Meldal, M. Peptidotriazoles on Solid Phase: [1,2,3]-Triazoles by Regiospecific Copper(I)-Catalyzed 1,3-Dipolar Cycloadditions of Terminal Alkynes to Azides. *Journal of Organic Chemistry* **2002**, *67* (9). https://doi.org/10.1021/jo011148j.

(110) Haberkant, P.; Van Meer, G. Protein-Lipid Interactions: Paparazzi Hunting for Snap-Shots. *Biol Chem* **2009**, *390* (8), 795–803. https://doi.org/10.1515/BC.2009.074.

(111) Haberkant, P.; Holthuis, J. C. M. Fat & Fabulous: Bifunctional Lipids in the Spotlight. *Biochim Biophys Acta Mol Cell Biol Lipids* **2014**, *1841* (8), 1022–1030. https://doi.org/10.1016/j.bbalip.2014.01.003.

(112) Bockelmann, S.; Mina, J. G. M.; Korneev, S.; Hassan, D. G.; Müller, D.; Hilderink, A.; Vlieg, H. C.; Raijmakers, R.; Heck, A. J. R.; Per, H.; Holthuis, J. C. M. A Search for Ceramide Binding Proteins Using Bifunctional Lipid Analogs Yields CERT-Related Protein StarD7. *J Lipid Res* **2018**, *59* (3), 515–530. https://doi.org/10.1194/jlr.M082354.

(113) Haberkant, P.; Stein, F.; Höglinger, D.; Gerl, M. J.; Brügger, B.; Van Veldhoven, P. P.; Krijgsveld, J.; Gavin, A. C.; Schultz, C. Bifunctional Sphingosine for Cell-Based Analysis of Protein-Sphingolipid Interactions. *ACS Chem Biol* **2016**, *11* (1), 222–230. https://doi.org/10.1021/acschembio.5b00810.

(114) Chakrabarti, P.; Khorana, H. G. New Approach to the Study of Phospholipid-Protein Interactions in Biological Membranes. Synthesis of Fatty Acids and Phospholipids Containing Photosensitive Groups. *Biochemistry* **1975**, *14* (23). https://doi.org/10.1021/bi00694a001.

(115) Peng, T.; Hang, H. C. Bifunctional Fatty Acid Chemical Reporter for Analyzing S-Palmitoylated Membrane Protein-Protein Interactions in Mammalian Cells. *J Am Chem Soc* **2015**, *137* (2), 556–559. https://doi.org/10.1021/ja502109n.

(116) De Carvalho, C. C. C. R.; Caramujo, M. J. The Various Roles of Fatty Acids. *Molecules* **2018**, *23* (10). https://doi.org/10.3390/molecules23102583.

(117) West, A. V.; Muncipinto, G.; Wu, H. Y.; Huang, A. C.; Labenski, M. T.; Jones, L. H.; Woo, C. M. Labeling Preferences of Diazirines with Protein Biomolecules. *J Am Chem Soc* **2021**, *143* (17), 6691–6700. https://doi.org/10.1021/jacs.1c02509.

(118) Seath, C. P.; Trowbridge, A. D.; Muir, T. W.; Macmillan, D. W. C. Reactive Intermediates for Interactome Mapping. *Chem Soc Rev* **2021**, *50* (5), 2911–2926. https://doi.org/10.1039/d0cs01366h.

(119) Trowbridge, A. D.; Seath, C. P.; Rodriguez-Rivera, F. P.; Li, B. X.; Dul, B. E.; Schwaid, A. G.; Geri, J. B.; Oakley, J. V; Fadeyi, O. O.; Oslund, R. C.; Ah Ryu, K.; White, C.; Reyes-Robles, T.; Tawa, P.; Parker, D. L.; C MacMillan, D. W. Small Molecule Photocatalysis Enables Drug Target Identification via Energy Transfer. *Proc Natl Acad Sci U S A* **2022**, *119* (34). https://doi.org/10.1101/2021.08.02.454797.

(120) Geri, J. B.; Oakley, J. V; Reyes-Robles, T.; Wang, T.; McCarver, S. J.; White, C. H.; Rodriguez-Rivera, F. P.; Parker Jr, D. L.; Hett, E. C.; Fadeyi, O. O.; Oslund, R. C.; C MacMillan, D. W. Microenvironment Mapping via Dexter Energy Transfer on Immune Cells. *Science (1979)* **2020**, *367*, 1091–1097.

(121) Martin, B. R.; Wang, C.; Adibekian, A.; Tully, S. E.; Cravatt, B. F. Global Profiling of Dynamic Protein Palmitoylation. *Nat Methods* **2012**, *9* (1), 84–89. https://doi.org/10.1038/nmeth.1769.

(122) Peng, T.; Yuan, X.; Hang, H. C. Turning the Spotlight on Protein-Lipid Interactions in Cells. *Curr Opin Chem Biol* **2014**, *21*, 144–153. https://doi.org/10.1016/j.cbpa.2014.07.015.

(123) Fedoryshchak, R. O.; Gorelik, A.; Shen, M.; Shchepinova, M. M.; Pérez-Dorado, I.; Tate, E. W. Discovery of Lipid-Mediated Protein-Protein Interactions in Living Cells Using Metabolic Labeling with Photoactivatable Clickable Probes. *Chem Sci* **2023**, *14* (9), 2419–2430. https://doi.org/10.1039/d2sc06116c.

(124) Trowbridge, A. D.; Seath, C. P.; Rodriguez-Rivera, F. P.; Li, B. X.; Dul, B. E.; Schwaid, A. G.; Buksh, B. F.; Geri, J. B.; Oakley, J. V; Fadeyi, O. O.; Oslund, R. C.; Ryu, K. A.; White, C.; Reyes-Robles, T.; Tawa, P.; Parker, D. L.; Macmillan, D. W. C.; Dougherty, D.; Liu, D. Small Molecule Photocatalysis Enables Drug Target Identification via Energy Transfer. *Proc Natl Acad Sci U S A* **2022**, *119* (34). https://doi.org/10.1073/pnas.

(125) Kallemeijn, W. W.; Lanyon-Hogg, T.; Panyain, N.; Goya Grocin, A.; Ciepla, P.; Morales-Sanfrutos, J.; Tate, E. W. Proteome-Wide Analysis of Protein Lipidation Using Chemical Probes: In-Gel Fluorescence Visualization, Identification and Quantification of N-Myristoylation, N- and S-Acylation, O-Cholesterylation, S-Farnesylation and S-Geranylgeranylation. *Nat Protoc* **2021**, *16* (11), 5083–5122. https://doi.org/10.1038/s41596-021-00601-6.

(126) Tyanova, S.; Temu, T.; Sinitcyn, P.; Carlson, A.; Hein, M. Y.; Geiger, T.; Mann, M.; Cox, J. The Perseus Computational Platform for Comprehensive Analysis of (Prote)Omics Data. *Nat Methods* **2016**, *13* (9), 731–740. https://doi.org/10.1038/nmeth.3901.

(127) Zhou, Y.; Zhou, B.; Pache, L.; Chang, M.; Khodabakhshi, A. H.; Tanaseichuk, O.; Benner, C.; Chanda, S. K. Metascape Provides a Biologist-Oriented Resource for the Analysis of Systems-Level Datasets. *Nat Commun* **2019**, *10* (1). https://doi.org/10.1038/s41467-019-09234-6.

(128) Szklarczyk, D.; Kirsch, R.; Koutrouli, M.; Nastou, K.; Mehryary, F.; Hachilif, R.; Gable, A. L.; Fang, T.; Doncheva, N. T.; Pyysalo, S.; Bork, P.; Jensen, L. J.; Von Mering, C. The STRING Database in 2023: Protein-Protein Association Networks and Functional Enrichment Analyses for Any Sequenced Genome of Interest. *Nucleic Acids Res* **2023**, *51* (1), 638–646. https://doi.org/10.1093/nar/gkac1000.

(129) Love, M. I.; Huber, W.; Anders, S. Moderated Estimation of Fold Change and Dispersion for RNA-Seq Data with DESeq2. *Genome Biol* **2014**, *15* (12). https://doi.org/10.1186/s13059-014-0550-8.

(130) Zwiener, I.; Frisch, B.; Binder, H. Transforming RNA-Seq Data to Improve the Performance of Prognostic Gene Signatures. *PLoS One* **2014**, *9* (1). https://doi.org/10.1371/journal.pone.0085150.

(131) Kanehisa, M.; Goto, S. KEGG: Kyoto Encyclopedia of Genes and Genomes. *Nucleic Acids Res* **2000**, *28* (1), 27–30.

(132) Agrawal, A.; Balcı, H.; Hanspers, K.; Coort, S. L.; Martens, M.; Slenter, D. N.; Ehrhart, F.; Digles, D.; Waagmeester, A.; Wassink, I.; Abbassi-Daloii, T.; Lopes, E. N.; Iyer, A.; Acosta, J. M.; Willighagen, L. G.; Nishida, K.; Riutta, A.; Basaric, H.; Evelo, C. T.; Willighagen, E. L.; Kutmon, M.; Pico, A. R. WikiPathways 2024: Next Generation Pathway Database. *Nucleic Acids Res* **2024**, *52* (1), 679–689. https://doi.org/10.1093/nar/gkad960.

(133) Korotkevich, G.; Sukhov, V.; Sergushichev, A. Fast Gene Set Enrichment Analysis. Preprint of BioRxiv. *bioRxiv* **2019**.

(134) Schefe, J. H.; Lehmann, K. E.; Buschmann, I. R.; Unger, T.; Funke-Kaiser, H. Quantitative Real-Time RT-PCR Data Analysis: Current Concepts and the Novel "Gene Expression's C T Difference" Formula. *J Mol Med* **2006**, *84* (11), 901–910. https://doi.org/10.1007/s00109-006-0097-6.

(135) Licciardello, M. P.; Workman, P. The Era of High-Quality Chemical Probes. *RSC Med Chem* **2022**, *13* (12), 1446–1459. https://doi.org/10.1039/d2md00291d.

(136) Kustatscher, G.; Collins, T.; Gingras, A. C.; Guo, T.; Hermjakob, H.; Ideker, T.; Lilley, K. S.; Lundberg, E.; Marcotte, E. M.; Ralser, M.; Rappsilber, J. Understudied Proteins: Opportunities and Challenges for Functional Proteomics. *Nat Methods* **2022**, *19* (7), 774–779. https://doi.org/10.1038/s41592-022-01454-x.

(137) Oprea, T. I.; Bologa, C. G.; Brunak, S.; Campbell, A.; Gan, G. N.; Gaulton, A.; Gomez, S. M.; Guha, R.; Hersey, A.; Holmes, J.; Jadhav, A.; Jensen, L. J.; Johnson, G. L.; Karlson, A.; Leach, A. R.; Ma'ayan, A.; Malovannaya, A.; Mani, S.; Mathias, S. L.; McManus, M. T.; Meehan, T. F.; Von Mering, C.; Muthas, D.; Nguyen, D. T.; Overington, J. P.; Papadatos, G.; Qin, J.; Reich, C.; Roth, B. L.; Schürer, S. C.; Simeonov, A.; Sklar, L. A.; Southall, N.; Tomita, S.; Tudose, I.; Ursu, O.; Vidović, D.; Waller, A.; Westergaard, D.; Yang, J. J.; Zahoránszky-Köhalmi, G. Unexplored Therapeutic Opportunities in the Human Genome. *Nat Rev Drug Discov* **2018**, *17* (5), 317–332. https://doi.org/10.1038/nrd.2018.14.

(138) Haberkant, P.; Raijmakers, R.; Wildwater, M.; Sachsenheimer, T.; Brügger, B.; Maeda, K.; Houweling, M.; Gavin, A. C.; Schultz, C.; Van Meer, G.; Heck, A. J. R.; Holthuis, J. C. M. In Vivo Profiling and Visualization of Cellular Protein-Lipid Interactions Using Bifunctional Fatty Acids. *Angewandte Chemie - International Edition* **2013**, *52* (14), 4033–4038. https://doi.org/10.1002/anie.201210178.

(139) Niphakis, M. J.; Lum, K. M.; Cognetta, A. B.; Correia, B. E.; Ichu, T. A.; Olucha, J.; Brown, S. J.; Kundu, S.; Piscitelli, F.; Rosen, H.; Cravatt, B. F. A Global Map of Lipid-Binding Proteins and Their Ligandability in Cells. *Cell* **2015**, *161* (7), 1668–1680. https://doi.org/10.1016/j.cell.2015.05.045.

(140) Fürstner, A.; Leitner, A.; Méndez, M.; Krause, H. Iron-Catalyzed Cross-Coupling Reactions. *J Am Chem Soc* **2002**, *124* (46), 13856–13863. https://doi.org/10.1021/ja027190t.

(141) Fiandanese, V.; Marchese, G.; Martina, V.; Ronzini, L. Iron Catalyzed Cross-Coupling Reactions of Acyl Chlorides with Grignard Reagents. A Mild, General, and Convenient Synthesis of Aliphatic and Aromatic Ketones. *Tetrahedron Lett* **1984**, *25* (42), 4805–4808. https://doi.org/https://doi.org/10.1016/S0040-4039(01)81525-2.

(142) Nahm, S.; Weinreb, S. M. N-METHOXY-N-METHYLAMIDES AS EFFECTIVE ACYLATING AGENTS. *Tetrahedron Lett* **1981**, *22* (39), 3815–3818.

(143) Krasovskiy, A.; Knochel, P. Convenient Titration Method for Organometallic Zinc, Magnesium, and Lanthanide Reagents. *Synthesis (Stuttg)* **2006**, No. 5, 890–891. https://doi.org/10.1055/s-2006-926345.

(144) Corey, E. J.; Seebach, D. Synthesis of 1,N-Dicarbonyl Derivates Using Carbanions from 1,3-Dithianes. *Angewandte Chemie International Edition in English* **1965**, *4* (12). https://doi.org/10.1002/anie.196510771.

(145) Wang, X.; Sun, Z.; Li, T.; Perveen, S.; Li, P. Chemoenzymatic β-Specific Methylene C(Sp3)-H Deuteration of Carboxylic Acids. *Green Chemistry* **2024**, *26* (7), 3767–3775. https://doi.org/10.1039/d4gc00082j.

(146) Ramishetti, S.; Hazan-Halevy, I.; Palakuri, R.; Chatterjee, S.; Naidu Gonna, S.; Dammes, N.; Freilich, I.; Kolik Shmuel, L.; Danino, D.; Peer, D. A Combinatorial Library of Lipid Nanoparticles for RNA Delivery to Leukocytes. *Advanced Materials* **2020**, *32* (12). https://doi.org/10.1002/adma.201906128.

(147) Gundoju, N. R.; Bokam, R.; Yalavarthi, N. R.; Buddana, S. K.; Prakasham, R. S.; Ponnapalli, M. G. Total Syntheses of Surinone B, Alatanones A–B, and Trineurone A. *J Asian Nat Prod Res* **2019**, *21* (3). https://doi.org/10.1080/10286020.2018.1460362.

(148) Yu, B.; Yu, H.; Hui, Y.; Han, X. Trichloroacetimidate as an Efficient Protective Group for Alcohols. *Synlett* **1999**, No. 6, 753–755.

(149) Okamoto, S.; Kasatkin, A.; Zubaidha, P. K.; Sato, F. Intramolecular Nucleophilic Acyl Substitution Reactions Mediated by XTi(O-i-Pr) 3 (X) Cl, O-i-Pr)/2i-PrMgBr Reagent. Efficient Synthesis of Functionalized Organotitanium Compounds from Unsaturated Compounds. *Journal of American Chemical Society* **1996**, *118*, 2208–2216.

(150) Girard, A. L.; Lhermet, R.; Fressigné, C.; Durandetti, M.; Maddaluno, J. Influence of the Acetylenic Substituent on the Intramolecular Carbolithiation of Alkynes. *European J Org Chem* **2012**, No. 15, 2895–2905. https://doi.org/10.1002/ejoc.201101777.

(151) Hodgson, D. M.; Labande, A. H.; Pierard, F. Y. T. M.; Expósito Castro, M. A. The Scope of Catalytic Enantioselective Tandem Carbonyl Ylide Formation - Intramolecular [3 + 2] Cycloadditions. *Journal of Organic Chemistry* **2003**, *68* (16), 6153–6159. https://doi.org/10.1021/jo0343735.

(152) Rodier, F.; Rajzmann, M.; Parrain, J. L.; Chouraqui, G.; Commeiras, L. Diastereoselective Access to Polyoxygenated Polycyclic Spirolactones through a Rhodium-Catalyzed [3+2] Cycloaddition Reaction: Experimental and Theoretical Studies. *Chemistry - A European Journal* **2013**, *19* (7), 2467–2477. https://doi.org/10.1002/chem.201203155.

(153) Ziegler, H. J.; Bruckner, P.; Binon, F. O-Acylation of Dl-Carnitine Chloride. *Journal of Organic Chemistry* **1967**, *32* (12). https://doi.org/10.1021/jo01287a057.

(154) Karakaya, I.; Primer, D. N.; Molander, G. A. Photoredox Cross-Coupling: Ir/Ni Dual Catalysis for the Synthesis of Benzylic Ethers. *Org Lett* **2015**, *17* (13), 3294–3297. https://doi.org/10.1021/acs.orglett.5b01463.

(155) Miller, D. C.; Ganley, J. M.; Musacchio, A. J.; Sherwood, T. C.; Ewing, W. R.; Knowles, R. R. Anti-Markovnikov Hydroamination of Unactivated Alkenes with Primary Alkyl Amines. *J Am Chem Soc* **2019**, *141* (42), 16590–16594. https://doi.org/10.1021/jacs.9b08746.

(156) Lethu, S.; Matsuoka, S.; Murata, M. Highly Efficient Preparation of Selectively Isotope Cluster-Labeled Long Chain Fatty Acids via Two Consecutive Csp3-Csp3 Cross-Coupling Reactions. *Org Lett* **2014**, *16* (3), 844–847. https://doi.org/10.1021/ol4036159.

(157) Hailutaffa, D.; Kathiresan, M.; Walder, L. Tuning the Hydrophilic, Hydrophobic, and Ion Exchange Properties of Mesoporous TiO2. *Langmuir* **2009**, *25* (9), 5371–5379. https://doi.org/10.1021/la8038126.

(158) Grunwald, M. A.; Haenle, J. C.; Kreß, K. C.; Forschner, R.; Wöhrle, T.; Frey, W.; Giesselmann, F.; Laschat, S. Mesomorphic Properties of Cyanobiphenyl Dimers with a Central Malonate Unit. *Liq Cryst* **2018**, *45* (11), 1626–1636. https://doi.org/10.1080/02678292.2018.1468500.

(159) Greaves, J.; Munro, K. R.; Davidson, S. C.; Riviere, M.; Wojno, J.; Smith, T. K.; Tomkinson, N. C. O.; Chamberlain, L. H. Molecular Basis of Fatty Acid Selectivity in the ZDHHC Family of S-Acyltransferases Revealed by Click Chemistry. *Proc Natl Acad Sci U S A* **2017**, *114* (8), E1365–E1374. https://doi.org/10.1073/pnas.1612254114.

(160) McDermott, L. A Convenient Method for the Removal of Tetrabutylammonium Salts from Desilylation Reactions. *Organic Syntheses* **2022**, *99*, 53–67. https://doi.org/10.15227/orgsyn.099.0053.

(161) Grigorieva, N. Y.; Smirnov, A. G.; Popovsky, V. A.; Stepanov, A. V; Zelinsky, N. D. Highly Stereoselective Synthesis of 2,55disubstituted (E,E))Pentaa2,44dienals*. *Izvestiya Akademii Nauk. Seriya Khimicheskaya* **2009**, *58* (2), 310–314.

(162) Mohammadlou, A.; Joshi, C.; Smith, B. P.; Zheng, L.; Corio, S. A.; Canestraight, V. M.; Kohlbouni, S. T.; Taimoory, S. M.; Borhan, B.; Staples, R.; Vetticatt, M. J.; Wulff, W. D. A Lewis Acid-Controlled Enantiodivergent Epoxidation of Aldehydes. *ACS Catal* **2023**, *13* (19), 13117–13126. https://doi.org/10.1021/acscatal.3c03929.

(163) Woodcock, S. R.; Marwitz, A. J. V.; Bruno, P.; Branchaud, B. P. Synthesis of Nitrolipids. All Four Possible Diastereomers of Nitrooleic Acids: (E)- and (Z)-, 9- and 10-Nitro-Octadec-9-Enoic Acids. *Org Lett* **2006**, *8* (18), 3931–3934. https://doi.org/10.1021/ol0613463.

(164) Thurnhofer, S.; Vetter, W. Synthesis of (S)-(+)-Enantiomers of Food-Relevant (n-5)-Monoenoic and Saturated Anteiso-Fatty Acids by a Wittig Reaction. *Tetrahedron* **2007**, *63* (5), 1140–1145. https://doi.org/10.1016/j.tet.2006.11.059.

(165) Wang, L.; Tachrim, Z. P.; Kurokawa, N.; Ohashi, F.; Sakihama, Y.; Hashidoko, Y.; Hashimoto, M. Base-Mediated One-Pot Synthesis of Aliphatic Diazirines for Photoaffinity Labeling. *Molecules* **2017**, *22* (8). https://doi.org/10.3390/molecules22081389.

(166) Heindl, S.; Riomet, M.; Matyasovsky, J.; Lemmerer, M.; Malzer, N.; Maulide, N. Chemoselective γ-Oxidation of β,γ-Unsaturated Amides with TEMPO. *Angewandte Chemie - International Edition* **2021**, *60* (35), 19123–19127. https://doi.org/10.1002/anie.202104023.

(167) World Health Organisation (WHO). *Breast cancer*. https://www.who.int/news-room/fact-sheets/detail/breast-cancer.

(168) Welsh, J. E. Animal Models for Studying Prevention and Treatment of Breast Cancer. In *Animal Models for Studying Prevention and Treatment of Breast Cancer. Animal Models for the Study of Human Disease.*; 2013; pp 997–1018. https://doi.org/10.1016/B978-0-12-415894-8.00040-3.

(169) Liu, K.; Newbury, P. A.; Glicksberg, B. S.; Zeng, W. Z. D.; Paithankar, S.; Andrechek, E. R.; Chen, B. Evaluating Cell Lines as Models for Metastatic Breast Cancer through Integrative Analysis of Genomic Data. *Nat Commun* **2019**, *10* (1). https://doi.org/10.1038/s41467-019-10148-6.

(170) Palmer, J. W.; Tandler, B.; Hoppel, C. L. Biochemical Properties of Subsarcolemmal and Interfibrillar Mitochondria Isolated from Rat Cardiac Muscle. *J Biol Chem* **1977**, *252* (23), 8731–8739.

(171) Heather, L. C.; Carr, C. A.; Stuckey, D. J.; Pope, S.; Morten, K. J.; Carter, E. E.; Edwards, L. M.; Clarke, K. Critical Role of Complex III in the Early Metabolic Changes Following Myocardial Infarction. *Cardiovasc Res* **2010**, *85* (1), 127–136. https://doi.org/10.1093/cvr/cvp276.

(172) Jin, S. J.; Hoppel, C. L.; Tserng, K. Y. Incomplete Fatty Acid Oxidation: The Production and Epimerization of 3-Hydroxy Fatty Acids. *Journal of Biological Chemistry* **1992**, *267* (1), 119–125. https://doi.org/10.1016/s0021-9258(18)48467-0.

(173) Decker, T.; Lohmann-Matthes, M.-L. *A Quick and Simple Method for the Quantitation of Lactate Dehydrogenase Release in Measurements of Cellular Cytotoxicity and Tumor Necrosis Factor (TNF) Activity*; 1988; Vol. 15.

(174) *Mammalian Cell Viability*; Martin J. Stoddart, Ed.; Springer, 2011.

(175) Schmiedeknecht, K.; Kaufmann, A.; Bauer, S.; Solis, F. V. L-Lactate as an Indicator for Cellular Metabolic Status: An Easy and Cost-Effective Colorimetric L-Lactate Assay. *PLoS One* **2022**, *17*. https://doi.org/10.1371/journal.pone.0271818.

(176) Kakimoto, P. A.; Serna, J. D. C.; de Miranda Ramos, V.; Zorzano, A.; Kowaltowski, A. J. Increased Glycolysis Is an Early Consequence of Palmitate Lipotoxicity Mediated by Redox Signaling. *Redox Biol* **2021**, *45*. https://doi.org/10.1016/j.redox.2021.102026.

(177) Jin, S. J.; Hoppel, C. L.; Tserng, K. Y. Incomplete Fatty Acid Oxidation: The Production and Epimerization of 3-Hydroxy Fatty Acids. *Journal of Biological Chemistry* **1992**, *267* (1), 119–125. https://doi.org/10.1016/s0021-9258(18)48467-0.

(178) Kerr, M.; Dennis, K. M. J. H.; Carr, C. A.; Fuller, W.; Berridge, G.; Rohling, S.; Aitken, C. L.; Lopez, C.; Fischer, R.; Miller, J. J.; Clarke, K.; Tyler, D. J.; Heather, L. C. Diabetic Mitochondria Are Resistant to Palmitoyl CoA Inhibition of Respiration, Which Is Detrimental during Ischemia. *FASEB Journal* **2021**, *35* (8). https://doi.org/10.1096/fj.202100394R.

(179) Ly, L. D.; Xu, S.; Choi, S.-K.; Ha, C.-M.; Thoudam, T.; Cha, S.-K.; Wiederkehr, A.; Wollheim, C. B.; Lee, I.-K.; Park, K.-S. Oxidative Stress and Calcium Dysregulation by Palmitate in Type 2 Diabetes. *Exp Mol Med* **2017**, *49* (2). https://doi.org/10.1038/emm.2016.157.

(180) Xu, S.; Nam, S. M.; Kim, J. H.; Das, R.; Choi, S. K.; Nguyen, T. T.; Quan, X.; Choi, S. J.; Chung, C. H.; Lee, E. Y.; Lee, I. K.; Wiederkehr, A.; Wollheim, C. B.; Cha, S. K.; Park, K. S. Palmitate Induces ER Calcium Depletion and Apoptosis in Mouse Podocytes Subsequent to Mitochondrial Oxidative Stress. *Cell Death Dis* **2015**, *6* (11). https://doi.org/10.1038/cddis.2015.331.

(181) Zorov, D. B.; Vorobjev, I. A.; Popkov, V. A.; Babenko, V. A.; Zorova, L. D.; Pevzner, I. B.; Silachev, D. N.; Zorov, S. D.; Andrianova, N. V.; Plotnikov, E. Y. Lessons from the Discovery of Mitochondrial Fragmentation (Fission): A Review and Update. *Cells* **2019**, *8* (2). https://doi.org/10.3390/cells8020175.

(182) Basen-Engquist, K.; Chang, M. Obesity and Cancer Risk: Recent Review and Evidence. *Curr Oncol Rep* **2011**, *13* (1), 71–76. https://doi.org/10.1007/s11912-010-0139-7.

(183) Pati, S.; Irfan, W.; Jameel, A.; Ahmed, S.; Shahid, R. K. Obesity and Cancer: A Current Overview of Epidemiology, Pathogenesis, Outcomes, and Management. *Cancers (Basel)* **2023**, *15* (2). https://doi.org/10.3390/cancers15020485.

(184) Seiler, A.; Chen, M. A.; Brown, R. L.; Fagundes, C. P. Obesity, Dietary Factors, Nutrition, and Breast Cancer Risk. *Curr Breast Cancer Rep* **2018**, *10* (1), 14–27. https://doi.org/10.1007/s12609-018-0264-0.

(185) Brown, K. A. Metabolic Pathways in Obesity-Related Breast Cancer. *Nat Rev Endocrinol* **2021**, *17* (6), 350–363. https://doi.org/10.1038/s41574-021-00487-0.

(186) Devericks, E. N.; Carson, M. S.; McCullough, L. E.; Coleman, M. F.; Hursting, S. D. The Obesity-Breast Cancer Link: A Multidisciplinary Perspective. *Cancer and Metastasis Reviews* **2022**, *41* (3), 607–625. https://doi.org/10.1007/s10555-022-10043-5.

(187) Barr, R. L.; Lopaschuk, G. D. Methodology for Measuring in Vitro/Ex Vivo Cardiac Energy Metabolism. *J Pharmacol Toxicol Methods* **2000**, *43*, 141–152.

(188) Malandraki-Miller, S.; Lopez, C. A.; Alonaizan, R.; Purnama, U.; Perbellini, F.; Pakzad, K.; Carr, C. A. Metabolic Flux Analyses to Assess the Differentiation of Adult Cardiac Progenitors after Fatty Acid Supplementation. *Stem Cell Res* **2019**, *38*. https://doi.org/10.1016/j.scr.2019.101458.

(189) Mariscal, J.; Vagner, T.; Kim, M.; Zhou, B.; Chin, A.; Zandian, M.; Freeman, M. R.; You, S.; Zijlstra, A.; Yang, W.; Di Vizio, D. Comprehensive Palmitoyl-Proteomic Analysis Identifies Distinct Protein Signatures for Large and Small Cancer-Derived Extracellular Vesicles. *J Extracell Vesicles* **2020**, *9* (1). https://doi.org/10.1080/20013078.2020.1764192.

(190) Pradhan, A. J.; Lu, D.; Parisi, L. R.; Shen, S.; Berhane, I. A.; Galster, S. L.; Bynum, K.; Monje-Galvan, V.; Gokcumen, O.; Chemler, S. R.; Qu, J.; Kay, J. G.; Atilla-Gokcumen, G. E. Protein Acylation by Saturated Very Long Chain Fatty Acids and Endocytosis Are Involved in Necroptosis. *Cell Chem Biol* **2021**, *28* (9), 1298–1309. https://doi.org/10.1016/j.chembiol.2021.03.012.

(191) Schreiber, S. N.; Emter, R.; Hock, M. B.; Knutti, D.; Cardenas, J.; Podvinec, M.; Oakeley, E. J.; Kralli, A. The Estrogen-Related Receptor (ERR) Functions in PPAR Coactivator 1 (PGC-1)-Induced Mitochondrial Biogenesis. *Proc Natl Acad Sci U S A* **2004**, *101* (17), 6472–6477.

(192) Mootha, V. K.; Handschin, C.; Arlow, D.; Xie, X.; St Pierre, J.; Sihag, S.; Yang, W.; Altshuler, D.; Puigserver, P.; Patterson, N.; Willy, P. J.; Schulman, I. G.; Heyman, R. A.; Lander, E. S.; Spiegelman, B. M. Err and Gabpa/b Specify PGC-1-Dependent Oxidative Phosphorylation Gene Expression That Is Altered in Diabetic Muscle. *Proc Natl Acad Sci U S A* **2004**, *101* (17), 6570–6575.

(193) Schreiber, S. N.; Knutti, D.; Brogli, K.; Uhlmann, T.; Kralli, A. The Transcriptional Coactivator PGC-1 Regulates the Expression and Activity of the Orphan Nuclear Receptor Estrogen-Related Receptor α (ERRα). *Journal of Biological Chemistry* **2003**, *278* (11), 9013–9018. https://doi.org/10.1074/jbc.M212923200.

(194) Deblois, G.; Hall, J. A.; Perry, M. C.; Laganière, J.; Ghahremani, M.; Park, M.; Hallett, M.; Giguère, V. Genome-Wide Identification of Direct Target Genes Implicates Estrogen-Related Receptor α as a Determinant of Breast Cancer Heterogeneity. *Cancer Res* **2009**, *69* (15), 6149–6157. https://doi.org/10.1158/0008-5472.CAN-09-1251.

(195) Stein, R. A.; Chang, C. Y.; Kazmin, D. A.; Way, J.; Schroeder, T.; Wergin, M.; Dewhirst, M. W.; McDonnell, D. P. Estrogen-Related Receptor α Is Critical for the Growth of Estrogen Receptor-Negative Breast Cancer. *Cancer Res* **2008**, *68* (21), 8805–8812. https://doi.org/10.1158/0008-5472.CAN-08-1594.

(196) Zhang, M. M.; Wu, P. Y. J.; Kelly, F. D.; Nurse, P.; Hang, H. C. Quantitative Control of Protein S-Palmitoylation Regulates Meiotic Entry in Fission Yeast. *PLoS Biol* **2013**, *11* (7). https://doi.org/10.1371/journal.pbio.1001597.

(197) Pradhan, A. J.; Lu, D.; Parisi, L. R.; Shen, S.; Berhane, I. A.; Galster, S. L.; Bynum, K.; Monje-Galvan, V.; Gokcumen, O.; Chemler, S. R.; Qu, J.; Kay, J. G.; Atilla-Gokcumen, G. E. Protein Acylation by Saturated Very Long Chain Fatty Acids and Endocytosis Are Involved in Necroptosis. *Cell Chem Biol* **2021**, *28* (9), 1298-1309.e7. https://doi.org/10.1016/j.chembiol.2021.03.012.

(198) Won, S. J.; Martin, B. R. Temporal Profiling Establishes a Dynamic S-Palmitoylation Cycle. *ACS Chem Biol* **2018**, *13* (6), 1560–1568. https://doi.org/10.1021/acschembio.8b00157.

(199) Zhao, H. L.; Liu, L. Z.; Sui, Y.; Ho, S. K. S.; Tam, S. K.; Lai, F. M. M.; Chan, J. C. N.; Tong, P. C. Y. Fatty Acids Inhibit Insulin-Mediated Glucose Transport Associated with Actin Remodeling in Rat L6 Muscle Cells. *Acta Diabetol* **2010**, *47* (4), 331–339. https://doi.org/10.1007/s00592-010-0225-1.

(200) Wigner, P.; Zielinski, K.; Labieniec-Watala, M.; Marczak, A.; Szwed, M. Doxorubicin–Transferrin Conjugate Alters Mitochondrial Homeostasis and Energy Metabolism in Human Breast Cancer Cells. *Sci Rep* **2021**, *11* (1). https://doi.org/10.1038/s41598-021-84146-4.

(201) Homma, Y.; Hiragi, S.; Fukuda, M. Rab Family of Small GTPases: An Updated View on Their Regulation and Functions. *FEBS Journal* **2021**, *288* (1), 36–55. https://doi.org/10.1111/febs.15453.

(202) Rocks, O.; Peyker, A.; Bastiaens, P. I. Spatio-Temporal Segregation of Ras Signals: One Ship, Three Anchors, Many Harbors. *Curr Opin Cell Biol* **2006**, *18* (4), 351–357. https://doi.org/10.1016/j.ceb.2006.06.007.

(203) Shen, L. F.; Chen, Y. J.; Liu, K. M.; Haddad, A. N. S.; Song, I. W.; Roan, H. Y.; Chen, L. Y.; Yen, J. J. Y.; Chen, Y. J.; Wu, J. Y.; Chen, Y. T. Role of S-Palmitoylation by ZDHHC13 in Mitochondrial Function and Metabolism in Liver. *Sci Rep* **2017**, *7* (1). https://doi.org/10.1038/s41598-017-02159-4.

(204) Petty, E.; Pillus, L. Balancing Chromatin Remodeling and Histone Modifications in Transcription. *Trends in Genetics* **2013**, *29* (11), 621–629. https://doi.org/10.1016/j.tig.2013.06.006.

(205) Kumar, S.; Pamulapati, H.; Tikoo, K. Fatty Acid Induced Metabolic Memory Involves Alterations in Renal Histone H3K36me2 and H3K27me3. *Mol Cell Endocrinol* **2016**, *422*, 233–242. https://doi.org/10.1016/j.mce.2015.12.019.

(206) Hall, E.; Volkov, P.; Dayeh, T.; Bacos, K.; Rönn, T.; Nitert, M. D.; Ling, C. Effects of Palmitate on Genome-Wide MRNA Expression and DNA Methylation Patterns in Human Pancreatic Islets. *BMC Med* **2014**, *103* (12).

(207) Ji, B.; Skup, M. Roles of Palmitoylation in Structural Long-Term Synaptic Plasticity. *Mol Brain* **2021**, *14* (1). https://doi.org/10.1186/s13041-020-00717-y.

(208) Navarro-Lérida, I.; Sánchez-Perales, S.; Calvo, M.; Rentero, C.; Zheng, Y.; Enrich, C.; Del Pozo, M. A. A Palmitoylation Switch Mechanism Regulates Rac1 Function and Membrane Organization. *EMBO Journal* **2012**, *31* (3), 534–551. https://doi.org/10.1038/emboj.2011.446.

(209) Tian, T.; Li, X.; Zhang, J. MTOR Signaling in Cancer and Mtor Inhibitors in Solid Tumor Targeting Therapy. *Int J Mol Sci* **2019**, *20* (3). https://doi.org/10.3390/ijms20030755.

(210) Hatanaka, M.; Maier, B.; Sims, E. K.; Templin, A. T.; Kulkarni, R. N.; Evans-Molina, C.; Mirmira, R. G. Palmitate Induces MRNA Translation and Increases ER Protein Load in Islet SS-Cells via Activation of the Mammalian Target of Rapamycin Pathway. *Diabetes* **2014**, *63* (10), 3404–3415. https://doi.org/10.2337/db14-0105.

(211) Takahashi, K.; Yamanaka, S. Induction of Pluripotent Stem Cells from Mouse Embryonic and Adult Fibroblast Cultures by Defined Factors. *Cell* **2006**, *126* (4), 663–676. https://doi.org/10.1016/j.cell.2006.07.024.

(212) Ye, L.; Swingen, C.; Zhang, J. Induced Pluripotent Stem Cells and Their Potential for Basic and Clinical Sciences. *Curr Cardiol Rev* **2013**, *9* (1), 63–72.

(213) Andrysiak, K.; Stępniewski, J.; Dulak, J. Human-Induced Pluripotent Stem Cell-Derived Cardiomyocytes, 3D Cardiac Structures, and Heart-on-a-Chip as Tools for Drug Research. *European Journal of Physiology* **2021**, *473* (7), 1061–1085. https://doi.org/10.1007/s00424-021-02536-z.

(214) Takahashi, K.; Tanabe, K.; Ohnuki, M.; Narita, M.; Ichisaka, T.; Tomoda, K.; Yamanaka, S. Induction of Pluripotent Stem Cells from Adult Human Fibroblasts by Defined Factors. *Cell* **2007**, *131* (5), 861–872. https://doi.org/10.1016/j.cell.2007.11.019.

(215) Harrison, S. P.; Baumgarten, S. F.; Verma, R.; Lunov, O.; Dejneka, A.; Sullivan, G. J. Liver Organoids: Recent Developments, Limitations and Potential. *Front Med (Lausanne)* **2021**, *8*. https://doi.org/10.3389/fmed.2021.574047.

(216) McCauley, K. B.; Hawkins, F.; Serra, M.; Thomas, D. C.; Jacob, A.; Kotton, D. N. Efficient Derivation of Functional Human Airway Epithelium from Pluripotent Stem Cells via Temporal Regulation of Wnt Signaling. *Cell Stem Cell* **2017**, *20* (6), 844-857.e6. https://doi.org/10.1016/j.stem.2017.03.001.

(217) Lian, X.; Zhang, J.; Azarin, S. M.; Zhu, K.; Hazeltine, L. B.; Bao, X.; Hsiao, C.; Kamp, T. J.; Palecek, S. P. Directed Cardiomyocyte Differentiation from Human Pluripotent Stem Cells by Modulating Wnt/β-Catenin Signaling under Fully Defined Conditions. *Nat Protoc* **2013**, *8* (1), 162–175. https://doi.org/10.1038/nprot.2012.150.

(218) Ke, J.; Pan, J.; Lin, H.; Gu, J. Diabetic Cardiomyopathy: A Brief Summary on Lipid Toxicity. *ESC Heart Fail* **2023**, *10* (2), 776–790. https://doi.org/10.1002/ehf2.14224.

(219) Leggat, J.; Bidault, G.; Vidal-Puig, A. Lipotoxicity: A Driver of Heart Failure with Preserved Ejection Fraction? *Clin Sci* **2021**, *135* (19), 2265–2283. https://doi.org/10.1042/CS20210127.

(220) Fialho, M. da L. S.; Purnama, U.; Dennis, K. M. J. H.; Aparicio, C. N. M.; Castro-Guarda, M.; Massourides, E.; Tyler, D. J.; Carr, C. A.; Heather, L. C. Activation of HIF1α Rescues the Hypoxic Response and Reverses Metabolic Dysfunction in the Diabetic Heart. *Diabetes* **2021**, *70* (11), 2518–2531. https://doi.org/10.2337/DB21-0398.

(221) Onuh, J. O.; Qiu, H. Serum Response Factor-Cofactor Interactions and Their Implications in Disease. *FEBS Journal* **2021**, *288* (10), 3120–3134. https://doi.org/10.1111/febs.15544.

(222) Liu, X.; Wang, Z. Z.; Meng, S.; Zang, F.; Zhang, H.; Wang, J.; Chen, Y. Z. Systematic Analysis Reveals Distinct Roles of USF Family Proteins in Various Cancer Types. *International Journal of Biological Markers* **2023**, *38* (3–4), 243–252. https://doi.org/10.1177/03936155231206135.

(223) Davey, R. A.; Grossmann, M. Androgen Receptor Structure, Function and Biology: From Bench to Bedside. *Clin Biochem Rev* **2016**, *37* (1), 3.

(224) Tan, N. Y.; Khachigian, L. M. Sp1 Phosphorylation and Its Regulation of Gene Transcription. *Mol Cell Biol* **2009**, *29* (10), 2483–2488. https://doi.org/10.1128/mcb.01828-08.

(225) Sun, Y.; Cheng, Z.; Liu, S. MCM2 in Human Cancer: Functions, Mechanisms, and Clinical Significance. *Molecular Medicine* **2022**, *28* (1). https://doi.org/10.1186/s10020-022-00555-9.

(226) Di Tullio, F.; Schwarz, M.; Zorgati, H.; Mzoughi, S.; Guccione, E. The Duality of PRDM Proteins: Epigenetic and Structural Perspectives. *FEBS Journal* **2022**, *289* (5), 1256–1275. https://doi.org/10.1111/febs.15844.

(227) Jiang, L.; Zhang, H.; Xiao, D.; Wei, H.; Chen, Y. Farnesoid X Receptor (FXR): Structures and Ligands. *Comput Struct Biotechnol J* **2021**, *19*, 2148–2159. https://doi.org/10.1016/j.csbj.2021.04.029.

(228) Hernandez-Quiles, M.; Broekema, M. F.; Kalkhoven, E. PPARgamma in Metabolism, Immunity, and Cancer: Unified and Diverse Mechanisms of Action. *Front Endocrinol (Lausanne)* **2021**, *12*. https://doi.org/10.3389/fendo.2021.624112.

(229) Kelemen, K. The Role of Nucleophosmin 1 (NPM1) Mutation in the Diagnosis and Management of Myeloid Neoplasms. *Life* **2022**, *12* (1). https://doi.org/10.3390/life12010109.

(230) Anderson, L. A.; Perkins, N. D. Regulation of RelA (P65) Function by the Large Subunit of Replication Factor C. *Mol Cell Biol* **2003**, *23* (2), 721–732. https://doi.org/10.1128/mcb.23.2.721-732.2003.

(231) Azeez, J. M.; Susmi, R.; Remadevi, V.; Ravindran, V.; Sujatha, A. S.; Nair, R.; Ayswarya, S.; Sreeja, S. New Insights into the Functions of Progesterone Receptor (PR) Isoforms and Progesterone Signaling. *Am J Cancer Res* **2021**, *11* (11), 5214–5232.

(232) Li, H. S.; Zhou, Y. N.; Li, L.; Li, S. F.; Long, D.; Chen, X. L.; Zhang, J. B.; Feng, L.; Li, Y. P. HIF-1α Protects against Oxidative Stress by Directly Targeting Mitochondria. *Redox Biol* **2019**, *25*. https://doi.org/10.1016/j.redox.2019.101109.

(233) Milazzo, G.; Mercatelli, D.; Di Muzio, G.; Triboli, L.; De Rosa, P.; Perini, G.; Giorgi, F. M. Histone Deacetylases (HDACs): Evolution, Specificity, Role in Transcriptional Complexes, and Pharmacological Actionability. *Genes (Basel)* **2020**, *11* (5). https://doi.org/10.3390/genes11050556.

(234) Gharibeh, L.; Yamak, A.; Whitcomb, J.; Lu, A.; Joyal, M.; Komati, H.; Liang, W.; Fiset, C.; Nemer, M. GATA6 Is a Regulator of Sinus Node Development and Heart Rhythm. *Proc Natl Acad Sci U S A* **2020**, *118* (1). https://doi.org/10.1073/pnas.2007322118.

(235) Fiordelisi, A.; Iaccarino, G.; Morisco, C.; Coscioni, E.; Sorriento, D. NfkappaB Is a Key Player in the Crosstalk between Inflammation and Cardiovascular Diseases. *Int J Mol Sci* **2019**, *20* (7). https://doi.org/10.3390/ijms20071599.

(236) Aubrey, B. J.; Strasser, A.; Kelly, G. L. Tumor-Suppressor Functions of the TP53 Pathway. *Cold Spring Harb Perspect Med* **2016**, *6* (5). https://doi.org/10.1101/cshperspect.a026062.

(237) Beaulieu, M. E.; Castillo, F.; Soucek, L. Structural and Biophysical Insights into the Function of the Intrinsically Disordered Myc Oncoprotein. *Cells* **2020**, *9* (4). https://doi.org/10.3390/cells9041038.

(238) Wortel, I. M. N.; van der Meer, L. T.; Kilberg, M. S.; van Leeuwen, F. N. Surviving Stress: Modulation of ATF4-Mediated Stress Responses in Normal and Malignant Cells. *Trends in Endocrinology and Metabolism* **2017**, *28* (11), 794–806. https://doi.org/10.1016/j.tem.2017.07.003.

(239) Ling, S. S. M.; Chen, Y. T.; Wang, J.; Richards, A. M.; Liew, O. W. Ankyrin Repeat Domain 1 Protein: A Functionally Pleiotropic Protein with Cardiac Biomarker Potential. *Int J Mol Sci* **2017**, *18* (7). https://doi.org/10.3390/ijms18071362.

(240) Goetze, J. P.; Bruneau, B. G.; Ramos, H. R.; Ogawa, T.; de Bold, M. K.; de Bold, A. J. Cardiac Natriuretic Peptides. *Nat Rev Cardiol* **2020**, *17* (11), 698–717. https://doi.org/10.1038/s41569-020-0381-0.

(241) Yi, M.; Negishi, M.; Lee, S. J. Estrogen Sulfotransferase (SULT1E1): Its Molecular Regulation, Polymorphisms, and Clinical Perspectives. *J Pers Med* **2021**, *11* (3). https://doi.org/10.3390/jpm11030194.

(242) Huang, K. W.; Wang, I. H.; Fu, P.; Krum, H.; Bach, L. A.; Wang, B. H. Insulin-like Growth Factor-1 Directly Affects Cardiac Cellular Remodelling via Distinct Pathways. *IJC Heart and Vasculature* **2021**, *36*. https://doi.org/10.1016/j.ijcha.2021.100852.

(243) Ock, S.; Ham, W.; Kang, C. W.; Kang, H.; Lee, W. S.; Kim, J. IGF-1 Protects against Angiotensin II-Induced Cardiac Fibrosis by Targeting ASMA. *Cell Death Dis* **2021**, *12* (7). https://doi.org/10.1038/s41419-021-03965-5.

(244) Xu, J.; Zhou, Q.; Xu, W.; Cai, L. Endoplasmic Reticulum Stress and Diabetic Cardiomyopathy. *Exp Diabetes Res* **2012**, *2012*. https://doi.org/10.1155/2012/827971.

(245) He, Y.; Zhou, L.; Fan, Z.; Liu, S.; Fang, W. Palmitic Acid, but Not High-Glucose, Induced Myocardial Apoptosis Is Alleviated by N-Acetylcysteine Due to Attenuated Mitochondrial-Derived ROS Accumulation-Induced Endoplasmic Reticulum Stress. *Cell Death Dis* **2018**, *9* (5). https://doi.org/10.1038/s41419-018-0593-y.

(246) Ly, L. D.; Xu, S.; Choi, S.-K.; Ha, C.-M.; Thoudam, T.; Cha, S.-K.; Wiederkehr, A.; Wollheim, C. B.; Lee, I.-K.; Park, K.-S. Oxidative Stress and Calcium Dysregulation by Palmitate in Type 2 Diabetes. *Exp Mol Med* **2017**, *49* (2). https://doi.org/10.1038/emm.2016.157.

(247) Oh, Y. S.; Bae, G. D.; Baek, D. J.; Park, E. Y.; Jun, H. S. Fatty Acid-Induced Lipotoxicity in Pancreatic Beta-Cells during Development of Type 2 Diabetes. *Front Endocrinol (Lausanne)* **2018**, *9*. https://doi.org/10.3389/fendo.2018.00384.

(248) Eijkelenboom, A.; Burgering, B. M. T. FOXOs: Signalling Integrators for Homeostasis Maintenance. *Nat Rev Mol Cell Biol* **2013**, *14* (2), 83–97. https://doi.org/10.1038/nrm3507.

(249) Braicu, C.; Buse, M.; Busuioc, C.; Drula, R.; Gulei, D.; Raduly, L.; Rusu, A.; Irimie, A.; Atanasov, A. G.; Slaby, O.; Ionescu, C.; Berindan-Neagoe, I. A Comprehensive Review on MAPK: A Promising Therapeutic Target in Cancer. *Cancers (Basel)* **2019**, *11* (10). https://doi.org/10.3390/cancers11101618.

(250) Budi, E. H.; Schaub, J. R.; Decaris, M.; Turner, S.; Derynck, R. TGF-β as a Driver of Fibrosis: Physiological Roles and Therapeutic Opportunities. *Journal of Pathology* **2021**, *254* (4), 358–373. https://doi.org/10.1002/path.5680.

(251) Iorga, A.; Cunningham, C. M.; Moazeni, S.; Ruffenach, G.; Umar, S.; Eghbali, M. The Protective Role of Estrogen and Estrogen Receptors in Cardiovascular Disease and the Controversial Use of Estrogen Therapy. *Biol Sex Differ* **2017**, *8* (1), 33. https://doi.org/10.1186/s13293-017-0152-8.

(252) Aryan, L.; Younessi, D.; Zargari, M.; Banerjee, S.; Agopian, J.; Rahman, S.; Borna, R.; Ruffenach, G.; Umar, S.; Eghbali, M. The Role of Estrogen Receptors in Cardiovascular Disease. *Int J Mol Sci* **2020**, *21* (12), 1–26. https://doi.org/10.3390/ijms21124314.

(253) Regitz-Zagrosek, V.; Kararigas, G. Mechanistic Pathways of Sex Differences in Cardiovascular Disease. *Physiol Rev* **2017**, *97*, 1–37. https://doi.org/10.1152/physrev.00021.2015.-Major.

(254) Ferreira, C.; Trindade, F.; Ferreira, R.; Neves, J. S.; Leite-Moreira, A.; Amado, F.; Santos, M.; Nogueira-Ferreira, R. Sexual Dimorphism in Cardiac Remodeling: The Molecular Mechanisms Ruled

by Sex Hormones in the Heart. *J Mol Med* **2022**, *100* (2), 245–267. https://doi.org/10.1007/s00109-021-02169-w.

(255) Hönig, S. M. N.; Lemmen, C.; Rarey, M. Small Molecule Superposition: A Comprehensive Overview on Pose Scoring of the Latest Methods. *WIRES: Comput Mol Sci* **2023**, *13* (2). https://doi.org/10.1002/wcms.1640.

(256) Brown, B. P.; Mendenhall, J.; Meiler, J. BCL::MolAlign: Three-Dimensional Small Molecule Alignment for Pharmacophore Mapping. *J Chem Inf Model* **2019**, *59* (2), 689–701. https://doi.org/10.1021/acs.jcim.9b00020.

(257) Sargsyan, K.; Grauffel, C.; Lim, C. How Molecular Size Impacts RMSD Applications in Molecular Dynamics Simulations. *J Chem Theory Comput* **2017**, *13* (4), 1518–1524. https://doi.org/10.1021/acs.jctc.7b00028.

(258) Takashima, H.; Kitamura, K.; Tanabe, K.; Nagashima, U. Is Large-Scale Ab Initio Hartree-Fock Calculation Chemically Accurate? Toward Improved Calculation of Biological Molecule Properties. *J Comput Chem* **1999**, *20* (4), 443–454. https://doi.org/10.1002/(SICI)1096-987X(199903)20:4<443::AID-JCC5>3.0.CO;2-B.

(259) Kruse, H.; Grimme, S. A Geometrical Correction for the Inter- and Intra-Molecular Basis Set Superposition Error in Hartree-Fock and Density Functional Theory Calculations for Large Systems. *Journal of Chemical Physics* **2012**, *136* (15). https://doi.org/10.1063/1.3700154.

(260) Luchini, G.; Alegre-Requena, J. V.; Funes-Ardoiz, I.; Paton, R. S. GoodVibes: Automated Thermochemistry for Heterogeneous Computational Chemistry Data. *F1000Res* **2020**, *9*. https://doi.org/10.12688/f1000research.22758.1.

(261) Richards, A. *Technical Note on ARC Facility and Service Deployment for Publication Reference*; 2015. http://www.arc.ox.ac.uk.

(262) Chemical Computing Group ULC. Molecular Operating Environment (MOE), 2020.0901. *Scientific Computing & Instrumentation*. 2020.

(263) DeLano, W. L. The PyMOL Molecular Graphics System, Version 2.3. *Schrödinger LLC*. 2020.

(264) Sargsyan, K.; Grauffel, C.; Lim, C. How Molecular Size Impacts RMSD Applications in Molecular Dynamics Simulations. *J Chem Theory Comput* **2017**, *13* (4), 1518–1524. https://doi.org/10.1021/acs.jctc.7b00028.

(265) Wei Dai, Y. Y. Genomic Instability and Cancer. *J Carcinog Mutagen* **2014**, *5* (2). https://doi.org/10.4172/2157-2518.1000165.

(266) Negrini, S.; Gorgoulis, V. G.; Halazonetis, T. D. Genomic Instability an Evolving Hallmark of Cancer. *Nat Rev Mol Cell Biol* **2010**, *11* (3), 220–228. https://doi.org/10.1038/nrm2858.

(267) Lopaschuk, G. D.; Jaswal, J. S. Energy Metabolic Phenotype of the Cardiomyocyte during Development, Differentiation, and Postnatal Maturation. *J Cardiovasc Pharmacol* **2010**, *56* (2). https://doi.org/10.1097/FJC.0b013e3181e74a14.

(268) Bartelds, B.; Knoester, H.; Smid, G. B.; Takens, J.; Henk Visser, ; G; Luit, ; Feike, P. ; Van Der Leij, R.; Gertie, ; Beaufort-Krol, C. M.; Zijlstra, W. G.; Hugo, ; Heymans, S. A.; Kuipers, J. R. G. Perinatal Changes in Myocardial Metabolism in Lambs. *Circulation* **2000**, *102*, 926–931.

(269) Ascuitto, R. J.; Ross-Ascuitto, N. T. Substrate Metabolism in the Developing Heart. *Semin Perinatol* **1996**, *20* (6), 542–563.

(270) Tapon, N.; Hall, A. Rho, Rac and Cdc42 GTPases Regulate the Organization of the Actin Cytoskeleton. *Curr Opin Cell Biol* **1997**, *9* (1). https://doi.org/10.1016/S0955-0674(97)80156-1.

(271) Tie, Y.; Tang, F.; Peng, D.; Zhang, Y.; Shi, H. TGF-Beta Signal Transduction: Biology, Function and Therapy for Diseases. *Molecular Biomedicine* **2022**, *3* (1). https://doi.org/10.1186/s43556-022-00109-9.

(272) Corbet, C.; Bastien, E.; Santiago de Jesus, J. P.; Dierge, E.; Martherus, R.; Vander Linden, C.; Doix, B.; Degavre, C.; Guilbaud, C.; Petit, L.; Michiels, C.; Dessy, C.; Larondelle, Y.; Feron, O. TGFβ2-Induced Formation of Lipid Droplets Supports Acidosis-Driven EMT and the Metastatic Spreading of Cancer Cells. *Nat Commun* **2020**, *11* (1). https://doi.org/10.1038/s41467-019-14262-3.

(273) Nieves, B. J.; D'Amore, P. A.; Bryan, B. A. The Function of Vascular Endothelial Growth Factor. *BioFactors* **2009**, *35* (4), 332–337. https://doi.org/10.1002/biof.46.

(274) Goel, H. L.; Mercurio, A. M. VEGF Targets the Tumour Cell. *Nat Rev Cancer* **2013**, *13* (12), 871–882. https://doi.org/10.1038/nrc3627.

(275) McDonnell, C. M.; Ghanim, M.; Mike Southern, J.; Kelly, V. P.; Connon, S. J. De-Novo Designed β-Lysine Derivatives Can Both Augment and Diminish the Proliferation Rates of E. Coli through the Action of Elongation Factor P. *Bioorg Med Chem Lett* **2022**, *59*. https://doi.org/10.1016/j.bmcl.2022.128545.

(276) He, J.; Bai, Z.-Q.; Yuan, P.-F.; Wu, L.-Z.; Liu, Q. Supporting Information Highly Efficient Iridium-Based Photosensitizers for Thia-Paternò-Büchi Reaction and Aza-Photocyclization. *ACS Catal* **2021**, *11* (1), 446–451.

Appendix

Appendix A - Buffers and reagents for hand-poured electrophoresis gels

Resolving gel buffer	500 mL	**Stacking gel buffer**	500 mL	**10X Running buffer**	1L	**Loading dye**	50 mL
1.5 M Tris base	90.83 g	0.5 M Tris-HCl	30.28 g	0.25 M tris-base	30.3 g	187.5 mM Tris HCl	1.136 g
0.4% SDS	2.0 g	0.4% SDS	2.0 g	1% SDS	10 g	6% SDS	3.0 g
				1.92 M Glycine	144 g	30% Glycerol	15 mL
Add 450 mL dH_2O, pH to 8.8 and make up to 500 mL		pH 6.8		No need to pH		pH 6.8	
						Brilliant Blue	~0.1 g

Makes (x2) 12% gels – using a 10 or 15 well comb:

Reagents	**Resolving Gel**	**Stacking Gel**
Acrylamide/Bis-acrylamide solution (30%)	7.5 mL	1.7 mL
Resolving gel buffer	6.25 mL	2.5 mL
dH_2O	5.0 mL	3.75 mL
10% ammonium persulfate	125 µL	40 µL
Tetramethylethylenediamine (TEMED)	50 µL	40 µL

Appendix B - Quantification of pulldown enrichment of proteomic targets of Probe 1 in *MDA-MB-231* cells (n=3)

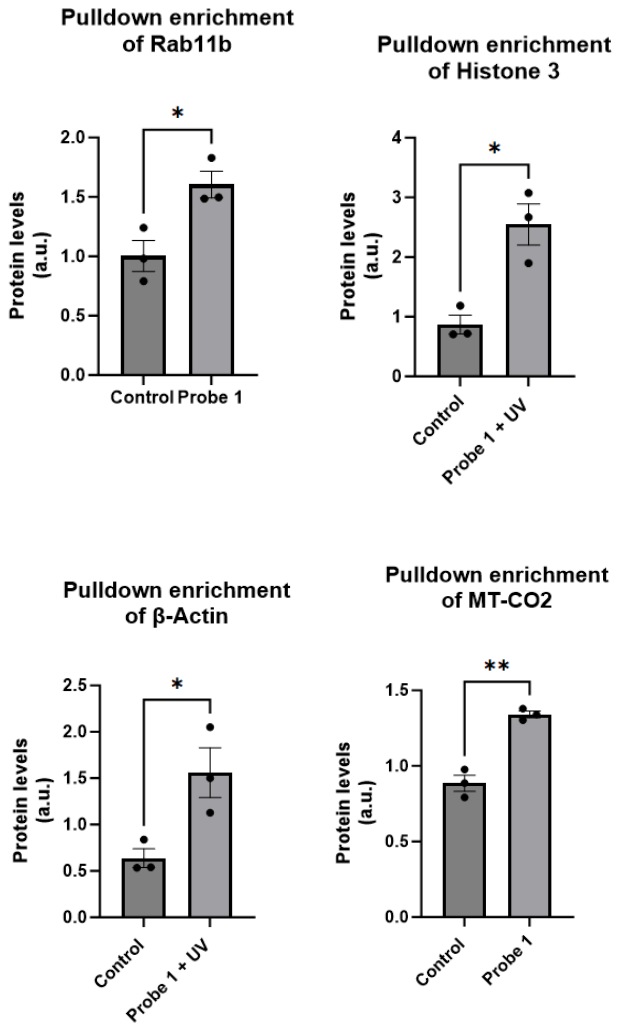

Appendix C - Quantification of pulldown enrichment of proteomic targets of Probe 1 in hiPSC cardiomyocytes (n=3)

